

1 CERN-ACC-Note-2020-0002  
2 Version v2.0  
3 Geneva, July 24, 2020  
4



5 **The Large Hadron-Electron Collider at the HL-LHC**

6 **LHeC Study Group**



7 To be submitted to J.Phys. G



## Abstract

The Large Hadron electron Collider (LHeC) constitutes the unique means for moving the physics of deep inelastic scattering to the energy and intensity frontier of particle physics, by colliding a novel, high energy, intense electron beam with one of the proton or ion beams of the High Luminosity-Large Hadron Collider (HL-LHC). This report represents a thorough update of the initial Conceptual Design Report (CDR) of the LHeC, published in 2012. It comprises new results on the far reaching physics programme on parton structure of the proton and heavier nuclei, QCD dynamics, electroweak and top-quark physics. It is shown that the LHeC will open a new chapter of nuclear particle physics by extending the kinematic range in electron-nucleus scattering by several orders of magnitude than previous experiments. Due to an enhanced luminosity goal, the high centre of mass energy and the cleanliness of the neutral and charged current final states, the LHeC has a very remarkable Higgs physics programme and a promising potential to discover new physics beyond the Standard Model. The design for its operation is for concurrent operation with the HL-LHC operation. Building on the 2012 CDR, the report represents a detailed updated design of the energy recovery electron linac (ERL) including new lattice, magnet, superconducting radio frequency technology and interaction region designs. A lower energy, high current, 3-turn ERL facility, PERLE at Orsay, is described which uses the basic LHeC configuration parameters and serves as a development facility for the design and operation of the LHeC. The electron accelerator frequency is now chosen to be 801.58 MHz and the first 5-cell Niobium cavity was built with a  $Q_0$  of  $3 \cdot 10^{10}$  exceeding the design goal. An updated detector design, including a forward hadron tagger, is presented as a base for the acceptance, resolution and calibration goals which arise from the Higgs and parton density function physics programme. While the paper is dedicated to the LHeC, it also presents novel results on the Future Circular Collider in electron-hadron mode, FCC-*eh*, which is designed to utilise the same ERL technology, and would further extend the rich physics programme of the LHeC to even higher center-of-mass energies.

## LHeC Study Group

35

36

37 P. Agostini<sup>1</sup>, H. Aksakal<sup>2</sup>, H. Alan<sup>3</sup>, S. Alekhin<sup>4,5</sup>, P. P. Allport<sup>6</sup>, N. Andari<sup>7</sup>, K. D. J. Andre<sup>8,9</sup>,  
38 D. Angal-Kalinin<sup>10,11</sup>, S. Antusch<sup>12</sup>, L. Aperio Bella<sup>13</sup>, L. Apolinario<sup>14</sup>, R. Apsimon<sup>15,11</sup>, A. Apyan<sup>16</sup>,  
39 G. Arduini<sup>9</sup>, V. Ari<sup>17</sup>, A. Armbruster<sup>9</sup>, N. Armesto<sup>1</sup>, B. Auchmann<sup>9</sup>, K. Aulenbacher<sup>18,19</sup>,  
40 G. Azuelos<sup>20</sup>, S. Backovic<sup>21</sup>, I. Bailey<sup>15,11</sup>, S. Bailey<sup>22</sup>, F. Balli<sup>7</sup>, S. Behera<sup>23</sup>, O. Behnke<sup>24</sup>,  
41 I. Ben-Zvi<sup>25</sup>, J. Bernauer<sup>26,27</sup>, S. Bertolucci<sup>9,28</sup>, S. S. Biswal<sup>29</sup>, J. Blümlein<sup>24</sup>, A. Bogacz<sup>30</sup>,  
42 M. Bonvini<sup>31</sup>, M. Boonekamp<sup>32</sup>, F. Bordry<sup>9</sup>, G. R. Boroun<sup>33</sup>, L. Bottura<sup>9</sup>, S. Bousson<sup>7</sup>,  
43 A. O. Bouzas<sup>34</sup>, C. Bracco<sup>9</sup>, J. Bracinik<sup>6</sup>, D. Britzger<sup>35</sup>, S. J. Brodsky<sup>36</sup>, C. Bruni<sup>7</sup>, O. Brüning<sup>9</sup>,  
44 H. Burkhardt<sup>9</sup>, O. Cakir<sup>17</sup>, R. Calaga<sup>9</sup>, A. Caldwell<sup>37</sup>, A. Caliskan<sup>38</sup>, S. Camarda<sup>9</sup>,  
45 N. C. Catalan-Lasheras<sup>9</sup>, K. Cassou<sup>39</sup>, J. Cepila<sup>40</sup>, V. Cetinkaya<sup>41</sup>, V. Chetvertkova<sup>9</sup>, B. Cole<sup>42</sup>,  
46 B. Coleppa<sup>43</sup>, A. Cooper-Sarkar<sup>22</sup>, E. Cormier<sup>44</sup>, A. S. Cornell<sup>45</sup>, R. Corsini<sup>9</sup>, E. Cruz-Alaniz<sup>8</sup>,  
47 J. Currie<sup>46</sup>, D. Curtin<sup>47</sup>, M. D’Onofrio<sup>8</sup>, J. Dainton<sup>15</sup>, E. Daly<sup>30</sup>, A. Das<sup>48</sup>, S. P. Das<sup>49</sup>, L. Dassa<sup>9</sup>,  
48 J. de Blas<sup>46</sup>, L. Delle Rose<sup>50</sup>, H. Denizli<sup>51</sup>, K. S. Deshpande<sup>52</sup>, D. Douglas<sup>30</sup>, L. Duarte<sup>53</sup>,  
49 K. Dupraz<sup>39,54</sup>, S. Dutta<sup>55</sup>, A. V. Efremov<sup>56</sup>, R. Eichhorn<sup>57</sup>, K. J. Eskola<sup>3</sup>, E. G. Ferreira<sup>1</sup>,  
50 O. Fischer<sup>58</sup>, O. Flores-Sánchez<sup>59</sup>, S. Forte<sup>60,61</sup>, A. Gaddi<sup>9</sup>, J. Gao<sup>62</sup>, T. Gehrman<sup>63</sup>,  
51 A. Gehrman-De Ridder<sup>63,64</sup>, F. Gerigk<sup>9</sup>, A. Gilbert<sup>65</sup>, F. Giuli<sup>66</sup>, A. Glazov<sup>24</sup>, N. Glover<sup>46</sup>,  
52 R. M. Godbole<sup>67</sup>, B. Goddard<sup>9</sup>, V. Gonçalves<sup>68</sup>, G. A. Gonzalez-Sprinberg<sup>53</sup>, A. Goyal<sup>69</sup>, J. Grames<sup>30</sup>,  
53 E. Granados<sup>9</sup>, A. Grassellino<sup>70</sup>, Y. O. Gunaydin<sup>2</sup>, Y. C. Guo<sup>71</sup>, V. Guzey<sup>72</sup>, C. Gwenlan<sup>22</sup>,  
54 A. Hammad<sup>12</sup>, C. C. Han<sup>73,74</sup>, L. Harland-Lang<sup>22</sup>, F. Haug<sup>9</sup>, F. Hautmann<sup>22</sup>, D. Hayden<sup>75</sup>,  
55 J. Hessler<sup>37</sup>, I. Helenius<sup>3</sup>, J. Henry<sup>30</sup>, J. Hernandez-Sanchez<sup>59</sup>, H. Hesari<sup>76</sup>, T. J. Hobbs<sup>77</sup>, N. Hod<sup>78</sup>,  
56 G. H. Hoffstaetter<sup>57</sup>, B. Holzer<sup>9</sup>, C. G. Honorato<sup>59</sup>, B. Hounsell<sup>8,11,39</sup>, N. Hu<sup>39</sup>, F. Hug<sup>18,19</sup>,  
57 A. Huss<sup>9,46</sup>, A. Hutton<sup>30</sup>, R. Islam<sup>23,79</sup>, S. Iwamoto<sup>80</sup>, S. Jana<sup>58</sup>, M. Jansova<sup>81</sup>, E. Jensen<sup>9</sup>, T. Jones<sup>8</sup>,  
58 J. M. Jowett<sup>9</sup>, W. Kaabi<sup>39</sup>, M. Kado<sup>31</sup>, D. A. Kalinin<sup>10,11</sup>, H. Karadeniz<sup>82</sup>, S. Kawaguchi<sup>83</sup>, U. Kaya<sup>84</sup>,  
59 R. A. Khalek<sup>85</sup>, H. Khanpour<sup>76,86</sup>, A. Kilic<sup>87</sup>, M. Klein<sup>8</sup>, U. Klein<sup>8</sup>, M. Köksal<sup>88</sup>, F. Kocak<sup>87</sup>,  
60 M. Korostelev<sup>22</sup>, P. Kostka<sup>8</sup>, M. Krelina<sup>89</sup>, J. Kretzschmar<sup>8</sup>, S. Kuday<sup>90</sup>, G. Kulipanov<sup>91</sup>, M. Kumar<sup>92</sup>,  
61 M. Kuze<sup>83</sup>, T. Lappi<sup>3</sup>, F. Larios<sup>34</sup>, A. Latina<sup>9</sup>, P. Laycock<sup>25</sup>, G. Lei<sup>93</sup>, E. Levitchev<sup>91</sup>, S. Levonian<sup>24</sup>,  
62 A. Levy<sup>94</sup>, R. Li<sup>95,96</sup>, X. Li<sup>62</sup>, H. Liang<sup>62</sup>, V. Litvinenko<sup>25,26</sup>, M. Liu<sup>71</sup>, T. Liu<sup>97</sup>, W. Liu<sup>98</sup>, Y. Liu<sup>99</sup>,  
63 S. Liuti<sup>100</sup>, E. Lobodzinska<sup>24</sup>, D. Longuevergne<sup>39</sup>, X. Luo<sup>101</sup>, W. Ma<sup>62</sup>, M. Machado<sup>102</sup>, S. Mandal<sup>103</sup>,  
64 H. Mäntysaari<sup>3,104</sup>, F. Marhauser<sup>30</sup>, C. Marquet<sup>105</sup>, A. Martens<sup>39</sup>, R. Martin<sup>9</sup>, S. Marzani<sup>106,107</sup>,  
65 J. McFayden<sup>9</sup>, P. McIntosh<sup>10</sup>, B. Mellado<sup>92</sup>, F. Meot<sup>57</sup>, A. Milanese<sup>9</sup>, J. G. Milhano<sup>14</sup>, B. Milityn<sup>10,11</sup>,  
66 M. Mitra<sup>108</sup>, S. Moch<sup>24</sup>, M. Mohammadi Najafabadi<sup>76</sup>, S. Mondal<sup>104</sup>, S. Moretti<sup>109</sup>, T. Morgan<sup>46</sup>,  
67 A. Morreale<sup>26</sup>, P. Nadolsky<sup>77</sup>, F. Navarra<sup>110</sup>, Z. Nergiz<sup>111</sup>, P. Newman<sup>6</sup>, J. Niehues<sup>46</sup>, E. W. Nissen<sup>9</sup>,  
68 M. Nowakowski<sup>112</sup>, N. Okada<sup>113</sup>, G. Olivier<sup>39</sup>, F. Olness<sup>77</sup>, G. Olry<sup>39</sup>, J. A. Osborne<sup>9</sup>, A. Ozansoy<sup>17</sup>,  
69 R. Pan<sup>95,96</sup>, B. Parker<sup>25</sup>, M. Patra<sup>114</sup>, H. Paukkunen<sup>3</sup>, Y. Peinaud<sup>39</sup>, D. Pellegrini<sup>9</sup>,  
70 G. Perez-Segurana<sup>15,11</sup>, D. Perini<sup>9</sup>, L. Perrot<sup>39</sup>, N. Pietralla<sup>115</sup>, E. Pilicer<sup>87</sup>, B. Pire<sup>105</sup>, J. Pires<sup>14</sup>,  
71 R. Placakyte<sup>116</sup>, M. Poelker<sup>30</sup>, R. Polifka<sup>117</sup>, A. Pollini<sup>28,118</sup>, P. Poulose<sup>23</sup>, G. Pownall<sup>22</sup>,  
72 Y. A. Pupkov<sup>91</sup>, F. S. Queiroz<sup>119</sup>, K. Rabbertz<sup>120</sup>, V. Radescu<sup>121</sup>, R. Rahaman<sup>122</sup>, S. K. Rai<sup>108</sup>,  
73 N. Raicevic<sup>123</sup>, P. Ratoff<sup>15,11</sup>, A. Rashed<sup>124</sup>, D. Raut<sup>125</sup>, S. Raychaudhuri<sup>114</sup>, J. Repond<sup>126</sup>,  
74 A. H. Rezaeian<sup>127,128</sup>, R. Rimmer<sup>30</sup>, L. Rinolfi<sup>9</sup>, J. Rojo<sup>85</sup>, A. Rosado<sup>59</sup>, X. Ruan<sup>92</sup>, S. Russenschuck<sup>9</sup>,  
75 M. Sahin<sup>129</sup>, C. A. Salgado<sup>1</sup>, O. A. Sampayo<sup>130</sup>, K. Satendra<sup>23</sup>, N. Satyanarayan<sup>131</sup>, B. Schenke<sup>25</sup>,  
76 K. Schirm<sup>9</sup>, H. Schopper<sup>9</sup>, M. Schott<sup>19</sup>, D. Schulte<sup>9</sup>, C. Schwanenberger<sup>24</sup>, T. Sekine<sup>83</sup>, A. Senol<sup>51</sup>,  
77 A. Seryi<sup>30</sup>, S. Setiniyaz<sup>15,11</sup>, L. Shang<sup>132</sup>, X. Shen<sup>95,96</sup>, N. Shipman<sup>9</sup>, N. Sinha<sup>133</sup>, W. Slominski<sup>134</sup>,  
78 S. Smith<sup>10,11</sup>, C. Solans<sup>9</sup>, M. Song<sup>135</sup>, H. Spiesberger<sup>19</sup>, J. Stanyard<sup>9</sup>, A. Starostenko<sup>91</sup>, A. Stasto<sup>136</sup>,  
79 A. Stocchi<sup>39</sup>, M. Strikman<sup>136</sup>, M. J. Stuart<sup>9</sup>, S. Sultansoy<sup>84</sup>, H. Sun<sup>101</sup>, M. Sutton<sup>137</sup>,  
80 L. Szymanowski<sup>138</sup>, I. Tapan<sup>87</sup>, D. Tapia-Takaki<sup>139</sup>, M. Tanaka<sup>83</sup>, Y. Tang<sup>140</sup>, A. T. Tasci<sup>141</sup>,  
81 A. T. Ten-Kate<sup>9</sup>, P. Thonet<sup>9</sup>, R. Tomas-Garcia<sup>9</sup>, D. Tommasini<sup>9</sup>, D. Trbojevic<sup>25,57</sup>, M. Trott<sup>142</sup>,  
82 I. Tsurin<sup>8</sup>, A. Tudora<sup>9</sup>, I. Turk Cakir<sup>82</sup>, K. Tywoniuk<sup>143</sup>, C. Vallerand<sup>39</sup>, A. Valloni<sup>9</sup>, D. Verney<sup>39</sup>,  
83 E. Vilella<sup>8</sup>, D. Walker<sup>46</sup>, S. Wallon<sup>39</sup>, B. Wang<sup>95,96</sup>, K. Wang<sup>95,96</sup>, K. Wang<sup>144</sup>, X. Wang<sup>101</sup>,  
84 Z. S. Wang<sup>145</sup>, H. Wei<sup>146</sup>, C. Welsch<sup>8,11</sup>, G. Willering<sup>9</sup>, P. H. Williams<sup>10,11</sup>, D. Wollmann<sup>9</sup>,  
85 C. Xiaohao<sup>13</sup>, T. Xu<sup>147</sup>, C. E. Yaguna<sup>148</sup>, Y. Yamaguchi<sup>83</sup>, Y. Yamazaki<sup>149</sup>, H. Yang<sup>150</sup>, A. Yilmaz<sup>82</sup>,  
86 P. Yock<sup>151</sup>, C. X. Yue<sup>71</sup>, S. G. Zadeh<sup>152</sup>, O. Zenaiev<sup>9</sup>, C. Zhang<sup>153</sup>, J. Zhang<sup>154</sup>, R. Zhang<sup>62</sup>,  
87 Z. Zhang<sup>39</sup>, G. Zhu<sup>95,96</sup>, S. Zhu<sup>132</sup>, F. Zimmermann<sup>9</sup>, F. Zomer<sup>39</sup>, J. Zurita<sup>155,156</sup> and P. Zurita<sup>35</sup>

88 <sup>1</sup> Universidade de Santiago de Compostela (USC), Santiago de Compostela, Spain  
89 <sup>2</sup> Kahramanmaras Sutcu Imam University, Kahramanmaras, Turkey  
90 <sup>3</sup> University of Jyväskylä, Jyväskylä, Finland  
91 <sup>4</sup> Universität Hamburg, Hamburg, Germany  
92 <sup>5</sup> Institute of High Energy Physics (IHEP), Protvino, Russia  
93 <sup>6</sup> University of Birmingham, Birmingham, United Kingdom  
94 <sup>7</sup> Université Paris-Saclay, Saint-Aubin, France  
95 <sup>8</sup> University of Liverpool, Liverpool, United Kingdom  
96 <sup>9</sup> European Organization for Nuclear Research (CERN), Genève, Switzerland  
97 <sup>10</sup> Science and Technology Facilities Council (STFC) - Daresbury Laboratory, Daresbury, United  
98 Kingdom  
99 <sup>11</sup> Cockcroft Institute of Accelerator Science and Technology, Daresbury, United Kingdom  
100 <sup>12</sup> Universität Basel, Basel, Switzerland  
101 <sup>13</sup> Chinese Academy of Sciences - Institute of High Energy Physics (IHEP), Beijing, China  
102 <sup>14</sup> Laboratório de Instrumentação e Física Experimental de Partículas (LIP), Lisbon, Portugal  
103 <sup>15</sup> University of Lancaster, Lancaster, United Kingdom  
104 <sup>16</sup> A. Alikhanian National Laboratory (AANL), Yerevan, Armenia  
105 <sup>17</sup> Ankara University, Ankara, Turkey  
106 <sup>18</sup> Johannes Gutenberg University Mainz (JGU) - PRISMA Cluster of Excellence, Mainz, Germany  
107 <sup>19</sup> Johannes Gutenberg-Universität Mainz (JGU), Mainz, Germany  
108 <sup>20</sup> Université de Montréal, Montreal, Canada  
109 <sup>21</sup> University of Montenegro, Podgorica, Montenegro  
110 <sup>22</sup> University of Oxford, Oxford, United Kingdom  
111 <sup>23</sup> Department of Physics, Indian Institute of Technology, Guwahati, Assam, India  
112 <sup>24</sup> Deutsches Elektronen-Synchrotron (DESY), Hamburg, Germany  
113 <sup>25</sup> Brookhaven National Laboratory (BNL), Upton, USA  
114 <sup>26</sup> Stony Brook University, Stony Brook, USA  
115 <sup>27</sup> BNL Research Center, RIKEN, Upton, NY, USA  
116 <sup>28</sup> Università di Bologna, Bologna, Italy  
117 <sup>29</sup> Ravenshaw University, Cuttack, India  
118 <sup>30</sup> Thomas Jefferson National Accelerator Facility (Jefferson Lab), Newport News, USA  
119 <sup>31</sup> Istituto Nazionale di Fisica Nucleare (INFN) - Sezione di Roma, Rome, Italy  
120 <sup>32</sup> Commissariat à l’Energie Atomique (CEA) - Institut de Recherche sur les Lois Fondamentales de  
121 l’Univers (IRFU), Gif-sur-Yvette, France  
122 <sup>33</sup> Razi University, Kermanshah, Iran  
123 <sup>34</sup> Centro de Investigación y Estudios Avanzados (CINVESTAV), San Pedro, Mexico  
124 <sup>35</sup> Universität Regensburg, Regensburg, Germany  
125 <sup>36</sup> SLAC National Accelerator Laboratory, Menlo Park, USA  
126 <sup>37</sup> Max-Planck-Institut für Physik, Munich, Germany  
127 <sup>38</sup> Gumushane University, Gumushane, Turkey  
128 <sup>39</sup> Université Paris-Saclay, CNRS/IN2P3, IJCLab, Orsay, France  
129 <sup>40</sup> Faculty of Nuclear Sciences and Physical Engineering, Czech Technical University in Prague, Prague,  
130 Czech Republic  
131 <sup>41</sup> Kutahya Dumlupinar University, Kutahya, Turkey  
132 <sup>42</sup> Columbia University, New York, USA  
133 <sup>43</sup> Indian Institute of Technology (IIT), Gandhinagar, India  
134 <sup>44</sup> Centre Lasers Intenses et Applications (CELIA), Bordeaux, France  
135 <sup>45</sup> University of Johannesburg (UJ), Johannesburg, South Africa  
136 <sup>46</sup> Institute for Particle Physics Phenomenology, Durham University, Durham, United Kingdom  
137 <sup>47</sup> University of Toronto, Toronto, Canada  
138 <sup>48</sup> Osaka University, Osaka, Japan  
139 <sup>49</sup> Universidad de los Andes, Santiago, Columbia  
140 <sup>50</sup> Istituto Nazionale di Fisica Nucleare (INFN) - Sezione di Firenze, Firenze, Italy  
141 <sup>51</sup> Bolu Abant İzzet Baysal University, Bolu, Turkey  
142 <sup>52</sup> University of Maryland, College Park, USA  
143 <sup>53</sup> Universidad de la Republica - Instituto de Física Facultad de Ciencias (IFFC), Montevideo, Uruguay

144 54 Université Paris-Sud, Orsay, France  
145 55 Sri Guru Tegh Badadur Khalsa College, Delhi, India  
146 56 Joint Institute for Nuclear Research (JINR), Dubna, Russia  
147 57 Cornell University, Ithaca, USA  
148 58 Max-Planck-Institut für Kernphysik, Heidelberg, Germany  
149 59 Benemerita Universidad Autonoma de Puebla (BUAP), Puebla, Mexico  
150 60 Università degli Studi di Milano, Milano, Italy  
151 61 Istituto Nazionale di Fisica Nucleare (INFN) - Sezione di Milano, Milano, Italy  
152 62 University of Science and Technology of China (USTC), Hefei, China  
153 63 Department of Physics, Universität Zürich, Zurich, Switzerland  
154 64 Institute for Theoretical Physics, ETH, Zurich, Switzerland  
155 65 Northwestern University, Evanston, USA  
156 66 University of Rome Tor Vergata and INFN, Sezione di Roma 2, Rome, Italy  
157 67 Indian Institute of Science (IISc), Bangalore, India  
158 68 Universidade Federal de Pelotas (UFPEL), Pelotas, Brazil  
159 69 University of Delhi, Delhi, India  
160 70 Fermi National Accelerator Laboratory (FNAL), Batavia, USA  
161 71 Liaoning Normal University (LNNU), Dalian, China  
162 72 Petersburg Nuclear Physics Institute (PNPI), Petersburg, Russia  
163 73 University of Tokyo, Tokyo, Japan  
164 74 Kavli Institute for the Physics and Mathematics of the Universe (KIPMU), Kashiwa, Japan  
165 75 Michigan State University, East Lansing, USA  
166 76 Institute for Research in Fundamental Sciences (IPM), Tehran, Iran  
167 77 Southern Methodist University, Dallas, USA  
168 78 Weizmann Institute of Science, Rehovot, Israel  
169 79 Department of Physics, Mathabanga College, Cooch Behar, West Bengal, India  
170 80 Università degli Studi di Padova, Padua, Italy  
171 81 Université de Strasbourg, Strasbourg, France  
172 82 Giresun University, Giresun, Turkey  
173 83 Tokyo Institute of Technology, Tokyo, Japan  
174 84 TOBB University of Economic and Technology (TOBB ETU), Ankara, Turkey  
175 85 Vrije University, Amsterdam, Netherlands  
176 86 University of Science and Technology of Mazandaran, Behshahr, Iran  
177 87 Uludag University, Bursa, Turkey  
178 88 Sivas Cumhuriyet University, Sivas, Turkey  
179 89 Universidad Tecnica Federico Santa Maria, Valparaiso, Chile  
180 90 Istanbul Aydin University, Istanbul, Turkey  
181 91 Siberian Branch of Russian Academy of Science - Budker Institute of Nuclear Physics (BINP),  
182 Novosibirsk, Russia  
183 92 University of the Witwatersrand, Johannesburg, South Africa  
184 93 Tsinghua University, Beijing, China  
185 94 Tel-Aviv University, Tel Aviv, Israel  
186 95 Zhejiang Institute of Modern Physics (ZIMP), Hangzhou, China  
187 96 Zhejiang University (ZJU), Hangzhou, China  
188 97 Xiamen University (XMU), Xiamen, China  
189 98 University College London, London, United Kingdom  
190 99 Henan Institute of Science and Technology (HIST), Xinxiang, China  
191 100 University of Virginia, Charlottesville, USA  
192 101 Dalian University of Technology (DLUT), Dalian, China  
193 102 Universidade Federal do Rio Grande do Sul (UFRGS), Porto Alegre, Brazil  
194 103 Institut de Física Corpuscular – CSIC/Universitat de València, Paterna (Valencia), Spain  
195 104 University of Helsinki, Helsinki, Finland  
196 105 CPHT, CNRS, Ecole Polytechnique, I. P. Paris, France  
197 106 University Genova, Genova, Italy  
198 107 Istituto Nazionale di Fisica Nucleare (INFN) - Sezione di Genova, Genova, Italy  
199 108 Harish-Chandra Research Institute (HRI), Allahabad, India

200 109 University of Southampton, Southampton, United Kingdom  
201 110 Universidade de Sao Paulo (USP), Sao, Paolo  
202 111 Nigde Omer Halisdemir University, Nigde, Turkey  
203 112 Universidad de los Andes, Carrera, Colombia  
204 113 The University of Alabama, Tuscaloosa, USA  
205 114 Tata Institute of Fundamental Research (TIFR), Mumbai, India  
206 115 Technische Universität Darmstadt, Darmstadt, Germany  
207 116 Homeday GmbH Berlin, Berlin, Germany  
208 117 Charles University, Praque, Czech Republic  
209 118 Istituto Nazionale di Fisica Nucleare (INFN) - Sezione di Bologna, Bologna, Italy  
210 119 Univ. Federal do Rio Grande do Norte, Natal, Brazil  
211 120 Karlsruher Institut für Technologie (KIT), Karlsruhe, Germany  
212 121 IBM Deutschland RnD, GmbH, Urbar, Germany  
213 122 Indian Institute of Science Education and Research (IISER), Kolkata, India  
214 123 Univ. of Montenegro, Podgorica, YUOGSLAVIA  
215 124 Shippensburg University of Pennsylvania, Shippensburg, Pennsylvania, USA  
216 125 University of Delaware, Newark, USA  
217 126 Argonne National Laboratory, Argonne, USA  
218 127 Oracle, San Fransisco, USA  
219 128 Applied AI Center of Excellence, San Francisco, USA  
220 129 Usak University, Usak, Turkey  
221 130 National University of Mar del Plata, Mar del Plata, Argentina  
222 131 Oklahoma State University (OSU), Stillwater, USA  
223 132 Peking University (PKU), Beijing, China  
224 133 Institute of Mathematical Sciences (IMSc), Chennai, India  
225 134 Jagiellonian University, Cracow, Poland  
226 135 Anhui University (AHU), Hefei, China  
227 136 Pennsylvania State University (PSU), University Park, USA  
228 137 University of Sussex, Sussex, United Kingdom  
229 138 Narodowe Centrum Badań Jądrowych (NCBJ), Warsaw, Poland  
230 139 Kansas State University, Manhattan, USA  
231 140 Korea Institute for Advanced Study (KIAS), Cheongryangri-dong, Korea  
232 141 Kastamonu University, Kastamonu, Turkey  
233 142 Københavns, Universitet - Niels Bohr Institutet (NBI), Copenhagen  
234 143 University of Bergen, Bergen, Norway  
235 144 Wuhan University of Technology, Wuhan, China  
236 145 Asia Pacific Center for Theoretical Physics (APCTP), Pohang, Korea  
237 146 University of California (UC), Riverside, USA  
238 147 Hebrew University of Jerusalem - Racah Inst. of Physics, Jerusalem, Israel  
239 148 Universidad Pedagógica y Tecnológica de Colombia, Tunja, Colombia  
240 149 Kobe University, Kobe, Japan  
241 150 Lawrence Berkeley National Laboratory (LBNL), Berkeley, USA  
242 151 Fellow Royal Astronomical Society of New Zealand (FRASNZ), Auckland, New Zealand  
243 152 Universität Rostock, Rostock, Germany  
244 153 National Center for Theoretical Sciences (NCTS), Hsinchu, Taiwan  
245 154 Nankai University (NKU), Tianjin, China  
246 155 Karlsruher Institut für Technologie (KIT) - Institut für Theoretische Teilchenphysik (TTP),  
247 Karlsruhe, Germany  
248 156 Karlsruher Institut für Technologie (KIT) - Institut für Kernphysik (IKP), Karlsruhe, Germany

# Preface

249

250 This paper represents the updated design study of the Large Hadron-electron Collider, the  
251 LHeC, a TeV energy scale electron-hadron (*eh*) collider which may come into operation during  
252 the third decade of the lifetime of the Large Hadron Collider (LHC) at CERN. It is an account,  
253 accompanied by numerous papers in the literature, for many years of study and development,  
254 guided by an International Advisory Committee (IAC) which was charged by the CERN Direc-  
255 torate to advise on the directions of energy frontier electron-hadron physics at CERN. End of  
256 2019 the IAC summarised its observations and recommendations in a brief report to the Director  
257 General of CERN, which is here reproduced as an Appendix.

258 The paper outlines a unique, far reaching physics programme on deep inelastic scattering (DIS),  
259 a design concept for a new generation collider detector, together with a novel configuration  
260 of the intense, high energy electron beam. This study builds on the previous, detailed LHeC  
261 Conceptual Design Report (CDR), which was published eight years ago [1]. It surpasses the  
262 initial study in essential characteristics: i) the depth of the physics programme, owing to the  
263 insight obtained mainly with the LHC, and ii) the luminosity prospect, for enabling a novel Higgs  
264 facility to be built and the prospects to search for and discover new physics to be strengthened.  
265 It builds on recent and forthcoming progress of modern technology, due to major advances  
266 especially of the superconducting RF technology and as well new detector techniques.

267 Unlike in 2012, there has now a decision been taken to configure the LHeC as an electron linac-  
268 proton or nucleus ring configuration, which leaves the ring-ring option [1, 2] as a backup. In  
269 *ep*, the high instantaneous luminosity of about  $10^{34} \text{ cm}^{-2} \text{ s}^{-1}$  may be achieved with the electron  
270 accelerator built as an energy recovery linac (ERL) and because the brightness of the LHC ex-  
271 ceeds early expectations by far, not least through the upgrade of the LHC to its high luminosity  
272 version, the HL-LHC [3, 4]. For *ePb* collisions, the corresponding per nucleon instantaneous lu-  
273 minosity would be about  $10^{33} \text{ cm}^{-2} \text{ s}^{-1}$ . The LHeC is designed to be compatible with concurrent  
274 operation with the LHC. It thus represents a unique opportunity to advance particle physics by  
275 building on the singular investments which CERN and its global partners have made into the  
276 LHC facility.

277 Extending much beyond the CDR, a new configuration for a low energy ERL facility, termed  
278 PERLE [5], has been designed and is moving ahead to be built at Orsay by an international  
279 collaboration. The major parameters of PERLE have been taken from the LHeC, such as  
280 the 3-turn configuration, source, the 802 MHz frequency and cavity-cryomodule technology, in  
281 order to make PERLE a suitable facility for the development of LHeC ERL technology and the  
282 accumulation of operating experience prior to and later in parallel with the LHeC. In addition,  
283 the PERLE facility has a striking low energy physics programme, industrial applications and  
284 will be an enabler for ERL technology as the first facility to operate in the 10 MW power regime.



285 While the 2012 CDR focussed the physics discussion on the genuine physics of deep inelastic  
286 scattering leading much beyond HERA, a new focus arose through the challenges and opportu-  
287 nities posed by the HL-LHC. It is demonstrated that DIS at the LHeC can play a crucial role  
288 in sustaining and enriching the LHC programme, a consequence of the results obtained at the  
289 LHC, i.e. the discovery of the Higgs boson, the non-observation of supersymmetry (SUSY) or  
290 other non Standard Model (SM) exotic particles and, not least, the unexpected realisation of  
291 the huge potential of the LHC for discovery through precision measurements in the strong and  
292 electroweak sectors. Thus, it was felt time to summarise the recent seven years of LHeC devel-  
293 opment, also in support of the current discussions on the future of particle physics, especially  
294 at the energy frontier. Both for the LHeC [6–8] and PERLE [9], documents were submitted for  
295 consideration to the European Strategy for Particle Physics Update.

296 The LHeC has something of a once in our lifetime opportunity for substantial progress in particle  
297 physics. It comprises, with a linac shorter than the pioneering two-mile linac at SLAC, a most  
298 ambitious and exciting physics programme, the introduction of novel accelerator technology and  
299 the complete exploitation of the unique values of and spendings into the LHC. It requires proba-  
300 bly less courage than that of Pief Panowsky and colleagues half a century ago. Finally, not least,  
301 one may realise that the power LHeC needed without the energy recovery technique is beyond  
302 1 GW while the electron beam is dumped at injection energy. It so appears to be a significant  
303 step towards green accelerator technology, a major general desire and requirement of our times.  
304 This paper aims at substantiating these statements in the various chapters following.

305

306 Oliver Brüning (CERN) and Max Klein (University of Liverpool)

# Contents

308	<b>Preface</b>	<b>5</b>
309	<b>1 Introduction</b>	<b>13</b>
310	1.1 The Context . . . . .	13
311	1.1.1 Particle Physics - an unfinished Area of Fundamental Science . . . . .	13
312	1.1.2 Deep Inelastic Scattering and HERA . . . . .	15
313	1.2 The Paper . . . . .	16
314	1.2.1 The LHeC Physics Programme . . . . .	16
315	1.2.2 The Accelerator . . . . .	18
316	1.2.3 PERLE . . . . .	19
317	1.2.4 The Detector . . . . .	20
318	1.3 Outline . . . . .	21
319	<b>2 LHeC Configuration and Parameters</b>	<b>22</b>
320	2.1 Introduction . . . . .	22
321	2.2 Cost Estimate, Default Configuration and Staging . . . . .	23
322	2.3 Configuration Parameters . . . . .	24
323	2.4 Luminosity . . . . .	25
324	2.4.1 Electron-Proton Collisions . . . . .	26
325	2.4.2 Electron-Ion Collisions . . . . .	27
326	2.5 Linac Parameters . . . . .	27
327	2.6 Operation Schedule . . . . .	28
328	<b>3 Parton Distributions - Resolving the Substructure of the Proton</b>	<b>31</b>
329	3.1 Introduction . . . . .	31
330	3.1.1 Partons in Deep Inelastic Scattering . . . . .	32
331	3.1.2 Fit Methodology and HERA PDFs . . . . .	33
332	3.2 Simulated LHeC Data . . . . .	36
333	3.2.1 Inclusive Neutral and Charged Current Cross Sections . . . . .	36
334	3.2.2 Heavy Quark Structure Functions . . . . .	39
335	3.3 Parton Distributions from the LHeC . . . . .	41
336	3.3.1 Procedure and Assumptions . . . . .	41
337	3.3.2 Valence Quarks . . . . .	44
338	3.3.3 Light Sea Quarks . . . . .	45
339	3.3.4 Strange Quark . . . . .	46
340	3.3.5 Heavy Quarks . . . . .	49
341	3.3.6 The Gluon PDF . . . . .	51
342	3.3.7 Luminosity and Beam Charge Dependence of LHeC PDFs . . . . .	53

343	3.3.8	Weak Interactions Probing Proton Structure . . . . .	56
344	3.3.9	Parton-Parton Luminosities . . . . .	59
345	3.4	The 3D Structure of the Proton . . . . .	62
346	<b>4</b>	<b>Exploration of Quantum Chromodynamics</b>	<b>69</b>
347	4.1	Determination of the strong coupling constant . . . . .	69
348	4.1.1	Strong coupling from inclusive jet cross sections . . . . .	70
349	4.1.2	Pinning Down $\alpha_s$ with Inclusive and Jet LHeC Data . . . . .	74
350	4.1.3	Strong coupling from other processes . . . . .	77
351	4.2	Discovery of New Strong Interaction Dynamics at Small $x$ . . . . .	78
352	4.2.1	Resummation at small $x$ . . . . .	79
353	4.2.2	Disentangling non-linear QCD dynamics at the LHeC . . . . .	82
354	4.2.3	Low $x$ and the Longitudinal Structure Function $F_L$ . . . . .	87
355	4.2.4	Associated jet final states at low $x$ . . . . .	93
356	4.2.5	Relation to Ultrahigh Energy Neutrino and Astroparticle physics . . . . .	94
357	4.3	Diffractive Deep Inelastic Scattering at the LHeC . . . . .	96
358	4.3.1	Introduction and Formalism . . . . .	96
359	4.3.2	Pseudodata for diffractive structure functions . . . . .	101
360	4.3.3	Potential for constraining diffractive PDFs at the LHeC and FCC-eh . . . . .	101
361	4.3.4	Hadronic Final States in Diffraction and hard rapidity gap processes . . . . .	103
362	4.4	Theoretical Developments . . . . .	105
363	4.4.1	Prospects for Higher Order pQCD in DIS . . . . .	105
364	4.4.2	Theoretical Concepts on the Light Cone . . . . .	107
365	<b>5</b>	<b>Electroweak and Top Quark Physics</b>	<b>112</b>
366	5.1	Electroweak Physics with Inclusive DIS data . . . . .	112
367	5.1.1	Electroweak effects in inclusive NC and CC DIS cross sections . . . . .	112
368	5.1.2	Methodology of a combined EW and QCD fit . . . . .	113
369	5.1.3	Weak boson masses $M_W$ and $M_Z$ . . . . .	114
370	5.1.4	Further mass determinations . . . . .	116
371	5.1.5	Weak Neutral Current Couplings . . . . .	117
372	5.1.6	The neutral current $\rho_{\text{NC}}$ and $\kappa_{\text{NC}}$ parameters . . . . .	118
373	5.1.7	The effective weak mixing angle $\sin^2 \theta_{\text{W}}^{\text{eff},\ell}$ . . . . .	119
374	5.1.8	Electroweak effects in charged-current scattering . . . . .	121
375	5.1.9	Conclusion . . . . .	121
376	5.2	Direct $W$ and $Z$ Production and Anomalous Triple Gauge Couplings . . . . .	122
377	5.2.1	Direct $W$ and $Z$ Production . . . . .	122
378	5.2.2	Anomalous Triple Gauge Couplings . . . . .	123
379	5.3	Top Quark Physics . . . . .	125
380	5.3.1	$Wtq$ Couplings . . . . .	126
381	5.3.2	Top Quark Polarisation . . . . .	127
382	5.3.3	Top- $\gamma$ and Top- $Z$ Couplings . . . . .	128
383	5.3.4	Top-Higgs Coupling . . . . .	129
384	5.3.5	Top Quark PDF and the Running of $\alpha_s$ . . . . .	129
385	5.3.6	FCNC Top Quark Couplings . . . . .	130
386	5.3.7	Other Top Quark Property Measurements and Searches for New Physics . . . . .	132
387	5.3.8	Summary of Top Quark Physics . . . . .	132
388	<b>6</b>	<b>Nuclear Particle Physics with Electron-Ion Scattering at the LHeC</b>	<b>134</b>
389	6.1	Introduction . . . . .	134

390	6.2	Nuclear Parton Densities . . . . .	136
391	6.2.1	Pseudodata . . . . .	137
392	6.2.2	Nuclear gluon PDFs in a global-fit context . . . . .	140
393	6.2.3	nPDFs from DIS on a single nucleus . . . . .	141
394	6.3	Nuclear diffraction . . . . .	146
395	6.3.1	Exclusive vector meson diffraction . . . . .	146
396	6.3.2	Inclusive diffraction on nuclei . . . . .	151
397	6.4	New Dynamics at Small $x$ with Nuclear Targets . . . . .	153
398	6.5	Collective effects in dense environments – the ‘ridge’ . . . . .	154
399	6.6	Novel QCD Nuclear Phenomena at the LHeC . . . . .	154
400	<b>7</b>	<b>Higgs Physics with LHeC</b>	<b>158</b>
401	7.1	Introduction . . . . .	158
402	7.2	Higgs Production in Deep Inelastic Scattering . . . . .	159
403	7.2.1	Kinematics of Higgs Production . . . . .	159
404	7.2.2	Cross Sections and Rates . . . . .	161
405	7.3	Higgs Signal Strength Measurements . . . . .	162
406	7.3.1	Higgs Decay into Bottom and Charm Quarks . . . . .	164
407	7.3.2	Higgs Decay into WW . . . . .	170
408	7.3.3	Accessing Further Decay Channels . . . . .	172
409	7.3.4	Systematic and Theoretical Errors . . . . .	173
410	7.4	Higgs Coupling Analyses . . . . .	175
411	7.5	Measuring the Top-quark–Higgs Yukawa Coupling . . . . .	177
412	7.6	Higgs Decay into Invisible Particles . . . . .	181
413	<b>8</b>	<b>Searches for Physics Beyond the Standard Model</b>	<b>184</b>
414	8.1	Introduction . . . . .	184
415	8.2	Extensions of the SM Higgs Sector . . . . .	184
416	8.2.1	Modifications of the Top-Higgs interaction . . . . .	185
417	8.2.2	Charged scalars . . . . .	185
418	8.2.3	Neutral scalars . . . . .	186
419	8.2.4	Modifications of Higgs self-couplings . . . . .	187
420	8.2.5	Exotic Higgs boson decays . . . . .	188
421	8.3	Searches for supersymmetry . . . . .	188
422	8.3.1	Search for the SUSY Electroweak Sector: prompt signatures . . . . .	189
423	8.3.2	Search for the SUSY Electroweak Sector: long-lived particles . . . . .	190
424	8.3.3	R-parity violating signatures . . . . .	191
425	8.4	Feebly Interacting Particles . . . . .	192
426	8.4.1	Searches for heavy neutrinos . . . . .	192
427	8.4.2	Fermion triplets in type III seesaw . . . . .	193
428	8.4.3	Dark photons . . . . .	194
429	8.4.4	Axion-like particles . . . . .	195
430	8.5	Anomalous Gauge Couplings . . . . .	196
431	8.5.1	Radiation Amplitude Zero . . . . .	198
432	8.6	Theories with heavy resonances and contact interaction . . . . .	198
433	8.6.1	Leptoquarks . . . . .	198
434	8.6.2	$Z'$ mediated charged lepton flavour violation . . . . .	200
435	8.6.3	Vector-like quarks . . . . .	200
436	8.6.4	Excited fermions ( $\nu^*, e^*, u^*$ ) . . . . .	201
437	8.6.5	Colour octet leptons . . . . .	201

438	8.6.6	Quark substructure and Contact interactions . . . . .	202
439	8.7	Summary and conclusion . . . . .	202
440	<b>9</b>	<b>Influence of the LHeC on Physics at the HL-LHC</b>	<b>204</b>
441	9.1	Precision Electroweak Measurements at the HL-LHC . . . . .	204
442	9.1.1	The effective weak mixing angle . . . . .	204
443	9.1.2	The $W$ -boson mass . . . . .	206
444	9.1.3	Impact on electroweak precision tests . . . . .	208
445	9.2	Higgs Physics . . . . .	210
446	9.2.1	Impact of LHeC data on Higgs cross section predictions at the LHC . . .	210
447	9.2.2	Higgs Couplings from a simultaneous analysis of $pp$ and $ep$ collision data	212
448	9.3	Further precision SM measurements at the HL-LHC . . . . .	214
449	9.4	High Mass Searches at the LHC . . . . .	219
450	9.4.1	Strongly-produced supersymmetric particles . . . . .	219
451	9.4.2	Contact interactions . . . . .	219
452	9.5	PDFs and the HL-LHC and the LHeC . . . . .	220
453	9.5.1	PDF Prospects with the HL-LHC and the LHeC . . . . .	220
454	9.5.2	Parton luminosities at the HL-LHC . . . . .	222
455	9.5.3	PDF Sensitivity: Comparing HL-LHC and LHeC . . . . .	223
456	9.6	Impact of New Small- $x$ Dynamics on Hadron Collider Physics . . . . .	223
457	9.7	Heavy Ion Physics with $eA$ Input . . . . .	225
458	<b>10</b>	<b>The Electron Energy Recovery Linac</b>	<b>230</b>
459	10.1	Introduction – Design Goals . . . . .	230
460	10.2	The ERL Configuration of the LHeC . . . . .	231
461	10.2.1	Baseline Design – Lattice Architecture . . . . .	232
462	10.2.2	30 GeV ERL Options . . . . .	243
463	10.2.3	Component Summary . . . . .	243
464	10.3	Electron-Ion Collisions . . . . .	244
465	10.4	Beam-Beam Interactions . . . . .	245
466	10.4.1	Effect on the electron beam . . . . .	246
467	10.4.2	Effect on the proton beam . . . . .	247
468	10.5	Arc Magnets . . . . .	248
469	10.5.1	Dipole magnets . . . . .	248
470	10.5.2	Quadrupole magnets . . . . .	249
471	10.6	LINAC and SRF . . . . .	250
472	10.6.1	Choice of Frequency . . . . .	251
473	10.6.2	Cavity Prototype . . . . .	252
474	10.6.3	Cavity-Cryomodule . . . . .	255
475	10.6.4	Electron sources and injectors . . . . .	258
476	10.6.5	Positrons - INCOMPLETE Being edited . . . . .	262
477	10.6.6	Compensation of Synchrotron Radiation Losses . . . . .	264
478	10.6.7	LINAC Configuration and Infrastructure . . . . .	266
479	10.7	Interaction Region . . . . .	266
480	10.7.1	Layout . . . . .	266
481	10.7.2	Proton Optics . . . . .	268
482	10.7.3	Electron Optics . . . . .	276
483	10.7.4	Interaction Region Magnet Design . . . . .	284
484	10.8	Civil Engineering . . . . .	287
485	10.8.1	Placement and Geology . . . . .	288

486	10.8.2	Underground infrastructure . . . . .	289
487	10.8.3	Construction Methods . . . . .	290
488	10.8.4	Civil Engineering for FCC-eh . . . . .	291
489	10.8.5	Cost estimates . . . . .	294
490	10.8.6	Spoil management . . . . .	294
491	<b>11</b>	<b>Technology of ERL and PERLE</b>	<b>295</b>
492	11.1	Energy Recovery Linac Technology - Status and Prospects . . . . .	295
493	11.1.1	ERL Applications . . . . .	295
494	11.1.2	Challenges . . . . .	295
495	11.1.3	ERL Landscape . . . . .	298
496	11.2	The ERL Facility PERLE . . . . .	299
497	11.2.1	Configuration . . . . .	300
498	11.2.2	Importance of PERLE towards the LHeC . . . . .	300
499	11.2.3	PERLE Layout and Beam Parameters . . . . .	301
500	11.2.4	PERLE Lattice . . . . .	301
501	11.2.5	The Site . . . . .	303
502	11.2.6	Staging Strategy and Time Schedule . . . . .	304
503	11.2.7	Concluding Remark . . . . .	306
504	<b>12</b>	<b>Experimentation at the LHeC</b>	<b>307</b>
505	12.1	Introduction . . . . .	307
506	12.2	Overview of Main Detector Elements . . . . .	309
507	12.3	Inner Tracking . . . . .	310
508	12.3.1	Overview and Performance . . . . .	310
509	12.3.2	Silicon Technology Choice . . . . .	314
510	12.4	Calorimetry . . . . .	317
511	12.5	Muon Detector . . . . .	320
512	12.6	Forward and Backward Detectors . . . . .	322
513	12.6.1	Zero-Degree (Neutron) Calorimeter . . . . .	322
514	12.7	Detector Installation and Infrastructure . . . . .	325
515	12.8	Detector Design for a Low Energy FCC-eh . . . . .	328
516	<b>13</b>	<b>Conclusion</b>	<b>332</b>
517	<b>A</b>	<b>Statement of the International Advisory Committee</b>	<b>336</b>



# 518 Chapter 1

## 519 Introduction

### 520 1.1 The Context

#### 521 1.1.1 Particle Physics - an unfinished Area of Fundamental Science

522 Despite its striking success, the Standard Model (SM) has been recognised to have major defi-  
523 ciencies. These may be summarised in various ways. Some major questions can be condensed  
524 as follows:

- 525 • **Higgs boson** Is the electroweak scale stabilised by new particles, interactions, symme-  
526 tries? Is the Higgs boson discovered in 2012 the SM Higgs boson, what is its potential?  
527 Do more Higgs bosons exist as predicted, for example, in super-symmetric theories?
- 528 • **Elementary Particles** The SM has 61 identified particles: 12 leptons, 36 quarks and  
529 anti-quarks, 12 mediators, 1 Higgs boson. Are these too many or too few? Do right-handed  
530 neutrinos exist? Why are there three families? What makes leptons and quarks different?  
531 Do leptoquarks exist, is there a deeper substructure?
- 532 • **Strong Interactions** What is the true parton dynamics and structure inside the proton,  
533 inside other hadrons and inside nuclei – at different levels of resolution? How is confinement  
534 explained and how do partons hadronise? How can the many body dynamics of the Quark  
535 Gluon Plasma (QGP) state be described in terms of the elementary fields of Quantum  
536 Chromodynamics? What is the meaning of the AdS/CFT relation and of supersymmetry  
537 in strong interactions? Do axions, odderons, instantons exist?
- 538 • **GUT** Is there a genuine, grand unification of the interactions at high scales, would this  
539 include gravitation? What is the correct value of the strong coupling constant, is lattice  
540 theory correct in this respect? Is the proton stable?
- 541 • **Neutrinos** Do Majorana or/and sterile neutrinos exist, is there CP violation in the  
542 neutrino sector?
- 543 • **Dark Matter** Is dark matter constituted of elementary particles or has it another origin?  
544 Do hidden or dark sectors of nature exist and would they be accessible to accelerator  
545 experiments?

546 These and other open problems are known, and they have been persistent questions to Particle  
547 Physics. They are intimately related and any future strategic programme should not be confined  
548 to only one or a few of these. The field of particle physics is far from being understood,



549 despite the phenomenological success of the  $SU_L(2) \times U(1) \times SU_c(3)$  gauge field theory termed  
550 the Standard Model. Attempts to declare its end [10] are in contradiction not only to the  
551 experience from a series of past revolutions in science but indeed contrary to the incomplete  
552 status of particle physics as sketched above. The question is not why to end particle physics but  
553 how to proceed. The answer is not hidden in philosophy but requires new, better, affordable  
554 experiments. Indeed the situation is special as expressed by Guido Altarelli a few years ago: *It is*  
555 *now less unconceivable that no new physics will show up at the LHC... We expected complexity*  
556 *and instead we have found a maximum of simplicity. The possibility that the Standard model*  
557 *holds well beyond the electroweak scale must now be seriously considered [11].* This is reminiscent  
558 of the time before 1969, prior to anything like a Standard Model, when gauge theory was just  
559 for theorists, while a series of new accelerators, such as the 2 mile electron linac at Stanford or  
560 the SPS at CERN, were planned which resulted in a complete change of the paradigm of particle  
561 physics.

562 Ingenious theoretical hypotheses, such as on the existence of extra dimensions, on SUSY, of un-  
563 particles or the embedding in higher gauge groups, like E8, are a strong motivation to develop  
564 high energy physics rigorously further. In this endeavour, a substantial increase of precision,  
565 the conservation of diversity of projects and the extension of kinematic coverage are a necessity,  
566 likely turning out to be of fundamental importance. The strategic question in this context,  
567 therefore, is not just which new collider should be built next, as one often hears, but how we  
568 may challenge the current and incomplete knowledge best. A realistic step to progress comprises  
569 a new  $e^+e^-$  collider, built probably in Asia, and complementing the LHC with an electron energy  
570 recovery linac to synchronously operate  $ep$  with  $pp$  at the LHC, the topic of this paper.

571 One may call these machines first technology generation colliders as their technology has been  
572 proven to principally work [12]. Beyond these times, there is a long-term future reaching to  
573 the year 2050 and much beyond, of a second, further generation of hadron, lepton and electron-  
574 hadron colliders. CERN has recently published a design study of a future circular  $hh$ ,  $eh$  and  
575  $e^+e^-$  collider (FCC) complex [13–15], which would provide a corresponding base. For electron-  
576 hadron scattering this opens a new horizon with the FCC-eh, an about 3 TeV centre-of-mass  
577 system (cms) energy collider which in this paper is also considered, mostly for comparison with  
578 the LHeC. A prospect similar to FCC is also being developed in China [16, 17].

579 A new collider for CERN at the level of  $\mathcal{O}(10^{10})$  CHF cost should have the potential to change the  
580 paradigm of particle physics with direct, high energy discoveries in the 10 TeV mass range. This  
581 may only be achieved with the FCC-hh including an  $eh$  experiment. The FCC-hh/eh complex  
582 does access physics to several hundred TeV, assisted by a qualitatively new level of QCD/DIS.  
583 A prime, very fundamental goal of the FCC-pp is the clarification of the Higgs vacuum potential  
584 which can not be achieved in  $e^+e^-$ . This collider therefore has an overriding justification beyond  
585 the unknown prospects of finding new physics nowadays termed “exotics”. It accesses rare Higgs  
586 boson decays, high scales and, when combined with  $ep$ , it measures the SM Higgs couplings to  
587 below percent precision. There is a huge, fundamental program on electroweak and strong  
588 interactions, flavour and heavy ions for FCC-hh to be explored. This represents CERN’s unique  
589 opportunity to build on the ongoing LHC program, for many decades ahead. The size of the  
590 FCC-hh requires this to be established as a global enterprise. The HL-LHC and the LHeC can  
591 be understood as very important steps towards this major new facility, both in terms of physics  
592 and technology. The present report outlines a road towards realising a next generation, energy  
593 frontier electron-hadron collider as part of this program, which would maximally exploit and  
594 support the LHC.

### 595 1.1.2 Deep Inelastic Scattering and HERA

596 The field of deep inelastic lepton-hadron scattering (DIS) [18] was born with the discovery [19,20]  
597 of partons [21, 22] about 50 years ago. It readily contributed fundamental insights, for example  
598 on the development of QCD with the confirmation of fractional quark charges and of asymptotic  
599 freedom or with the spectacular finding that the weak isospin charge of the right-handed electron  
600 was zero [23] which established the Glashow-Weinberg-Salam “Model of Leptons” [24] as the  
601 base of the united electroweak theory. The quest to reach higher energies in accelerator based  
602 particle physics led to generations of colliders, with HERA [25] as the so far only electron-proton  
603 one.

604 HERA collided electrons (and positrons) of  $E_e = 27.6$  GeV energy off protons of  $E_p = 920$  GeV  
605 energy achieving a centre of mass energy,  $\sqrt{s} = 2\sqrt{E_e E_p}$ , of about 0.3 TeV. It therefore extended  
606 the kinematic range covered by fixed target experiments by two orders of magnitude in Bjorken  
607  $x$  and in four-momentum transfer squared,  $Q^2$ , with its limit  $Q_{max}^2 = s$ . HERA was built in less  
608 than a decade, and it operated for 16 years. Together with the Tevatron and LEP, HERA was  
609 pivotal to the development of the Standard Model.

610 HERA had a unique collider physics programme and success [26]. It established QCD as the cor-  
611 rect description of proton substructure and parton dynamics down to  $10^{-19}$  m. It demonstrated  
612 electroweak theory to hold in the newly accessed range, especially with the measurement of  
613 neutral and charged current  $ep$  scattering cross sections beyond  $Q^2 \sim M_{W,Z}^2$  and with the proof  
614 of electroweak interference at high scales through the measurement of the interference struc-  
615 ture functions  $F_2^{\gamma Z}$  and  $xF_3^{\gamma Z}$ . The HERA collider has provided the core base of the physics  
616 of parton distributions, not only in determining the gluon, valence, light and heavy sea quark  
617 momentum distributions in a much extended range, but as well in supporting the foundation of  
618 the theory of unintegrated, diffractive, photon, neutron PDFs through a series of correspond-  
619 ing measurements. It discovered the rise of the parton distributions towards small momentum  
620 fractions,  $x$ , supporting early QCD expectations on the asymptotic behaviour of the structure  
621 functions [27]. Like the Tevatron and LEP/SLC colliders which explored the Fermi scale of  
622 a few hundred GeV energy, determined by the vacuum expectation value of the Higgs field,  
623  $v = 1/\sqrt{\sqrt{2}G_F} = 2M_W/g \simeq 246$  GeV, HERA showed too that there was no supersymmetric or  
624 other exotic particle with reasonable couplings existing at the Fermi energy scale.

625 HERA established electron-proton scattering as an integral part of modern high energy particle  
626 physics. It demonstrated the richness of DIS physics, and the feasibility of constructing and  
627 operating energy frontier  $ep$  colliders. What did we learn to take into a next, higher energy  $ep$   
628 collider design? Perhaps there arose three lessons about:

- 629 • *the need for higher energy*, for three reasons: i) to make charged currents a real, precision  
630 part of  $ep$  physics, for instance for the complete unfolding of the flavour composition of  
631 the sea and valence quarks, ii) to produce heavier mass particles (Higgs, top, exotics) with  
632 favourable cross sections, and iii) to discover or disprove the existence of gluon saturation  
633 for which one needs to measure at lower  $x \propto Q^2/s$ , i.e. higher  $s$  than HERA had available;
- 634 • *the need for much higher luminosity*: the first almost ten years of HERA provided just a  
635 hundred  $\text{pb}^{-1}$ . As a consequence, HERA could not accurately access the high  $x$  region,  
636 and it was inefficient and short of statistics in resolving puzzling event fluctuations;
- 637 • *the complexity of the interaction region* when a bent electron beam caused synchrotron  
638 radiation while the opposite proton beam generated quite some halo background through  
639 beam-gas and beam-wall proton-ion interactions.

640 Based on these and further lessons a first LHeC paper was published in 2006 [28]. The LHeC  
 641 design was then intensely worked on, and a comprehensive CDR appeared in 2012 [1]. This has  
 642 now been pursued much further still recognising that the LHC is the only existing base to realise  
 643 a TeV energy scale electron-hadron collider in the accessible future. It offers highly energetic,  
 644 intense hadron beams, a long time perspective and a unique infrastructure and expertise, i.e.  
 645 everything required for an energy frontier DIS physics and innovative accelerator programme.

## 646 1.2 The Paper

### 647 1.2.1 The LHeC Physics Programme

648 This paper presents a design concept of the LHeC, using a 50 GeV energy electron beam to  
 649 be scattered off the LHC hadron beams (proton and ion) in concurrent operation<sup>1</sup>. Its main  
 650 characteristics are presented in **Chapter 2**. The instantaneous luminosity is designed to be  
 651  $10^{34} \text{ cm}^{-2}\text{s}^{-1}$  exceeding that of HERA, which achieved a few times  $10^{31} \text{ cm}^{-2}\text{s}^{-1}$ , by a factor of  
 652 several hundreds. The kinematic range nominally is extended by a factor of about 15, but in fact  
 653 by a larger amount because of the hugely increased luminosity which is available for exploring  
 654 the maximum  $Q^2$  and large  $x \leq 1$  regions, which were major deficiencies at HERA. The coverage  
 655 of the  $Q^2$ ,  $x$  plane by previous and future DIS experiments is illustrated in Fig. 1.1.

656 The LHeC would provide a major extension of the DIS kinematic range as is required for the  
 657 physics programme at the energy frontier. For the LHC, the  $ep/A$  detector would be a new  
 658 major experiment. A number of major themes would be explored with significant discovery  
 659 potential. These are presented in quite some detail in seven chapters of this paper dedicated to  
 660 physics:

- 661 • Based on the unique hadron beams of the LHC and employing a point-like probe, the  
 662 LHeC would represent the world's cleanest, high resolution microscope for exploring the  
 663 substructure of and dynamics inside matter, which may be termed the Hubble telescope  
 664 for the smallest dimensions. The first chapter on physics, **Chapter 3**, is devoted to the  
 665 measurement of parton distributions with the LHeC, and it also presents the potential to  
 666 resolve proton structure in 3D.
- 667 • **Chapter 4** is devoted to the deep exploration of QCD. A key deliverable of the LHeC is  
 668 the clarification of the parton interaction dynamics at small Bjorken  $x$ , in the new regime  
 669 of very high parton densities but small coupling which HERA discovered but was unable  
 670 to clarify for its energy was limited. It is first shown that the LHeC can measure  $\alpha_s$  to  
 671 per mille accuracy followed by various studies to illustrate the unique potential of the  
 672 LHeC to pin down the dynamics at small  $x$ . The chapter also covers the seminal potential  
 673 for diffractive DIS to be developed. It concludes with brief presentations on theoretical  
 674 developments on pQCD and of novel physics on the light cone.
- 675 • The maximum  $Q^2$  exceeds the  $Z$ ,  $W$  boson mass values (squared) by two orders of magni-  
 676 tude. The LHeC, supported by variations of beam parameters and high luminosity, thus  
 677 offers a unique potential to test the electroweak SM in the spacelike region with unprece-  
 678 dented precision. The high  $ep$  cms energy leads to the copious production of top quarks,  
 679 of about  $2 \cdot 10^6$  single top and  $5 \cdot 10^4$   $t\bar{t}$  events. Top production could not be observed

---

<sup>1</sup>The CDR in 2012 used a 60 GeV beam energy. Recent considerations of cost, effort and synchrotron radiation effects led to preference of a small reduction of the energy. Various physics studies presented here still use 60 GeV. While for BSM, top and Higgs physics the high energy is indeed important, the basic conclusions remain valid if eventually the energy was indeed chosen somewhat smaller than previously considered. This is further discussed below. A decision on the energy would come with the approval obviously.

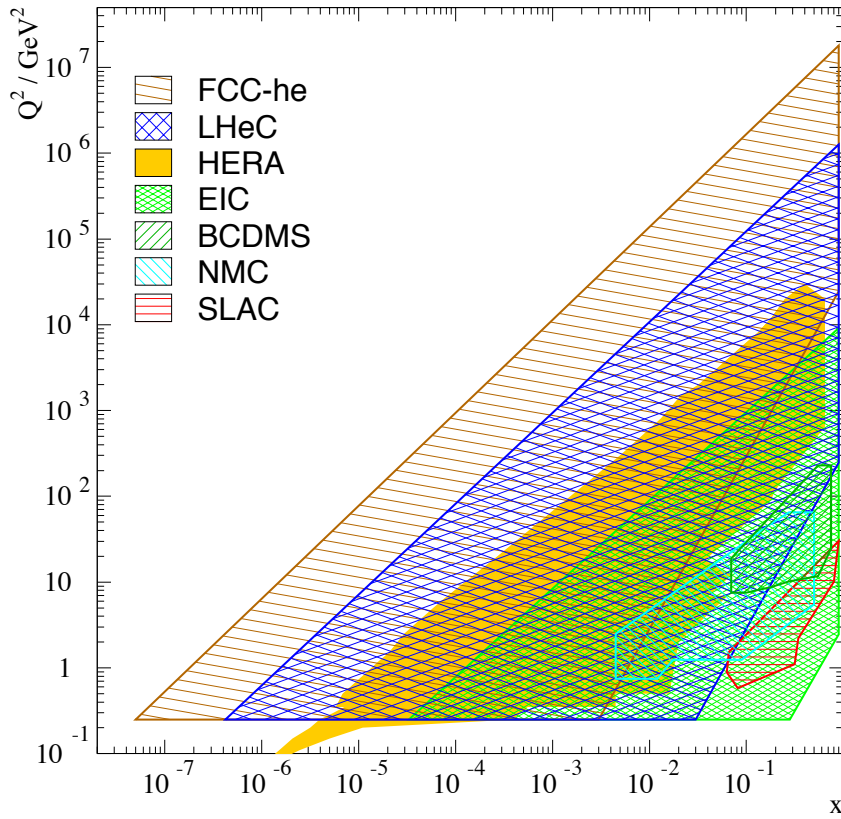


**Figure 1.1:** Coverage of the kinematic plane in deep inelastic lepton-proton scattering by some initial fixed target experiments, with electrons (SLAC) and muons (NMC, BCDMS), and by the  $ep$  colliders: the EIC (green), HERA (yellow), the LHeC (blue) and the FCC-eh (brown). The low  $Q^2$  region for the colliders is here limited to about  $0.2 \text{ GeV}^2$ , which is covered by the central detectors, roughly and perhaps using low electron beam data. Electron taggers may extend this to even lower  $Q^2$ . The high  $Q^2$  limit at fixed  $x$  is given by the line of inelasticity  $y = 1$ . Approximate limitations of acceptance at medium  $x$ , low  $Q^2$  are illustrated using polar angle limits of  $\eta = -\ln \tan \theta/2$  of 4, 5, 6 for the EIC, LHeC, and FCC-eh, respectively. These lines are given by  $x = \exp \eta \cdot \sqrt{Q^2}/2E_p$ , and can be moved to larger  $x$  when  $E_p$  is lowered below the nominal values.

680 at HERA but will thus become a central theme of precision and discovery physics with  
681 the LHeC. In particular, the top momentum fraction, top couplings to the photon, the  $W$   
682 boson and possible flavour changing neutral currents (FCNC) interactions can be studied  
683 in a uniquely clean environment (**Chapter 5**).

684 • The LHeC extends the kinematic range in lepton-nucleus scattering by nearly four orders  
685 of magnitude. It thus will transform nuclear particle physics completely, by resolving the  
686 hitherto hidden parton dynamics and substructure in nuclei and clarifying the QCD base  
687 for the collective dynamics observed in QGP phenomena (**Chapter 6**).

688 • The clean DIS final state in neutral and charged current scattering and the high integrated  
689 luminosity enable a high precision Higgs physics programme with the LHeC. The Higgs  
690 production cross section is comparable to the one of  $Z$ -strahlung at  $e^+e^-$ . This opens  
691 unexpected extra potential to independently test the Higgs sector of the SM, with high

692 precision insight especially into the  $H - WW/ZZ$  and  $H - bb/cc$  couplings (**Chapter 7**).

- 693 • As a new, unique, luminous TeV scale collider, the LHeC has an outstanding opportunity  
694 to discover new physics, such as in the exotic Higgs, dark matter, heavy neutrino and QCD  
695 areas (**Chapter 8**).
- 696 • With concurrent  $ep$  and  $pp$  operation, the LHeC would transform the LHC into a 3-beam,  
697 twin collider of greatly improved potential which is sketched in **Chapter 9**. Through  
698 ultra-precise strong and electroweak measurements, the  $ep$  experiment would make the  
699 HL-LHC complex a much more powerful search and measurement laboratory than current  
700 expectations, based on  $pp$  only, do entail. The joint  $pp/ep$  LHC facility together with a  
701 novel  $e^+e^-$  collider will make a major step in the study of the SM Higgs Boson, leading  
702 far beyond the HL-LHC. Putting  $pp$  and  $ep$  results together, as is illustrated for PDFs,  
703 will lead to new insight, especially when compared with its single  $pp$  and  $ep$  components.

704 The development of particle physics, the future of CERN, the exploitation of the singular LHC  
705 investments, the culture of accelerator art, all make the LHeC a unique project of great interest.  
706 It is challenging in terms of technology, affordable given budget constraints and it may still be  
707 realised in the two decades of currently projected LHC lifetime.

## 708 1.2.2 The Accelerator

709 The LHeC provides an intense, high energy electron beam to collide with the LHC. It represents  
710 the highest energy application of energy recovery linac (ERL) technology which is increasingly  
711 recognised as one of the major pilot technologies for the development of particle physics because  
712 it utilises and stimulates superconducting RF technology progress, and it increases intensity  
713 while keeping the power consumption low.

714 The LHeC instantaneous luminosity is determined through the integrated luminosity goal of  
715  $\mathcal{O}(1) \text{ ab}^{-1}$  caused by various physics reasons. The electron beam energy is chosen to achieve TeV  
716 cms collision energy and enable competitive searches and precision Higgs boson measurements.  
717 A cost-physics-energy evaluation is presented here which points to choosing  $E_e \simeq 50 \text{ GeV}$  as  
718 a new default value, which was 60 GeV before [1]. The wall-plug power has been constrained  
719 to 100 MW. Two super-conducting linacs of about 900 m length, which are placed opposite to  
720 each other, accelerate the passing electrons by 8.3 GeV each. This leads to a final electron beam  
721 energy of about 50 GeV in a 3-turn racetrack energy recovery linac configuration.

722 For measuring at very low  $Q^2$  and for determining the longitudinal structure function  $F_L$ , see  
723 below, the electron beam energy may be reduced to a minimum of about 10 GeV. For maximising  
724 the acceptance at large Bjorken  $x$ , the proton beam energy,  $E_p$ , may be reduced to 1 TeV. This  
725 determines a minimum cms energy of 200 GeV, below HERA's 319 GeV. If the ERL may be  
726 combined in the further future with the double energy HE-LHC [29], the proton beam energy  
727  $E_p$  could reach 14 TeV and  $\sqrt{s}$  be increased to 1.7 TeV. This is extended to 3.5 TeV for the FCC-  
728 he with a 50 TeV proton energy beam. We thus have the unique, exciting prospect for future  
729 DIS  $ep$  scattering at CERN with an energy range from below HERA to the few TeV region,  
730 at hugely increased luminosity and based on much more sophisticated experimental techniques  
731 than had been available at HERA times.

732 A spectacular extension of the kinematic range will be expected for deep inelastic lepton-nucleus  
733 scattering which was not pursued at DESY. Currently, highest energy  $lN$  data are due to fixed  
734 target muon-nucleus experiments, such as NMC and COMPASS, with a maximum  $\sqrt{s}$  of about  
735 20 GeV which permits a maximum  $Q^2$  of  $400 \text{ GeV}^2$ . This will be extended with the EIC at

736 Brookhaven to about  $10^4 \text{ GeV}^2$ . The corresponding numbers for  $ePb$  scattering at LHeC (FCC-  
737 he) are  $\sqrt{s} \simeq 0.74$  (2.2) TeV and  $Q_{max}^2 = 0.54$  (4.6)  $10^6 \text{ GeV}^2$ . The kinematic range in  $eA$   
738 scattering will thus be extended through the LHeC (FCC-he) by three (four) orders of magnitude  
739 as compared to the current status. This will thoroughly alter the understanding of parton and  
740 collective dynamics inside nuclei.

741 The ERL beam configuration is located inside the LHC ring but outside its tunnel, which  
742 minimises any interference with the main hadron beam infrastructure. The electron accelerator  
743 may thus be built independently, to a considerable extent, of the status of operation of the  
744 proton machine. The length of the ERL has configuration to be a fraction  $1/n$  of the LHC  
745 circumference as is required for the  $e$  and  $p$  matching of bunch patterns. Here the return arcs  
746 count as two single half rings. The chosen electron beam energy of 50 GeV leads, for  $n = 5$ , to  
747 a circumference  $U$  of 5.4 km for the electron racetrack <sup>2</sup>. A 3-pass ERL configuration had been  
748 adopted also for the FCC-he albeit maintaining the original 60 GeV as default which had a 9 km  
749 circumference.

750 For the LHC, the ERL would be tangential to IP2. According to current plans, IP2 is given  
751 to the ALICE detector with a program extending to LS4, the first long shutdown following the  
752 three year pause of the LHC operation for upgrading the luminosity performance and detectors.  
753 There are plans for a new heavy ion detector to move into IP2. The LS4 shutdown is currently  
754 scheduled to begin in 2031 with certain likelihood of being postponed to 2032 or later as recent  
755 events seem to move LS3 forward and extend its duration to three years.

756 For FCC-he the preferred position is interaction point L, for geological reasons mainly, and the  
757 time of operation fully depending on the progress with FCC-hh, beginning at the earliest in the  
758 late 40ies if CERN went for the hadron collider directly after the LHC.

759 The LHeC operation is transparent to the LHC collider experiments owing to the low lepton  
760 bunch charge and resulting small beam-beam tune shift experienced by the protons. The LHeC  
761 is thus designed to run simultaneously with  $pp$  (or  $pA$  or  $AA$ ) collisions with a dedicated final  
762 operation of a few years.

763 The paper presents in considerable detail the design of the LHeC (**Chapter 10**), i.e. the optics  
764 and lattice, components, magnets, as well as designs of the linac and interaction region besides  
765 special topics such as the prospects for electron-ion scattering, positron-proton operation and a  
766 novel study of beam-beam interaction effects. With the more ambitious luminosity goal, with  
767 a new lattice adapted to 50 GeV, with progress on the IR design, a novel analysis of the civil  
768 engineering works and, especially, the production and successful test [30] of the first SC cavity  
769 at the newly chosen default frequency of 801.58 MHz, this report considerably extends beyond  
770 the initial CDR. This holds especially since several LHeC institutes have recently embarked on  
771 the development of the ERL technology with a low energy facility, PERLE, to be built at IJC  
772 Laboratory at Orsay.

### 773 1.2.3 PERLE

774 Large progress has been made in the development of superconducting, high gradient cavities  
775 with quality factors,  $Q_0$ , beyond  $10^{10}$ . This will enable the exploitation of ERLs in high-energy  
776 physics colliders, with the LHeC as a prime example, while considerations are also brought  
777 forward for future  $e^+e^-$  colliders [31] and for proton beam cooling with an ERL tangential to  
778 eRHIC. The status and challenges of energy recovery linacs are summarised in **Chapter 11**.

---

<sup>2</sup>The circumference may eventually be chosen to be 6.8 km, the length of the SPS, which would relax certain parameters and ease an energy upgrade.

779 This chapter also presents the design, status and prospects for the ERL development facility  
780 PERLE. The major parameters of PERLE have been taken from the LHeC, such as the 3-turn  
781 configuration, source, frequency and cavity-cryomodule technology, in order to make PERLE a  
782 suitable facility for the development of LHeC ERL technology and the accumulation of operating  
783 experience prior to and later in parallel with the LHeC.

784 An international collaboration has been established to build PERLE at Orsay. With the design  
785 goals of 500 MeV electron energy, obtained in three passes through two cryo-modules and of  
786 20 mA, corresponding to 500 nC charge at 40 MHz bunch frequency, PERLE is set to become  
787 the first ERL facility to operate at 10 MW power. Following its CDR [5] and a paper submitted  
788 to the European strategy [9], work is directed to build a first dressed cavity and to release  
789 a TDR by 2021/22. Besides its value for accelerator and ERL technology, PERLE is also  
790 of importance for pursuing a low energy physics programme, see [5], and for several possible  
791 industrial applications. It also serves as a local hub for the education of accelerator physicists  
792 at a place, previously called Linear Accelerator Laboratory (LAL), which has long been at the  
793 forefront of accelerator design and operation.

794 There are a number of related ERL projects as are characterised in Chapter 11. The realisation  
795 of the ERL for the LHeC at CERN represents a unique opportunity not only for physics and  
796 technology but as well for a next and the current generation of accelerator physicists, engineers  
797 and technicians to realise an ambitious collider project while the plans for very expensive next  
798 machines may take shape. Similarly, this holds for a new generation of detector experts, as  
799 the design of the upgrade of the general purpose detectors (GPDs) at the LHC is reaching  
800 completion, with the question increasingly posed about opportunities for new collider detector  
801 construction to not lose the expertise nor the infrastructure for building trackers, calorimeters  
802 and alike. The LHeC offers the opportunity for a novel  $4\pi$  particle physics detector design,  
803 construction and operation. As a linac-ring collider, it may serve one detector of a size smaller  
804 than CMS and larger than H1 or ZEUS.

#### 805 1.2.4 The Detector

806 **Chapter 12** on the detector relies to a large extent on the very detailed write-up on the kinemat-  
807 ics, design considerations, and realisation of a detector for the LHeC presented in the CDR [1].  
808 In the previous report one finds detailed studies not only on the central detector and its magnets,  
809 a central solenoid for momentum measurements and an extended dipole for ensuring head-on  $ep$   
810 collisions, but as well on the forward ( $p$  and  $n$ ) and backward ( $e$  and  $\gamma$ ) tagging devices. The  
811 work on the detector as presented here was focussed on an optimisation of the performance and  
812 on the scaling of the design towards higher proton beam energies. It presents a new, consistent  
813 design and summaries of the essential characteristics in support of many physics analyses this  
814 paper entails.

815 The most demanding performance requirements arise from the  $ep$  Higgs measurement pro-  
816 gramme, especially the large acceptance and high precision desirable for heavy flavour tagging  
817 and the requirement to resolve the hadronic final state. This has been influenced by both the  
818 rapidity acceptance extensions and the technology progress of the HL-LHC detector upgrades.  
819 A key example, also discussed, is the HV-CMOS Silicon technology, for which the LHeC is an  
820 ideal application due to the much limited radiation level as compared to  $pp$ .

821 Therefore we have now completed two studies of design: previously, of a rather conventional  
822 detector with limited cost and, here, of a more ambitious device. Both of these designs appear  
823 feasible. This regards also the installation. The paper presents a brief description of the installa-  
824 tion of the LHeC detector at IP2 with the result that it may proceed within two years, including

825 the dismantling of the there residing detector. This calls for modularity and pre-mounting of  
826 detector elements on the surface, as was done for CMS too. It will be for the LHeC detector  
827 Collaboration, to be established with and for the approval of the project, to eventually design  
828 the detector according to its understanding and technical capabilities.

### 829 1.3 Outline

830 The paper is organised as follows. For a brief overview, Chapter 2 summarises the LHeC charac-  
831 teristics. Chapter 3 presents the physics of the LHeC seen as a microscope for measuring PDFs  
832 and exploring the 3D structure of the proton. Chapter 4 contains further means to explore QCD,  
833 especially low  $x$  dynamics, together with two sections on QCD theory developments. Chapter 5  
834 describes the electroweak and top physics potential of the LHeC. Chapter 6 presents the seminal  
835 nuclear particle physics potential of the LHeC, through luminous electron-ion scattering explor-  
836 ing an unexplored kinematic territory. Chapter 7 presents a detailed analysis of the opportunity  
837 for precision SM Higgs boson physics with charged and neutral current  $ep$  scattering. Chapter 8  
838 is a description of the salient opportunities to discover physics beyond the Standard Model with  
839 the LHeC, including non-SM Higgs physics, right-handed neutrinos, physics of the dark sector,  
840 heavy resonances and exotic substructure phenomena. Chapter 8 describes the interplay of  $ep$   
841 and  $pp$  physics, i.e. the necessity to have the LHeC for fully exploiting the potential of the LHC  
842 facility, e.g. through the large increase of electroweak precision measurements, the considerable  
843 extension of search ranges and the joint  $ep$  and  $pp$  Higgs physics potential. Chapter 9 presents  
844 the update of the design on the electron accelerator with many novel results such as on the  
845 lattice and interaction region, updated parameters for  $ep$  and  $eA$  scattering, new specifications  
846 of components, updates on the electron source, . . . The chapter also presents the encouraging re-  
847 sults of the first LHeC 802 MHz cavity. Chapter 10 is devoted, first, to the status and challenges  
848 of energy recovery based accelerators and, second, to the description of the PERLE facility be-  
849 tween its CDR and a forthcoming TDR. Chapter 11 describes the update of the detector studies  
850 towards an optimum configuration in terms of acceptance and performance. Chapter 12 presents  
851 a summary of the paper including a time line for realising the LHeC to operate with the LHC.



## Chapter 2

# LHeC Configuration and Parameters

### 2.1 Introduction

The Conceptual Design Report (CDR) of the LHeC was published in 2012 [1]. The CDR default configuration uses a 60 GeV energy electron beam derived from a racetrack, three-turn, intense energy recovery linac (ERL) achieving a cms energy of  $\sqrt{s} = 1.3$  TeV, where  $s = 4E_p E_e$  is determined by the electron and proton beam energies,  $E_e$  and  $E_p$ . In 2012, the Higgs boson,  $H$ , was discovered which has become a central topic of current and future high energy physics. The Higgs production cross section in charged current (CC) deep inelastic scattering (DIS) at the LHeC is roughly 100 fb. The Large Hadron Collider has so far not led to the discovery of any exotic phenomenon. This forces searches to be pursued, in  $pp$  but as well in  $ep$ , with the highest achievable precision in order to access a maximum range of phase space and possibly rare channels. The DIS cross section at large  $x$  roughly behaves like  $(1-x)^3/Q^4$ , demanding very high luminosities for exploiting the unknown regions of Bjorken  $x$  near 1 and very high  $Q^2$ , the negative four-momentum transfer squared between the electron and the proton. For the current update of the design of the LHeC this has set a luminosity goal about an order of magnitude higher than the  $10^{33} \text{ cm}^{-2} \text{ s}^{-1}$  which had been adopted for the CDR. There arises the potential, as described subsequently in this paper, to transform the LHC into a high precision electroweak, Higgs and top quark physics facility.

The  $ep$  Higgs production cross section rises approximately with  $E_e$ . New physics may be related to the heaviest known elementary particle, the top quark, the  $ep$  production cross section of which rises more strongly than linearly with  $E_e$  in the LHeC kinematic range as that is not very far from the  $t\bar{t}$  threshold. Searches for heavy neutrinos, SUSY particles, etc. are the more promising the higher the energy is. The region of deep inelastic scattering and pQCD requires that  $Q^2$  be larger than  $M_p^2 \simeq 1 \text{ GeV}^2$ . Access with DIS to very low Bjorken  $x$  requires high energies because of  $x = Q^2/s$ , for inelasticity  $y = 1$ . In DIS, one needs  $Q^2 > M_p^2 \simeq 1 \text{ GeV}^2$ . Physics therefore requires a maximally large energy. However, cost and effort set realistic limits such that twice the HERA electron beam energy, of about 27 GeV, appeared as a reasonable and affordable target value.

In the CDR [1] the default electron energy was chosen to be 60 GeV. This can be achieved with an ERL circumference of 1/3 of that of the LHC. Recently, the cost was estimated in quite some detail [32], comparing also with other accelerator projects. Aiming at a cost optimisation and providing an option for a staged installation, the cost estimate lead to defining a new default configuration of  $E_e = 50$  GeV with the option of starting in an initial phase with a beam energy of  $E_e = 30$  GeV and a a circumference of 5.4 km which is 1/5 of the LHC length. Lowering

887  $E_e$  is also advantageous for mastering the synchrotron radiation challenges in the interaction  
 888 region. Naturally, the decision on  $E_e$  is not taken now. This paper comprises studies with  
 889 different energy configurations, mainly  $E_e = 50$  and  $60$  GeV, which are close in their centre of  
 890 mass energy values of  $1.2$  and  $1.3$  TeV, respectively.

891 Up to beam energies of about  $60$  GeV, the ERL cost is dominated by the cost for the supercon-  
 892 ducting RF of the linacs. Up to this energy the ERL cost scales approximately linearly with the  
 893 beam energy. Above this energy the return arcs represent the main contribution to the cost and  
 894 to the ERL cost scaling is no longer linear. Given the non-linear dependence of the cost on  $E_e$ ,  
 895 for energies larger than about  $60$  GeV, significantly larger electron beam energy values may only  
 896 be justified by overriding arguments, such as, for example, the existence of leptoquarks<sup>1</sup>. Higher  
 897 values of  $\sqrt{s}$  are also provided with enlarged proton beam energies by the High Energy LHC  
 898 ( $E_p = 13.5$  TeV) [29] and the FCC-hh [15] with  $E_p$  between  $20$  and possibly  $75$  TeV, depending  
 899 on the dipole magnet technology.

## 900 2.2 Cost Estimate, Default Configuration and Staging

901 In 2018 a detailed cost estimate was carried out [32] following the guidance and practice of  
 902 CERN accelerator studies. The assumptions were also compared with the DESY XFEL cost.  
 903 The result was that for the  $60$  GeV configuration about half of the total cost was due to the two  
 904 SC linacs. The cost of the arcs decreases more strongly than linearly with decreasing energy,  
 905 about  $\propto E^4$  for synchrotron radiation losses and  $\propto E^3$  when emittance dilution is required to be  
 906 avoided [33]. It was therefore considered to set a new default of  $50$  GeV with a circumference of  
 907  $1/5$  of that of the LHC, see Sect. 2.3, compared to  $1/3$  for  $60$  GeV. Furthermore, an initial phase  
 908 at  $30$  GeV was considered, within the  $1/5$  configuration but with only partially equipped linacs.  
 909 The HERA electron beam energy was  $27$  GeV. The main results, taken from [32] are reproduced  
 910 in Tab. 2.1.

911 The choice of a default of  $50$  GeV at  $1/5$  of the LHC circumference results, as displayed, in  
 912 a total cost of  $1,075$  MCHF for the initial  $30$  GeV configuration and an additional, upgrade  
 913 cost to  $50$  GeV of  $296$  MCHF. If one restricted the LHeC to a non-upgradeable  $30$  GeV only  
 914 configuration one would, still in a triple racetrack configuration, come to roughly a  $1$  km long  
 915 structure with two linacs of about  $500$  m length, probably in a single linac tunnel configuration.  
 916 The cost of this version of the LHeC is roughly  $800$  MCHF, i.e. about half the  $60$  GeV estimated  
 917 cost. However, this would essentially reduce the LHeC to a QCD and electroweak machine, still  
 918 very powerful but accepting substantial losses in its Higgs, top and BSM programme.

919 A detailed study was made on the cost of the civil engineering, which is also discussed subse-  
 920 quently. This concerned a comparison of the  $1/3$  vs the  $1/5$  LHC circumference versions, and  
 921 the FCC-eh. The result is illustrated in Fig. 2.1. It shows that the CE cost for the  $1/5$  version is  
 922 about a quarter of the total cost. The reduction from  $1/3$  to  $1/5$  economises about  $100$  MCHF.

923 Choices of the final energy will be made later. They depend not only on a budget but also on the  
 924 future development of particle physics at large. For example, it may turn out that, for some years  
 925 into the future, the community may not find the  $\mathcal{O}(10)$  GCHF required to build any of the  $e^+e^-$

---

<sup>1</sup>If these existed with a mass of say  $M = 1.5$  TeV this would require, at the LHC with  $E_p = 7$  TeV, to choose  $E_e$  to be larger than  $90$  GeV, and to pay for it. Leptoquarks would be produced by  $ep$  fusion and appear as resonances, much like the  $Z$  boson in  $e^+e^-$  and would therefore fix  $E_e$  (given certain  $E_p$  which at the FCC exceeds  $7$  TeV). The genuine DIS kinematics, however, is spacelike, the exchanged four-momentum squared  $q^2 = -Q^2$  being negative, which implies that the choice of the energies is less constrained than in an  $e^+e^-$  collider aiming at the study of the  $Z$  or  $H$  bosons.

Component	CDR 2012 (60 GeV)	Stage 1 (30 GeV)	Default (50 GeV)
SRF System	805	402	670
SRF R+D and Prototyping	31	31	31
Injector	40	40	40
Arc Magnets and Vacuum	215	103	103
SC IR Magnets	105	105	105
Source and Dump System	5	5	5
Cryogenic Infrastructure	100	41	69
General Infrastructure and Installation	69	58	58
Civil Engineering	386	289	289
Total Cost	1756	1075	1371

**Table 2.1:** Summary of cost estimates, in MCHF, from [32]. The 60 GeV configuration is built with a 9 km triple racetrack configuration as was considered in the CDR [1]. It is taken as the default configuration for FCC-eh, with an additional CE cost of 40 MCHF due to the larger depth on point L (FCC) as compared to IP2 (LHC). Both the 30 and the 50 GeV assume a 5.4 km configuration, i.e. the 30 GeV is assumed to be a first stage of LHeC upgradeable to 50 GeV ERL. Whenever a choice was to be made on estimates, in [32] the conservative number was chosen.

926 colliders currently considered. Then the only way to improve on the Higgs measurements beyond  
927 HL-LHC substantially is the high energy (50 – 60 GeV), high luminosity ( $\int L = 1 \text{ ab}^{-1}$ ) LHeC.  
928 Obviously, physics and cost are intimately related. Based on such considerations, but also taking  
929 into account technical constraints as resulting from the amount of synchrotron radiation losses  
930 in the interaction region and the arcs, we have chosen 50 GeV in a 1/5 of U(LHC) configuration  
931 as the new default. This economises about 400 MCHF as compared to the CDR configuration.

932 If the LHeC ERL were built, it may later be transferred, with some reconfiguration and upgrades,  
933 to the FCC to serve as the FCC-eh. The FCC-eh has its own location, L, for the ERL which  
934 requires a new accelerator tunnel. It has been decided to keep the 60 GeV configuration for the  
935 FCC, as described in the recently published CDR of the FCC [15]. The LHeC ERL configuration  
936 may also be used as a top-up injector for the  $Z$  and possibly  $WW$  phase of the FCC-e should  
937 the FCC-ee indeed precede the FCC-hh/eh phase.

## 938 2.3 Configuration Parameters

939 A possible transition from the 60 GeV to the 50 GeV configuration of the LHeC was already  
940 envisaged in 2018, as considered in the paper submitted to the European Strategy [7]. The  
941 machine layout shown in that paper is reproduced in Fig. 2.2. It is a rough sketch illustrating  
942 the reduction from a 60 GeV to a 50 GeV configuration, which results not only in a reduction of  
943 capital costs, as discussed above, but also of effort.

944 The ERL configuration has been recently revisited [33] considering its dependence on the electron  
945 beam energy. Applying a dimension scaling which preserves the emittance dilution, the results  
946 have been obtained as are summarised in Tab. 2.2. The 1/5 configuration is chosen as the new  
947 LHeC default while the CDR on the LHeC from 2012 and the recent CDR on FCC-eh have used  
948 the 1/3 configuration. The energy and configuration may be decided as physics, cost and effort  
949 dictate, once a decision is taken.

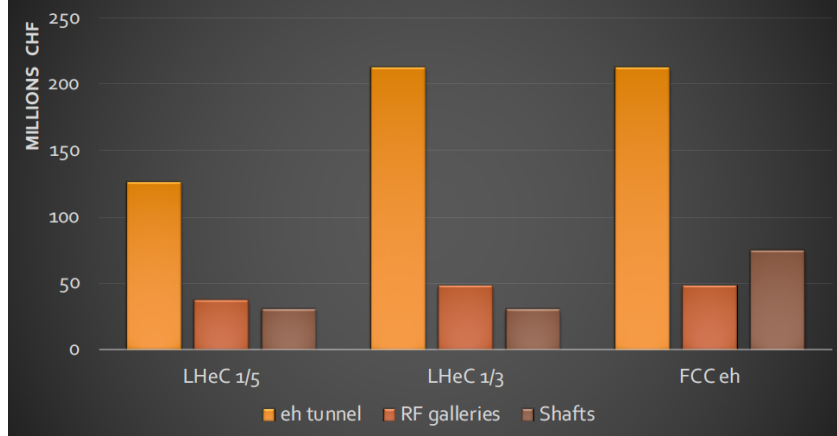


**Figure 2.1:** Cost estimate for the civil engineering work for the tunnel, rf galleries and shafts for the LHeC at 1/5 of the LHC circumference (left), at 1/3 (middle) and the FCC-eh (right). The unit costs and percentages are consistent with FCC and CLIC unit prices. The estimate is considered reliable to 30%. The cost estimates include: Site investigations: 2%, Preliminary design, tender documents and project changes: 12% and the Contractors profit: 3%. Surface site work is not included, which for LHeC exists with IP2.

Parameter	Unit	LHeC option			
		1/3 LHC	1/4 LHC	1/5 LHC	1/6 LHC
Circumference	m	9000	6750	5332	4500
Arc radius	$m \cdot 2\pi$	1058	737	536	427
Linac length	$m \cdot 2$	1025	909	829	758
Spreader and recombiner length	$m \cdot 4$	76	76	76	76
Electron energy	GeV	61.1	54.2	49.1	45.2

**Table 2.2:** Scaling of the electron beam energy, linac and further accelerator element dimensions with the choice of the total circumference in units  $1/n$  of the LHC circumference. For comparison, the CERN SPS has a circumference of 6.9 km, only somewhat larger than 1/4 of that of the LHC.

## 950 2.4 Luminosity

951 The luminosity  $L$  for the LHeC in its linac-ring configuration is determined as

$$L = \frac{N_e N_p n_p f_{rev} \gamma_p}{4\pi \epsilon_p \beta^*} \cdot \prod_{i=1}^3 H_i, \quad (2.1)$$

952 where  $N_{e(p)}$  is the number of electrons (protons) per bunch,  $n_p$  the number of proton bunches  
953 in the LHC,  $f_{rev}$  the revolution frequency in the LHC [the bunch spacing in a batch is given  
954 by  $\Delta$ , equal to 25 ns for protons in the LHC] and  $\gamma_p$  the relativistic factor  $E_p/M_p$  of the proton  
955 beam. Further,  $\epsilon_p$  denotes the normalised proton transverse beam emittance and  $\beta^*$  the proton  
956 beta function at the IP, assumed to be equal in  $x$  and  $y$ . The luminosity is moderated by the  
957 hourglass factor,  $H_1 = H_{geo} \simeq 0.9$ , the pinch or beam-beam correction factor,  $H_2 = H_{b-b} \simeq 1.3$ ,  
958 and the filling factor  $H_3 = H_{coll} \simeq 0.8$ , should an ion clearing gap in the electron beam be  
959 required. This justifies taking the product of these factors. As the product is close to unity, the  
960 factors are not listed for simplicity in the subsequent tables.

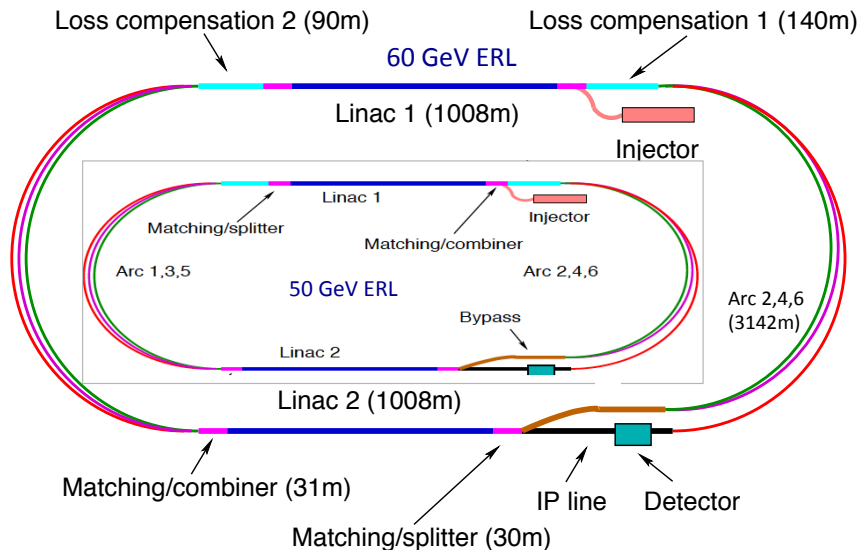


**Figure 2.2:** Schematic view of the three-turn LHeC configuration with two oppositely positioned electron linacs and three arcs housed in the same tunnel. Two configurations are shown: Outer: Default  $E_e = 60$  GeV with linacs of about 1 km length and 1 km arc radius leading to an ERL circumference of about 9 km, or 1/3 of the LHC length. Inner: Sketch for  $E_e = 50$  GeV with linacs of about 0.8 km length and 0.55 km arc radius leading to an ERL circumference of 5.4 km, or 1/5 of the LHC length, which is smaller than the size of the SPS. The 1/5 circumference configuration is flexible: it entails the possibility to stage the project as funds of physics dictate by using only partially equipped linacs, and it also permits upgrading to somewhat higher energies if one admits increased synchrotron power losses and operates at higher gradients.

961 The electron beam current is given as

$$I_e = eN_e f, \quad (2.2)$$

962 where  $f$  is the bunch frequency  $1/\Delta$ . The current for the LHeC is limited by the charge delivery  
 963 of the source. In the new default design we have  $I_e = 20$  mA which results from a charge of  
 964 500 pC for the bunch frequency of 40 MHz. It is one of the tasks of the PERLE facility to  
 965 investigate the stability of the 3-turn ERL configuration in view of the challenge for each cavity  
 966 to hold the sixfold current due to the simultaneous acceleration and deceleration of bunches at  
 967 three different beam energies each.

### 968 2.4.1 Electron-Proton Collisions

969 The design parameters of the luminosity were recently provided in a note describing the FCC-eh  
 970 configuration [34], including the LHeC. Tab.2.3 represents an update comprising in addition  
 971 the initial 30 GeV configuration and the lower energy version of the FCC-hh based on the LHC  
 972 magnets<sup>2</sup>. For the LHeC, as noted above, we assume  $E_e = 50$  GeV while for FCC-eh we retain  
 973 60 GeV. Since the source limits the electron current, the peak luminosity may be taken not to  
 974 depend on  $E_e$ . Studies of the interaction region design, presented in this paper, show that one

<sup>2</sup>The low energy FCC-pp collider, as of today, uses a 6 T LHC magnet in a 100 km tunnel. If, sometime in the coming decades, high field magnets become available based on HTS technology, then a 20 TeV proton beam energy may even be achievable in the LHC tunnel. To this extent the low energy FCC considered here and an HTS based HE-LHC would be comparable options in terms of their energy reach.

975 may be confident of reaching a  $\beta^*$  of 10 cm but it will be a challenge to reach even smaller values.  
 976 Similarly, it will be quite a challenge to operate with a current much beyond 20 mA. That has  
 977 nevertheless been considered [35] for a possible dedicated LHeC operation mode for a few years  
 following the  $pp$  operation program.

Parameter	Unit	LHeC				FCC-eh	
		CDR	Run 5	Run 6	Dedicated	$E_p=20$ TeV	$E_p=50$ TeV
$E_e$	GeV	60	30	50	50	60	60
$N_p$	$10^{11}$	1.7	2.2	2.2	2.2	1	1
$\epsilon_p$	$\mu\text{m}$	3.7	2.5	2.5	2.5	2.2	2.2
$I_e$	mA	6.4	15	20	50	20	20
$N_e$	$10^9$	1	2.3	3.1	7.8	3.1	3.1
$\beta^*$	cm	10	10	7	7	12	15
Luminosity	$10^{33} \text{ cm}^{-2}\text{s}^{-1}$	1	5	9	23	8	15

**Table 2.3:** Summary of luminosity parameter values for the LHeC and FCC-eh. Left: CDR from 2012; Middle: LHeC in three stages, an initial run, possibly during Run 5 of the LHC, the 50 GeV operation during Run 6, both concurrently with the LHC, and a final, dedicated, stand-alone  $ep$  phase; Right: FCC-eh with a 20 and a 50 TeV proton beam, in synchronous operation.

978

979 The peak luminosity values exceed those at HERA by 2–3 orders of magnitude. The operation  
 980 of HERA in its first, extended running period, 1992-2000, provided an integrated luminosity  
 981 of about  $0.1 \text{ fb}^{-1}$  for the collider experiments H1 and ZEUS. This may now be expected to be  
 982 taken in a day of initial LHeC operation.

## 983 2.4.2 Electron-Ion Collisions

984 The design parameters and luminosity were also provided recently [34] for collisions of electrons  
 985 and lead nuclei (fully stripped  $^{208}\text{Pb}^{82+}$  ions). Tab. 2.4 is an update of the numbers presented  
 986 there for consistency with the Run 6 LHeC configuration in Tab. 2.3 and with the addition  
 987 of parameters corresponding to the  $E_p = 20$  TeV FCC-hh configuration. Further discussion of  
 988 this operating mode and motivations for the parameter choices in this table are provided in  
 989 Section 10.3.

990 One can expect the average luminosity during fills to be about 50% of the peak in Tab. 2.4  
 991 and we assume an overall operational efficiency of 50%. Then, a year of  $eA$  operation, possibly  
 992 composed by combining shorter periods of operation, would have the potential to provide an  
 993 integrated data set of about 5 (25)  $\text{fb}^{-1}$  for the LHeC (FCC-eh), respectively. This exceeds  
 994 the HERA electron-proton luminosity value by about tenfold for the LHeC and much more at  
 995 FCC-eh while the fixed target nuclear DIS experiment kinematics is extended by 3–4 orders of  
 996 magnitude. These energy frontier electron-ion configurations therefore have the unique potential  
 997 to radically modify our present view of nuclear structure and parton dynamics. This is discussed  
 998 in Chapter 4.

## 999 2.5 Linac Parameters

1000 The brief summary of the main LHeC characteristics here concludes with a table of the main  
 1001 ERL parameters for the new default electron energy of 50 GeV, Tab. 2.5, which are discussed in  
 1002 detail in Chapter 8.

Parameter	Unit	LHeC	FCC-eh ( $E_p=20$ TeV)	FCC-eh ( $E_p=50$ TeV)
Ion energy $E_{Pb}$	PeV	0.574	1.64	4.1
Ion energy/nucleon $E_{Pb}/A$	TeV	2.76	7.88	19.7
Electron beam energy $E_e$	GeV	50	60	60
Electron-nucleon CMS $\sqrt{s_{eN}}$	TeV	0.74	1.4	2.2
Bunch spacing	ns	50	100	100
Number of bunches		1200	2072	2072
Ions per bunch	$10^8$	1.8	1.8	1.8
Normalised emittance $\epsilon_n$	$\mu\text{m}$	1.5	1.5	1.5
Electrons per bunch	$10^9$	6.2	6.2	6.2
Electron current	mA	20	20	20
IP beta function $\beta_A^*$	cm	10	10	15
e-N Luminosity	$10^{32}\text{cm}^{-2}\text{s}^{-1}$	7	14	35

**Table 2.4:** Baseline parameters of future electron-ion collider configurations based on the electron ERL, in concurrent  $eA$  and  $AA$  operation mode with the LHC and the two versions of a future hadron collider at CERN. Following established convention in this field, the luminosity quoted, at the start of a fill, is the *electron-nucleon* luminosity which is a factor  $A$  larger than the usual (i.e. electron-nucleus) luminosity.

## 2.6 Operation Schedule

The LHeC parameters are determined to be compatible with a parasitic operation with the nominal HL-LHC proton-proton operation. This implies limiting the electron bunch current to sufficiently small values so that the proton beam-beam parameter remains small enough to be negligible for the proton beam dynamics.

Assuming a ten year construction period for the LHeC after approval of the project and a required installation window of two years for the LHeC detector, the earliest realistic operation period for the LHeC coincides with the LHC Run 5 period in 2032 and with a detector installation during LS4 which is currently scheduled during 2030 and would need to be extended by one year to 2031. The baseline HL-LHC operation mode assumes 160 days of proton operation, 20 days of ion operation and 20 days of machine development time for the Run 4 period, amounting to a total of 200 operation days per year. After the Run 4 period the HL-LHC does not consider ion operation at present and assumes 190 days for proton operation. The HL-LHC project assumes an overall machine efficiency of 54% (e.g. fraction of scheduled operation time spent in physics production) and we assume that the ERL does not contribute to significant additional downtime for the operation. Assuming an initial 15 mA of electron beam current, a  $\beta^*$  of 10 cm and HL-LHC proton beam parameters, the LHeC reaches a peak luminosity of  $0.5 \cdot 10^{34} \text{cm}^{-2}\text{s}^{-1}$ . Assuming further a proton beam lifetime of 16.7 hours, a proton fill length of 11.7 hours and an average proton beam turnaround time of 4 hours, the LHeC can reach in this configuration an annual integrated luminosity of  $20 \text{fb}^{-1}$ .

For the evaluation of the physics potential it is important to note that the Run 5 initial  $ep$  operation period may accumulate about  $50 \text{fb}^{-1}$  of integrated luminosity. This is the hundredfold value which H1 (or ZEUS) took over a HERA lifetime of 15 years. As one may expect, for details see Chapter 3, such a huge DIS luminosity is ample for pursuing basically the complete QCD programme. In particular, the LHeC would deliver on time for the HL-LHC precision analyses the external, precise PDFs and with just a fraction of the  $50 \text{fb}^{-1}$  the secrets of low  $x$  parton dynamics would unfold. Higher  $ep$  luminosity is necessary for ultimate precision and for the top, BSM and the Higgs programme of the LHeC to be of competitive value.

Parameter	Unit	Value
Frequency	MHz	801.58
Bunch charge	pC	499
Bunch spacing	ns	24.95
Electron current	mA	20
Injector energy	MeV	500
Gradient	MV/m	19.73
Cavity length, active	m	0.918
Cavity length, flange-to-flange	m	1.5
Cavities per cryomodule		4
Length of cryomodule	m	7
Acceleration per cryomodule	MeV	72.45
Total number of cryomodules		112
Acceleration energy per pass	GeV	8.1

**Table 2.5:** Basic LHeC ERL characteristics for the default configuration using two such linacs located opposite to each other in a racetrack of 5.4 km length. Each linac is passed three times for acceleration and three times for deceleration.

1031 For the Run 6 period of the HL-LHC, the last of the HL-LHC operation periods, we assume  
1032 that the number of machine development sessions for the LHC can be suppressed, providing  
1033 an increase in the operation time for physics production from 190 days to 200 days per year.  
1034 Furthermore, we assume that the electron beam parameters can be slightly further pushed.  
1035 Assuming a  $\beta^*$  reduced to 7 cm, an electron beam current of up to 25 mA and still nominal  
1036 HL-LHC proton beam parameters, the LHeC reaches a peak performance of  $1.2 \cdot 10^{34} \text{ cm}^{-2} \text{ s}^{-1}$   
1037 and an annual integrated luminosity of  $50 \text{ fb}^{-1}$ . This would add up to an integrated luminosity  
1038 of a few hundred  $\text{fb}^{-1}$ , a strong base for top, BSM and Higgs physics at the LHeC.

1039 Beyond the HL-LHC exploitation period, the electron beam parameters could be further pushed  
1040 in dedicated  $ep$  operation, when the requirement of a parasitic operation to the HL-LHC proton-  
1041 proton operation may no longer be imposed. The proton beam lifetime without proton-proton  
1042 collisions would be significantly larger than in the HL-LHC configuration. In the following we  
1043 assume a proton beam lifetime of 100 hours and a proton beam efficiency of 60 % without proton-  
1044 proton beam collisions. The electron beam current in this configuration would only be limited  
1045 by the electron beam dynamics and the SRF beam current limit. Assuming that electron beam  
1046 currents of up to 50 mA, the LHeC would reach a peak luminosity of  $2.4 \cdot 10^{34} \text{ cm}^{-2} \text{ s}^{-1}$  and an  
1047 annual integrated luminosity of up to  $180 \text{ fb}^{-1}$ . Table 2.6 summarises the LHeC configurations  
1048 over these three periods of operation.

1049 Depending on the years available for a dedicated final operation (or through an extension of  
1050 the  $pp$  LHC run, currently not planned but interesting for collecting 4 instead of  $3 \text{ ab}^{-1}$  to, for  
1051 example, observe di-Higgs production at the LHC), a total luminosity of  $1 \text{ ab}^{-1}$  could be available  
1052 for the LHeC. This would double the precision of Higgs couplings measured in  $ep$  as compared to  
1053 the default HL-LHC run period with  $ep$  added as described. It would also significantly enlarge  
1054 the potential to observe or/and quantify rare and new physics phenomena. Obviously such  
1055 considerations are subject to the grand developments at CERN. A period with most interesting  
1056 physics and on-site operation activity could be particularly welcome for narrowing a possible  
1057 large time gap between the LHC and its grand successor, the FCC-hh. One may, however, be  
1058 interested in ending LHC on time. It thus is important for the LHeC project to recognise its  
1059 particular value as an asset of the HL-LHC, and on its own, with even less than the ultimate  
1060 luminosity, albeit values which had been dreamt of at HERA.



Parameter	Unit	Run 5 Period	Run 6 Period	Dedicated
Brightness $N_p/(\gamma\epsilon_p)$	$10^{17}\text{m}^{-1}$	2.2/2.5	2.2/2.5	2.2/2.5
Electron beam current	mA	15	25	50?
Proton $\beta^*$	m	0.1	0.7	0.7
Peak luminosity	$10^{34}\text{cm}^{-2}\text{s}^{-1}$	0.5	1.2	2.4
Proton beam lifetime	h	16.7	16.7	100
Fill duration	h	11.7	11.7	21
Turnaround time	h	4	4	3
Overall efficiency	%	54	54	60
Physics time / year	days	160	180	185
Annual integrated lumi.	$\text{fb}^{-1}$	20	50	180

**Table 2.6:** The LHeC performance levels during different operation modes.

## Chapter 3

# Parton Distributions - Resolving the Substructure of the Proton

### 3.1 Introduction

Since the discovery of quarks in the famous  $ep \rightarrow eX$  scattering experiment at Stanford [19,20], the deep inelastic scattering process has been established as the most reliable method to resolve the substructure of protons, which was immediately recognised, not least by Feynman [18]. Since that time, a series of electron, muon and neutrino DIS experiments validated the Quark-Parton Model and promoted the development of Quantum Chromodynamics. A new quality of this physics was realised with HERA, the first electron-proton collider built, which extended the kinematic range in momentum transfer squared to  $Q_{max}^2 = s \simeq 10^5 \text{ GeV}^2$ , for  $s = 4E_e E_p$ . Seen from today's perspective, largely influenced by the LHC, it is necessary to advance to a further level in these investigations, with higher energy and much increased luminosity than HERA could achieve. This is a major motivation for building the LHeC, with an extension of the  $Q^2$  and  $1/x$  range by more than an order of magnitude and an increase of the luminosity by a factor of almost a thousand. QCD may breakdown, be embedded in a higher gauge symmetry, or unconfined colour might be observed; These phenomena raise a number a series of fundamental questions of the QCD theory [36] and highlight the importance of a precision DIS programme with the LHeC.

The subsequent chapter is mainly devoted to the exploration of the seminal potential of the LHeC to resolve the substructure of the proton in an unprecedented range, with the first ever complete and coherent measurement of the full set of parton distribution functions (PDFs) in one experiment. The precise determination of PDFs, consistently to high orders pQCD, is crucial for the interpretation of LHC physics, i.e. its precision electroweak and Higgs measurements as well as the exploration of the high mass region where new physics may occur when the HL-LHC operates. Extra constraints on PDFs arise also from  $pp$  scattering as is discussed in a later chapter. Conceptually, however, the LHeC provides the singular opportunity to completely separate the PDF determination from proton-proton physics. This approach is not only more precise for the PDFs, but it is theoretically more accurate and enables incisive tests of QCD, by confronting independent predictions with LHC (and later FCC) measurements, as well as providing an indispensable base for reliable interpretations of searches for new physics.

While the resolution of the longitudinal, collinear structure of the proton is key to the physics programme of the LHeC (and the LHC), the  $ep$  collider provides further fundamental insight

1094 in the structure of the proton: semi-inclusive measurements of jets and vector mesons, and  
 1095 especially Deeply Virtual Compton Scattering, a process established at HERA, will shed light  
 1096 on also the transverse structure of the proton in a new kinematic range. This is presented at  
 1097 the end of the current chapter.

### 1098 3.1.1 Partons in Deep Inelastic Scattering

1099 Parton Distribution Functions  $xf(x, Q^2)$  represent a probabilistic view on hadron substructure  
 1100 at a given distance,  $1/\sqrt{Q^2}$ . They depend on the parton type  $f = (q_i, g)$ , for quarks and  
 1101 gluons, and must be determined from experiment, most suitably DIS, as perturbative QCD  
 1102 is not prescribing the parton density at a given momentum fraction Bjorken  $x$ . PDFs are  
 1103 important also for they determine Drell-Yan, hadron-hadron scattering processes, supposedly  
 1104 universally through the QCD factorisation theorem [37]<sup>1</sup>. The PDF programme of the LHeC  
 1105 is of unprecedented reach for the following reasons:

- 1106 • For the first time it will resolve the partonic structure of the proton (and nuclei) com-  
 1107 pletely, i.e. determine the  $u_v, d_v, u, d, s, c, b$ , and gluon momentum distributions through  
 1108 neutral and charged current cross section as well as direct heavy quark PDF measure-  
 1109 ments, performed in a huge kinematic range of DIS, from  $x = 10^{-6}$  to 0.9 and from  $Q^2$   
 1110 above 1 to  $10^6$  GeV<sup>2</sup>. The LHeC explores the strange density and the momentum fraction  
 1111 carried by top quarks [39] which was impossible at HERA.
- 1112 • Very high luminosity and unprecedented precision, owing to both new detector technology  
 1113 and the redundant evaluation of the event kinematics from the leptonic and hadronic final  
 1114 states, will lead to extremely high PDF precision.
- 1115 • Because of the high LHeC energy, the weak probes ( $W, Z$ ) dominate the interaction  
 1116 at larger  $Q^2$  which permits the up and down sea and valence quark distributions to be  
 1117 resolved in the full range of  $x$ . Thus no additional data will be required<sup>2</sup>: that is, there  
 1118 is no influence from higher twists nor nuclear uncertainties or data inconsistencies, which  
 1119 are main sources of uncertainty of current so-called global PDF determinations.

1120 While PDFs are nowadays often seen as merely a tool for interpreting LHC data, in fact what  
 1121 really is involved is a new understanding of strong interaction dynamics and the deeper resolution  
 1122 of substructure extending into hitherto uncovered phase space regions, in particular the small  $x$   
 1123 region, by virtue of the very high energy  $s$ , and the very small spatial dimension ( $1/\sqrt{Q^2}$ ) and  
 1124 the  $x \rightarrow 1$  region, owing to the high luminosity and energy. The QPM is not tested well enough,  
 1125 despite decades of DIS and other experiments, and QCD is not developed fully either in these  
 1126 kinematic regimes.

1127 Examples of issues of fundamental interest for the LHeC to resolve are: i) the long awaited  
 1128 resolution of the behaviour of  $u/d$  near the kinematic limit ( $x \rightarrow 1$ ); ii) the flavour democracy of  
 1129 the light quark sea (is  $d \simeq u \simeq s$  ??); iii) the existence of quark-level charge-symmetry [40]; iv)  
 1130 the behaviour of the ratio  $\bar{d}/\bar{u}$  at small  $x$ ; v) the turn-on and the values of heavy quark PDFs;  
 1131 vi) the value of the strong coupling constant and vii) the question of the dynamics, linear or  
 1132 non-linear, at small  $x$  where the gluon and quark densities rise.

---

<sup>1</sup>In his referee report on the LHeC CDR, in 2012, Guido Altarelli noted on the factorisation theorem in QCD for hadron colliders that: “many people still advance doubts. Actually this question could be studied experimentally, in that the LHeC, with its improved precision, could put bounds on the allowed amount of possible factorisation violations (e.g. by measuring in DIS the gluon at large  $x$  and then comparing with jet production at large  $p_T$  in hadron colliders).” This question was addressed also in a previous LHeC paper [38].

<sup>2</sup>The LHeC may be operated at basically HERA energies and collect a fb<sup>-1</sup> of luminosity for cross checks and maximising the high  $x$ , medium  $Q^2$  acceptance, see Sect. 3.2.

1133 Of special further interest is the gluon distribution, for the gluon self-interaction prescribes all  
 1134 visible mass, the gluon-gluon fusion process dominates Higgs production at hadron colliders  
 1135 (the LHC and the FCC) and because its large  $x$  behaviour, essentially unknown today, affects  
 1136 predictions of BSM cross sections at the LHC.

1137 The LHeC may be understood as an extension of HERA to a considerable extent. It has the  
 1138 reach in  $x \propto 1/s$  to resolve the question of new strong interaction dynamics at small  $x$  and it  
 1139 accesses high  $Q^2$ , much larger than  $M_{W,Z}^2$ , with huge luminosity to make accurate use of weak  
 1140 NC and CC cross sections in DIS PDF physics for the first time. QCD analyses of HERA data  
 1141 are still ongoing. For obvious reasons, there is no quantitative analysis of LHC related PDF  
 1142 physics possible without relying on the HERA data, and often on its QCD analyses. These  
 1143 are introduced briefly next. Albeit with certain assumptions and limited luminosity, HERA  
 1144 completely changed the field of PDF physics as compared to the times of solely fixed target  
 1145 data, see Ref. [41], and it opened the era of physics of high parton densities at small  $x$ .

### 1146 3.1.2 Fit Methodology and HERA PDFs

1147 The methodology of PDF determinations with HERA data has been developed over decades by  
 1148 the H1 and ZEUS Collaborations [26, 42, 43], in close contact with many theorists. It has been  
 1149 essentially adopted with suitable modifications for the LHeC PDF prospect study as is detailed  
 1150 subsequently.

1151 HERAPDF fits use information from both  $e^\pm p$  neutral current and charged current scattering  
 1152 from exclusively the  $ep$  collider experiments, H1 and ZEUS, up to high  $Q^2 = 30\,000\text{ GeV}^2$  and  
 1153 down to about  $x = 5 \cdot 10^{-5}$ . The precision of the HERA combined data is below 1.5% over the  
 1154  $Q^2$  range of  $3 < Q^2 < 500\text{ GeV}^2$  and remains below 3% up to  $Q^2 = 3000\text{ GeV}^2$ . The precision  
 1155 for large  $x > 0.5$  is rather poor due to limited luminosity and high- $x$  acceptance limitations at  
 1156 medium  $Q^2$ .

1157 The QCD analysis is performed at LO, NLO and NNLO within the  $xFitter$  framework [42,  
 1158 44, 45], and the latest version is the HERAPDF2.0 family [43]. The DGLAP evolution of the  
 1159 PDFs, as well as the light-quark coefficient functions, are calculated using QCDNUM [46, 47].  
 1160 The contributions of heavy quarks are calculated in the general-mass variable-flavour-number  
 1161 (GMVFN) scheme of Refs. [48, 49]. Experimental uncertainties are determined using the Hessian  
 1162 method imposing a  $\chi^2+1$  criterion. This is usually impossible in global fits over rather incoherent  
 1163 data sets originating from different processes and experiments, but has been a major advantage  
 1164 of the solely HERA based QCD analyses.

1165 In the HERAPDF analysis, as well as subsequently in the LHeC study, the starting scale is  
 1166 chosen to be  $Q_0^2 = 1.9\text{ GeV}^2$  such that it is below the charm mass,  $m_c^2$ . The data is restricted to  
 1167  $Q_{min}^2 \geq 3.5\text{ GeV}^2$  in order to stay in the DIS kinematic range. The forward hadron final state  
 1168 acceptance introduces a lower  $W$  cut which removes the region which otherwise is potentially  
 1169 sensitive to higher twist effects [50]. The strong coupling constant is set to  $\alpha_s(M_Z) = 0.118$ <sup>3</sup>.  
 1170 All these assumptions are varied in the evaluation of model uncertainties on the resulting fit.  
 1171 These variations will essentially have no significant effect with the LHeC as the sensitivity to  
 1172 the quark masses, for example, is hugely improved with respect to HERA,  $\alpha_s$  known to 1–2 per  
 1173 mille, and the kinematic range of the data is much extended.

---

<sup>3</sup>The strong coupling constant cannot be reliably determined from inclusive HERA data alone. DIS results, including fixed target data, have provided values which tend to be lower [51] than the here chosen value, see for a discussion Ref. [52]. As is further presented in detail in Sect. 4.1 the LHeC reaches a sensitivity to  $\alpha_s$  at the per mille level based on inclusive and jet data as well as their combination.

1174 In HERAPDF fits, the quark distributions at the initial  $Q_0^2$  are represented by the generic form

$$xq_i(x) = A_i x^{B_i} (1-x)^{C_i} P_i(x), \quad (3.1)$$

1175 where  $i$  specifies the flavour of the quark distribution and  $P_i(x) = (1 + D_i x + E_i x^2)$ . The  
 1176 inclusive NC and CC cross sections determine four independent quark distributions, essentially  
 1177 the sums of the up and down quark and anti-quark densities. These may be decomposed into  
 1178 any four other distributions of up and down quarks with an ad-hoc assumption on the fraction  
 1179 of strange to anti-down quarks which has minimal numeric effect on the PDFs, apart from that  
 1180 on  $x_s$  itself. The parameterised quark distributions,  $xq_i$ , are chosen to be the valence quark  
 1181 distributions ( $xu_v$ ,  $xd_v$ ) and the light anti-quark distributions ( $x\bar{u}$ ,  $x\bar{d}$ ). This has been adopted  
 1182 for the LHeC also.

1183 The parameters  $A_{u_v}$  and  $A_{d_v}$  are fixed using the quark counting rule. The normalisation and  
 1184 slope parameters,  $A$  and  $B$ , of  $\bar{u}$  and  $\bar{d}$  are set equal such that  $x\bar{u} = x\bar{d}$  at  $x \rightarrow 0$ , a crucial  
 1185 assumption which the LHeC can validate. The strange quark PDF  $x\bar{s}$  is set as a fixed fraction  
 1186  $r_s = 0.67$  of  $x\bar{d}$ . This fraction is varied in the determination of model uncertainties. By default  
 1187 it is assumed that  $x_s = x\bar{s}$  and that  $u$  and  $d$  sea and anti-quarks have the same distributions  
 1188 also. These assumptions will be resolved by the LHeC and their uncertainties will essentially be  
 1189 eliminated, see Sect. 3.3.4. The  $D$  and  $E$  parameters are used only if required by the data, fol-  
 1190 lowing a  $\chi^2$  saturation procedure [42]. This leads for HERAPDF2.0 to two non-zero parameters,  
 1191  $E_{u_v}$  and  $D_{\bar{u}}$ .

1192 The gluon distribution is parameterised differently

$$xg(x) = A_g x^{B_g} (1-x)^{C_g} - A'_g x^{B'_g} (1-x)^{C'_g}. \quad (3.2)$$

1193 The normalisation parameter  $A_g$  is calculated using the momentum sum rule. Variations of  
 1194 the PDFs were also considered with  $A'_g = 0$  which for earlier HERA data fits had been the  
 1195 default choice. The appearance of this second term may be understood as coming from a not-  
 1196 well constrained behaviour of  $xg(x, Q^2)$  at small  $x$ . In fact,  $xg$  is resembling a valence-quark  
 1197 distribution at  $Q^2 \simeq Q_0^2$ . The much extended  $Q^2$  range of the LHeC at a given small  $x$  and the  
 1198 access to much smaller  $x$  values than probed at HERA will quite certainly enable this behaviour  
 1199 to be clarified. Since also  $C'_g$  had been set to just a large value, there is negligible effect of that  
 1200 second term in Eq. (3.2) on the resulting PDF uncertainties. Consequently  $A'_g$  is set to zero in  
 1201 the LHeC study.

1202 Alternative parameterisations are used in the evaluation of the parameterisation uncertainty.  
 1203 These variations include: introducing extra parameters  $D$ ,  $E$  for each quark distribution; the  
 1204 removal of primed gluon parameters; and the relaxation of assumptions about the low- $x$  sea.  
 1205 These fits provide alternative extracted PDFs with similar fit  $\chi^2$ . The maximum deviation  
 1206 from the central PDF at each value of  $x$  is taken as an envelope and added in quadrature  
 1207 with the experimental and model uncertainties to give the total uncertainty. As for the model  
 1208 uncertainties, the extended range and improved precision of the LHeC data may well be expected  
 1209 to render such variations negligible.

1210 The results of the HERA PDF analysis [43] are shown in Fig. 3.1 for the HERAPDF2.0NNLO  
 1211 PDF set, displaying experimental, model and parameterisation uncertainties separately. The  
 1212 structure of the proton is seen to depend on the resolution  $\propto 1/\sqrt{Q^2}$ , with which it is probed.  
 1213 At  $Q^2$  of about  $1 - 2 \text{ GeV}^2$ , corresponding to  $0.2 \text{ fm}$ , the parton contents may be decomposed  
 1214 as is shown in Figure 3.1 top. The gluon distribution at  $Q^2 \simeq 2 \text{ GeV}^2$  has a valence like shape,  
 1215 i.e. at very low  $x$  the momentum is carried by sea quarks, see Fig. 3.1 (top). At medium  
 1216  $x \sim 0.05$  the gluon density dominates over all quark densities. At largest  $x$ , above 0.3, the

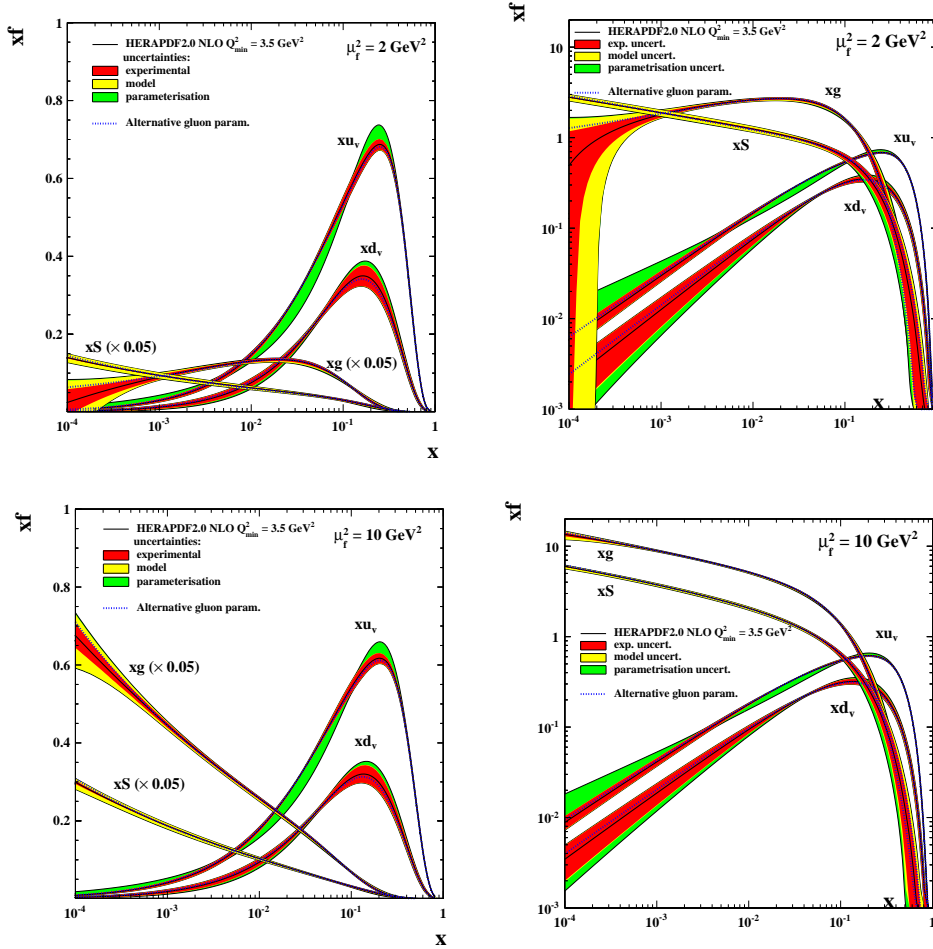


**Figure 3.1:** Parton distributions as determined by the QCD fit to the combined H1 and ZEUS data at  $Q^2 = 1.9 \text{ GeV}^2$  (top) and at  $Q^2 = 10 \text{ GeV}^2$  (bottom). The color coding represents the experimental, model and parameterisation uncertainties separately. Here  $xS = 2x(\bar{u} + \bar{d})$  denotes the total sea quark density. Note that  $xg$  and  $xS$  are scaled by  $1/20$  in the left side plots with a linear  $y$  scale.

1217 proton structure is dominated by the up and down valence quarks. This picture evolves such  
 1218 that below  $10^{-16} \text{ m}$ , for  $x \leq 0.1$ , the gluon density dominates also over the sea quark density,  
 1219 see Figure 3.1 (bottom). The valence quark distributions are rather insensitive to the resolution  
 1220 which reflects their non-singlet transformation behaviour in QCD.

1221 The HERAPDF set differs from other PDF sets in that: i) it represents a fit to a consistent data  
 1222 set with small correlated systematic uncertainties; ii) it uses data on solely a proton target such  
 1223 that no heavy target corrections are needed and the assumption of strong isospin invariance,  
 1224  $d_{\text{proton}} = u_{\text{neutron}}$ , is not required; iii) a large  $x, Q^2$  region is covered such that no regions where  
 1225 higher twist effects are important are included in the analysis.

1226 The limitations of HERA PDFs are known as well: i) the data is limited in statistics such  
 1227 that the region  $x > 0.5$  is poorly constrained; ii) the energy is limited such that the very low  
 1228  $x$  region, below  $x \simeq 10^{-4}$ , is not or not reliably accessed; iii) limits of luminosity and energy  
 1229 implied that the potential of the flavour resolution through weak interactions, in NC and CC,  
 1230 while remarkable, could not be utilised accurately and  $\alpha_s$  not been determined alongside PDFs  
 1231 in solely inclusive fits; iv) while the strange quark density was not accessed by H1 and ZEUS,  
 1232 only initial measurements of  $xc$  and  $xb$  could be performed. The strong success with respect

1233 to the fixed target PDF situation *ante* HERA has yet been most remarkable. The thorough  
 1234 clarification of parton dynamics and the establishment of a precision PDF base for the LHC and  
 1235 later hadron colliders, however, make a next generation, high energy and luminosity  $ep$  collider  
 1236 a necessity.

1237 The PDF potential of the LHeC is presented next. This study follows closely the first extended  
 1238 analysis, developed for the CDR and detailed subsequently in Ref. [53]. The main differences  
 1239 compared to that analysis result from the choice of the Linac-Ring LHeC configuration, with  
 1240 preferentially  $e^-p$  of high polarisation (and much less  $e^+p$ ) combined with an order of magnitude  
 1241 enhanced luminosity and developments of the apparatus design.

## 1242 3.2 Simulated LHeC Data

### 1243 3.2.1 Inclusive Neutral and Charged Current Cross Sections

1244 In order to estimate the uncertainties of PDFs from the LHeC, several sets of LHeC inclusive  
 1245 NC/CC DIS data with a full set of uncertainties have been simulated and are described in the  
 1246 following. The systematic uncertainties of the DIS cross sections have a number of sources,  
 1247 which can be classified as uncorrelated and correlated across bin boundaries. For the NC case,  
 1248 the uncorrelated sources, apart from event statistics, are a global efficiency uncertainty, due  
 1249 for example to tracking or electron identification errors, as well as uncertainties due to photo-  
 1250 production background, calorimeter noise and radiative corrections. The correlated uncertainties  
 1251 result from imperfect electromagnetic and hadronic energy scale and angle calibrations. In the  
 1252 classic  $ep$  kinematic reconstruction methods used here, the scattered electron energy  $E'_e$  and  
 1253 polar electron angle  $\theta_e$ , complemented by the energy of the hadronic final state  $E_h$ , can be  
 1254 employed to determine  $Q^2$  and  $x$  in a redundant way.

1255 Briefly,  $Q^2$  is best determined with the electron kinematics and  $x$  is calculated from  $y = Q^2/sx$ .  
 1256 At large  $y$ , the inelasticity is best measured using the electron energy,  $y_e \simeq 1 - E'_e/E_e$ . At low  
 1257  $y$ , the relation  $y_h = E_h \sin^2(\theta_h/2)/E_e$  can be used to provide a measurement of the inelasticity  
 1258 with the hadronic final state energy  $E_h$  and angle  $\theta_h$ . This results in the uncertainty  $\delta y_h/y_h \simeq$   
 1259  $\delta E_h/E_h$ , which is determined by the  $E_h$  calibration uncertainty to good approximation.

1260 There have been various refined methods proposed to determine the DIS kinematics, such as the  
 1261 double angle method [54], which is commonly used to calibrate the electromagnetic energy scale,  
 1262 or the so-called  $\Sigma$  method [55], which exhibits reduced sensitivity to QED radiative corrections,  
 1263 see a discussion in Ref. [56]. For the estimate of the cross section uncertainty the electron method  
 1264 ( $Q_e^2, y_e$ ) is used at large  $y$ , while at low  $y$  we use  $Q_e^2, y_h$ , which is transparent and accurate to  
 1265 better than a factor of two. In much of the phase space, moreover, it is rather the uncorrelated  
 1266 efficiency or further specific errors than the kinematic correlations, which dominate the cross  
 1267 section measurement precision.

1268 The assumptions used in the simulation of pseudodata are summarised in Tab. 3.1. The proce-  
 1269 dure was gauged with full H1 Monte Carlo simulations and the assumptions are corresponding  
 1270 to H1's achievements with an improvement by at most a factor of two. Using a numerical proce-  
 1271 dure developed in Ref. [57], the scale uncertainties are transformed to kinematics-dependent  
 1272 correlated cross-section uncertainties caused by imperfect measurements of  $E'_e$ ,  $\theta_e$  and  $E_h$ . These  
 1273 data uncertainties were imposed for all data sets, NC and CC, as are subsequently listed and  
 1274 described.

1275 The design of the LHeC assumes that it operates with the LHC in the high luminosity phase,  
 1276 following LS4 at the earliest. As detailed in Chapter 2, it is assumed there will be an initial phase,

Source of uncertainty	Uncertainty
Scattered electron energy scale $\Delta E'_e/E'_e$	0.1 %
Scattered electron polar angle	0.1 mrad
Hadronic energy scale $\Delta E_h/E_h$	0.5 %
Radiative corrections	0.3 %
Photoproduction background (for $y > 0.5$ )	1 %
Global efficiency error	0.5 %

**Table 3.1:** Assumptions used in the simulation of the NC cross sections on the size of uncertainties from various sources. The top three are uncertainties on the calibrations which are transported to provide correlated systematic cross section errors. The lower three values are uncertainties of the cross section caused by various sources.

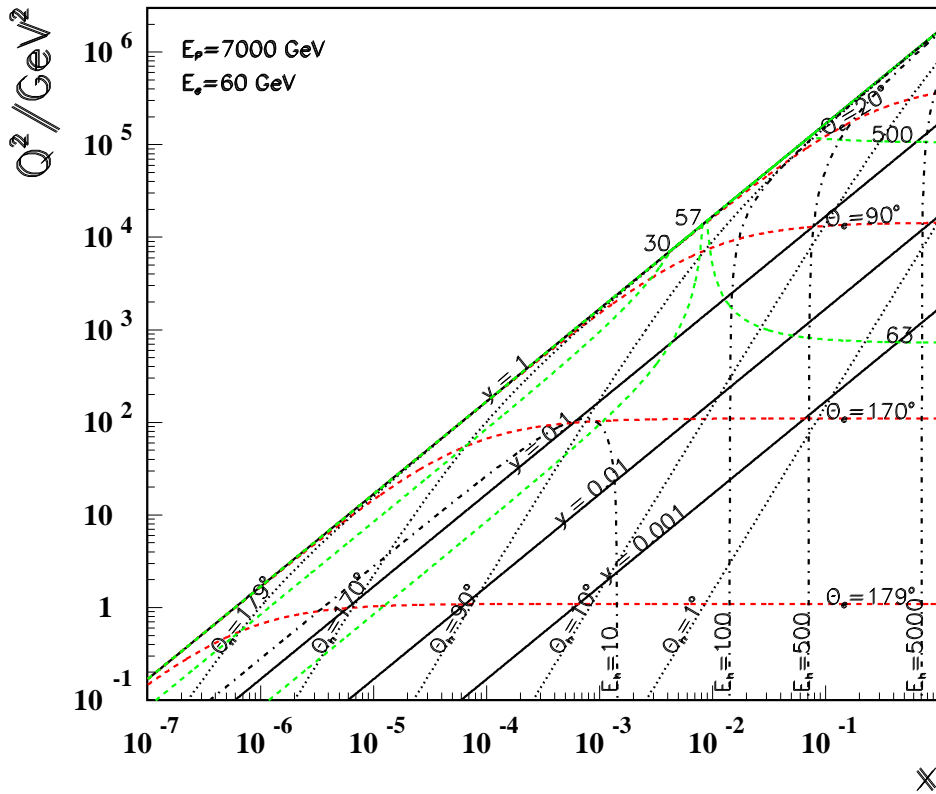


**Figure 3.2:** Kinematic plane covered with the maximum beam energies at the LHeC. Red dashed: Lines of constant scattered electron polar angle. Note that low  $Q^2$  is measured with electrons scattered into the backward region, highest  $Q^2$  is reached with Rutherford backscattering; Black dotted: lines of constant angle of the hadronic final state; Black solid: Lines of constant inelasticity  $y = Q^2/sx$ ; Green dashed: Lines of constant scattered electron energy  $E'_e$ . Most of the central region is covered by what is termed the kinematic peak, where  $E'_e \simeq E_e$ . The small  $x$  region is accessed with small energies  $E'_e$  below  $E_e$  while the very forward, high  $Q^2$  electrons carry TeV energies; Black dashed-dotted: lines of constant hadronic final state energy  $E_h$ . Note that the very forward, large  $x$  region sees very high hadronic energy deposits too.

1277 during which the LHeC may collect  $50 \text{ fb}^{-1}$  of data. This may begin with a sample of  $5 \text{ fb}^{-1}$ .  
1278 Such values are very high when compared with HERA, corresponding to the hundred(ten)-fold  
1279 of luminosity which H1 collected in its lifetime of about 15 years. The total luminosity may



1280 come close to  $1 \text{ ab}^{-1}$ .

1281 The bulk of the data is assumed to be taken with electrons, possibly at large negative helicity  
 1282  $P_e$ , because this configuration maximises the number of Higgs bosons that one can produce at  
 1283 the LHeC:  $e^-$  couples to  $W^-$  which interacts primarily with an up-quark and the CC cross  
 1284 section is proportional to  $(1 - P_e)$ . However, for electroweak physics there is a strong interest to  
 1285 vary the polarisation and charge <sup>4</sup>. It was considered that the  $e^+p$  luminosity may reach  $1 \text{ fb}^{-1}$   
 1286 while the tenfold has been simulated for sensitivity studies. A dataset has also been produced  
 1287 with reduced proton beam energy as that enlarges the acceptance towards large  $x$  at smaller  
 $Q^2$ . The full list of simulated sets is provided in Tab. 3.2.

Parameter	Unit	Data set								
		D1	D2	D3	D4	D5	D6	D7	D8	D9
Proton beam energy	TeV	7	7	7	7	1	7	7	7	7
Lepton charge		-1	-1	-1	-1	-1	+1	+1	-1	-1
Longitudinal lepton polarisation		-0.8	-0.8	0	-0.8	0	0	0	+0.8	+0.8
Integrated luminosity	$\text{fb}^{-1}$	5	50	50	1000	1	1	10	10	50

**Table 3.2:** Summary of characteristic parameters of data sets used to simulate neutral and charged current  $e^\pm$  cross section data, for a lepton beam energy of  $E_e = 50 \text{ GeV}$ . Sets D1-D4 are for  $E_p = 7 \text{ TeV}$  and  $e^-p$  scattering, with varying assumptions on the integrated luminosity and the electron beam polarisation. The data set D1 corresponds to possibly the first year of LHeC data taking with the tenfold of luminosity which H1/ZEUS collected in their lifetime. Set D5 is a low  $Ep$  energy run, essential to extend the acceptance at large  $x$  and medium  $Q^2$ . D6 and D7 are sets for smaller amounts of positron data. Finally, D8 and D9 are for high energy  $e^-p$  scattering with positive helicity as is important for electroweak NC physics. These variations of data taking are subsequently studied for their effect on PDF determinations.

1288

1289 The highest energies obviously give access to the smallest  $x$  at a given  $Q^2$ , and to the maximum  
 1290  $Q^2$  at fixed  $x$ . This is illustrated with the kinematic plane and iso-energy and iso-angle lines,  
 1291 see Fig. 3.2. It is instructive to see how the variation of the proton beam energy changes  
 1292 the kinematics considerably and enables additional coverage of various regions. This is clear  
 1293 from Fig. 3.3 which shows the kinematic plane choosing the approximate minimum energies  
 1294 the LHeC could operate with. There are striking changes one may note which are related to  
 1295 kinematics (c.f. Ref. [57]). For example, one can see that the line of  $\theta_e = 179^\circ$  now corresponds  
 1296 to  $Q^2 \simeq 0.1 \text{ GeV}^2$  which is due to lowering  $E_e$  as compared to  $1 \text{ GeV}^2$  in the maximum energy  
 1297 case, cf. Fig. 3.2. Similarly, comparing the two figures one finds that the lower  $Q^2$ , larger  
 1298  $x$  region becomes more easily accessible with lower energies, in this case solely owing to the  
 1299 reduction of  $E_p$  from 7 to 1 TeV. It is worthwhile to note that the LHeC, when operating at  
 1300 these low energies, would permit a complete repetition of the HERA programme, within a short  
 1301 period of special data taking.

1302 The coverage of the kinematic plane is illustrated in the plot of the  $x, Q^2$  bin centers of data  
 1303 points used in simulations, see Fig. 3.4 [58]. The full coverage at highest Bjorken- $x$ , i.e. very  
 1304 close to  $x = 1$ , is enabled by the high luminosity of the LHeC. This was impossible to achieve for  
 1305 HERA as the NC/CC DIS cross sections decrease proportional to some power of  $(1 - x)$  when  
 1306  $x$  approaches 1, as has long been established with Regge counting [59–61].

1307 It has been a prime goal, leading beyond previous PDF studies, to understand the importance of

<sup>4</sup>With a linac source, the generation of an intense positron beam is very challenging and will not be able to compete with the electron intensity. This is discussed in the accelerator chapter.

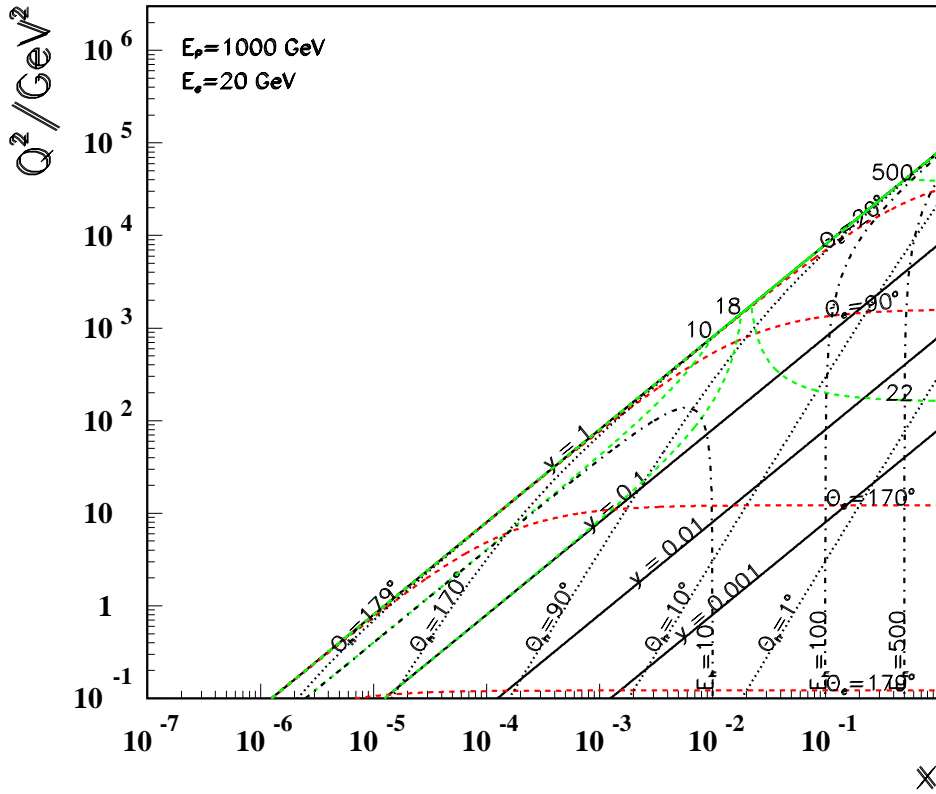


**Figure 3.3:** Kinematic plane covered with the minimum beam energies at LHeC. The meaning of the curves is the same as in the previous figure. This coverage is very similar to that by HERA as the energies are about the same.

1308 these varying data taking conditions for measuring PDFs with the LHeC. This holds especially  
 1309 for the question about what can be expected from an initial, lower luminosity LHeC operation  
 1310 period, which is of highest interest for the LHC analyses during the HL-LHC phase. Some  
 1311 special data sets of lowered electron energy have also been produced in order to evaluate the  
 1312 potential to measure  $F_L$ , see Sect. 4.2.3. These data sets have not been included in the bulk  
 1313 PDF analyses presented subsequently in this Chapter.

### 1314 3.2.2 Heavy Quark Structure Functions

1315 The LHeC is the ideal environment for a determination of the strange, charm and bottom  
 1316 density distributions which is necessary for a comprehensive unfolding of the parton contents  
 1317 and dynamics in protons and nuclei. The principal technique is charm tagging (in CC for  
 1318  $xs$ , in NC for  $xc$ ) and bottom tagging (in NC for  $xb$ ). The beam spot of the LHeC has a  
 1319 transverse extension of about  $(7 \mu\text{m})^2$ . The inner Silicon detectors has a resolution of typically  
 1320 10 microns to be compared with decay lengths of charm and beauty particles of hundreds of  
 1321  $\mu\text{m}$ . The experimental challenges then are the beam pipe radius, coping at the LHeC with  
 1322 strong synchrotron radiation effects, and the forward tagging acceptance, similar to the HL-  
 1323 LHC challenges albeit much easier through the absence of pile-up in  $ep$ . Very sophisticated  
 1324 techniques are being developed at the LHC in order to identify bottom production through  
 1325 jets [62] which are not touched upon here.

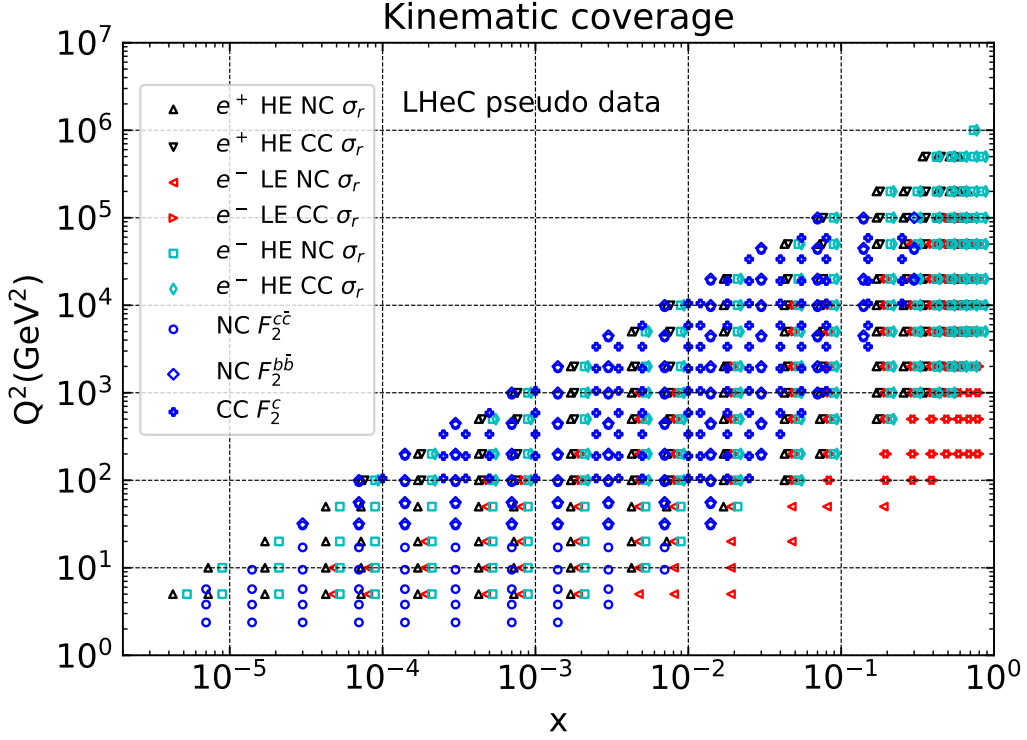


**Figure 3.4:** Illustration of the  $x, Q^2$  values of simulated cross section and heavy quark density data used in LHeC studies. The red points illustrate the gain in acceptance towards large  $x$  at fixed  $Q^2$  when  $E_p$  is lowered, see text.

1326 A simulation was made of the possible measurements of the anti-strange density (Fig. 3.5) using  
 1327 impact parameter tagging in  $ep$  CC scattering, and of the charm and beauty structure functions  
 1328 using  $c$  and  $b$  tagging in NC (Figs. 3.6, 3.7). The results served as input for the PDF study  
 1329 subsequently presented.

1330 Following experience on heavy flavour tagging at HERA and ATLAS, assumptions were made  
 1331 on the charm and beauty tagging efficiencies, to be 10 % and 60 %, respectively. The light-quark  
 1332 background in the charm analysis is assumed to be controllable to per cent level, while the  
 1333 charm background in the beauty tagging sample is assumed to be 10 %. The tagging efficiencies  
 1334 and background contaminations affect the statistical error which for the assumed  $100 \text{ fb}^{-1}$  is  
 1335 negligible, apart from edges of phase space as the figures illustrate for all three distribution.

1336 An additional uncorrelated systematic error is assumed in the simulated strange and beauty  
 1337 quark measurements of 3 % while for charm a 2 % error is used. These errors determine the mea-  
 1338 surement uncertainties in almost the full kinematic range. At higher  $Q^2$  and  $x$ , these increase,  
 1339 for example to 10, 5 and 7 % for  $xs$ ,  $xc$  and  $xb$ , respectively, at  $x \simeq 0.1$  and  $Q^2 \simeq 10^5 \text{ GeV}^2$ . As  
 1340 is specified in the figures, the  $x$  and  $Q^2$  ranges of these measurements extend over 3, 5 and 4  
 1341 orders of magnitude for  $s$ ,  $c$  and  $b$ . The coverage of very high  $Q^2$  values, much beyond  $M_Z^2$ , per-  
 1342 mits to determine the  $c$  and  $b$  densities probed in  $\gamma Z$  interference interactions for the first time.  
 1343 At HERA,  $xs$  was not directly accessible while pioneering measurements of  $xc$  and  $xb$  could be  
 1344 performed [63], albeit in a smaller range and less precise than shall be achieved with the LHeC.  
 1345 These measurements, as discussed below and in much detail in the 2012 LHeC CDR [1], are of  
 1346 vital importance for the development of QCD and for the interpretation of precision LHC data.

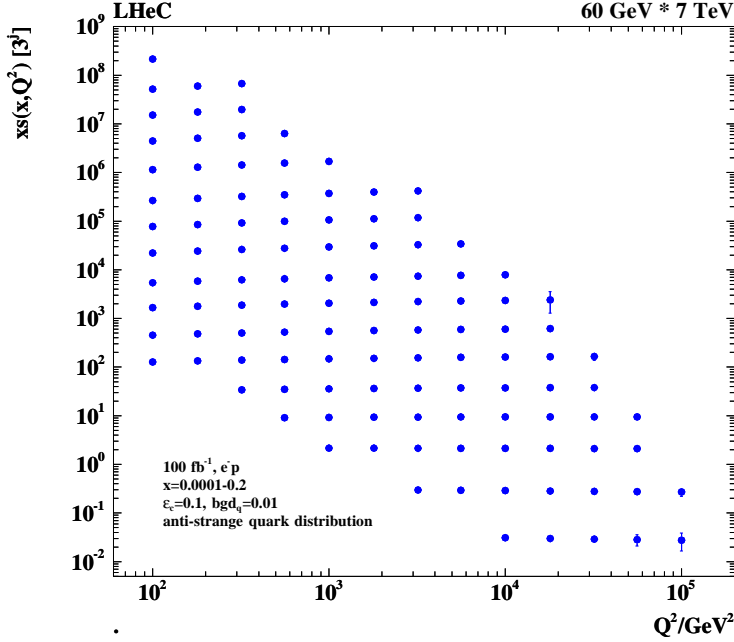


**Figure 3.5:** Simulation of the measurement of the (anti)-strange quark distribution,  $x\bar{s}(x, Q^2)$ , in charged current  $e^-p$  scattering through the t-channel reaction  $W^- \bar{s} \rightarrow c$ . The data are plotted with full systematic and statistical errors added in quadrature, mostly non-visible. The covered  $x$  range extends from  $10^{-4}$  (top left bin), determined by the CC trigger threshold conservatively assumed to be at  $Q^2 = 100 \text{ GeV}^2$ , to  $x \simeq 0.2$  (bottom right) determined by the forward tagging acceptance limits, which could be further extended by lowering  $E_p$ .

### 1347 3.3 Parton Distributions from the LHeC

#### 1348 3.3.1 Procedure and Assumptions

1349 In this section, PDF constraints from the simulation of LHeC inclusive NC and CC cross section  
 1350 measurements and heavy quark densities are investigated. The analysis closely follows the one  
 1351 for HERA as presented above.

1352 The expectations on PDFs for the “LHeC inclusive” dataset, corresponding to the combination  
 1353 of datasets D4+D5+D6+D9, are presented, see Tab. 3.2. These datasets have the highest sen-  
 1354 sitivity to general aspects of PDF phenomenology. Since the data are recorded concurrently to  
 1355 the HL-LHC operation they will become available only after the end of the HL-LHC. There-  
 1356 fore, these PDFs will be valuable for re-analysis or re-interpretation of (HL-)LHC data, and for  
 1357 further future hadron colliders.

1358 In order that LHeC will be useful already during the lifetime of the HL-LHC, it is of high rele-  
 1359 vance that the LHeC can deliver PDFs of transformative precision already on a short timescale.  
 1360 Therefore, in the present study particular attention is paid to PDF constraints that can be ex-  
 1361 tracted from the first  $50 \text{ fb}^{-1}$  of electron-proton data, which corresponds to the first three years  
 1362 of LHeC operation. The dataset is labelled D2 in Tab. 3.2 and also referred to as “LHeC 1st run”  
 1363 in the following.

1364 Already the data recorded during the initial weeks of data taking will be highly valuable and  
 1365 impose new PDF constraints. This is because already the initial instantaneous luminosity will  
 1366 be comparably high, and the kinematic range is largely extended in comparison to the HERA

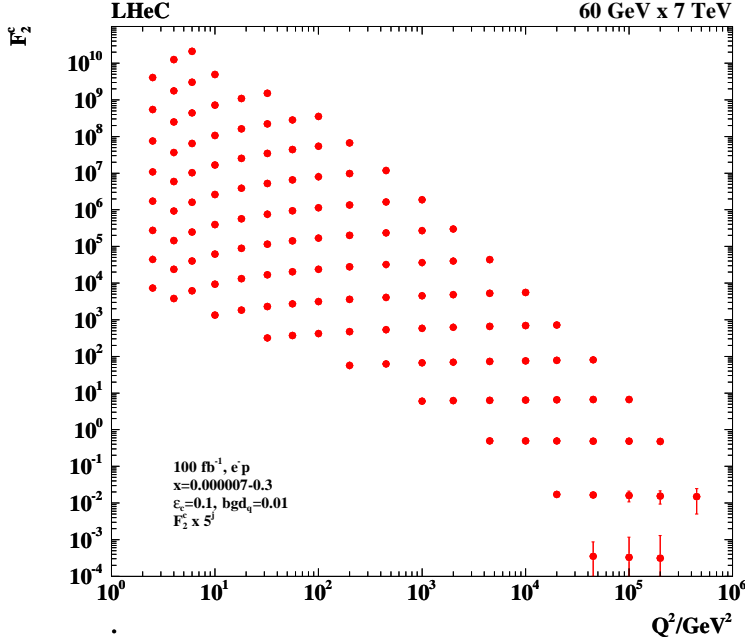


**Figure 3.6:** Simulation of the measurement of the charm quark distribution expressed as  $F_2^c = e_c^2 x(c + \bar{c})$  in neutral current  $e^-p$  scattering. The data are plotted with full systematic and statistical errors added in quadrature, mostly invisible. The minimum  $x$  (left top bin) is at  $7 \cdot 10^{-6}$ , and the data extend to  $x = 0.3$  (right bottom bin). The simulation uses a massless scheme and is only indicative near threshold albeit the uncertainties entering the QCD PDF analysis are estimated consistently.

1367 data. These initial analyses will provide the starting point for the LHeC PDF programme. It  
 1368 may be recalled that the HERA I data period (1992-2000) provided just  $0.1 \text{ fb}^{-1}$  of data which  
 1369 was ample for discovering the rise of  $F_2$  and of  $xg$  towards small  $x$  at low  $Q^2$ , and still today  
 1370 these data form the most important ingredient to the combined legacy HERA data [43]. The  
 1371 sets in Tab. 3.2 comprise D1, with  $5 \text{ fb}^{-1}$ , still the tenfold of what H1 collected in 15 years, and  
 1372 D3, which resembles D2 but has the electron polarisation set to zero.

1373 Additional dedicated studies of the impact of  $s, c, b$  data on the PDFs are then also presented,  
 1374 based on  $10 \text{ fb}^{-1}$  of  $e^-p$  simulated data. Further important PDF constraints that would be  
 1375 provided by measurements of  $F_L$  and jets are not considered in the present study. These remarks  
 1376 are significant in that they mean one has to be cautious when comparing the LHeC PDF potential  
 1377 with some global fits:  $F_L$  will resolve the low  $x$  non-linear parton interaction issue, see Sect. 4.2.3,  
 1378 and jets are important to pin down the gluon density behaviour at large  $x$  as well as providing  
 1379 a precision measurement of  $\alpha_s$ , Sect. 4.1.

1380 To assess the importance of different operating conditions, the impact of datasets with: differ-  
 1381 ing amounts of integrated luminosity (D1 vs. D4); positrons (D6 vs. D7); and with different  
 1382 polarisation states for the leptons (D3 vs. D8) are also considered.

1383 In the following, PDF fits are presented, which make use of the simulated data and NLO QCD  
 1384 predictions. Fits in NNLO have been performed as a cross check. The analysis follows closely  
 1385 the HERAPDF procedure (c.f. Sect. 3.1.2 and Ref. [43]). The parametric functions in Eqs. (3.1)  
 1386 and (3.2) are used, and the parameterised PDFs are the valence distributions  $xu_v$  and  $xd_v$ , the  
 1387 gluon distribution  $xg$ , and the  $x\bar{U}$  and  $x\bar{D}$  distributions, using  $x\bar{U} = x\bar{u}$  and  $x\bar{D} = x\bar{d} + x\bar{s}$ .  
 1388 In total the following 14 parameters are set free for the nominal fits:  $B_g, C_g, D_g, B_{uv}, C_{uv}$ ,

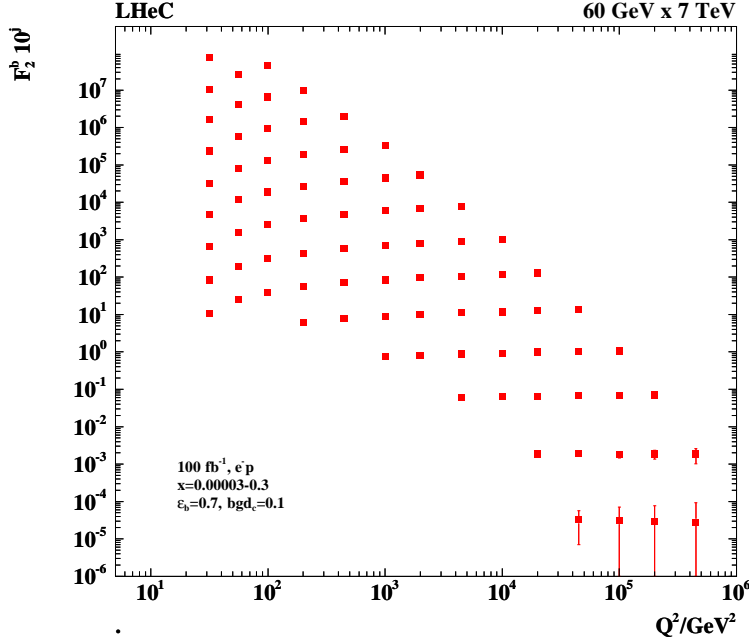


**Figure 3.7:** Simulation of the measurement of the bottom quark distribution expressed as  $F_2^b = e_b^2 x(b+\bar{b})$  in neutral current  $e^-p$  scattering. The data are plotted with full systematic and statistical errors added in quadrature, mostly invisible. The minimum  $x$  (left top bin) is at  $3 \cdot 10^{-5}$ , and the data extend to  $x = 0.3$  (right bottom bin). The simulation uses a massless scheme and is only indicative near threshold albeit the uncertainties entering the QCD PDF analysis are estimated consistently.

1389  $E_{uv}, B_{dv}, C_{dv}, A_{\bar{U}}, B_{\bar{U}}, C_{\bar{U}}, A_{\bar{D}}, B_{\bar{D}}, C_{\bar{D}}$ . These fit parameters are similar to HERAPDF2.0,  
 1390 albeit to some extent more flexible due to the stronger constraints from the LHeC. Note, the  $B$   
 1391 parameters for  $u_v$  and  $d_v$ , and the  $A$  and  $B$  parameters for  $\bar{U}$  and  $\bar{D}$  are fitted independently,  
 1392 such that the up and down valence and sea quark distributions are uncorrelated in the analysis,  
 1393 whereas for HERAPDF2.0  $x\bar{u} \rightarrow x\bar{d}$  as  $x \rightarrow 0$  is imposed. The other main difference is that no  
 1394 negative gluon term has been included, i.e.  $A'_g = 0$  but  $D_g \neq 0$ .

1395 This ansatz is natural to the extent that the NC and CC inclusive cross sections determine  
 1396 the sums of up and down quark distributions, and their anti-quark distributions, as the four  
 1397 independent sets of PDFs, which may be transformed to the ones chosen if one assumes  $u_v =$   
 1398  $U - \bar{U}$  and  $d_v = D - \bar{D}$ , i.e. the equality of anti- and sea-quark distributions of given flavour. For  
 1399 the majority of the QCD fits presented here, the strange quark distribution at  $Q_0^2$  is assumed to  
 1400 be a constant fraction of  $\bar{D}$ ,  $x\bar{s} = f_s x\bar{D}$  with  $f_s = 0.4$  as for HERAPDF, while this assumption  
 1401 is relaxed for the fits including simulated  $s, c, b$  data.

1402 Note, that the prospects presented here are illustrations for a different era of PDF physics, which  
 1403 will be richer and deeper than one may be able to simulate now. For instance, without real data  
 1404 one cannot determine the actual parameterisation needed for the PDFs. In particular the low  $x$   
 1405 kinematic region was so far unexplored and the simulated data relies on a simple extrapolation  
 1406 of current PDFs, and no reliable data or model is available that provides constraints on this  
 1407 region<sup>5</sup>. The LHeC data explores new corners of phase space with high precision, and therefore

<sup>5</sup>It is expected that real LHeC data, and also the inclusion of further information such as  $F_L$ , will certainly lead to a quite different optimal parameterisation ansatz than was used in the present analysis. Though, it has been checked that with a more relaxed set of parameters, very similar results on the PDF uncertainties are obtained, which justifies the size of the prospected PDF uncertainties.

1408 it will have a great potential, much larger than HERA had, to determine the parameterisation.  
 1409 As another example, with LHeC data one can directly derive relations for how the valence quarks  
 1410 are determined with a set of NC and CC cross section data in a redundant way, since the gluon  
 1411 distribution at small  $x$  can be determined from the  $Q^2$  derivative of  $F_2$  and from a measurement  
 1412 of  $F_L$ . The question of the optimal gluon parameterisation may then be settled by analysing  
 1413 these constraints and not by assuming some specific behaviour of a given fit.

1414 Furthermore, the precise direct determinations of  $s$ ,  $c$  and  $b$  densities with measurements of the  
 1415 impact parameter of their decays, will put the treatment of heavy flavours in PDF analyses on  
 1416 a new level. The need for the phenomenological introduction of the  $f_s$  factor will disappear and  
 1417 the debate on the value of fixed and variable heavy flavour schemes will be settled.

### 1418 3.3.2 Valence Quarks

1419 Since the first measurements of DIS physics, it had been proposed to identify partons with quarks  
 1420 and to consider the proton to consist of valence quarks together with “an indefinite number of  
 1421  $(q\bar{q})$  pairs” [64]. 50 years later there are still basic questions unanswered about the behaviour of  
 1422 valence quarks, such as the  $d_v/u_v$  ratio at large  $x$ , and PDF fits struggle to resolve the flavour  
 1423 composition and interaction dynamics of the sea. The LHeC is the most suited machine to  
 1424 resolve these challenges.

1425 The precision that can be expected for the valence quark distributions from the LHeC is illus-  
 1426 trated in Fig. 3.8, and compared to a variety of modern PDF sets. Today, the knowledge of  
 1427 the valence quark distributions, particularly at large  $x$ , is fairly limited as it can be derived  
 1428 from the Figure. This is due to the limited HERA luminosity, challenging systematics that rise  
 1429  $\propto 1/(1-x)$ , and to nuclear correction uncertainties. At low  $x$  the valence quark distributions  
 1430 are very small compared to the sea quarks and cannot be separated easily from these.

1431 The  $u$  valence quark distribution is much better known than the  $d$  valence, since it enters with a  
 1432 four-fold weight in  $F_2$  due to the electric quark charge ratio squared. Nevertheless, a substantial  
 1433 improvement in  $d_v$  by the LHeC is also visible, because the relative weight of  $d_v$  to  $u_v$  is changing  
 1434 favourably towards the down quark due to the influence of weak NC and CC interactions at  
 1435 high  $Q^2$  where the LHeC is providing very accurate data. The strong constraints to the highest  
 1436  $x$  valence distributions are due to the very high integrated luminosity. Note, at the HL-LHC,  
 1437 albeit its high integrated luminosity, the highest  $x$  are there only accessible as convolutions with  
 1438 partons at lower  $x$ , and those can therefore not be well constrained.

1439 Note that the “LHeC 1st run” PDF, displayed by the yellow band in Fig. 3.8, includes only  
 1440 electron, i.e. no positron, data. In fact, from the  $e^\pm p$  cross section differences access to valence  
 1441 quarks at low  $x$  can be obtained. As has already been illustrated in the CDR from 2012 [1] the  
 1442 sum of  $2u_v + d_v$  may be measured directly with the NC  $\gamma Z$  interference structure function  $x F_3^{\gamma Z}$   
 1443 down to  $x \simeq 10^{-4}$  with very good precision. Thus the LHeC will have a direct access to the  
 1444 valence quarks at small  $x$ . This also tests the assumption of the equality of sea- and anti-quark  
 1445 densities which if different would cause  $x F_3^{\gamma Z}$  to rise towards small  $x$ .

1446 As becomes evident in Fig. 3.8 there is a striking difference and even contradiction between the  
 1447 estimates of the uncertainties of the parton distributions between the various fit groups. This is  
 1448 due to different fit technologies but as well a result of different choices of data and assumptions  
 1449 on the  $d/u$  ratio. Such major uncertainties would be resolved by the LHeC.

1450 The precise determinations of the valence quark distributions at large  $x$  have strong implications  
 1451 for physics at the HL-LHC, in particular for BSM searches. The precise determinations of the  
 1452 valence quarks will resolve the long standing mystery of the behaviour of the  $d/u$  ratio at large  $x$ ,

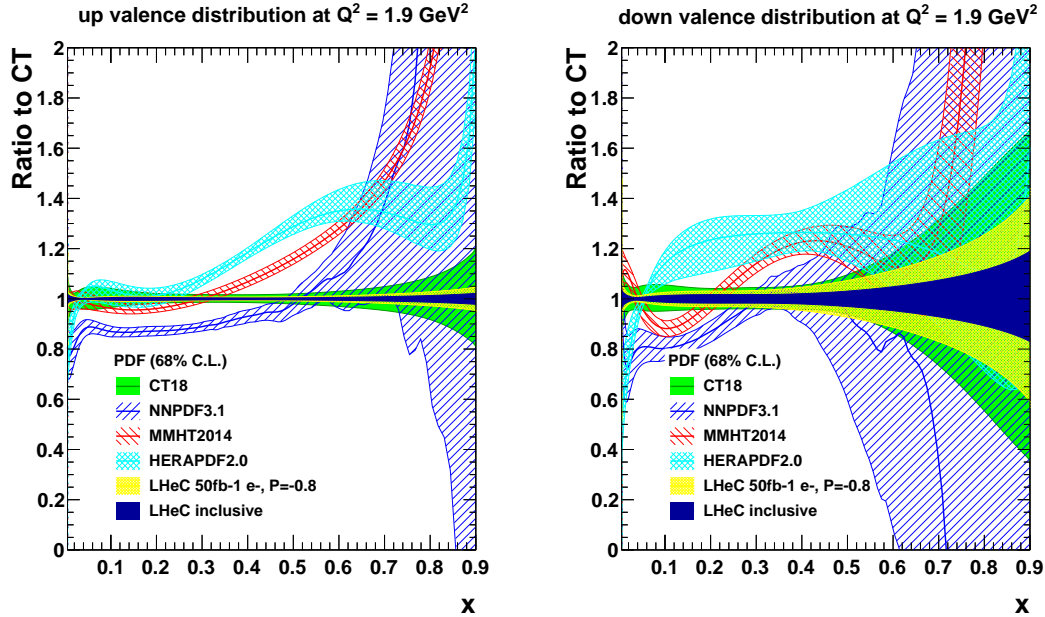


**Figure 3.8:** Valence quark distributions at  $Q^2 = 1.9 \text{ GeV}^2$  as a function of  $x$ , presented as the ratio to the CT14 [65] central values. The yellow band corresponds to the “LHeC 1st run” PDFs (D2), while the dark blue shows the final “LHeC inclusive” PDFs based on the data sets (D4+D5+D6+D9), as described in Sect. 3.3.1. For the purposes of illustrating the improvement to the uncertainties more clearly, the central value of the LHeC PDF has been scaled to the CT14 PDF, which itself is displayed by the green band.

1453 see Fig. 3.9. As exemplarily shown in Fig. 3.9, there are currently conflicting theoretical pictures  
 1454 for the central value of the  $d/u$  ratio, albeit the large uncertainty bands of the different PDF  
 1455 sets mainly overlap. As of today, the constraints from data are inconclusive statistically and  
 1456 also suffer from large uncertainties from the use of DIS data on nuclear targets, which therefore  
 1457 cause those large uncertainties.

### 1458 3.3.3 Light Sea Quarks

1459 Our knowledge today about the anti-quark distributions is fairly poor and uncertainties are very  
 1460 large at smaller values of  $x$ , and also at the highest  $x$ . In particular, at low  $x$  the size of the  
 1461 anti-quark PDFs are large and they contribute significantly to precision SM measurements at  
 1462 the HL-LHC. At high  $x$ , sea and valence need to be properly distinguished and accurately be  
 1463 measured for reliable BSM searches at high mass.

1464 Our knowledge about the anti-quark PDFs will be changed completely with LHeC data. Pre-  
 1465 cise constraints are obtained with inclusive NC/CC DIS data despite the relaxation of any  
 1466 assumptions in the fit ansatz that would force  $\bar{u} \rightarrow \bar{d}$  as  $x \rightarrow 0$ , as it is present in other PDF  
 1467 determinations today. At smaller  $Q^2$  in DIS one measures essentially  $F_2 \propto 4\bar{U} + \bar{D}$ . Thus, at  
 1468 HERA, with limited precision at high  $Q^2$ , one could not resolve the two parts, and neither will  
 1469 that be possible at any other lower energy  $ep$  collider which cannot reach small  $x$ . At the LHeC,  
 1470 in contrast, the CC DIS cross sections are measured very well down to  $x$  values even below  $10^{-4}$ ,  
 1471 and in addition there are strong weak current contributions to the NC cross section which probe  
 1472 the flavour composition differently than the photon exchange does. This enables this distinction  
 1473 of  $\bar{U}$  and  $\bar{D}$  at the LHeC.



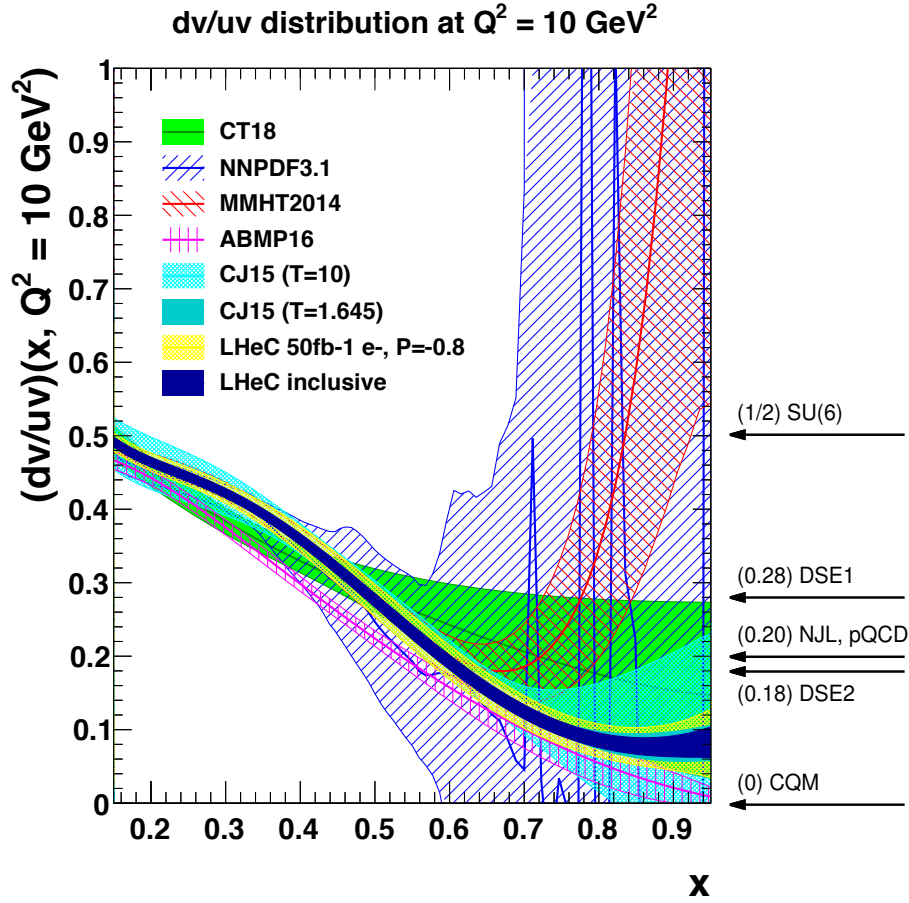


**Figure 3.9:** The  $d_v/u_v$  distribution at  $Q^2 = 10 \text{ GeV}^2$  as a function of  $x$ . The yellow band corresponds to the “LHeC 1st run” PDFs (D2), while the dark blue shows the final “LHeC inclusive” result. Both LHeC PDFs shown are scaled to the central value of CT14.

1474 The distributions of  $\bar{U}$  and  $\bar{D}$  for the PDFs from the 1st run and the “LHeC inclusive data” are  
 1475 shown in Figs. 3.10 and 3.11 for  $Q^2 = 1.9 \text{ GeV}^2$  and  $Q^2 = 10^4 \text{ GeV}^2$ , respectively, and compared  
 1476 to present PDF analyses. One observes a striking increase in precision for both  $\bar{U}$  and  $\bar{D}$  which  
 1477 persists from low to high scales. The relative uncertainty is large at high  $x \geq 0.5$ . However, in  
 1478 that region the sea-quark contributions are already very tiny. In the high  $x$  region one recognises  
 1479 the value of the full LHeC data sample fitted over the initial one while the uncertainties below  
 1480  $x \simeq 0.1$  of both the small and the full data sets are of comparable, very small size.

### 1481 3.3.4 Strange Quark

1482 The determination of the strange PDF has generated significant controversy in the literature for  
 1483 more than a decade. Fixed-target neutrino DIS measurements [66–70] typically prefer a strange  
 1484 PDF that is roughly half of the up and down sea distribution;  $\kappa = (s + \bar{s})/(\bar{u} + \bar{d}) \sim 0.5$ . The  
 1485 recent measurements from the LHC [71–74] and related studies [75, 76] suggest a larger strange  
 1486 quark distribution, that may potentially even be larger than the up and down sea quarks. The  
 1487  $x$  dependence of  $xs$  is essentially unknown, and it may differ from that of  $x\bar{d}$ , or  $x(\bar{u} + \bar{d})$ , by  
 1488 more than a normalisation factor.

1489 The precise knowledge of the strange quark PDF is of high relevance, since it provides a signif-

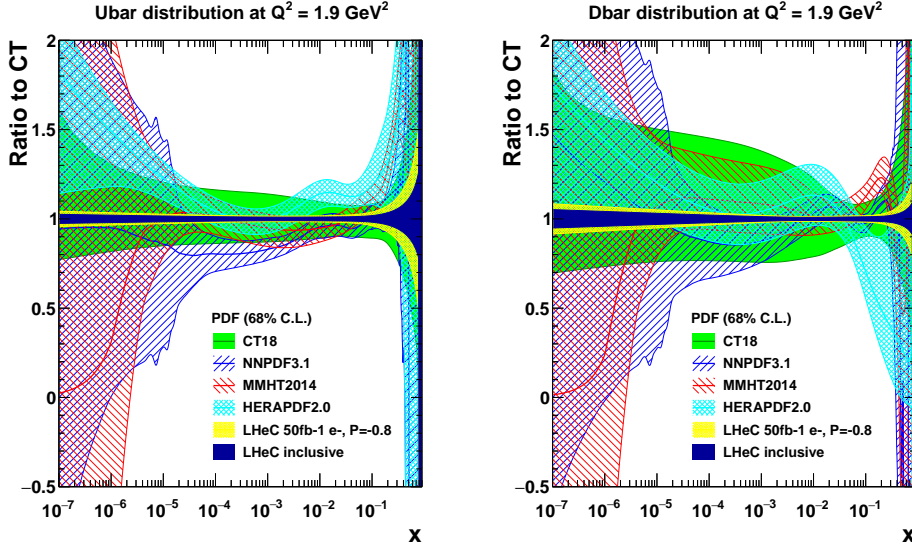


**Figure 3.10:** Sea quark distributions at  $Q^2 = 1.9 \text{ GeV}^2$  as a function of  $x$ , presented as the ratio to the CT14 central values. The yellow band corresponds to the “LHeC 1st run” PDFs (D2), while the dark blue shows the final “LHeC inclusive” PDFs (D4+D5+D6+D9), as described in the text. Both LHeC PDFs shown are scaled to the central value of CT14.

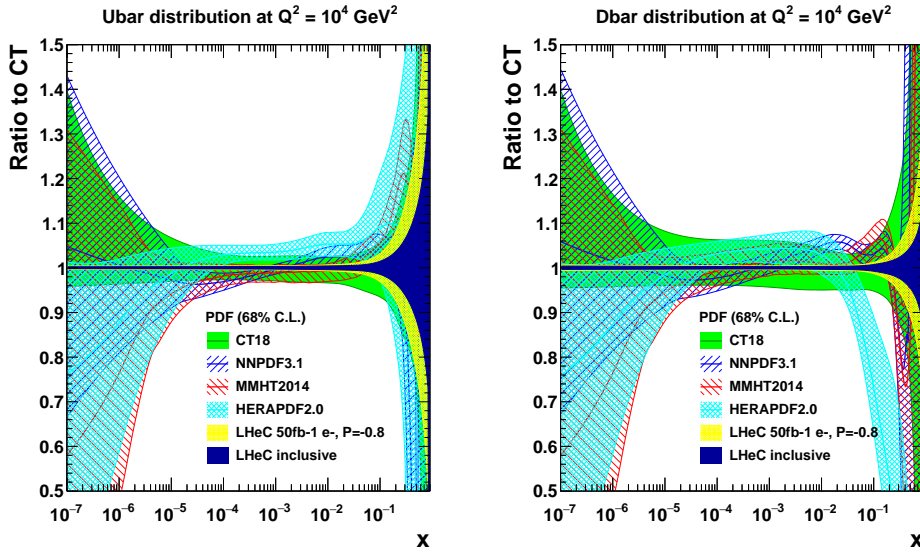


**Figure 3.11:** Sea quark distributions at  $Q^2 = 10^4 \text{ GeV}^2$  as a function of  $x$ , presented as the ratio to the CT14 central values. The yellow band corresponds to the “LHeC 1st run” PDFs (D2), while the dark blue shows the final “LHeC inclusive” PDFs (D4+D5+D6+D9), as described in the text. Both LHeC PDFs shown are scaled to the central value of CT14.

1490 icant contribution to *standard candle* measurements at the HL-LHC, such as  $W/Z$  production,  
 1491 and it imposes a significant uncertainty on the  $W$  mass measurements at the LHC. The question  
 1492 of light-sea flavour ‘democracy’ is of principle relevance for QCD and the parton model. For the  
 1493 first time, as has been presented in Sect. 3.2.2,  $x\bar{s}(x, Q^2)$  can be accurately measured, namely  
 1494 through the charm tagging  $Ws \rightarrow c$  reaction in CC  $e^-p$  scattering at the LHeC. The inclusion  
 1495 of the CC charm data in the PDF analysis will settle the question of how strange the strange

1496 quark distribution really is <sup>6</sup>. This prospect has been analysed within the LHeC fit framework  
 1497 here introduced and as well studied in detail in a profiling analysis using *xFitter*. Both analyses  
 1498 yield rather compatible results and are presented in the following.

1499 In the standard LHeC fit studies, the parameterised PDFs are the four quark distributions  $xu_v$ ,  
 1500  $xd_v$ ,  $x\bar{U}$ ,  $x\bar{D}$  and  $xg$  (constituting a 4+1 parameterisation), as the inclusive NC and CC data  
 1501 determine only the sums of the up and down quark and anti-quark distribution, as discussed  
 1502 previously. The strange quark PDF is then assumed to be a constant fraction of  $x\bar{d}$ .

1503 With the strange quark data available, the LHeC PDF fit parameterisations can be extended  
 1504 to include  $xs = x\bar{s}$ , parameterised as  $A_s x^{B_s} (1-x)^{C_s}$  <sup>7</sup>. For the fits presented in the following,  
 1505 the  $\bar{d}$  and  $\bar{s}$  are treated now separately, and therefore a total of five quark distributions are  
 1506 parameterised ( $xu_v$ ,  $xd_v$ ,  $x\bar{U}$ ,  $x\bar{d}$ ,  $x\bar{s}$ ) as well as  $g$ . This provides a 5+1 parameterisation, and  
 1507 the total number of free parameters of the PDF fit then becomes 17.

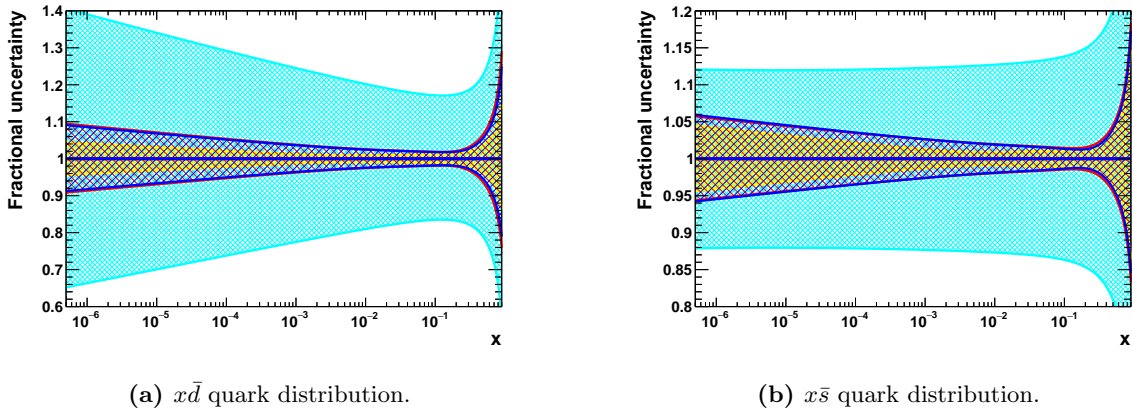


**Figure 3.12:** PDF uncertainties at  $Q^2 = 1.9 \text{ GeV}^2$  as a function of  $x$  for the  $\bar{d}$  and  $\bar{s}$  distributions. The yellow band displays the uncertainties of the nominal “LHeC inclusive” PDF, which was obtained in a 4+1 PDF fit. From the same dataset, results of the more flexible 5+1 fit (see text) are displayed as a cyan band. The red band displays the results, when in addition an LHeC measurement of the  $\bar{s}$  quark density is included. When even further including LHeC measurements of  $F_2^c$  and  $F_2^b$ , the PDF fits yields uncertainties as displayed by the blue band.

1508 Results of the 5+1 PDF fits are shown in Fig. 3.12, where fits to inclusive NC/CC DIS data are  
 1509 displayed as reference (both for the 4+1 and 5+1 ansatz) and the fits where in addition strange  
 1510 density measurements and even further measurements of  $F_2^{c,b}$  are considered. As expected, the  
 1511 uncertainties of the 5+1 fit to the inclusive DIS data, especially on the  $\bar{d}$  and  $\bar{s}$  distributions  
 1512 (c.f. Fig. 3.12), become substantially larger in comparison to the respective 4+1 fit, since the  $\bar{d}$   
 1513 and  $\bar{s}$  distributions are treated now separately. This demonstrates that the inclusive DIS data  
 1514 alone does not have the flavour separating power to determine the individual distributions very  
 1515 precisely.

1516 When including an LHeC measurement of the  $\bar{s}$  quark density based on  $10 \text{ fb}^{-1}$  of  $e^-p$  data, the  
 1517 uncertainties on the  $\bar{d}$  and  $\bar{s}$  PDFs become significantly smaller. By chance, those uncertainties

<sup>6</sup>The provision of positron-proton data will enable very interesting tests of charge symmetry, i.e. permit to search for a difference between the strange and the anti-strange quark densities. This has not been studied in this paper.

<sup>7</sup>It is worth mentioning that the  $W, Z$  data [71] essentially determine only a moment of  $xs$  at  $x \sim 0.02$ , not the  $x$  dependence. Therefore, in analyses of HERA and ATLAS data such as Ref. [76], there is no determination attempted of the relevant parameter,  $B_s$ , which instead is set equal to  $B_{\bar{d}}$ . The kinematic dependence of  $xs$  is basically not determined by LHC data while the hint to the strange being unsuppressed has been persistent.

1518 are then comparable to the 4+1 fit in which  $x\bar{s}$  is linked to  $x\bar{d}$  by a constant fraction.

1519 The constraints from a measurement of charm quark production cross sections in charged current  
 1520 DIS have also been studied in a profiling analysis using *xFitter* [77]. The treatment of heavy  
 1521 quark production to higher orders in pQCD is discussed extensively in this paper. At leading-  
 1522 order QCD, the subprocess under consideration is  $W s \rightarrow c$ , where the  $s$  represents an intrinsic  
 strange quark. Fig. 3.13 displays the tight constraints obtained for the strange PDF when

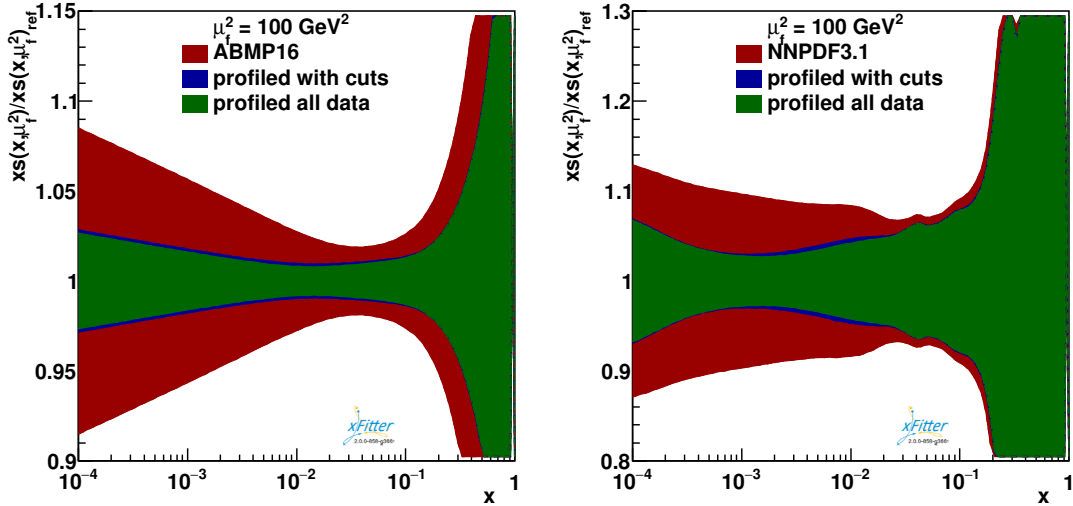


**Figure 3.13:** Constraints on the strange quark PDF  $x s$  using simulated data for charged-current production of charm quarks at the LHeC, from a profiling study [77] using the ABMP16 (left) and the NNPDF3.1 (right) PDF sets. The red band displays the nominal PDF uncertainties, and the green and blue bands the improved uncertainties due to the LHeC strange quark data.

1523 using the LHeC pseudo-data for the CC charm production channel. The results of this profiling  
 1524 analysis, both when based on the ABM16 and the NNPDF3.1 PDF sets, and of the direct fit  
 1525 presented above, are very similar, reaching about 3 – 5 % precision for  $x$  below  $\simeq 0.01$   
 1526

1527 In a variation of the study [77], a large reduction of uncertainties is already observed when  
 1528 restricting the input data to the kinematic range where the differences between the different  
 1529 heavy flavour schemes (VFNS and FFNS) are not larger than the present PDF uncertainties.  
 1530 This further indicates that the PDF constraints are stable and independent of the particular  
 1531 heavy-flavour scheme.

1532 It may thus be concluded that the LHeC, through high luminosity, energy and precise kinematic  
 1533 reconstruction, will be able to solve a long standing question about the role of the strange-quark  
 1534 density in the proton, and its integration into a consistent QCD treatment of parton dynamics.

### 1535 3.3.5 Heavy Quarks

1536 One of the unsolved mysteries of the Standard Model is the existence of three generations of  
 1537 quarks and leptons. The strongly interacting fermion sector contains altogether six quarks with  
 1538 masses differing by up to five orders of magnitude. This hierarchy of masses is on one hand a  
 1539 challenge to explain, on the other hand it offers a unique opportunity to explore dynamics at a  
 1540 variety of different scales and thus develop different facets of the strong interaction. While the  
 1541 light quarks at low scales are non-perturbative and couple strongly, the heavier quarks charm,  
 1542 bottom and top are separated from the soft sea by their masses and thus can serve as a suitable  
 1543 additional probe for the soft part of QCD.

1544 There are a number of deep and unresolved questions that can be posed in the context of  
1545 the proton structure: what is the individual contribution of the different quark flavours to the  
1546 structure functions?; are heavy quarks like charm and bottom radiatively generated or is there  
1547 also an intrinsic heavy quark component in the proton?; to what extent do the universality and  
1548 factorisation theorems work in the presence of heavy quarks? It is therefore imperative to be  
1549 able to perform precise measurements of each individual quark flavour and their contribution to  
1550 the proton structure. The LHeC is the ideal place for these investigations because it resolves the  
1551 complete composition of the proton flavour by flavour. In particular, as shown in Sect. 3.2.2, the  
1552 LHeC provides data on  $F_2^c$  and  $F_2^b$  extending over nearly 5 and 6 orders of magnitude in  $x, Q^2$ ,  
1553 respectively. These are obtained through charm and beauty tagging with high precision in NC  
1554  $ep$  scattering. A thorough PDF analysis of the LHeC data thus can be based on the inclusive  
1555 NC/CC cross sections and tagged  $s, c, b$  data. In addition, one may use DIS jets, here used for  
1556 the  $\alpha_s$  prospective study (Sect. 4.1) and low energy data, here analysed for resolving the low  $x$   
1557 dynamics with a precision measurement of  $F_L$  (Sect. 4.2.3). The current studies in this chapter  
1558 therefore must be understood as indicative only as we have not performed a comprehensive  
1559 analysis using all these data as yet <sup>8</sup>.

1560 The production of heavy quarks at HERA (charm and bottom) is an especially interesting  
1561 process as the quark mass introduces a new scale ( $m = m_{c,b}$ ) which was neither heavy or light  
1562 (see e.g. reviews [78, 79]). Actually, the treatment of heavy quark mass effects is essential in PDF  
1563 fits which include data from fixed target to collider energies and thus require the computation  
1564 of physical cross sections over a large range of perturbative scales  $\mu^2$ . With these scales passing  
1565 through (or close to) the thresholds for charm, bottom and, eventually, top, precise computations  
1566 demand the incorporation of heavy quark mass effects close to threshold,  $\mu^2 \sim m^2$ , and the  
1567 resummation of collinear logarithms  $\ln(\mu^2/m^2)$  at scales far above the threshold,  $\mu^2 \gg m^2$ . The  
1568 first problem can be dealt with through the use of massive matrix elements for the generation  
1569 of heavy quark-antiquark pairs but keeping a fixed number of parton densities (fixed flavour  
1570 number schemes, FFNS). On the other hand, the proper treatment of resummation is achieved  
1571 through the use of variable flavour number schemes (VFNS) which consider an increasing number  
1572 of massless parton species, evolved through standard DGLAP, when the scale is increased above  
1573 heavy quark mass thresholds. At present, calculations involving heavy quarks in DIS in different  
1574 schemes (generalised mass VFNS) with different numbers of active flavours participating to  
1575 DGLAP evolution are combined to derive an expression for the coefficient functions which is valid  
1576 both close to threshold, and far above it. Such multi-scale problems are particularly difficult,  
1577 and numerous techniques were developed to cope with this challenging problem [50, 80–88].  
1578 Additional complications, see e.g. Ref. [89], arise when the possibility of a non-perturbative  
1579 origin of heavy quark distributions is allowed above the heavy quark mass threshold - intrinsic  
1580 heavy flavour. The ABMP16 analysis [51] underlines that the available DIS data are compatible  
1581 with solely an FFNS treatment assuming that the heavy quarks are generated in the final state.

1582 At the LHeC, as illustrated in Figs. 3.6, 3.7, the large polar angle acceptance and the high  
1583 centre-of-mass energy allow heavy quark physics to be investigated from below threshold to  
1584 almost  $10^6 \text{ GeV}^2$ . The extended reach in comparison to HERA is dramatic. This permits to  
1585 comprehensively explore the *asymptotic* high energy limit where  $m_{c,b}^2/Q^2 \rightarrow 0$ , as well as the  
1586 low energy *decoupling* region  $m_{c,b}^2/Q^2 \sim 1$ .

1587 For the PDF determination the obviously direct impact of the tagged charm and bottom data  
1588 will be on the determination of  $xc$  and  $xb$ , and the clarification of their appropriate theoretical

---

<sup>8</sup>This is to be considered when one compares the precision of the inclusive PDF fits with so-called global analyses, for example regarding the behaviour of  $xg$  at large  $x$ .

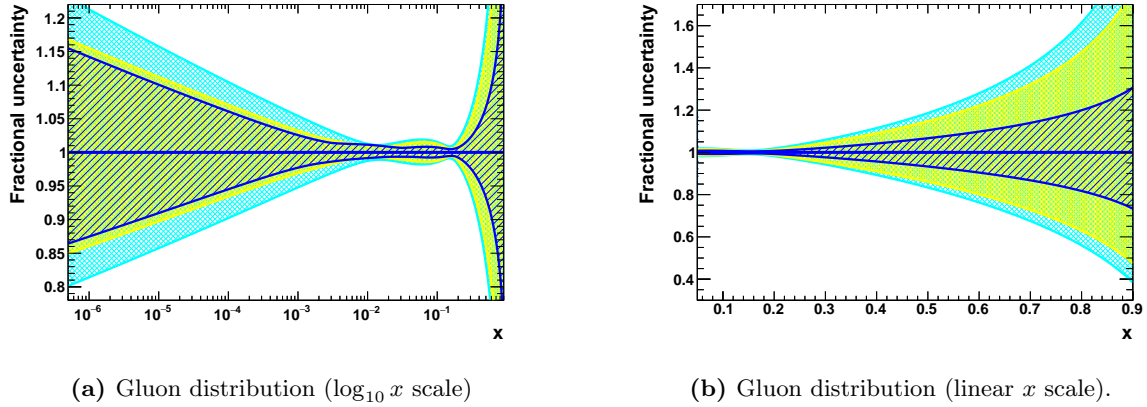


**Figure 3.14:** PDF uncertainties at  $Q^2 = 1.9 \text{ GeV}^2$  as a function of  $x$  to illustrate the constraints from additional heavy quark sensitive measurements at LHeC. Displayed is the gluon distribution on a logarithmic and linear scale. The yellow band illustrates the uncertainties of the nominal “LHeC inclusive” PDF, obtained in a 4+1 PDF fit. When further including LHeC measurements of  $F_2^c$  and  $F_2^b$ , the PDF fits yields uncertainties as displayed by the blue band.

1589 treatment. In addition, however, there is a remarkable improvement achieved for the determi-  
 1590 nation of the gluon density, see Fig. 3.14. The determination of  $xg$  will be discussed in much  
 1591 more detail in the following section.

1592 These channels will also strongly improve the determination of the charm and bottom quark  
 1593 masses and bring these uncertainties down to about  $\delta m_{c(b)} \simeq 3(10) \text{ MeV} [1]^9$ . These accuracies  
 1594 are crucial for eliminating the corresponding model uncertainties in the PDF fit. Precision  
 1595 tagged charm and bottom data are also essential for the determination of the  $W$ -boson mass in  
 1596  $pp$ , and the extraction of the Higgs  $\rightarrow c\bar{c}$  and  $b\bar{b}$  couplings in  $ep$ , as is discussed further below.

### 1597 3.3.6 The Gluon PDF

1598 The LHeC, with hugely increased precision and extended kinematic range of DIS, i.e. the  
 1599 most appropriate process to explore  $xg(x, Q^2)$ , can pin down the gluon distribution much more  
 1600 accurately than it is known today. This primarily comes from the extension of range and  
 1601 precision in the measurement of  $\partial F_2 / \partial \ln Q^2$ , which at small  $x$  is a direct measure of  $xg$ . The  
 1602 precision determination of the quark distributions, discussed previously, also strongly constrains  
 1603  $xg$ . Further sensitivity arises with the high- $y$  part of the NC cross section which is controlled  
 1604 by the longitudinal structure function as is discussed in Sect. 4.2.3.

1605 The result for the gluon distribution from the LHeC inclusive NC/CC data fits is presented in  
 1606 Fig. 3.15, and compared to several other PDF sets. On the left, the distribution is presented  
 1607 as a ratio to CT14, and is displayed on a log- $x$  scale to highlight the small  $x$  region. On the  
 1608 right, the  $xg$  distribution is shown on a linear- $x$  scale, accentuating the region of large  $x$ . The  
 1609 determination of  $xg$  will be radically improved with the LHeC NC and CC precision data, which  
 1610 provide constraints on  $\partial F_2 / \partial \ln Q^2$  down to very low  $x$  values,  $\geq 10^{-5}$ , and large  $x \leq 0.8$ .

1611 Below  $x \simeq 5 \cdot 10^{-4}$ , the HERA data have almost vanishing constraining power due to kinematic  
 1612 range limitations, as one needs a lever arm to determine the  $Q^2$  derivative, and so the gluon

<sup>9</sup>Such precision demands the availability of calculations with higher orders in pQCD, and those computations are already ongoing [90–92]. Note that in PDF fits the heavy quark mass is an effective parameter that has to be related with the pole mass, see e.g. Ref. [93] and refs. therein.

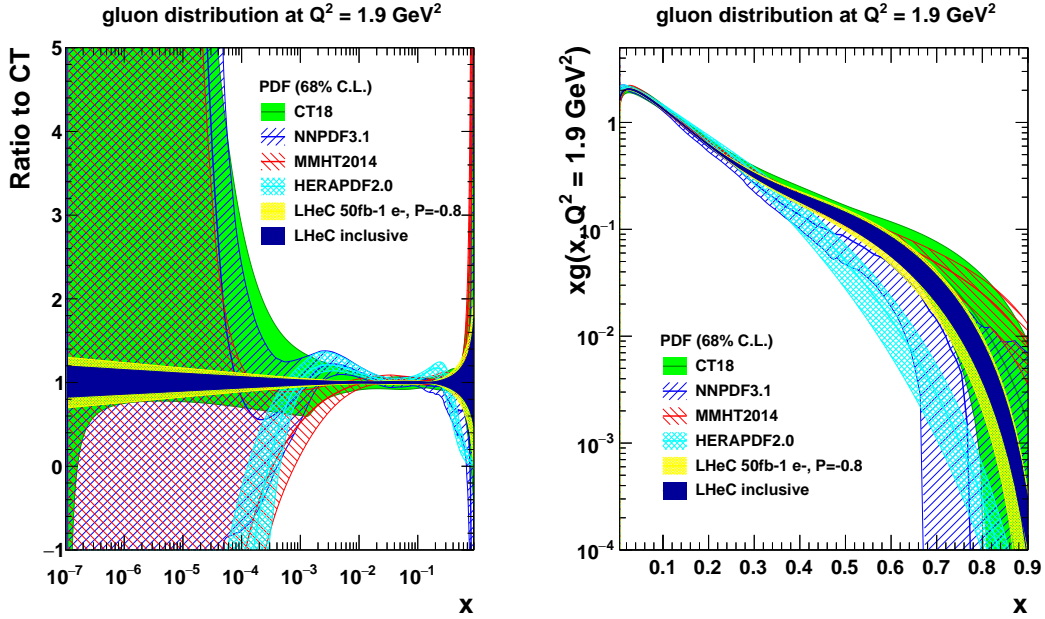


**Figure 3.15:** Gluon distribution at  $Q^2 = 1.9 \text{ GeV}^2$  as a function of  $x$ , highlighting (left) the low  $x$  and (right) the high  $x$  regions. The yellow band corresponds to the “LHeC 1st run” PDFs (D2), while the dark blue shows the “LHeC inclusive” PDFs (D4+D5+D6+D9), as described in the text. Both LHeC PDFs shown are scaled to the central value of CT14. The smooth extension of the LHeC  $xg$  uncertainty bands below  $x \simeq 10^{-5}$  is an artefact of the parameterisation.

1613 is simply not determined at lower  $x$ . This can be seen in all modern PDF sets. With the  
 1614 LHeC, a precision of a few per cent at small  $x$  becomes possible down to nearly  $10^{-5}$ . This  
 1615 should resolve the question of non-linear parton interactions at small  $x$  (cf. Sect. 4.2). It also  
 1616 has direct implications for the LHC (and even stronger for the FCC): with the extension of the  
 1617 rapidity range to about 4 at the HL-LHC by ATLAS and CMS, Higgs physics will become small  
 1618  $x$  physics for which  $xg$  must be known very accurately since  $gg \rightarrow H$  is the dominant production  
 1619 mechanism.

1620 At large  $x \geq 0.3$ , the gluon distribution becomes very small and large variations appear in  
 1621 its determination from several PDF groups, differing by orders of magnitude. That is related  
 1622 to uncertainties on jet measurements, theoretical uncertainties, and the fact that HERA did  
 1623 not have sufficient luminosity to cover the high  $x$  region where, moreover, the sensitivity to  $xg$   
 1624 diminishes, since the valence quark evolution is insensitive to it. For the LHeC, the sensitivity  
 1625 at large  $x$  comes as part of the overall package: large luminosity allowing access to  $x$  values close  
 1626 to 1, fully constrained quark distributions and strong constraints at small  $x$  which feed through  
 1627 to large  $x$  via the momentum sum rule. The high precision illustrated will be crucial for BSM  
 1628 searches at high scales. It is also important for testing QCD factorisation and scale choices, as  
 1629 well as pinning down electroweak effects.

1630 The analysis presented here has not made use of the additional information that can be provided  
 1631 at the LHeC in measurements of  $F_2^{c,b}$  (see Sect. 3.3.5) or  $F_L$ . The large  $x$  situation can be  
 1632 expected to further improve by using LHeC jet data, providing further, direct constraints at  
 1633 large  $x$  which, however, have not yet been studied in comparable detail.

1634 The LHeC is the ideal laboratory to resolve all unknowns of the gluon density, which is the  
 1635 origin for all visible mass in the universe, and one of the particular secrets of particle physics for

1636 the gluon cannot directly be observed but is confined inside hadrons. It is obvious that resolving  
 1637 this puzzle is an energy frontier DIS task and goal, including electron-ion scattering since the  
 1638 gluon inside heavy matter is known even much less. Therefore, the special importance of this  
 1639 part of high energy PDF physics is not primarily related to the smallness of uncertainties: it is  
 1640 about a consistent understanding and resolution of QCD at all regions of spatial and momentum  
 1641 dimensions which the LHeC will explore.

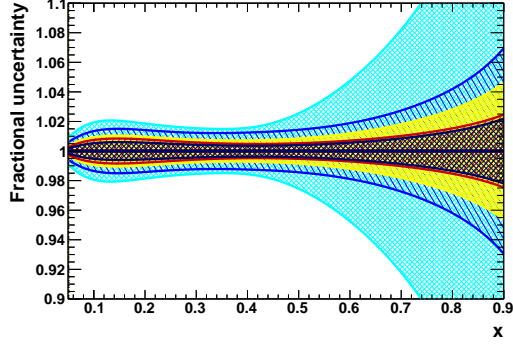
### 1642 3.3.7 Luminosity and Beam Charge Dependence of LHeC PDFs

1643 It is informative to study the transition of the PDF uncertainties from the “LHeC 1st run”  
 1644 PDFs, which exploits only a single electron-proton dataset, D2, through to the “LHeC final  
 1645 inclusive” PDFs, which makes use of the full datasets D4+D5+D6+D9 as listed in Tab. 3.2, i.e.  
 1646 including high luminosity data (D4), small sets of low energy  $E_p = 1$  TeV and positron data  
 1647 (D5 and D6) together with  $10 \text{ fb}^{-1}$  of opposite helicity data. Various intermediate PDF fits are  
 1648 performed using subsets of the data in order to quantify the influence of the beam parameters  
 1649 on the precision of the various PDFs. All fits use the same, standard 4+1 fit parameterisation  
 1650 and exclude the use of  $s$ ,  $c$ ,  $b$  data, the effect of which was evaluated before. The fits do neither  
 1651 include the low electron energy data sets generated for the  $F_L$  analysis, cf. Sect. 4.2.3, nor any  
 1652 jet  $ep$  data. The emphasis is on the development of the  $u_v$ ,  $d_v$ , total sea and  $xg$  uncertainty.

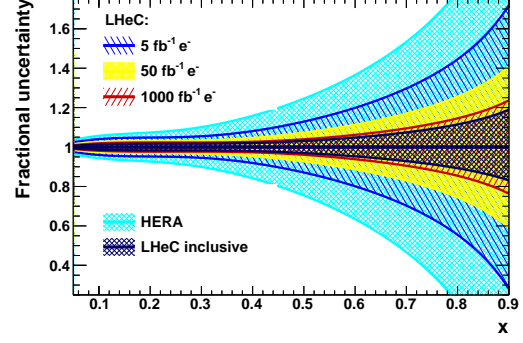
1653 A first study, Fig. 3.16, shows the influence of the integrated luminosity. This compares four  
 1654 cases, three with evolving luminosity, from 5 over 50 to  $1000 \text{ fb}^{-1}$ . These assumptions, according  
 1655 to the luminosity scenarios presented elsewhere, correspond to year 1 (D1), the initial 3 years  
 1656 (D2) and to the maximum attainable integrated luminosity (D4). The fourth case is represented  
 1657 by what is denoted the LHeC inclusive fit. One observes a number of peculiarities. For example,  
 1658 the initial  $5 \text{ fb}^{-1}$  (yellow in Fig. 3.16), i.e. the tenfold of what H1 collected over its lifetime (albeit  
 1659 with different beam parameters), leads i) to an extension of the HERA range to low and higher  
 1660  $x$ , ii) to high precision at small  $x$ , for example of the sea quark density of 5% below  $x = 10^{-5}$   
 1661 or iii) of also 5% for  $u_v$  at very high  $x = 0.8$ . With  $50 \text{ fb}^{-1}$  the down valence distribution is  
 1662 measured to within 20% accuracy at  $x = 0.8$ , an improvement by about a factor of two as  
 1663 compared to the  $5 \text{ fb}^{-1}$  case, and a major improvement to what is currently known about  $x d_v$  at  
 1664 large  $x$ , compare with Fig. 3.8. The very high luminosity, here taken to be  $1 \text{ ab}^{-1}$ , leads to a next  
 1665 level of high precision, for example of 2% below  $x = 10^{-5}$  for the total sea. The full data set  
 1666 further improves, especially the  $x d_v$  and the gluon at high  $x$ . The valence quark improvement  
 1667 is mostly linked to the positron data while the gluon improvement is related to the extension of  
 1668 the lever arm towards small values of  $Q^2$  as the reduction of  $E_p$  extends the acceptance at large  
 1669  $x$ . The visible improvement through the final inclusive fit is probably related to the increased  
 1670 precision at high  $x$  for there exists a momentum sum rule correlation over the full  $x$  range. In  
 1671 comparison to the analogous HERA fit, it becomes clear, that the vast majority of the gain  
 1672 comes already from the first  $5 - 50 \text{ fb}^{-1}$ .

1673 The second study presented here regards the impact on the PDF uncertainties when adding  
 1674 additionally positron data of different luminosity to a baseline fit on  $50 \text{ fb}^{-1}$  of  $e^-p$  data, the  
 1675 “LHeC 1st run” dataset. The results are illustrated in Fig. 3.17. It is observed, that the addition  
 1676 of positron data does bring benefits, which, however, are not striking in their effect on the here  
 1677 considered PDFs. A prominent improvement is obtained for the  $d$ -valence PDF, primarily due  
 1678 to the sensitivity gained via the CC cross section of the positron data. The benefit of the precise  
 1679 access to NC and CC weak interactions by the LHeC is clearer when one studies the cross  
 1680 sections and their impact on PDFs. This is illustrated in the subsequent section.

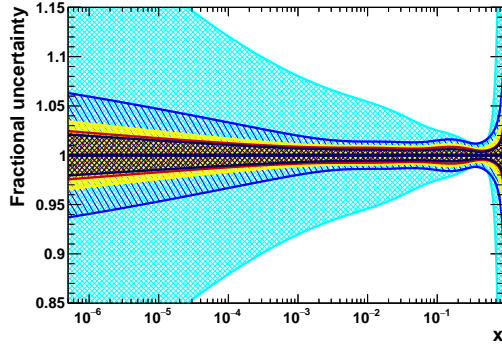




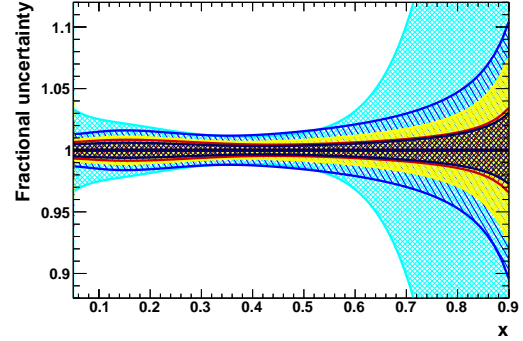
(a)  $u$ -valence distribution.



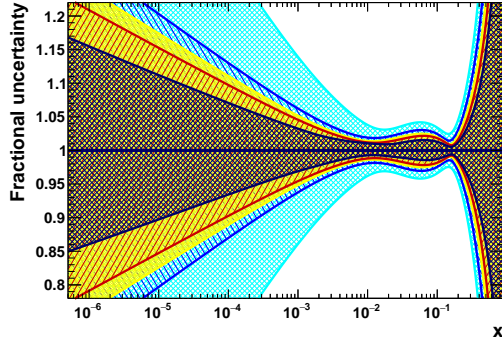
(b)  $d$ -valence distribution.



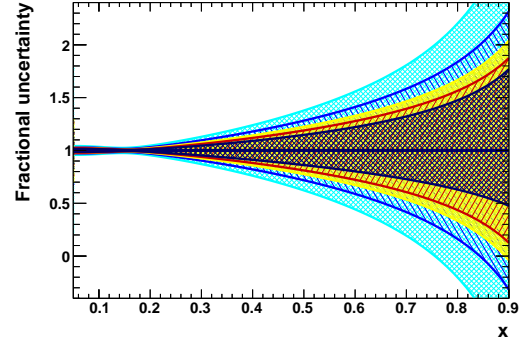
(c) Sea quark distribution ( $\log_{10} x$  scale).



(d) Sea quark distribution (linear  $x$  scale).

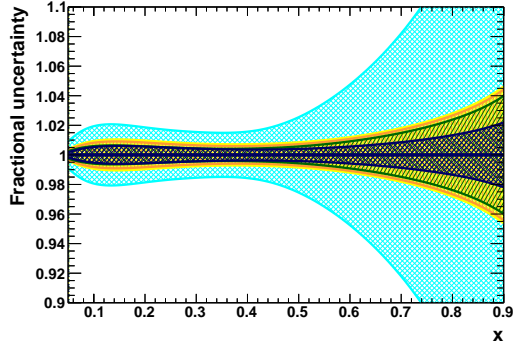


(e) Gluon distribution ( $\log_{10} x$  scale).

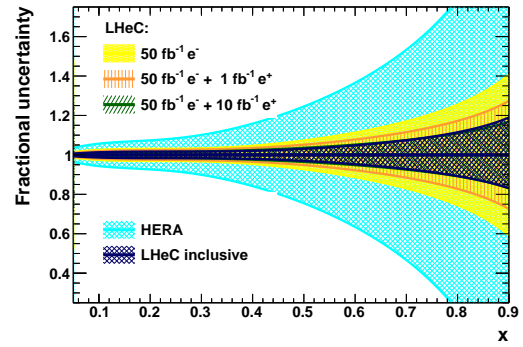


(f) Gluon distribution (linear  $x$  scale).

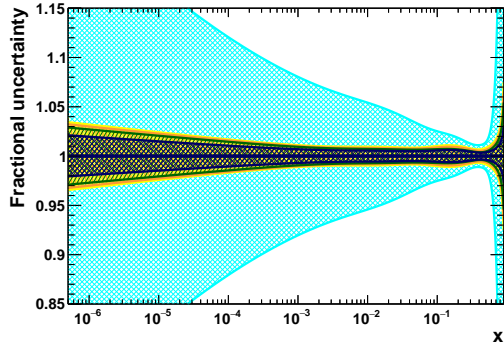
**Figure 3.16:** PDF distributions at  $Q^2 = 1.9 \text{ GeV}^2$  as a function of  $x$ , illustrating the impact of different amounts of integrated luminosity. The blue, yellow and red bands correspond to LHeC PDFs using electron-only NC and CC inclusive measurements with 5, 50 and  $1000 \text{ fb}^{-1}$  (datasets D1, D2 and D4), respectively. The yellow band is therefore equivalent to the “LHeC 1st run” PDF. For reference, the dark blue band shows the results of the final “LHeC inclusive” PDF. For comparison, the cyan band represents an identical PDF fit using HERA combined inclusive NC and CC data [43], restricted to solely the experimental uncertainties. Note that this, unlike the LHeC, extends everywhere beyond the narrow limits of the  $y$  scale of the plots.



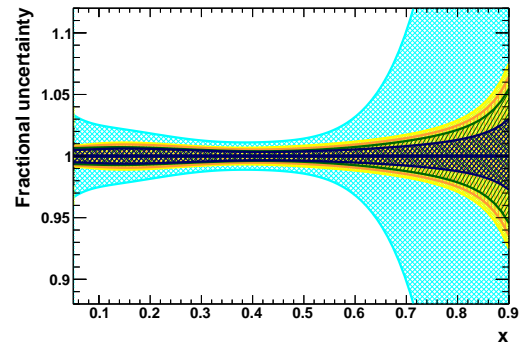
(a)  $u$ -valence distribution.



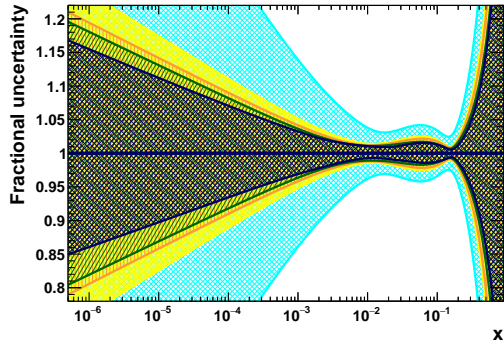
(b)  $d$ -valence distribution.



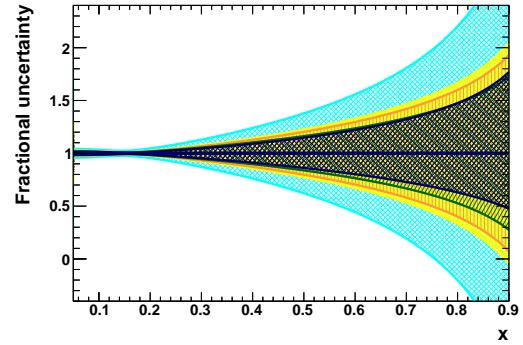
(c) Sea quark distribution ( $\log_{10} x$  scale).



(d) Sea quark distribution (linear  $x$  scale).



(e) Gluon distribution ( $\log_{10} x$  scale).



(f) Gluon distribution (linear  $x$  scale).

**Figure 3.17:** PDF distributions at  $Q^2 = 1.9 \text{ GeV}^2$  as a function of  $x$ , illustrating the impact of including positron data. The yellow (“LHeC 1st run”) and dark blue (“LHeC final inclusive”) and cyan bands (HERA data) are as in Fig. 3.16. The orange band corresponds to a fit with  $1 \text{ fb}^{-1}$  of inclusive NC and CC positron-proton data, in addition to  $50 \text{ fb}^{-1}$  of electron-proton data (D2+D6), while the green band is similar, but with  $10 \text{ fb}^{-1}$  of positron-proton data (D2+D7).

### 3.3.8 Weak Interactions Probing Proton Structure

It had long been considered to use the weak interactions to probe proton structure in deep inelastic scattering [94]. First important steps in this direction could be pursued with HERA, especially with the measurements of the polarisation and beam charge asymmetries in NC  $ep$  scattering by H1 and ZEUS [43]. This area of research will become a focus at the LHeC, because the  $Q^2$  range extends by 2-3 orders of magnitude beyond the weak scale  $Q^2 \simeq M_{W,Z}^2$ , with hugely increased luminosity. In Sect. 5.1 below, the emphasis is on accessing the electroweak theory parameters at a new level of sensitivity. Here we illustrate the importance of using the  $Z$  and also  $W$  exchange for pinning down the parton contents of the proton. This has been implicit for the QCD fits presented above, it yet emerges clearly only when one considers cross sections directly, their asymmetries with respect to beam charge and polarisation, and certain kinematic limits.

Parity violation is accessed in NC DIS through a variation of the lepton beam helicity,  $P$ , as can be deduced from [94]

$$\frac{\sigma_{r,NC}^{\pm}(P_R) - \sigma_{r,NC}^{\pm}(P_L)}{P_R - P_L} = \mp \kappa_Z g_A^e F_2^{\gamma Z} - (\kappa_Z g_A^e)^2 \frac{Y_-}{Y_+} x F_3^Z \quad (3.3)$$

where  $\sigma_{r,NC}$  denotes the double differential NC scattering cross section scaled by  $Q^4 x / 2\pi\alpha^2 Y_+$ . Here  $\kappa_Z$  is of the order of  $Q^2/M_Z^2$ ,  $F_2^{\gamma Z} = 2x \sum Q_q g_V^q(q - \bar{q})$  and the NC vector couplings are determined as  $g_V^f = I_{3,L}^f - 2Q_f \sin^2 \theta_W$ , where  $Q_f$  is the electric charge and  $I_{3,L}^f$  the left handed weak isospin charge of the fermion  $f = e, q$ , which also determines the axial vector couplings  $g_A^f$ , with  $g_A^e = -1/2$ . At LHeC (unlike FCC-he) the second term in Eq. 3.3 is suppressed with respect to the first one as it results from pure  $Z$  exchange and because the  $Y$  factor is small,  $\propto y$  since  $Y_{\mp} = (1 \mp (1 - y)^2)$ .

For the approximate value of the weak mixing angle  $\sin^2 \theta_W = 1/4$  one obtains  $g_V^e = 0$ ,  $g_V^u = 1/6$  and  $g_V^d = -1/3$ . Consequently, one may write to good approximation

$$F_2^{\gamma Z}(x, Q^2) = 2x \sum_q Q_q g_V^q(q - \bar{q}) \simeq x \frac{2}{9} [U + \bar{U} + D + \bar{D}] \quad (3.4)$$

The beam helicity asymmetry therefore determines the total sea. A simulation is shown in Fig. 3.18 for integrated luminosities of  $10 \text{ fb}^{-1}$  and helicities of  $P = \pm 0.8$ . Apparently, this asymmetry will provide a very precise measurement of the total sea. The combination of up and down quarks accessed with  $F_2^{\gamma Z}$  (Eq. 3.4) is different from that provided by the known function

$$F_2(x, Q^2) = 2x \sum_q Q_q^2(q - \bar{q}) = x \frac{1}{9} [4(U + \bar{U}) + D + \bar{D}] \quad (3.5)$$

because of the difference of the photon and  $Z$  boson couplings to quarks. Following Eq. 3.3, the beam polarisation asymmetry

$$A^{\pm} = \frac{\sigma_{NC}^{\pm}(P_R) - \sigma_{NC}^{\pm}(P_L)}{\sigma_{NC}^{\pm}(P_R) + \sigma_{NC}^{\pm}(P_L)} \simeq \mp (P_L - P_R) \kappa_Z g_A^e \frac{F_2^{\gamma Z}}{F_2} \quad (3.6)$$

measures to a very good approximation the  $F_2$  structure function ratio. The different composition of up and down quark contributions to  $F_2^{\gamma Z}$  and  $F_2$ , see above, indicates that the weak neutral current interactions will assist to separate the up and down quark distributions which HERA had to link together by setting  $B_d = B_u$ .

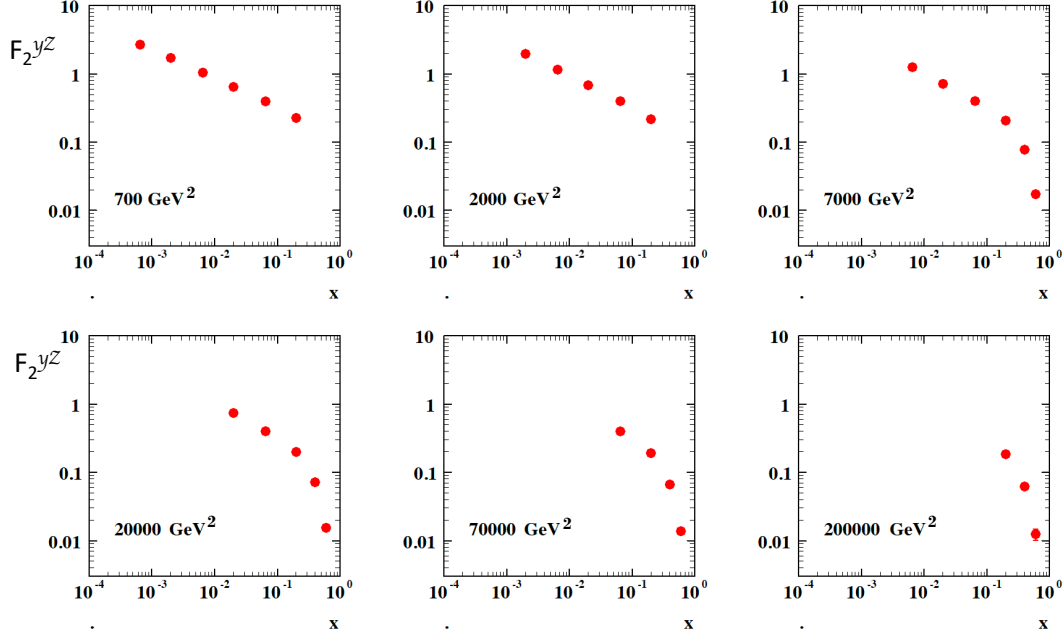


**Figure 3.18:** Prospective measurement of the photon-Z interference structure function  $F_2^{\gamma Z}(x, Q^2)$  at the LHeC using polarised electron beams of helicity  $\pm 0.8$  and an integrated luminosity of  $10 \text{ fb}^{-1}$  for each state. The uncertainties are only statistical.

1714 Inserting  $P_L = -P_R = -P$  and considering the large  $x$  limit, one observes that the asymmetry  
 1715 measures the  $d/u$  ratio of the valence quark distributions according to

$$A^\pm \simeq \pm \kappa_Z P \frac{1 + d_v/u_v}{4 + d_v/u_v}. \quad (3.7)$$

1716 This quantity will be accessible with very high precision, as Fig. 3.18 illustrates, which is one  
 1717 reason, besides the CC cross sections, why the  $d/u$  ratio comes out to be so highly constrained  
 1718 by the LHeC (see Fig. 3.9).

1719 A further interesting quantity is the the lepton beam charge asymmetry, which is given as

$$\sigma_{r,NC}^+(P_1) - \sigma_{r,NC}^-(P_2) = \kappa_Z a_e [-(P_1 + P_2)F_2^{\gamma Z} - \frac{Y_-}{Y_+} (2xF_3^{\gamma Z} + \kappa_Z a_e (P_1 - P_2)xF_3^Z)] \quad (3.8)$$

1720 neglecting terms  $\propto g_V^e$ . For zero polarisation this provides directly a parity conserving measure-  
 1721 ment of the structure function

$$xF_3^{\gamma Z}(x, Q^2) = 2x \sum_q Q_q g_A^q (q - \bar{q}) = \frac{2}{3}x(U - \bar{U}) + \frac{1}{3}x(D - \bar{D}). \quad (3.9)$$

1722 The appearance of this function in weak NC DIS resembles that of  $xW^3$  in CC, or fixed target  
 1723 neutrino-nucleon, scattering. It enables one to resolve the flavour contents of the proton. The  
 1724 function  $xF_3^{\gamma Z}$  was first measured by the BCDMS Collaboration in  $\mu^\pm C$  scattering [95] at the  
 1725 SPS.

1726 The HERA result is shown in Fig. 3.19. It covers the range from about  $x = 0.05$  to  $x = 0.6$  with  
 1727 typically 10% statistical precision. Assuming that sea and anti-quark densities are equal, such  
 1728 as  $u_s = \bar{u}$  or  $d_s = \bar{d}$ ,  $xF_3^{\gamma Z}$  is given as  $x/3(2u_v + d_v)$ . This function therefore accesses valence

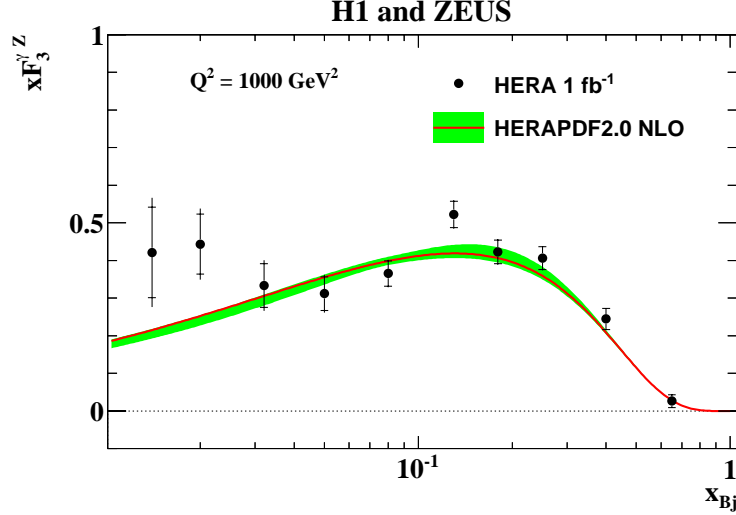


**Figure 3.19:** Combination of H1 and ZEUS measurement of the structure function  $xF_3^{\gamma^Z}(x, Q^2)$  as a function of  $x$  projected to a fixed  $Q^2$  value of  $2000 \text{ GeV}^2$ , from [43]. The inner error bar represents the statistical uncertainty.

1729 quarks down to small values of  $x$  where their densities become much smaller than that of the  
 1730 sea quarks. Since the  $Q^2$  evolution of the non-singlet valence quark distributions is very weak,  
 1731 it has been customary to project the various charge asymmetry measurements to some lowish  
 1732 value of  $Q^2$  and present the measurement as the  $x$  dependence of  $xF_3^{\gamma^Z}$ .

1733 If, however, there would be differences between the sea and anti-quarks, if  $s \neq \bar{s}$ , for example,  
 1734 one expected a rise of  $xF_3^{\gamma^Z}$  towards low  $x$ . This may be a cause for the undershoot of the  
 1735 QCD fit below the HERA data near to  $x \simeq 0.01$ , see Fig. 3.19, which yet are not precise enough.  
 1736 However, it is apparent that, besides providing constraints on the valence quark densities, this  
 1737 measurement indeed has the the potential to discover a new anti-symmetry in the quark sea.

1738 Such a discovery would be enabled by the LHeC as is illustrated in Fig. 3.20 with an extension  
 1739 of the kinematic range by an order of magnitude towards small  $x$  and a much increased precision  
 1740 in the medium  $x$  region. The simulation is performed for 10 and for  $1 \text{ fb}^{-1}$  of  $e^+p$  luminosity.  
 1741 Obviously it would be very desirable to reach high values of integrated luminosity in positron-  
 1742 proton scattering too.

1743 It is finally of interest to consider the role of precisely measured cross sections in CC scattering.  
 1744 The coupling of the  $W$  boson to quarks is flavour dependent resulting in the relations

$$\sigma_{r,CC}^+ = (1 + P)[x\bar{U} + (1 - y)^2xD], \quad (3.10)$$

$$\sigma_{r,CC}^- = (1 - P)[xU + (1 - y)^2x\bar{D}]. \quad (3.11)$$

1745 Here  $\sigma_{r,CC}$  is the double differential charged current DIS cross section scaled by a factor  $2\pi x \cdot$   
 1746  $(M_W^2 + Q^2)^2 / (G_F M_W^2)^2$  with the Fermi constant  $G_F$  and the  $W$  boson mass  $M_W$ . The positron  
 1747 beam at the LHeC is most likely unpolarised,  $P = 0$ . Maximum rate in  $e^-p$  is achieved with  
 1748 large negative polarisation. In the valence-quark approximation, the  $e^+p$  CC cross section is  
 1749 proportional to  $(1 - y)^2 x d_v$  while  $\sigma_{r,CC}^- \propto u_v$ . This provides direct, independent measurements  
 1750 of  $d_v$  and  $u_v$  as had been illustrated already in the LHeC CDR [1].

1751 Inclusive NC and CC DIS accesses four combinations of parton distributions, as is obvious from

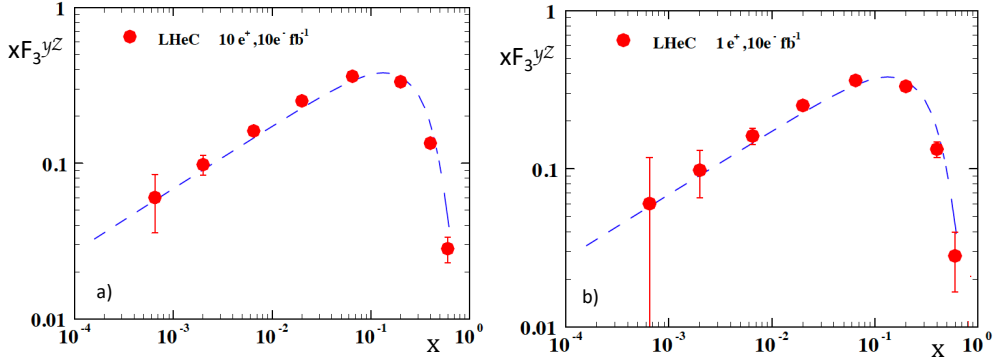


**Figure 3.20:** Prospective measurement of the photon-Z interference structure function  $xF_3^{\gamma Z}(x, Q^2)$  at the LHeC projected to a fixed  $Q^2$  value of  $2000 \text{ GeV}^2$ . The result corresponds to a cross section charge asymmetry for an unpolarised  $e^-p$  beam with  $10 \text{ fb}^{-1}$  luminosity combined with unpolarised  $e^+p$  beams of a)  $10 \text{ fb}^{-1}$  (left) and b)  $1 \text{ fb}^{-1}$  (right). The error bars represent the statistical uncertainty. The curve is drawn to guide the eye. It is possible that the measurement would discover a rise of  $xF_3^{\gamma Z}$  towards low  $x$  should there exist so far unknown differences between sea and anti-quark densities, see text.

1752 Eq. 3.10 for CC above and from the NC relation

$$\sigma_{r,NC}^{\pm} \simeq [c_u(U + \bar{U}) + c_d(D + \bar{D})] + \kappa_Z[d_u(U - \bar{U}) + d_d(D - \bar{D})]$$

with  $c_{u,d} = Q_{u,d}^2 + \kappa_Z(-g_V^e \mp P g_A^e) Q_{u,d} g_V^{u,d}$  and  $d_{u,d} = \pm g_A^e g_A^{u,d} Q_{u,d}$ , (3.12)

1753 restricted to photon and  $\gamma Z$  interference contributions. These four PDF combinations are com-  
 1754 plemented by the  $s$ ,  $c$ ,  $b$  measurements introduced before. The parton contents can therefore  
 1755 be completely resolved, which was impossible at HERA.

1756 It is the high energy and high luminosity access to DIS, the high precision NC/CC and tagged  
 1757 heavy quark measurement programme, which makes the LHeC the uniquely suited environment  
 1758 to uncover the secrets of parton structure and dynamics. This will establish a new level with  
 1759 possible discoveries of strong interaction physics and also provide the necessary base for precision  
 1760 electroweak and Higgs measurements at the LHC, for massively extending the range of BSM  
 1761 searches and reliably interpreting new physics signals in hadron-hadron scattering at the LHC.

### 1762 3.3.9 Parton-Parton Luminosities

1763 The energy frontier in accelerator particle physics is the LHC, with a cms energy of  $\sqrt{s} =$   
 1764  $2E_p \simeq 14 \text{ TeV}$ , with the horizon of a future circular hadron collider, the FCC-hh, reaching  
 1765 energies up to  $\sqrt{s} = 100 \text{ TeV}$ . Proton-proton collider reactions are characterised by the Drell-Yan  
 1766 scattering [96]. To leading order, the double differential Drell-Yan scattering cross section [97]  
 1767 for the neutral current reaction  $pp \rightarrow (\gamma, Z)X \rightarrow e^+e^-X$  and the charged current (CC) reaction  
 1768  $pp \rightarrow W^{\pm}X \rightarrow e\nu X$ , can be written as

$$\frac{d^2\sigma}{dM dy} = \frac{4\pi\alpha^2(M)}{9} \cdot 2M \cdot P(M) \cdot \Phi(x_1, x_2, M^2) \quad [\text{nb GeV}^{-1}]. \quad (3.13)$$

1769 Here  $M$  is the mass of the  $e^+e^-$  and  $e^+\nu$  and  $e^-\bar{\nu}$  systems for the NC and CC process, respec-  
 1770 tively, and  $y$  is the boson rapidity. The cross section implicitly depends on the Bjorken  $x$  values

1771 of the incoming quark  $q$  and its anti-quark  $\bar{q}$ , which are related to the rapidity  $y$  as

$$x_1 = \sqrt{\tau}e^y \quad x_2 = \sqrt{\tau}e^{-y} \quad \tau = \frac{M^2}{s}. \quad (3.14)$$

1772 For the NC process, the cross section is a sum of a contribution from photon and  $Z$  exchange  
 1773 as well as an interference term. In the case of photon exchange, the propagator term  $P(M)$  and  
 1774 the parton distribution term  $\Phi$  are given by

$$P_\gamma(M) = \frac{1}{M^4} \quad \Phi_\gamma = \sum_q Q_q^2 F_{q\bar{q}} \quad (3.15)$$

$$F_{q\bar{q}} = x_1 x_2 \cdot [q(x_1, M^2)\bar{q}(x_2, M^2) + \bar{q}(x_1, M^2)q(x_2, M^2)]. \quad (3.16)$$

1775 Similar to DIS, the corresponding formulae for the  $\gamma Z$  interference term read as

$$P_{\gamma Z} = \frac{\kappa_Z g_V^e (M^2 - M_Z^2)}{M^2 [(M^2 - M_Z^2)^2 + (\Gamma_Z M_Z)^2]} \quad \Phi_{\gamma Z} = \sum_q 2Q_q g_V^q F_{q\bar{q}} \quad (3.17)$$

1776 The interference contribution is small being proportional to the vector coupling of the electron  
 1777  $g_V^e$ . One also sees in Eq 3.17 that the interference cross section contribution changes sign from  
 1778 plus to minus as the mass increases and passes  $M_Z$ . The expressions of  $P$  and  $\Phi$  for the pure  $Z$   
 1779 exchange part are

$$P_Z = \frac{\kappa_Z^2 (g_V^e{}^2 + g_A^e{}^2)}{(M^2 - M_Z^2)^2 + (\Gamma_Z M_Z)^2} \quad \Phi_Z = \sum_q (g_V^q{}^2 + g_A^q{}^2) F_{q\bar{q}}. \quad (3.18)$$

1780 For the CC cross section the propagator term is

$$P_W = \frac{\kappa_W^2}{(M^2 - M_W^2)^2 + (\Gamma_W M_W)^2} \quad (3.19)$$

1781 and the charge dependent parton distribution forms are

$$\Phi_{W^+} = x_1 x_2 [V_{ud}^2 (u_1 \bar{d}_2 + u_2 \bar{d}_1) + V_{cs}^2 (c_1 \bar{s}_2 + c_2 \bar{s}_1) + V_{us}^2 (u_1 \bar{s}_2 + u_2 \bar{s}_1) + V_{cd}^2 (c_1 \bar{d}_2 + c_2 \bar{d}_1)] \quad (3.20)$$

$$\Phi_{W^-} = x_1 x_2 [V_{ud}^2 (\bar{u}_1 d_2 + \bar{u}_2 d_1) + V_{cs}^2 (\bar{c}_1 s_2 + \bar{c}_2 s_1) + V_{us}^2 (\bar{u}_1 s_2 + \bar{u}_2 s_1) + V_{cd}^2 (\bar{c}_1 d_2 + \bar{c}_2 d_1)], \quad (3.21)$$

1782  
 1783 with  $\kappa_W = 1/(4 \sin^2 \Theta)$  and  $q_i = q_i(x, M^2)$  and the CKM matrix elements  $V_{ij}$ . The expressions  
 1784 given here are valid in the QPM. At higher order pQCD, Drell-Yan scattering comprises also  
 1785 quark-gluon and gluon-gluon contributions. Certain production channels are sensitive to specific  
 1786 parton-parton reactions, Higgs production, for example, originating predominantly from gluon-  
 1787 gluon fusion. Based on the factorisation theorem [37] one therefore opened a further testing  
 1788 ground for PDFs, and much of the current PDF analyses is about constraining parton distri-  
 1789 butions by Drell-Yan scattering measurements and semi-inclusive production processes, such as  
 1790 top, jet and charm production, at the LHC. An account of this field is provided below, including  
 1791 a study as to how LHeC would add to the “global” PDF knowledge at the time of the HL-LHC.

1792 There are drawbacks to the use of Drell-Yan and other hadron collider data for the PDF deter-  
 1793 mination and advantages for  $ep$  scattering: i) DIS has the ability to prescribe the reaction type  
 1794 and the kinematics ( $x$ ,  $Q^2$ ) through the reconstruction of solely the leptonic vertex; ii) there  
 1795 are no colour reconnection and, for the lepton vertex, no hadronisation effects disturbing the  
 1796 theoretical description; iii) the most precise LHC data, on  $W$  and  $Z$  production, are located at

1797 a fixed equivalent  $Q^2 = M_{W,Z}^2$  and represent a snapshot at a fixed scale which in DIS at the  
 1798 LHeC varies by more than 5 orders of magnitude <sup>10</sup>.

1799 There are further difficulties inherent to the use of LHC data for PDF determinations, such as  
 1800 hadronisation corrections and incompatibility of data. For example, the most recent CT18 [98]  
 1801 global PDF analysis had to arrange for a separate set (CT18A) because the standard fit would  
 1802 not respond well to the most precise ATLAS  $W$ ,  $Z$  data taken at 7 TeV cms. The intent to  
 1803 include all data can only be realised with the introduction of so-called  $\chi^2$  tolerance criteria  
 1804 which fundamentally affect the meaning of the quoted PDF uncertainties.

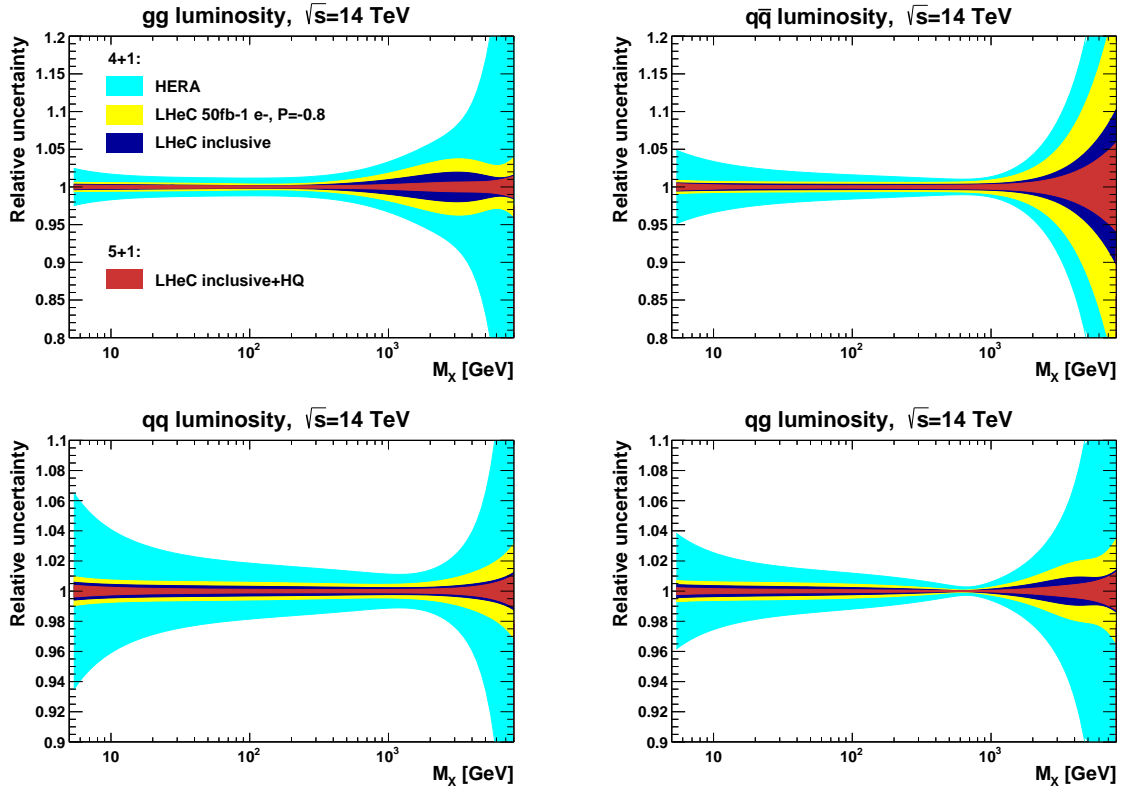


**Figure 3.21:** Uncertainty bands for parton luminosities as a function of the mass  $M_X = \sqrt{s x_1 x_2}$  for LHC energies. Light blue: fit to HERA data using the same parameterisation as the LHeC fits shown; yellow: expectation from the first run period of the LHeC with solely  $e^-p$  operation; dark blue: inclusive fit, based on the data sets (D4+D5+D6+D9) in Tab. 3.2; red: fit to the inclusive data adding simulated heavy flavour  $s$ ,  $c$ ,  $b$  data with a 5 quark distribution parameterisation as introduced above.

1805 Conceptually, the LHeC enables us to change this approach completely. Instead of trying to use  
 1806 all previous and current PDF sensitive data, to which nowadays one has no alternative, it replaces  
 1807 these by pure  $ep$  collider DIS data. Then one will bring order back into the PDF field: parton  
 1808 distributions, completely resolved, and from a single process, extending over nearly six orders  
 1809 of magnitude and calculated from NLO pQCD up to probably even N<sup>4</sup>LO (see Sect. 4.4.1).  
 1810 These PDFs will be applicable for i) identifying new dynamics and symmetries; ii) testing

<sup>10</sup>This is mitigated by measurements of Drell-Yan scattering at low masses, which are less precise, however. At high masses,  $M = \sqrt{s x_1 x_2} \gg M_{W,Z}$ , one soon reaches the region where new physics may occur, i.e. there arises the difficulty to separate unknown physics from the uncertainty of the quark and gluon densities at large  $x$ . High mass Drell Yan searches often are performed at the edge of the data statistics, i.e. they can not really be guided by data but miss a reliable guidance for the behaviour of the SM background around and beyond a (non-) resonant effect they would like to discover.



1811 factorisation; iii) confronting other PDF analyses at that time; iv) performing high precision  
 1812 Higgs and electroweak analyses, and v) interpreting any peculiar HL-LHC signal for BSM using  
 1813 that independent PDF. higg It has been customary, which is obvious from Eqs. 3.15, 3.20 and  
 1814 3.21, to express the usefulness of various PDF determinations and prospects for the LHC, and  
 1815 similarly the FCC, with four so-called parton luminosities which are defined as

$$L_{ab}(M_X) = \int dx_a dx_b \sum_q F_{ab} \delta(M_X^2 - s x_a x_b) \quad (3.22)$$

1816 where  $F_{ab}$  for  $(a, b) = (q\bar{q})$  is defined in Eq. 3.15 and  $(a, b)$  could also be  $(g, q)$ ,  $(g, \bar{q})$  and  
 1817  $(gg)$ , without a sum over quarks in the latter case. The expectations for the quark and gluon  
 1818 related four parton luminosities are presented in Fig. 3.21. The LHeC provides very precise  
 1819 parton luminosity predictions in the complete range of  $M_X$  up to the high mass edge of the  
 1820 search range at the LHC. This eliminates the currently sizeable PDF uncertainty of precision  
 1821 electroweak measurements at the LHC, as for example for the anticipated measurement of  $M_W$   
 1822 to within  $10^{-4}$  uncertainty, see below. One may also notice that the gluon-gluon luminosity  
 1823 (left top in Fig. 3.21) is at a per cent level for the Higgs mass  $M_X = M_H \simeq 125$  GeV. This is  
 1824 evaluated further in the chapter on Higgs physics with the LHeC.

### 1825 3.4 The 3D Structure of the Proton

1826 As is evident from the discussion in the previous Sections, the LHeC machine will be able to  
 1827 measure the collinear parton distribution functions with unprecedented accuracy in its extended  
 1828 range of  $x$  and  $Q^2$ . Thus, it will provide a new insight into the details of the one-dimensional  
 1829 structure of the proton and nuclei, including novel phenomena at low  $x$ . In addition to collinear  
 1830 dynamics, the LHeC opens a new window into proton and nuclear structure by allowing a precise  
 1831 investigation of the partonic structure in more than just the one dimension of the longitudinal  
 1832 momentum. Precision DIS thus gives access to multidimensional aspects of hadron structure.  
 1833 This can be achieved by accurately measuring processes with more exclusive final states like  
 1834 production of jets, semi-inclusive production of hadrons and exclusive processes, in particular the  
 1835 elastic diffractive production of vector mesons and deeply virtual Compton (DVCS) scattering  
 1836 that were explored in the 2012 LHeC CDR [1]. These processes have the potential to provide  
 1837 information not only on the longitudinal distribution of partons in the proton or nucleus, but also  
 1838 on the dependence of the parton distribution on transverse momenta and momentum transfer.  
 1839 Therefore, future, high precision DIS machines like the LHeC or the Electron Ion Collider (EIC)  
 1840 in the US [99], open a unique window into the details of the 3D structure of hadrons. Note  
 1841 that the measurement of these processes requires a detector with large acceptance,  $|\eta| < 4$ , see  
 1842 e.g. [1, 100]. The current LHeC central detector design covers  $|\eta| \lesssim 4.5$ , see Chapter 12.

1843 The most general quantity that can be defined in QCD, that would contain very detailed infor-  
 1844 mation about the partonic content of the hadron, is the Wigner distribution [101]. This function  
 1845  $W(x, \mathbf{k}, \mathbf{b})$  is a 1+4 dimensional function. One can think of it as the “mother” or “master” par-  
 1846 ton distribution, from which lower-dimensional distributions can be obtained. In the definition  
 1847 of the Wigner function,  $\mathbf{k}$  is the transverse momentum of the parton and  $\mathbf{b}$  is the 2-dimensional  
 1848 impact parameter, which can be defined as a Fourier conjugate to the momentum transfer of  
 1849 the process. The other, lower dimensional parton distributions can be obtained by integrating  
 1850 out different variables. Thus, transverse momentum dependent (TMD) parton distributions  
 1851 (or unintegrated parton distribution functions)  $f_{\text{TMD}}(x, \mathbf{k})$  can be obtained by integrating out  
 1852 the impact parameter  $\mathbf{b}$  in the Wigner function, while the generalised parton densities (GPD),  
 1853  $f_{\text{GPD}}(x, \mathbf{b})$ , can be obtained from the Wigner function through the integration over the trans-  
 1854 verse momentum  $\mathbf{k}$ . In the regime of small  $x$ , or high energy, a suitable formalism is that of

1855 the dipole picture [102–107], where the fundamental quantity which contains the details of the  
 1856 partonic distribution is the dipole amplitude  $N(x, \mathbf{r}, \mathbf{b})$ . This object contains the dependence  
 1857 on the impact parameter  $\mathbf{b}$  as well as another transverse size  $\mathbf{r}$ , the dipole size, which can be  
 1858 related to the transverse momentum of the parton  $\mathbf{k}$  through a Fourier transform. The impor-  
 1859 tant feature of the dipole amplitude is that it should obey the unitarity limit  $N \leq 1$ . The dipole  
 1860 amplitude  $N$  within this formalism can be roughly interpreted as a Wigner function in the high  
 1861 energy limit, as it contains information about the spatial distribution of the partons in addition  
 1862 to the dependence on the longitudinal momentum fraction  $x$ .

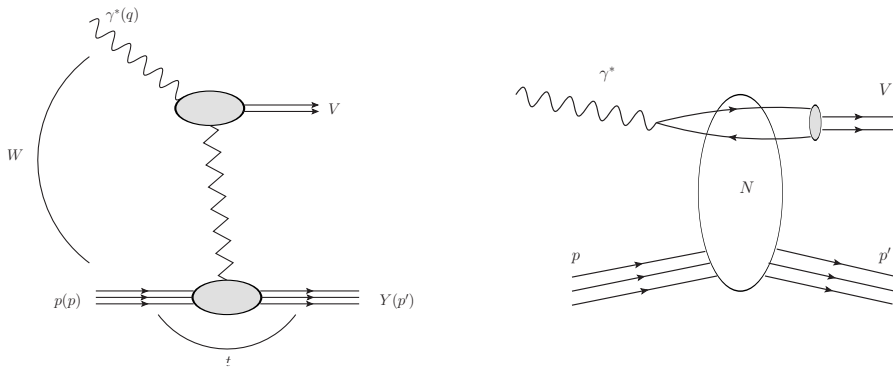


**Figure 3.22:** Left: diagram for the quasi-elastic production of the vector meson. Right: schematic illustration of the same process, quasi-elastic vector meson production, within the framework of the dipole picture. The initial virtual photon, fluctuates into a quark-antiquark pair which then scatters off the hadronic target and forms the vector meson. The details of the hadronic interaction of the dipole with the target are encoded in the dipole amplitude  $N$ .

1863 Detailed simulations of elastic  $J/\psi$  vector meson production were performed for the LHeC  
 1864 kinematic region and beyond [1], using the formalism of the dipole picture. This particular  
 1865 process is shown in Fig. 3.22, left plot. The proton is scattered elastically with momentum  
 1866 transfer  $t$ , and the vector meson is produced, which is separated from the final state proton  
 1867 by a rapidity gap. Of particular importance is the measurement of the  $t$  slope of this process,  
 1868 since it can be related directly to the impact parameter distribution and is thus sensitive to the  
 1869 transverse variation of the partonic density in the target. The first type of analysis like this,  
 1870 in the context of elastic scattering, was performed by Amaldi and Schubert [108], where it was  
 1871 demonstrated that the Fourier transform of the elastic cross section yields access to the impact  
 1872 parameter profile of the scattering amplitude. This method can be used in the context of vector  
 1873 meson scattering in DIS, where the transverse distribution of partons, in the perturbative regime,  
 1874 can be extracted through the appropriate Fourier transform [109]. The additional advantage of  
 1875 studying diffractive vector meson production is the fact that the partonic distributions can be  
 1876 studied as a function of the hard scale in this process given by the mass of the vector meson  $M_V^2$   
 1877 in the photoproduction case or  $Q^2$  (or more precisely a combination of  $Q^2$  and  $M_V^2$ ) in the case  
 1878 of the diffractive DIS production of vector mesons, as well as the energy  $W$  of the photon-proton  
 1879 system available in the process which is closely related to  $x$ .

1880 The differential cross section for elastic vector meson production can be expressed in the following  
 1881 form:

$$\frac{d\sigma^{\gamma^* p \rightarrow J/\psi p}}{dt} = \frac{1}{16\pi} |\mathcal{A}(x, Q, \Delta)|^2, \quad (3.23)$$

1882 where the amplitude for the process of elastic diffractive vector meson production in the high

1883 energy limit, in the dipole picture, is given by

$$1884 \quad \mathcal{A}(x, Q, \Delta) = \sum_{h\bar{h}} \int d^2\mathbf{r} \int dz \Psi_{h\bar{h}}^*(z, \mathbf{r}, Q) \mathcal{N}(x, \mathbf{r}, \Delta) \Psi_{h\bar{h}}^V(z, \mathbf{r}) . \quad (3.24)$$

1884 In the above formula,  $\Psi_{h\bar{h}}^*(z, \mathbf{r}, Q)$  is the photon wave function which describes the splitting  
 1885 of the virtual photon  $\gamma^*$  into a  $q\bar{q}$  pair. This wave function can be calculated in perturbative  
 1886 QCD. The function  $\Psi_{h\bar{h}}^V(z, \mathbf{r})$  is the wave function of the vector meson. Finally,  $\mathcal{N}(x, \mathbf{r}, \Delta)$  is the  
 1887 dipole amplitude which contains all the information about the interaction of the quark-antiquark  
 1888 dipole with the target. The formula (3.24) can be interpreted as the process of fluctuation of the  
 1889 virtual photon into a  $q\bar{q}$  pair, which subsequently interacts with the target through the dipole  
 1890 amplitude  $\mathcal{N}$  and then forms the vector meson, given by the amplitude  $\Psi^V$ , see Fig. 3.22, right  
 1891 plot. The two integrals in the definition Eq. (3.24) are performed over the dipole size which is  
 1892 denoted by  $\mathbf{r}$ , and  $z$  which is the longitudinal momentum fraction of the photon carried by the  
 1893 quark. The scattering amplitude depends on the value of the momentum transfer  $\Delta$ , which is  
 1894 related to the Mandelstam variable  $t = -\Delta^2$ . The sum is performed over the helicity states of  
 1895 the quark and antiquark.

1896 The dipole amplitude  $\mathcal{N}(x, \mathbf{r}, \Delta)$  can be related to the dipole amplitude in coordinate space  
 1897 through the appropriate Fourier transform

$$N(x, \mathbf{r}, \mathbf{b}) = \int d^2\Delta e^{i\Delta \cdot \mathbf{b}} \mathcal{N}(x, \mathbf{r}, \Delta) . \quad (3.25)$$

1898 We stress that  $\mathbf{r}$  and  $\mathbf{b}$  are two different transverse sizes here. The dipole size  $\mathbf{r}$  is conjugate  
 1899 to the transverse momentum of the partons  $\mathbf{k}$ , whereas the impact parameter is roughly the  
 1900 distance between the centre of the scattering target to the centre-of-mass of the quark-antiquark  
 1901 dipole and is related to the Fourier conjugate variable, the momentum transfer  $\Delta$ .

1902 The dipole amplitude  $N(x, \mathbf{r}, \mathbf{b})$  contains rich information about the dynamics of the hadronic  
 1903 interaction. It is a 5-dimensional function and it depends on the longitudinal momentum frac-  
 1904 tion, and two two-dimensional coordinates. The dependence on the longitudinal momentum  
 1905 fraction is obviously related to the evolution with the centre-of-mass energy of the process,  
 1906 while the dependence on  $\mathbf{b}$  provides information about the spatial distribution of the partons in  
 1907 the target. The dipole amplitude is related to the distribution of gluons in impact parameter  
 1908 space. The dipole amplitude has a nice property that its value should be bounded from above  
 1909 by the unitarity requirement  $N \leq 1$ . The complicated dependence on energy, dipole size and  
 1910 impact parameter of this amplitude can provide a unique insight into the dynamics of QCD,  
 1911 and on the approach to the dense partonic regime. Besides, from Eqs. (3.23), (3.24) and (3.25) it  
 1912 is evident that the information about the spatial distribution in impact parameter  $\mathbf{b}$  is related  
 1913 through the Fourier transform to the dependence of the cross section on the momentum transfer  
 1914  $t = -\Delta^2$ .

1915 To see how the details of the distribution, and in particular the approach to unitarity, can  
 1916 be studied through the VM elastic production, calculations based on the dipole model were  
 1917 performed [110], and extended to energies which can be reached at the LHeC as well as the  
 1918 FCC-eh. The parameterisations used in the calculation were the so-called IP-Sat [111, 112]  
 1919 and b-CGC [113] models. In both cases the impact parameter dependence has to be modelled  
 1920 phenomenologically. In the IP-Sat model the dipole amplitude has the following form

$$N(x, \mathbf{r}, \mathbf{b}) = 1 - \exp \left[ -\frac{\pi^2 r^2}{2N_c} \alpha_s(\mu^2) x g(x, \mu^2) T_G(b) \right] , \quad (3.26)$$

1921 where  $xg(x, \mu^2)$  is the collinear gluon density, evolved using LO DGLAP (without quarks), from  
 1922 an initial scale  $\mu_0^2$  up to the scale  $\mu^2$  set by the dipole size  $\mu^2 = \frac{4}{r^2} + \mu_0^2$ .  $\alpha_s(\mu^2)$  is the strong  
 1923 coupling. The parameterisation of the gluon density at the initial scale  $\mu_0^2$  is given by

$$xg(x, \mu_0^2) = A_g x^{-\lambda_g} (1-x)^{5.6}, \quad (3.27)$$

1924 and the impact parameter profile for the gluon by

$$T_G(b) = \frac{1}{2\pi B_G} \exp(-b^2/2B_G). \quad (3.28)$$

An alternative parameterisation is given by the b-CGC model [113] which has the form

$$N(x, \mathbf{r}, \mathbf{b}) = \begin{cases} N_0 \left(\frac{rQ_s}{2}\right)^{2\gamma_{\text{eff}}} & \text{for } rQ_s \leq 2, \\ 1 - \exp(-\mathcal{A} \ln^2(\mathcal{B}rQ_s)) & \text{for } rQ_s > 2. \end{cases} \quad (3.29)$$

1925 Here the effective anomalous dimension  $\gamma_{\text{eff}}$  and the saturation scale  $Q_s$  of the proton explicitly  
 1926 depend on the impact parameter and are defined as

$$\begin{aligned} \gamma_{\text{eff}} &= \gamma_s + \frac{1}{\kappa \lambda \ln 1/x} \ln \left( \frac{2}{rQ_s} \right), \\ Q_s(x, b) &= \left( \frac{x_0}{x} \right)^{\lambda/2} \exp \left[ -\frac{b^2}{4\gamma_s B_{\text{CGC}}} \right] \text{ GeV}, \end{aligned} \quad (3.30)$$

1927 where  $\kappa = \chi''(\gamma_s)/\chi'(\gamma_s)$ , with  $\chi(\gamma)$  being the leading-logarithmic BFKL kernel eigenvalue  
 1928 function [114]. The parameters  $\mathcal{A}$  and  $\mathcal{B}$  in Eq.(3.29) are determined uniquely from the matching  
 1929 of the dipole amplitude and its logarithmic derivatives at the limiting value of  $rq_s = 2$ . The  
 1930 b-CGC model is constructed by smoothly interpolating between two analytically known limiting  
 1931 cases [113], namely the solution of the BFKL equation in the vicinity of the saturation line for  
 1932 small dipole sizes  $r < 2/Q_s$ , and the solution of the BK equation deep inside the saturation  
 1933 region for large dipole sizes  $r > 2/Q_s$ .

1934 The parameters  $\mu_0, A_g, \lambda_g$  of the IP-Sat model and  $N_0, \gamma_s, x_0\lambda$  of the b-CGC model were fitted  
 1935 to obtain the best description of the inclusive data for the structure function  $F_2$  at HERA. The  
 1936 slope parameters  $B_g$  and  $B_{\text{CGC}}$ , which control the  $b$ -dependence in both models, were fitted to  
 1937 obtain the best description of elastic diffractive  $J/\psi$  production, in particular its  $t$ -dependence,  
 1938 at small values of  $t$ .

1939 In Figs. 3.23 and 3.24 we show the simulated differential cross section  $d\sigma/dt$  as a function of  $|t|$   
 1940 and study its variation with energy and virtuality, and its model dependence. First, in Fig. 3.23  
 1941 we show the differential cross section as a function of  $t$  for fixed energy  $W = 1 \text{ TeV}$ , in the case of  
 1942 the photoproduction of  $J/\psi$  (left plot) and for the case of DIS with  $Q^2 = 10 \text{ GeV}^2$  (right plot).  
 1943 The energy  $W$  corresponds to the LHeC kinematics. There are three different calculations in  
 1944 each plot, using the IP-sat model, the b-CGC model and the 1-Pomeron approximation. The  
 1945 last one is obtained by keeping just the first non-trivial term in the expansion of the eikonalised  
 1946 formula of the IP-Sat amplitude (3.26). First, let us observe that all three models coincide  
 1947 for very low values of  $t$ , where the dependence on  $t$  is exponential. This is because for low  
 1948  $|t|$ , relatively large values of impact parameter are probed in Eq. (3.24) where the amplitude  
 1949 is small, and therefore the tail in impact parameter is Gaussian in all three cases. Since the  
 1950 Fourier transform of the Gaussian in  $b$  is an exponential in  $t$ , the result at low  $t$  follows. On  
 1951 the other hand, the three scenarios differ significantly for large values of  $|t|$ . In the case of the

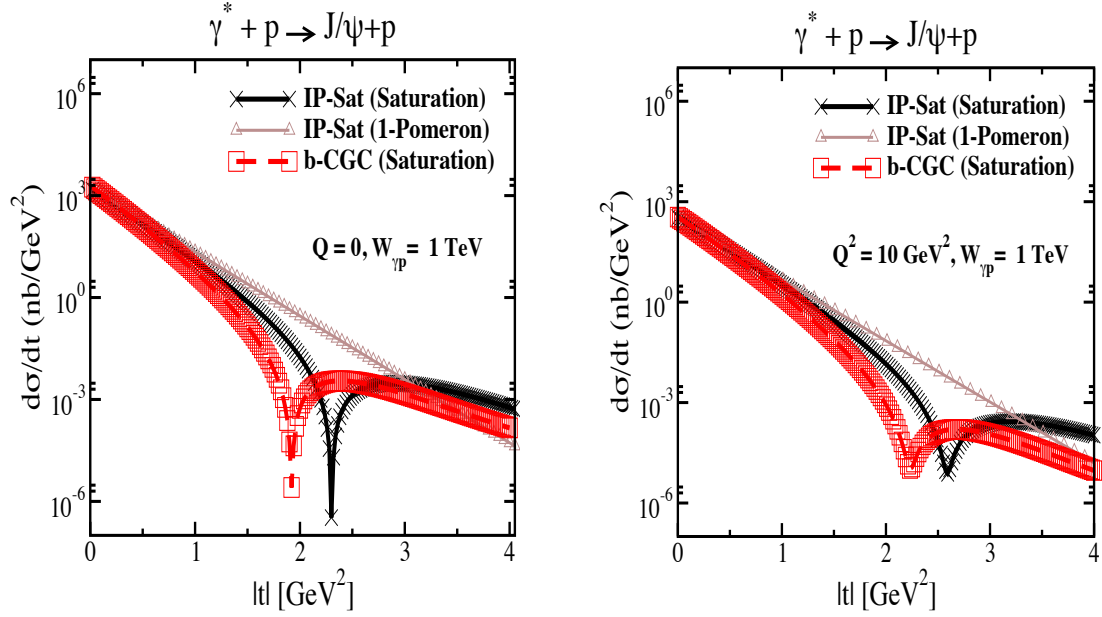


**Figure 3.23:** Differential cross section for the elastic  $J/\psi$  production as a function of  $|t|$  within the IP-Sat (saturation), b-CGC and 1-Pomeron models at a fixed  $W_{\gamma p} = 1$  TeV, which corresponds to the LHeC kinematics, and for two different values of photon virtuality  $Q = 0$  and  $Q^2 = 10$  GeV $^2$ . The thickness of points includes the uncertainties associated with the freedom to choose different values for the charm quark mass within the range  $m_c = 1.2 - 1.4$  GeV.

1952 1-Pomeron approximation the dependence is still exponential, without any dips, which is easily  
 1953 understood since the impact parameter profile is perfectly Gaussian in this case. For the two  
 1954 other scenarios, dips in  $d\sigma/dt$  as a function in  $t$  emerge. They signal the departure from the  
 1955 Gaussian profile in  $b$  for small values of  $b$  where the system is dense. A similar pattern can be  
 1956 observed when performing the Fourier transform of the Wood-Saxon distribution, which is the  
 1957 typical distribution used for the description of the matter density in nuclei. When  $Q^2$  is increased  
 1958 the pattern of dips also changes. This is illustrated in Fig. 3.23. It is seen that the dips move to  
 1959 higher values of  $|t|$  for DIS than for photoproduction. This can be understood from the dipole  
 1960 formula Eq. (3.24) which contains the integral over the dipole size. Larger values of  $Q^2$  select  
 1961 smaller values of dipole size  $r$ , where the amplitude is smaller and thus in the dilute regime,  
 1962 where the profile in  $b$  is again Gaussian. On the other hand, small scales select large dipole sizes  
 1963 for which the dipole amplitude is larger and thus the saturation effects more prominent, leading  
 1964 to the distortion of the impact parameter profile and therefore to the emergence of dips in the  
 1965 differential cross section  $d\sigma/dt$  when studied as a function of  $t$ .

1966 In Fig. 3.24 we show the same calculation but for even higher energy  $W = 2.5$  TeV, which could  
 1967 be explored in the FCC-eh. In this case we see that the dips move to lower values of  $|t|$ . This  
 1968 can be easily understood, as with increasing energy the dipole scattering amplitude increases,  
 1969 and thus the dilute-dense boundary shifts to larger values of  $b$ , meaning that the deviation from  
 1970 the exponential fall off occurs for smaller values of  $|t|$ . Similar studies [110] show also the change  
 1971 of the position of the dips with the mass of the vector meson: for lighter vector mesons like  
 1972  $\rho, \omega, \phi$  the dips occur at smaller  $t$  than for the heavier vector mesons  $J/\psi$  or  $\Upsilon$ . We note that,  
 1973 of course, the positions of the dips depend crucially on the details of the models, which are  
 1974 currently not constrained by the existing HERA data. We also note the sizeable uncertainties  
 1975 due to the charm quark mass (the fits to inclusive HERA data from which parameters of the  
 1976 models have been extracted are performed at each fixed value of the charm mass that is then

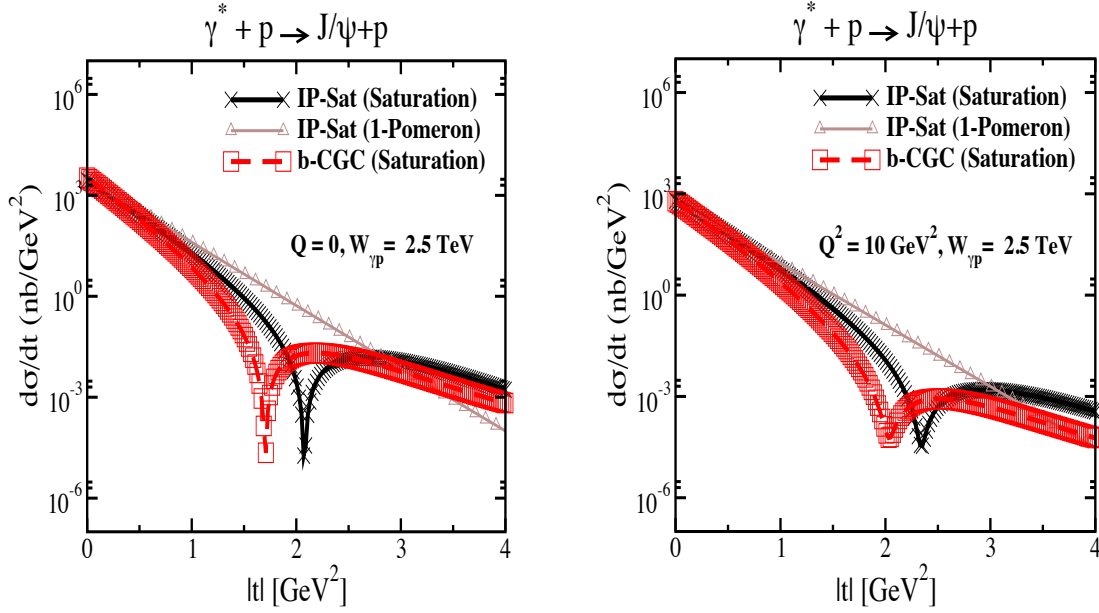


**Figure 3.24:** Differential cross section for elastic  $J/\psi$  production as a function of  $|t|$  within the IP-Sat (saturation), b-CGC and 1-Pomeron models at a fixed  $W_{\gamma p} = 2.5$  TeV, which corresponds to the region that can be explored by FCC-eh, and for two different values of photon virtuality  $Q = 0$  (left plot) and  $Q^2 = 10$  GeV $^2$  (right plot). The thickness of points includes the uncertainties associated with the freedom to choose different values for the charm quark mass within the range  $m_c = 1.2 - 1.4$  GeV .

1977 used to compute exclusive  $J/\psi$  production).

1978 We thus see that the precise measurement of the  $t$ -slope in the elastic production of vector mesons  
 1979 at the LHeC, and its variation with  $x$  and scales, provide a unique opportunity to explore the  
 1980 transition between the dilute and dense partonic regimes. As mentioned earlier, elastic diffractive  
 1981 production is one among several different measurements which can be performed to explore the  
 1982 3D structure of the hadron. Another one is Deeply Virtual Compton Scattering which is a  
 1983 process sensitive to the spatial distribution of quarks inside the hadron. Previous preliminary  
 1984 analyses [1] indicate a huge potential of LHeC for the measurement of DVCS. Another example  
 1985 of a process that could be studied at the LHeC, is diffractive exclusive dijet production. It  
 1986 has been suggested [115] that this process is sensitive to the Wigner function, and that the  
 1987 transverse momentum and spatial distribution of partons can be extracted by measuring this  
 1988 process. The transverse momentum of jets would be sensitive to the transverse momentum of  
 1989 the participating partons, whereas the momentum transfer of the elastically scattered proton  
 1990 would give a handle on the impact parameter distribution of the partons in the target [116–118],  
 1991 thus giving a possibility to extract information about the Wigner distribution.

1992 So far we have referred to coherent diffraction, i.e. to a scenario in which the proton remains  
 1993 intact after the collision. There also exists incoherent diffraction, where the proton gets excited  
 1994 into some state with the quantum numbers of the proton and separated from the rest of the  
 1995 event by a large rapidity gap. In order to apply the dipole formalism to the incoherent case,  
 1996 see Sec. 6.3.1 where the formulae applicable for both protons and nuclei are shown. Here one  
 1997 must consider a more involved structure of the proton (e.g. as composed by a fixed [119–122]  
 1998 or a growing number with  $1/x$  of hot spots [123–125]). As discussed in Sec. 6.3.1, coherent  
 1999 diffraction is sensitive to the gluon distribution in transverse space, while incoherent diffraction  
 2000 is particularly sensitive to fluctuations of the gluon distribution. A prediction of the model with  
 2001 a growing number of hot spots, both in models where this increasing number is implemented

2002 by hand [123–125] and in those where it is dynamically generated [122] from a fixed number  
2003 at larger  $x$ , is that the ratio of incoherent to coherent diffraction will decrease with  $W$ , and  
2004 that this decrease is sensitive to the details of the distribution of hot spots, and thus, to the  
2005 fluctuations of the gluon distribution in transverse space. In order to check these ideas, both  
2006 the experimental capability to separate coherent from incoherent diffraction and a large lever  
2007 arm in  $W$ , as available at the LHeC, are required.

2008 In conclusion, measurements at the LHeC (particularly exclusive diffractive production of vector  
2009 mesons, photons and other final states like dijets) will offer unprecedented opportunities to  
2010 unravel the three-dimensional structure of hadrons in a kinematic region complementary to that  
2011 at the EIC. Note that, such structure varies with  $x$  or energy, so its measurement at small  
2012 enough  $x$  is key as input for both analytic calculations and Monte Carlo simulators at high  
2013 energy hadron colliders. And the large lever arms both in  $x$  and  $Q^2$ , as those offered by the  
2014 LHeC, are required to understand the perturbative evolution of such quantities, as much as it  
2015 is required for collinear PDFs. Ultraperipheral collisions at the LHC, see Refs. [126, 127] and  
2016 references therein, offer an alternative albeit less precise and for photoproduction.

## Chapter 4

# Exploration of Quantum Chromodynamics

The gauge theory formalism of Quantum Chromodynamics (QCD) provides a very successful description of strong interactions between confined partons. Despite the undoubted success of QCD, the strong force still remains one of the least known fundamental sectors of (particle) physics which needs to be explored much deeper.

For an improved understanding of strong interactions and to answer a variety of those open questions additional measurements with highest precision have to be performed. At the LHeC, deep-inelastic electron-proton and lepton-nucleus reactions will extend tests of QCD phenomena to a new and yet unexplored domain up to the TeV scale and to  $x$  values as low as  $10^{-6}$ , and QCD measurements can be performed with very high experimental precision. This is because the proton is a *strongly* bound system and in deep-inelastic scattering (DIS) the exchanged *colourless* photon (or  $Z$ ) between the electron and the parton inside the proton acts as a neutral observer with respect to the phenomena of the strong force. In addition, the over-constrained kinematic system in DIS allows for precise (*in-situ*) calibrations of the detector to measure the kinematics of the scattered lepton, and, more importantly here, also the hadronic final state. In DIS, in many cases, the virtuality of the exchanged  $\gamma/Z$  boson often provides a reasonable scale to stabilise theoretical predictions.

In this Chapter, selected topics of QCD studies at the LHeC are discussed.

### 4.1 Determination of the strong coupling constant

Quantum Chromodynamics (QCD) [128, 129] has been established as the theory of strong interactions within the Standard Model of particle physics. While there are manifold aspects both from the theoretical and from the experimental point-of-view, by far the most important parameter of QCD is the coupling strength which is most commonly expressed at the mass of the  $Z$  boson,  $M_Z$ , as  $\alpha_s(M_Z)$ . Its (renormalisation) scale dependence is given by the QCD gauge group SU(3) [130, 131]. Predictions for numerous processes in  $e^+e^-$ ,  $pp$  or  $ep$  collisions are then commonly performed in the framework of perturbative QCD, and (the lack of) higher-order QCD corrections often represent limiting aspects for precision physics. Therefore, the determination of the strong coupling constant  $\alpha_s(M_Z)$  constitutes one of the most crucial tasks for future precision physics, while at the same time the study of the scale dependence of  $\alpha_s$  provides an inevitable test of the validity of QCD as the theory of strong interactions and the portal for



2049 GUT theories.

2050 Different processes and methodologies can be considered for a determination of  $\alpha_s(M_Z)$  (see e.g.  
 2051 reviews [132–134]). Since QCD is an asymptotically free theory, with free behaviour at high scales  
 2052 but confinement at low scales, a high sensitivity to the value of  $\alpha_s(M_Z)$  is naturally obtained  
 2053 from low-scale measurements. However, the high-scale behaviour must then be calculated by  
 2054 solving the renormalisation group equation, which implies the strict validity of the theory and  
 2055 an excellent understanding of all subleading effects, such as the behaviour around quark-mass  
 2056 thresholds.

2057 Precision measurements at the LHeC offer the unique opportunity to exploit many of these  
 2058 aspects. Measurements of jet production cross sections or inclusive NC and CC DIS cross  
 2059 sections provide a high sensitivity to the value of  $\alpha_s(M_Z)$ , since these measurements can be  
 2060 performed at comparably low scales and with high experimental precision. At the same time,  
 2061 the LHeC provides the opportunity to test the running of the strong coupling constant over a  
 2062 large kinematic range. In this Section, the prospects for a determination of the strong coupling  
 2063 constant with inclusive jet cross sections and with inclusive NC/CC DIS cross sections are  
 2064 studied.

#### 2065 4.1.1 Strong coupling from inclusive jet cross sections

2066 The measurement of inclusive jet or di-jet production cross sections in NC DIS provides a high  
 2067 sensitivity to the strong coupling constant and to the gluon PDF of the proton. This is because  
 2068 jet cross sections in NC DIS are measured in the Breit reference frame [135], where the virtual  
 2069 boson  $\gamma^*$  or  $Z$  collides head-on with the struck parton from the proton and the outgoing jets are  
 2070 required to have a non-zero transverse momentum in that reference frame. The leading order  
 QCD diagrams are QCD Compton and boson-gluon fusion and are both  $\mathcal{O}(\alpha_s)$ , see Fig. 4.1.

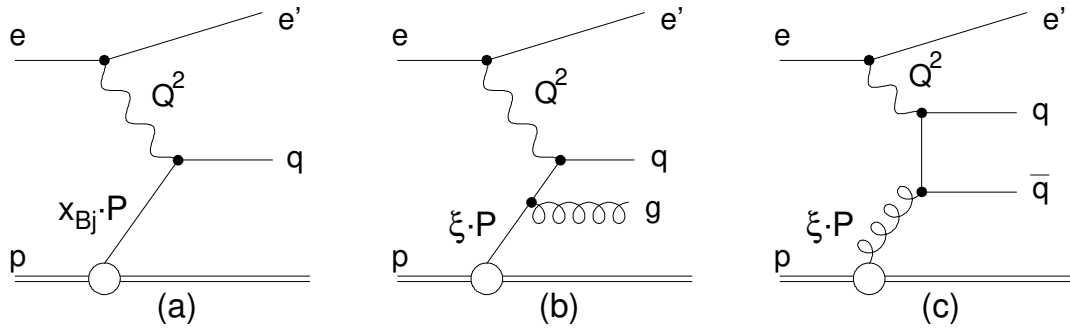


**Figure 4.1:** Leading order diagrams for inclusive DIS (a) and jet production (b,c) in the Breit frame (taken from Ref. [136]).

2071

2072 At HERA, jets are most commonly defined by the longitudinally invariant  $k_t$  jet algorithm [137]  
 2073 with a distance parameter  $R = 1.0$  [136, 138–154]. This provides an infrared safe jet definition  
 2074 and the chosen distance parameter guarantees a small dependence on non-perturbative effects,  
 2075 such as hadronisation. Differently than in  $pp$  at the LHC [155–158], jet algorithms at the LHeC  
 2076 do not require any pile-up subtraction and any reduction of the dependence on minimum bias  
 2077 or underlying event, due to the absence of such effects. Therefore, for this study we adopt the  
 2078 choices made at HERA.

2079 In Fig. 4.2 the next-to-next-to-leading order QCD (NNLO) predictions [159, 160] for cross sec-  
 2080 tions for inclusive jet production in NC DIS as a function of the transverse momentum of the jets  
 2081 in the Breit frame are displayed. The calculations are performed for an electron beam energy of

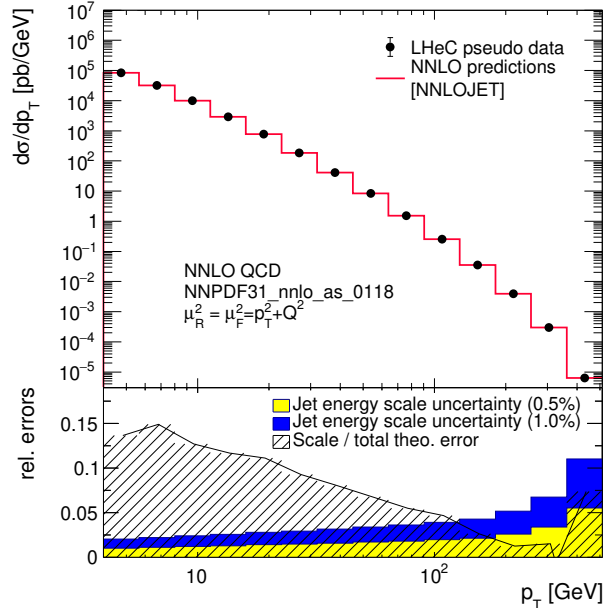


**Figure 4.2:** Inclusive jet cross sections calculated in NNLO QCD as a function of the jet transverse momentum in the Breit frame,  $p_T$ . The shaded area indicates NNLO scale uncertainties and the yellow band shows the estimated experimental jet energy scale uncertainty (JES) of 0.5%. The blue band shows a very conservative assumption on the JES of 1%.

2082  $E_e = 60$  GeV and include  $\gamma/Z$  and  $Z$  exchange terms and account for the electron polarisation  
 2083  $P_e = -0.8$ . The NC DIS kinematic range is set to  $Q^2 > 4$  GeV<sup>2</sup>. The calculations are performed  
 2084 using the NNLOJET program [161] interfaced to the APPLfast library [162–164] which provides  
 2085 a generic interface to the APPLgrid [165, 166] and fastNLO [167, 168] interpolation grid code.

2086 The kinematically accessible range in jet- $p_T$  ranges over two orders of magnitude,  $4 < p_T \lesssim$   
 2087  $400$  GeV. The size of the cross section extends over many orders in magnitude, thus imposing  
 2088 challenging demands on LHeC experimental conditions, triggers and DAQ bandwidth, calibra-  
 2089 tion, and data processing capabilities. The scale uncertainty of the NNLO predictions is about  
 2090 10% at low values of  $p_T$  and significantly decreases with increasing values of  $p_T$ . Future improved  
 2091 predictions will further reduce these theoretical uncertainties.

2092 For the purpose of estimating the uncertainty of  $\alpha_s(M_Z)$  in a determination from inclusive jet  
 2093 cross sections at the LHeC, double-differential cross sections as a function of  $Q^2$  and  $p_T$  with  
 2094 a full set of experimental uncertainties are generated. Altogether 509 cross section values are  
 2095 calculated in the kinematic range  $8 < Q^2 < 500\,000$  GeV<sup>2</sup> and  $4 < p_T < 512$  GeV, and the bin  
 2096 grid is similar to the ones used by CMS, H1 or ZEUS [43, 155, 164, 169]. The various error sources  
 2097 considered are summarised in Tab. 4.1. The uncertainties related to the reconstruction of the  
 2098 NC DIS kinematic variables,  $Q^2$ ,  $y$  and  $x_{bj}$ , are similar to the estimates for the inclusive NC DIS  
 2099 cross sections (see section 3.2). For the reconstruction of hadronic final state particles which are  
 2100 the input to the jet algorithm, jet energy scale uncertainty (JES), calorimetric noise and the polar  
 2101 angle uncertainty are considered. The size of the uncertainties is gauged with achieved values by  
 2102 H1, ZEUS, ATLAS and CMS [145, 153, 170, 171]. The size of the dominant JES one is assumed  
 2103 to be 0.5% for reconstructed particles in the laboratory rest frame, yielding an uncertainty of  
 2104 0.2–4.4% on the cross section after the boost to the Breit frame. A JES uncertainty of 0.5%  
 2105 is well justified by improved calorimeters, since already H1 and ZEUS reported uncertainties  
 2106 of 1% [145, 153, 172], and ATLAS and CMS achieved 1% over a wide range in  $p_T$  [170, 171],

2107 albeit the presence of pile-up and the considerably more complicated definition of a reference  
 2108 object for the in-situ calibration. The size of the JES uncertainty is also displayed in Fig. 4.2.  
 2109 The calorimetric noise of  $\pm 20$  MeV on every calorimeter cluster, as reported by H1, yields an  
 2110 uncertainty of up to 0.7% on the jet cross sections. A minimum size of the statistical uncertainty  
 2111 of 0.15% is imposed for each cross section bin. An overall normalisation uncertainty of 1.0%  
 2112 is assumed, which will be mainly dominated by the luminosity uncertainty. In addition, an  
 2113 uncorrelated uncertainty component of 0.6% collects various smaller error sources, such as for  
 2114 instance radiative corrections, unfolding or model uncertainties. Studies on the size and the  
 correlation model of these uncertainties are performed below.

Exp. uncertainty	Shift	Size on $\sigma$ [%]
Statistics with $1 \text{ ab}^{-1}$	min. 0.15 %	0.15–5
Electron energy	0.1 %	0.02–0.62
Polar angle	2 mrad	0.02–0.48
Calorimeter noise	$\pm 20$ MeV	0.01–0.74
Jet energy scale (JES)	0.5 %	0.2–4.4
Uncorrelated uncert.	0.6 %	0.6
Normalisation uncert.	1.0 %	1.0

**Table 4.1:** Anticipated uncertainties of inclusive jet cross section measurements at the LHeC.

2115

2116 The value and uncertainty of  $\alpha_s(M_Z)$  is obtained in a  $\chi^2$ -fit of NNLO predictions [159, 160] to  
 2117 the simulated data with  $\alpha_s(M_Z)$  being a free fit parameter. The methodology follows closely  
 2118 analyses of HERA jet data [164, 169] and the  $\chi^2$  quantity is calculated from relative uncertainties,  
 2119 i.e. those of the right column of Tab. 4.1. The predictions for the cross section  $\sigma$  account for  
 2120 both  $\alpha_s$ -dependent terms in the NNLO calculations, i.e. in the DGLAP operator and the hard  
 2121 matrix elements, by using

$$\sigma = f_{\mu_0} \otimes P_{\mu_0 \rightarrow \mu_F}(\alpha_s(M_Z)) \otimes \hat{\sigma}(\alpha_s(M_Z), \mu), \quad (4.1)$$

2122 where  $f_{\mu_0}$  are the PDFs at a scale of  $\mu_0 = 30$  GeV, and  $P_{\mu_0 \rightarrow \mu_F}$  denotes the DGLAP operator,  
 2123 which is dependent on the value of  $\alpha_s(M_Z)$ . The  $\alpha_s$  uncertainty is obtained by linear error  
 2124 propagation and is validated with a separate study of the  $\Delta\chi^2 = 1$  criterion.

2125 In the fit of NNLO QCD predictions to the simulated double-differential LHeC inclusive jet cross  
 2126 sections an uncertainty of

$$\Delta\alpha_s(M_Z)(\text{jets}) = \pm 0.00013_{(\text{exp})} \pm 0.00010_{(\text{PDF})} \quad (4.2)$$

2127 is found. The PDF uncertainty is estimated from a PDF set obtained from LHeC inclusive DIS  
 2128 data (see Sec. 3.3). These uncertainties promise a determination of  $\alpha_s(M_Z)$  with the highest  
 2129 precision and would represent a considerable reduction of the current world average value with  
 2130 a present uncertainty of  $\pm 0.00110$  [133].

2131 The uncertainty of  $\alpha_s$  is studied for different values of the experimental uncertainties for the  
 2132 inclusive jet cross section measurement and for different assumption on bin-to-bin correlations,  
 2133 expressed by the correlation coefficient  $\rho$ , of individual uncertainty sources, as shown in Fig. 4.3.  
 2134 It is observed that, even for quite conservative scenarios,  $\alpha_s(M_Z)$  will be determined with an  
 2135 uncertainty smaller than 2‰. For this, it is important to keep the size of the uncorrelated  
 2136 uncertainty or the uncorrelated components of other systematic uncertainties under good control.  
 2137 This is also visible from Fig. 4.3 (bottom right), where the contributions of the individual  
 2138 uncertainty sources to the total uncertainty of  $\alpha_s(M_Z)$  are displayed, and it is seen that the

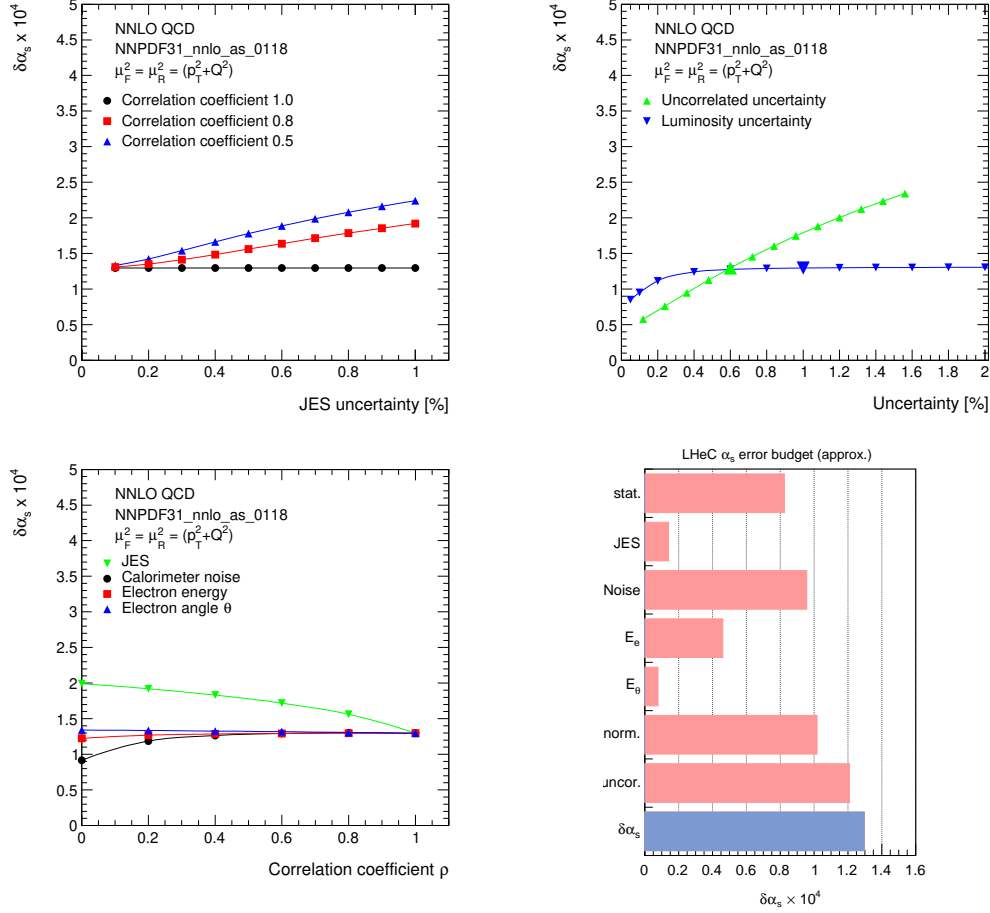


**Figure 4.3:** Studies of the size and correlations of experimental uncertainties impacting the uncertainty of  $\alpha_s(M_Z)$ . Top left: Study of the value of the correlation coefficient  $\rho$  for different systematic uncertainties. Common systematic uncertainties are considered as fully correlated,  $\rho = 1$ . Top right: Size of the JES uncertainty for three different values of  $\rho_{\text{JES}}$ . Bottom left: Impact of the uncorrelated and normalisation uncertainties on  $\Delta\alpha_s(M_Z)$ . Bottom right: Contribution of individual sources of experimental uncertainty to the total experimental uncertainty of  $\alpha_s(M_Z)$ .

2139 uncorrelated and the normalisation uncertainty are the largest individual uncertainty compo-  
 2140 nents. It is further observed, that the size of the statistical uncertainty (stat.) is non-negligible,  
 2141 which is, however, strongly dependent on the *ad hoc* assumption on the minimum size of 0.15%.  
 2142 The noise uncertainty contributes mainly to jets at low- $p_T$ , and since these have a particular  
 2143 high sensitivity to  $\alpha_s(M_Z)$ , due to their low scale  $\mu_R$ . It is of great importance to keep this  
 2144 experimental uncertainty well under control, or make better use of track-based information for  
 2145 the measurement of jets.

2146 In the present formalism theoretical uncertainties from scale variations of the NNLO predictions  
 2147 amount to about  $\Delta\alpha_s(M_Z) = 0.0035$  (NNLO). These can be reduced with suitable cuts in  $p_T$  or  
 2148  $Q^2$  to about  $\Delta\alpha_s(M_Z) \approx 0.0010$ . However, it is expected that improved predictions, e.g. with  
 2149 resummed contributions or  $N^3\text{LO}$  predictions will significantly reduce these uncertainties in the  
 2150 future. Uncertainties on non-perturbative hadronisation effects will have to be considered as  
 2151 well, but these will be under good control due to the measurements of charged particle spectra  
 2152 at the LHeC and improved phenomenological models.

## 2153 4.1.2 Pinning Down $\alpha_s$ with Inclusive and Jet LHeC Data

2154 The dependence of the coupling strength as a function of the renormalisation scale  $\mu_R$  is predicted  
 2155 by QCD, which is often called the *running* of the strong coupling. Its study with experimental  
 2156 data represents an important consistency and validity test of QCD. Using inclusive jet cross  
 2157 sections the running of the strong coupling can be tested by determining the value of  $\alpha_s$  at  
 2158 different values of  $\mu_R$  by grouping data points with similar values of  $\mu_R$  and determining the  
 2159 value of  $\alpha_s(\mu_R)$  from these subsets of data points. The assumptions on the running of  $\alpha_s(\mu_R)$   
 2160 are then imposed only for the limited range of the chosen interval, and not to the full measured  
 2161 interval as in the previous study. Here we set  $\mu_R^2 = Q^2 + p_T^2$ <sup>1</sup>. The experimental uncertainties  
 from the fits to subsets of the inclusive jet pseudodata are displayed in Fig. 4.4. These results

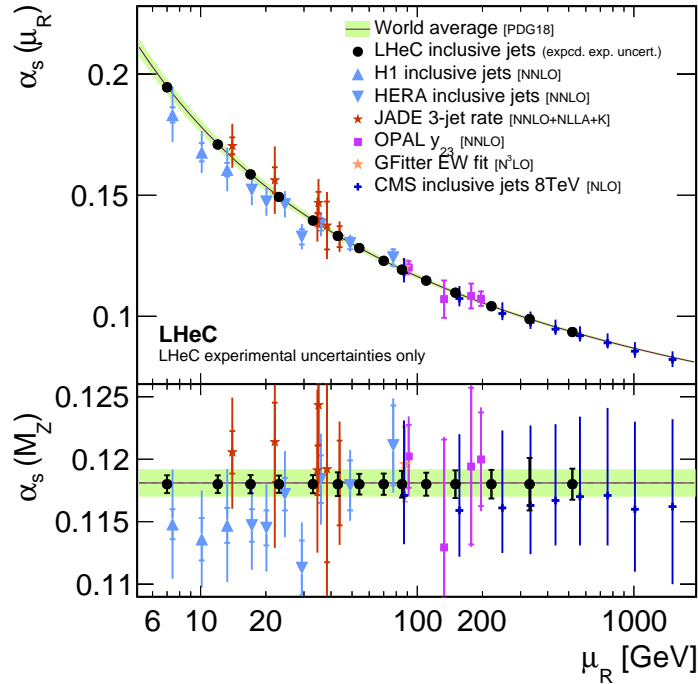


**Figure 4.4:** Uncertainties of  $\alpha_s(M_Z)$  and corresponding  $\alpha_s(\mu_R)$  in a determination of  $\alpha_s$  using LHeC inclusive jet cross sections at different values of  $\mu_R^2 = Q^2 + p_T^2$ . Only experimental uncertainties are shown for LHeC and are compared with a number of presently available measurements and the world average value.

2162 demonstrate a high sensitivity to  $\alpha_s$  over two orders of magnitude in renormalisation scale up  
 2163 to values of about  $\mu_R \approx 500$  GeV. In the range  $6 < \mu_R \lesssim 200$  GeV the experimental uncertainty  
 2164 is found to be smaller than the expectation from the world average value [180]. This region is of  
 2165 particular interest since it connects the precision determinations from lattice calculations [181]  
 2166 or  $\tau$  decay measurements [182], which are at low scales  $\mathcal{O}(\text{GeV})$ , to the measurements at the  
 2167  $Z$  pole [183] and to the applications to scales which are relevant for the LHC, e.g. for Higgs  
 2168

<sup>1</sup>The choice of the scales follows a *conventional* scale setting procedure and uncertainties for the scale choice and for unknown higher order terms are estimated by varying the scales. Such variations are sensitive only to the terms which govern the behaviour of the running coupling, and may become unreliable due to renormalons [173]. An alternative way to fix the scales is provided by the Principle of Maximum Conformality (PMC) [174–178]. The PMC method was recently applied to predictions of event shape observables in  $e^+e^- \rightarrow \text{hadrons}$  [179]. When applying the PMC method to observables in DIS, the alternative scale setting provides a profound alternative to verify the running of  $\alpha_s(\mu_R)$ . Such a procedure could be particularly relevant for DIS event shape observables, where the leading-order terms are insensitive to  $\alpha_s$  and conventional scale choices may not be adequately related to the  $\alpha_s$ -sensitive higher order QCD corrections.

2169 or top-quark physics or high-mass searches. This kinematic region of scales  $\mathcal{O}(10 \text{ GeV})$  cannot  
 2170 be accessed by (HL-)LHC experiments because of limitations due to pile-up and underlying  
 2171 event [184].

2172 Inclusive DIS cross sections are sensitive to  $\alpha_s(M_Z)$  through higher-order QCD corrections,  
 2173 contributions from the  $F_L$  structure function and the scale dependence of the cross section at  
 2174 high  $x$  (*scaling violations*). The value of  $\alpha_s(M_Z)$  can then be determined in a combined fit  
 2175 of the PDFs and  $\alpha_s(M_Z)$  [169]. While a simultaneous determination of  $\alpha_s(M_Z)$  and PDFs is  
 2176 not possible with HERA inclusive DIS data alone due to its limited precision and kinematic  
 2177 coverage [43, 169], the large kinematic coverage, high precision and the integrated luminosity of  
 2178 the LHeC data will allow for the first time such an  $\alpha_s$  analysis.

2179 For the purpose of the determination of  $\alpha_s(M_Z)$  from inclusive NC/CC DIS data, a combined  
 2180 PDF+ $\alpha_s$  fit to the simulated data is performed, similar to the studies presented above, in  
 2181 Chapter 3. Other technical details are outlined in Ref. [169]. In this fit, however, the numbers  
 2182 of free parameters of the gluon parameterisation is increased, since the gluon PDF and  $\alpha_s(M_Z)$   
 2183 are highly correlated and LHeC data are sensitive to values down to  $x < 10^{-5}$ , which requires  
 2184 additional freedom for the gluon parameterisation. The inclusive data are restricted to  $Q^2 \geq$   
 2185  $5 \text{ GeV}^2$  in order to avoid a region where effects beyond fixed-order perturbation theory may  
 2186 become sizeable [43, 185].

2187 Exploiting the full LHeC inclusive NC/CC DIS data with  $E_e = 50 \text{ GeV}$ , the value of  $\alpha_s(M_Z)$  can  
 2188 be determined with an uncertainty  $\Delta\alpha_s(M_Z) = \pm 0.00038$ . With a more optimistic assumption  
 2189 on the dominant uncorrelated uncertainty of  $\delta\sigma_{(\text{uncor.})} = 0.25 \%$ , an uncertainty as small as

$$\Delta\alpha_s(M_Z)(\text{incl. DIS}) = \pm 0.00022_{(\text{exp+PDF})} \quad (4.3)$$

2190 is achieved. This would represent a considerable improvement over the present world average  
 2191 value. Given these small uncertainties, theoretical uncertainties from missing higher orders or  
 2192 heavy quark effects have to be considered in addition. In a dedicated study, the fit is repeated  
 2193 with a reduced data set which can be accumulated already during a single year of operation <sup>2</sup>,  
 2194 corresponding to about  $\mathcal{L} \sim 50 \text{ fb}^{-1}$ . Already these data will be able to improve the world  
 2195 average value. These studies are displayed in Fig. 4.5.

2196 High sensitivity to  $\alpha_s(M_Z)$  and an optimal treatment of the PDFs is obtained by using inclusive  
 2197 jet data together with inclusive NC/CC DIS data in a combined determination of  $\alpha_s(M_Z)$  and  
 2198 the PDFs. The jet data will provide an enhanced sensitivity to  $\alpha_s(M_Z)$ , while inclusive DIS data  
 2199 has the highest sensitivity to the determination of the PDFs. In such combined QCD analyses,  
 2200 also heavy quark data may be further analysed to determine  $m_c$  and  $m_b$ . However, since jet  
 2201 cross sections have sufficiently high scale ( $p_T \gg m_b$ ) these are fairly insensitive to the actual  
 2202 value of the heavy quark masses. Contrary, heavy quark data is predominantly sensitive to the  
 2203 quark mass parameters rather than to  $\alpha_s(M_Z)$ , and their correlation is commonly found to be  
 2204 small in such combined analyses, see e.g. Ref [51]. Infact, at LHeC the masses of charm and  
 2205 bottom quarks can be determined with high precision and uncertainties of 3 MeV and 10 MeV  
 2206 are expected, respectively [1]. Therefore, for our sole purpose of estimating the uncertainty of  
 2207  $\alpha_s(M_Z)$  from LHeC data, we do not consider heavy quark data, nor free values of  $m_c$  or  $m_b$   
 2208 in the analysis, and we leave the outcome of such a complete QCD analysis to the time when  
 2209 real data are available and the actual value of the parameters are of interest. At this time, also  
 2210 better theoretical predictions will be used, including higher order corrections, heavy quark mass  
 2211 effects or higher-twist terms, as can be expected from steady progress [186–191].

<sup>2</sup>Two different assumptions are made. One fit is performed with only electron data corresponding to  $\mathcal{L} \sim 50 \text{ fb}^{-1}$ , and an alternative scenario considers further positron data corresponding to  $\mathcal{L} \sim 1 \text{ fb}^{-1}$ .

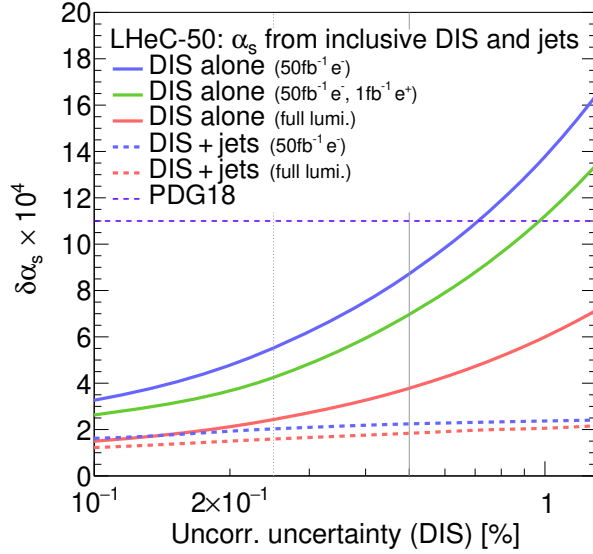


**Figure 4.5:** Uncertainties of  $\alpha_s(M_Z)$  from simultaneous fits of  $\alpha_s(M_Z)$  and PDFs to inclusive NC/CC DIS data as a function of the size of the uncorrelated uncertainty of the NC/CC DIS data. The full lines indicate the uncertainties obtained with different assumptions on the data taking scenario and integrated luminosity. The dashed lines indicate results where, additionally to the inclusive NC/CC DIS data, inclusive jet cross section data are considered.

2212 For this study, the double-differential inclusive jet data as described above, and additionally  
 2213 the inclusive NC/CC DIS data with  $E_e = 50 \text{ GeV}$  as introduced in Sec. 3.2, are employed.  
 2214 Besides the normalisation uncertainty, all sources of systematic uncertainties are considered as  
 2215 uncorrelated between the two processes. A fit of NNLO QCD predictions to these data sets is  
 2216 then performed, and  $\alpha_s(M_Z)$  and the parameters of the PDFs are determined. The methodology  
 2217 follows closely the methodology sketched in Sect. 3. Using inclusive jet and inclusive DIS data  
 2218 in a single analysis, the value of  $\alpha_s(M_Z)$  is determined with an uncertainty of

$$\Delta\alpha_s(M_Z)(\text{incl. DIS \& jets}) = \pm 0.00018_{(\text{exp+PDF})}. \quad (4.4)$$

2219 This result will improve the world average value considerably. However, theoretical uncertainties  
 2220 are not included and new mathematical tools and an improved understanding of QCD will  
 2221 be needed in order to achieve small values similar to the experimental ones. The dominant  
 2222 sensitivity in this study arises from the jet data. This can be seen from Fig. 4.5, where  $\Delta\alpha_s(M_Z)$   
 2223 changes only moderately with different assumptions imposed on the inclusive NC/CC DIS data.  
 2224 Assumptions made for the uncertainties of the inclusive jet data have been studied above, and  
 2225 these results can be translated easily to this PDF+ $\alpha_s$  fit.

2226 The expected values for  $\alpha_s(M_Z)$  obtained from inclusive jets or from inclusive NC/CC DIS data  
 2227 are compared in Fig. 4.6 with present determinations from global fits based on DIS data (called  
 2228 *PDF fits*) and the world average value [133]. It is observed that LHeC will have the potential  
 2229 to improve considerably the world average value. Already after one year of data taking, the  
 2230 experimental uncertainties of the NC/CC DIS data are competitive with the world average  
 2231 value. The measurement of jet cross sections will further improve that value (not shown).

2232 Furthermore, LHeC will be able to address a long standing puzzle. All  $\alpha_s$  determinations from  
 2233 global fits based on NC/CC DIS data find a lower value of  $\alpha_s(M_Z)$  than determinations in the  
 2234 lattice QCD framework, from  $\tau$  decays or in a global electroweak fit. With the expected precision  
 2235 from LHeC this discrepancy will be resolved.

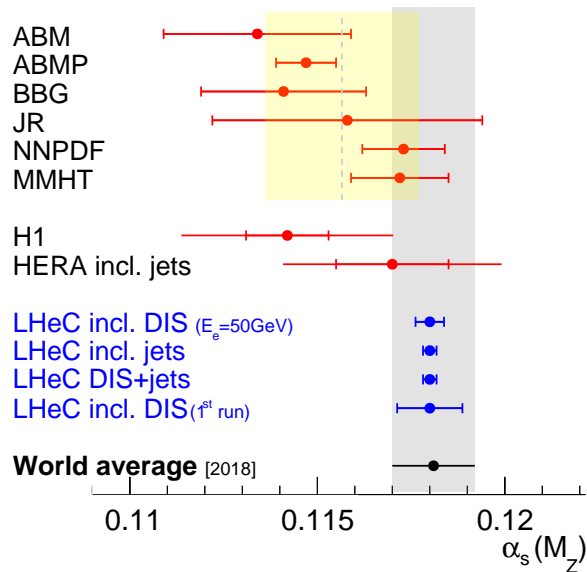


Figure 4.6: Summary of  $\alpha_s(M_Z)$  values in comparison with present values.

### 4.1.3 Strong coupling from other processes

A detailed study for the determination of  $\alpha_s(M_Z)$  from NC/CC DIS and from inclusive jet data was presented in the previous paragraphs. However, a large number of additional processes and observables that are measured at the LHeC can also be considered for a determination of  $\alpha_s(M_Z)$ . Suitable observables or processes are di-jet and multi-jet production, heavy flavour production, jets in photoproduction or event shape observables. These processes all exploit the  $\alpha_s$  dependence of the hard interaction. Using suitable predictions, also *softer* processes can be exploited for an  $\alpha_s$  determination. Examples could be jet shapes or other substructure observables, or charged particle multiplicities.

Since  $\alpha_s(M_Z)$  is a parameter of a phenomenological model, the total uncertainty of  $\alpha_s(M_Z)$  is always a sum of experimental and theoretical uncertainties which are related to the definition of the observable and to the applied model, e.g. hadronisation uncertainties, diagram removal/subtraction uncertainties or uncertainties from missing higher orders. Therefore, credible prospects for the total uncertainty of  $\alpha_s(M_Z)$  from other observables or processes altogether are difficult to predict, even more since LHeC will explore a new kinematic regime that was previously unmeasured.

In a first approximation, for any process the sensitivity to  $\alpha_s(M_Z)$  scales with the order  $n$  of  $\alpha_s$  in the leading-order diagram,  $\alpha_s^n$ . The higher the power  $n$  the higher the sensitivity to  $\alpha_s(M_Z)$ . Consequently, the experimental uncertainty of an  $\alpha_s$  fit may reduce with increasing power  $n$ . Already at HERA three-jet cross section were proven to have a high sensitivity to  $\alpha_s(M_Z)$  albeit their sizeable statistical uncertainties [136, 146]. At the LHeC, due to the higher  $\sqrt{s}$  and huge integrated luminosity, as well as the larger acceptance of the detector, three-, four- or five-jet cross sections represent highly sensitive observables for a precise determination of  $\alpha_s(M_Z)$ , and high experimental precision can be achieved. In these cases, fixed order pQCD predictions may become limiting factors, since they are more complicated for large  $n$ .

Di-jet observables are expected to yield a fairly similar experimental uncertainty than inclusive



2262 jet cross sections, as studied in the previous paragraphs, since both have  $n = 1$  at LO. How-  
 2263 ever, their theoretical uncertainties may be smaller, since di-jet observables are less sensitive to  
 2264 additional higher-order radiation, in particular at lower scales where  $\alpha_s(\mu_R)$  is larger.

2265 Event shape observables in DIS exploit additional radiation in DIS events (see e.g. review [192]  
 2266 or HERA measurements [193, 194]). Consequently, once measured at the LHeC the experi-  
 2267 mental uncertainties of  $\alpha_s(M_Z)$  from these observables are expected to become very similar  
 2268 to that in Eq. (4.4), since both the event sample and the process is similar to the inclusive  
 2269 jet cross sections<sup>3</sup>. However, different reconstruction techniques of the observables may yield  
 2270 reduced experimental uncertainties, and the calculation of event shape observables allow for  
 2271 the resummation of large logarithms, and steady theoretical advances promise small theoretical  
 2272 uncertainties [195–201].

2273 Jet production cross sections in photoproduction represents a unique opportunity for another  
 2274 precision determination of  $\alpha_s(M_Z)$ . Such measurements have been performed at HERA [202–  
 2275 205]. The sizeable photoproduction cross section provides a huge event sample, which is statis-  
 2276 tically independent from NC DIS events, and already the leading-order predictions are sensitive  
 2277 to  $\alpha_s(M_Z)$  [206]. Also its running can be largely measured since the scale of the process is well  
 2278 estimated by the transverse momentum of the jets  $\mu_R \sim p_T^{\text{jet}}$ . Limiting theoretical aspects are  
 2279 due to the presence of a quasi-real photon and the poorly known photon PDF [207, 208].

2280 A different class of observables represent heavy flavour (HF) cross sections, which are discussed in  
 2281 Sec. 3.3.5. Due to flavour conservation, these are commonly proportional to  $\mathcal{O}(\alpha_s^1)$  at leading-  
 2282 order. However, when considering inclusive HF cross sections above the heavy quark mass  
 2283 threshold heavy quarks can be factorised into the PDFs, and the leading structure functions  
 2284  $F_2^{c,b}$  are sensitive to  $\alpha_s$  only beyond the LO approximation (see reviews [78, 79], recent HERA  
 2285 measurements [63, 209] and references therein). The presence of the heavy quark mass as an  
 2286 additional scale stabilises perturbative calculations, and reduced theoretical uncertainties are  
 2287 expected.

2288 At the LHeC the structure of jets and the formation of hadrons can be studied with unprece-  
 2289 dented precision. This is so because of the presence of a single hadron in the initial state.  
 2290 Therefore, limiting effects like the underlying event or pile-up are absent or greatly diminished.  
 2291 Precise measurements of jet shape observables, or the study of jet substructure observables [210],  
 2292 are highly sensitive to the value of  $\alpha_s(M_Z)$ , because parton shower and hadronisation take place  
 2293 at lower scales where the strong coupling becomes large and an increased sensitivity to  $\alpha_s(M_Z)$   
 2294 is attained [162, 211].

2295 Finally, also the determination of  $\alpha_s(M_Z)$  from inclusive NC DIS cross sections can be improved.  
 2296 For NC DIS the dominant sensitivity to  $\alpha_s$  arises from the  $F_L$  structure function and from scaling  
 2297 violations of  $F_2$  at lower values of  $Q^2$  but at very high values of  $x$ . Dedicated measurements of  
 2298 these kinematic regions will further improve the experimental uncertainties from the estimated  
 2299 values in Eq. (4.3).

## 2300 4.2 Discovery of New Strong Interaction Dynamics at Small $x$

2301 The LHeC machine will offer access to a completely novel kinematic regime of DIS characterised  
 2302 by very small values of  $x$ . From the kinematical plane in  $(x, Q^2)$  depicted in Fig. 1.1, it is clear  
 2303 that the LHeC will be able to probe Bjorken- $x$  values as low as  $10^{-6}$  for perturbative values of

---

<sup>3</sup>It shall be noted, that event shape observables in NC DIS can be defined in the laboratory rest frame or the Breit frame.

2304  $Q^2$ . At low values of  $x$  various phenomena may occur which go beyond the standard collinear  
 2305 perturbative description based on DGLAP evolution. Since the seminal works of Balitsky,  
 2306 Fadin, Kuraev and Lipatov [114, 212, 213] it has been known that, at large values of centre-of-  
 2307 mass energy  $\sqrt{s}$  or, to be more precise, in the Regge limit, there are large logarithms of energy  
 2308 which need to be resummed. Thus, even at low values of the strong coupling  $\alpha_s$ , logarithms of  
 2309 energy  $\ln s$  may be sufficiently large, such that terms like  $(\alpha_s \ln s)^n$  will start to dominate the  
 2310 cross section.

2311 In addition, other novel effects may appear in the low  $x$  regime, which are related to the high  
 2312 gluon densities. At large parton densities the recombination of the gluons may become important  
 2313 in addition to the gluon splitting. This is known as the parton saturation phenomenon in QCD,  
 2314 and is deeply related to the restoration of the unitarity in QCD. As a result, the linear evolution  
 2315 equations will need to be modified by the additional nonlinear terms in the gluon density. In the  
 2316 next two subsections we shall explore the potential and sensitivity of the LHeC to these small  
 2317  $x$  phenomena in  $ep$  collisions. Note also that, being a density effect, the non-linear phenomena  
 2318 leading to parton saturation are enhanced by increasing the mass number of the nucleus in  $eA$ .  
 2319 Chapter 6, devoted to the physics opportunities with  $eA$  collisions at the LHeC, discusses this  
 2320 aspect, see also Ref. [1].

#### 2321 4.2.1 Resummation at small $x$

2322 The calculation of scattering amplitudes in the high-energy limit and the resummation of  
 2323  $(\alpha_s \ln s)^n$  series in the leading logarithmic order was performed in Refs. [114, 212, 213] and it  
 2324 resulted in the famous BFKL evolution equation. This small  $x$  evolution equation, written for  
 2325 the so-called gluon Green's function or the unintegrated gluon density, is a differential equation  
 2326 in  $\ln 1/x$ . An important property of this equation is that it keeps the transverse momenta un-  
 2327 ordered along the gluon cascade. This has to be contrasted with DGLAP evolution which is  
 2328 differential in the hard scale  $Q^2$  and relies on the strong ordering in the transverse momenta of  
 2329 the exchanged partons in the parton cascade. The solution to the BFKL equation is a gluon  
 2330 density which grows sharply with decreasing  $x$ , as a power i.e.  $\sim x^{-\omega_{IP}}$ , where  $\omega_{IP}$  is the hard  
 2331 Pomeron intercept, and in the leading logarithmic approximation equals  $\frac{N_c \alpha_s}{\pi} 4 \ln 2$ , which gives  
 2332 a value of about 0.5 for typical values of the strong coupling. The leading logarithmic (LLx)  
 2333 result yielded a growth of the gluon density which was too steep for the experimental data at  
 2334 HERA. The next-to-leading logarithmic (NLLx) calculation performed in the late 90s [214, 215]  
 2335 resulted in large negative corrections to the LLx value of the hard Pomeron intercept and yielded  
 2336 some instabilities in the cross section [216–219] and it is important to account for subleading  
 2337 effects, since these are large [220, 221].

2338 The appearance of the large negative corrections at NLLx motivated the search for the appro-  
 2339 priate resummation which would stabilize the result. It was understood very early that the large  
 2340 corrections which appear in BFKL at NLLx are mostly due to the kinematics [222–224] as well as  
 2341 DGLAP terms and the running of the strong coupling. First attempts at combining the BFKL  
 2342 and DGLAP dynamics together with the proper kinematics [225–227] yielded encouraging re-  
 2343 sults, and allowed a description of HERA data on structure functions with good accuracy. The  
 2344 complete resummation program was developed in a series of works [228–244]. In these works  
 2345 the resummation for the gluon Green's function and the splitting functions was developed.

2346 The low- $x$  resummation was recently applied to the description of structure function data at  
 2347 HERA using the methodology of NNPDF [245]. It was demonstrated that the resummed fits  
 2348 provide a better description of the structure function data than the pure DGLAP based fits at  
 2349 fixed NNL order. In particular, it was shown that the  $\chi^2$  of the fits does not vary appreciably

2350 when more small  $x$  data are included in the case of the fits which include the effects of the small- $x$   
 2351 resummation. On the other hand, the fits based on NNLO DGLAP evolution exhibit a worsening  
 2352 of their quality in the region of low  $x$  and low to moderate values of  $Q^2$ . This indicates that  
 2353 there is some tension in the fixed order fits based on DGLAP, and that resummation alleviates  
 2354 it. In addition, it was shown that the description of the longitudinal structure function  $F_L$   
 2355 from HERA data is improved in the fits with the small  $x$  resummation. This analysis suggests  
 2356 that the small  $x$  resummation effects are indeed visible in the HERA kinematic region. Such  
 2357 effects will be strongly magnified at the LHeC, which probes values of  $x$  more than one order  
 2358 of magnitude lower than HERA. The NNPDF group also performed simulation of the structure  
 2359 functions  $F_2$  and  $F_L$  with and without resummation in the LHeC range as well as for the next  
 2360 generation electron-hadron collider FCC-eh [245]. The predictions for the structure functions as  
 2361 a function of  $x$  for fixed values of  $Q^2$  are shown in Figs. 4.7.

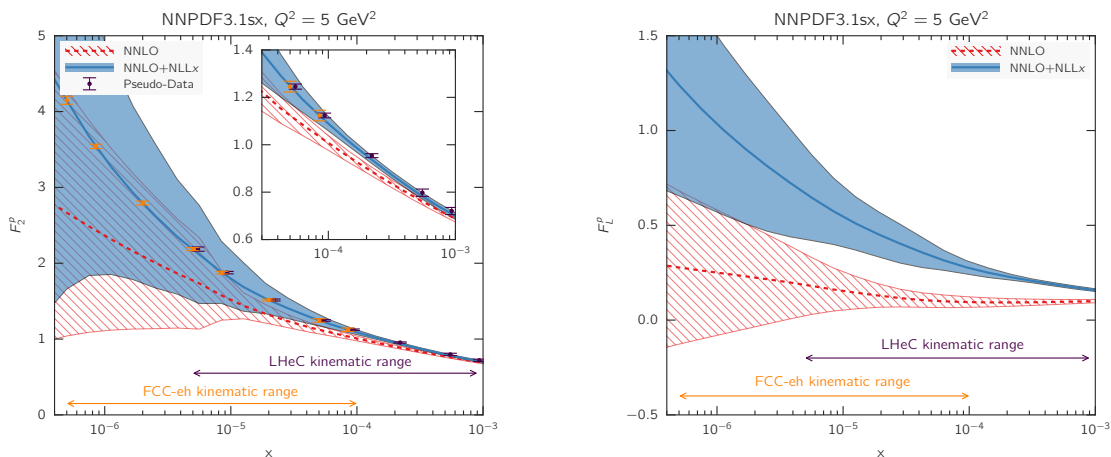


**Figure 4.7:** Predictions for the  $F_2$  and  $F_L$  structure functions using the NNPDF3.1sx NNLO and NNLO+NLL $x$  fits at  $Q^2 = 5 \text{ GeV}^2$  for the kinematics of the LHeC and FCC-eh. In the case of  $F_2$ , we also show the expected total experimental uncertainties based on the simulated pseudodata, assuming the NNLO+NLL $x$  values as the central prediction. A small offset has been applied to the LHeC pseudodata as some of the values of  $x$  overlap with the FCC-eh pseudodata points. The inset in the left plot shows a magnified view in the kinematic region  $x > 3 \times 10^{-5}$ , corresponding to the reach of HERA data. Figure taken from Ref. [245].

2362 The simulations were done using APFEL [246] together with the HELL package [247] which  
 2363 implements the small  $x$  resummation. From Fig. 4.7 it is clear that LHeC will have much higher  
 2364 sensitivity to discriminate between fixed order and resummed scenarios than the HERA collider,  
 2365 with even better discrimination at the FCC-eh. The differences between the central values for  
 2366 the two predictions are of the order of 15% for the case of  $F_2$  and this is much larger than  
 2367 the projected error bar on the reduced cross section or structure function  $F_2$  which could be  
 2368 measured at LHeC. For comparison, the simulated pseudodata for  $F_2$  are shown together with  
 2369 the expected experimental uncertainties. The total uncertainties of the simulated pseudodata  
 2370 are at the few percent level at most, and are therefore much smaller than the uncertainties  
 2371 coming from the PDFs in most of the kinematic range.

2372 It is evident that fits to the LHeC data will have power to discriminate between the different  
 2373 frameworks. In the right plot in Fig. 4.7, the predictions for the longitudinal structure function  
 2374 are shown. We see that in the case of the  $F_L$  structure function, the differences between the  
 2375 fixed order and resummed predictions are even larger, consistently over the entire range of  $x$ .  
 2376 This indicates the importance of the measurement of the longitudinal structure function  $F_L$

2377 which can provide further vital constraints on the QCD dynamics in the low  $x$  region due to its  
 2378 sensitivity to the gluon density in the proton.

2379 To further illustrate the power of a high energy DIS collider like the LHeC in exploring the  
 2380 dynamics at low  $x$ , fits which include the simulated data were performed. The NNLO+NLLx  
 2381 resummed calculation was used to obtain the simulated pseudodata, both for the LHeC, in a  
 2382 scenario of a 60 GeV electron beam on a 7 TeV proton beam as well as in the case of the FCC-eh  
 2383 scenario with a 50 TeV proton beam. All the experimental uncertainties for the pseudodata have  
 2384 been added in quadrature. Next, fits were performed to the DIS HERA as well as LHeC and  
 2385 FCC-eh pseudodata using the theory with and without the resummation at low  $x$ . Hadronic  
 2386 data like jet, Drell-Yan or top, were not included for this analysis but, as demonstrated in [245],  
 2387 these data do not have much of the constraining power at low  $x$ , and therefore the results of  
 2388 the analysis at low  $x$  are independent of the additional non-DIS data sets. The quality of the  
 2389 fits characterised by the  $\chi^2$  was markedly worse when the NNLO DGLAP framework was used  
 2390 to fit the HERA data and the pseudodata from LHeC and/or FCC-eh than was the case with  
 2391 resummation. To be precise, the  $\chi^2$  per degree of freedom for the HERA data set was equal to  
 2392 1.22 for the NNLO fit, and 1.07 for the resummed fit. For the case of the LHeC/FCC-eh the  $\chi^2$   
 2393 per degree of freedom was equal to 1.71/2.72 and 1.22/1.34 for NNLO and NNLO+resummation  
 2394 fits, respectively. These results demonstrate the huge discriminatory power of the new DIS  
 2395 machines between the DGLAP and resummed frameworks, and the large sensitivity to the low  
 2396  $x$  region while simultaneously probing low to moderate  $Q^2$  values.

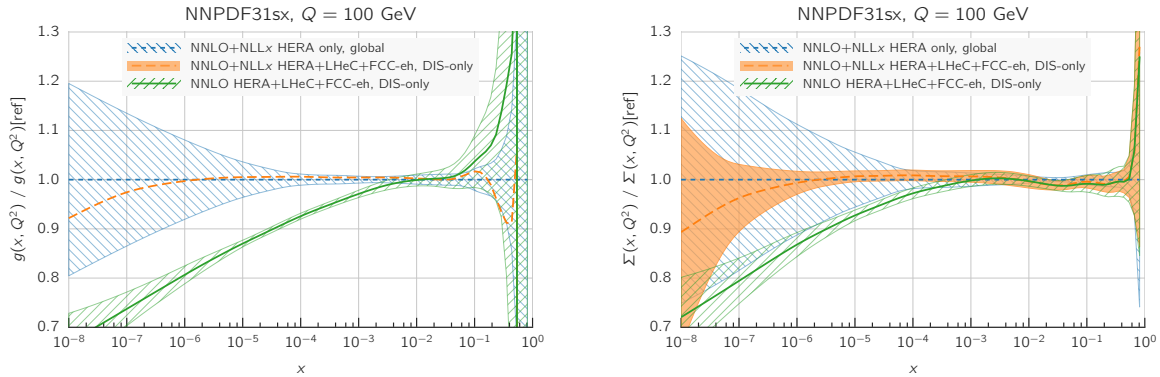


**Figure 4.8:** Comparison between the gluon (left plot) and the quark singlet (right plot) PDFs in the NNPDF3.1sx NNLO+NLLx fits without (blue hatched band) and with the LHeC+FCC-eh pseudodata (orange band) on inclusive structure functions. For completeness, we also show the results of the corresponding NNPDF3.1sx NNLO fit with LHeC+FCC-eh pseudodata (green hatched band). Figure taken from Ref. [245].

2397 In Fig. 4.8 the comparison of the gluon and quark distributions from the NNLO + NLLx fits is  
 2398 shown at  $Q = 100$  GeV as a function of  $x$ , with and without including the simulated pseudodata  
 2399 from LHeC as well as FCC-eh. The differences at large  $x$  are due to the fact that only DIS  
 2400 data were included in the fits, and not the hadronic data. The central values of the extracted  
 2401 PDFs using only HERA or using HERA and the simulated pseudodata coincide with each  
 2402 other, but a large reduction in uncertainty is visible when the new data are included. The  
 2403 uncertainties from the fits based on the HERA data only increase sharply already at  $x \sim 10^{-4}$ .  
 2404 On the other hand, including the pseudodata from LHeC and/or FCC-eh can extend this regime  
 2405 by order(s) of magnitude down in  $x$ . Furthermore, fits without resummation, based only on  
 2406 NNLO DGLAP, were performed to the HERA data and the pseudodata. We see that in this  
 2407 case the extracted gluon and singlet quark densities differ significantly from the fits using the

2408 NNLO+NLLx. Already at  $x = 10^{-4}$  the central values of the gluon differ by 10% and at  
2409  $x = 10^{-5}$ , which is the LHeC regime, the central values for the gluon differ by 15%. This  
2410 difference is much larger than the precision with which the gluon can be extracted from the DIS  
2411 data, which is of the order of  $\sim 1\%$ .

2412 The presented analysis demonstrates that the fixed order prediction based on the DGLAP  
2413 evolution would likely fail to describe accurately the structure function data in the new DIS  
2414 machines and that in that regime new dynamics including resummation are mandatory for  
2415 quantitative predictions. Therefore, the LHeC machine has an unprecedented potential to pin  
2416 down the details of the QCD dynamics at low values of Bjorken  $x$ .

#### 2417 4.2.2 Disentangling non-linear QCD dynamics at the LHeC

2418 As mentioned previously the kinematic extension of the LHeC will allow unprecedented tests of  
2419 the strong interaction in the extremely low  $x$  region, and allow for the tests of the novel QCD  
2420 dynamics at low  $x$ . The second effect, in addition to resummation, that may be expected is  
2421 the parton saturation phenomenon, which may manifest itself as the deviation from the linear  
2422 DGLAP evolution, and the emergence of the saturation scale.

2423 In particular, it has been argued that the strong growth of the gluon PDF at small- $x$  should  
2424 eventually lead to gluon recombination [248] to avoid violating the unitary bounds. The onset  
2425 of such non-linear dynamics, also known as saturation, has been extensively searched but so  
2426 far there is no conclusive evidence of its presence, at least within the HERA inclusive structure  
2427 function measurements. In this context, the extended kinematic range of the LHeC provides  
2428 unique avenues to explore the possible onset of non-linear QCD dynamics at small- $x$ . The  
2429 discovery of saturation, a radically new regime of QCD, would then represent an important  
2430 milestone in our understanding of the strong interactions.

2431 The main challenge in disentangling saturation lies in the fact that non-linear corrections are  
2432 expected to be moderate even at the LHeC, since they are small (if present at all) in the region  
2433 covered by HERA. Therefore, great care needs to be employed in order to separate such effects  
2434 from those of standard DGLAP linear evolution. Indeed, it is well known that HERA data at  
2435 small- $x$  in the perturbative region can be equally well described, at least at the qualitative level,  
2436 both by PDF fits based on the DGLAP framework as well as by saturation-inspired models.  
2437 However, rapid progress both in theory calculations and methodological developments have  
2438 pushed QCD fits to a new level of sophistication, and recently it has been shown that subtle but  
2439 clear evidence of BFKL resummation at small- $x$  is present in HERA data, both for inclusive and  
2440 for heavy quark structure functions [249, 250]. Such studies highlight how it should be possible  
2441 to tell apart non-linear from linear dynamics using state-of-the-art fitting methods even if these  
2442 are moderate, provided that they are within the LHeC reach.

2443 Here we want to assess the sensitivity of the LHeC to detect the possible onset of non-linear  
2444 saturation dynamics. This study will be carried out by generalising a recent analysis [58] that  
2445 quantified the impact of LHeC inclusive and semi-inclusive measurements on the PDF4LHC15  
2446 PDFs [251, 252] by means of Hessian profiling [253]. There, the LHeC pseudodata was generated  
2447 assuming that linear DGLAP evolution was valid in the entire LHeC kinematic range using the  
2448 PDF4LHC15 set as input. To ascertain the possibility of pinning down saturation at the LHeC,  
2449 here we have revisited this study but now generating the LHeC pseudodata by means of a  
2450 saturation-inspired calculation. By monitoring the statistical significance of the tension that  
2451 will be introduced (by construction) between the saturation pseudodata and the DGLAP theory  
2452 assumed in the PDF fit, we aim to determine the likelihood of disentangling non-linear from

2453 linear evolution effects at the LHeC. See also [254] for previous related studies along the same  
 2454 direction.

### 2455 Analysis settings

2456 In this study we adopt the settings of [58, 255], to which we refer the interested reader for  
 2457 further details. In Ref. [58] the impact on the proton PDFs of inclusive and semi-inclusive  
 2458 neutral-current (NC) and charged current (CC) DIS structure functions from the LHeC was  
 2459 quantified. These results were then compared with the corresponding projections for the PDF  
 2460 sensitivity of the High-Luminosity upgrade of the LHC (HL-LHC). In Fig. 3.4 the kinematic  
 2461 range in the  $(x, Q^2)$  plane of the LHeC pseudodata employed in that analysis is displayed, which  
 2462 illustrated how the LHeC can provide unique constraints on the behaviour of the quark and  
 2463 gluon PDFs in the very small- $x$  region.

2464 Since non-linear dynamics are known to become sizeable only at small- $x$ , for the present analysis  
 2465 it is sufficient to consider the NC  $e^-p$  inclusive scattering cross sections from proton beam  
 2466 energies of  $E_p = 7$  TeV and  $E_p = 1$  TeV. In Fig. 4.9 we show the bins in  $(x, Q^2)$  for which  
 2467 LHeC pseudodata for inclusive structure functions has been generated according to a saturation-  
 2468 based calculation. Specifically, we have adopted here the DGLAP-improved saturation model  
 2469 of Ref. [256], in which the scattering matrix is modelled through eikonal iteration of two gluon  
 2470 exchanges. This model was further extended to include heavy flavour in Ref. [257]. The specific  
 2471 parameters that we use were taken from Fit 2 in Ref. [258], where parameterisations are provided  
 2472 that can be used for  $x < 0.01$  and  $Q^2 < 700$  GeV<sup>2</sup>. These parameters were extracted from a fit  
 2473 to the HERA legacy inclusive structure function measurements [43] restricted to  $x < 0.01$  and  
 2474  $0.045 < Q^2 < 650$  GeV<sup>2</sup>. In contrast to other saturation models, the one we assume here [258]  
 2475 provides a reasonable description for large  $Q^2$  in the small  $x$  region, where it ensure a smooth  
 2476 transition to standard fixed-order perturbative results.

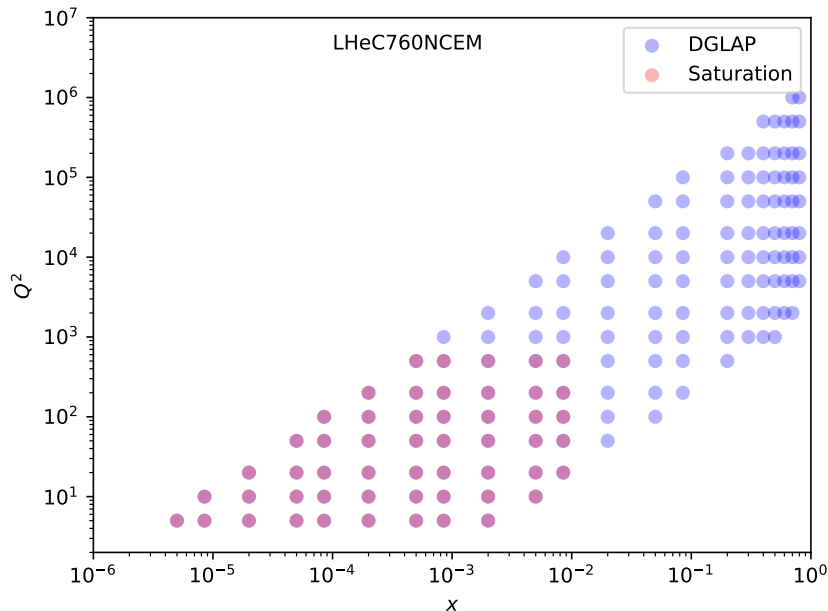


**Figure 4.9:** The kinematic coverage of the NC  $e^-p$  scattering pseudodata at the LHeC, where the blue (red) points indicate those bins for which DGLAP (saturation) predictions are available.

2477 Note that the above discussion refers only to the generated LHeC pseudodata: all other aspects  
 2478 of the QCD analysis of Ref. [58] are left unchanged. In particular, the PDF profiling will be

2479 carried out using theory calculations obtained by means of DGLAP evolution with the NNLO  
2480 PDF4LHC15 set (see also Ref. [259]), with heavy quark structure functions evaluated by means of  
2481 the FONLL-B general-mass variable flavour number scheme [86]. In order to ensure consistency  
2482 with the PDF4LHC15 prior, here we will replace the DGLAP pseudodata by the saturation  
2483 calculation only in the kinematic region for  $x \lesssim 10^{-4}$ , rather than for all the bins indicated in  
2484 red in Fig. 4.9. The reason for this choice is that PDF4LHC15 already includes HERA data  
2485 down to  $x \simeq 10^{-4}$  which is successfully described via the DGLAP framework, and therefore if we  
2486 assume departures from DGLAP in the LHeC pseudodata this should only be done for smaller  
2487 values of  $x$ .

## 2488 Results and discussion

2489 Using the analysis settings described above, we have carried out the profiling of PDF4LHC15  
2490 with the LHeC inclusive structure function pseudodata, which for  $x \leq 10^{-4}$  ( $x > 10^{-4}$ ) has  
2491 been generated using the GBW saturation (DGLAP) calculations, and compare them with the  
2492 results of the profiling where the pseudodata follows the DGLAP prediction. We have generated  
2493  $N_{\text{exp}} = 500$  independent sets LHeC pseudodata, each one characterised by different random  
2494 fluctuations (determined by the experimental uncertainties) around the underlying central value.

2495 To begin with, it is instructive to compare the data versus theory agreement,  $\chi^2/n_{\text{dat}}$ , between  
2496 the pre-fit and post-fit calculations, in order to assess the differences between the DGLAP and  
2497 saturation cases. In the upper plots of Fig. 4.10 we show the distributions of pre-fit and post-fit  
2498 values of  $\chi^2/n_{\text{dat}}$  for the  $N_{\text{exp}} = 500$  sets of generated LHeC pseudodata. We compare the results  
2499 of the profiling of the LHeC pseudodata based on DGLAP calculations in the entire range of  
2500  $x$  with those where the pseudodata is based on the saturation model in the region  $x < 10^{-4}$ .  
2501 Then in the bottom plot we compare of the post-fit  $\chi^2$  distributions between the two scenarios.  
2502 Note that in these three plots the ranges in the  $x$  axes are different.

2503 From this comparison we can observe that for the case where the pseudodata is generated using  
2504 a consistent DGLAP framework (PDF4LHC15) as the one adopted for the theory calculations  
2505 used in the fit, as expected the agreement is already good at the pre-fit level, and it is further  
2506 improved at the post-fit level. However the situation is rather different in the case where a  
2507 subset of the LHeC pseudodata is generated using a saturation model: at the pre-fit level the  
2508 agreement between theory and pseudodata is poor, with  $\chi^2/n_{\text{dat}} \simeq 7$ . The situation markedly  
2509 improves at the post-fit level, where now the  $\chi^2/n_{\text{dat}}$  distributions peaks around 1.3. This result  
2510 implies that the DGLAP fit manages to absorb most of the differences in theory present in  
2511 the saturation pseudodata. This said, the DGLAP fit cannot entirely *fit away* the non-linear  
2512 corrections: as shown in the lower plot of Fig. 4.10, even at the post-fit level one can still tell  
2513 apart the  $\chi^2/n_{\text{dat}}$  distributions between the two cases, with the DGLAP (saturation) pseudodata  
2514 peaking at around 0.9 (1.3). This comparison highlights that it is not possible for the DGLAP  
2515 fit to completely absorb the saturation effects into a PDF redefinition.

2516 In order to identify the origin of the worse agreement between theory predictions and LHeC  
2517 pseudodata in the saturation case, it is illustrative to take a closer look at the pulls defined as

$$P(x, Q^2) = \frac{\mathcal{F}_{\text{dat}}(x, Q^2) - \mathcal{F}_{\text{fit}}(x, Q^2)}{\delta_{\text{exp}}\mathcal{F}(x, Q^2)}, \quad (4.5)$$

2518 where  $\mathcal{F}_{\text{fit}}$  is the central value of the profiled results for the observable  $\mathcal{F}$  (in this case the reduced  
2519 neutral current DIS cross section),  $\mathcal{F}_{\text{dat}}$  is the corresponding central value of the pseudodata,  
2520 and  $\delta_{\text{exp}}\mathcal{F}$  represents the associated total experimental uncertainty. In Fig. 4.11 we display the  
2521 pulls between the post-fit prediction and the central value of the LHeC pseudodata for different

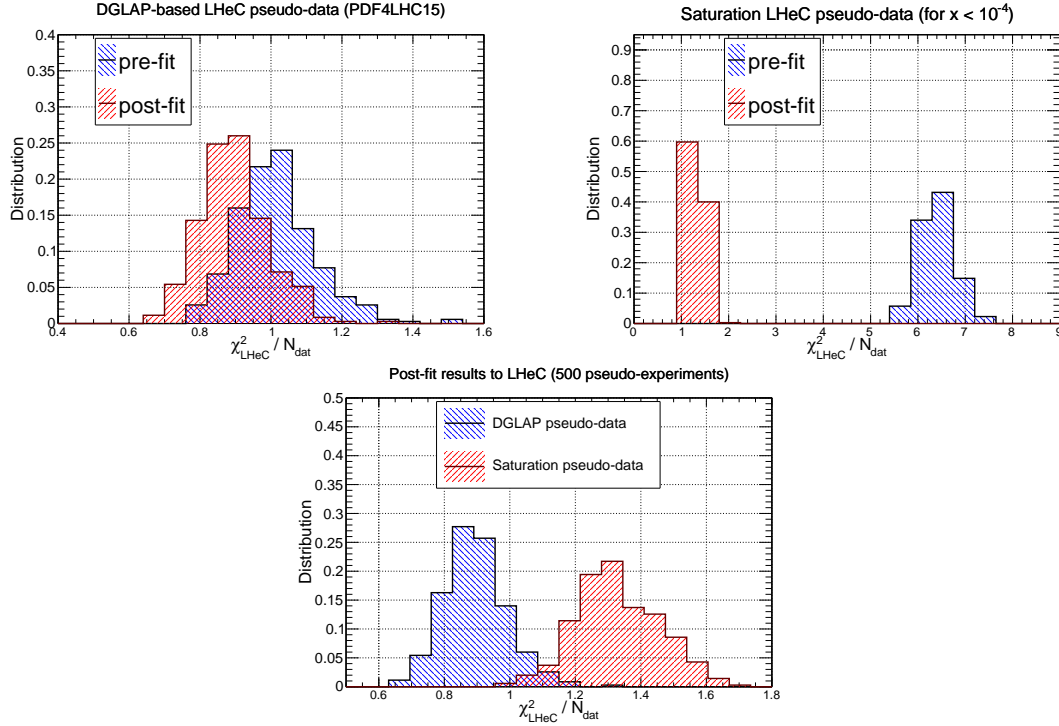


**Figure 4.10:** Upper plots: the distribution of pre-fit and post-fit values of  $\chi^2/n_{\text{dat}}$  for the  $N_{\text{exp}} = 500$  sets of generated LHeC pseudodata. We compare the results of the profiling of the LHeC pseudodata based on DGLAP calculations in the entire range of  $x$  (left) with those where the pseudodata is based on the saturation model in the region  $x < 10^{-4}$  (right plot). Bottom plot: comparison of the post-fit  $\chi^2/n_{\text{dat}}$  distributions between these two scenarios for the pseudodata generation.

2522 bins in  $Q^2$ . We compare the cases where the pseudodata has been generated using a consistent  
 2523 theory calculation (DGLAP) with that based on the GBW saturation model.

2524 The comparisons in Fig. 4.11 show first of all that in the DGLAP case the pulls are  $\mathcal{O}(1)$  in  
 2525 the entire kinematical range. This is of course expected, given that the LHeC pseudodata is  
 2526 generated using the same theory as the one subsequently used for the fit. In the case where  
 2527 the pseudodata has been partially generated with the saturation calculation, on the other hand,  
 2528 one finds a systematic tension between the theory used for the fit (DGLAP) and the one used  
 2529 to generate the pseudodata (saturation). Indeed, we find that at the smallest values of  $x$  the  
 2530 theory prediction overshoots the data by a significant amount, while at higher  $x$  the opposite  
 2531 behaviour takes place. One can also see that in the region  $10^{-4} \lesssim x \lesssim 10^{-3}$  the fit undershoots  
 2532 the pseudodata by a large amount.

2533 These comparisons highlight how a QCD fit to the saturation pseudodata is obtained as a  
 2534 compromise between opposite trends: the theory wants to overshoot the data at very small  $x$   
 2535 and undershoot it at larger values of  $x$ . These tensions result in a distorted fit, explaining the  
 2536 larger  $\chi^2/n_{\text{dat}}$  values as compared to the DGLAP case. Such a behaviour can be partially traced  
 2537 back by the different scaling in  $Q^2$  between DGLAP and GBW: while a different  $x$  dependence  
 2538 could eventually be absorbed into a change of the PDFs at the parameterisation scale  $Q_0$ , this  
 2539 is not possible with a  $Q^2$  dependence.

2540 The pull analysis of Fig. 4.11 highlights how in order to tell apart linear from non-linear QCD  
 2541 evolution effects at small- $x$  it would be crucial to ensure a lever arm in  $Q^2$  as large as possible  
 2542 in the perturbative region. This way it becomes possible to disentangle the different scaling



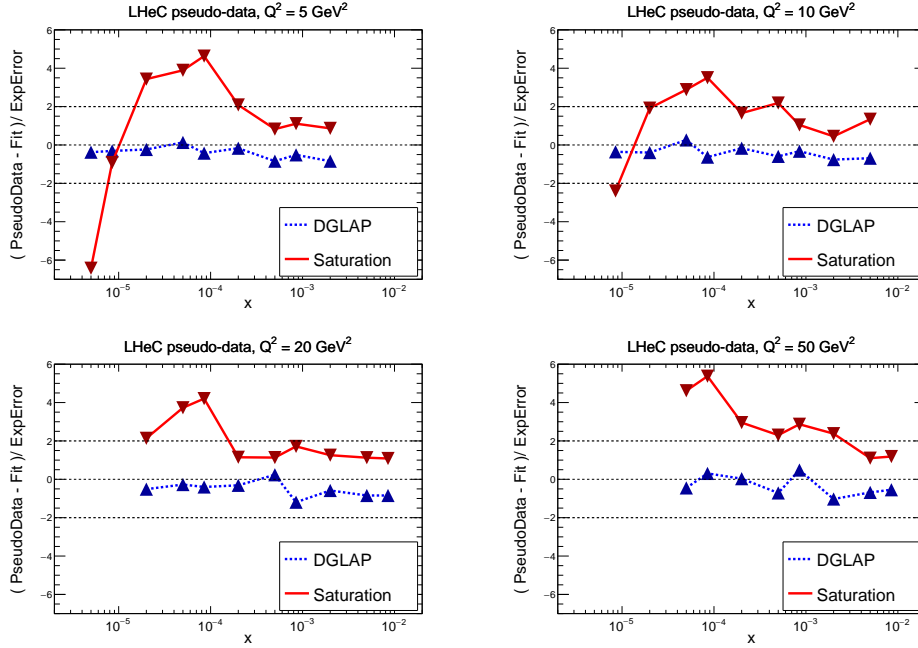


**Figure 4.11:** The pulls between the central value of the LHeC pseudodata and post-fit prediction, Eq. (4.5), for four different bins in  $Q^2$ . We compare the results of the profiling where the LHeC pseudodata has been generated using a consistent DGLAP theory with that partially based on the saturation calculations.

2543 in  $Q^2$  for the two cases. The lack of a sufficiently large lever arm in  $Q^2$  at HERA at small  $x$   
 2544 could explain in part why both frameworks are able to describe the same structure function  
 2545 measurements at the qualitative level. Furthermore, we find that amplifying the significance  
 2546 of these subtle effects can be achieved by monitoring the  $\chi^2$  behaviour in the  $Q^2$  bins more  
 2547 affected by the saturation corrections. The reason is that the total  $\chi^2$ , such as that reported  
 2548 in Fig. 4.10, is somewhat less informative since the deviations at small- $Q$  are washed out by  
 2549 the good agreement between theory and pseudodata in the rest of the kinematical range of the  
 2550 LHeC summarised in Figs. 3.4 and 4.9.

2551 To conclude this analysis, in Fig. 4.12 we display the comparison between the PDF4LHC15  
 2552 baseline with the results of the PDF profiling of the LHeC pseudodata for the gluon (left) and  
 2553 quark singlet (right) for  $Q = 10 \text{ GeV}$ . We show the cases where the pseudodata is generated  
 2554 using DGLAP calculations and where it is partially based on the GBW saturation model (for  
 2555  $x \lesssim 10^{-4}$ ). We find that the distortion induced by the mismatch between theory and pseudodata  
 2556 in the saturation case is typically larger than the PDF uncertainties expected once the LHeC  
 2557 constraints are taken into account. While of course in a realistic situation such a comparison  
 2558 would not be possible, the results of Fig. 4.12 show that saturation-induced effects are expected  
 2559 to be larger than the typical PDF errors in the LHeC era, and thus that it should be possible to  
 2560 tell them apart using for example tools such as the pull analysis of Fig. 4.11 or other statistical  
 2561 methods.

## 2562 Summary

2563 Here we have assessed the feasibility of disentangling DGLAP evolution from non-linear effects at  
 2564 the LHeC. By means of a QCD analysis where LHeC pseudodata is generated using a saturation  
 2565 model, we have demonstrated that the LHeC should be possible to identify non-linear effects  
 2566 with large statistical significance, provided their size is the one predicted by current calculations

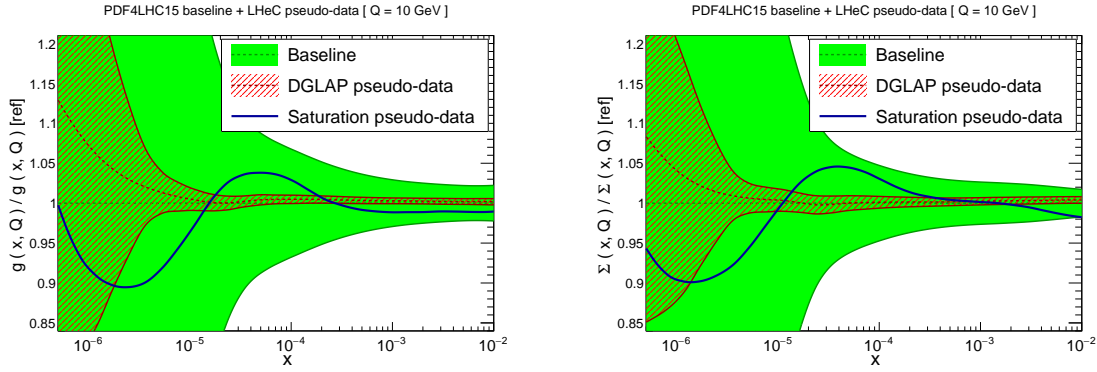


**Figure 4.12:** Comparison between the PDF4LHC15 baseline (green band) with the results of the profiling of the LHeC pseudodata for the gluon (left) and quark singlet (right) for  $Q = 10$  GeV. We show the cases where the pseudodata is generated using DGLAP calculations (red hatched band) and where it is partially based on the GBW saturation model (blue curve).

2567 such as the that of [258] that have been tuned to HERA data. A more refined analysis would  
 2568 require to study whether or not small- $x$  BFKL resummation effects can partially mask the  
 2569 impact of non-linear dynamics, though this is unlikely since the main difference arises in their  
 2570  $Q^2$  scaling. The discovery of non-linear dynamics would represent an important milestone for  
 2571 the physics program of the LHeC, demonstrating the onset of a new gluon-dominated regime of  
 2572 the strong interactions and paving the way for detailed studies of the properties of this new state  
 2573 of matter. Such discovery would have also implications outside nuclear and particle physics, for  
 2574 instance it would affect the theory predictions for the scattering of ultra-high energy neutrinos  
 2575 with matter [260].

### 2576 4.2.3 Low $x$ and the Longitudinal Structure Function $F_L$

#### 2577 DIS Cross Section and the Challenge to Access $F_L$

2578 The inclusive, deep inelastic electron-proton scattering cross section at low  $Q^2 \ll M_Z^2$ ,

$$\frac{Q^4 x}{2\pi\alpha^2 Y_+} \cdot \frac{d^2\sigma}{dx dQ^2} = \sigma_r \simeq F_2(x, Q^2) - f(y) \cdot F_L(x, Q^2) = F_2 \cdot \left(1 - f(y) \frac{R}{1+R}\right) \quad (4.6)$$

2579 is defined by two proton structure functions,  $F_2$  and  $F_L$ , with  $y = Q^2/sx$ ,  $Y_+ = 1 + (1-y)^2$   
 2580 and  $f(y) = y^2/Y_+$ . The cross section may also be expressed [261] as a sum of two contributions,  
 2581  $\sigma_r \propto (\sigma_T + \epsilon\sigma_L)$ , referring to the transverse and longitudinal polarisation state of the exchanged  
 2582 boson, with  $\epsilon$  characterising the ratio of the longitudinal to the transverse polarisation. The  
 2583 ratio of the longitudinal to transverse cross sections is termed

$$R(x, Q^2) = \frac{\sigma_L}{\sigma_T} = \frac{F_L}{F_2 - F_L}, \quad (4.7)$$

2584 which is related to  $F_2$  and  $F_L$  as given above. Due to the positivity of the cross sections  $\sigma_{L,T}$   
 2585 one observes that  $F_L \leq F_2$ . The reduced cross section  $\sigma_r$ , Eq. (4.6), is therefore a direct measure  
 2586 of  $F_2$ , apart from a limited region of high  $y$  where a contribution of  $F_L$  may be sizeable. To  
 2587 leading order, for spin 1/2 particles, one expected  $R = 0$ . The initial measurements of  $R$  at  
 2588 SLAC [262, 263] showed that  $R$  was indeed small,  $R \simeq 0.18$ , which was taken as evidence for  
 2589 quarks to carry spin 1/2.

2590 The task to measure  $F_L$  thus requires to precisely measure the inclusive DIS cross section near  
 2591 to  $y = 1$  and to then disentangle the two structure functions by exploiting the  $f(y) = y^2/Y_+$

2592 variation which depends on  $x$ ,  $Q^2$  and  $s$ . By varying the centre-of-mass (cms) beam energy,  $s$ , one  
 2593 can disentangle  $F_2$  and  $F_L$  obtaining independent measurements at each common, fixed point of  
 2594  $x$ ,  $Q^2$ . This is particularly challenging not only because the  $F_L$  part is small, calling for utmost  
 2595 precision, but also because it requires to measure at high  $y$ . The inelasticity  $y = 1 - E'/E_e$ ,  
 2596 however, is large only for scattered electron energies  $E'_e$  much smaller than the electron beam  
 2597 energy  $E_e$ , for example  $E'_e = 2.7$  GeV for  $y = 0.9$  at HERA <sup>4</sup>. In the region where  $E'$  is a few GeV  
 2598 only, the electron identification becomes a major problem and the electromagnetic ( $\pi^0 \rightarrow \gamma\gamma$ )  
 2599 and hadronic backgrounds, mainly from unrecognised photoproduction, rise strongly.

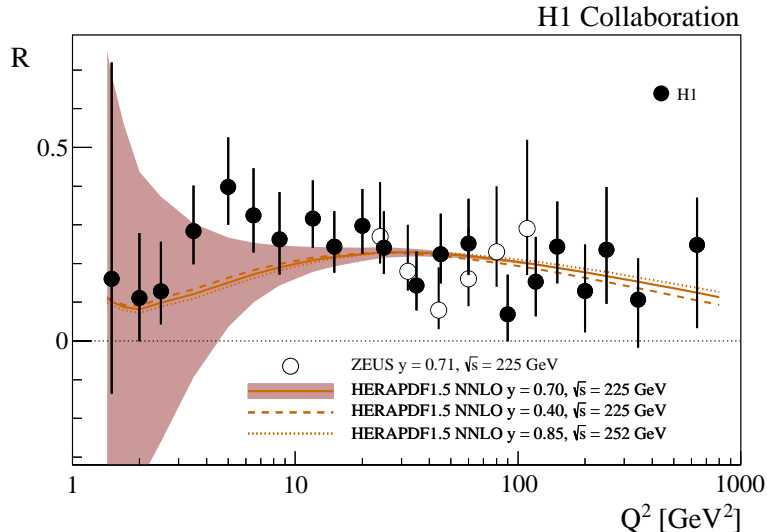


**Figure 4.13:** Measurement of the structure function ratio  $R = F_L/(F_2 - F_L)$  by H1 (solid points) and ZEUS (open circles), from a variation of proton beam energy in the final half year of HERA operation. The curve represents an NNLO QCD fit analysis of the other HERA data. This becomes uncertain for  $Q^2$  below 10 GeV<sup>2</sup> where the  $Q^2$  dependence of  $F_2$  at HERA does not permit an accurate determination of the gluon density which dominates the prediction on  $F_L$ .

2600 The history and achievements on  $F_L$ , the role of HERA and the prospects as sketched in the  
 2601 CDR of the LHeC, were summarised in detail in [52]. The measurement of  $F_L$  at HERA [264]  
 2602 was given very limited time and it collected about 5.9 and 12.2 pb<sup>-1</sup> of data at reduced beam  
 2603 energies which were analysed together with about 100 pb<sup>-1</sup> at nominal HERA energies. The  
 2604 result may well be illustrated with the data obtained on the ratio  $R(x, Q^2)$  shown in Fig. 4.13.  
 2605 To good approximation,  $R(x, Q^2)$  is a constant which was determined as  $R = 0.23 \pm 0.04$ ,  
 2606 in good agreement with the SLAC values of  $R \simeq 0.18$  despite the hugely extended kinematic  
 2607 range. The rather small variation of  $R$  towards small  $x$ , at fixed  $y = Q^2/sx$ , may appear to be  
 2608 astonishing as one observed  $F_2$  to strongly rise towards low  $x$ . A constant  $R$  of e.g. 0.25 means  
 2609 that  $F_2 = (1 + R)F_L/R$  is five times larger than  $F_L$ , and that they rise together, as they have  
 2610 a common origin, the rise of the gluon density. This can be understood in approximations to  
 2611 the DGLAP expression of the  $Q^2$  derivative of  $F_2$  and the so-called Altarelli-Martinelli relation  
 2612 of  $F_L$  to the parton densities [265, 266], see the discussion in Ref. [52]. The resulting H1 value  
 2613 also obeyed the condition  $R \leq 0.37$ , which had been obtained in a rigorous attempt to derive  
 2614 the dipole model for inelastic DIS [267].

<sup>4</sup>The nominal electron beam energy  $E_e$  at the LHeC is doubled as compared to HERA. Ideally one would like to vary the proton beam energy in an  $F_L$  measurement at the LHeC, which yet would affect the hadron collider operation. In the present study it was therefore considered to lower  $E_e$  which may be done independently of the HL-LHC.

## 2615 Parton Evolution at Low $x$

2616 Parton distributions are to be extracted from experiment as their  $x$  dependence and flavour  
2617 sharing are not predicted in QCD. They acquire a particular meaning through the theoretical  
2618 prescription of their kinematic evolution. PDFs, as they are frequently used for LHC analyses,  
2619 are predominantly defined through the now classic DGLAP formalism, in which the  $Q^2$  depen-  
2620 dence of parton distributions is regulated by splitting functions while the DIS cross section,  
2621 determined by the structure functions, is calculable by folding the PDFs with coefficient func-  
2622 tions. Deep inelastic scattering is known to be the most suited process to extract PDFs from  
2623 the experiment, for which the HERA collider has so far delivered the most useful data. Through  
2624 factorisation theorems the PDFs are considered to be universal such that PDFs extracted in  $ep$   
2625 DIS shall be suited to describe for example Drell-Yan scattering cross sections in  $pp$  at the LHC.  
2626 This view has been formulated to third order pQCD already and been quite successful in the  
2627 interpretation of LHC measurements, which by themselves also constrain PDFs in parton-parton  
2628 scattering sub-processes.

2629 As commented in Sec. 4.2.1, the question has long been posed about the universal validity of  
2630 the DGLAP formalism, especially for the region of small Bjorken  $x$  where logarithms  $\propto \ln(1/x)$   
2631 become very sizeable. This feature of the perturbation expansion is expected to significantly  
2632 modify the splitting functions. This in turn changes the theory underlying the physics of parton  
2633 distributions, and predictions for the LHC and its successor will correspondingly have to be  
2634 altered. This mechanism, for an equivalent  $Q^2$  of a few  $\text{GeV}^2$ , is illustrated in Fig. 4.14, taken  
2635 from Ref. [250]. It shows the  $x$  dependence of the gluon-gluon and the quark-gluon splitting  
2636 functions,  $P_{gg}$  and  $P_{qg}$ , calculated in DGLAP QCD. It is observed that at NNLO  $P_{gg}$  strongly  
2637 decreases towards small  $x$ , becoming smaller than  $P_{qg}$  for  $x$  below  $10^{-4}$ . Resummation of  
2638 the large  $\ln(1/x)$  terms, see Ref. [250], here performed to next-to-leading log  $x$ , restores the  
2639 dominance of the  $gg$  splitting over the  $qg$  one. Consequently, the gluon distribution in the  
2640 resummed theory exceeds the one derived in pure DGLAP. While this observation has been  
2641 supported by the HERA data, it yet relies on limited kinematic coverage and precision. The  
2642 LHeC will examine this in detail, at a hugely extended range and is thus expected to resolve the  
2643 long known question about the validity of the BFKL evolution and the transition from DGLAP  
2644 to BFKL as  $x$  decreases while  $Q^2$  remains large enough for pQCD to apply.

## 2645 Kinematics of Higgs Production at the HL-LHC

2646 The clarification of the evolution and the accurate and complete determination of the parton  
2647 distributions is of direct importance for the LHC. This can be illustrated with the kinematics of  
2648 Higgs production at HL-LHC which is dominated by gluon-gluon fusion. With the luminosity  
2649 upgrade, the detector acceptance is being extended into the forward region to pseudorapidity  
2650 values of  $|\eta| = 4$ , where  $\eta = \ln \tan \theta/2$  is a very good approximation of the rapidity. In Drell-Yan  
2651 scattering of two partons with Bjorken  $x$  values of  $x_{1,2}$  these are related to the rapidity via the  
2652 relation  $x_{1,2} = \exp(\pm\eta) \cdot M/\sqrt{s}$  where  $\sqrt{s} = 2E_p$  is the cms energy and  $M$  the mass of the  
2653 produced particle. It is interesting to see that  $\eta = \pm 4$  corresponds to  $x_1 = 0.5$  and  $x = 0.00016$   
2654 for the SM Higgs boson of mass  $M = 125 \text{ GeV}$ . Consequently, Higgs physics at the HL-LHC  
2655 will depend on understanding PDFs at high  $x$ , a challenge resolved by the LHeC too, and on  
2656 clarifying the evolution at small  $x$ . At the FCC-hh, in its 100 TeV energy version, the small  $x$   
2657 value for  $\eta = 4$  will be as low as  $2 \cdot 10^{-5}$ . Both the laws of QCD and the resulting phenomenology  
2658 of particle production at the HL-LHC and its successor demand to clarify the evolution of the  
2659 parton contents at small  $x$  as a function of the resolution scale  $Q^2$  [268–270]. This concerns in  
2660 particular the unambiguous, accurate determination of the gluon distribution, which dominates  
2661 the small- $x$  parton densities and as well the production of the Higgs boson in  $pp$  scattering.

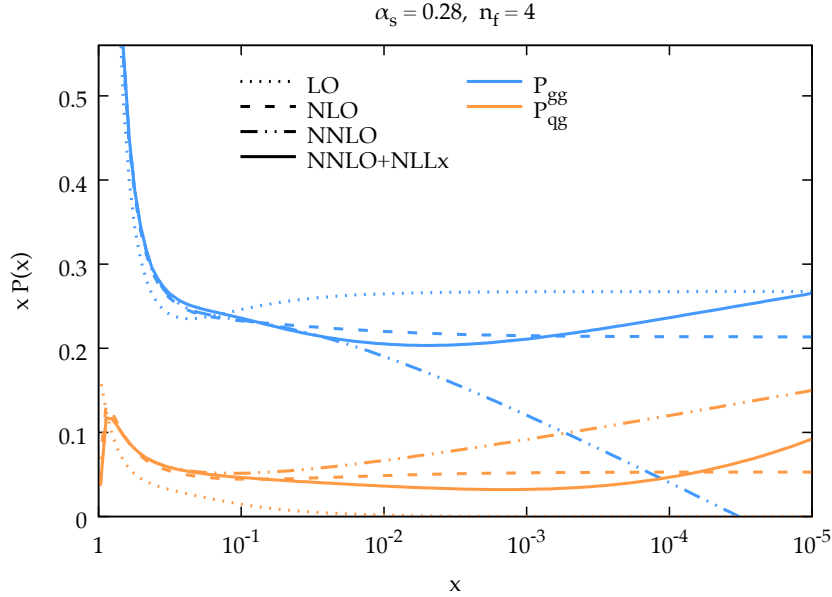


**Figure 4.14:** Calculation of splitting functions  $P_{gg}$  (top, blue) and  $P_{qg}$  (bottom, brown) in resummed NNLO (solid) as compared to non-resummed calculations at LO (dotted), NLO (dashed) and NNLO (dashed-dotted) as functions of  $x$  for  $n_f = 4$  at a large value of  $\alpha_s$  corresponding to a  $Q^2$  of a few  $\text{GeV}^2$ , from Ref. [250]. The resummed calculation is seen to restore the dominance of  $P_{gg}$  over  $P_{qg}$  as  $x$  becomes small (towards the right side), which is violated at NNLO.

## 2662 Indications for Resummation in H1 $F_L$ Data

2663 The simultaneous measurement of the two structure functions  $F_2$  and  $F_L$  is the cleanest way  
 2664 to establish new parton dynamics at low  $x$ . This holds because their independent constraints  
 2665 on the dominating gluon density at low  $x$  ought to lead to consistent results. In other words,  
 2666 one may constrain all partons with a complete PDF analysis of the inclusive cross section in  
 2667 the kinematic region where its  $F_L$  part is negligible and confront the  $F_L$  measurement with  
 2668 this result. A significant deviation from  $F_L$  data signals the necessity to introduce new, non-  
 2669 DGLAP physics in the theory of parton evolution, especially at small  $x$ . The salient value of the  
 2670  $F_L$  structure function results from its inclusive character enabling a clean theoretical treatment  
 2671 as has early on been recognised [265, 266]. This procedure has recently been illustrated [250]  
 2672 using the H1 data on  $F_L$  [271] which are the only accurate data from HERA at smallest  $x$ . The  
 2673 result is shown in Fig. 4.15. One observes the trend described above: the resummed prediction  
 2674 is higher than the pure NNLO curve, and the description at smallest  $x$ , below  $5 \cdot 10^{-4}$ , appears  
 2675 to be improved. The difference between the two curves increases as  $x$  decreases. However, due  
 2676 to the peculiarity of the DIS kinematics, which relates  $x$  to  $Q^2/sy$ , one faces the difficulty of  
 2677  $Q^2$  decreasing with  $x$  at fixed  $s$  for large  $y \geq 0.6$ , which is the region of sensitivity to  $F_L$ . Thus  
 2678 one not only wishes to improve substantially the precision of the  $F_L$  data but also to increase  
 2679 substantially  $s$  in order to avoid the region of non-perturbative behaviour while testing theory  
 2680 at small  $x$ . This is the double and principal advantage which the LHeC offers - a much increased  
 2681 precision and more than a decade of extension of kinematic range.

## 2682 The Longitudinal Structure Function at the LHeC

2683 Following the method described above, inclusive cross section data have been simulated for  
 2684  $E_p = 7 \text{ TeV}$  and three electron beam energies  $E_e$  of 60, 30 and 20 GeV. The assumed integrated

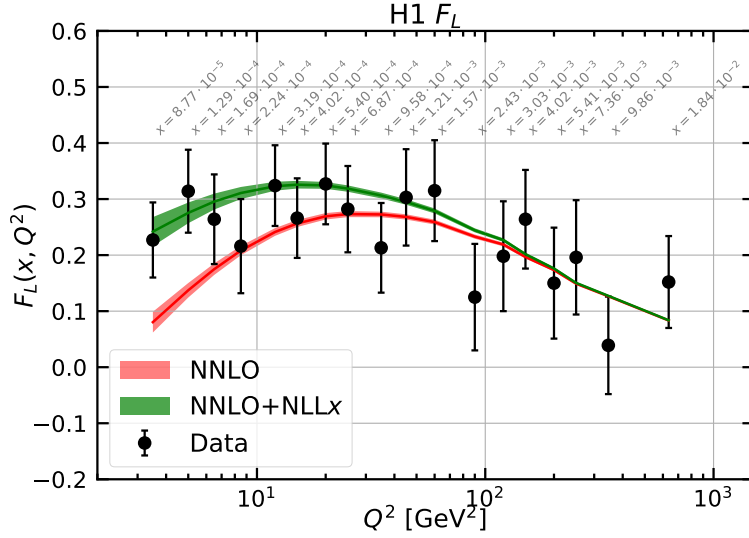


**Figure 4.15:** Measurement of the longitudinal structure function  $F_L$ , obtained as an average results over a number of  $x$  dependent points at fixed  $Q^2$ , plotted vs  $Q^2$  with the corresponding  $x$  values indicated in grey. Red curve: NNLO fit to the H1 cross section data; green curve: NNLO fit including NLLx resummation, from Ref. [250].

2685 luminosity values are 10, 1 and again  $1 \text{ fb}^{-1}$ , respectively. These are about a factor of a hundred  
2686 larger than the corresponding H1 luminosities. At large  $y$ , the kinematics is best reconstructed  
2687 using the scattered electron energy,  $E'_e$ , and polar angle,  $\theta_e$ . The experimental methods to  
2688 calibrate the angular and energy measurements are described in [264]. For the present study  
2689 similar results are assumed: for  $E'_e$  a scale uncertainty of 0.5% at small  $y$  (compared to 0.2%  
2690 with H1) rising linearly to 1.2%, in the range of  $y = 0.4$  to 0.9. For the polar angle, given  
2691 the superior quality of the anticipated LHeC Silicon tracker as compared to the H1 tracker,  
2692 it is assumed that  $\theta_e$  may be calibrated to 0.2mrad, as compared to 0.5mrad at H1. The  
2693 residual photo-production background contamination is assumed to be 0.5% at largest  $y$ , twice  
2694 better than with H1. There is further an assumption made on the radiative corrections which  
2695 are assumed to be uncertain to 1% and treated as a correlated error. The main challenge is to  
2696 reduce the uncorrelated uncertainty, which here was varied between 0.2 and 0.5%. This is about  
2697 ten to three times more accurate than the H1 result which may be a reasonable assumption: the  
2698 hundred fold increase in statistics sets a totally different scale to the treatment of uncorrelated  
2699 uncertainties, as from imperfect simulations, trigger efficiency or Monte Carlo statistics. It  
2700 is very difficult to transport previous results to the modern and future conditions. It could,  
2701 however, be an important fix point if one knows that the most precise measurement of  $Z$  boson  
2702 production by ATLAS at the LHC had a total systematic error of just 0.5% [272].

2703 The method here used is that of a simple straight-line fit of  $\sigma_r = F_2 - f(y)F_L$  (Eq. (4.6)), in  
2704 which  $F_L$  is obtained as the slope of the  $f(y)$  dependence<sup>5</sup>. The predictions for  $F_2$  and  $F_L$  were  
2705 obtained using LO formulae for the PDF set of MSTW 2008. In this method any common factor  
2706 does not alter the absolute uncertainty of  $F_L$ . This also implies that the estimated absolute error  
2707 on  $F_L$  is independent of whether  $F_L$  is larger or smaller than here assumed. For illustration,  
2708  $F_L$  was scaled by a factor of two. Since  $f(y) \propto y^2$ , the accuracy is optimised with a non-linear  
2709 choice of lowered beam energies. The fit takes into account cross section uncertainties and their

<sup>5</sup>Better results were achieved by H1 using a  $\chi^2$  minimisation technique, see Ref. [273], which for the rough estimate on the projected  $F_L$  uncertainty at the LHeC has not been considered.

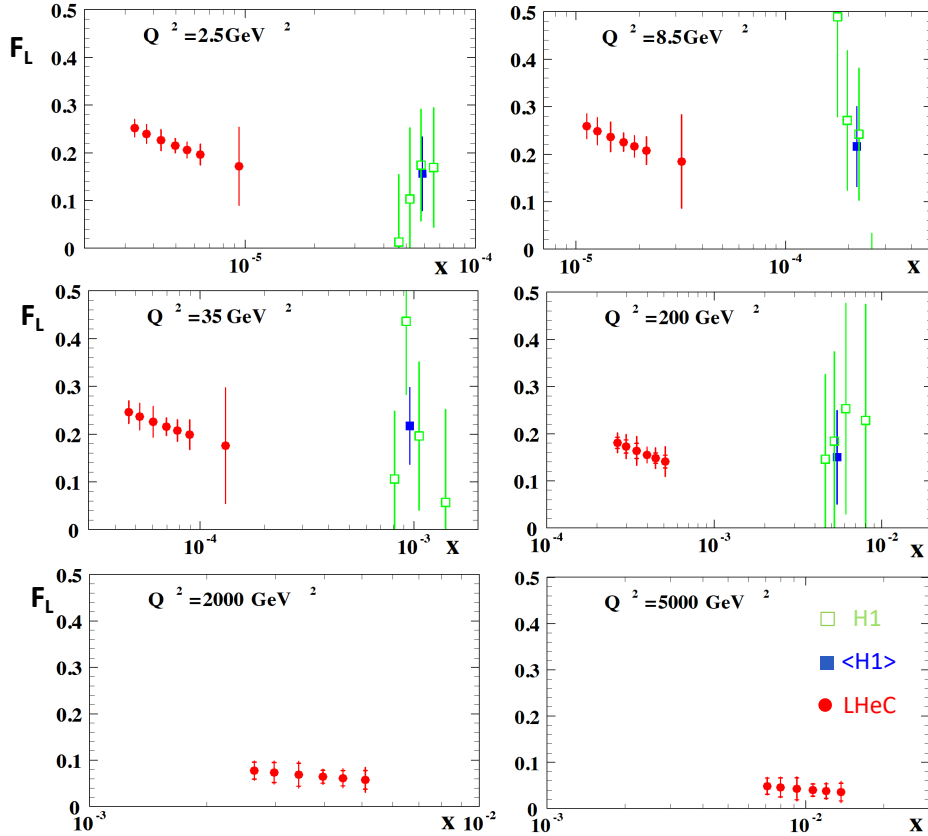


**Figure 4.16:** H1 measurement and LHeC simulation of data on the longitudinal structure function  $F_L(x, Q^2)$ . Green: Data by H1, for selected  $Q^2$  intervals from Ref. [271]; Blue: Weighted average of the (green) data points at fixed  $Q^2$ ; Red: Simulated data from an  $F_L$  measurement at the LHeC with varying beam energy, see text. The H1 error bars denote the total measurement uncertainty. The LHeC inner error bars represent the data statistics, visible only for  $Q^2 \geq 200 \text{ GeV}^2$ , while the outer error bars are the total uncertainty. Since the  $F_L$  measurement is sensitive only at high values of inelasticity,  $y = Q^2/sx$ , each  $Q^2$  value is sensitive only to a certain limited interval of  $x$  values which increase with  $Q^2$ . Thus each panel has a different  $x$  axis. The covered  $x$  range similarly varies with  $s$ , i.e. H1  $x$  values are roughly twenty times larger at a given  $Q^2$ . There are no H1 data for high  $Q^2$ , beyond  $1000 \text{ GeV}^2$ , see Ref. [271].

2710 correlations, calculated numerically following [57, 274], by considering each source separately  
 2711 and adding the results of the various correlated sources to one correlated systematic error which  
 2712 is added quadratically to the statistical and uncorrelated uncertainties to obtain one total error.

2713 The result is illustrated in Fig. 4.16 presenting the  $x$ -dependent results, for some selected  $Q^2$   
 2714 values, of both H1, with their average over  $x$ , and the prospect LHeC results. It reflects the  
 2715 huge extension of kinematic range, towards low  $x$  and high  $Q^2$  by the LHeC as compared to  
 2716 HERA. It also illustrates the striking improvement in precision which the LHeC promises to  
 2717 provide. The  $F_L$  measurement will cover an  $x$  range from  $2 \cdot 10^{-6}$  to above  $x = 0.01$ . Surely,  
 2718 when comparing with Fig. 4.15, one can safely expect that any non-DGLAP parton evolution  
 2719 would be discovered with such data, in their combination with a very precise  $F_2$  measurement.

2720 A few comments are in order on the variation of the different error components with the kine-  
 2721 matics, essentially  $Q^2$  since the whole  $F_L$  sensitivity is restricted to high  $y$  which in turn for each  
 2722  $Q^2$  defines a not wide interval of  $x$  values covered. One observes in Fig. 4.16 that the precision  
 2723 is spoiled towards large  $x \propto 1/y$ , see e.g. the result for  $Q^2 = 8.5 \text{ GeV}^2$ . The assumptions on

2724 the integrated luminosity basically define a  $Q^2$  range for the measurement. For example, the  
 2725 statistical uncertainty for  $Q^2 = 4.5 \text{ GeV}^2$  and  $x = 10^{-5}$ , a medium  $x$  value at this  $Q^2$  interval,  
 2726 is only 0.6 % (or 0.001 in absolute for  $F_L = 0.22$ ). At  $Q^2 = 2000 \text{ GeV}^2$  it rises to 21 % (or 0.012  
 2727 for  $F_L = 0.064$ ). One thus can perform the  $F_L$  measurement at the LHeC, with a focus on only  
 2728 small  $x$ , with much less luminosity than the  $1 \text{ fb}^{-1}$  here used. The relative size of the various  
 2729 systematic error sources also varies considerably, which is due to the kinematic relations between  
 2730 angles and energies and their dependence on  $x$  and  $Q^2$ . This is detailed in [57]. It implies, for ex-  
 2731 ample, that the 0.2 mrad polar angle scale uncertainty becomes the dominant error at small  $Q^2$ ,  
 2732 which is the backward region where the electron is scattered near the beam axis in the direction  
 2733 of the electron beam. For large  $Q^2$ , however, the electron is more centrally scattered and the  
 2734  $\theta_e$  calibration requirement may be more relaxed. The  $E'_e$  scale uncertainty has a twice smaller  
 2735 effect than that due to the  $\theta_e$  calibration at lowest  $Q^2$  but becomes the dominant correlated  
 2736 systematic error source at high  $Q^2$ . The here used overall assumptions on scale uncertainties  
 2737 are therefore only rough first approximations and would be replaced by kinematics and detector  
 2738 dependent requirements when this measurement may be pursued. These could also exploit the  
 2739 cross calibration opportunities which result from the redundant determination of the inclusive  
 2740 DIS scattering kinematics through both the electron and the hadronic final state. This had been  
 2741 noted very early at HERA times, see Ref. [54,56,274] and was worked out in considerable detail  
 2742 by both H1 and ZEUS using independent and different methods. A feature used by H1 in their  
 2743  $F_L$  measurement includes a number of decays such as  $\pi^0 \rightarrow \gamma\gamma$  and  $J/\psi \rightarrow e^+e^-$  for calibrating  
 2744 the low energy measurement or  $K_s^0 \rightarrow \pi^+\pi^-$  and  $\Lambda \rightarrow p\pi$  for the determination of tracker scales,  
 2745 see Ref. [264].

2746 It is obvious that the prospect to measure  $F_L$  as presented here is striking. For nearly a decade,  
 2747 Guido Altarelli was a chief theory advisor to the development of the LHeC. In 2011, he publishes  
 2748 an article [273], in honour of Mario Greco, about *The Early Days of QCD (as seen from Rome)*  
 2749 in which he describes one of his main achievements [265], and persistent irritation, regarding  
 2750 the longitudinal structure function,  $F_L$ , and its measurement: *... The present data, recently*  
 2751 *obtained by the H1 experiment at DESY, are in agreement with our [!this] LO QCD prediction*  
 2752 *but the accuracy of the test is still far from being satisfactory for such a basic quantity.* The  
 2753 LHeC developments had not been rapid enough to let Guido see results of much higher quality  
 2754 on  $F_L$  with which the existence of departures from the DGLAP evolution, to high orders pQCD,  
 2755 may be expected to most safely be discovered.

#### 2756 4.2.4 Associated jet final states at low $x$

2757 The dynamical effects from resummation or nonlinear corrections which we have discussed above  
 2758 can arise at the LHeC not only in the inclusive structure functions, as we have illustrated so far,  
 2759 but also in more exclusive observables describing the structure of the jet final states associated  
 2760 to low- $x$  DIS. Here we update the discussion in Ref. [1].

2761 Baseline predictions for jet final states in DIS are obtained from perturbative finite-order cal-  
 2762 culations (see e.g. Refs. [200,275] for third-order calculations), supplemented by parton-shower  
 2763 Monte Carlo generators for realistic event simulation (as e.g. in Ref. [199]). But owing to the  
 2764 large phase space opening up at LHeC energies and the complex kinematics possibly involv-  
 2765 ing multiple hard scales, jet events are potentially sensitive to soft-gluon coherence effects of  
 2766 initial-state radiation [222,276–278], which go beyond finite-order perturbative evaluations and  
 2767 collinear parton showers, and show up as logarithmic  $x \rightarrow 0$  corrections to all orders of perturba-  
 2768 tion theory. These corrections can be resummed, and combined with large- $x$  contributions, via  
 2769 CCFM exclusive evolution equations [222,276], and affect the structure of jet multiplicities and  
 2770 angular jet correlations [278] as well as heavy quark distributions [277]. Observables based on



2771 forward jets, transverse energy flow, azimuthal correlations constitute probes of low- $x$  dynamics  
 2772 in DIS final states [279–281]. Phenomenological studies started with HERA [282–284] and will  
 2773 continue with the LHeC.

2774 Computational tools are being developed to address the structure of multi-jet final states by  
 2775 including low- $x$  dynamical effects. These include CCFM Monte Carlo tools [285, 286], off-shell  
 2776 matrix element parton-level generators [287, 288], BFKL Monte Carlo generators [289–291]. Fur-  
 2777 thermore, exclusive parton branching formalisms are being proposed in which not only gluon  
 2778 distributions but also quark distributions are treated at unintegrated level in transverse momen-  
 2779 tum [292–294]. This is instrumental in connecting low- $x$  approaches with DGLAP approaches  
 2780 to parton showers beyond leading order [295, 296]. Current applications of these new develop-  
 2781 ments are mostly being carried out for final states in hadron-hadron collisions, but extensions to  
 2782 lepton-hadron collisions are underway (see e.g. Ref. [288]), and likely to trigger further advances  
 2783 in the field.

#### 2784 4.2.5 Relation to Ultrahigh Energy Neutrino and Astroparticle physics

2785 The small- $x$  region probed by the LHeC is also very important in the context of ultra-high energy  
 2786 neutrino physics and astroparticle physics. Highly energetic neutrinos provide a unique window  
 2787 into the Universe, due to their weak interaction with matter, for a review see for example [297].  
 2788 They can travel long distances from distant sources, undeflected by the magnetic fields inside  
 2789 and in between galaxies, and thus provide complementary information to cosmic rays, gamma  
 2790 rays and gravitational wave signals. The IceCube observatory on Antarctica [298] is sensitive  
 2791 to neutrinos with energies from 100 GeV up (above 10 GeV with the use of their Deep Core  
 2792 detector). Knowledge about low- $x$  physics becomes indispensable in two contexts: neutrino  
 2793 interactions and neutrino production. At energies beyond the TeV scale the dominant part of the  
 2794 cross section is due to the neutrino DIS CC and NC interaction with the hadronic targets [297].

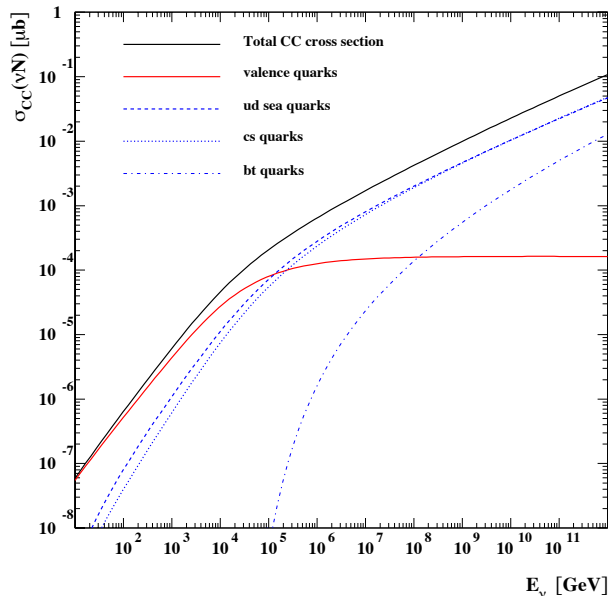


**Figure 4.17:** Charged current cross section for the neutrino - nucleon interaction on a isoscalar target as a function of neutrino energy. The total CC cross section is broken down into several contributions due to valence, up-down, strange-charm and bottom-top quarks. The calculation was based on Ref. [299].

2795 In Fig. 4.17 we show the charged current neutrino cross section as a function of the neutrino  
 2796 energy for an isoscalar target (in the laboratory frame where the target is at rest), using a  
 2797 calculation [299] based on the resummed model in [227]. We see that at energies below  $\sim 50$  TeV  
 2798 the cross section grows roughly linearly with energy, and in this region it is dominated by  
 2799 contributions from the large- $x$  valence region. Beyond that energy the neutrino cross section  
 2800 grows slower, roughly as a power  $\sim E_\nu^\lambda$  with  $\lambda \simeq 0.3$ . This high energy behaviour is totally  
 2801 controlled by the small- $x$  behaviour of the parton distributions. The dominance of the sea  
 2802 contributions to the cross section is clearly seen in Fig. 4.17. To illustrate more precisely the  
 2803 contributing values of  $x$  and  $Q^2$ , in Fig. 4.18 we show the differential cross section for the CC  
 2804 interaction  $xQ^2 d\sigma^{CC}/dx dQ^2$  for a neutrino energy  $E_\nu = 10^{11}$  GeV (in the frame where the  
 2805 hadronic target is at rest). We see a clear peak of the cross section at roughly a value of  
 2806  $Q^2 = M_W^2$  and an  $x$  value

$$x \simeq \frac{M_W^2}{2ME_\nu}, \quad (4.8)$$

which in this case is about  $3 \times 10^{-8}$ . We note that IceCube extracted the DIS cross section from

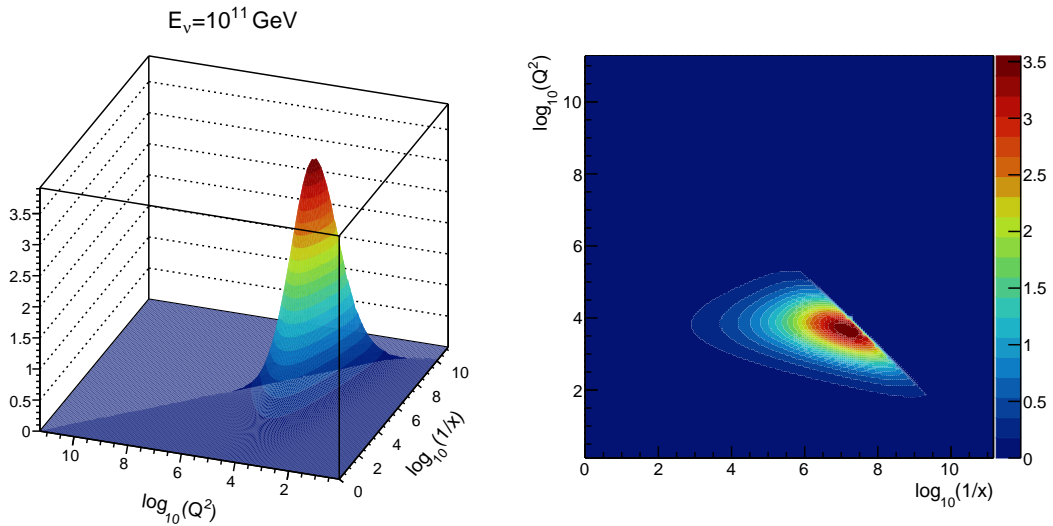


**Figure 4.18:** Differential charged current neutrino cross section  $10^5 \cdot xQ^2 d\sigma^{CC}/dx dQ^2$  [nb] as a function of  $Q^2$  and  $x$  for fixed neutrino energy  $E_\nu = 10^{11}$  GeV. Left: surface plot; right: contour plot.

2807

2808 neutrino observations [300] in the region of neutrino energies 10 – 1000 TeV. The extraction  
 2809 is consistent, within the large error bands, with the predictions based on the QCD, like those  
 2810 illustrated in Fig. 4.17. It is important to note that the IceCube extraction is limited to these  
 2811 energies by the statistics due to the steeply falling flux of neutrinos at high energy. We thus  
 2812 see that the neutrino interaction cross section at high energies is sensitive to a region which is  
 2813 currently completely unconstrained by existing precision DIS data.

2814 Another instance where dynamics at low  $x$  are crucial for neutrino physics is in understand-  
 2815 ing the mechanisms of ultra-high energy neutrino production. The neutrinos are produced in  
 2816 interactions which involve hadrons, either in  $\gamma p$  or in  $pp$  interactions. They emerge as decay  
 2817 products of pions, kaons and charmed mesons, and possibly beauty mesons if the energy is high  
 2818 enough [301]. For example, in the atmosphere neutrinos are produced in the interactions of the  
 2819 highly energetic cosmic rays with nitrogen and oxygen nuclei. The lower energy part of the  
 2820 atmospheric neutrino spectrum, up to about 100 TeV or so, is dominated by the decay of pions  
 2821 and kaons. This is called the conventional atmospheric neutrino flux. Above that energy the

2822 neutrino flux is dominated by the decay of the shorter-lived charmed mesons. Thus, this part of  
2823 the neutrino flux is called the prompt-neutrino flux. The reason why the prompt-neutrino flux  
2824 dominates at high energies is precisely related to the life-time of the intermediate mesons (and  
2825 also baryons like  $\Lambda_c$ ). The longer lived pions and kaons have a high probability of interacting  
2826 before they decay, thus degrading their energy and leading to a steeply falling neutrino flux.  
2827 The cross section for the production of charmed mesons is smaller than that for pions and kaons,  
2828 but the charmed mesons  $D^\pm$ ,  $D^0$ ,  $D_s$  and baryon  $\Lambda_c$  live shorter than pions and kaons, and thus  
2829 decay prior to any interaction. Thus, at energies about 100 TeV the prompt neutrino flux will  
2830 dominate over the conventional atmospheric neutrino flux. Therefore, the knowledge of this part  
2831 of the spectrum is essential as it provides a background for the sought-after astrophysical neu-  
2832 trinos [302]. Charmed mesons in high energy hadron-hadron interactions are produced through  
2833 gluon-gluon fusion into  $c\bar{c}$  pairs, where one gluon carries rather large  $x$  and the other one carries  
2834 very small  $x$ . Since the scales are small, of the order of the charm masses, the values of the  
2835 longitudinal momentum fractions involved are also very small and thus the knowledge of the  
2836 parton distributions in this region is essential [303]. The predictions for the prompt neutrino  
2837 flux become extremely sensitive to the behaviour of the gluon distribution at low  $x$  (and low  
2838  $Q^2$ ), where novel QCD phenomena like resummation as well as gluon saturation are likely to  
2839 occur [304].

2840 In addition, the LHeC measurements could help pin down one enduring mystery - what is  
2841 the composition of the most energetic cosmic rays? The best measurements of composition at  
2842 energies above  $10^{18}$  eV are based on studies of how showers develop in the atmosphere. The main  
2843 observable is the depth (in the atmosphere) of shower maximum - so called  $X_{\max}$ . The absolute  
2844 value of  $X_{\max}$  and the elongation rate  $dX_{\max}/dE$  of cosmic-rays depends on the assumed details  
2845 of the hadronic physics. A change in the elongation rate, observed by the Auger observatory  
2846 has often been interpreted as a signature for composition change (i.e. from mostly protons to  
2847 mostly iron) with increasing energy [305, 306]. However, new hadronic phenomena, such as a  
2848 color glass condensate, might also lead to a change in the elongation rate. Seeing saturation in  
2849 a Large Hadron electron Collider would help select between these two options [307, 308].

2850 Finally, the low- $x$  dynamics will become even more important at the HL-LHC and FCC hadron  
2851 colliders, see Sect. 9.6. With increasing centre-of-mass energy, hadron colliders will probe values  
2852 of  $x$  previously unconstrained by HERA data. It is evident that all the predictions in  $pp$   
2853 interactions at high energy will heavily rely on the PDF extrapolations to the small  $x$  region  
2854 which carry large uncertainties. As discussed in detail in this Section, resummation will play an  
2855 increasingly important role in the low  $x$  region of PDFs. A precision DIS machine is thus an  
2856 indispensable tool for constraining the QCD dynamics at low  $x$  with great precision as well as  
2857 for providing complementary information and independent measurements to hadronic colliders.

## 2858 4.3 Diffractive Deep Inelastic Scattering at the LHeC

### 2859 4.3.1 Introduction and Formalism

2860 An important discovery of HERA was the observation of a large ( $\sim 10\%$ ) fraction of diffractive  
2861 events in DIS [309, 310]. In these events the proton stays intact or dissociates into a state with  
2862 the proton quantum numbers, despite undergoing a violent, highly energetic collision, and is  
2863 separated from the rest of the produced particles by a large rapidity gap. In a series of ground-  
2864 breaking papers (see Ref. [311] for a review), the HERA experiments determined the deep  
2865 inelastic structure of the  $t$ -channel exchange in these events in the form of diffractive parton  
2866 densities.

2867 The precise measurement of diffraction in DIS is of great importance for our understanding of the  
 2868 strong interaction. First, the mechanism through which a composite strongly interacting object  
 2869 interacts perturbatively while keeping colour neutrality [312–318] offers information about the  
 2870 confinement mechanism. Second, diffraction is known to be highly sensitive to the low- $x$  partonic  
 2871 content of the proton and its evolution with energy [319–322] and it therefore has considerable  
 2872 promise to reveal deviations from standard linear evolution through higher twist effects or,  
 2873 eventually, non-linear dynamics. Third, it allows checks of basic theory predictions such as the  
 2874 relation between diffraction in  $ep$  scattering and nuclear shadowing [323]. Finally, the accurate  
 2875 extraction of diffractive parton distribution functions facilitates tests of the range of validity of  
 2876 perturbative factorisation [324–326]. The potential studies of inclusive diffraction that would be  
 2877 possible at the LHeC are presented here (see Ref. [327] for further details). They substantially  
 2878 extend the kinematic coverage of the HERA analyses, leading to much more detailed tests of  
 2879 theoretical ideas than have been possible hitherto. Although we work here at NLO of QCD, it is  
 2880 worth noting that similar analyses in the HERA context have recently extended to NNLO [328].

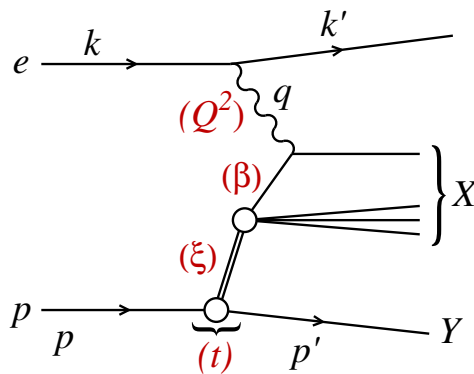


**Figure 4.19:** A diagram of a diffractive NC event in DIS together with the corresponding variables, in the one-photon exchange approximation. The large rapidity gap is between the system  $X$  and the scattered proton (or its low mass excitation)  $Y$ .

2881 In Fig. 4.19 we show a diagram depicting a neutral current diffractive deep inelastic event.  
 2882 Charged currents could also be considered and were measured at HERA [329] but with large  
 2883 statistical uncertainties and in a very restricted region of phase space. Although they could be  
 2884 measured at both the LHeC and the FCC-eh with larger statistics and more extended kinematics,  
 2885 in this first study we limit ourselves to neutral currents. The incoming electron or positron, with  
 2886 four momentum  $k$ , scatters off the proton, with incoming four momentum  $p$ , and the interaction  
 2887 proceeds through the exchange of a virtual photon with four-momentum  $q$ . The kinematic  
 2888 variables for such an event include the standard deep inelastic variables

$$Q^2 = -q^2, \quad x = \frac{-q^2}{2p \cdot q}, \quad y = \frac{p \cdot q}{p \cdot k}, \quad (4.9)$$

2889 where  $Q^2$  describes the photon virtuality,  $x$  is the Bjorken variable and  $y$  the inelasticity of the  
 2890 process. In addition, the variables

$$s = (k + p)^2, \quad W^2 = (q + p)^2, \quad (4.10)$$

2891 are the electron-proton centre-of-mass energy squared and the photon-proton centre-of-mass  
 2892 energy squared, respectively. A distinguishing feature of the diffractive event  $ep \rightarrow eXY$  is the  
 2893 presence of the large rapidity gap between the diffractive system, characterised by the invariant  
 2894 mass  $M_X$  and the final proton (or its low-mass excitation)  $Y$  with four momentum  $p'$ . In

2895 addition to the standard DIS variables listed above, diffractive events are also characterised by  
 2896 an additional set of variables defined as

$$t = (p - p')^2, \quad \xi = \frac{Q^2 + M_X^2 - t}{Q^2 + W^2}, \quad \beta = \frac{Q^2}{Q^2 + M_X^2 - t}. \quad (4.11)$$

2897 In the above  $t$  is the squared four-momentum transfer at the proton vertex,  $\xi$  (alternatively  
 2898 denoted by  $x_{IP}$ ) can be interpreted as the momentum fraction of the *diffractive exchange* with  
 2899 respect to the hadron, and  $\beta$  is the momentum fraction of the parton with respect to the  
 2900 diffractive exchange. The two momentum fractions combine to give Bjorken- $x$ ,  $x = \beta\xi$ .

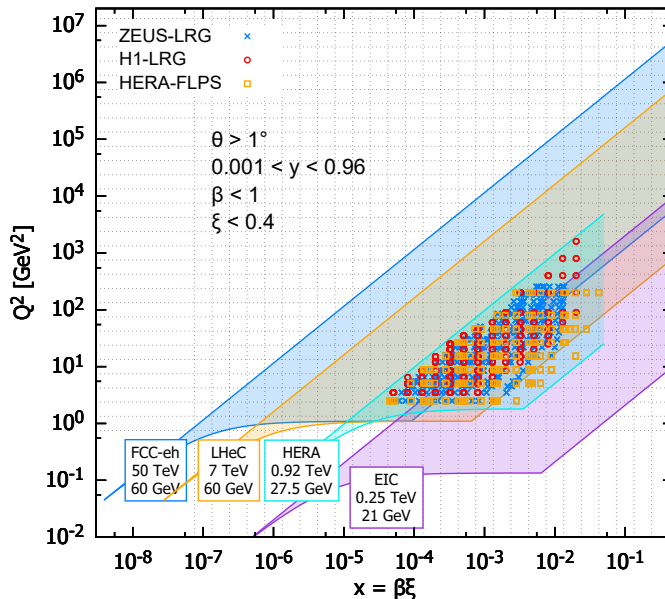


**Figure 4.20:** Kinematic phase space for inclusive diffraction in  $(x, Q^2)$  for the EIC (magenta region), the LHeC (orange region) and the FCC-eh (dark blue region) as compared with the HERA data (light blue region, ZEUS-LRG [330], H1-LRG [331], HERA-FLPS [332]). The acceptance limit for the electron in the detector design has been assumed to be  $1^\circ$ , and we take  $\xi < 0.4$ .

2901 The kinematic range in  $(\beta, Q^2, \xi)$  that we consider at the LHeC is restricted by the following  
 2902 cuts:

- 2903 •  $Q^2 \geq 1.8 \text{ GeV}^2$ : due to the fact that the initial distribution for the DGLAP evolution is  
 2904 parameterised at  $\mu_0^2 = 1.8 \text{ GeV}^2$ . The renormalization and factorisation scales are taken  
 2905 to be equal to  $Q^2$ .
- 2906 •  $\xi < 0.4$ : constrained by physical and experimental limitations. This rather high  $\xi$  value is  
 2907 an experimental challenge and physically enters the phase-space region where the Pomeron  
 2908 contribution should become negligible compared with sub-leading exchanges. Within the  
 2909 two-component model, see Eq. (4.16) below, at high  $\xi$  the cross section is dominated by  
 2910 the secondary Reggeon contribution, which is poorly fixed by the HERA data. We present  
 2911 this high  $\xi$  ( $> 0.1$ ) region for illustrative purpose and for the sake of discussion of the fit  
 2912 results below.

2913 In Fig. 4.20 the accessible kinematic range in  $(x, Q^2)$  is shown for three machines: HERA, LHeC  
 2914 and FCC-eh. For the LHeC design the range in  $x$  is increased by a factor  $\sim 20$  over HERA  
 2915 and the maximum available  $Q^2$  by a factor  $\sim 100$ . The FCC-eh machine would further increase  
 2916 this range with respect to LHeC by roughly one order of magnitude in both  $x$  and  $Q^2$ . We

2917 also show the EIC kinematic region for comparison. The three different machines are clearly  
 2918 complementary in their kinematic coverage, with LHeC and EIC adding sensitivity at lower and  
 2919 higher  $x$  than HERA, respectively.

2920 In Fig. 4.21 the phase space in  $(\beta, Q^2)$  is shown for fixed  $\xi$  for the LHeC. The LHeC machine  
 2921 probes very small values of  $\xi$ , reaching  $10^{-4}$  with a wide range of  $\beta$ . Of course, the ranges in  
 2922  $\beta$  and  $\xi$  are correlated since  $x = \beta\xi$ . Therefore, for small values of  $\xi$  only large values of  $\beta$  are  
 2923 accessible while for large  $\xi$  the range in  $\beta$  extends to very small values.

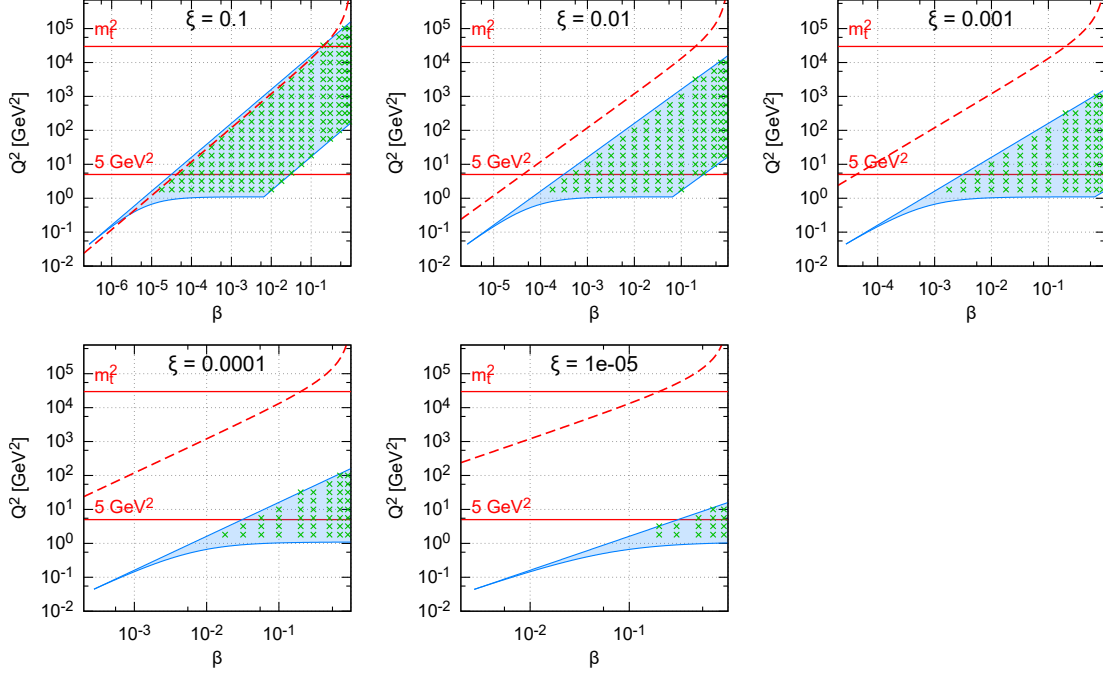


**Figure 4.21:** Kinematic phase space for inclusive diffraction in  $(\beta, Q^2)$  for fixed values of  $\xi$  for the LHeC design. The horizontal lines indicate correspondingly,  $Q^2 = 5 \text{ GeV}^2$ , the lowest data value for the DGLAP fit performed in this study and  $m_t^2$  the 6-flavour threshold. The dashed line marks the kinematic limit for  $t\bar{t}$  production.

2924 Diffractive cross sections in the neutral current case can be presented in the form of the reduced  
 2925 cross sections integrated over  $t$  [329]:

$$\frac{d^3\sigma^D}{d\xi d\beta dQ^2} = \frac{2\pi\alpha_{\text{em}}^2}{\beta Q^4} Y_+ \sigma_{\text{red}}^{\text{D}(3)}, \quad (4.12)$$

2926 where  $Y_+ = 1 + (1-y)^2$  and the reduced cross sections can be expressed in terms of two diffractive  
 2927 structure functions  $F_2^{\text{D}}$  and  $F_L^{\text{D}}$ . In the one-photon approximation, the relations are

$$\sigma_{\text{red}}^{\text{D}(3)} = F_2^{\text{D}(3)}(\beta, \xi, Q^2) - \frac{y^2}{Y_+} F_L^{\text{D}(3)}(\beta, \xi, Q^2). \quad (4.13)$$

2928 In this analysis we neglect  $Z^0$  exchange, though it should be included in future studies.

2929 Both  $\sigma_{\text{red}}^{\text{D}(3)}$  and  $\sigma_{\text{red}}^{\text{D}(4)}$  have been measured at the HERA collider [309, 310, 329–331, 333–336] and  
 2930 used to obtain QCD-inspired parameterisations.

2931 The standard perturbative QCD approach to diffractive cross sections is based on collinear  
 2932 factorisation [324–326]. It was demonstrated that, similarly to the inclusive DIS cross section,

2933 the diffractive cross section can be written, up to terms of order  $\mathcal{O}(\Lambda^2/Q^2)$ , where  $\Lambda$  is the  
 2934 hadronic scale, in a factorised form

$$d\sigma^{ep \rightarrow eXY}(\beta, \xi, Q^2, t) = \sum_i \int_{\beta}^1 dz d\hat{\sigma}^{ei} \left( \frac{\beta}{z}, Q^2 \right) f_i^D(z, \xi, Q^2, t), \quad (4.14)$$

2935 where the sum is performed over all parton flavours (gluon,  $d$ -quark,  $u$ -quark, etc.). The hard  
 2936 scattering partonic cross section  $d\hat{\sigma}^{ei}$  can be computed perturbatively in QCD and is the same  
 2937 as in the inclusive deep inelastic scattering case. The long distance part  $f_i^D$  corresponds to the  
 2938 diffractive parton distribution functions, which can be interpreted as conditional probabilities  
 2939 for partons in the proton, provided the proton is scattered into the final state system  $Y$  with  
 2940 specified 4-momentum  $p'$ . They are evolved using the DGLAP evolution equations [337–340]  
 2941 similarly to the inclusive case. The analogous formula for the  $t$ -integrated structure functions  
 2942 reads

$$F_{2/L}^{D(3)}(\beta, \xi, Q^2) = \sum_i \int_{\beta}^1 \frac{dz}{z} C_{2/L,i} \left( \frac{\beta}{z} \right) f_i^{D(3)}(z, \xi, Q^2), \quad (4.15)$$

2943 where the coefficient functions  $C_{2/L,i}$  are the same as in inclusive DIS.

2944 Fits to the diffractive structure functions usually [329, 335] parameterise the diffractive PDFs in  
 2945 a two component model, which is a sum of two diffractive exchange contributions,  $\mathbb{P}$  and  $\mathbb{R}$ :

$$f_i^{D(4)}(z, \xi, Q^2, t) = f_{\mathbb{P}}^p(\xi, t) f_i^{\mathbb{P}}(z, Q^2) + f_{\mathbb{R}}^p(\xi, t) f_i^{\mathbb{R}}(z, Q^2). \quad (4.16)$$

2946 For both of these terms proton vertex factorisation is separately assumed, meaning that the  
 2947 diffractive exchange can be interpreted as colourless objects called a *Pomeron* or a *Reggeon*  
 2948 with parton distributions  $f_i^{\mathbb{P},\mathbb{R}}(\beta, Q^2)$ . The flux factors  $f_{\mathbb{P},\mathbb{R}}^p(\xi, t)$  represent the probability  
 2949 that a Pomeron/Reggeon with given values  $\xi, t$  couples to the proton. They are parameterised  
 2950 using the form motivated by Regge theory,

$$f_{\mathbb{P},\mathbb{R}}^p(\xi, t) = A_{\mathbb{P},\mathbb{R}} \frac{e^{B_{\mathbb{P},\mathbb{R}}t}}{\xi^{2\alpha_{\mathbb{P},\mathbb{R}}(t)-1}}, \quad (4.17)$$

2951 with a linear trajectory  $\alpha_{\mathbb{P},\mathbb{R}}(t) = \alpha_{\mathbb{P},\mathbb{R}}(0) + \alpha'_{\mathbb{P},\mathbb{R}} t$ . The diffractive PDFs relevant to the  
 2952  $t$ -integrated cross sections read

$$f_i^{D(3)}(z, \xi, Q^2) = \phi_{\mathbb{P}}^p(\xi) f_i^{\mathbb{P}}(z, Q^2) + \phi_{\mathbb{R}}^p(\xi) f_i^{\mathbb{R}}(z, Q^2), \quad (4.18)$$

2953 with

$$\phi_{\mathbb{P},\mathbb{R}}^p(\xi) = \int dt f_{\mathbb{P},\mathbb{R}}^p(\xi, t). \quad (4.19)$$

2954 Note that, the notions of *Pomeron* and *Reggeon* used here to model hard diffraction in DIS are,  
 2955 in principle, different from those describing the soft hadron-hadron interactions; in particular,  
 2956 the parameters of the fluxes may be different.

2957 The diffractive parton distributions of the Pomeron at the initial scale  $\mu_0^2 = 1.8 \text{ GeV}^2$  are  
 2958 parameterised as

$$z f_i^{\mathbb{P}}(z, \mu_0^2) = A_i z^{B_i} (1-z)^{C_i}, \quad (4.20)$$

2959 where  $i$  is a gluon or a light quark and the momentum fraction  $z = \beta$  in the case of quarks. In the  
 2960 diffractive parameterisations the contributions of all the light quarks (anti-quarks) are assumed  
 2961 to be equal. For the treatment of heavy flavours, a variable flavour number scheme (VFNS)  
 2962 is adopted, where the charm and bottom quark DPDFs are generated radiatively via DGLAP

2963 evolution, and no intrinsic heavy quark distributions are assumed. The structure functions are  
 2964 calculated in a General-Mass Variable Flavour Number scheme (GM-VFNS) [341, 342] which  
 2965 ensures a smooth transition of  $F_{2,L}$  across the flavour thresholds by including  $\mathcal{O}(m_h^2/Q^2)$  correc-  
 2966 tions. The parton distributions for the Reggeon component are taken from a parameterisation  
 2967 which was obtained from fits to the pion structure function [343, 344].

2968 In Eq. (4.16) the normalisation factors of fluxes,  $A_{P,R}$  and of DPDFs,  $A_i$  enter in the product.  
 2969 To resolve the ambiguity we fix<sup>6</sup>  $A_P$  and use  $f_i^R(z, Q^2)$  normalised to the pion structure function,  
 2970 which results in  $A_i$  and  $A_R$  being well defined free fit parameters. For full details, see Ref. [327].

### 2971 4.3.2 Pseudodata for diffractive structure functions

2972 The reduced cross sections are extrapolated using the ZEUS-SJ DPDFs. Following the scenario  
 2973 of the ZEUS fit [335] we work within the VFNS scheme at NLO accuracy. The transition scales  
 2974 for DGLAP evolution are fixed by the heavy quark masses,  $\mu^2 = m_h^2$  and the structure functions  
 2975 are calculated in the Thorne–Roberts GM-VFNS [345]. The Reggeon PDFs are taken from the  
 2976 GRV pion set [344], the numerical parameters are taken from Tables 1 and 3 of Ref. [335], the  
 2977 heavy quark masses are  $m_c = 1.35$  GeV,  $m_b = 4.3$  GeV, and  $\alpha_s(M_Z^2) = 0.118$ .

2978 The pseudodata were generated using the extrapolation of the fit to HERA data, which pro-  
 2979 vides the central values, amended with a random Gaussian smearing with standard deviation  
 2980 corresponding to the relative error  $\delta$ . An uncorrelated 5% systematic error was assumed giving  
 2981 a total uncertainty

$$\delta = \sqrt{\delta_{\text{sys}}^2 + \delta_{\text{stat}}^2}. \quad (4.21)$$

2982 The statistical error was computed assuming a very modest integrated luminosity of  $2 \text{ fb}^{-1}$ , see  
 2983 Ref. [34, 35]. For the binning adopted in this study, the statistical uncertainties have a very  
 2984 small effect on the uncertainties in the extracted DPDFs. Obviously, a much larger luminosity  
 2985 would allow a denser binning that would result in smaller DPDF uncertainties.

2986 In Fig. 4.22 we show a subset of the simulated data for the diffractive reduced cross section  $\xi\sigma_{\text{red}}$   
 2987 as a function of  $\beta$  in selected bins of  $\xi$  and  $Q^2$  for the LHeC. For the most part the errors are  
 2988 very small, and are dominated by the systematics. The breaking of Regge factorisation evident  
 2989 at large  $\xi$  comes from the large Reggeon contribution in that region, whose validity could be  
 2990 further investigated at the LHeC.

### 2991 4.3.3 Potential for constraining diffractive PDFs at the LHeC and FCC-eh

2992 With the aim of establishing the experimental precision with which DPDFs could be extracted  
 2993 when LHeC data become available, we generate the central values of the pseudodata using the  
 2994 central set of the ZEUS-SJ fit that are distributed according to a Gaussian with experimental  
 2995 width given by Eq. (4.21), that also provides the uncertainty in the pseudodata. We then include  
 2996 the pseudodata in a fit alongside the existing HERA data using the same functional form and,  
 2997 as expected, obtain a  $\chi^2/\text{ndf} \sim 1$ , which demonstrates the consistency of the approach.

2998 To evaluate the experimental precision with which the DPDFs can be determined, several pseu-  
 2999 dodata sets, corresponding to independent random error samples, were generated. Each pseudo-  
 3000 data set was fitted separately. The minimal value of  $Q^2$  for the data considered in the fits was set  
 3001 to  $Q_{\text{min}}^2 = 5 \text{ GeV}^2$ . The reason for this cut-off is to show the feasibility of the fits including just  
 3002 the range in which standard twist-2 DGLAP evolution is expected to be trustable. At HERA,  
 3003 the  $Q_{\text{min}}^2$  values giving acceptable DGLAP (twist-2) fits were  $8 \text{ GeV}^2$  [329] and  $5 \text{ GeV}^2$  [330] for

---

<sup>6</sup>Here, as in the HERA fits,  $A_P$  is fixed by normalizing  $\phi_P^p(0.003) = 1$ .



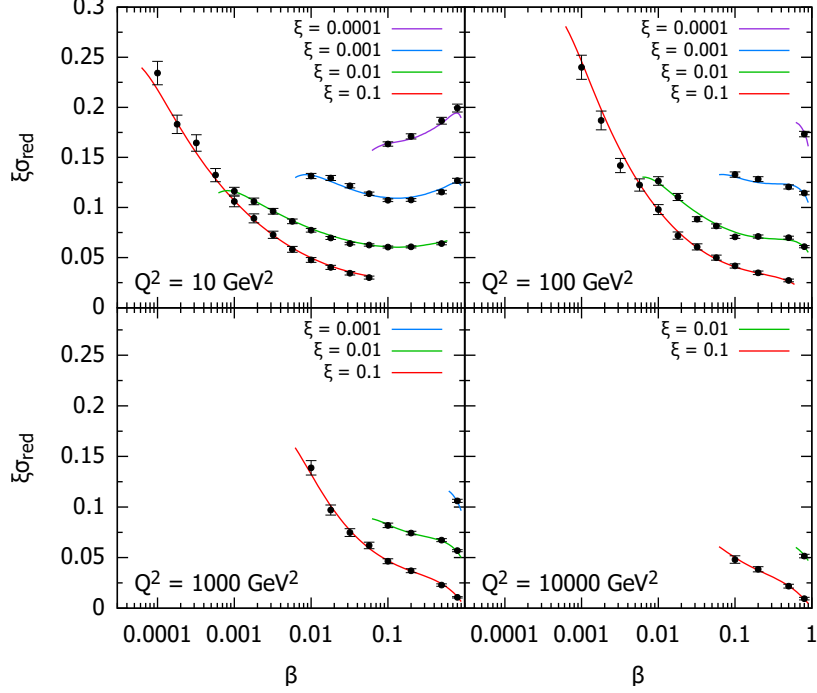


**Figure 4.22:** Selected subset of the simulated data for the diffractive reduced cross section as a function of  $\beta$  in bins of  $\xi$  and  $Q^2$  for  $ep$  collisions at the LHeC. The curves for  $\xi = 0.01, 0.001, 0.0001$  are shifted up by 0.04, 0.08, 0.12, respectively.

3004 H1 and ZEUS, respectively. The maximum value of  $\xi$  was set by default to  $\xi_{\max} = 0.1$ , above  
 3005 which the cross section starts to be dominated by the Reggeon exchange. The binning adopted  
 3006 in this study corresponds roughly to 4 bins per order of magnitude in each of  $\xi, \beta, Q^2$ . For  
 3007  $Q_{\min}^2 = 5 \text{ GeV}^2$ ,  $\xi_{\max} = 0.1$  and below the top threshold this results in 1229 and 1735 pseudo-  
 3008 data points for the LHeC and FCC-eh, respectively. The top-quark region adds 17 points for the  
 3009 LHeC and 255 for FCC-eh. Lowering  $Q_{\min}^2$  down to  $1.8 \text{ GeV}^2$  we get 1589 and 2171 pseudodata  
 3010 points, while increasing  $\xi$  up to 0.32 adds around 180 points for both proposed machines.

3011 The potential for determination of the gluon DPDF was investigated by fitting the inclusive  
 3012 diffractive DIS pseudodata with two models with different numbers of parameters, named S and  
 3013 C (see Ref. [327]) with  $\alpha_{IP,IR}(0)$  fixed, in order to focus on the shape of the Pomeron's PDFs. At  
 3014 HERA, both S and C fits provide equally good descriptions of the data with  $\chi^2/\text{ndf} = 1.19$  and  
 3015 1.18, respectively, despite different gluon DPDF shapes. The LHeC pseudodata are much more  
 3016 sensitive to gluons, resulting in  $\chi^2/\text{ndf}$  values of 1.05 and 1.4 for the S and C fits, respectively.  
 3017 This motivates the use of the larger number of parameters in the fit-S model, which we employ  
 3018 in the following studies. It also shows clearly the potential of the LHeC and the FCC-eh to  
 3019 better constrain the low- $x$  gluon and, therefore, unravel eventual departures from standard  
 3020 linear evolution.

3021 In Fig. 4.23 the diffractive gluon and quark distributions are shown for the LHeC and FCC-eh,  
 3022 respectively, as a function of momentum fraction  $z$  for fixed scales  $\mu^2 = 6, 20, 60, 200 \text{ GeV}^2$ .  
 3023 The bands labelled A, B, C denote fits to three statistically independent pseudodata replicas,  
 3024 obtained from the same central values and statistical and systematic uncertainties. Hereafter the  
 3025 uncertainty bands shown correspond to  $\Delta\chi^2 = 2.7$  (90% CL). Also the extrapolated ZEUS-SJ  
 3026 DPDFs are shown with error bands marked by the '/' hatched area. Note that the depicted  
 3027 uncertainty bands come solely from experimental errors, neglecting theoretical sources, such as

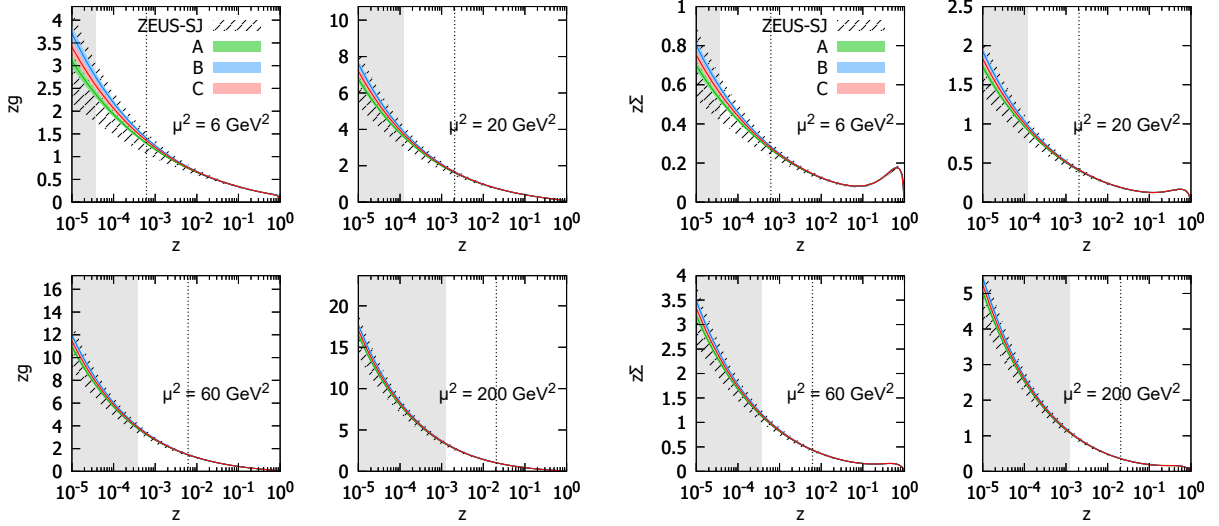


**Figure 4.23:** Diffractive PDFs for gluon and quark in the LHeC kinematics as a function of momentum fraction  $z$  for fixed values of scale  $\mu^2$ . Results of fits to three (A,B,C) pseudodata replicas are shown together with the experimental error bands. For comparison, the extrapolated ZEUS-SJ fit is also shown (black) with error bands marked with the hatched pattern. The vertical dotted lines indicate the HERA kinematic limit. The bands indicate only the experimental uncertainties.

3028 fixed input parameters and parameterisation biases. The extrapolation beyond the reach of  
 3029 LHeC/FCC-eh is marked in grey and the HERA kinematic limit is marked with the vertical  
 3030 dotted line. The stability of the results with respect to the independent pseudodata replicas  
 3031 used for the analysis is evident, so in the following only one will be employed. The low  $x$  DPDF  
 3032 determination accuracy improves with respect to HERA by a factor of 5–7 for the LHeC and  
 3033 10–15 for the FCC-eh and completely new kinematic regimes are accessed.

3034 For a better illustration of the precision, in Fig. 4.24 the relative uncertainties are shown for  
 3035 parton distributions at different scales. The different bands show the variation with the upper  
 3036 cut on the available  $\xi$  range, from 0.01 to 0.32. In the best constrained region of  $z \simeq 0.1$ ,  
 3037 the precision reaches the 1% level. We observe only a modest improvement in the achievable  
 3038 accuracy of the extracted DPDFs with the change of  $\xi$  by an order of magnitude from 0.01  
 3039 to 0.1. An almost negligible effect is observed when further extending the  $\xi$  range up to 0.32.  
 3040 This is encouraging, since the measurement for the very large values of  $\xi$  is challenging. It  
 3041 reflects the dominance of the secondary Reggeon in this region. We stress again that only  
 3042 experimental errors are included in our uncertainty bands. Neither theoretical uncertainties nor  
 3043 the parameterisation biases are considered. For a detailed discussion of this and other aspects  
 3044 of the fits, see Ref. [327].

#### 3045 4.3.4 Hadronic Final States in Diffraction and hard rapidity gap processes

3046 Various diffractive processes offer unique opportunity to investigate the factorization properties  
 3047 and can help to disentangle DGLAP vs BFKL dynamics.

3048 The factorisation properties of diffractive DIS were a major topic of study at HERA [311] and  
 3049 are highly relevant to the interpretation of diffractive processes at the LHC [346]. A general the-  
 3050 oretical framework is provided by the proof [324] of a hard scattering collinear QCD factorisation  
 3051 theorem for semi-inclusive DIS scattering processes such as  $ep \rightarrow epX$ . This implies that the  
 3052 DPDFs extracted in fits to inclusive diffractive DIS may be used to predict perturbative cross

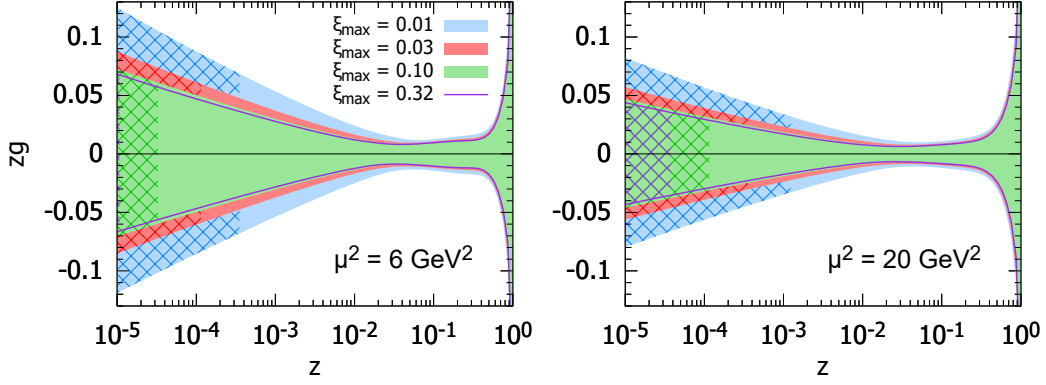


**Figure 4.24:** Relative uncertainties on the diffractive gluon PDFs for the LHeC kinematics. Two different choices of scales are considered  $\mu^2 = 6$  and  $\mu^2 = 20 \text{ GeV}^2$ . The blue, red, green bands and magenta line correspond to different maximal values of  $\xi = 0.01, 0.03, 0.1, 0.32$ , respectively. The cross-hatched areas show kinematically excluded regions. The bands indicate only the experimental uncertainties, see the text.

3053 sections for hadronic final state observables such as heavy flavour or jet production. Testing this  
 3054 factorisation pushes at the boundaries of applicability of perturbative QCD and will be a major  
 3055 topic of study at the LHeC.

3056 Tests of diffractive factorisation at HERA are strongly limited by the kinematics. The mass of  
 3057 the dissociation system  $X$  is limited to approximately  $M_X < 30 \text{ GeV}$ , which implies for example  
 3058 that jet transverse momenta cannot be larger than about  $15 \text{ GeV}$  and more generally leaves very  
 3059 little phase space for any studies at perturbative scales. As well as restricting the kinematic range  
 3060 of studies, this restriction also implied large hadronisation and scale uncertainties in theoretical  
 3061 predictions, which in turn limit the precision with which tests can be made.

3062 The higher centre-of-mass energy of the LHeC opens up a completely new regime for diffractive  
 3063 hadronic final state observables in which masses and transverse momenta are larger and theo-  
 3064 retical uncertainties are correspondingly reduced. For example,  $M_X$  values in excess of  $250 \text{ GeV}$   
 3065 are accessible, whilst remaining in the region  $\xi < 0.05$  where the leading diffractive (pomeron)  
 3066 exchange dominates. The precision of tests is also improved by the development of techniques  
 3067 for NNLO calculations for diffractive jets [347].

3068 Fig. 4.25 shows a simulation of the expected diffractive jet cross section at the LHeC, assuming  
 3069 DPDFs extrapolated from H1 at HERA [329], using the NLOJET++ framework [348]. An  
 3070 integrated luminosity of  $100 \text{ fb}^{-1}$  is assumed and the kinematic range considered is  $Q^2 > 2 \text{ GeV}^2$ ,  
 3071  $0.1 < y < 0.7$  and scattered electron angles larger than  $1^\circ$ . Jets are reconstructed using the  $k_T$   
 3072 algorithm with  $R = 1$ . The statistical precision remains excellent up to jet transverse momenta  
 3073 of almost  $50 \text{ GeV}$  and the theoretical scale uncertainties (shaded bands) are substantially reduced  
 3074 compared with HERA measurements. Comparing a measurement of this sort of quality with  
 3075 predictions refined using DPDFs from inclusive LHeC data would clearly provide an exacting  
 3076 test of diffractive factorisation.

3077 Further interesting hadronic final state observables that were studied at HERA and could be  
 3078 extended at the LHeC include open charm production, thrust and other event shapes, charged  
 3079 particle multiplicities and energy flows. In addition, the LHeC opens up completely new chan-  
 3080 nels, notably diffractive beauty,  $W$  and  $Z$  production, the latter giving complementary sensitivity  
 3081 to the quark densities to that offered by inclusive diffraction.

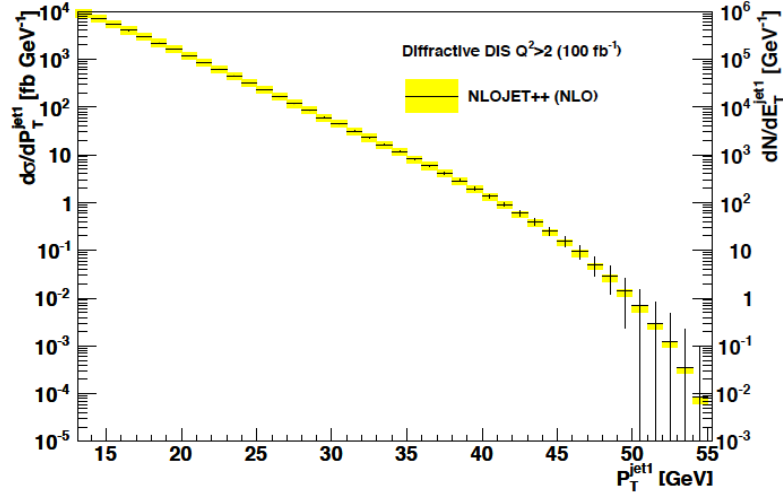


**Figure 4.25:** Simulated diffractive dijet cross section as a function of leading jet transverse momentum in the kinematic range  $Q^2 > 2 \text{ GeV}^2$  and  $0.1 < y < 0.7$ , with scattered electron angles in excess of  $1^\circ$ . The error bars indicate predicted statistical uncertainties for a luminosity of  $100 \text{ fb}^{-1}$ . The coloured bands correspond to theoretical uncertainties when varying the renormalisation and factorisation scales by factors of 2.

3082 Of separate interest are hard rapidity gap processes, for example  $\gamma^* p \rightarrow J/\psi + \text{rapidity gap}(\Delta y) +$   
 3083  $Y$  at large  $-t \gg 1 \text{ GeV}^2$ . In such processes DGLAP evolution is strongly suppressed and  
 3084 therefore this is an ideal laboratory to investigate BFKL dynamics. The dependence of the  
 3085 process on  $\Delta y$  is expected to be given by  $\sigma \sim \Delta y^{2\omega_P(t)}$ . Here, the effective pomeron trajectory  
 3086 is parameterized as  $\alpha_P(t) = 1 + \omega(t)$ . The current models give  $\omega$  between 0.5 (LO BFKL) and  
 3087  $\omega = 0.2 - 0.3$  for the resummed BFKL. With a proper large acceptance detector one would be  
 3088 able to study dependence on  $\Delta y$  in a wide rapidity interval as well as the dependence on the  
 3089 momentum transfer  $t$ . Hence this process offers a powerful test for the theoretical predictions  
 3090 of the properties of the BFKL pomeron.

## 3091 4.4 Theoretical Developments

### 3092 4.4.1 Prospects for Higher Order pQCD in DIS

3093 With its large anticipated luminosity, the LHeC will be able to perform highly precise mea-  
 3094 surements for a wide variety of final states in deep inelastic scattering, often exploring novel  
 3095 kinematical ranges, challenging the theory of QCD at an unprecedented level of accuracy, and  
 3096 enabling precision determinations of QCD parameters and of the proton's parton structure. For  
 3097 this program to succeed, it will be mandatory to be able to confront the LHeC precision data  
 3098 with equally precise theoretical predictions.

3099 In the Standard Model, these predictions can be obtained through a perturbative expansion  
 3100 to sufficiently high order. These calculations are performed in the larger framework of QCD  
 3101 factorization [37] and exploit the process-independence of parton distributions, whose evolution  
 3102 is controlled by the DGLAP equations. The DGLAP splitting functions are known to NNLO  
 3103 level for already quite some time [349, 350], and important progress has been made recently  
 3104 towards their N3LO terms [90, 91]. Moreover, mixed QCD/QED corrections to them have been  
 3105 derived [351], enabling a consistent combination of QCD and electroweak effects.

3106 The physics opportunities that are offered already by the HERA legacy data set have motivated

3107 substantial recent activity in precision QCD calculations for deeply inelastic processes. At the  
3108 inclusive level, the QCD coefficients for the inclusive DIS structure functions are known to three  
3109 loops (N3LO) for some time [352], they were improved upon recently by the computation of heavy  
3110 quark mass effects [353, 354]. Fully differential predictions for final states with jets, photons,  
3111 heavy quarks or hadrons are generally available to NLO in QCD, often dating back to the HERA  
3112 epoch. Technical developments that were made in the context of fully differential higher-order  
3113 QCD calculations for LHC processes have enabled substantial advances in the theory precision  
3114 of DIS jet cross sections. Fully differential predictions for single jet production are now available  
3115 to NNLO [198] and N3LO [200, 275] for neutral-current and charged current DIS, and two-jet  
3116 production [159, 160, 355] has been computed to NNLO. The latter calculations are performed  
3117 with fully differential parton-level final state information, thereby allowing their extension to jet  
3118 production in diffractive DIS [347] and to DIS two-parton event shapes [201]. The newly derived  
3119 NNLO jet cross sections were partly used in the projections for LHeC precision jet studies in  
3120 Sections 4.1.2 and 4.3.4 above.

3121 NLO calculations have been largely automated in QCD [356–358] and the electroweak the-  
3122 ory [359, 360], and are now available in multi-purpose event generator programs [361–363] for  
3123 processes of arbitrary multiplicity. These can be combined with parton shower approximations  
3124 to provide NLO-accurate predictions for fully exclusive final states. Although most of the ap-  
3125 plications of these tools were to hadron collider observables, they are also ready to be used for  
3126 DIS processes [199], thereby offering novel opportunities for precision studies for LHeC. In this  
3127 context, electroweak corrections may become particularly crucial for high-mass final states at  
3128 the LHeC, and have been largely unexplored up to now. A similar level of automation has not  
3129 yet been reached so far at NNLO, where calculations are performed on a process-by-process ba-  
3130 sis. For DIS processes, fully differential NNLO calculations for three-jet final states or for heavy  
3131 quark production could become feasible in the near-term future. Moreover, a whole set of cal-  
3132 culations at this order for specific final states (involving jets, vector bosons or heavy quarks) in  
3133 photoproduction could be readily taken over by adapting the respective hadron collider results.

3134 The all-order resummation of large logarithmic corrections to hadron collider processes has  
3135 made very substantial advances in the recent past, owing to the emergence of novel systematic  
3136 frameworks from soft-collinear effective theory, or in momentum space resummation. As a  
3137 result, threshold logarithms and transverse-momentum logarithms in benchmark hadron collider  
3138 processes can now be resummed up to the third subleading logarithmic order (N3LL). A similar  
3139 accuracy has been reached for selected event shapes in electron-positron annihilation. For DIS  
3140 event shapes, currently available predictions include only up to NLL resummation [364]. With  
3141 the newly available frameworks, they could be improved by two more logarithmic orders, as  
3142 demonstrated in exploratory work on the DIS one-jettiness event shape [196, 197]. Applications  
3143 of this framework to final states in DIS the small- $x$  limit (see Section 4.2) are largely unexplored,  
3144 and may provide important novel insights into the all-order dynamics in the high-energy limit.

3145 The full exploitation of future LHeC data will require novel precision calculations for a variety  
3146 of benchmark processes, often combining fixed-order, resummation and parton shower event  
3147 generation to obtain theory predictions of matching accuracy. Recent advances in calculational  
3148 techniques and an increasing degree of automation will help to enable this progress. A close  
3149 interplay between experiment and theory will then be crucial to combine data and predictions  
3150 into precision measurements of physics parameters and into probes of fundamental particle  
3151 dynamics.

## 3152 4.4.2 Theoretical Concepts on the Light Cone

### 3153 Intrinsic Heavy Quark Phenomena

3154 One of the most interesting nonperturbative quantum field theoretic aspects of hadron light front  
 3155 wavefunctions in QCD are the intrinsic heavy-quark Fock states [365–367]. Consider a heavy-  
 3156 quark loop insertion to the proton’s self-energy. The heavy-quark loop can be attached by gluons  
 3157 to just one valence quark. The cut of such diagrams yields the standard DGLAP gluon splitting  
 3158 contribution to the proton’s heavy quark structure function. In this case, the heavy quarks are  
 3159 produced at very small  $x$ . However, the heavy quark loop can also be attached to two or more  
 3160 valence quarks in the proton self-energy. In the case of QED this corresponds to the light-by-  
 3161 light lepton loop insertion in an atomic wavefunction. In the case of QCD, the heavy quark  
 3162 loop can be attached by three gluons to two or three valence quarks in the proton self-energy.  
 3163 This is a non-Abelian insertion to the hadron’s self-energy. The cut of such diagrams gives the  
 3164 *intrinsic* heavy-quark contribution to the proton’s light-front wavefunction. In the case of QCD,  
 3165 the probability for an intrinsic heavy  $Q\bar{Q}$  pair scales as  $\frac{1}{M_Q^2}$ ; this is in contrast to heavy  $\ell\bar{\ell}$  lepton  
 3166 pairs in QED where the probability for heavy lepton pairs in an atomic wavefunction scales as  
 3167  $\frac{1}{M_\ell^2}$ . This difference in heavy-particle scaling in mass distinguishes Abelian from non-Abelian  
 3168 theories.

3169 A basic property of hadronic light-front wavefunctions is that they have strong fall-off with the  
 3170 invariant mass of the Fock state. For example, the Light-Front Wave Functions (LFWFs) of the  
 3171 colour-confining AdS/QCD models [368]  $\mathcal{M}^2 = [\sum_i k_i^\mu]^2$  of the Fock state constituents. This  
 3172 means that the probability is maximised when the constituents have equal true rapidity, i.e.  
 3173  $x_i \propto (\vec{k}_{\perp i}^2 + m_i^2)^{1/2}$ . Thus the heavy quarks carry most of the momentum in an intrinsic heavy  
 3174 quark Fock state. For example, the charm quark in the intrinsic charm Fock state  $|uudc\bar{c}\rangle$  of a  
 3175 proton carries about 40% of the proton’s momentum:  $x_c \sim 0.4$ . After a high-energy collision,  
 3176 the co-moving constituents can then recombine to form the final state hadrons. along the proton.  
 3177 Thus, in a  $ep$  collision the comoving  $udc$  quarks from the  $|uudc\bar{c}\rangle$  intrinsic 5-quark Fock state can  
 3178 recombine to a  $\Lambda_c$ , where  $x_{\Lambda_c} = x_c + x_u + x_d \sim 0.5$ . Similarly, the comoving  $dcc$  in the  $|uudc\bar{c}\bar{c}\bar{c}\rangle$   
 3179 intrinsic 7-quark Fock state can recombine to a  $\Xi(ccd)^+$ , with  $x_{\Xi(ccd)} = x_c + x_c + x_d \sim 0.9$ .

3180 Therefore, in the intrinsic heavy quark model the wavefunction of a hadron in QCD can be rep-  
 3181 resented as a superposition of Fock state fluctuations, e.g.  $|n_V\rangle, |n_V g\rangle, |n_V Q\bar{Q}\rangle, \dots$  components  
 3182 where  $n_V \equiv dds$  for  $\Sigma^-$ ,  $uud$  for proton,  $\bar{u}d$  for  $\pi^-$  and  $u\bar{d}$  for  $\pi^+$ . Charm hadrons can be  
 3183 produced by coalescence in the wavefunctions of the moving hadron. Doubly-charmed hadrons  
 3184 require fluctuations such as  $|n_V c\bar{c}\bar{c}\bar{c}\rangle$ . The probability for these Fock state fluctuations to come  
 3185 on mass shell is inversely proportional to the square of the quark mass,  $\mathcal{O}(m_Q^{-2n})$  where  $n$   
 3186 is the number of  $Q\bar{Q}$  pairs in the hadron. Thus the natural domain for heavy hadrons pro-  
 3187 duced from heavy quark Fock states is  $\vec{k}_{\perp Q}^2 \sim m_Q^2$  and high light-front momentum fraction  
 3188  $x_Q$  [365, 366, 366, 367]. For example, the rapidity regime for double-charm hadron production  
 3189  $y_{ccd} \sim 3$  at low energies is well within the kinematic experiment domain of a fixed target ex-  
 3190 periment such as SELEX at the Tevatron [369]. Note that the intrinsic heavy-quark mechanism  
 3191 can account for many previous observations of forward heavy hadron production single and  
 3192 double  $J/\psi$  production by pions observed at high  $x_F > 0.4$  in the low energy fixed target NA3  
 3193 experiment, the high  $x_F$  production of  $pp \rightarrow \Lambda_c + X$  and  $pp \rightarrow \Lambda_b + X$  observed at the ISR;  
 3194 single and double  $\Upsilon(b\bar{b})$  production, as well as *quadra-bottom* tetraquark  $[bb\bar{b}\bar{b}]$  production ob-  
 3195 served recently by the AnDY experiment at RHIC [370]. In addition the EMC collaboration  
 3196 observed that the charm quark distribution in the proton at  $x = 0.42$  and  $Q^2 = 75 \text{ GeV}^2$  is 30  
 3197 times larger than expected from DGLAP evolution. All of these experimental observations are  
 3198 naturally explained by the intrinsic heavy quark mechanism. The SELEX observation [369] of

3199 double charm baryons at high  $x_F$  reflects production from double intrinsic heavy quark Fock  
 3200 states of the baryon projectile. Similarly, the high  $x_F$  domain – which would be accessible at  
 3201 forward high  $x_F$  – is the natural production domain for heavy hadron production at the LHeC.

3202 The production of heavy hadrons based on intrinsic heavy quark Fock states is thus remarkable  
 3203 efficient and greatly extends the kinematic domain of the LHeC, e.g. for processes such as  
 3204  $\gamma^*b \rightarrow Z^0b$ . This is in contrast with the standard production cross sections based on gluon  
 3205 splitting, where only a small fraction of the incident momentum is effective in creating heavy  
 3206 hadrons.

### 3207 **Light-Front Holography and Superconformal Algebra**

3208 The LHeC has the potential of probing the high mass spectrum of QCD, such as the spectroscopy  
 3209 and structure of hadrons consisting of heavy quarks. Insights into this new domain of hadron  
 3210 physics can now be derived by new non-perturbative colour-confining methods based on light-  
 3211 front (LF) holography. A remarkable feature is universal Regge trajectories with universal  
 3212 slopes in both the principal quantum number  $n$  and internal orbital angular momentum  $L$ . A  
 3213 key feature is di-quark clustering and supersymmetric relations between the masses of meson,  
 3214 baryons, and tetraquarks. In addition the running coupling is determined at all scales, including  
 3215 the soft domain relevant to rescattering corrections to LHeC processes. The combination of  
 3216 lightfront holography with superconformal algebra leads to the novel prediction that hadron  
 3217 physics has supersymmetric properties in both spectroscopy and dynamics.

3218 **Light-front holography and recent theoretical advances** Five-dimensional AdS<sub>5</sub> space  
 3219 provides a geometrical representation of the conformal group. Remarkably, AdS<sub>5</sub> is holograph-  
 3220 ically dual to 3 + 1 spacetime at fixed LF time  $\tau$  [371]. A colour-confining LF equation for  
 3221 mesons of arbitrary spin  $J$  can be derived from the holographic mapping of the *soft-wall model*  
 3222 modification of AdS<sub>5</sub> space for the specific dilaton profile  $e^{+\kappa^2 z^2}$ , where  $z$  is the fifth dimension  
 3223 variable of the five-dimensional AdS<sub>5</sub> space. A holographic dictionary maps the fifth dimension  
 3224  $z$  to the LF radial variable  $\zeta$ , with  $\zeta^2 = b_\perp^2(1 - x)$ . The same physics transformation maps  
 3225 the AdS<sub>5</sub> and (3 + 1) LF expressions for electromagnetic and gravitational form factors to each  
 3226 other [372].

3227 A key tool is the remarkable dAFF principle [373] which shows how a mass scale can appear in a  
 3228 Hamiltonian and its equations of motion while retaining the conformal symmetry of the action.  
 3229 When applying it to LF holography, a mass scale  $\kappa$  appears which determines universal Regge  
 3230 slopes, and the hadron masses. The resulting *LF Schrödinger Equation* incorporates colour  
 3231 confinement and other essential spectroscopic and dynamical features of hadron physics, includ-  
 3232 ing Regge theory, the Veneziano formula [374], a massless pion for zero quark mass and linear  
 3233 Regge trajectories with the universal slope in the radial quantum number  $n$  and the internal  
 3234 orbital angular momentum  $L$ . The combination of LF dynamics, its holographic mapping to  
 3235 AdS<sub>5</sub> space, and the dAFF procedure provides new insight into the physics underlying colour  
 3236 confinement, the non-perturbative QCD coupling, and the QCD mass scale. The  $q\bar{q}$  mesons and  
 3237 their valence LFWFs are the eigensolutions of the frame-independent a relativistic bound-state  
 3238 LF Schrödinger equation.

3239 The mesonic  $q\bar{q}$  bound-state eigenvalues for massless quarks are  $M^2(n, L, S) = 4\kappa^2(n + L + S/2)$ .  
 3240 This equation predicts that the pion eigenstate  $n = L = S = 0$  is massless for zero quark mass.  
 3241 When quark masses are included in the LF kinetic energy  $\sum_i \frac{k_{\perp i}^2 + m^2}{x_i}$ , the spectroscopy of mesons  
 3242 are predicted correctly, with equal slope in the principal quantum number  $n$  and the internal

3243 orbital angular momentum  $L$ . A comprehensive review is given in Ref. [371].

3244

3245 **The QCD Running Coupling at all Scales from Light-Front Holography** The QCD  
3246 running coupling  $\alpha_s(Q^2)$  sets the strength of the interactions of quarks and gluons as a function  
3247 of the momentum transfer  $Q$  (see Sec. 4.1). The dependence of the coupling  $Q^2$  is needed to  
3248 describe hadronic interactions at both long and short distances [375]. It can be defined [376] at  
3249 all momentum scales from a perturbatively calculable observable, such as the coupling  $\alpha_s^{g_1}(Q^2)$ ,  
3250 which is defined using the Bjorken sum rule [377], and determined from the sum rule prediction  
3251 at high  $Q^2$  and, below, from its measurements [378–380]. At high  $Q^2$ , such *effective charges*  
3252 satisfy asymptotic freedom, obey the usual pQCD renormalisation group equations, and can be  
3253 related to each other without scale ambiguity by commensurate scale relations [381].

3254 The high  $Q^2$  dependence of  $\alpha_s^{g_1}(Q^2)$  is predicted by pQCD. In the small  $Q^2$  domain its functional  
3255 behaviour can be predicted by the dilaton  $e^{+\kappa^2 z^2}$  soft-wall modification of the AdS<sub>5</sub> metric,  
3256 together with LF holography [382], as  $\alpha_s^{g_1}(Q^2) = \pi e^{-Q^2/4\kappa^2}$ . The parameter  $\kappa$  determines the  
3257 mass scale of hadrons and Regge slopes in the zero quark mass limit, and it was shown that it can  
3258 be connected to the mass scale  $\Lambda_s$ , which controls the evolution of the pQCD coupling [382–384].  
3259 Measurements of  $\alpha_s^{g_1}(Q^2)$  [385,386] are remarkably consistent with this predicted Gaussian form,  
3260 and a fit gives  $\kappa = 0.513 \pm 0.007$  GeV, see Fig. 4.26.

3261 The matching of the high and low  $Q^2$  regimes of  $\alpha_s^{g_1}(Q^2)$  determines a scale  $Q_0$ , which sets the  
3262 interface between perturbative and non-perturbative hadron dynamics. This connection can be  
3263 done for any choice of renormalisation scheme and one obtains an effective QCD coupling at all  
3264 momenta. In the  $\overline{\text{MS}}$  scheme one gets  $Q_0 = 0.87 \pm 0.08$  GeV [387]. The corresponding value of  
3265  $\Lambda_{\overline{\text{MS}}}$  agrees well with the measured world average value and its value allows to compute hadron  
3266 masses using the AdS/QCD superconformal predictions for hadron spectroscopy. The value of  
3267  $Q_0$  can further be used to set the factorization scale for DGLAP evolution [338–340] or the ERBL  
3268 evolution of distribution amplitudes [388,389]. The use of the scale  $Q_0$  to resolve the factorization  
3269 scale uncertainty in structure functions and fragmentation functions, in combination with the  
3270 scheme-independent *principle of maximum conformality* (PMC) [177] for setting renormalization  
3271 scales, can greatly improve the precision of pQCD predictions for collider phenomenology at  
3272 LHeC and HL-LHC.

3273 **Superconformal Algebra and Hadron Physics with LHeC data** If one generalises LF  
3274 holography using *superconformal algebra* the resulting LF eigensolutions yield a unified Regge  
3275 spectroscopy of mesons, baryons and tetraquarks, including remarkable supersymmetric relations  
3276 between the masses of mesons and baryons of the same parity <sup>7</sup> [390,391]. This generalisation  
3277 further predicts hadron dynamics, including vector meson electroproduction, hadronic LFWFs,  
3278 distribution amplitudes, form factors, and valence structure functions [392,393]. Applications  
3279 to the deuteron elastic form factors and structure functions are given in Refs. [394,395]

3280 The eigensolutions of superconformal algebra predict the Regge spectroscopy of mesons, baryons,  
3281 and tetraquarks of the same parity and twist as equal-mass members of the same 4-plet repre-  
3282 sentation with a universal Regge slope [396–398]. A comparison with experiment is shown in  
3283 Fig. 4.27. The  $q\bar{q}$  mesons with orbital angular momentum  $L_M = L_B + 1$  have the same mass as  
3284 their baryonic partners with orbital angular momentum  $L_B$  [396,399].

---

<sup>7</sup>QCD is not supersymmetrical in the usual sense, since the QCD Lagrangian is based on quark and gluonic fields, not squarks or gluinos. However, its hadronic eigensolutions conform to a representation of superconformal algebra, reflecting the underlying conformal symmetry of chiral QCD and its Pauli matrix representation.



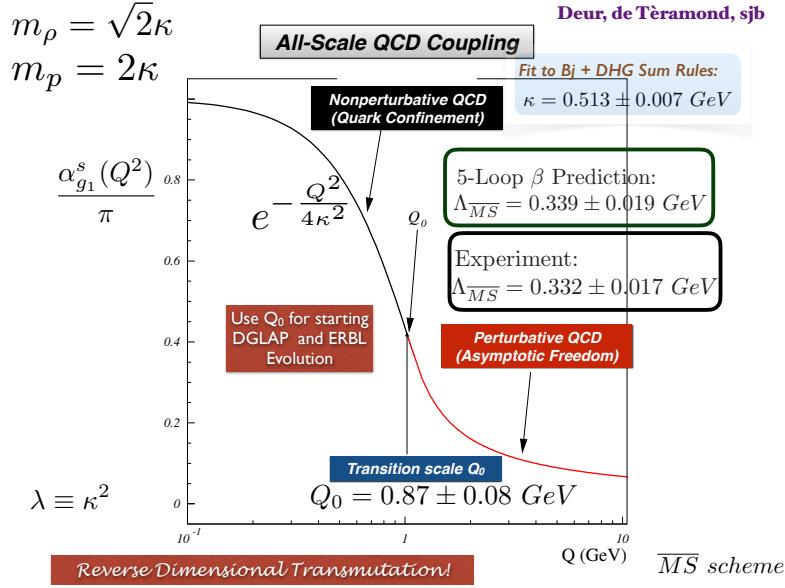


**Figure 4.26:** Prediction for the running coupling  $\alpha_{g_1}^s(Q^2)$  at all scales. At lower  $Q^2$  predictions are obtained from LF Holography and at higher  $Q^2$  from perturbative QCD. The magnitude and derivative of the perturbative and non-perturbative coupling are matched at the scale  $Q_0$ . This matching connects the perturbative scale  $\Lambda_{\overline{MS}}$  to the non-perturbative scale  $\kappa$  which underlies the hadron mass scale.

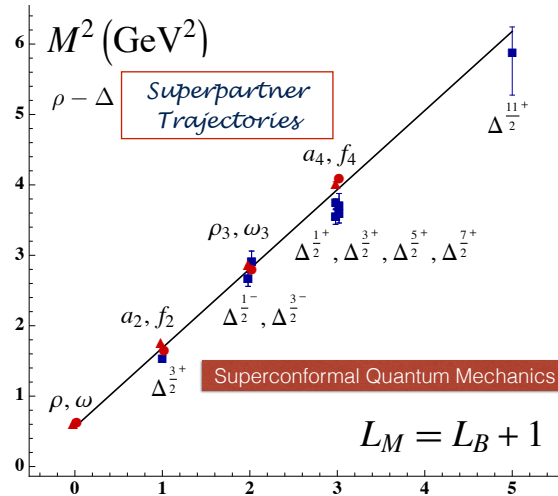


**Figure 4.27:** Comparison of the  $\rho/\omega$  meson Regge trajectory with the  $J = 3/2$   $\Delta$  baryon trajectory. Superconformal algebra predicts the mass degeneracy of the meson and baryon trajectories if one identifies a meson with internal orbital angular momentum  $L_M$  with its superpartner baryon with  $L_M = L_B + 1$ . See Refs. [396, 399].

3285 The predictions from LF holography and superconformal algebra can also be extended to mesons,  
 3286 baryons, and tetraquarks with strange, charm and bottom quarks. Although conformal symme-  
 3287 try is strongly broken by the heavy quark masses, the basic underlying supersymmetric mech-  
 3288 anism, which transforms mesons to baryons (and baryons to tetraquarks), still holds and gives  
 3289 remarkable mass degeneracy across the entire spectrum of light, heavy-light and double-heavy

3290 hadrons.

3291 The 4-plet symmetry of quark-antiquark mesons, quark-diquark baryons, and diquark-antidiquark  
3292 tetraquarks are important predictions by superconformal algebra [387,390]. Recently the AnDY  
3293 experiment at RHIC has reported the observation of a state at 18 GeV which can be identified  
3294 with the  $[bb][\bar{b}\bar{b}]$  tetraquark [370]. The states with heavy quarks such as the  $[bb][\bar{b}\bar{b}]$  tetraquark  
3295 can be produced at the LHeC, especially at high  $x_F$  along the proton beam direction. New  
3296 measurements at the LHeC are therefore inevitable to manifest the superconformal nature of  
3297 hadronic bound states.

## Chapter 5

# Electroweak and Top Quark Physics

### 5.1 Electroweak Physics with Inclusive DIS data

With the discovery of the Standard Model (SM) Higgs boson at the CERN LHC experiments and subsequent measurements of its properties, all fundamental parameters of the SM have now been measured directly and with remarkable precision. To further establish the validity of the theory of electroweak interactions [24,400–403], validate the mechanism of electroweak symmetry breaking and the nature of the Higgs sector [404–406], new electroweak measurements have to be performed at highest precision. Such high-precision measurements can be considered as a portal to new physics, since non-SM contributions, as for instance loop-insertions, may cause significant deviations for some precisely measurable and calculable observables. At the LHeC, the greatly enlarged kinematic reach to higher mass scales in comparison to HERA [407–409] and the large targeted luminosity will enable electroweak measurements in  $ep$  scattering with higher precision than ever before.

#### 5.1.1 Electroweak effects in inclusive NC and CC DIS cross sections

Electroweak NC interactions in inclusive  $e^\pm p$  DIS are mediated by exchange of a virtual photon ( $\gamma$ ) or a  $Z$  boson in the  $t$ -channel, while CC DIS is mediated exclusively by  $W$ -boson exchange as a purely *weak* process. Inclusive NC DIS cross sections are expressed in terms of generalised structure functions  $\tilde{F}_2^\pm$ ,  $x\tilde{F}_3^\pm$  and  $\tilde{F}_L^\pm$  at EW leading order (LO) as

$$\frac{d^2\sigma^{\text{NC}}(e^\pm p)}{dx dQ^2} = \frac{2\pi\alpha^2}{xQ^4} \left[ Y_+ \tilde{F}_2^\pm(x, Q^2) \mp Y_- x\tilde{F}_3^\pm(x, Q^2) - y^2 \tilde{F}_L^\pm(x, Q^2) \right], \quad (5.1)$$

where  $\alpha$  denotes the fine structure constant. The terms  $Y_\pm = 1 \pm (1-y)^2$ , with  $y = Q^2/sx$ , describe the helicity dependence of the process. The generalised structure functions are separated into contributions from pure  $\gamma$ - and  $Z$ -exchange and their interference [94,133]:

$$\tilde{F}_2^\pm = F_2 - (g_V^e \pm P_e g_A^e) \kappa_Z F_2^{\gamma Z} + [(g_V^e g_V^e + g_A^e g_A^e) \pm 2P_e g_V^e g_A^e] \kappa_Z^2 F_2^Z, \quad (5.2)$$

$$\tilde{F}_3^\pm = -(g_A^e \pm P_e g_V^e) \kappa_Z F_3^{\gamma Z} + [2g_V^e g_A^e \pm P_e (g_V^e g_V^e + g_A^e g_A^e)] \kappa_Z^2 F_3^Z. \quad (5.3)$$

Similar expressions hold for  $\tilde{F}_L$ . In the naive quark-parton model, which corresponds to the LO QCD approximation, the structure functions are calculated as

$$[F_2, F_2^{\gamma Z}, F_2^Z] = x \sum_q [Q_q^2, 2Q_q g_V^q, g_V^q g_V^q + g_A^q g_A^q] \{q + \bar{q}\}, \quad (5.4)$$

$$x [F_3^{\gamma Z}, F_3^Z] = x \sum_q [2Q_q g_A^q, 2g_V^q g_A^q] \{q - \bar{q}\}, \quad (5.5)$$

representing two independent combinations of the quark and anti-quark momentum distributions,  $xq$  and  $x\bar{q}$ . In Eq. (5.3), the quantities  $g_V^f$  and  $g_A^f$  stand for the vector and axial-vector couplings of a fermion ( $f = e$  or  $f = q$  for electron or quark) to the  $Z$  boson, and the coefficient  $\kappa_Z$  accounts for the  $Z$ -boson propagator including the normalisation of the weak couplings. Both parameters are fully calculable from the electroweak theory. The (effective) coupling parameters depend on the electric charge,  $Q_f$  and the third component of the weak-isospin,  $I_{L,f}^3$ . Using  $\sin^2\theta_W = 1 - \frac{M_W^2}{M_Z^2}$ , one can write

$$g_V^f = \sqrt{\rho_{\text{NC},f}} (I_{L,f}^3 - 2Q_f \kappa_{\text{NC},f} \sin^2\theta_W), \quad \text{and} \quad (5.6)$$

$$g_A^f = \sqrt{\rho_{\text{NC},f}} I_{L,f}^3 \quad \text{with } f = (e, u, d). \quad (5.7)$$

3317 The parameters  $\rho_{\text{NC},f}$  and  $\kappa_{\text{NC},f}$  are calculated as real parts of complex form factors which  
 3318 include the higher-order loop corrections [410–412]. They contain non-leading flavour-specific  
 3319 components.

3320 Predictions for CC DIS are written in terms of the CC structure functions  $W_2$ ,  $xW_3$  and  $W_L$  and  
 3321 higher-order electroweak effects are collected in two form factors  $\rho_{\text{CC},e\bar{q}}$  and  $\rho_{\text{CC},e\bar{q}}$  [413, 414].

3322 In this study, the on-shell scheme is adopted for the calculation of higher-order corrections.  
 3323 This means that the independent parameters are chosen as the fine structure constant  $\alpha$  and  
 3324 the masses of the weak bosons, the Higgs boson and the fermions. The weak mixing angle is  
 3325 then fixed and  $G_F$  is a prediction, whose higher-order corrections are included in the well-known  
 3326 correction factor  $\Delta r$  [415–417] (see discussion of further contributions in Ref. [133]).

3327 The predicted single-differential inclusive NC and CC DIS cross sections for polarised  $e^-p$  scat-  
 3328 tering as a function of  $Q^2$  are displayed in Fig. 5.1. For NC DIS and at higher  $Q^2$ , electroweak  
 3329 effects are important through  $\gamma Z$  interference and pure  $Z$ -exchange terms and the polarisation  
 3330 of the LHeC electron beam of  $P_e = \pm 0.8$  will considerably alter the cross sections. For CC DIS,  
 3331 the cross section scales linearly with  $P_e$ . Two different electron beam energies are displayed in  
 3332 Fig. 5.1, and albeit the impact of a reduction from  $E_e = 60$  to  $50$  GeV appears to be small, a  
 3333 larger electron beam energy would yield higher precision for the measurement of electroweak  
 3334 parameters, since these are predominantly sensitive to the cross sections at highest scales, as  
 3335 will be shown in the following.

### 3336 5.1.2 Methodology of a combined EW and QCD fit

3337 A complete electroweak analysis of DIS data has to consider PDFs together with electroweak  
 3338 parameters [419]. In this study, the uncertainties of electroweak parameters are obtained in  
 3339 a combined fit of electroweak parameters and the PDFs, and the inclusive NC and CC DIS  
 3340 pseudodata (see Sec. 4.3.2) are explored as input data. The PDFs are parameterised with 13  
 3341 parameters at a starting scale  $Q_0^2$  and NNLO DGLAP evolution is applied [46, 47]. In this  
 3342 way, uncertainties from the PDFs are taken into account, which is very reasonable, since the  
 3343 PDFs will predominantly be determined from those LHeC data in the future. The details of

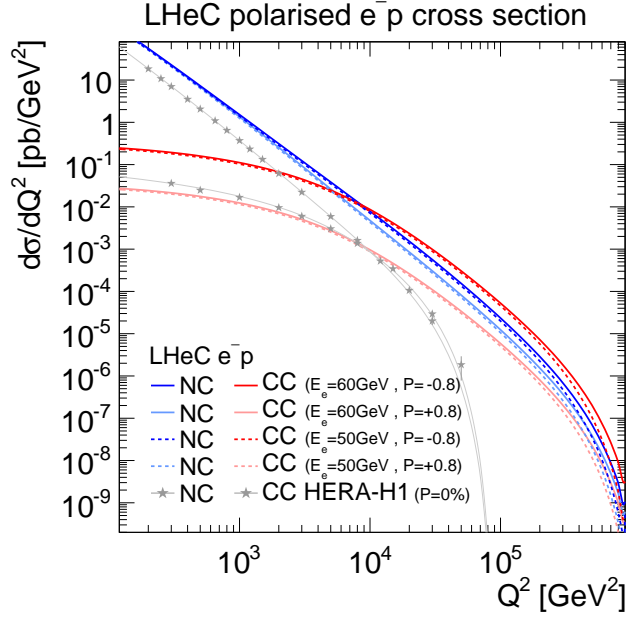


**Figure 5.1:** Single differential cross sections for polarised  $e^-p$  NC and CC DIS at LHeC for two different electron beam energies ( $E_e$ ). Cross sections for longitudinal electron beam polarisations of  $P_e = -0.8$  and  $+0.8$  are displayed. For comparison also measurements at centre-of-mass energies of  $\sqrt{s} = 920$  GeV by H1 at HERA for unpolarised ( $P_e = 0\%$ ) electron beams are displayed [418].

3344 the PDF fit are altogether fairly similar to the PDF fits outlined in Chapter. 3. Noteworthy  
 3345 differences are that additionally EW effects are included into the calculation by considering the  
 3346 full set of 1-loop electroweak corrections [420], and the  $\chi^2$  quantity [145], which is input to the  
 3347 minimisation and error propagation, is based on normal-distributed relative uncertainties. In  
 3348 this way, a dependence on the actual size of the simulated cross sections is avoided. The size of  
 3349 the pseudodata are therefore set equivalent to the predictions [421].

### 3350 5.1.3 Weak boson masses $M_W$ and $M_Z$

The expected uncertainties for a determination of the weak boson masses,  $M_W$  and  $M_Z$ , are determined in the PDF+EW-fit, where one of the masses is determined together with the PDFs, while the other mass parameter is taken as external input. The expected uncertainties for  $M_W$  are

$$\begin{aligned} \Delta M_W(\text{LHeC-60}) &= \pm 8_{(\text{exp})} \pm 5_{(\text{PDF})} \text{ MeV} = 10_{(\text{tot})} \text{ MeV} \quad \text{and} \quad (5.8) \\ \Delta M_W(\text{LHeC-50}) &= \pm 9_{(\text{exp})} \pm 8_{(\text{PDF})} \text{ MeV} = 12_{(\text{tot})} \text{ MeV} \end{aligned}$$

for LHeC with  $E_e = 60$  GeV or 50 GeV, respectively. The breakdown into experimental and PDF uncertainties is obtained by repeating the fit with PDF parameters fixed. These uncertainties are displayed in Fig. 5.2 and compared to the values obtained by LEP2 [423], Tevatron [422], ATLAS [424] and the PDG value [180]. The LHeC measurement will become the most precise measurement from one single experiment and will greatly improve over the best measurement achieved by H1, which was  $M_W(\text{H1}) = 80.520 \pm 0.115$  GeV [409]. If the dominating uncorrelated

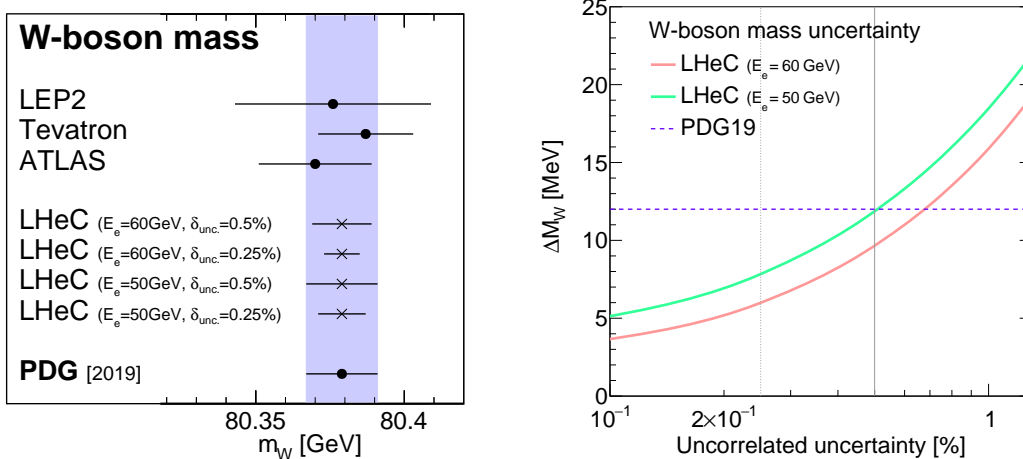


**Figure 5.2:** Left: Measurements of the  $W$ -boson mass assuming fixed values for the top-quark and  $Z$ -boson masses at the LHeC for different scenarios in comparison with today’s measurements [422–424] and the world average value (PDG19) [180]. For LHeC, prospects for  $E_e = 60$  GeV and  $50$  GeV are displayed, as well as results for the two scenarios with  $0.5\%$  or  $0.25\%$  uncorrelated uncertainty (see text). Right: Comparison of the precision for  $M_W$  for different assumptions of the uncorrelated uncertainty of the pseudodata. The uncertainty of the world average value is displayed as horizontal line. The nominal (and alternative) size of the uncorrelated uncertainty of the inclusive NC/CC DIS pseudodata is indicated by the vertical line (see text).

uncertainties can be reduced from the prospected  $0.5\%$  to  $0.25\%$ <sup>1</sup>, a precision for  $M_W$  of up to

$$\begin{aligned} \Delta M_W(\text{LHeC-60}) &= \pm 5_{(\text{exp})} \pm 3_{(\text{PDF})} \text{ MeV} = 6_{(\text{tot})} \text{ MeV} \quad \text{and} \\ \Delta M_W(\text{LHeC-50}) &= \pm 6_{(\text{exp})} \pm 6_{(\text{PDF})} \text{ MeV} = 8_{(\text{tot})} \text{ MeV} \end{aligned} \quad (5.9)$$

3351 for LHeC-60 and LHeC-50 may be achieved, respectively. A complete dependence of the expected  
3352 total experimental uncertainty  $\Delta M_W$  on the size of the uncorrelated uncertainty component is  
3353 displayed in Fig. 5.2, and with a more optimistic scenario an uncertainty of up to  $\Delta M_W \approx 5$  MeV  
3354 can be achieved. In view of such a high accuracy, it will be important to study carefully  
3355 theoretical uncertainties. For instance the parameteric uncertainty due to the dependence on  
3356 the top-quark mass of  $0.5$  GeV will yield an additional error of  $\Delta M_W = 2.5$  MeV. Also higher-  
3357 order corrections, at least the dominating 2-loop corrections in DIS will have to be studied and  
3358 kept under control. Then, the prospected determination of the  $W$ -boson mass from LHeC data  
3359 will be among the most precise determinations and significantly improve the world average value  
3360 of  $M_W$ . It will also become competitive with its prediction from global EW fits with present  
3361 uncertainties of about  $\Delta M_W = 7$  MeV [180, 425, 426].

3362 While the determination of  $M_W$  from LHeC data is competitive with other measurements, the  
3363 experimental uncertainties of a determination of  $M_Z$  are estimated to be about  $11$  MeV and  
3364  $13$  MeV for LHeC-60 and LHeC-50, respectively. Therefore, the precision of the determination  
3365 of  $M_Z$  at LHeC cannot compete with the precise measurements at the  $Z$ -pole by LEP+SLD and  
3366 future  $e^+e^-$  colliders may even improve on that.

3367 A simultaneous determination of  $M_W$  and  $M_Z$  is displayed in Fig. 5.3 (left). Although the  
3368 precision of these two mass parameters is only moderate, a meaningful test of the high-energy

<sup>1</sup>Due to performance reasons, the pseudodata are generated for a rather coarse grid. With a binning which is closely related to the resolution of the LHeC detector, much finer grids in  $x$  and  $Q^2$  are feasible. Already such a change would alter the uncertainties of the fit parameters. However, such an effect can be reflected by a changed uncorrelated uncertainty, and a value of  $0.25\%$  appears like an optimistic, but achievable, alternative scenario.

3369 behaviour of electroweak theory is obtained by using  $G_F$  as additional input: The high precision  
 3370 of the  $G_F$  measurement [427] yields a very shallow error ellipse and a precise test of the SM  
 3371 can be performed with only NC and CC DIS cross sections alone. Such a fit determines and  
 3372 simultaneously tests the high-energy behaviour of electroweak theory, while using only low-  
 3373 energy parameters  $\alpha$  and  $G_F$  as input (plus values for masses like  $M_t$  and  $M_H$  needed for loop  
 corrections).

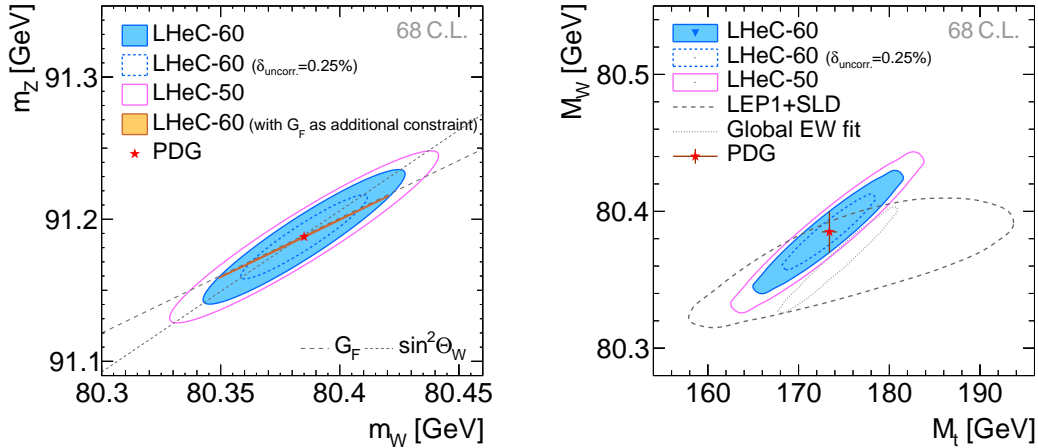


**Figure 5.3:** Simultaneous determination of the top-quark mass  $M_t$  and  $W$ -boson mass  $M_W$  from LHeC-60 or LHeC-50 data (left). Simultaneous determination of the  $W$ -boson and  $Z$ -boson masses from LHeC-60 or LHeC-50 data (right).

3374

### 3375 5.1.4 Further mass determinations

3376 Inclusive DIS data are sensitive to the top-quark mass  $M_t$  indirectly through radiative correc-  
 3377 tions.  $M_t$ -dependent terms are dominantly due to corrections from the gauge boson self-energy  
 3378 corrections. They are contained in the  $\rho$  and  $\kappa$  parameters and in the correction factor  $\Delta r$ .  
 3379 The leading contributions are proportional to  $M_t^2$ . This allows for an indirect determination  
 3380 of the top-quark mass using LHeC inclusive DIS data, and a determination of  $M_t$  will yield an  
 3381 uncertainty of  $\Delta M_t = 1.8 \text{ GeV}$  to  $2.2 \text{ GeV}$ . Assuming an uncorrelated uncertainty of the DIS  
 3382 data of 0.25 % the uncertainty of  $M_t$  becomes as small as

$$\Delta M_t = 1.1 \text{ to } 1.4 \text{ GeV} \quad (5.10)$$

3383 for 60 and 50 GeV electron beams, respectively. This would represent a very precise indirect  
 3384 determination of the top-quark mass from purely electroweak corrections and thus being fully  
 3385 complementary to measurements based on real  $t$ -quark production, which often suffer from  
 3386 sizeable QCD corrections. The precision achievable in this way will be competitive with indirect  
 3387 determinations from global EW fits after the HL-LHC [428].

3388 More generally, and to some extent depending on the choice of the renormalisation scheme, the  
 3389 leading self-energy corrections are proportional to  $\frac{M_t^2}{M_W^2}$  and thus a simultaneous determination  
 3390 of  $M_t$  and  $M_W$  is desirable. The prospects for a simultaneous determination of  $M_t$  and  $M_W$  is  
 3391 displayed in Fig. 5.3 (right). It is remarkable that the precision of the LHeC is superior to that of  
 3392 the LEP+SLD combination [429]. In an optimistic scenario an uncertainty similar to the global  
 3393 electroweak fit [426] can be achieved. In a fit without PDF parameters similar uncertainties

3394 are found (not shown), which illustrates that the determination of EW parameters is to a large  
 3395 extent independent of the QCD phenomenology and the PDFs.

3396 The subleading contributions to self-energy corrections have a Higgs-boson mass dependence  
 3397 and are proportional to  $\log \frac{M_H^2}{M_W^2}$ . When fixing all other EW parameters the Higgs boson mass  
 3398 could be constrained indirectly through these loop corrections with an experimental uncertainty  
 3399 of  $\Delta m_H = {}^{+29}_{-23}$  to  ${}^{+24}_{-20}$  GeV for different LHeC scenarios, which is again similar to the indirect  
 3400 constraints from a global electroweak fit [426], but not competitive with direct measurements.

### 3401 5.1.5 Weak Neutral Current Couplings

3402 The vector and axial-vector couplings of up-type and down-type quarks to the  $Z$ ,  $g_V^q$  and  $g_A^q$ ,  
 see Eq. (5.7), are determined in a fit of the four coupling parameters together with the PDFs.

Coupling parameter	PDG value	Expected uncertainties		
		LHeC-60	LHeC-60 ( $\delta_{\text{uncor.}}=0.25\%$ )	LHeC-50
$g_A^u$	0.50 ${}^{+0.04}_{-0.05}$	0.0022	0.0015	0.0035
$g_A^d$	-0.514 ${}^{+0.050}_{-0.029}$	0.0055	0.0034	0.0083
$g_V^u$	0.18 $\pm 0.05$	0.0015	0.0010	0.0028
$g_V^d$	-0.35 ${}^{+0.05}_{-0.06}$	0.0046	0.0027	0.0067

**Table 5.1:** Light-quark weak NC couplings ( $g_A^u, g_A^d, g_V^u, g_V^d$ ) and their currently most precise values from the PDG [180] compared with the prospected uncertainties for different LHeC scenarios. The LHeC prospects are obtained in a simultaneous fit of the PDF parameters and all four coupling parameters determined at a time.

3403

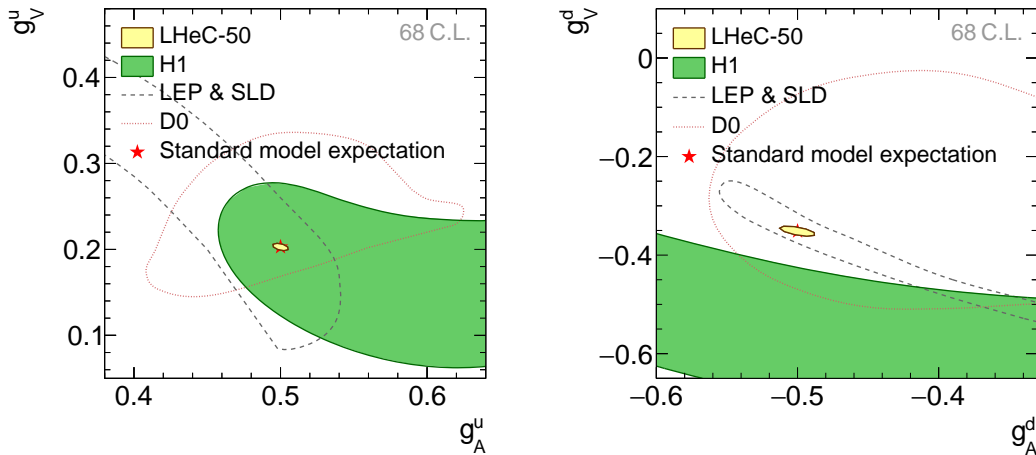


**Figure 5.4:** Weak NC vector and axial-vector couplings of  $u$ -type (left) and  $d$ -type quarks (right) at 68 % confidence level (C.L.) for simulated LHeC data with  $E_e = 50$  GeV. The LHeC expectation is compared with results from the combined LEP+SLD experiments [429], a single measurement from D0 [430] and one from H1 [409]. The standard model expectations are displayed by a red star, partially hidden by the LHeC prospects.

3404 The resulting uncertainties are collected in Tab. 5.1. The two-dimensional uncertainty contours  
 3405 at 68 % confidence level obtained from LHeC data with  $E_e = 50$  GeV are displayed in Fig. 5.4  
 3406 for the two quark families and compared with available measurements. While all the current  
 3407 determinations from  $e^+e^-$ ,  $ep$  or  $p\bar{p}$  data have a similar precision, the future LHeC data will



3408 greatly improve the precision of the weak neutral-current couplings and expected uncertainties  
 3409 are an order of magnitude smaller than the currently most precise ones [180]. An increased  
 3410 electron beam energy of  $E_e = 60$  GeV or improved experimental uncertainties would further  
 3411 improve this measurement.

3412 The determination of the couplings of the electron to the  $Z$  boson,  $g_V^e$  and  $g_A^e$ , can be determined  
 3413 at the LHeC with uncertainties of up to  $\Delta g_V^e = 0.0013$  and  $\Delta g_A^e = \pm 0.0009$ , which is similar  
 3414 to the results of a single LEP experiment and about a factor three larger than the LEP+SLD  
 3415 combination [429].

### 3416 5.1.6 The neutral-current $\rho_{\text{NC}}$ and $\kappa_{\text{NC}}$ parameters

3417 Beyond Born approximation, the weak couplings are subject to higher-order loop corrections.  
 3418 These corrections are commonly parameterised by quantities called  $\rho_{\text{NC}}$ ,  $\kappa_{\text{NC}}$  and  $\rho_{\text{CC}}$ . They are  
 3419 sensitive to contributions beyond the SM and the structure of the Higgs sector. It is important  
 3420 to keep in mind that these effective coupling parameters depend on the momentum transfer  
 3421 and are, indeed, form factors rather than constants. It is particularly interesting to investigate  
 3422 the so-called effective weak mixing angle defined as  $\sin^2\theta_W^{\text{eff}} = \kappa_{\text{NC}}\sin^2\theta_W$ . At the  $Z$ -pole it  
 3423 is well accessible through asymmetry measurements in  $e^+e^-$  collisions. In DIS at the LHeC,  
 3424 the scale dependence of the effective weak mixing angle is not negligible. It can be determined  
 3425 only together with the  $\rho$  parameter due to the  $Q^2$  dependence and the presence of the photon  
 3426 exchange terms. Therefore, we introduce (multiplicative) anomalous contributions to these  
 3427 factors, denoted as  $\rho'_{\text{NC,CC}}$  and  $\kappa'_{\text{NC}}$ , and test their agreement with unity (for more details see  
 3428 Ref. [409]), and uncertainties of these parameters are obtained in a fit together with the PDFs.  
 The two-dimensional uncertainty contours of the anomalous form factors  $\rho'_{\text{NC},f}$  and  $\kappa'_{\text{NC},f}$  are

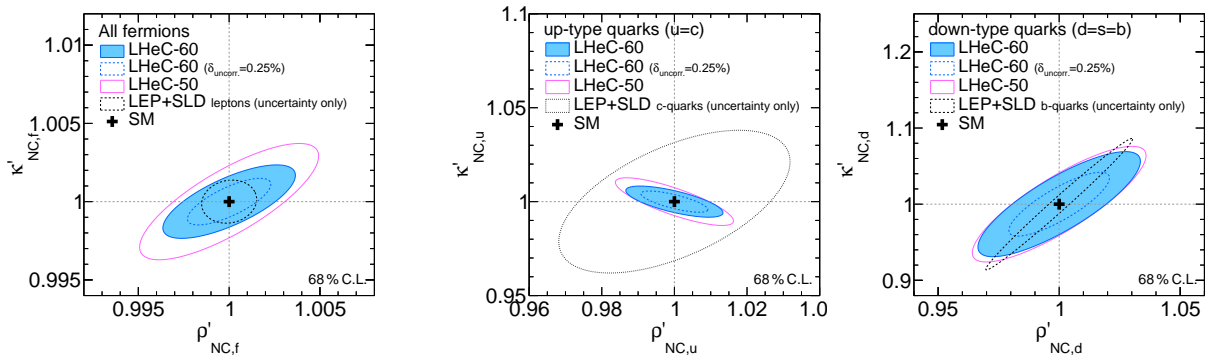


**Figure 5.5:** Expectations at 68% confidence level for the determination of the  $\rho'_{\text{NC}}$  and  $\kappa'_{\text{NC}}$  parameters assuming a single anomalous factor equal for all fermions (left). The results for three different LHeC scenarios are compared with the achieved uncertainties from the LEP+SLD combination [429] for the determination the respective leptonic quantities. Right: uncertainties for the simultaneous determination of the anomalous form factors for  $u$  and  $d$ -type quarks, assuming known values for the electron parameters. The values are compared with uncertainties reported by LEP+SLD for the determination of the values  $\rho_{\text{NC},(c,b)}$  and  $\sin^2\theta_W^{\text{eff},(c,b)}$  for charm or bottom quarks, respectively.

3429 displayed for three different LHeC scenarios in Fig. 5.5 (left), and compared with uncertainties  
 3430 from the LEP+SLD combination <sup>2</sup> [429]. It is found that these parameters can be determined  
 3431

<sup>2</sup>Since in the LEP+SLD analysis the values of  $\rho_{\text{NC}}$  and  $\kappa_{\text{NC}}\sin^2\theta_W$  are determined, we compare only the size of the uncertainties in these figures. Furthermore it shall be noted, that LEP is mainly sensitive to the parameters of leptons or heavy quarks, while LHeC data is more sensitive to light quarks ( $u, d, s$ ), and thus the LHeC measurements are highly complementary.

3432 with very high experimental precision.

3433 Assuming the couplings of the electron are given by the SM, the anomalous form factors for  
 3434 the two quark families can be determined and results are displayed in Fig. 5.5 (right). Since  
 3435 these measurements represent unique determinations of parameters sensitive to the light-quark  
 3436 couplings, we can compare only with nowadays measurements of the parameters for heavy-quarks  
 3437 of the same charge and it is found that the LHeC will provide high-precision determinations of  
 3438 the  $\rho'_{\text{NC}}$  and  $\kappa'_{\text{NC}}$  parameters.

3439 A meaningful test of the SM can be performed by determining the effective coupling parameters  
 3440 as a function of the momentum transfer. In case of  $\kappa'_{\text{NC}}$ , this is equivalent to measuring the  
 3441 running of the effective weak mixing angle,  $\sin^2 \theta_{\text{W}}^{\text{eff}}(\mu)$  (see also Sec. 5.1.7). However, DIS is quite  
 3442 complementary to other measurements since the process is mediated by space-like momentum  
 3443 transfer, i.e.  $q^2 = -Q^2 < 0$  with  $q$  being the boson four-momentum. Prospects for a determi-  
 3444 nation of  $\rho'_{\text{NC}}$  or  $\kappa'_{\text{NC}}$  at different  $Q^2$  values are displayed in Fig. 5.6 and compared to results  
 obtained by H1. The value of  $\kappa'_{\text{NC}}(\mu)$  can be easily translated to a measurement of  $\sin^2 \theta_{\text{W}}^{\text{eff}}(\mu)$ .

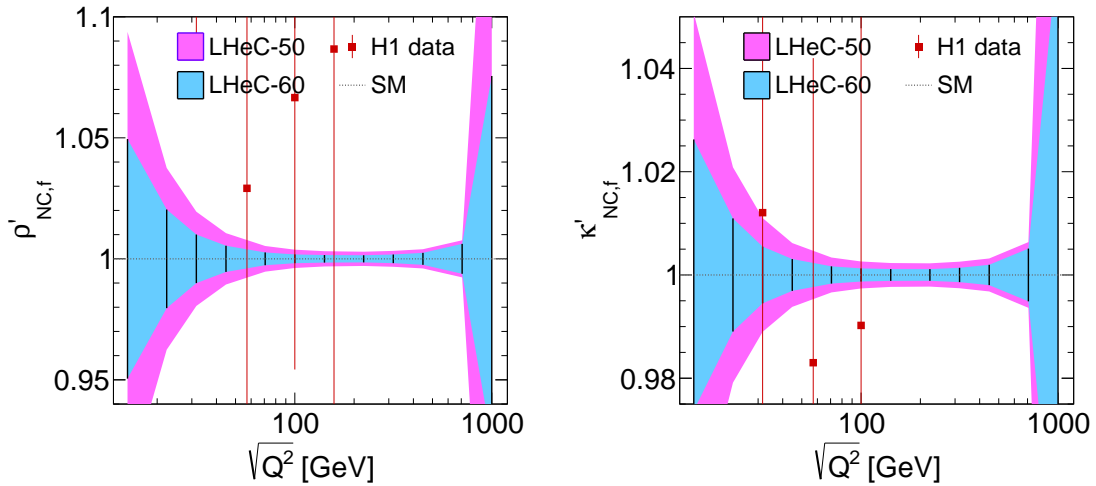


**Figure 5.6:** Test of the scale dependence of the anomalous  $\rho$  and  $\kappa$  parameters for two different LHeC scenarios. For the case of LHeC-60, i.e.  $E_e = 60$  GeV, we assume an uncorrelated uncertainty of 0.25%. The uncertainties of the parameter  $\kappa'_{\text{NC},f}$  can be interpreted as sensitivity to the scale-dependence of the weak mixing angle,  $\sin^2 \theta_{\text{W}}^{\text{eff}}(\mu)$ .

3445

3446 From Fig. 5.6 one can conclude that this quantity can be determined with a precision of up to  
 3447 0.1% and better than 1% over a wide kinematic range of about  $25 < \sqrt{Q^2} < 700$  GeV.

### 3448 5.1.7 The effective weak mixing angle $\sin^2 \theta_{\text{W}}^{\text{eff},\ell}$

3449 The leptonic effective weak mixing angle is defined as  $\sin^2 \theta_{\text{W}}^{\text{eff},\ell}(\mu^2) = \kappa_{\text{NC},\ell}(\mu^2) \sin^2 \theta_{\text{W}}$ . Due to  
 3450 its high sensitivity to loop corrections it represents an ideal quantity for precision tests of the  
 3451 Standard Model. Its value is scheme dependent and it exhibits a scale dependence. Near the  
 3452  $Z$  pole,  $\mu^2 = M_Z^2$ , its value was precisely measured at LEP and at SLD. Those analyses were  
 3453 based on the measurement of asymmetries and their interpretation in terms of the leptonic weak  
 3454 mixing angle was simplified by the fact that many non-leptonic corrections and contributions  
 3455 from box graphs cancel or can be taken into account by subtracting their SM predictions. The  
 3456 highest sensitivity to  $\sin^2 \theta_{\text{W}}^{\text{eff},\ell}(M_Z)$  to date arises from a measurement of  $A_{\text{fb}}^{0,b}$  [429], where  
 3457 the non-universal flavour-specific corrections to the quark couplings are taken from the SM

3458 and consequently these measurements are interpreted to be sensitive only to the universal, i.e.  
 3459 flavour-independent <sup>3</sup>, non-SM contributions to  $\kappa_{\text{NC}}$ . Applying this assumption also to the DIS  
 3460 cross sections, the determination of  $\kappa'_{\text{NC},f}$  can directly be interpreted as a sensitivity study of  
 3461 the leptonic effective weak mixing angle  $\sin^2 \theta_{\text{W}}^{\text{eff},\ell}$ .

Fit parameters	Parameter of interest	SM value	Expected uncertainties			
			LHeC-50 ( $\delta_{\text{uncor.}} = 0.50\%$ )	LHeC-60	LHeC-50 ( $\delta_{\text{uncor.}} = 0.25\%$ )	LHeC-60
$\kappa'_{\text{NC},f}$ , PDFs	$\sin^2 \theta_{\text{W}}^{\text{eff},\ell}(M_Z^2)$	0.23154	0.00033	0.00025	0.00022	0.00015
$\kappa'_{\text{NC},f}, \rho'_{\text{NC},f}$ , PDFs	$\sin^2 \theta_{\text{W}}^{\text{eff},\ell}(M_Z^2)$	0.23154	0.00071	0.00036	0.00056	0.00023
$\kappa'_{\text{NC},e}$ , PDFs	$\sin^2 \theta_{\text{W}}^{\text{eff},e}(M_Z^2)$	0.23154	0.00059	0.00047	0.00038	0.00028
$\kappa'_{\text{NC},e}, \kappa'_{\text{NC},u}, \kappa'_{\text{NC},d}$ , PDFs	$\sin^2 \theta_{\text{W}}^{\text{eff},e}(M_Z^2)$	0.23154	0.00111	0.00095	0.00069	0.00056
$\kappa'_{\text{NC},f}$	$\sin^2 \theta_{\text{W}}^{\text{eff},\ell}(M_Z^2)$	0.23154	0.00028	0.00023	0.00017	0.00014

**Table 5.2:** Determination of  $\sin^2 \theta_{\text{W}}^{\text{eff},\ell}(M_Z^2)$  with inclusive DIS data at the LHeC for different scenarios. Since the value of the effective weak mixing angle at the  $Z$  pole cannot be determined directly in DIS, a fit of the  $\kappa'_{\text{NC},f}$  parameter is performed instead and its uncertainty is translated to  $\sin^2 \theta_{\text{W}}^{\text{eff},\ell}(M_Z^2)$ . Different assumptions on the fit parameters are studied, and results include uncertainties from the PDFs. Only the last line shows results where the PDF parameters are kept fixed. See text for more details.

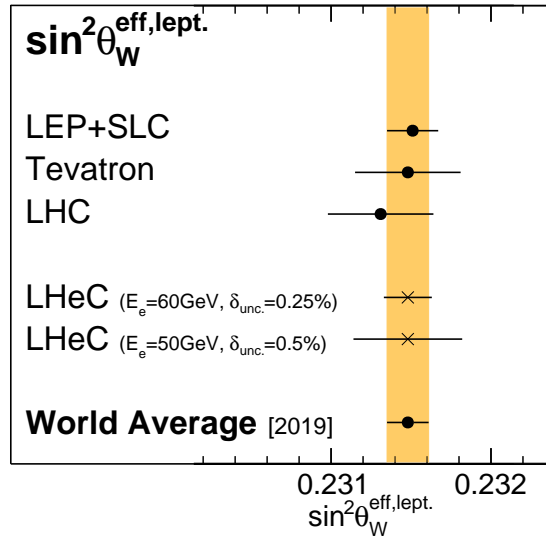


**Figure 5.7:** Comparison of the determination of  $\sin^2 \theta_{\text{W}}^{\text{eff},\ell}(M_Z^2)$  from LHeC inclusive DIS data with recent averaged values. Results from LEP+SLC [429], Tevatron [431], LHC [432–435] and the world average value [435] are all obtained from a combination of various separate measurements (not shown individually) (see also Ref. [436] for additional discussions). For LHeC, the experimental and PDF uncertainties are displayed.

3462 The prospects for a determination of  $\sin^2 \theta_{\text{W}}^{\text{eff},\ell}$  are listed in Tab. 5.2. Two fits have been studied:  
 3463 one with a fixed parameter  $\rho'_{\text{NC}}$  and one where  $\sin^2 \theta_{\text{W}}^{\text{eff},\ell}$  is determined together with  $\rho'_{\text{NC}}$  (see  
 3464 Fig. 5.5 (left)). At the LHeC, it will be possible to determine the value of  $\sin^2 \theta_{\text{W}}^{\text{eff},\ell}(M_Z^2)$  with  
 3465 an experimental uncertainty of up to

$$\Delta \sin^2 \theta_{\text{W}}^{\text{eff},\ell} = \pm 0.00015, \quad (5.11)$$

<sup>3</sup>Flavour-specific tests have been discussed to some extent in the previous Section.

3466 where PDF uncertainties are already included. If the PDF parameters are artificially kept fixed,  
 3467 the uncertainties are of very similar size, which demonstrates that these measurements are fairly  
 3468 insensitive to the QCD effects and the PDFs. The uncertainties are compared <sup>4</sup> to recent average  
 3469 values in Fig. 5.7. One can see that the LHeC measurement has the potential to become the  
 3470 most precise single measurement in the future with a significant impact to the world average  
 3471 value. It is obvious that a conclusive interpretation of experimental results with such a high  
 3472 precision will require correspondingly precise theoretical predictions, and the investigation of  
 3473 two-loop corrections for DIS will become important.

3474 This LHeC measurement will become competitive with measurements at the HL-LHC [184].  
 3475 Since in  $pp$  collisions one of the dominant uncertainties is from the PDFs [433, 434, 437–439],  
 3476 future improvements can (only) be achieved with a common analysis of LHeC and HL-LHC  
 3477 data. Such a study will yield highest experimental precision and the challenging theoretical  
 3478 and experimental aspects for a complete understanding of such an analysis will deepen our  
 3479 understanding of the electroweak sector.

3480 It may be further of interest, to determine the value of the effective weak mixing angle of the  
 3481 electron separately in order to compare with measurements in  $pp$  and test furthermore lepton-  
 3482 specific contributions to  $\kappa_{\text{NC,lept.}}$ . Such fits are summarised in Table 5.2 and a reasonable  
 3483 precision is achieved with LHeC.

### 3484 5.1.8 Electroweak effects in charged-current scattering

3485 The charged-current sector of the SM can be uniquely measured at high scales over many orders  
 3486 of magnitude in  $Q^2$  at the LHeC, due to the excellent tracking detectors, calorimetry, and high-  
 3487 bandwidth triggers. Similarly as in the NC case, the form factors of the effective couplings of  
 3488 the fermions to the  $W$  boson can be measured. In the SM formalism, only two of these form  
 3489 factors are present,  $\rho_{CC,eq}$  and  $\rho_{CC,e\bar{q}}$ . We thus introduce two anomalous modifications to them,  
 3490  $\rho_{CC,(eq/e\bar{q})} \rightarrow \rho'_{CC,(eq/e\bar{q})}\rho_{CC,(eq/e\bar{q})}$  (see Ref. [409]). The prospects for the determination of these  
 3491 parameters are displayed in Fig. 5.8, and it is found, that with the LHeC these parameters can  
 3492 be determined with a precision up to 0.2–0.3%. Also their  $Q^2$  dependence can be uniquely  
 3493 studied with high precision up to  $\sqrt{Q^2}$  values of about 400 GeV.

### 3494 5.1.9 Conclusion

3495 With LHeC inclusive NC and CC DIS data, unique measurements of electroweak parameters can  
 3496 be performed with highest precision. Since inclusive DIS is mediated through space-like momen-  
 3497 tum transfer ( $t$ -channel exchange) the results are often complementary to other experiments,  
 3498 such as  $pp$  or  $e^+e^-$  collider experiments, where measurements are performed in the time-like  
 3499 regime and most often at the  $Z$  peak. Among many other quantities, measurements of the weak  
 3500 couplings of the light quarks,  $u$  and  $d$ , or their anomalous form factors  $\rho'_{\text{NC},u/d}$  and  $\kappa'_{\text{NC},u/d}$ ,  
 3501 can be performed uniquely due to the important contributions of valence quarks in the initial  
 3502 state. Also scale dependent measurements of weak interactions can be performed over a large  
 3503 range in  $\sqrt{Q^2}$ , which provides an interesting portal to BSM physics. The  $W$  boson mass can be  
 3504 determined with very small experimental uncertainties, such that theoretical uncertainties are  
 3505 expected to become more important than experimental uncertainties. While the parameters of

---

<sup>4</sup>It shall be noted, that in order to compare the LHeC measurements with the  $Z$ -pole measurements at  $\mu^2 = M_Z^2$  in a conclusive way, one has to assume the validity of the SM framework. In particular the scale-dependence of  $\kappa_{\text{NC},\ell}$  must be known in addition to the flavour-specific corrections. On the other hand, the scale dependence can be tested itself with the LHeC data which cover a large range of space-like  $Q^2$ . In this aspect, DIS provides a unique opportunity for precision measurements in the space-like regime ( $\mu^2 < 0$ ) as has been discussed in the previous Section, see Fig. 5.6 (right).

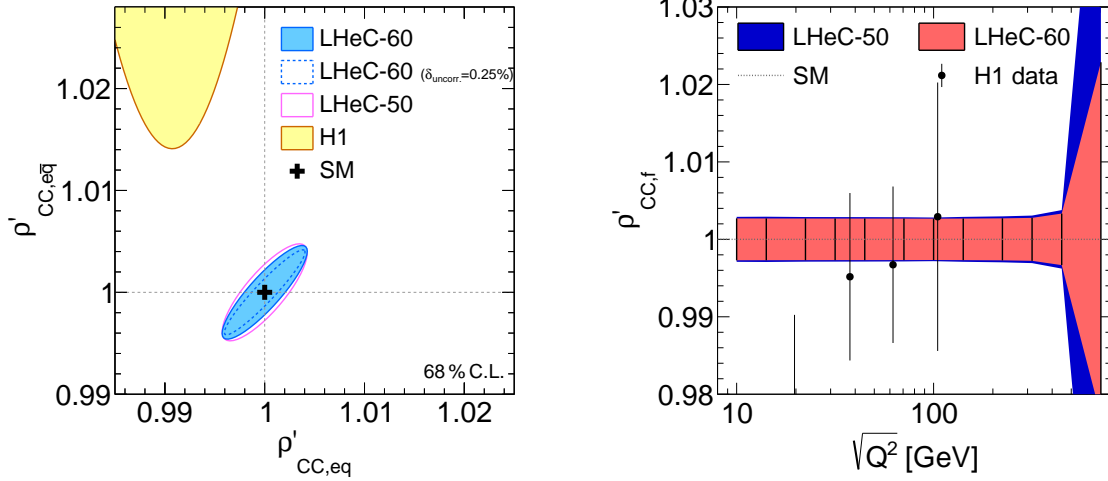


**Figure 5.8:** Left: anomalous modifications of the charged current form factors  $\rho'_{CC,eq}$  and  $\rho'_{CC,e\bar{q}}$  for different LHeC scenarios in comparison with the H1 measurement [409]. Right: scale dependent measurement of the anomalous modification of the charged current form factor  $\rho'_{CC}(Q^2)$ , assuming  $\rho'_{CC,eq} = \rho'_{CC,e\bar{q}} = \rho'_{CC}$ .

3506 the PDFs are determined together with the EW parameters in the present study, it is found  
 3507 that the PDFs do not induce a limitation of the uncertainties. Considering the dominating  
 3508 top-quark mass dependence of higher-order electroweak effects, one can realise that the LHeC  
 3509 will be competitive with the global electroweak fit after the HL-LHC era [184, 428].

3510 Besides proving its own remarkable prospect on high-precision electroweak physics, the LHeC  
 3511 will further significantly improve the electroweak measurements in  $pp$  collisions at the LHC by  
 3512 reducing the presently sizeable influence of PDF and  $\alpha_s$  uncertainties. This is discussed in Sec. 9.

## 3513 5.2 Direct $W$ and $Z$ Production and Anomalous Triple Gauge 3514 Couplings

### 3515 5.2.1 Direct $W$ and $Z$ Production

3516 The direct production of single  $W$  and  $Z$  bosons as a crucial signal represents an important  
 3517 channel for EW precision measurements. The production of  $W$  bosons has been measured at  
 3518  $\sqrt{s} \simeq 320$  GeV at HERA [440–442]. With the full  $e^\pm p$  data set collected by the H1 and ZEUS  
 3519 experiments together, corresponding to an integrated luminosity of about  $\mathcal{L} \sim 1 \text{ fb}^{-1}$ , a few  
 3520 dozens of  $W$  boson event candidates have been identified in the  $e$ ,  $\mu$  or  $\tau$  decay channel.

3521 Detailed studies of direct  $W/Z$  production in  $ep$  collisions at higher centre-of-mass energies have  
 3522 been presented in the past, see Refs. [443–445]. These theoretical studies were performed for  
 3523 a proton beam energy of  $E_p = 8$  TeV and electron beam energies of  $E_e = 55$  GeV or 100 GeV,  
 3524 which correspond to a very similar centre-of-mass energy as the LHeC. Measurements at the  
 3525 LHeC will benefit considerably from the large integrated luminosity, in comparison to earlier  
 3526 projections.

3527 The  $W$  or  $Z$  direct production in  $e^-p$  collisions can be classified into five processes

$$\begin{aligned}
 e^-p &\rightarrow e^-W^+j, & e^-p &\rightarrow e^-W^-j, \\
 e^-p &\rightarrow \nu_e^-W^-j, & e^-p &\rightarrow \nu_e^-Zj
 \end{aligned}
 \tag{5.12}$$

3528 and

$$e^- p \rightarrow e^- Z j, \quad (5.13)$$

3529 where  $j$  denotes the hadronic the final state (i.e. the *forward jet*). According to the above  
 3530 classification, the four processes in Eq.(5.12) can be used to study Tripe Gauge Couplings  
 3531 (TGCs), e.g.  $WW\gamma$  and  $WWZ$  couplings, since some contributing diagrams represent Vector  
 3532 Boson Fusion (VBF) processes. The process shown in Eq.(5.13) does not contain any TGC  
 3533 vertex. The processes for positron-proton collisions can be easily derived from Eqs. (5.12)  
 3534 and (5.13), but are not discussed further here due to the small integrated luminosity of the  
 3535 LHeC  $e^+p$  data.

3536 The MadGraph5\_v2.4.2 program [361] is employed for matrix element calculation and event gen-  
 3537 eration and the PDF NNPDF23\_nlo.as\_0119\_qed [446] is used. Technical cuts on the transverse  
 3538 momentum of the outgoing scattered lepton,  $p_T^\ell$ , of 10 GeV or alternatively 5 GeV, are imposed  
 3539 and other basic cuts are  $p_T^j > 20$  GeV,  $|\eta_{e,j}| < 5$  and  $\Delta R_{ej} < 0.4$ . The resulting Standard Model  
 total cross sections of the above processes are listed in Tab. 5.3.

Process	$E_e = 50$ GeV, $E_p = 7$ TeV $p_T^e > 10$ GeV	$E_e = 60$ GeV, $E_p = 7$ TeV $p_T^e > 10$ GeV	$E_e = 60$ GeV, $E_p = 7$ TeV $p_T^e > 5$ GeV
$e^- W^+ j$	1.00 pb	1.18 pb	1.60 pb
$e^- W^- j$	0.930 pb	1.11 pb	1.41 pb
$\nu_e^- W^- j$	0.796 pb	0.956 pb	0.956 pb
$\nu_e^- Z j$	0.412 pb	0.502 pb	0.502 pb
$e^- Z j$	0.177 pb	0.204 pb	0.242 pb

**Table 5.3:** The SM predictions of direct  $W$  and  $Z$  production cross sections in  $e^-p$  collisions for different collider beam energy options,  $E_e$ , and final state forward electron transverse momentum cut,  $p_T^e$ . Two different electron beam energy options are considered,  $E_e = 50$  GeV and 60 GeV.

3540

3541 The process with the largest production cross section in  $e^-p$  scattering is the single  $W^+$  boson  
 3542 production. This will be the optimal channel of both the SM measurement and new physics  
 3543 probes in the EW sector. Also, this channel is experimentally preferred since the  $W^+$  is produced  
 3544 in NC scattering, so the beam electron is measured in the detector, and the  $W$ -boson has opposite  
 3545 charge to the beam lepton and thus in a leptonic decay an opposite charge lepton and missing  
 3546 transverse momentum is observed. Altogether, it is expected that a few million of direct  $W$ -  
 3547 boson events are measured at LHeC.

3548 Several  $10^5$  direct  $Z$  events are measured, which corresponds approximately to the size of the  
 3549 event sample of the SLD experiment [429], but at the LHeC these  $Z$  bosons are predominantly  
 3550 produced in VBF events.

3551 All these total cross sections increase significantly with smaller transverse momentum of the  
 3552 outgoing scattered lepton. Therefore it will become important to decrease that threshold with  
 3553 dedicated electron taggers, see Chapter 12.

## 3554 5.2.2 Anomalous Triple Gauge Couplings

3555 The measurement of gauge boson production processes provides a precise measurement of the  
 3556 triple gauge boson vertex. The measurement is sensitive to new physics contributions in *anoma-*  
 3557 *lous* Triple Gauge Couplings (aTGC). The LHeC has advantages of a higher centre-of-mass  
 3558 energy and easier kinematic analysis in the measurement of aTGCs.

3559 In the effective field theory language, aTGCs in the Lagrangian are generally parameterised as

$$\begin{aligned}
\mathcal{L}_{TGC}/g_{WWV} &= ig_{1,V}(W_{\mu\nu}^+W_{\mu}^-V_{\nu} - W_{\mu\nu}^-W_{\mu}^+V_{\nu}) + i\kappa_V W_{\mu}^+W_{\nu}^-V_{\mu\nu} + \frac{i\lambda_V}{M_W^2}W_{\mu\nu}^+W_{\nu\rho}^-V_{\rho\mu} \\
&+ g_5^V \epsilon_{\mu\nu\rho\sigma}(W_{\mu}^+\overleftrightarrow{\partial}_{\rho}W_{\nu}^-)V_{\sigma} - g_4^V W_{\mu}^+W_{\nu}^-(\partial_{\mu}V_{\nu} + \partial_{\nu}V_{\mu}) \\
&+ i\tilde{\kappa}_V W_{\mu}^+W_{\nu}^-\tilde{V}_{\mu\nu} + \frac{i\tilde{\lambda}_V}{M_W^2}W_{\lambda\mu}^+W_{\mu\nu}^-\tilde{V}_{\nu\lambda},
\end{aligned} \tag{5.14}$$

3560 where  $V = \gamma, Z$ . The gauge couplings  $g_{WW\gamma} = -e$ ,  $g_{WWZ} = -e \cot \theta_W$  and the weak mixing  
3561 angle  $\theta_W$  are from the SM.  $\tilde{V}_{\mu\nu}$  and  $A \overleftrightarrow{\partial}_{\mu} B$  are defined as  $\tilde{V}_{\mu\nu} = \frac{1}{2}\epsilon_{\mu\nu\rho\sigma}V_{\rho\sigma}$ ,  $A \overleftrightarrow{\partial}_{\mu} B = A(\partial_{\mu}B) -$   
3562  $(\partial_{\mu}A)B$ , respectively. There are five aTGCs ( $g_{1,Z}$ ,  $\kappa_V$ , and  $\lambda_V$ ) conserving the  $C$  and  $CP$   
3563 condition with electromagnetic gauge symmetry requires  $g_{1,\gamma} = 1$ . Only three of them are  
3564 independent because  $\lambda_Z = \lambda_{\gamma}$  and  $\Delta\kappa_Z = \Delta\kappa_{\gamma} - \tan^2 \theta_W \Delta\kappa_{\gamma}$  [447–449]. The LHeC can set  
3565 future constraints on  $\Delta\kappa_{\gamma}$  and  $\lambda_{\gamma}$ .

3566 In the direct  $Z/\gamma$  production process, the anomalous  $WWZ$  and  $WW\gamma$  couplings can be sep-  
3567 arately measured without being influenced by their interference [450, 451]. In the direct  $W$   
3568 production process, both the deviation in signal cross section and the kinematic distributions  
3569 can effectively constrain the  $WW\gamma$  aTGC, while anomalous  $WWZ$  contribution in this channel  
3570 is insensitive as a result of the suppression from  $Z$  boson mass [452–454].

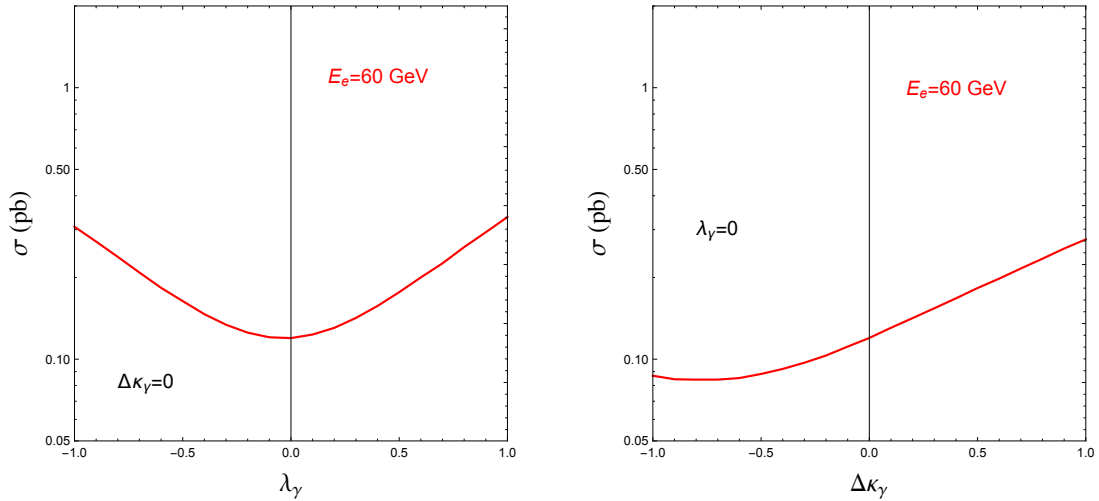


**Figure 5.9:** Total cross sections of the  $e^- p \rightarrow e^- \mu^+ \nu_{\mu} j$  process with varying  $\lambda_{\gamma}$  (left plot) and  $\Delta\kappa_{\gamma}$  (right plot).

3571 The  $W$  decay into muon channel is the expected optimal measurement for the anomalous  $WW\gamma$   
3572 coupling because of the discrimination of final states and mistagging efficiencies [452]. Fig. 5.9  
3573 shows the cross section of single  $W^+$  production process followed by  $W^+ \rightarrow \mu^+ \nu_{\mu}$  decay, with  
3574 different  $\lambda_{\gamma}$  and  $\Delta\kappa_{\gamma}$  values. Large anomalous coupling leads to measurable deviation to the  
3575 SM prediction. The cross section increases monotonically with  $\Delta\kappa_{\gamma}$  and the absolute value of  
3576  $\lambda_{\gamma}$  within the region of  $-1.0 \leq \lambda_{\gamma}/\Delta\kappa_{\gamma} \leq 1.0$ .

3577 Kinematic analysis is necessary for the precise aTGC measurement. At LHeC, the  $e^- p \rightarrow$   
3578  $e^- W^{\pm} j$  process with leptonic  $W$  boson decay can be fully reconstructed because the unde-  
3579 tected neutrino information is reconstructed either with energy-momentum conservation or the  
3580 recoil mass method. This allows to use angular correlation observables, which are sensitive to  
3581 the  $W$  boson polarization. Helicity amplitude calculation indicates that a non-SM value of  $\lambda_{\gamma}$

3582 leads to a significant enhancement in the transverse polarization fraction of the  $W$  boson in the  
 3583  $e^-p \rightarrow e^-W^+j$  process, while a non-SM value of  $\Delta\kappa_\gamma$  leads to enhancement in the longitudinal  
 3584 component fraction [443]. The angle  $\theta_{\ell W}$  is defined as the angle between the decay product  
 3585 lepton  $\ell$  in the  $W$  rest frame and  $W$  moving direction in the collision rest frame. Making use  
 3586 of the energetic final states in the forward direction, a second useful angle  $\Delta\phi_{ej}$  is defined as  
 3587 the separation of final state jet and electron on the azimuthal plane. In an optimised analysis,  
 3588 assuming an integrated luminosity of  $1 \text{ ab}^{-1}$ , the observable  $\Delta\phi_{ej}$  can impose stringent con-  
 3589 straints on both  $\lambda_\gamma$  and  $\Delta\kappa_\gamma$ , and uncertainties within  $[-0.007, 0.0056]$  and  $[-0.0043, 0.0054]$   
 3590 are achieved, respectively. The  $\cos\theta_{\mu W}$  observable is also sensitive to  $\Delta\kappa_\gamma$  at the same order,  
 3591 but fails to constrain  $\lambda_\gamma$ . The analysis is described in detail in Ref. [452].

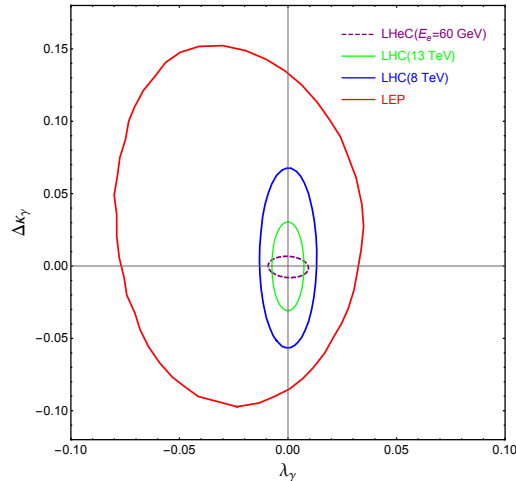


**Figure 5.10:** The 95% C.L. exclusion limit on the  $\Delta\kappa_\gamma$ - $\lambda_\gamma$  plane. The purple dashed contour is the projected LHeC exclusion limit with  $1 \text{ ab}^{-1}$  integrated luminosity [452]. The blue, green and red contours are current bounds from LHC [455, 456] and LEP [457].

3592 Fig. 5.10 shows the two-parameter aTGC constraint on the  $\lambda_\gamma$ - $\Delta\kappa_\gamma$  plane based on a  $\chi^2$  analysis  
 3593 of  $\Delta\phi_{ej}$  at parton-level and assuming an electron beam energy of  $E_e = 60 \text{ GeV}$ . When comparing  
 3594 with the current LHC (blue and green) and LEP (red) bounds, the LHeC has the potential  
 3595 to significantly improve the constraints, in particular on the  $\Delta\kappa_\gamma$  parameter. The polarised  
 3596 electron beam is found to improve the aTGC measurement [451, 454]. In consideration of the  
 3597 *realistic* analysis at detector level, one expects  $2\text{-}3 \text{ ab}^{-1}$  integrated luminosity to achieve same  
 3598 results [452].

3599 One uncertainty in the aTGC measurement at the (HL-)LHC comes from the PDF uncertainty.  
 3600 Future LHeC PDF measurement will improve the precision of aTGC measurement in the  $x \simeq$   
 3601  $\mathcal{O}(10^{-2})$  region.

### 3602 5.3 Top Quark Physics

3603 SM top quark production at a future ep collider is dominated by single top quark production,  
 3604 mainly via CC DIS production. An example graph is shown in Fig. 5.11 (left). The total cross  
 3605 section is  $1.89 \text{ pb}$  at the LHeC [458] and with an electron beam energy of  $60 \text{ GeV}$ , and an LHC  
 3606 proton beam of  $7 \text{ TeV}$ , leading to a centre-of-mass energy of  $1.3 \text{ TeV}$ , respectively. The other  
 3607 important top quark production mode is  $t\bar{t}$  photoproduction with a total cross section of  $0.05 \text{ pb}$   
 3608 at the LHeC [459]. An example graph is shown in Fig. 5.11 (right). This makes a future LHeC a  
 3609 top quark factory and an ideal tool to study top quarks with a high precision, and to analyse in



3610 particular their electroweak interaction. Selected highlights in top quark physics are summarised  
 3611 here.

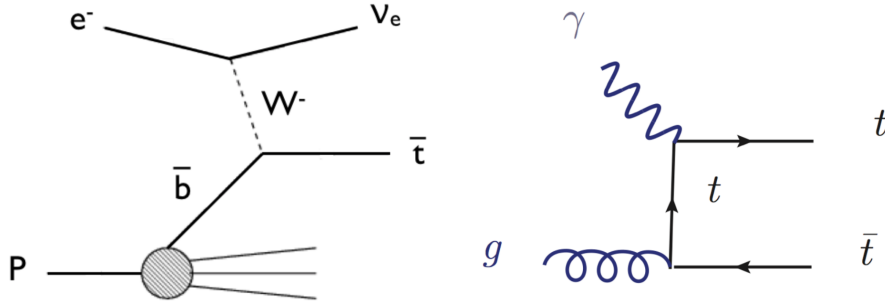


**Figure 5.11:** Example graphs for CC DIS top quark production (left) and top quark photoproduction (right).

### 3612 5.3.1 $Wtq$ Couplings

3613 The top quark couplings with gauge bosons can be modified significantly in models with new  
 3614 top (or third generation) partners, such as in some extensions of the minimal supersymmetric  
 3615 standard model, in little Higgs models, top-color models, top seesaw, top compositeness, and  
 3616 others. Testing them is therefore of utmost importance to find out whether there are other  
 3617 sources of electroweak symmetry breaking that are different from the standard Higgs mechanism.

3618 One flagship measurement is the direct measurement of the CKM matrix element  $|V_{tb}|$ , i.e.  
 3619 without making any model assumptions such as on the unitarity of the CKM matrix or the  
 3620 number of quark generations. An elaborate analysis of the single top quark CC DIS process  
 3621 at the LHeC including a detailed detector simulation using the DELPHES package [460] shows  
 3622 that already at  $100 \text{ fb}^{-1}$  of integrated luminosity an uncertainty of 1% can be expected. This  
 3623 compares to a total uncertainty of 4.1% of the currently most accurate result at the LHC Run-I  
 3624 performed by the CMS experiment [461].

3625 The same analysis [458] can also be used to search for anomalous left- and right-handed  $Wtb$   
 3626 vector  $(f_1^L, f_1^R)$  and tensor  $(f_2^L, f_2^R)$  couplings analyzing the following effective Lagrangian:

$$\mathcal{L}_{Wtb} = -\frac{g}{\sqrt{2}} \bar{b} \gamma^\mu V_{tb} (f_1^L P_L - f_1^R P_R) t W_\mu^- - \frac{g}{\sqrt{2}} \bar{b} \frac{i\sigma^{\mu\nu} q_\nu}{M_W} (f_2^L P_L - f_2^R P_R) t W_\mu^- + h.c. \quad (5.15)$$

3627 In the SM  $f_1^L = 1$  and  $f_1^R = f_2^L = f_2^R = 0$ . The effect of anomalous  $Wtb$  couplings is consistently  
 3628 evaluated in the production and the decay of the antitop quark, cf. Fig. 5.11 (left).<sup>5</sup> Using  
 3629 hadronic top quark decays only, the expected accuracies in a measurement of these couplings as  
 3630 a function of the integrated luminosity are presented in Fig. 5.12, derived from expected 95%  
 3631 C.L. limits on the cross section yields. The couplings can be measured with accuracies of 1%  
 3632 for the SM  $f_1^L$  coupling determining  $|V_{tb}|$  (as discussed above) and of 4% for  $f_2^L$ , 9% for  $f_2^R$ ,  
 3633 and 14% for  $f_1^R$  at  $1 \text{ ab}^{-1}$ .

3634 Similarly, the CKM matrix elements  $|V_{tx}|$  ( $x = d, s$ ) can be extracted using a parameterisation of  
 3635 deviations from their SM values with very high precision through  $W$  boson and bottom (light)  
 3636 quark associated production channels, where the  $W$  boson and  $b$ -jet (light jet  $j = d, s$ ) final

<sup>5</sup>Further studies of the top quark charged current coupling can be found in [462] There, a more general frame-  
 work is employed using the full basis of  $SU(2)_L \times U(1)$  operators, including the relevant four-fermion ones.

3637 states can be produced via s-channel single top quark decay or t-channel top quark exchange as  
 3638 outlined in [463]. As an example, analysing the processes

3639 Signal 1:  $pe^- \rightarrow \nu_e \bar{t} \rightarrow \nu_e W^- \bar{b} \rightarrow \nu_e \ell^- \nu_\ell \bar{b}$

3640 Signal 2:  $pe^- \rightarrow \nu_e W^- b \rightarrow \nu_e \ell^- \nu_\ell b$

3641 Signal 3:  $pe^- \rightarrow \nu_e \bar{t} \rightarrow \nu_e W^- j \rightarrow \nu_e \ell^- \nu_\ell j$

3642 in an elaborate analysis including a detailed detector simulation using the DELPHES pack-  
 3643 age [460], the expected accuracies on  $|V_{td}|$  and  $|V_{ts}|$  at the  $2\sigma$  confidence level (C.L.) are shown  
 3644 as a function of the integrated luminosity in Fig. 5.13. At  $1 \text{ ab}^{-1}$  of integrated luminosity and an  
 3645 electron polarization of 80%, the  $2\sigma$  limits improve on existing limits from the LHC [464] (inter-  
 3646 preted by [465]) by a factor of  $\approx 3.5$ . Analyzing Signal 3 alone, and even more when combining  
 3647 Signals 1, 2 and 3, will allow for the first time to achieve an accuracy of the order of the actual  
 3648 SM value of  $|V_{ts}^{\text{SM}}| = 0.04108_{-0.0057}^{+0.0030}$  as derived from an indirect global CKM matrix fit [466],  
 3649 and will therefore represent a direct high precision measurement of this important top quark  
 3650 property. In these studies, upper limits at the  $2\sigma$  level down to  $|V_{ts}| < 0.06$ , and  $|V_{td}| < 0.06$   
 3651 can be achieved.

### 3652 5.3.2 Top Quark Polarisation

3653 Single top quarks produced via the  $e^+p \rightarrow t\bar{\nu}$  processes possess a high degree of spin polarisation  
 3654 in terms of a basis which decomposes the top quark spin in its rest frame along the direction of  
 3655 the incoming  $e$  beam [467]. It has been investigated for  $\sqrt{s} = 1.6 \text{ TeV}$  in  $e^+p$  scattering, that the  
 3656 spin fraction defined as the ratio of the polarised cross section to the unpolarised one, reaches  
 3657 96% allowing a detailed study of top quark spin and polarisation. Exploring the angle between  
 3658 the momentum direction of the charged lepton from top quark decay and the spin quantisation  
 3659 axis in the top quark rest frame, anomalous  $Wtb$  couplings can be tested. Assuming a total  
 3660 systematic uncertainty of 10% the expected sensitivity for  $\sqrt{s} = 1.6 \text{ TeV}$  reaches  $\pm 3\%$  for  $f_2^L$ ,  
 3661 and  $\pm 7\%$  for  $f_2^R$  as defined in Eq. (5.15).

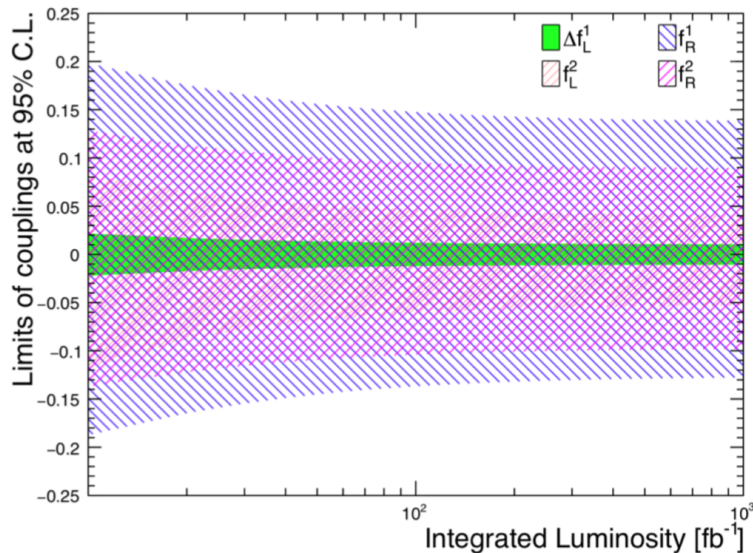


**Figure 5.12:** Expected sensitivities as a function of the integrated luminosity on the SM and anomalous  $Wtb$  couplings [458].

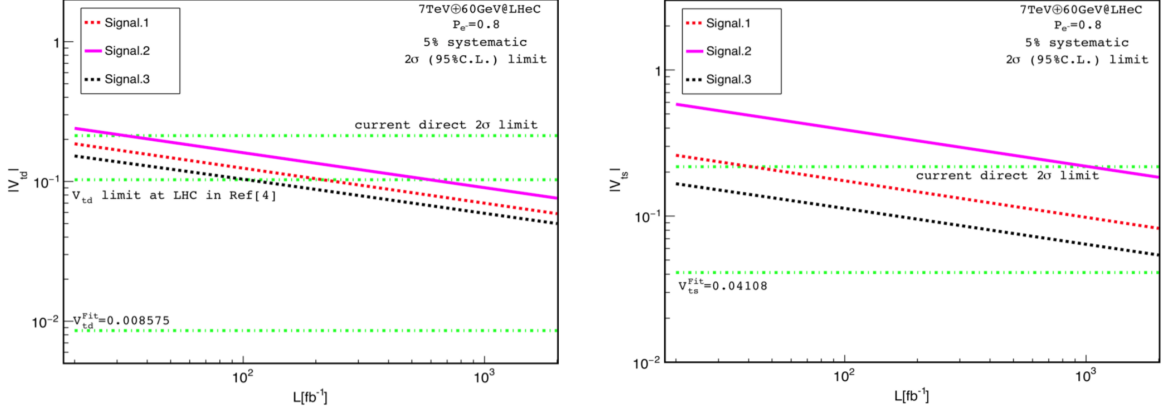


**Figure 5.13:** Expected sensitivities as a function of the integrated luminosity on  $|V_{td}|$  (left) and  $|V_{ts}|$  (right) [463].

### 5.3.3 Top- $\gamma$ and Top- $Z$ Couplings

The LHeC is particularly well suited to measure the  $t\bar{t}\gamma$  vertex, since in photoproduction of top quark pairs (see Fig. 5.11, right) the highly energetic incoming photon only couples to the top quark, and therefore the cross section directly depends on the  $t\bar{t}\gamma$  vertex. This provides a direct measurement of the coupling between the top quark and the photon and therefore of another important top quark property, the top quark charge. In contrast, at the LHC the  $t\bar{t}\gamma$  vertex is probed in  $t\bar{t}\gamma$  production, where the final state photon can also be produced from other vertices than the  $t\bar{t}\gamma$  vertex, such as from initial state radiation or from radiation off charged top quark decay products.

The LHeC also provides a high potential for measuring the  $t\bar{t}\gamma$  magnetic and electric dipole moments (MDM and EDM, respectively) in  $t\bar{t}$  production [459]. In an effective Lagrangian framework, effective  $t\bar{t}\gamma$  couplings can be written in terms of form factors:

$$\mathcal{L}_{Wtb} = e\bar{t}\left(Q_t\gamma^\mu A_\mu + \frac{1}{4m_t}\sigma^{\mu\nu}F_{\mu\nu}(\kappa + i\tilde{\kappa}\gamma_5)\right)t + h.c. \quad (5.16)$$

with the anomalous MDM of the top quark,  $\kappa$ , and the EDM of the top quark,  $\tilde{\kappa}$ . The top quark charge is given by  $eQ_t$ .

By solely measuring the  $t\bar{t}$  production cross section, remarkably tight bounds can be derived on the MDM and the EDM of the top quark as presented in Fig. 5.14. In this parton level study, for the computation of the cross section a set of appropriate phase-space cuts are imposed on the final-state momenta. Applying further cuts to remove the background will result in a substantial reduction of the signal. It is therefore assumed that this would lead to a statistical uncertainty of about 8%, represented by the dark inner ring in Fig. 5.14. To include uncertainties due to mistagging and to allow for other unspecified sources of systematic uncertainty, it is assumed that the total uncertainty will be about 16% corresponding to the full ring in Fig. 5.14. This would yield bounds of  $-0.13 < \kappa < 0.18$ , and  $|\tilde{\kappa}| < 0.38$ , respectively, at the  $2\sigma$  C.L. Figure 5.14 shows that the LHeC could greatly improve the limits imposed by the indirect constraints from  $b \rightarrow s\gamma$ , and even the limits imposed by a future measurement of  $t\bar{t}\gamma$  production at the LHC at  $\sqrt{s} = 14$  TeV.

Furthermore, the deep inelastic scattering (DIS) regime of  $t\bar{t}$  production will allow to probe the  $t\bar{t}Z$  coupling, albeit with less sensitivity [459].

### 3690 5.3.4 Top-Higgs Coupling

3691 The CP-nature of the top-Higgs coupling can be analysed at the LHeC in  $ep \rightarrow \bar{t}H$  production  
 3692 exploring the top quark polarisation and other angular variables such as the rapidity difference  
 3693 between the single top quark and the Higgs boson. Measuring just the fiducial inclusive produc-  
 3694 tion cross section gives already a powerful probe of the CP properties of the  $t\bar{t}H$  coupling [469].  
 3695 Further details are given in Section 7.5.

### 3696 5.3.5 Top Quark PDF and the Running of $\alpha_s$

3697 Parton distributions are usually released in a variable-flavor number scheme, in which the number  
 3698 of active flavors changes as the scale is raised [251]. However,  $n_f = 5$  is normally taken by default  
 3699 as a maximum number of flavors, even though in some PDF releases  $n_f = 6$  PDF sets are also  
 3700 made available [470]. The top PDF is unlikely to be required for precision phenomenology, even  
 3701 at very high scales, because the top threshold is high enough that collinear resummation is not  
 3702 necessary up to extremely large scales: indeed  $\frac{\alpha_s(M_t^2)}{\pi} \ln \frac{Q^2}{m_t^2} \sim \frac{1}{2}$  only for  $Q \gtrsim 10^6 m_t$ . On the  
 3703 other hand, the use of  $n_f = 6$  active flavors in the running of  $\alpha_s$  is important for precision  
 3704 phenomenology, since the value of  $\alpha_s$  with five and six active flavors already differ by about  
 3705 2% at the TeV scale [471]. Investigations of the top quark structure inside the proton are also  
 3706 discussed in Refs. [1, 39].

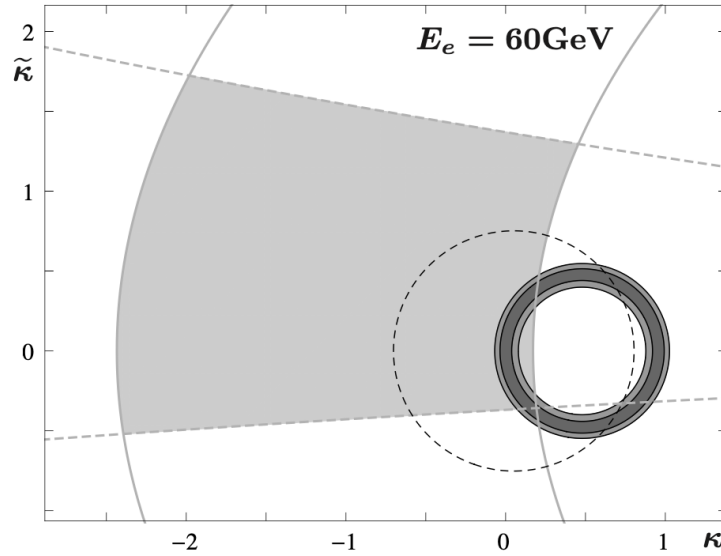


**Figure 5.14:** Allowed region of the magnetic dipole moment  $\kappa$  and the electric dipole moment  $\tilde{\kappa}$  of the top quark as expected in a measurement of the photoproduction cross section  $\sigma(e(\gamma)p(g) \rightarrow t\bar{t})$  in semileptonic final states, assuming an experimental uncertainty of 8% (dark grey), and of 16% (dark+medium grey) [459]. Light gray area: region allowed by the measurements of the branching ratio (solid gray lines) and the CP asymmetry (dashed gray lines) of  $B \rightarrow X_s \gamma$  [468]. Black dashed line: region allowed by a hypothetical experimental result for  $\sigma(pp \rightarrow t\bar{t}\gamma)$  utilizing semileptonic final states at the LHC at  $\sqrt{s} = 14$  TeV with phase-space cuts as defined in equations (5), (6) of Ref. [468] (including  $E_T^\gamma > 10$  GeV), and assuming an experimental uncertainty of 5%.

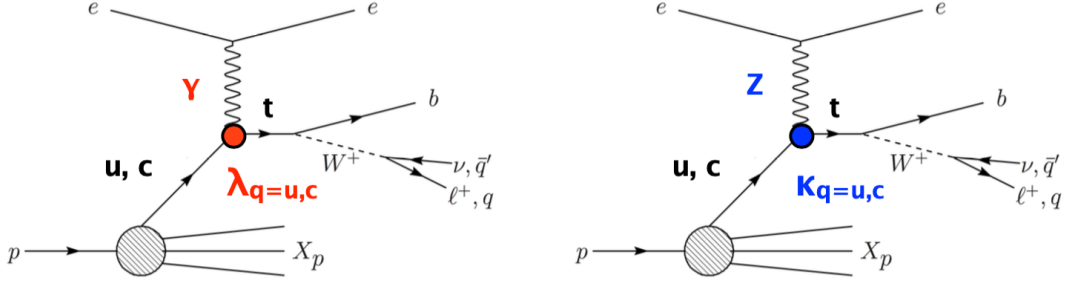


**Figure 5.15:** Example graphs for single top quark production via FCNC  $tq\gamma$  (left) and  $tuZ$  (right) couplings.

### 3707 5.3.6 FCNC Top Quark Couplings

3708 Like all the Flavour Changing Neutral Currents (FCNCs) the top quark FCNC interactions  
 3709 are also extremely suppressed in the SM, which renders them a good test of new physics. The  
 3710 contributions from FCNC to top interactions can be parameterised via an effective theory and  
 3711 studied by analysing specific processes.

3712 Single top quark NC DIS production can be used to search for FCNC  $tu\gamma$ ,  $tc\gamma$ ,  $tuZ$ , and  $tcZ$   
 3713 couplings [472, 473] as represented by the Lagrangian

$$\mathcal{L}_{\text{FCNC}} = \sum_{q=u,c} \left( \frac{g_e}{2m_t} \bar{t} \sigma^{\mu\nu} (\lambda_q^L P_L + \lambda_q^R P_R) q A_{\mu\nu} + \frac{g_W}{4c_W m_Z} \bar{t} \sigma^{\mu\nu} (\kappa_q^L P_L + \kappa_q^R P_R) q Z_{\mu\nu} \right) + h.c. , \quad (5.17)$$

3714 where  $g_e$  ( $g_W$ ) is the electromagnetic (weak) coupling constant,  $c_W$  is the cosine of the weak  
 3715 mixing angle,  $\lambda_q^{L,R}$  and  $\kappa_q^{L,R}$  are the strengths of the anomalous top FCNC couplings (the values  
 3716 of these couplings vanish at the lowest order in the SM). Top FCNC couplings as introduced in  
 3717 Eq. (5.17) would lead to Feynman graphs as shown in Fig. 5.15.

3718 In an elaborate analysis, events including at least one electron and three jets (hadronic top  
 3719 quark decay) with high transverse momentum and within the pseudorapidity acceptance range  
 3720 of the detector are selected. The distributions of the invariant mass of two jets (reconstructed  
 3721  $W$  boson mass) and an additional jet tagged as  $b$ -jet (reconstructed top quark mass) are used  
 3722 to further enhance signal over background events, mainly given by  $W$  + jets production. Signal  
 3723 and background interference effects are included. A detector simulation with DELPHES [460]  
 3724 is applied.

3725 The expected limits on the branching ratios  $\text{BR}(t \rightarrow q\gamma)$  and  $\text{BR}(t \rightarrow qZ)$  as a function of the  
 3726 integrated luminosity at the  $2\sigma$  C.L. are presented in Fig. 5.16 (left). Assuming an integrated  
 3727 luminosity of  $1 \text{ ab}^{-1}$ , limits of  $\text{BR}(t \rightarrow q\gamma) < 1 \cdot 10^{-5}$  and  $\text{BR}(t \rightarrow qZ) < 4 \cdot 10^{-5}$  are expected.  
 3728 This level of precision is close to actual predictions of concrete new phenomena models, such  
 3729 as SUSY, little Higgs, and technicolour, that have the potential to produce FCNC top quark  
 3730 couplings. The expected limits will improve on existing limits from the LHC by one order  
 3731 of magnitude [13]. They will be similar to limits expected from the High Luminosity-LHC  
 3732 (HL-LHC) with  $3000 \text{ fb}^{-1}$  [184], and will improve limits from the International Linear Collider  
 3733 (ILC) with  $500 \text{ fb}^{-1}$  at  $\sqrt{s} = 250 \text{ GeV}$  [474, 475] by an order of magnitude (see also Fig. 5.18).  
 3734 Figure 5.16 (right) shows how the sensitivity on  $\text{BR}(t \rightarrow q\gamma)$  and  $\text{BR}(t \rightarrow qZ)$ , respectively,  
 3735 changes as a function of the centre-of-mass energy. At a future FCC-ep [13] with, for example,  
 3736 an electron beam energy of  $60 \text{ GeV}$ , and a proton beam energy of  $50 \text{ TeV}$ , leading to a centre-of-  
 3737 mass energy of  $3.5 \text{ TeV}$ , the sensitivity to FCNC  $tq\gamma$  couplings even exceed expected sensitivities

3738 from the HL-LHC with  $3000 \text{ fb}^{-1}$  at  $\sqrt{s} = 14 \text{ TeV}$  [184].

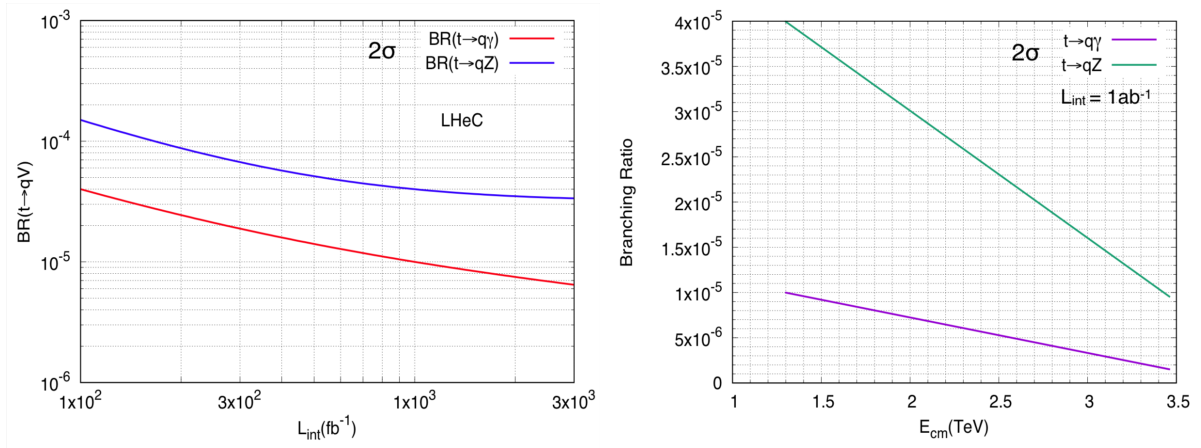


**Figure 5.16:** Expected sensitivities as a function of the integrated luminosity on FCNC  $t \rightarrow qV$  branching ratios (left) [472, 473]. The expected upper limits on FCNC  $t \rightarrow qV$  branching ratios are also shown as a function of the centre-of-mass-energy (right).

3739 A further study of the top quark FCNC through  $Z$ -boson has been performed in [476] for the  
 3740 LHeC including a DELPHES [460] detector simulation. The effective couplings for FCNC pro-  
 3741 cesses are of vector and tensor in nature, the latter corresponding to those in Eq. (5.17). The  
 3742 effect of these couplings is probed in the single top quark production (see Fig. 5.15 right). It is  
 3743 shown that the polar angle( $\theta$ ) of the electrons coming out of the primary vertex in association  
 3744 with the top quark polarization asymmetries constructed from the angular distribution of the  
 3745 secondary lepton arising from the top decay, allow to distinguish the Lorentz structure of the  
 3746 couplings. From a multi-parameter analysis, a reach of the  $\mathcal{O}(10^{-2})$  in the case of vector cou-  
 3747 plings and  $0.1 - 0.5 \text{ TeV}^{-1}$  in case of tensor couplings are obtained at an integrated luminosity  
 3748 of  $2 \text{ ab}^{-1}$  for 95% C.L.

3749 Another example for a sensitive search for anomalous top quark couplings is the one for FCNC  
 3750  $tqH$  couplings as defined in

$$\mathcal{L}_{\text{FCNC}} = \kappa_{tuH} \bar{t}uH + \kappa_{tcH} \bar{t}cH + h.c. \quad (5.18)$$

3751 This can be studied in CC DIS production as shown in Fig. 5.17 (left), where singly produced  
 3752 top anti-quarks could decay via such couplings into a light up-type anti-quark and a Higgs  
 3753 boson decaying into a bottom quark-antiquark pair,  $e^- p \rightarrow \nu_e \bar{t} \rightarrow \nu_e H \bar{q} \rightarrow \nu_e b \bar{b}$  [477]. Another  
 3754 signal involves the FCNC  $tqH$  coupling in the production vertex, i.e. a light quark from the  
 3755 proton interacts via  $t$ -channel top quark exchange with a  $W$  boson radiated from the initial  
 3756 electron producing a  $b$  quark and a Higgs boson decaying into a bottom quark-antiquark pair,  
 3757  $e^- p \rightarrow \nu_e H b \rightarrow \nu_e b \bar{b}$  [477]. This channel is similar in sensitivity to the previous one due to  
 3758 the clean experimental environment when requiring three identified  $b$ -jets. Largest backgrounds  
 3759 are given by  $Z \rightarrow b \bar{b}$ , SM  $H \rightarrow b \bar{b}$ , and single top quark production with hadronic top quark  
 3760 decays. A 5% systematic uncertainty for the background yields is added. Furthermore, the  
 3761 analysis assumes parameterised resolutions for electrons, photons, muons, jets and unclustered  
 3762 energy using typical parameters taken from the ATLAS experiment. Furthermore, a  $b$ -tag rate  
 3763 of 60%, a  $c$ -jet fake rate of 10%, and a light-jet fake rate of 1% is assumed. The selection is  
 3764 optimised for the different signal contributions separately. Fig. 5.17 (right), shows the expected  
 3765 upper limit on the branching ratio  $\text{Br}(t \rightarrow Hu)$  with  $1\sigma$ ,  $2\sigma$ ,  $3\sigma$ , and  $5\sigma$  C.L. as a function of  
 3766 the integrated luminosity for the  $e^- p \rightarrow \nu_e \bar{t} \rightarrow \nu_e H \bar{q} \rightarrow \nu_e b \bar{b}$  signal process. For an integrated  
 3767 luminosity of  $1 \text{ ab}^{-1}$ , upper limits of  $\text{Br}(t \rightarrow Hu) < 0.15 \cdot 10^{-3}$  are expected at the  $2\sigma$  C.L.

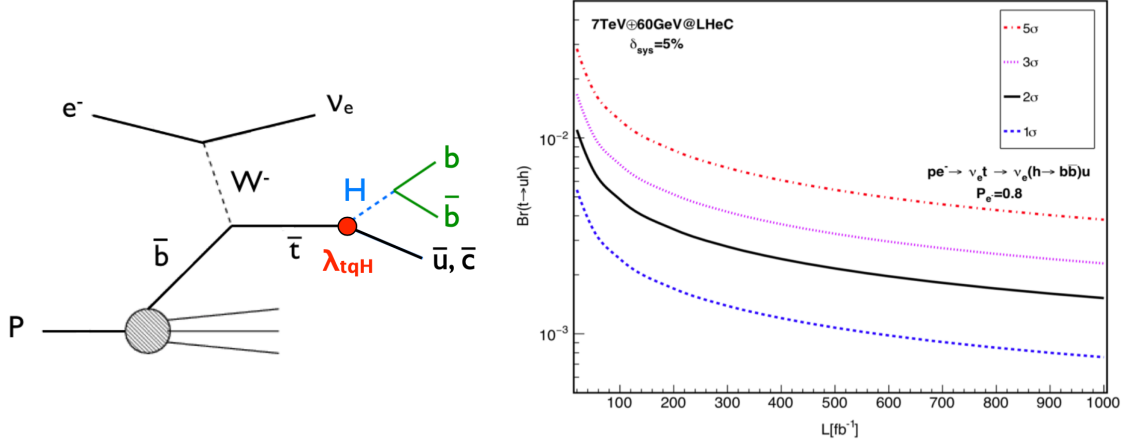


**Figure 5.17:** Example Feynman graph for associated single top quark and Higgs boson production via FCNC  $tqH$  couplings (left). Expected sensitivities as a function of the integrated luminosity on FCNC  $t \rightarrow uH$  branching ratios [477] (right).

3768 In Fig. 5.18 the different expected limits on various FCNC top quark couplings from the LHeC  
 3769 are summarised, and compared to results from the LHC and the HL-LHC. This clearly shows the  
 3770 competitiveness of the LHeC results, and documents the complementarity of the results gained  
 3771 at different colliders.

### 3772 5.3.7 Other Top Quark Property Measurements and Searches for New Physics

3773 Other exciting results not presented here involve, for example, the study of the CP-nature  
 3774 in  $t\bar{t}H$  production [469] (see Section 7.5), searches for anomalous  $t\bar{t}\gamma$  and  $t\bar{t}Z$  chromoelectric  
 3775 and chromomagnetic dipole moments in  $t\bar{t}$  production [459], the study of top quark spin and  
 3776 polarisation [467], and the investigation of the top quark structure function inside the proton [1,  
 3777 39].

### 3778 5.3.8 Summary of Top Quark Physics

3779 Top quark physics at the LHeC represents a very rich and diverse field of research involving  
 3780 high precision measurements of top quark properties, and sensitive searches for new physics.  
 3781 In particular the top couplings to the photon, the  $W$  boson and possible FCNC interactions  
 3782 can be studied in a uniquely clean environment. One signature analysis is the expected direct  
 3783 measurement of the CKM matrix element  $|V_{tb}|$  with a precision of less than 1% in CC DIS. In  
 3784 top quark pair photoproduction the magnetic and electric dipole moments of the top quark can  
 3785 be probed directly with higher sensitivity than indirect limits from  $b \rightarrow s\gamma$  and the potential  
 3786 limits from the LHC through  $t\bar{t}\gamma$  production. Furthermore, FCNC top quark couplings can  
 3787 be studied with a precision high enough to explore those couplings in a regime that might be  
 3788 affected by actual new phenomena models, such as SUSY, little Higgs, and technicolour.

3789 It has been shown [13], that results from future  $e^+e^-$ -colliders,  $eh$ -colliders, and  $hh$ -colliders  
 3790 deliver complimentary information and will therefore give us a more complete understanding of  
 3791 the properties of the heaviest elementary particle known to date, and of the top quark sector in  
 3792 general.

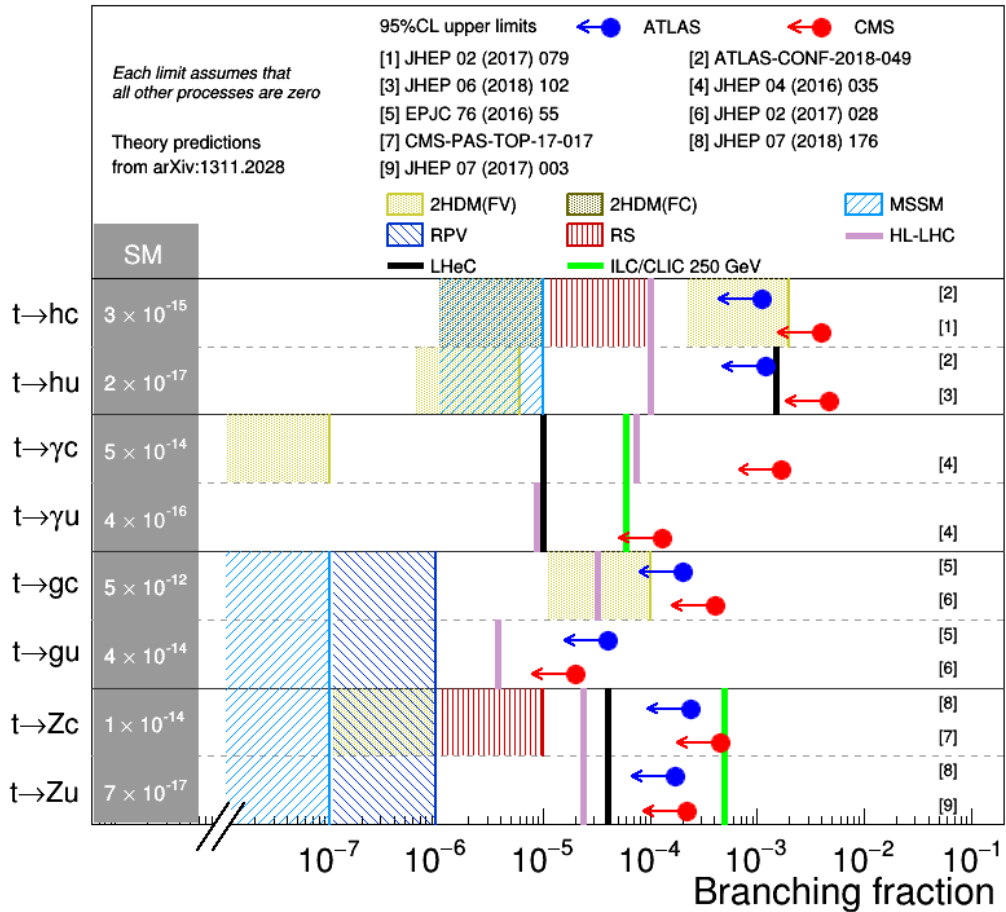


**Figure 5.18:** Summary of 95% C.L. limits on top quark branching fractions in searches for FCNC in top quark production or decays. The LHeC results (black lines) are compared to current LHC limits (blue and red dots), to HL-LHC predictions with  $3000 \text{ fb}^{-1}$  at  $\sqrt{s} = 14 \text{ TeV}$  [184] (magenta lines), and to predictions from a future ILC collider with  $500 \text{ fb}^{-1}$  at  $\sqrt{s} = 250 \text{ GeV}$  [474, 475] (green lines). The results are also compared to various theory predictions (hatched areas).



## Chapter 6

# Nuclear Particle Physics with Electron-Ion Scattering at the LHeC

### 6.1 Introduction

The LHeC accelerator, in addition to being a powerful machine for exploring proton structure, will allow for the first time studies of DIS off nuclei in a collider mode at the energy frontier. The nuclear structure has been previously studied in fixed target experiments with charged lepton and neutrino beams, see [67–69, 478–487] and references therein. Due to the energy limitations of the machines operating in this mode, the kinematic range covered by these experiments is rather narrow, mostly limited to relatively large values of  $x \geq 0.01$  and low to moderate  $Q^2$ , in the range  $Q^2 < 100 \text{ GeV}^2$ . The precise kinematic range covered by experiments is shown in Fig. 6.1, where the DIS experiments overlap to a large degree with the data from hadronic collisions using the Drell-Yan (DY) process. These fixed target DIS and DY data dominate the data sets used in the fits for the nuclear parton distribution functions. In addition, in some analyses of nuclear PDFs, data on inclusive single hadron production in  $d\text{Au}$  collisions at RHIC and on EW bosons and dijets in  $p\text{Pb}$  collisions at the LHC are included.

As is clear from Fig. 6.1, the LHeC will be able to cover a very large range in  $(x, Q^2)$  in  $eA$ , previously unexplored in experiments. It will extend the range in  $x$  down to  $\sim 10^{-6}$  and have a huge lever arm in  $Q^2$  from very low values up to  $\sim 10^6 \text{ GeV}^2$ . It will also be complementary to the EIC [99] machine, extending the range in  $x$  and  $Q^2$  by about two orders of magnitude with respect to it. The extension of these ranges will be even larger at the FCC-eh.

Due to large statistics and modern, specialised detectors, it will be possible to study nuclear structure at the LHeC with unprecedented precision in a kinematical range far wider than previously possible and with the controlled systematics of one single experiment. There are a large number of important physics topics that can be addressed in  $eA$  collisions at the LHeC:

- A precise determination of nuclear parton densities for a single nucleus (lead, and eventually lighter ions) will be possible. In particular, the current huge uncertainties in nuclear gluon and sea quark densities at low  $x$  will be dramatically improved using the data from the LHeC. In analogy to the proton PDF extraction described in previous sections, full flavour decomposition in the nuclear case could be achieved using both NC and CC data with heavy flavour identification.
- Precision measurement of semi-inclusive and exclusive processes will enable an exploration

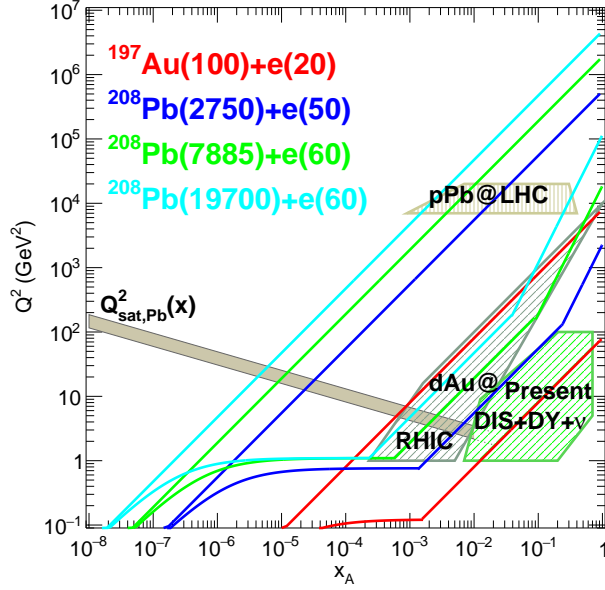


**Figure 6.1:** Kinematic regions in the  $x - Q^2$  plane explored by different data sets (charged lepton and neutrino DIS, DY,  $dAu$  at RHIC and  $pPb$  at the LHC) used in present nPDF analyses [488], compared to the ones achievable at the EIC (red), the LHeC (ERL against the HL-LHC beams, dark blue) and two FCC-eh versions (with Pb beams corresponding to proton energies  $E_p = 20$  TeV - green and  $E_p = 50$  TeV - light blue). Acceptance of the detector for the electrons is taken to be  $1^\circ < \theta < 179^\circ$ , and  $0.01(0.001) < y < 1$  for the EIC (all other colliders). The saturation scale  $Q_{sat}$  shown here for indicative purposes only, see also [489], has been drawn for a Pb nucleus considering an uncertainty  $\sim 2$  and a behaviour with energy following the model in [490]. Note that it only indicates a region where saturation effects are expected to be important but there is no sharp transition between the linear and non-linear regimes.

3825  
3826  
3827  
3828  
3829  
3830  
3831  
3832  
3833  
3834  
3835  
3836  
3837  
3838  
3839  
3840  
3841  
3842  
3843  
3844

of new details of the nuclear structure. Similarly to the proton case, DVCS and exclusive vector-meson production will provide unique insight into 3D nuclear structure.

- The LHeC will offer unprecedented opportunities to extract diffractive parton densities in nuclei for the first time. A first detailed analysis [327] indicates that the achievable precision on diffractive PDFs in nuclei will be comparable to that possible in the proton case. The measurements of diffraction on protons and nuclei as well as the inclusive structure functions in the nuclear case will allow us to explore the very important relation between nuclear shadowing and diffraction [491].
- The LHeC will be able to test and establish or exclude the phenomenon of parton saturation at low  $x$  in protons and nuclei. According to the Color Glass Condensate framework [492, 493], parton saturation is a density effect that can be achieved in two ways, either by decreasing the value of  $x$  or by increasing the size of the target by increasing  $A$ . The LHeC will be a unique machine to address both of their variations, such that the ideas of saturation could be precisely tested. It will be possible to search for parton saturation in a variety of ways which include, among others, the search for tensions in DGLAP fits, the study of the diffraction, in particular the ratios of diffractive to inclusive cross sections, and the study of particle azimuthal de-correlations.
- Finally, the LHeC machine in  $eA$  mode will have a huge impact onto physics explored in  $pA$  and  $AA$  collisions, see Sec. 9.7, where it will provide vital input and constraints on the ‘baseline’ initial state in nuclear collisions, measurements of the impact of a cold nuclear

3845 medium on hard probes and effects of hadronisation. It will also explore the initial state  
 3846 correlations on the final state observables relevant for understanding collectivity in small  
 3847 systems explored in  $pp$  or  $pA$  collisions.

3848 As commented below, these aims will require an experimental apparatus with large rapidity  
 3849 coverage and associated forward and backward electron, photons, hadron and nuclear detectors.  
 3850 In addition the detector design should allow to precisely measure diffractive events in  $eA$  and  
 3851 allow the clean separation of radiative events, most important for the case of DVCS and exclusive  
 3852 diffraction.

3853 Photonuclear interactions at high energies can also be studied through ultraperipheral collisions  
 3854 at RHIC and the LHC [126, 127, 308, 494] that offer an alternative although with less precision.  
 3855 This is briefly discussed in Chapter 9 where the relation between the LHeC and the HL-LHC is  
 3856 presented.

3857 In this Chapter we do not address issues on the nuclear modification on jet yields and fragmen-  
 3858 tation that are expected to show dramatic effects and to be of great importance for heavy-ion  
 3859 collisions. All these aspects were previously discussed in Ref. [1]. Besides, electron-deuteron  
 3860 collisions that offer additional possibilities for determining proton and neutron parton densities,  
 3861 and for studying weak interactions with neutron targets at high energies, are not considered  
 3862 here, see Ref. [1] where an analysis of parton densities in  $eD$  collisions can be found.

## 3863 6.2 Nuclear Parton Densities

3864 PDFs are essential ingredients in our understanding of the dynamics of the strong interaction.  
 3865 First, they encode important information about the structure of hadrons [495, 496]. Second, they  
 3866 are indispensable for the description of hadronic collisions within standard collinear factorisa-  
 3867 tion [37]. Concerning nuclei, it has been known for more than 40 years that structure functions  
 3868 are strongly affected by the nuclear environment [486, 487] so that they cannot be interpreted as  
 3869 a simple superposition of structure functions of free nucleons. In the standard approach, within  
 3870 collinear factorization, the nuclear modification is included in the parametrisation of the parton  
 3871 densities. This means that the parton densities in a bound nucleon are different from those in  
 3872 a free nucleon, and the difference is encoded in the non-perturbative initial conditions of the  
 3873 parton densities at some low, initial scale  $Q_0^2$ . The present status of nuclear parton densities  
 3874 (nPDFs), see for example [497, 498], can be summarised as follows:

- 3875 • Modern analyses [488, 499–501] are performed at next-to-leading order (NLO) and next-to-  
 3876 next-to-leading order (NNLO) [502, 503]. Differences between the different groups mainly  
 3877 arise from the different sets of data included in the analyses <sup>1</sup> and from the different  
 3878 functional forms employed for the initial conditions.
- 3879 • Many sets of data are presented as ratios of cross section for a given nucleus over that in  
 3880 deuterium, which is loosely bound and isoscalar. Therefore, it has become customary to  
 3881 work in terms of ratios of nPDFs:

$$R_i(x, Q^2) = \frac{f_i^A(x, Q^2)}{A f_i^p(x, Q^2)}, \quad i = u, d, s, c, b, g, \dots, \quad (6.1)$$

3882 with  $f_i^{p(A)}(x, Q^2)$  the corresponding parton density in a free proton  $p$  or in nucleus  $A$ .  
 3883 These nuclear modification factors are parametrised at initial scale  $Q_0^2$  (assuming isospin

---

<sup>1</sup>The main difference lies in the use or not of neutrino-Pb cross sections (whose usage has been controver-  
 sial [504–506], particularly the NuTeV data [68] from the Fe nucleus) from CHORUS and  $\pi^{0,\pm}$  transverse mo-  
 mentum spectra from  $dAu$  collisions at the Relativistic Heavy Ion Collider (RHIC).

3884 symmetry to hold). The nPDFs are then obtained multiplying the nuclear modification  
3885 factors by some given set of free proton PDFs.

- 3886 • The available data come from a large variety of nuclei and the number of data points for  
3887 any of them individually is very small compared to the proton analyses. In particular,  
3888 for the Pb nucleus there are less than 50 points coming from the fixed target DIS and  
3889 DY experiments and from particle production data in  $p$ Pb collisions at the LHC. The fit  
3890 for a single nucleus is therefore impossible and the modelling of the  $A$ -dependence of the  
3891 parameters in the initial conditions becomes mandatory [488, 501]. The most up to date  
3892 analyses include between 1000 and 2000 data points for 14 nuclei.
- 3893 • The kinematic coverage in  $Q^2$  and  $x$  with existing data is very small compared to that  
3894 of present hadronic colliders. The ultimate precision and large coverage of the kinematic  
3895 plane for nPDFs can only be provided by a high energy electron-ion collider. Meanwhile,  
3896 the only experimental collision system where nPDFs can be currently constrained are  
3897 hadronic and ultraperipheral collisions (UPCs). It is important to stress that extracting  
3898 PDFs from these collisions presents many theoretical challenges. These are related to the  
3899 question of applicability of collinear factorization for nuclear collisions, higher twist effects,  
3900 scale choices and other theoretical uncertainties.

3901 All parton species are very weakly constrained at small  $x < 10^{-2}$  [507], gluons are poorly  
3902 known at large  $x > 0.2$ , and the flavour decomposition is largely unknown - a natural fact  
3903 for  $u$  and  $d$  due to the approximate isospin symmetry in nuclei <sup>2</sup>. The impact of presently  
3904 available LHC data, studied using reweighting [253, 508] in [509, 510] and included in the fit  
3905 in [488], is quite modest with some constraints on the gluon and the strange quark in the region  
3906  $0.01 < x < 0.3$ . On the other hand, theoretical predictions for nuclear shadowing of quark and  
3907 gluon PDFs based on  $s$ -channel unitarity and diffractive nucleon PDFs are available down to  
3908  $x \sim 10^{-4} - 10^{-5}$  [491, 511–513]. Predictions on the flavour dependence of nuclear effects in the  
3909 antishadowing region [514] cannot be confirmed with present data.

3910 Future runs at the LHC will offer some further possibilities for improving our knowledge on  
3911 nPDFs [494]. However, the ideal place to determine parton densities is DIS, either at the Electron  
3912 Ion Collider (EIC) [99] in the USA or, in a much larger kinematic domain (see Fig. 6.1), at the  
3913 LHeC. DIS measurements in such configurations offer unprecedented possibilities to enlarge our  
3914 knowledge of parton densities through a complete unfolding of all flavours.

3915 In the following, we show the possibilities for constraining the PDFs for a Pb nucleus at the  
3916 LHeC. In the next subsection, Subsec. 6.2.1, we discuss the corresponding pseudodata for the  
3917 inclusive cross section in electron-nucleus scattering. Next, in Subsec. 6.2.2 we discuss how the  
3918 pseudodata will be introduced in a global nPDF fit. Finally, in Subsec. 6.2.3 it is demonstrated  
3919 how the PDFs of Pb can be extracted with a very good precision from the LHeC data only,  
3920 without requiring any other set of data.

### 3921 6.2.1 Pseudodata

3922 The LHeC provides measurements of  $eA$  scattering cross sections in the deep inelastic scattering  
3923 region  $Q^2 > 1 \text{ GeV}^2$  reaching values of  $Q^2$  up to about  $5 \cdot 10^5 \text{ GeV}^2$  and corresponding  $x$  values  
3924 between a few times  $10^{-6}$  and near to  $x = 1$ . This enables the determination of a complete  
3925 set of nPDFs in  $e$ Pb scattering at the LHeC from the inclusive neutral and charged current  
3926 cross sections with a clean separation of up and down valence and sea quark distributions. The

---

<sup>2</sup>The  $u$ - $d$  difference is suppressed by a factor  $2Z/A - 1$ .

3927 very high  $Q^2$  region which reaches much beyond the  $W$  mass squared makes the CC measure-  
 3928 ments extremely valuable for the separation of different flavours when taken together with the  
 3929 NC, from photon and  $Z$  boson exchange. Charm tagging in CC determines the anti-strange  
 3930 quark distribution in a wide kinematic range to typically 10 – 20 % precision, while charm and  
 3931 beauty tagging in NC provide high precision determinations of  $xc$  and  $xb$  from nuclei. Using  
 3932 coherent data from just this one experiment the uncertainties of these nPDFs will follow from  
 3933 a straightforward  $\Delta\chi^2 = 1$  criterion.

3934 The QCD analyses of pseudo LHeC cross section data illustrated subsequently employ sets of  
 3935 simulated NC and CC measurements under assumptions on precision which are summarised in  
 3936 Table 6.1, see Ref. [515]. The cross section simulation was done numerically employing deriva-  
 3937 tive formulae from [57] and found to compare well to a detailed Monte Carlo simulation when  
 3938 tested for the conditions of the H1 experiment. The assumptions made are all reasonable when  
 3939 comparing with the H1 achievements, allowing for further improvements owing to new detector  
 3940 techniques and higher statistics. The control of radiative corrections in  $eA$  scattering is a spe-  
 3941 cial challenge as these grow  $\propto Z^2$ . The LHeC detector thus needs to be equipped with reliable  
 3942 photon detectors and the exploitation of the energy-momentum conservation, via the  $E - p_z$   
 3943 cut, should further reduce the effect of photon radiation to a few per cent level. It is also to be  
 3944 noted that the semi-inclusive measurements of the  $s$ ,  $c$  and  $b$  quark distributions carry additional  
 uncertainties for tagging, acceptance and background influences.

Source of uncertainty	Error on the source or cross section
Scattered electron energy scale	0.1 %
Scattered electron polar angle	0.1 mrad
Hadronic energy scale	0.5 %
Calorimeter noise ( $y < 0.01$ )	1–3 %
Radiative corrections	1–2 %
Photoproduction background	1 %
Global efficiency error	0.7 %

**Table 6.1:** Summary of assumed systematic uncertainties for future inclusive cross section measurements at the LHeC.

3945

3946 Fig. 6.2 illustrates the kinematic reach of the NC+CC pseudodata at the LHeC and the FCC-eh,  
 3947 in  $ep$  and  $ePb$  collisions (for per nucleon integrated luminosities  $\leq 1$  and  $10 \text{ fb}^{-1}$  respectively). In  
 3948 addition to inclusive data, semi-inclusive measurements with flavour sensitivity are also included.  
 3949 They will allow us to determine the strange, charm and beauty (also the top) PDFs. The  
 3950 principal technique is charm tagging (in CC for  $xs$ , in NC for  $xc$ ) and beauty tagging (in NC  
 3951 for  $xb$ ). The beam spot of the LHeC has a transverse extension of about  $(7 \mu\text{m})^2$ . Modern Si  
 3952 detectors have a resolution of a few microns to be compared with typical decay lengths of charm  
 3953 and beauty particles of hundreds of  $\mu\text{m}$ . The experimental challenges then are the beam pipe  
 3954 radius, coping at the LHeC with strong synchrotron radiation effects, and the forward tagging  
 3955 acceptance, similar to the HL-LHC challenges.

3956 A study was made of the possible measurements of the anti-strange density in nuclei (see Fig. 6.3)  
 3957 using impact parameter tagging in  $eA$  CC scattering, and of the charm and beauty structure  
 3958 functions in NC (see Fig. 6.4). Following experience on heavy flavour tagging at HERA and  
 3959 ATLAS, assumptions were made on the charm and beauty tagging efficiencies to be 10 % and  
 3960 60 %, respectively. The light quark background in the charm analysis is assumed to be control-  
 3961 lable to per cent level, while the charm background in the beauty tagging sample is assumed  
 3962 to be 10 %. The tagging efficiencies and background contaminations affect the statistical error.

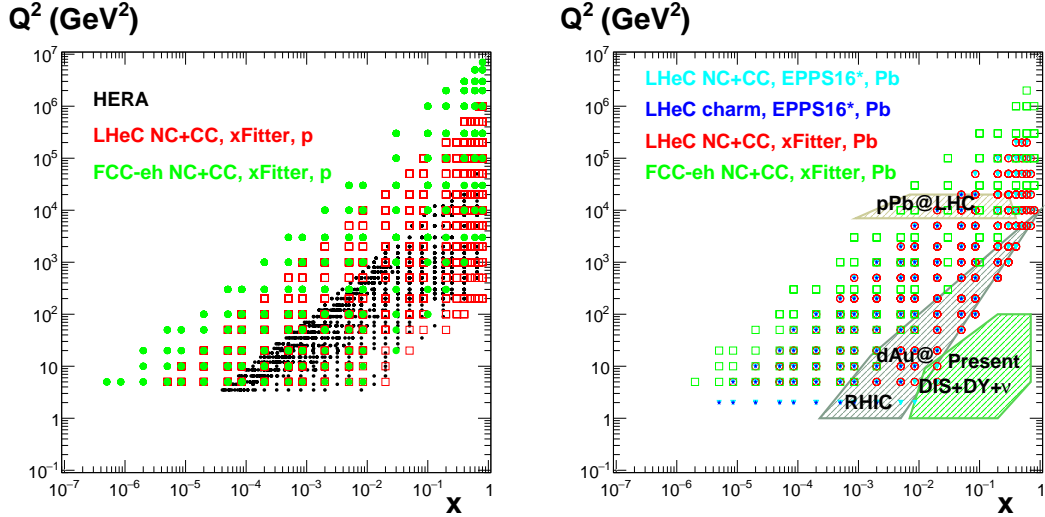


**Figure 6.2:** Left: kinematic  $x - Q^2$  plot of the NC+CC pseudodata on a proton at the LHeC (red symbols) and the FCC-eh (green symbols) used in the  $xFitter$  analysis in Section 6.2.3; data used in analysis at HERA (black symbols) are shown for comparison. Right: kinematic  $x - Q^2$  plot of the pseudodata on Pb used in the EPPS16 analysis at the LHeC (NC+CC, light blue symbols, and charm, dark blue symbols) in Section 6.2.2, and in the  $xFitter$  analysis in Subsec. 6.2.3 (at the LHeC, red symbols, and the FCC-eh, green symbols); the regions explored by currently available data sets (charged lepton and neutrino DIS, DY,  $dAu$  at RHIC and  $pPb$  at the LHC) used in present nPDF analyses [488] are shown for comparison.

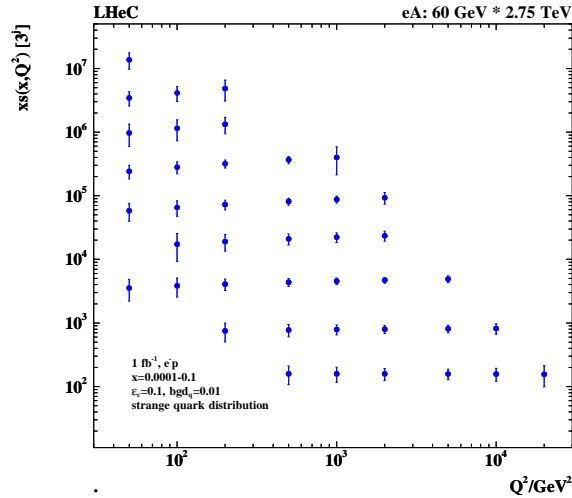


**Figure 6.3:** Simulation of the measurement of the (anti)-strange quark distribution  $x\bar{s}(x, Q^2)$  in charged current  $eA$  scattering through the  $t$ -channel reaction  $W^- \bar{s} \rightarrow c$ . The data are plotted with full systematic and statistical errors added in quadrature.

3963 Moreover, an additional systematic error is assumed in the simulated NC (CC) measurements  
 3964 of 3 (5) %. These result in very promising measurements of the heavier quark distributions: to  
 3965 about 10 – 20 % total uncertainty on the strange and 3 – 5 % on the charm and beauty mea-  
 3966 surements, for typically  $x$  between  $10^{-4}$  and 0.1 and  $Q^2$  extending from below threshold  $m_Q^2$  up  
 3967 to a few times  $10^4$   $\text{GeV}^2$ . The knowledge of the heavy quark densities is of prime relevance for  
 3968 understanding nuclear structure and the development of QCD as has often been emphasised.

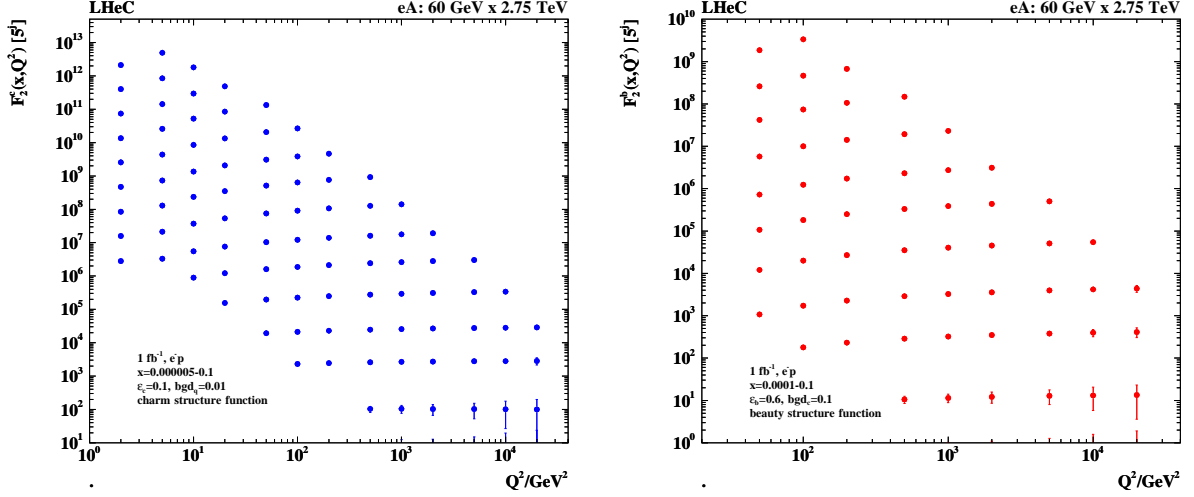


**Figure 6.4:** Left: Simulation of the measurement of the charm quark distribution expressed as  $F_2^c = e_c^2 x(c + \bar{c})$  in neutral current  $eA$  scattering; Right: Simulation of the measurement of the bottom quark distribution expressed as  $F_2^b = e_b^2 x(b + \bar{b})$  in neutral current  $eA$  scattering. The data are plotted with full systematic and statistical errors added in quadrature.

## 6.2.2 Nuclear gluon PDFs in a global-fit context

To illustrate the impact of the LHeC  $ePb$  pseudodata in the global context, they have been added [516] into the EPPS16 global analysis of nuclear PDFs [488]. The EPPS16 strategy is to parametrise the nuclear modification ratios  $R_i(x, Q^2)$  between the bound-proton PDFs  $f_i^{p/Pb}$  and proton PDFs  $f_i^p$ ,

$$R_i(x, Q^2) \equiv \frac{f_i^{p/Pb}(x, Q^2)}{f_i^p(x, Q^2)}, \quad (6.2)$$

at the charm mass threshold  $Q^2 = m_{charm}^2 = (1.3 \text{ GeV})^2$ . At higher  $Q^2$  the nuclear PDFs are obtained by solving the standard DGLAP evolution equations at next-to-leading order in QCD. As the LHeC pseudodata reach to significantly lower  $x$  than the data that were used in the EPPS16 analysis, an extended small- $x$  parametrisation was used for gluons, see Figure 6.5. The framework is almost identical to that in Ref. [517]. The introduced functional form allows for rather wild – arguably unphysical – behaviour at small- $x$  where e.g. significant enhancement is allowed. This is contrary to the theoretical expectations from the saturation conjecture and looks also to be an improbable scenario given the recent LHCb D and B meson measurements [518,519] which impressively indicate [520] gluon shadowing down to  $x \sim 10^{-5}$  at interaction scales as low as  $Q^2 \sim m_{charm}^2$ . On the other hand, given that there are no prior DIS measurements in this kinematic range for nuclei other than the proton, and that the D and B meson production in  $pPb$  collisions could be affected by strong final-state effects (which could eventually be resolved by e.g. measurements of forward prompt photons [521] in  $pPb$ ), we hypothesise that any kind of behaviour is possible at this stage. Anyway, with the extended parametrisation – called here EPPS16\* – the uncertainties in the small- $x$  regime get significantly larger than in the standard EPPS16 set. This is reflected as significantly larger PDF error bands in comparison to the projected LHeC pseudodata. It is shown in Figure 6.6 where EPPS16\* predictions are compared with the LHeC pseudodata for inclusive NC and CC reactions, as well as charm production in neutral-current scattering. The uncertainties are estimated using the Hessian method [522] and the same overall tolerance  $\Delta\chi^2 = 52$  as in the EPPS16 analysis has been used when defining the error bands. Because there are no small- $x$  data constraints for gluons, the

3995 gluon uncertainty is enormous and the Hessian method used for estimating the uncertainties is  
 3996 not particularly accurate, i.e. the true  $\Delta\chi^2 = 52$  error bands are likely to be even larger. At  
 3997 some point the downward uncertainty will be limited by positivity constraints e.g. for  $F_L$ , but  
 3998 will depend strongly on which  $Q^2$  is used to set the positivity constraints (e.g. in the EPPS16  
 3999 analysis  $F_L$  is required to remain positive at  $Q^2 = m_{charm}^2$ ).

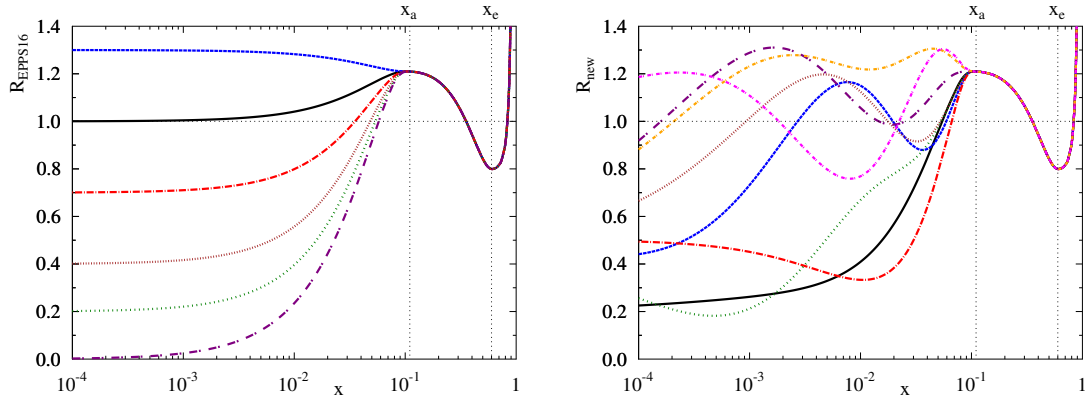


**Figure 6.5:** Left: Illustration of the functional behaviours allowed at small  $x$  in the EPPS16 analysis. Right: Illustration of the possible functional variations at small  $x$  in the extended parametrisation that we employ here.

4000 Upon including the LHeC  $e$ Pb pseudodata in the fit, the new nPDFs adapt to reproduce the  
 4001 pseudodata and their uncertainties are greatly reduced, as shown in Figure 6.7. The overall  
 4002 tolerance has been kept fixed to the default value  $\Delta\chi^2 = 52$ . The impact on the nuclear  
 4003 modification of the gluon PDF is illustrated in Figure 6.8 at two values of  $Q^2$ :  $Q^2 = 1.69 \text{ GeV}^2$   
 4004 (the parametrisation scale) and  $Q^2 = 10 \text{ GeV}^2$ . Already the inclusive pseudodata are able to  
 4005 reduce the small- $x$  gluon uncertainty quite significantly, and the addition of the charm data  
 4006 promises an even more dramatic reduction in the errors. The analysis indicates that the LHeC  
 4007 will nail the nuclear gluon PDF to a high precision down to  $x$  of at least  $10^{-5}$ .

### 4008 6.2.3 nPDFs from DIS on a single nucleus

4009 Another approach that becomes possible with the large kinematic coverage and volume of data  
 4010 for a single nucleus, Pb, at the LHeC and FCC-eh, is to perform a fit to only Pb data in order  
 4011 to extract the Pb PDFs, removing the need to interpolate between different nuclei. Then the  
 4012 corresponding ratios or nuclear modification factors for each parton species can be obtained  
 4013 using either a proton PDF set from a global fit or, as we do here (see [13, 523, 524]), from a  
 4014 fit to proton LHeC and FCC-eh pseudodata. In this way, there will be no need to introduce a  
 4015 nuclear size dependence in the parameters for the initial condition for DGLAP evolution. Such  
 4016 nPDFs can then be used for comparing to those obtained from global fits and for precision tests  
 4017 of collinear factorisation in nuclear collisions.

4018 The fits are performed using *xFitter* [525], where 484 (150) NC+CC Pb data points at the LHeC  
 4019 (FCC-eh) have been used in the fitted region  $Q^2 > 3.5 \text{ GeV}^2$ , see Fig. 6.2. A HERAPDF2.0-  
 4020 type parametrisation [43] has been employed to provide both the central values for the reduced  
 4021 cross sections (therefore, the extracted nuclear modification factors are centered at 1) and the  
 4022 fit functional form; in this way, neither theory uncertainties (treatment of heavy flavours, value  
 4023 of  $\alpha_s$ , order in the perturbative expansion) nor the uncertainty related to the functional form  
 4024 of the initial condition – parametrisation bias – are considered in our study, in agreement  
 4025 with our goal of estimating the *ultimate achievable experimental* precision in the extraction of



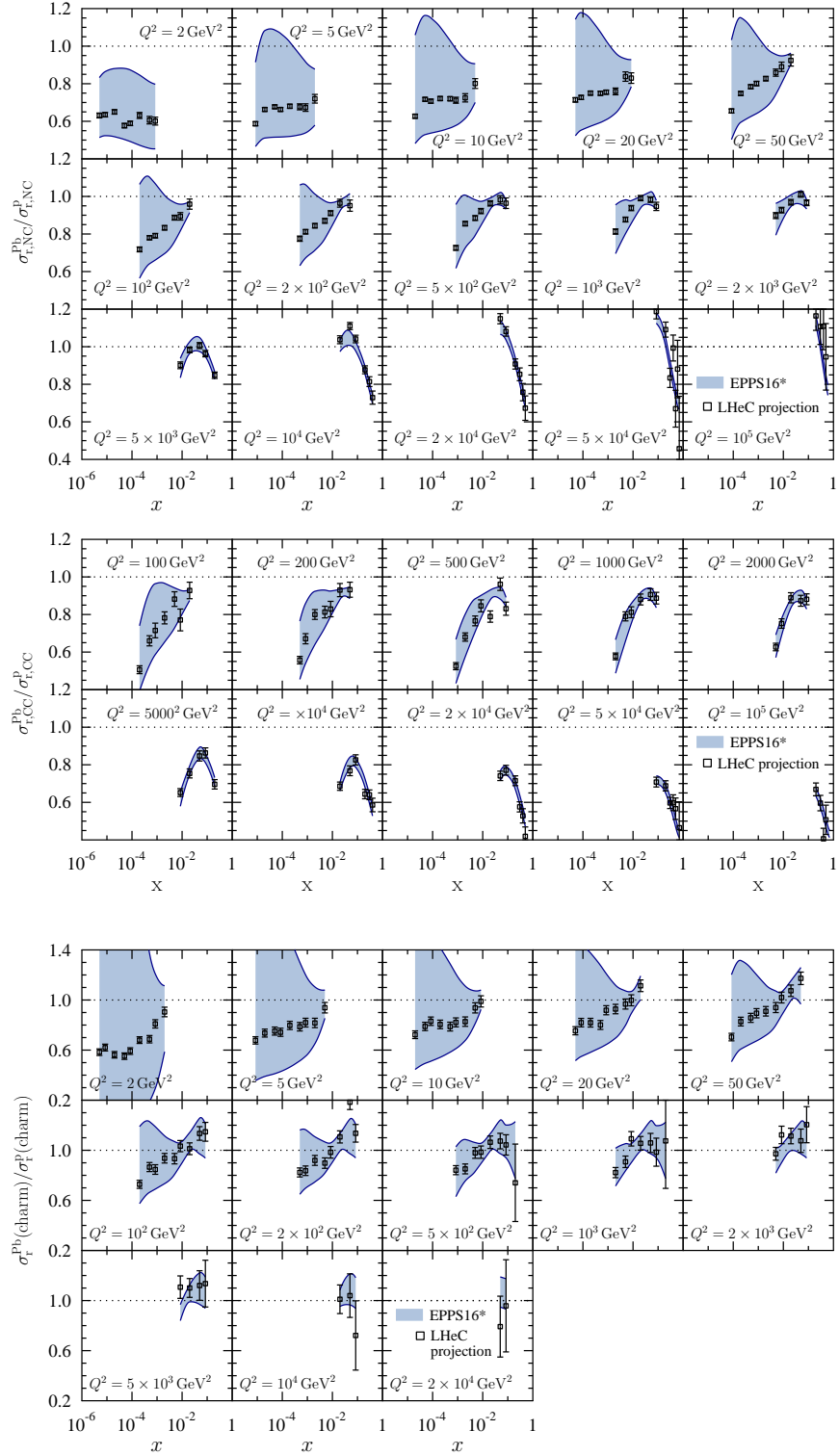


**Figure 6.6:** Top: Simulated ratios of neutral-current reduced cross sections between  $e\text{Pb}$  and  $ep$  collisions compared with the predictions from a EPPS16-type global fit of nuclear PDFs using an extended parametrisation for gluons. Middle: Charged-current cross section ratios. Bottom: Neutral-current charm-production cross section ratios.

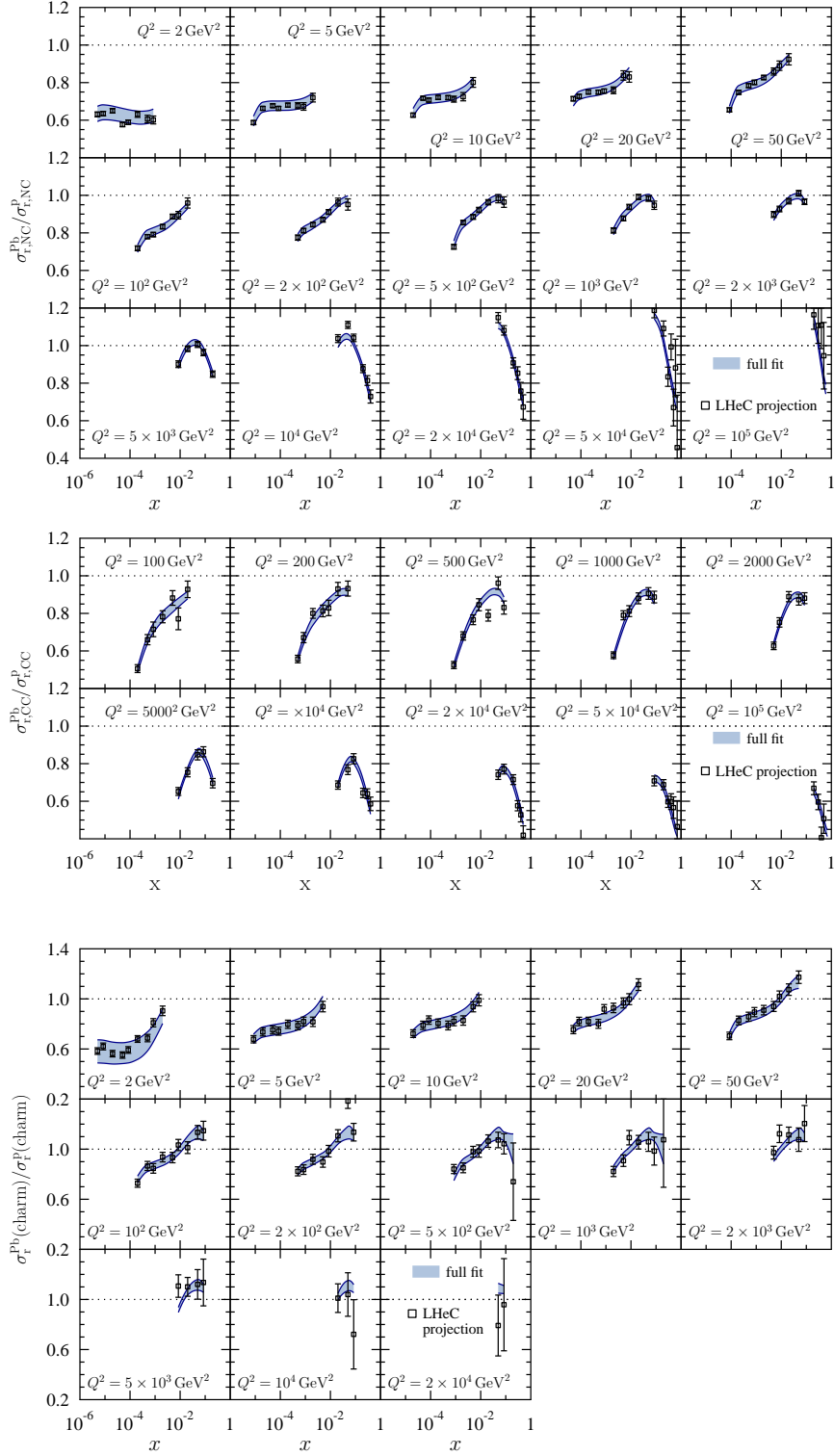


**Figure 6.7:** As Figure 6.6 but with fit results after including the LHeC pseudodata in the global analysis.

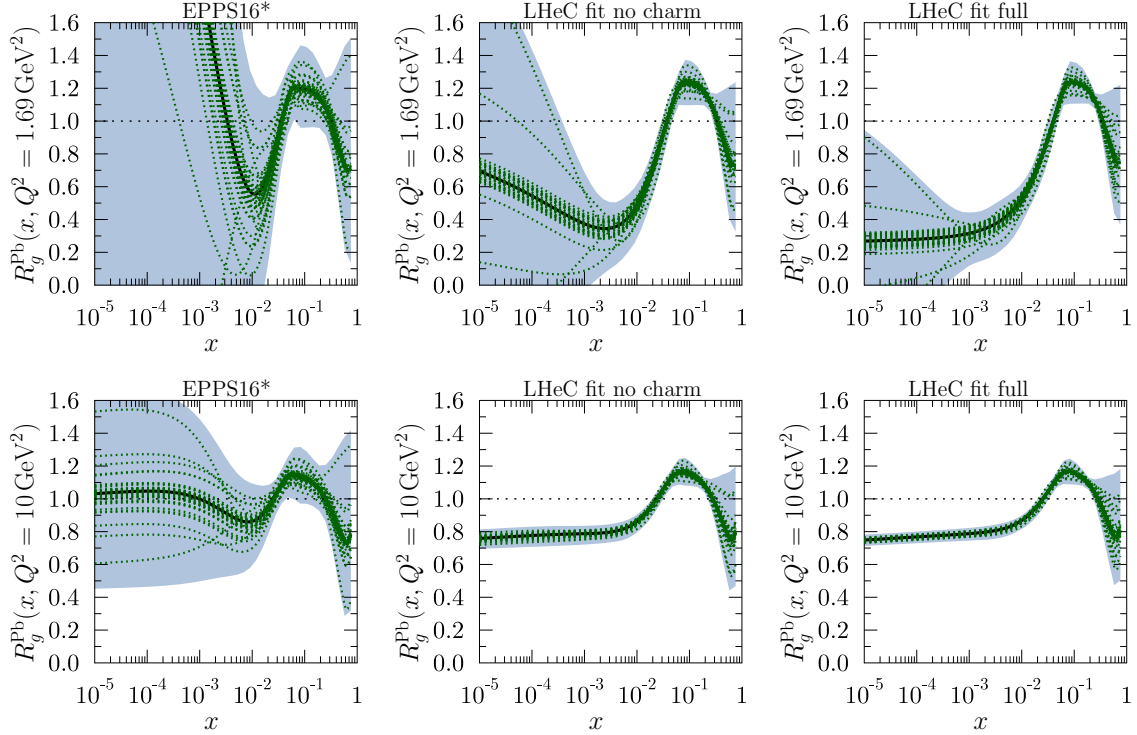


**Figure 6.8:** Upper panels: The gluon nuclear modification for the Pb nucleus at  $Q^2 = 1.69 \text{ GeV}^2$  in EPPS16\* (left), LHeC analysis without charm pseudodata (middle), and full LHeC analysis (right). The blue bands mark the total uncertainty and the green dotted curves correspond to individual Hessian error sets. Lower panels: As the upper panels but at  $Q^2 = 10 \text{ GeV}^2$ .

4026 nPDFs. We have worked at NNLO using the Roberts-Thorne improved heavy quark scheme,  
 4027 and  $\alpha_s(m_Z^2) = 0.118$ . The treatment of systematics and the tolerance  $\Delta\chi^2 = 1$  are identical to  
 4028 the approach in the HERAPDF2.0 fits, as achievable in a single experiment.

4029 The results for the relative uncertainties in the nuclear modification factors are shown in Figs. 6.9,  
 4030 6.10 and 6.11 for valence, sea and gluon, respectively. The uncertainties in these plots reflect  
 4031 the assumed uncertainties in the pseudodata, both statistics (mainly at large  $x$ ) and systematics  
 4032 from detector efficiencies, radiative corrections, etc., see Sec. 6.2.1. As expected, the uncertainty  
 4033 in the extraction of the valence at small  $x$  is sizeably larger than that for the sea and gluon.

4034 While a very high precision looks achievable at the LHeC and the FCC-eh, for the comparison  
 4035 with EPPS16 (or any other global fit) shown in the plots and with previous results including  
 4036 LHeC pseudodata in that setup, see Sect. 6.2.2 and [516,517], some caution is required. First, the  
 4037 effective EPPS16 tolerance criterion  $\Delta\chi^2 \simeq 52$  implies that naively the uncertainty bands should  
 4038 be compared after rescaling by a factor  $\sqrt{52}$ . Second, the treatment of systematics is rather  
 4039 different, considering correlations in the *xFitter* exercise and taking them as fully uncorrelated  
 4040 (and added quadratically to the statistical ones) in the EPPS16 approach. Finally, EPPS16  
 4041 uses parametrisations for the nuclear modification factors for different parton species while in  
 4042 *xFitter* just the (n)PDF combinations that enter the reduced cross sections are parametrised  
 4043 and employed for the fit <sup>3</sup>. With all these considerations in mind, the results shown in this  
 4044 Section are fully compatible with those in the previous one.

<sup>3</sup>In this respect let us note that, in analogy to proton PDFs, a full flavour decomposition can be achieved using both NC and CC with heavy flavour identification that will verify the existing ideas on flavour dependence of nuclear effects on parton densities [514].

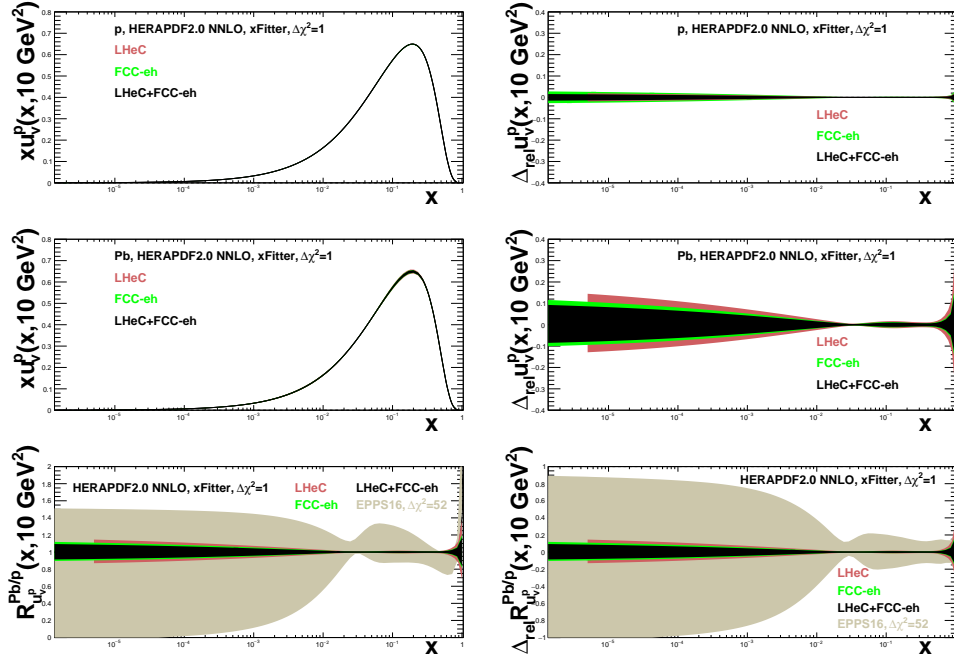


**Figure 6.9:** Distributions (left) and their relative uncertainties (right) of the valence  $u$ -quark density in the proton (top), Pb (middle) and the corresponding nuclear modification factor (bottom) in an analysis of  $ep$  and  $e\text{Pb}$  LHeC and FCC-eh NC plus CC pseudodata using  $x\text{Fitter}$  (both a single set of data and all combined), compared to the results of EPPS16 [488], see the text for details.

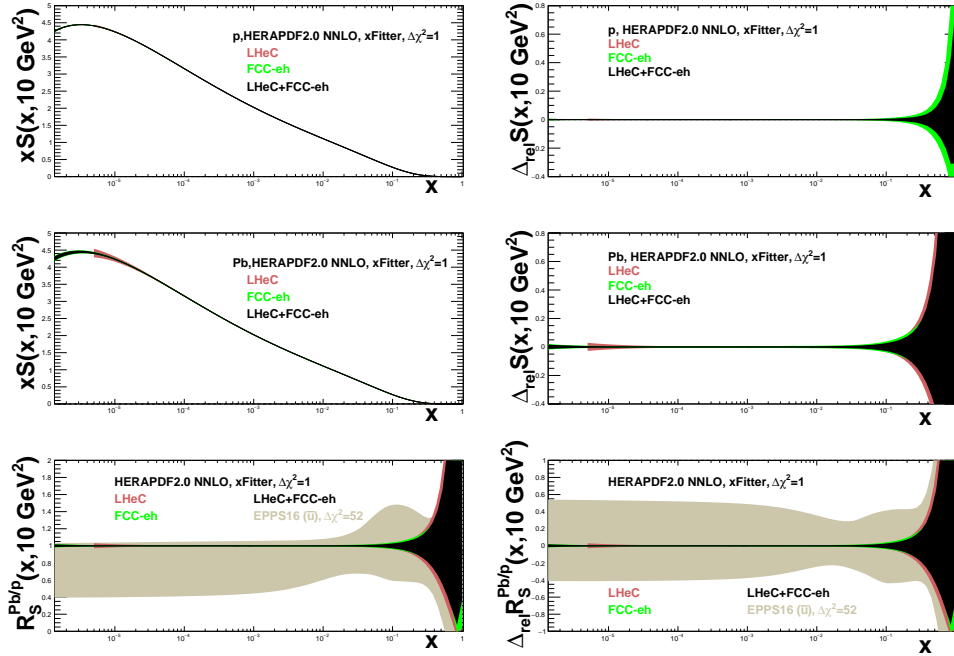


**Figure 6.10:** Distributions (left) and their relative uncertainties (right) of the sea quark density in the proton (top), Pb (middle) and the corresponding nuclear modifications factor (bottom) in an analysis of  $ep$  and  $e\text{Pb}$  LHeC and FCC-eh NC plus CC pseudodata using  $x\text{Fitter}$  (both a single set of data and all combined), compared to the results of EPPS16 [488] for  $\bar{u}$ , see the text for details.

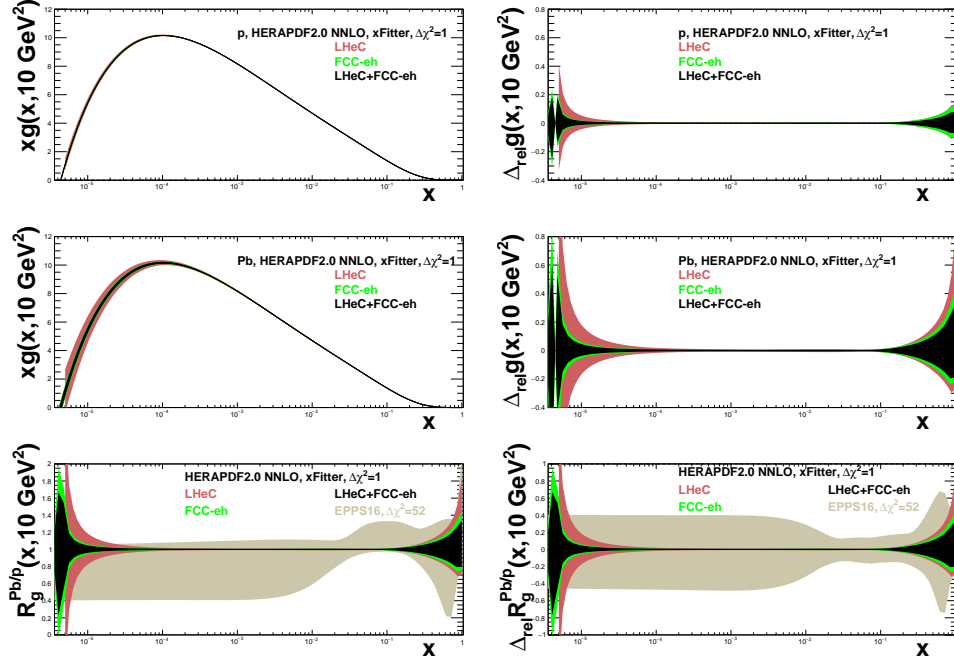


**Figure 6.11:** Distributions (left) and their relative uncertainties (right) of the gluon density in the proton (top), Pb (middle) and the corresponding nuclear modifications factor (bottom) in an analysis of  $ep$  and  $ePb$  LHeC and FCC-eh NC plus CC pseudodata using  $xFitter$  (both a single set of data and all combined), compared to the results of EPPS16 [488], see the text for details.

## 4045 6.3 Nuclear diffraction

4046 In Sec. 3.4 we have discussed specific processes which will probe the details of the 3D structure  
 4047 of the proton. The same processes can be studied in the context of electron-ion scattering  
 4048 and used to learn about the partonic structure of nuclei. Inclusive diffraction on nuclei can  
 4049 provide important information about the nuclear diffractive parton distribution similarly to the  
 4050 diffraction on the proton, see Sec. 4.3. Diffractive vector meson production can be studied in  
 4051 the nuclear case as well, e.g. within the framework of the dipole model suitable for high energy  
 4052 and including non-linear effects in density. In the nuclear case though, one needs to make a  
 4053 distinction between coherent and incoherent diffraction. In the coherent process, the nucleus  
 4054 scatters elastically and stays intact after the collision. In incoherent diffraction, the nucleus  
 4055 breaks up, and individual nucleons can be set free. Still, there will be a large rapidity gap between  
 4056 the produced diffractive system and the dissociated nucleus. It is expected that this process will  
 4057 dominate the diffractive cross section for medium and large values of momentum transfer. It is  
 4058 only in the region of small values of momentum transfer where elastic diffraction is the dominant  
 4059 contribution. Dedicated instrumentation in the forward region must be constructed in order to  
 4060 clearly distinguish between the two scenarios, see Chapter 10.

### 4061 6.3.1 Exclusive vector meson diffraction

4062 Calculations for the case of Pb for the coherent diffractive  $J/\psi$  production were performed  
 4063 using the dipole model [121], see Sec. 3.4. In order to apply the dipole model calculation to the  
 4064 nuclear case, one takes the independent scattering approximation that is Glauber theory [526].

4065 The dipole amplitude can then be represented in the form

$$N_A(x, \mathbf{r}, \mathbf{b}) = 1 - \prod_{i=1}^A [1 - N(x, \mathbf{r}, \mathbf{b} - \mathbf{b}_i)] . \quad (6.3)$$

4066 Here  $N(x, \mathbf{r}, \mathbf{b} - \mathbf{b}_i)$  is the dipole amplitude for the nucleon (see Sec. 3.4) and  $\mathbf{b}_i$  denotes the  
 4067 transverse positions of the nucleons in the nucleus. The interpretation of Eq. (6.3) is that  $1 - N$   
 4068 is the probability not to scatter off an individual nucleon, and thus  $\prod_{i=1}^A [1 - N(\mathbf{r}, \mathbf{b} - \mathbf{b}_i, x)]$  is  
 4069 the probability not to scatter off the entire nucleus.

4070 In addition, the following simulation includes the fluctuations of the density profile in the proton,  
 4071 following the prescription given in [119–121]. To include these proton structure fluctuations one  
 4072 assumes that the gluonic density of the proton in the transverse plane is distributed around  
 4073 three constituent quarks (hot spots). These hot spots are assumed to be Gaussian. In practical  
 4074 terms one replaces the proton profile  $T_p(\mathbf{b})$

$$T_p(\mathbf{b}) = \frac{1}{2\pi B_p} e^{-b^2/(2B_p)} , \quad (6.4)$$

4075 that appears in each individual nucleon scattering probability  $N(x, \mathbf{r}, \mathbf{b} - \mathbf{b}_i)$  by the function

$$T_p(\mathbf{b}) = \sum_{i=1}^3 T_q(\mathbf{b} - \mathbf{b}_{q,i}) , \quad (6.5)$$

4076 where the ‘quark’ density profile is given by

$$T_q(\mathbf{b}) = \frac{1}{2\pi B_q} e^{-b^2/(2B_q)} . \quad (6.6)$$

4077 Here  $\mathbf{b}_{q,i}$  are the location of the hotspots that are sampled from a two dimensional Gaussian  
 4078 distribution whose width is given by parameter  $B_{qc}$ . The free parameters  $B_q$  and  $B_{qc}$  were  
 4079 obtained in [120] by comparing with HERA data on coherent and incoherent  $J/\psi$  production at  
 4080 a photon-proton centre-of-mass energy  $W = 75$  GeV, corresponding to fractional hadronic target  
 4081 energy loss  $x_{IP} = 10^{-3}$ . The proton fluctuation parameters obtained are  $B_{qc} = 3.3$  GeV<sup>-2</sup> and  
 4082  $B_q = 0.7$  GeV<sup>-2</sup>.

4083 The results for the differential cross section at  $t = 0$  for coherent production of  $J/\psi$  as a  
 4084 function of (virtual) photon-proton energy  $W$  for fixed values of  $Q^2$  are shown in Figs. 6.12  
 4085 and Figs. 6.13. The calculations for Pb are compared to those on the proton target. We see  
 4086 that the cross sections for the nuclear case increase with energy slower than for the proton case  
 4087 and are always smaller. Note that, we have already rescaled the diffractive cross section by  
 4088 a factor  $A^2$ , as appropriate for comparison of the diffractive cross section on the proton and  
 4089 nucleus. In the absence of nuclear corrections their ratio should be equal to 1. The differences  
 4090 between the scattering off a nucleus and a proton are also a function of  $Q^2$ . They are larger  
 4091 for smaller values of  $Q^2$  and for photoproduction. This is understood from the dipole formulae,  
 4092 see Eqs. (3.23), (3.24), (3.25). As explained previously, larger values of scale  $Q^2$  select smaller  
 4093 size dipoles, for which the density effects are smaller. Similarly, the differences between the lead  
 4094 and proton cases are larger for higher energies. This is because the dipole amplitude grows with  
 4095 decreasing values of  $x$  which are probed when the energy is increased, and thus the non-linear  
 4096 density effects are more prominent at low values of  $x$  and  $Q^2$ .

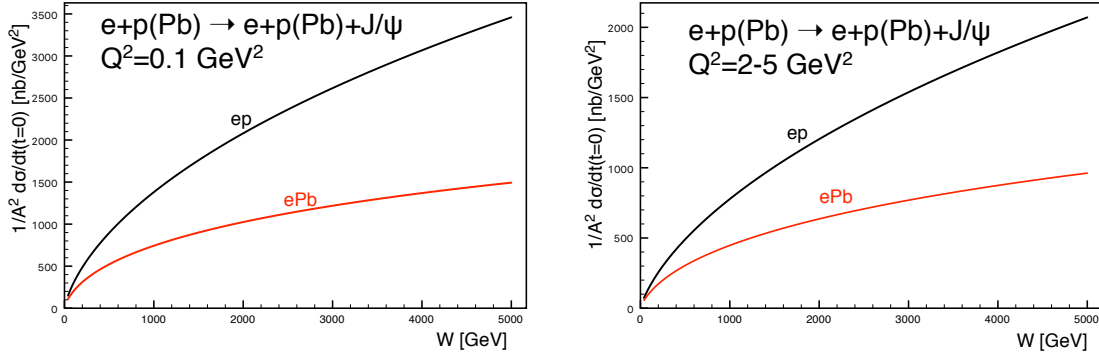


**Figure 6.12:** Cross section for the coherent diffractive production of the vector meson  $J/\psi$  in  $ePb$  (red solid curves) and  $ep$  (black solid curves) collisions, as a function of the energy  $W$ . Left: photoproduction case  $Q^2 \simeq 0$ , right:  $Q^2 = 2 - 5 \text{ GeV}^2$

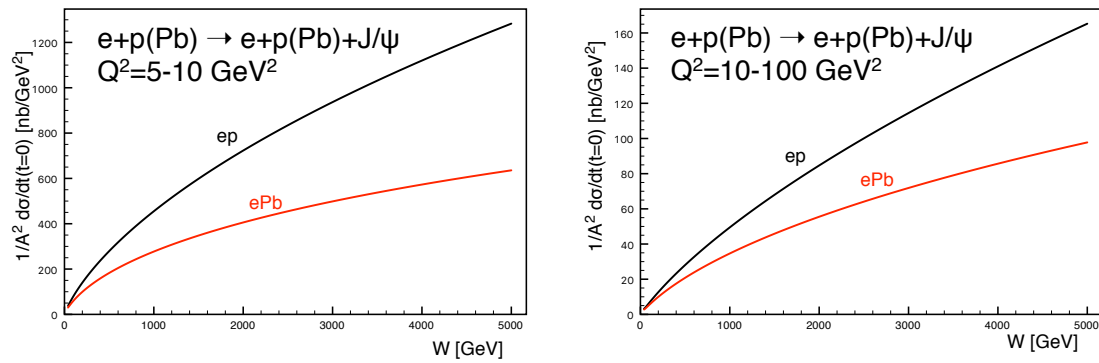


**Figure 6.13:** Cross section for the coherent diffractive production of the vector meson  $J/\psi$  in  $ePb$  (red solid curves) and  $ep$  (black solid curves) collisions, as a function of the energy  $W$ . Left:  $Q^2 = 5 - 10 \text{ GeV}^2$ , right:  $Q^2 = 10 - 100 \text{ GeV}^2$ .

4097 These findings can be summarised by inspecting the ratio of the cross sections, presented as a  
 4098 function of  $x$  defined as<sup>4</sup>

$$x = \frac{Q^2 + m_{J/\psi}^2}{Q^2 + W^2 + m_{J/\psi}^2 - m_N^2} \quad (6.7)$$

4099 which is shown in Fig. 6.14. We observe that the ratio is smaller for smaller values of  $Q^2$ ,  
 4100 and it decreases for decreasing values of  $x$ . The results from the dipole model calculations are  
 4101 compared with the ratio of the gluon density squared (evaluated at  $x$  and  $Q^2$ ) obtained from the  
 4102 nuclear PDFs using the EPPS16 set [488]. The reason why one can compare the diffractive cross  
 4103 section ratios with the ratios for the gluon density squared can be understood from Eqs. (3.23)  
 4104 and (3.24). The diffractive amplitude is proportional to the gluon density  $xg(x, Q^2)$ . On the  
 4105 other hand the diffractive cross section is proportional to the amplitude squared, thus having  
 4106 enhanced sensitivity to the gluon density. The nuclear PDFs have large uncertainties, which is  
 4107 indicated by the region between the two sets of dotted lines. The EPPS16 parametrisation is  
 4108 practically unconstrained in the region below  $x = 0.01$ . Nevertheless, the estimate based on the  
 4109 dipole model calculation and the central value of the EPPS16 parametrisation are consistent  
 4110 with each other. This strongly suggests that it will be hard to disentangle nuclear effects from  
 4111 saturation effects and that only through a detailed combined analysis of data on the proton and

<sup>4</sup>This choice to translate  $W$  and  $Q^2$  into  $x$  in the dipole model calculations differs from others in the literature but the difference is only significant at large  $x$  where the dipole model is not applicable.

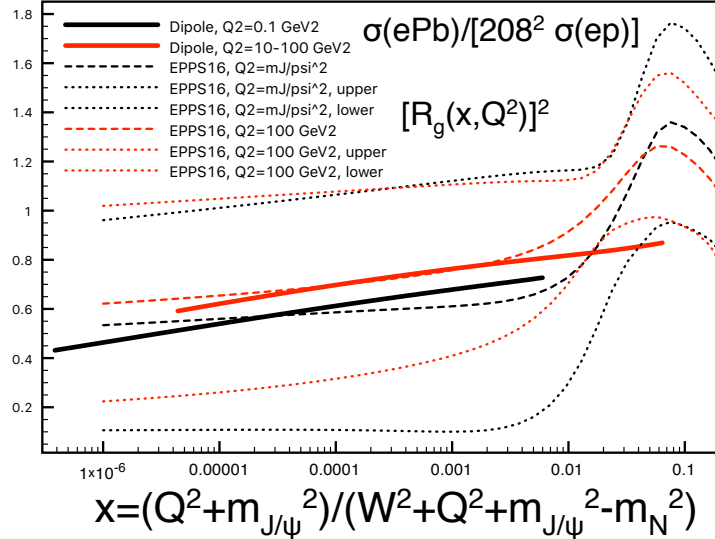


**Figure 6.14:** Ratio of coherent  $J/\psi$  production diffractive cross sections for Pb and proton as a function of the variable  $x$  (defined in Eq. (6.7) for the dipole model results). Solid lines: dipole model calculation, for  $Q^2 = 0.1 \text{ GeV}^2$  (black) and  $Q^2 = 10 - 100 \text{ GeV}^2$  (red). Dotted and dashed lines correspond to the nuclear ratio for the gluon density squared using the EPPS16 parametrisation [488] of the nuclear parton distribution functions. Black and red dashed lines are the central sets for  $Q^2 = M_{J/\psi}^2$  and  $Q^2 = 100 \text{ GeV}^2$ . The dotted lines correspond to the low and high edges of the Hessian uncertainty in the EPPS16 parametrisation. The difference between the two dotted lines is thus indicative of the parametrisation uncertainty for the nuclear ratio. These ratios, that can also be measured in ultraperipheral collisions [126], are larger than the values  $0.2 - 0.4$  at  $x \simeq 10^{-5}$  predicted by the relation between diffraction and nuclear shadowing [491].

4112 the nucleus firm conclusions can be established on the existence of a new non-linear regime of  
4113 QCD.

4114 The differential cross section  $d\sigma/dt$  as a function of the negative four momentum transfer squared  
4115  $-t$  for the case of coherent and incoherent production is shown in Fig. 6.15. Coherent and inco-  
4116 herent diffractive cross sections are computed from the dipole model in the following way. The  
4117 coherent diffractive cross section is obtained by averaging the diffractive scattering amplitude  
4118 over the target configurations and taking the square

$$\frac{d\sigma}{dt} = \frac{1}{16\pi} |\langle \mathcal{A}(x, Q, \Delta) \rangle|^2. \quad (6.8)$$

4119 Here the brackets  $\langle \dots \rangle$  refer to averages over different configurations of the target. The incoher-  
4120 ent cross section is obtained by subtracting the coherent cross section from the total diffractive  
4121 cross section. It is standardly assumed that it takes the form of a variance of the diffractive  
4122 scattering amplitude

$$\frac{d\sigma}{dt} = \frac{1}{16\pi} \left( \langle |\mathcal{A}(x, Q, \Delta)|^2 \rangle - |\langle \mathcal{A}(x, Q, \Delta) \rangle|^2 \right), \quad (6.9)$$

4123 which should be valid for small  $|t|$ . The  $t$  dependence, and the relation between the impact  
4124 parameter and  $t$  through the Fourier transform, makes diffractive scattering a sensitive probe  
4125 of the internal geometric structure of hadrons and nuclei, see Ref. [527] for an extraction of  
4126 the transverse profile of the nucleus in ultraperipheral collisions at RHIC; also Ref. [528] for an  
4127 study for the EIC. In particular, because the incoherent cross section has the form of a variance  
4128 of the amplitude, it is sensitive to the amount of fluctuations in impact parameter space.



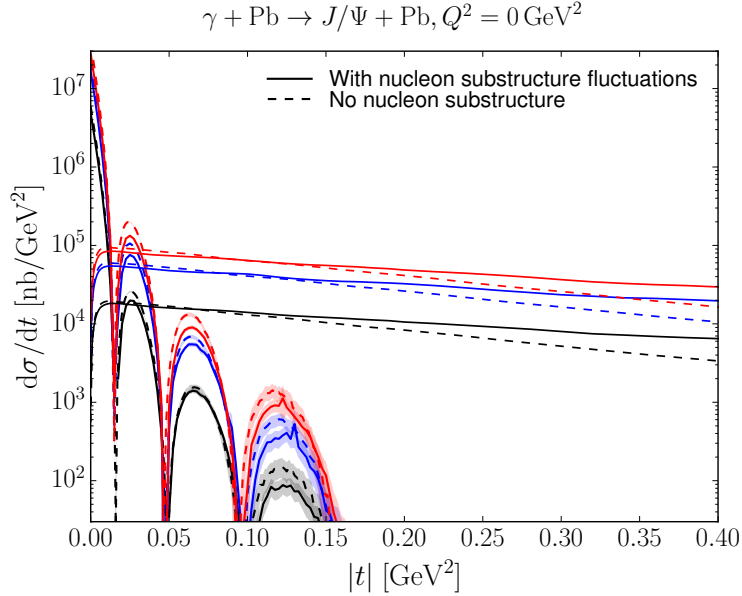


**Figure 6.15:** The differential cross sections for coherent and incoherent production of  $J/\psi$  in  $e\text{Pb}$  as a function of the negative four momentum transfer squared  $-t$ , for photoproduction,  $Q^2 = 0$ . The lines showing dips are for coherent production, and those extending to large  $|t|$  are for incoherent. The solid (dashed) lines are the results with (without) nucleon substructure fluctuations. Black, blue, red are for  $W = 0.1, 0.813, 2.5 \text{ TeV}$ , respectively.

4129 The results in Fig. 6.15 (results for higher  $Q^2$  are very similar) indicate that the incoherent  
 4130 production is dominant for most values of  $-t$ , except for the very small momentum transfers,  
 4131 about  $|t| < 0.02 \text{ GeV}^2$ . Thus, dedicated instrumentation which will allow us to distinguish  
 4132 between the two cases is essential if one wants to measure the coherent process in a reasonably  
 4133 wide range of  $|t|$ . As in the proton case, the coherent  $t$  distribution exhibits characteristic dips.  
 4134 However, in the case of the nuclear targets the dips occur for much smaller values of  $t$ . This is  
 4135 related to the much larger value of the dipole amplitude for a wide range of impact parameters  
 4136 in the case of nuclear targets compared to the proton case.

4137 Another interesting aspect, see Sec. 3.4, is the effect of the transverse structure of the target  
 4138 in nuclear coherent and incoherent diffraction [529]. For example, in the formulation shown  
 4139 above [121] a fixed number of hot spots was considered, while in [125] (see also [122] for a  
 4140 realisation using small- $x$  evolution) a growing number with  $1/x$  is implemented. In both cases,  
 4141 the ratio of incoherent to coherent diffraction decreases with  $W$ , being smaller for larger nuclei.  
 4142 This decrease is sensitive to the details of the distribution of hot spots - thus, to the fluctuations  
 4143 of the gluon distribution in transverse space. It also shows interesting dependencies on the  
 4144 mass of the produced vector meson and on  $Q^2$ , resulting in the ratio being smaller for lighter  
 4145 vector mesons and for lower  $Q^2$ . Besides, the hot spot treatment also has some effects on the  
 4146 distributions in momentum transfer, see Fig. 6.15. In order to check these ideas, both the  
 4147 experimental capability to separate coherent from incoherent diffraction, and a large lever arm  
 4148 in  $W$  and  $Q^2$  as available at the LHeC, are required.

4149 We thus conclude that by investigating coherent and incoherent diffractive scattering on nuclei,  
 4150 one gets unique insight into the spatial structure of matter in nuclei. On the one hand, the  
 4151 coherent cross section, which is obtained by averaging the amplitude before squaring it, is  
 4152 sensitive to the average spatial density distribution of gluons in transverse space. On the other  
 4153 hand, the incoherent cross section, which is governed by the variance of the amplitude with

4154 respect to the initial nucleon configurations of the nucleus, measures fluctuations of the gluon  
4155 density inside the nucleus. In the case of a nucleus, the diffractive production rate is controlled by  
4156 two different scales related to the proton and nucleus size. At momentum scales corresponding  
4157 to the nucleon size  $|t| \sim 1/R_p^2$  the diffractive cross section is almost purely incoherent. The  
4158  $t$ -distribution in coherent diffractive production off the nucleus gives rise to a dip-type structure  
4159 for both saturation and non-saturation models, while in the case of incoherent production at  
4160 small  $|t|$ , both saturation and non-saturation models do not lead to dips [121]. This is in drastic  
4161 contrast to the diffractive production off the proton where only saturation models lead to a  
4162 dip-type structure in the  $t$ -distribution at values of  $|t|$  that can be experimentally accessible.  
4163 Therefore, diffractive production offers a unique opportunity to measure the spatial distribution  
4164 of partons in the protons and nuclei. It is also an excellent tool to investigate the approach to  
4165 unitarity in the high energy limit of QCD.

4166 While we have focused here on  $J/\psi$  production, lighter vector mesons like  $\rho, \omega, \phi$  could also be  
4167 studied. They should show a different  $Q^2$  dependence and their larger sizes would make them  
4168 lie closer to the black disk regime. Also the dominance of two-jet events in photoproduction  
4169 would provide sensitivity to the approach to the unitarity limit [491].

### 4170 6.3.2 Inclusive diffraction on nuclei

4171 In Sec. 4.3, a study of the prospects for extracting diffractive parton densities in the proton was  
4172 presented following [327]. Similar considerations apply to diffraction in  $eA$  as to  $ep$  collisions.  
4173 The main difference is the larger contribution from incoherent diffraction <sup>5</sup>  $e + A \rightarrow e + X + A^*$   
4174 than from coherent diffraction  $e + A \rightarrow e + X + A$ , the former dominating for  $|t|$  larger than  
4175 a few hundredths of a  $\text{GeV}^2$ . In the following we focus on coherent diffraction, which could be  
4176 distinguished from the incoherent case using forward detectors [1].

4177 Assuming the same framework (collinear factorization for hard diffraction, such that Eq. (4.14),  
4178 and Regge factorization, Eq. (4.16) as introduced for  $ep$  in Sec. 4.3 also hold for  $eA$ ), nuclear  
4179 diffractive PDFs (nDPDFs) can be extracted from the diffractive reduced cross sections. It  
4180 should be noted that such nDPDFs have never been measured. With the same electron energy  
4181  $E_e = 60 \text{ GeV}$  and nuclear beams with  $E_N = 2.76 \text{ TeV/nucleon}$  for the LHeC, the kinematic  
4182 coverage is very similar to that shown in Fig. 4.20. For details, see Ref. [327].

4183 The nuclear modification factors for  $F_2^{D(3)}$  and  $F_L^{D(3)}$  from the FGS models [491] are shown in  
4184 Fig. 6.16 where, in analogy to Eq. (6.1), the diffractive nuclear modification factor reads

$$R_k^A(\beta, \xi, Q^2) = \frac{f_{k/A}^{D(3)}(\beta, \xi, Q^2)}{A f_{k/p}^{D(3)}(\beta, \xi, Q^2)}. \quad (6.10)$$

4185 The model in [491] employs Gribov inelastic shadowing [323] which relates diffraction in  $ep$   
4186 to nuclear shadowing for total and diffractive  $eA$  cross sections. It assumes that the nuclear  
4187 wave function squared can be approximated by the product of one-nucleon densities, neglects  
4188 the  $t$ -dependence of the diffractive  $\gamma^*$ -nucleon amplitude compared to the nuclear form factor,  
4189 introduces a real part in the amplitudes [530], and considers the colour fluctuation formalism  
4190 for the inelastic intermediate nucleon states [531]. There are two variants of the model, named  
4191 H and L, corresponding to different strengths of the colour fluctuations, giving rise to larger and  
4192 smaller probabilities for diffraction in nuclei with respect to that in proton, respectively. Results  
4193 from both model versions are shown in Figs. 6.16 and 6.17.

<sup>5</sup> $A^*$  denotes a final state in which the nucleus has dissociated to a system of at least two hadrons, but the rapidity gap signature that defines the diffractive event is still present.

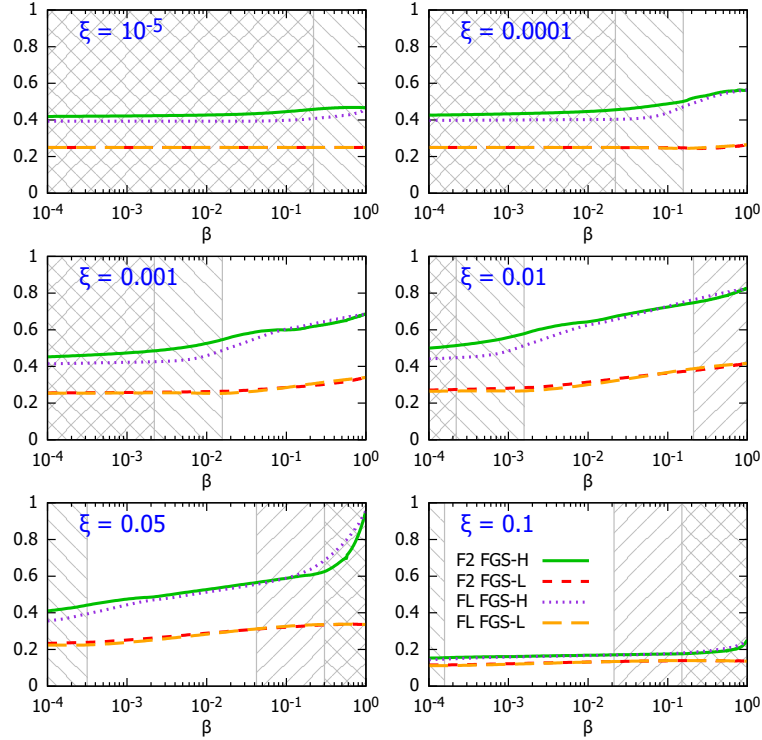


**Figure 6.16:** Nuclear modification factor, Eq. (6.10), for  $F_2^{D(3)}$  and  $F_L^{D(3)}$  in  $^{208}\text{Pb}$  versus  $\beta$ , at  $Q^2 = 10 \text{ GeV}^2$  and for different  $\xi$ , for the models H and L in [491]. The ‘\’ and ‘/’ hatched areas show kinematically excluded regions for  $E = 2.76$  and  $19.7 \text{ TeV/nucleon}$ , respectively.

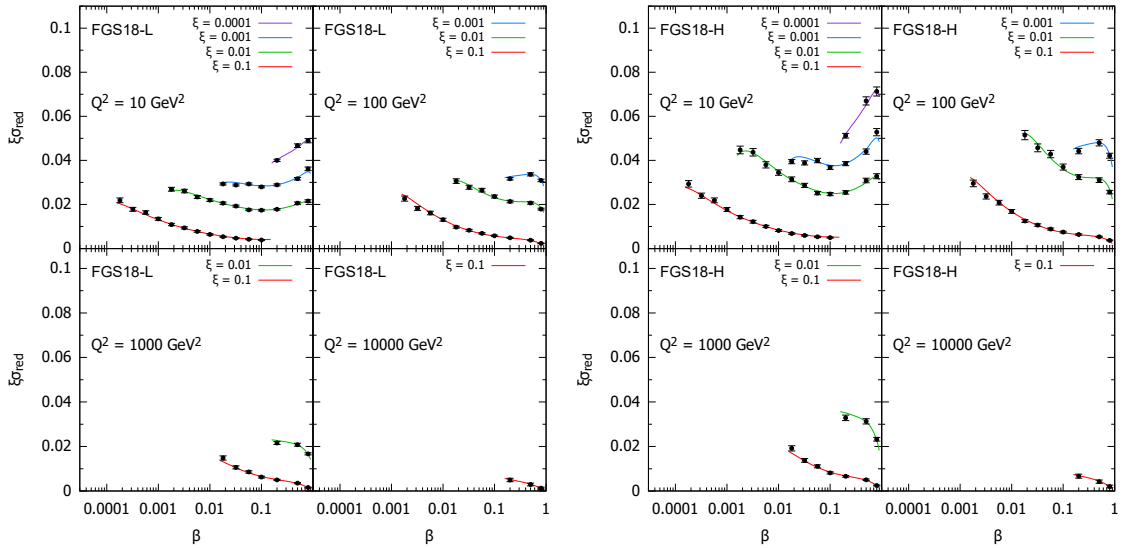


**Figure 6.17:** An indicative subset of simulated data for the diffractive reduced cross section as a function of  $\beta$  in bins of  $\xi$  and  $Q^2$  for  $e^{208}\text{Pb}$  collisions at the LHeC, in the models in [491]. The curves for  $\xi = 0.01, 0.001, 0.0001$  are shifted up by  $0.01, 0.02, 0.03$ , respectively.

4194 The pseudodata for the reduced cross sections are generated assuming 5% systematic error  
 4195 and statistic errors calculated for the integrated luminosity of  $2 \text{ fb}^{-1}$ . A selected subset of  
 4196 the simulated data is shown in Fig. 6.17. The large kinematic coverage and small uncertainty

4197 (dominated by the assumed systematics) illustrated in this figure compared to Fig. 4.22 make it  
 4198 clear that an accurate extraction of nDPDFs in  $^{208}\text{Pb}$  in an extended kinematic region, similar  
 4199 to that shown in Figs. 4.23 and 4.24, will be possible.

## 4200 6.4 New Dynamics at Small $x$ with Nuclear Targets

4201 As discussed in Sec. 4.2.1, theoretical expectations [493] indicate that fixed-order perturbation  
 4202 theory leading to the DGLAP evolution equations should eventually fail. When  $x$  decreases,  
 4203  $\alpha_s \ln 1/x$  becomes large and these large logarithms must be resummed, leading to the BFKL  
 4204 equation. Furthermore, when the parton density becomes large, the linear approximation that  
 4205 underlies both DGLAP and BFKL breaks, and non-linear processes must be taken into account  
 4206 to compute parton evolution. The CGC [492] offers a non-perturbative but weak coupling  
 4207 effective theory to treat dense parton systems in a systematic and controlled way. One of the  
 4208 important predictions of the CGC is that in a dense parton system saturation occurs leading to  
 4209 the emergence of a new dynamical scale – the saturation scale  $Q_{sat}$ , which increases with the  
 4210 energy.

4211 The parton density in a hadron becomes high both through evolution – when energy or  $1/x$   
 4212 becomes large, and/or when partons are accumulated by overlapping nucleons – when mass  
 4213 number  $A$  becomes large in a nucleus. In the nucleus rest frame, the virtual photon fluctuations  
 4214 at small  $x < (2m_N R_A)^{-1}$ , with  $m_N$  the nucleon mass and  $R_A$  the nuclear radius, acquire  
 4215 a lifetime larger than the time taken to traverse the nucleus and, thus, all partons within a  
 4216 transverse area  $\sim 1/Q^2$  are simultaneously probed. Actually, the parameter determining the  
 4217 transition between linear and non-linear dynamics is the parton density and, therefore, the onset  
 4218 of this new regime of QCD and its explanation must be tested, as commented in [1], exploring  
 4219 both decreasing values of  $x$  and increasing values of  $A$  in a kinematic  $x - Q^2$  region where,  
 4220 in order to be sensitive to differences in evolution, enough lever arm in  $Q^2 \gg \Lambda_{\text{QCD}}^2$  at small  
 4221  $x$  is available. The saturation scale  $Q_{sat}$  that characterises the typical gluon momentum in  
 4222 a saturated hadron wave function increases with nuclear size,  $Q_{sat}^2 \propto A^{1/3}$ . Therefore, in  $eA$   
 4223 collisions the perturbatively saturated regime is achieved at parametrically larger  $x$  than in a  
 4224 proton – a prediction not only of the CGC but of all multiple scattering models that anticipate  
 4225 an approach to the black disk, unitarity limit.

4226 The opportunities to establish the existence of saturation in lepton-nucleus collisions are nu-  
 4227 merous. They include inclusive observables, both total and diffractive cross sections, and less  
 4228 inclusive ones like correlations:

- 4229 • Tension in DGLAP fits for inclusive observables: As discussed in [1,254] and in Sec. 4.2.2,  
 4230 deviations from fixed-order perturbation theory can be tested by the tension that would  
 4231 appear in the description within a DGLAP fit of observables with different sensitivities to  
 4232 the sea and the glue, for example  $F_2$  and  $F_L$  (or reduced cross sections at different energies)  
 4233 or  $F_2^{\text{inclusive}}$  and  $F_2^{\text{heavy quarks}}$ . In [532], such an exercise was performed considering  $F_2$  and  
 4234  $F_L$  pseudodata for  $e\text{Au}$  collisions at the EIC [99] using reweighting techniques. While the  
 4235 results for EIC energies are shown not to be conclusive due to the reduced lever arm in  
 4236  $Q^2 > Q_{sat}^2 \gg \Lambda_{\text{QCD}}^2$ , the much larger centre-of-mass energies at the LHeC (and FCC-eh)  
 4237 should make possible a search for tensions between different observables.
- 4238 • Saturation effects in diffraction: A longstanding prediction of saturation [105, 533, 534]  
 4239 is a modification of the diffractive cross section in nuclei with respect to protons, with  
 4240 a suppression (enhancement) at small (large)  $\beta$  due to the approach of the nucleus to  
 4241 the black disk limit, where elastic and diffractive scattering become maximal, and the

behaviour of the different Fock components of the virtual photon wave function. Such effects can also be discussed in terms of a competition of nuclear shadowing with the probability that the event remains diffractive in the multiple scattering process [491]. This leads to the generic expectation of an enhancement of the ratio of the coherent diffractive cross section in nucleus over that in protons, in non-linear approaches with respect to linear ones [99].

- **Correlations:** Correlations have been considered for a long time as sensitive probes of the underlying production dynamics. For example, the cross section for the production of two jets with the same hardness and widely separated in rapidity, called Mueller-Navelet jets [535], was proposed as a test of BFKL versus DGLAP dynamics, but the effect of saturation has not been widely studied although it has the large potentiality of differentiating linear resummation from non-linear saturation where non-trivial nuclear effects could appear. Correlations between jets were analysed in [1] for the LHeC kinematics, both in inclusive and diffractive events, see the formalism in [536]. On the other hand, the azimuthal decorrelation of particles and jets when saturation effects are at work – at small  $x$ , studied by the difference between collisions involving proton and nuclei, was proposed long ago in  $d$ Au collisions at the Relativistic Hadron Collider [537, 538]. It was studied in [1] for the LHeC kinematics, see recent developments in [539] and the extension to forward dijet production in [540]. It could also be analysed in ultraperipheral collisions at the LHC, see Sec. 9.7.

## 6.5 Collective effects in dense environments – the ‘ridge’

One of the most striking discoveries [541] at the LHC is, that in all collision systems, from small ( $pp$  and  $pA$ ) to large ( $AA$ ), many of the features that are considered as indicative of the production of a dense hot partonic medium are observed (see e.g. reviews [542–544] and references therein). The most celebrated of such features is the long rapidity range particle correlations collimated in azimuth, named the ‘ridge’, shown in Fig. 6.18. The dynamics underlying this phenomena, either the formation of QGP and the existence of strong final state interactions, or some initial state dynamics that leaves imprint on the final observables, is under discussion [545]. While observed in photoproduction on Pb in UPCs at the LHC [546], its existence in smaller systems like  $e^+e^-$  [547] at LEP and  $ep$  at HERA [548] has been scrutinised, but the results are not conclusive.

In this respect, measurements in  $ep$  and  $eA$  collisions at the LHeC at considerable center-of-mass energies will offer crucial additional information. For example, the collision of the virtual photon with the proton at the LHeC can be considered as a high energy collision of two jets or ‘flux tubes’, as discussed in Refs. [551, 552] and illustrated in Fig. 6.18. This can lead to the production of ‘ridges’ and other novel configurations of gluons and quarks and will be measured uniquely at the LHeC.

## 6.6 Novel QCD Nuclear Phenomena at the LHeC

Beyond the topics discussed above there are many novel phenomena which can be explored in  $eA$  collisions at LHeC or FCC-eh, in a high energy regime and using dedicated instrumentation. We shall briefly review some of these phenomena, which can be understood utilizing the light-front framework of QCD, for a review see [553].

One of the most important theoretical tools in high energy physics is Dirac’s light-front (LF)

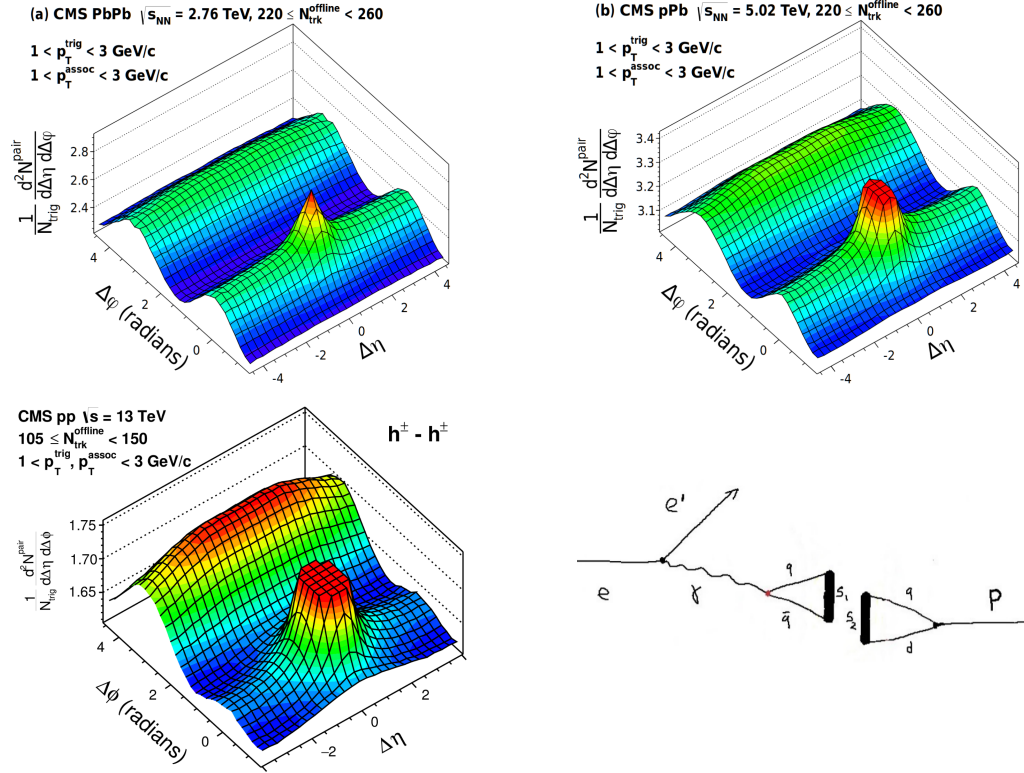


**Figure 6.18:** Left and top right: Collective effects seen in high-multiplicity two-particle azimuthal correlation, as observed by CMS in PbPb, pPb [549], and pp [550] collisions. Bottom right: Schematic illustration for the production of *ridge*-like effects in ep or eA scattering at the LHeC [551].

4285 time:  $\tau = x^+ = t + z/c$ , the time along the light-front [554], a concept which allows all of the  
 4286 tools and insights of Schrödinger's quantum mechanics and the Hamiltonian formalism to be  
 4287 applied to relativistic physics [553]. When one takes a photograph, the object is observed at a  
 4288 fixed LF time. Similarly, Compton  $\gamma p \rightarrow \gamma' p''$  and deep-inelastic lepton-proton scattering are  
 4289 measurements of proton structure at fixed LF time. Unlike ordinary *instant time*  $t$ , physics at  
 4290 fixed  $\tau$  is Poincaré invariant; i.e. independent of the observer's Lorentz frame. Observations  
 4291 at fixed  $\tau$  are made within the causal horizon. LF time  $\tau$  reduces to ordinary time  $t$  in the  
 4292 nonrelativistic limit  $c \rightarrow \infty$ .

4293 The LF wavefunctions (LFWF) of hadrons are superpositions of  $\Psi_n^H(x_i, \vec{k}_{\perp i}, \lambda_i) = \langle \Psi_H | n \rangle$ ,  
 4294 the Fock state projections of the eigensolution of the QCD LF Hamiltonian  $H_{QCD} | \Psi_H \rangle =$   
 4295  $M_H^2 | \Psi_H \rangle$ . They encode the underlying structure of bound states in quantum field theory and  
 4296 underlie virtually every observable in hadron physics. Hadronic LFWFs can also be measured  
 4297 directly by the Ashery method [555], the coherent diffractive dissociation of high energy hadrons  
 4298 into jets [556, 557]. In the diffractive dissociation of a high energy hadron into quark and gluon  
 4299 jets by two-gluon exchange, the cross-section measures the square of the second transverse  
 4300 derivative of the projectile LFWF. Similarly, the dissociation of a high energy atom such as  
 4301 positronium or *true muonium* ( $[\mu^+ \mu^-]$ ) can be used to measure the transverse derivative of its  
 4302 LFWFs.

4303 Hadronic LFWFs are defined at fixed  $\tau = -x^+ = t + z/c$ ; they are thus off-shell in the total  
 4304  $P^- = P^0 - P^z$ , not energy  $P^0$  [553]. Thus LFWFs are also off-shell in  $\mathcal{M}^2 = P^+ P^- - P_{\perp}^2 =$   
 4305  $[\sum_i k_i^{\mu}]^2 = \sum_i \frac{k_{\perp}^2 + m^2}{x}_i$ , the invariant mass squared of the constituents in the  $n$ -particle Fock  
 4306 state. LFWFs are thus functions of the invariant mass squared of the constituents in the

4307 Fock state. For a two-particle Fock state,  $\mathcal{M}^2 = \frac{k_{\perp}^2 + m^2}{x(1-x)}$ . Thus, the constituent transverse  
4308 momenta  $k_{\perp i}^2$  do appear alone as a separate factor in the LFWF; the transverse momenta are  
4309 always coupled to the longitudinal LF momentum fractions  $x_i$ . This is the light-front version  
4310 of rotational invariance. Only positive  $k_i^+ = k_i^0 + k_i^z \geq 0$  and  $0 \leq x_i = \frac{k_i^+}{P^+} \leq 1$  appear,  
4311 where  $\sum_i x_i = 1$ . In addition,  $J^z = \sum_i L_i^z + S_i^z$ , as well as  $P^+ = \sum_i k_i^+$  and  $\vec{P}_{\perp} = \sum_i \vec{k}_{\perp i}$  are  
4312 conserved at every vertex – essential covariant kinematical constraints. A remarkable property:  
4313 the anomalous gravitomagnetic moment of every LF Fock state vanishes at  $Q^2 = 0$ . The  
4314 LFWFs of bound states are off-shell in  $P^- = \sum_i k_i^-$ , but they tend to be maximal at minimal  
4315 off-shellness; i.e. minimal invariant mass. In fact, in the holographic LFWFs where colour is  
4316 confined, the LFWFs of hadrons have fast Gaussian fall-off in invariant mass. This feature also  
4317 underlie intrinsic heavy quark Fock states: the LFWFs have maximal support when all of the  
4318 constituents have the same rapidity  $y_i$ ; i.e.  $x_i \propto \sqrt{m_i^2 + k_{\perp i}^2}$ . Thus the heavy quarks have the  
4319 highest momentum fractions  $x_i$ .

4320 Conversely, light-front wavefunctions provide the boost-invariant transition amplitude which  
4321 convert the free quark and gluons into the hadronic eigenstates of QCD. Thus, knowing the  
4322 LFWFs allows one to compute *hadronization at the amplitude level* – how the coloured quarks  
4323 and gluons produced in a deep inelastic scattering event  $ep \rightarrow e'X$  at the LHeC are confined  
4324 and emerge as final-state hadrons.

4325 The LF formalism leads to many novel nuclear phenomena, such as *hidden colour* [558] *colour*  
4326 *transparency* [559], *nuclear-bound quarkonium* [560], *nuclear shadowing and antishadowing* of  
4327 nuclear structure functions, etc. For example, there are five distinct colour-singlet QCD Fock  
4328 state representations of the six colour-triplet quarks of the deuteron. These hidden-colour Fock  
4329 states become manifest when the deuteron fluctuates to a small transverse size, as in mea-  
4330 surements of the deuteron form factor at large momentum transfer. One can also probe the  
4331 hidden-colour Fock states of the deuteron by studying the final state of the dissociation of the  
4332 deuteron in deep inelastic lepton scattering at the LHeC  $eD \rightarrow e'X$ , where  $X$  can be  $\Delta^{++} + \Delta^-$ ,  
4333 six quark jets, or other novel colour-singlet final states.

4334 The LF wave functions provide the input for scattering experiments at the amplitude level,  
4335 encoding the structure of a projectile at a single light-front time  $\tau$  [553]. For example, consider  
4336 photon-ion collisions. The incoming photon probes the finite size structure of the incoming  
4337 nucleus at fixed LF time, like a photograph – not at a fixed instant time, which is acausal.  
4338 Since the nuclear state is an eigenstate of the LF Hamiltonian, its structure is independent of  
4339 its momentum, as required by Poincaré invariance. One gets the same answer in the ion rest  
4340 frame, the CM frame, or even if the incident particles move in the same direction, but collide  
4341 transversely. There are no colliding *pancakes* using the LF formalism.

4342 The resulting photon-ion cross-section is not point-like; it is shadowed:  $\sigma(\gamma A \rightarrow X) = A^{\alpha} \sigma(\gamma N \rightarrow$   
4343  $X)$ , where  $A$  is the mass number of the ion,  $N$  stands for a nucleon, and the power  $\alpha \approx 0.8$   
4344 reflects Glauber shadowing [561]. The shadowing stems from the destructive interference of  
4345 two-step and one-step amplitudes, where the two-step processes involve diffractive reactions on  
4346 a front-surface nucleon which shadows the interior nucleons. Thus the photon interacts primar-  
4347 ily on the front surface. Similarly, a high energy ion-ion collision  $A_1 + A_2 \rightarrow X$  involves the  
4348 overlap of the incident frame-independent LFWFs. The initial interaction on the front surface  
4349 of the colliding ions can resemble a shock wave.

4350 In the case of a deep inelastic lepton-nucleus collision  $\gamma^* A \rightarrow X$ , the two-step amplitude involves  
4351 a leading-twist diffractive deep inelastic scattering (DDIS)  $\gamma^* N_1 \rightarrow V^* N_1$  on a front surface  
4352 nucleon  $N_1$  and then the on-shell propagation of the vector system  $V^*$  to a downstream nucleon

4353  $N_2$  where it interacts inelastically:  $V^*N_2 \rightarrow X$ . If the DDIS involves Pomeron exchange, the two-  
4354 step amplitude interferes destructively with the one-step amplitude  $\gamma^*N_1 \rightarrow X$  thus producing  
4355 shadowing of the nuclear parton distribution function at low  $x < 0.1$ . On the other hand, if  
4356 the DDIS process involves  $I = 1$  Reggeon exchange, the interference is constructive, producing  
4357 *flavour-dependent* leading-twist antishadowing [561] in the domain  $0.1 < x < 0.2$ .

4358 One can also show that the Gribov-Glauber processes, which arise from leading-twist diffractive  
4359 deep inelastic scattering on nucleons and underly the shadowing and antishadowing of nuclear  
4360 structure functions [561], prevent the application of the operator product expansion to the  
4361 virtual Compton scattering amplitude  $\gamma^*A \rightarrow \gamma^*A$  on nuclei and thus negate the validity of the  
4362 momentum sum rule for deep inelastic nuclear structure functions [562].



## Chapter 7

# Higgs Physics with LHeC

### 7.1 Introduction

The Higgs boson was discovered in 2012 by ATLAS [563] and CMS [564] at the Large Hadron Collider (LHC). It is the most recently discovered and least explored part of the Standard Model. The Higgs Boson ( $H$ ) is of fundamental importance. It is related to the mechanism predicted by [405, 406, 565] and independently by [566], in which the intermediate vector bosons of the spontaneously broken electroweak symmetry acquire masses <sup>1</sup> while the photon remain massless. Fermions obtain a mass via the Yukawa couplings with the Higgs field. Following the discovery of the Higgs boson, its physics and thorough exploration has become a central theme of the physics programme at the LHC. Any high-energy future collider project, beginning with the high luminosity upgrade of the Large Hadron Collider, the HL-LHC, underway to collect data in a decade hence, has put the potential to precisely study the properties of the Higgs boson into its center of attention, for understanding its characteristics and hoping to open a new window into physics extending beyond the Standard Model, see for example [567, 568]. In this section we present the potential to explore the SM Higgs physics at the LHeC and to certain extent at FCC-eh also.

A first challenge on the physics of the Higgs boson is to establish whether it indeed satisfies the properties inherent to the Standard Model (SM) regarding its production and decay mechanisms. The SM neutral  $H$  boson decays into pairs of fermions,  $f\bar{f}$ . The dominant decay is  $H \rightarrow b\bar{b}$  with a branching fraction of about 58%. The branching scales with the square of the fermion mass,  $m_f^2$ . The next prominent fermionic decay therefore is  $H \rightarrow \tau^+\tau^-$  with 6.3% followed by the charm decay with a predicted branching fraction of 2.9%. The Higgs boson also decays into pairs of  $W$  and  $Z$  bosons at a rate of 21.5% and 2.6%, respectively. Loop diagrams enable the decay into gluon and photon pairs with a branching of 8.2 and 0.2%, respectively. The seven most frequent decay channels, ordered according to descending branching fractions, thus are into  $b\bar{b}$ ,  $W^+W^-$ ,  $gg$ ,  $\tau^+\tau^-$ ,  $c\bar{c}$ ,  $ZZ$  and  $\gamma\gamma$ . Together these are predicted to represent a total SM branching fraction of 99.9%. At the LHC these and rarer decays can be reconstructed, with the exception of the charm decay for reasons of prohibitive combinatorial background. The main purpose of this paper is to evaluate the prospects for precisely measuring these channels

---

<sup>1</sup>The mass of the  $W$  boson,  $M_W$ , is generated through the vacuum expectation value,  $\eta$ , of the Higgs field ( $\Phi$ ) and given by the simple relation  $M_W = g\eta/\sqrt{2}$  where  $g$  is the weak interaction coupling. Here  $\eta = \sqrt{-\mu^2/2\lambda}$  with the two parameters of the Higgs potential that is predicted to be  $V = -\mu^2\Phi^+\Phi - \lambda(\Phi^+\Phi)^2$ . The Higgs mass is given as  $M_H = 2\eta\sqrt{\lambda}$  while the mass of the  $Z$  boson is related to  $M_W$  with the electroweak mixing angle,  $M_Z = M_W/\cos\Theta_W$ .

4393 in electron-proton scattering.

## 4394 7.2 Higgs Production in Deep Inelastic Scattering

4395 In deep inelastic electron-proton scattering, the Higgs boson is predominantly produced through  
 4396  $WW$  fusion in charged current DIS (CC) scattering, Fig. 1. The next large Higgs production  
 4397 mode in  $ep$  is  $ZZ \rightarrow H$  fusion in neutral current DIS (NC) scattering, Fig. 1, which has a smaller  
 but still sizable cross section. These  $ep$  Higgs production processes are very clean for a number

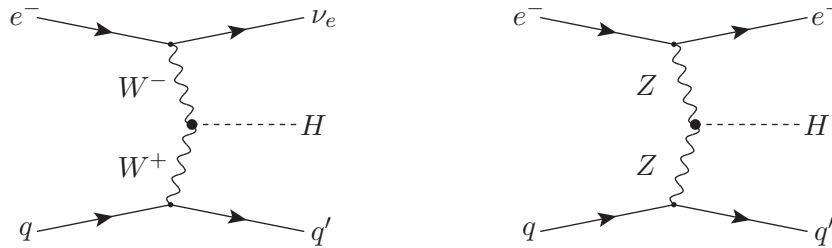


**Figure 7.1:** Higgs boson production in charged (left) and neutral (right) current deep inelastic electron-proton scattering to leading order.

4398 of reasons:

- 4400 • even at the high luminosity of  $10^{34} \text{ cm}^{-2}\text{s}^{-1}$  the inclusive pileup is only 0.1 (1) for the  
 4401 LHeC (FCC-eh) and the final state signature therefore free from event overlap, in contrast  
 4402 to the HL-LHC where it will typically be 150;
- 4403 • in  $ep$ , contrary to  $pp$ , there is no initial nor final state colour (re)connection;
- 4404 • the higher-order corrections are small. For the total CC process they were estimated [569]  
 4405 to be of the order of only 1% for the QCD part, subject to cut dependencies yielding  
 4406 shape changes up to 20%, and  $-5\%$  for the QED part (with a weak dependence on  
 4407 the PDF choice). The smallness of the QCD corrections was attributed mainly to the  
 4408 absorption of gluon and quark radiation effects in the evolution of the parton distributions  
 4409 (PDFs) [569]. The PDFs will be measured with very high precision at any of the  $ep$   
 4410 colliders here considered, see Chapter 3, thus allowing a unique self-consistency of Higgs  
 4411 cross section measurements.

4412 The NC reaction is even cleaner than the CC process as the scattered electron fixes the kinematics  
 4413 more accurately than the missing energy. While in  $pp$  both  $WW$  and  $ZZ$  processes are hardly  
 4414 distinguishable, in  $ep$  they uniquely are, which provides an important, precise constraint on the  
 4415  $WWH$  and  $ZZH$  couplings.

### 4416 7.2.1 Kinematics of Higgs Production

4417 At HERA the kinematics was conveniently reconstructed through event-wise measurements of  
 4418  $Q^2$  and  $y$ . The reconstruction of the kinematics in charged currents uses the inclusive hadronic  
 4419 final state measurements. Based on the energies  $E'_e$  and  $E_h$  and the polar angles  $\Theta_e$  and  $\Theta_h$   
 4420 of the scattered electron and the hadronic final state, respectively, one obtains a redundant  
 4421 determination of the kinematics in neutral current scattering. This permits a cross calibration  
 4422 of calorimetric measurements, of the electromagnetic and hadronic parts and of different regions

4423 of the detector, which is a major means to achieve superb, sub-percent precision in  $ep$  collider  
 4424 measurements. Methods have been developed to optimise the kinematics reconstruction and  
 4425 maximise the acceptance by exploiting the redundant determination of the scattering kinematics,  
 4426 see for example [55]. The basic DIS kinematic distributions of  $Q^2$ ,  $x$  and  $y$  for Higgs production  
 at  $\sqrt{s} = 3.5$  TeV are illustrated in Fig. 7.2. The average  $Q^2$  and  $x$  values probed are  $Q^2 \approx$

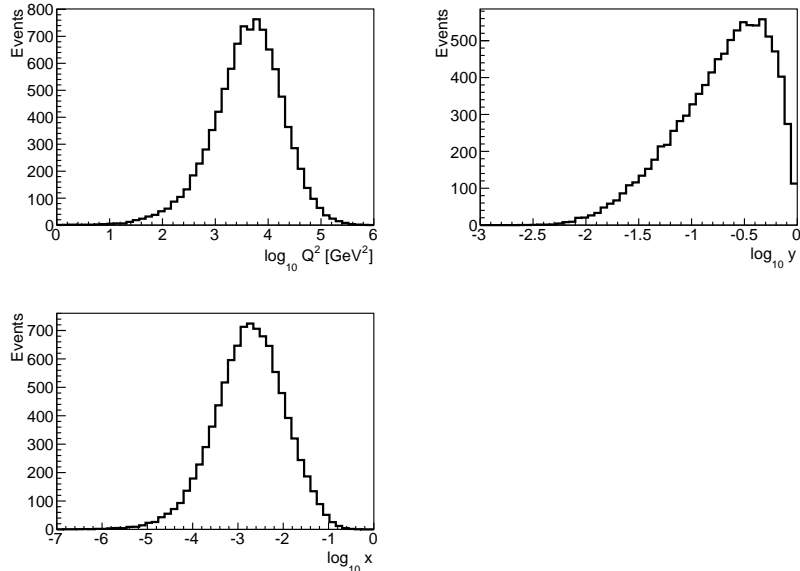


**Figure 7.2:** Distributions for  $ep \rightarrow \nu H X$  events, at parton-level, for the negative 4-momentum transfer squared,  $Q^2$  (top left), Bjorken  $x$  (bottom left) and the inelasticity  $y = Q^2/sx$  (top right) at  $\sqrt{s} = 3.5$  TeV (FCC-eh). Events generated with MadGraph [361], see Tab. 7.1.

4427

4428  $2000 \text{ GeV}^2$ ,  $x \approx 0.02$  at LHeC and  $Q^2 \approx 6500 \text{ GeV}^2$ ,  $x \approx 0.0016$  at FCC-eh.

4429 As is described in this paper elsewhere, constraints for a large pseudorapidity or polar angle,  
 4430  $\eta = \ln \tan \theta/2$ , acceptance of the apparatus arise i) for the backward region (the polar angle  
 4431 is defined w.r.t. the proton beam direction) from the need to reconstruct electrons at low  $Q^2$   
 4432 enabling low  $x$  physics and ii) for the forward region to cover a maximum region towards large  
 4433  $x$  at medium  $Q^2$  with the reconstruction of the hadronic final state. The acceptance therefore  
 4434 extends, for the LHeC, to pseudorapidities of  $\eta = \pm 5$ , which for the FCC-eh case is extended to  
 4435  $\eta = \pm 6$ . The large acceptance is in particular suitable for the reconstruction of Vector-Boson-  
 4436 Fusion Higgs boson event signatures, see Fig. 7.3 for the typical pseudorapidity distributions of  
 4437 Higgs boson event signature in DIS at the most asymmetric FCC-eh collider configuration.

4438 Geometric acceptances due to kinematic constraints in the pseudorapidity on the Higgs decay  
 4439 products for both LHeC and FCC-eh are further illustrated in Fig. 7.4. The acceptances are  
 4440 calculated for a basic selection of all final states with  $p_T > 15$  GeV and a coverage of the forward  
 4441 jet up to  $\eta = 5$  and  $\eta = 6$ , respectively, for both colliders. As seen from Fig. 7.4, the acceptances  
 4442 are higher for the less asymmetric LHeC beam configuration and about the same for hadronic  
 4443 calorimetry up to  $\eta = 5$  and  $\eta = 6$ . Hence, the LHeC calorimeter is designed for  $\eta = 5$ . The  
 4444 optimal hadronic calorimetry coverage for FCC-eh is clearly  $\eta = 6$  yielding significantly higher  
 4445 acceptances in comparison to an  $\eta = 5$  calorimetry. From Fig. 7.4, it is apparent that for both  
 4446 collider configurations the Higgs decay products would require tagging capabilities up  $\eta = 3.5$ ,  
 4447 e.g. for heavy flavour and tau decays. Suitably designed muon detectors covering  $\eta = 4$  appear  
 4448 feasible for both collider configurations, those would result in high  $H \rightarrow \mu\mu$  acceptances of about  
 4449 72 % (63 %) for LHeC (FCC-eh) for selecting all final states with  $p_T > 15$  GeV and a coverage

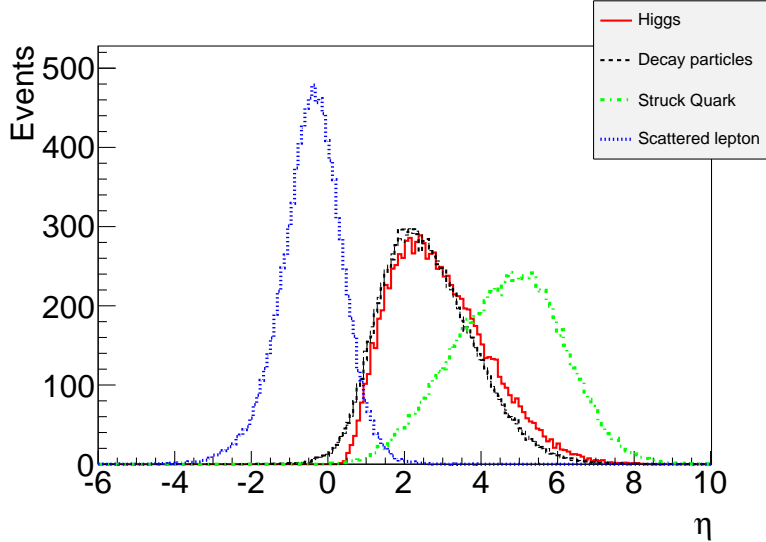


**Figure 7.3:** Pseudorapidity ( $\eta$ ) distributions, at parton-level, characterising the Vector-Boson-Fusion production and decay of the Higgs boson to  $WW$  in DIS scattering at FCC-eh. The scattered lepton (blue) in the NC case (or missing energy for CC) has an average  $\eta$  of about  $-0.5$ , i.e. it is scattered somewhat backwards (in electron beam direction). The pseudorapidity distributions of the generated Higgs boson (red) and its decay particles (black) are very similar and peak at  $\eta \simeq 2$ . The struck quark, especially at the FCC-eh as compared to LHeC, generates a very forward jet requiring forward calorimetry up to  $\eta \simeq 6$  as is foreseen in the FCC-eh detector design. Events are generated with MadGraph, see setup in Tab. 7.1.

4450 of the forward jet up to  $\eta = 5$  ( $\eta = 6$ ). A further extension to a  $1^\circ$  muon acceptance, would  
 4451 change the acceptances marginally to 72.9% (67.5%) for LHeC (FCC-eh).

## 4452 7.2.2 Cross Sections and Rates

4453 The cross sections for Higgs production in CC and NC DIS  $e^-$  scattering of a 60 GeV electron  
 4454 beam with protons at three different energies, for LHeC, HE-LHeC and FCC-eh, are summarised  
 4455 in Tab. 7.1. The cross sections are calculated to leading order with MadGraph (MG5 v2.5.1)  
 4456 using the CTEQ6L1 proton PDF and  $M_H = 125$  GeV. The CC  $e^-p$  cross section is directly pro-  
 4457 portional to the beam polarisation,  $P$ , as  $\sigma_{CC} \propto (1 - P)$  while the NC cross section only weakly  
 4458 depends on the polarisation [94]. It is observed that the CC Higgs production cross section at  
 4459 LHeC is comparable to that of a 250 GeV  $e^+e^-$  collider. One thus expects, roughly, results of  
 4460 comparable sensitivity. The difference being that  $e^+e^-$  favours the  $H$  to  $ZZ$  couplings while  $ep$   
 4461 is dominantly sensitive to  $WW \rightarrow H$  production. This provides a fundamental complementarity  
 4462 between  $e^+e^-$  and  $ep$  collider Higgs physics.

4463 The CC  $e^-p$  cross section is enlarged with the (negative) electron beam polarisation,  $P_e$ , while  
 4464 the NC cross section is less sensitive to  $P_e$ . The cross section at FCC-eh reaches values of pb.  
 4465 Combined with long operation time one reaches sub-permille precision of the Higgs couplings.  
 4466 Similarly, the  $HH$  cross section approaches 0.5 fb values only with the highest energy as expected  
 4467 for  $\sqrt{s} > 3$  TeV FCC-eh or CLIC-ee colliders. A first cut-based study to access the Higgs self-  
 4468 coupling at FCC-eh within 20% is detailed in Ref. [571]. Further prospects are not discussed here  
 4469 since measuring the  $HH$  coupling is one of the foremost tasks of HL-LHC and the FCC-hh [572].

4470 The polarised  $e^+p$  cross section is calculated to be significantly smaller than the  $e^-p$  value, by a  
 4471 factor of  $197/58 \simeq 6$  at the LHeC, mainly because the  $W^-u \rightarrow \bar{d}$  reaction is more frequent than

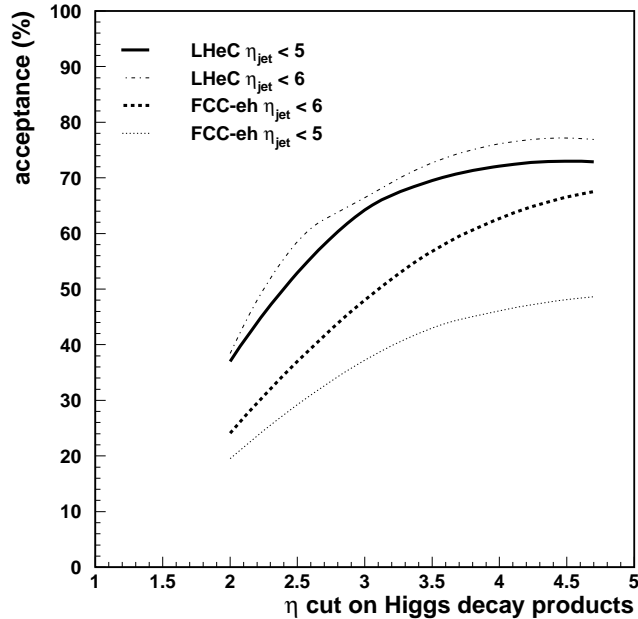


**Figure 7.4:** Acceptance of DIS Higgs candidates ( $y$  axis) in dependence on the pseudorapidity ( $\eta$ ) cut requirement on the Higgs decay products ( $x$  axis) for two scenarios of the coverage of the hadronic final states. All final states are selected with  $p_T > 15$  GeV. The forward jet is accepted up to  $\eta = 5$  and  $\eta = 6$  for LHeC (full and dashed-dotted lines), and FCC-eh (dotted and dashed lines), respectively. Calculations are at parton-level using MadGraph.

4472  $W^+d \rightarrow u$ . Furthermore, positron sources are currently considered to be much less intense (by  
4473 a factor of about ten or even a hundred) than electron sources. It is desirable to take  $e^+p$  data  
4474 at future  $ep$  colliders for electroweak physics but in the linac-ring version their amount will be  
4475 limited and unlikely suitable for precision Higgs physics.

4476 Table 7.2 provides an illustration of the statistics which is expected to be available in charged  
4477 and neutral current scattering for nine decay channels ordered by their branching ratios for the  
4478 nominal LHeC and FCC-eh configurations. The statistics at LHeC would be about ten times  
4479 lower than that at FCC-eh since the cross section is diminished by  $\simeq 1/5$  and due to a shorter  
4480 expected running time, i.e. the integrated luminosity is assumed to be half of that at FCC-eh.  
4481 Accessing rarer SM Higgs decay channels is the particular strength of luminous  $pp$  scattering at  
4482 highest energies rather than that of anticipated  $ep$  or  $e^+e^-$  colliders. The signal strength and  
4483 coupling analyses subsequently presented deal with the seven most frequent decays representing  
4484 99.9% of the SM Higgs decays. In addition, there is a significant potential for a measurement  
4485 of the  $H \rightarrow \mu\mu$  decay at the FCC-eh, which, as is seen in Tab. 7.2, may provide about 500  
4486 (45) events, from CC and NC DIS at FCC-eh (LHeC). Thus one may be able to measure this  
4487 process to about 6% precision at the FCC-eh and 18% at LHeC.

### 4488 7.3 Higgs Signal Strength Measurements

4489 Standard Model Higgs production in deep inelastic  $ep$  scattering proceeds via Vector-Boson-  
4490 Fusion in either charged or neutral current scattering as it is illustrated in Fig. 1. The scattering  
4491 cross sections, including the decay of the Higgs boson into a pair of particles  $A_i\bar{A}_i$  can be written

Parameter	Unit	LHeC	HE-LHeC	FCC-eh	FCC-eh
$E_p$	TeV	7	13.5	20	50
$\sqrt{s}$	TeV	1.30	1.77	2.2	3.46
$\sigma_{CC} (P = -0.8)$	fb	197	372	516	1038
$\sigma_{NC} (P = -0.8)$	fb	24	48	70	149
$\sigma_{CC} (P = 0)$	fb	110	206	289	577
$\sigma_{NC} (P = 0)$	fb	20	41	64	127
HH in CC	fb	0.02	0.07	0.13	0.46

**Table 7.1:** Total cross sections, in fb, for inclusive Higgs production,  $M_H = 125$  GeV, in charged and neutral current deep inelastic  $e^-p$  scattering for an unpolarised ( $P = 0$ ) and polarised ( $P = -0.8$ )  $E_e = 60$  GeV electron beam and four different proton beam energies,  $E_p$ , for LHeC, HE-LHeC and two FCC-eh versions. The c.m.s. energy squared in  $ep$  is  $s = 4E_e E_p$ . The last row shows the double-Higgs CC production cross sections in fb. The calculations are at LO QCD using the CTEQ6L1 PDF [570] and the default scale of MadGraph [361] with dependencies due to scale choices of 5-10%.

Channel	Fraction	Number of Events			
		Charged Current		Neutral Current	
		LHeC	FCC-eh	LHeC	FCC-eh
$b\bar{b}$	0.581	114 500	1 208 000	14 000	175 000
$W^+W^-$	0.215	42 300	447 000	5 160	64 000
$gg$	0.082	16 150	171 000	2000	25 000
$\tau^+\tau^-$	0.063	12 400	131 000	1 500	20 000
$c\bar{c}$	0.029	5700	60 000	700	9 000
$ZZ$	0.026	5 100	54 000	620	7 900
$\gamma\gamma$	0.0023	450	5 000	55	700
$Z\gamma$	0.0015	300	3 100	35	450
$\mu^+\mu^-$	0.0002	40	410	5	70
$\sigma$ [pb]		0.197	1.04	0.024	0.15

**Table 7.2:** Total event rates, and cross sections, for SM Higgs decays in the charged ( $ep \rightarrow \nu HX$ ) and neutral ( $ep \rightarrow eHX$ ) current production in polarised ( $P = -0.8$ ) electron-proton deep inelastic scattering at LHeC ( $\sqrt{s} = 1.3$  TeV) and FCC-eh ( $\sqrt{s} = 3.5$  TeV), for an integrated luminosity of 1 and 2  $\text{ab}^{-1}$ , respectively. The branching fractions are taken from [573]. The estimates are at LO QCD using the CTEQ6L1 PDF and the default scale of MadGraph, see setup in Tab. 7.1.

4492 as

$$\sigma_{CC}^i = \sigma_{CC} \cdot \frac{\Gamma^i}{\Gamma_H} \quad \text{and} \quad \sigma_{NC}^i = \sigma_{NC} \cdot \frac{\Gamma^i}{\Gamma_H}. \quad (7.1)$$

4493 Here the ratio of the partial to the total Higgs decay width defines the branching ratio,  $br_i$ ,  
4494 for each decay into  $A_i \bar{A}_i$ . The  $ep$  Higgs production cross section and the  $\text{O}(1) \text{ab}^{-1}$  luminosity  
4495 prospects enable to consider the seven most frequent SM Higgs decays, i.e. those into fermions  
4496 ( $b\bar{b}$ ,  $c\bar{c}$ ,  $\tau^+\tau^-$ ) and into gauge particles ( $WW$ ,  $ZZ$ ,  $gg$ ,  $\gamma\gamma$ ) with high precision at the LHeC  
4497 and its higher energy versions.

4498 In  $ep$  one obtains constraints on the Higgs production characteristics from CC and NC scattering,  
4499 which probe uniquely either the HWW and the HZZ production, respectively. Event by event  
4500 via the selection of the final state lepton which is either an electron (NC DIS) or missing energy  
4501 (CC DIS) those production vertices can be uniquely distinguished, in contrast to  $pp$ . In  $e^+e^-$ ,  
4502 at the ILC, one has considered operation at 250 GeV and separately at 500 GeV to optimise

4503 the  $HZZ$  versus the  $HWW$  sensitive production cross section measurements [574]. For CLIC  
 4504 the c.m.s. energy may be set to 380 GeV as a compromise working point for joint NC and CC  
 4505 measurements, including access to top production [575]. The salient advantage of the  $e^+e^-$   
 4506 reaction, similarly considered for the more recent circular collider proposals, CEPC [17] and  
 4507 FCC-ee [14], stems from the kinematic constraint of the Higgs-strahlung,  $e^+e^- \rightarrow Z^* \rightarrow ZH$ ,  
 4508 which determines the total Higgs production cross section independently of its decay.

4509 The sum of the branching ratios for the seven Higgs decay channels here under study for  $ep$  adds  
 4510 up to 99.87% of the total SM width [576]. As is discussed in Sect. 7.6, significant constraints  
 4511 of the  $H \rightarrow invisible$  decay can be set with  $ep$  also albeit not being able to exclude exotic,  
 4512 unnoticed Higgs decays. The accurate reconstruction of all decays considered here will present  
 4513 a severe constraint on the total cross section and with that of the total decay width of the  
 4514 Higgs boson in the SM. For the evaluation of the measurement accuracy, the cross section  
 4515 measurement prospects for a decay channel  $i$  are presented here as relative signal strengths  
 4516  $\mu^i(NC, CC)$ , obtained from division by the SM cross section.

4517 Initially, detailed simulations and Higgs extraction studies for LHeC were made for the dominant  
 4518  $H \rightarrow b\bar{b}$  [577–581] and the challenging  $H \rightarrow c\bar{c}$  [581–583] channels. The focus on the  $H \rightarrow b\bar{b}$   
 4519 decay has been driven not only by its dominance but as well by the difficulty of its accurate  
 4520 reconstruction at the LHC. It has been natural to extend this to the  $H \rightarrow c\bar{c}$  which currently is  
 4521 considered to not be observable at the HL-LHC, for permutation and large background reasons.  
 4522 The results of the updated  $b$  and  $c$  decay studies, using cuts and boosted decision tree (BDT)  
 4523 techniques, are presented below.

4524 A next detailed analysis has been performed for the  $H \rightarrow W^+W^-$  decay. The total of the  $WW$   
 4525 decays represents 21.5% of the Higgs branching into SM particles. There is a special interest  
 4526 in its reconstruction in the DIS charged current reaction as this channel uniquely determines  
 4527 the  $HWW$  coupling to its fourth power. A complete signal and background simulation and  
 4528 eventual BDT analysis of the  $H \rightarrow W^+W^-$  decay in charged currents has been performed  
 4529 which is subsequently described. Unlike at LHC, this uses the purely hadronic decays which in  
 4530  $pp$  are very difficult to exploit.

4531 Finally, as summarised below, an analysis using acceptance, efficiency and signal-to-background  
 4532 scale factors has been established for the residual four of the seven dominant decay channels,  
 4533 Tab. 7.2. This estimate could be successfully benchmarked with the detailed simulations for  
 4534 heavy quark and  $W$  decays. The present study therefore covers more than 99% of the SM Higgs  
 4535 decays, which in  $ep$  are redundantly measured, in both neutral and charged current reactions.  
 4536 This opens interesting prospects for precision Higgs physics in  $ep$ , but as well in combination  
 4537 with  $pp$ , i.e. of LHeC with HL-LHC, and later of FCC-eh with FCC-hh.

### 4538 7.3.1 Higgs Decay into Bottom and Charm Quarks

4539 The Higgs boson decays dominantly into  $b\bar{b}$  with a 58% branching ratio in the SM. Its reconstruc-  
 4540 tion at the LHC has been complicated by large combinatorial background. Recently this decay  
 4541 was established with signal strengths, relatively to the SM, of  $\mu_{bb} = 1.01 \pm 0.12(stat) \pm_{0.15}^{0.16}(exp)$   
 4542 by ATLAS [584] with a luminosity of  $79.8 \text{ fb}^{-1}$  and of  $\mu_{bb} = 1.01 \pm 0.22$  by CMS [585] with  
 4543 a luminosity of  $41.3 \text{ fb}^{-1}$ . This is a remarkable experimental LHC achievement since for long  
 4544 one expected to not be able to measure this decay to better than about 10% at the future  
 4545 HL-LHC. Meanwhile this expectation has become more optimistic with the updated HL-LHC  
 4546 prospects [586], however, the most hopeful assumption for the  $H \rightarrow c\bar{c}$  decay is a limit to two  
 4547 times the SM expectation.

4548 Because of the special importance of determining the frequent  $b\bar{b}$  decay most accurately, and  
4549 with it the full set of SM branchings, the prime attention of the LHeC Higgs prospect studies  
4550 has been given to those two channels. The first PGS detector-level study was published with  
4551 the CDR [1] before the announcement of the discovery of the Higgs boson and assuming  $M_H =$   
4552 120 GeV. This and subsequent analyses use samples generated by MadGraph5 [361], for both  
4553 signal and background events with fragmentation and hadronization via PYTHIA 6.4 [587] in an  
4554  $ep$  customised programme version<sup>2</sup>. Subsequent analyses have been updated to  $M_H = 125$  GeV  
4555 and to state-of-the art fast detector simulation with DELPHES 3 [589] as testbed for  $ep$  detector  
4556 configurations. Both cut-based and boosted decision tree (BDT) analyses were performed in  
4557 independent evaluations.

4558 As shown in the CDR, the  $H \rightarrow b\bar{b}$  decay could be measured via applying classical kinematic  
4559 selection requirements as follows:

- 4560 • CC DIS kinematic cuts of  $Q_h^2 > 500 \text{ GeV}^2$ ,  $y_h < 0.9$ , missing energy  $E_T^{\text{miss}} > 30 \text{ GeV}$ , and  
4561 no electrons in the final state to reject NC DIS;
- 4562 • at least three anti-kt  $R = 0.7$  jets with  $p_T > 20 \text{ GeV}$  which are subject to further b-tagging  
4563 requirements;
- 4564 • a Higgs candidate from two b-tagged jets with b-tagging efficiencies of 60 to 75 %, charm  
4565 (light quark) misidentification efficiencies of 10 to 5 % (1 %) ;
- 4566 • rejection of single-top events via requiring a dijet W candidate mass of greater than  
4567 130 GeV and a three-jet top candidate mass of larger than 250 GeV using a combina-  
4568 tion with one of the b-jets of the Higgs mass candidate;
- 4569 • a forward scattered jet with  $\eta > 2$ , and a large  $\Delta\phi_{b,MET} > 0.2$  between the b-tagged jet  
4570 and the missing energy.

4571 The dominant backgrounds are CC DIS multijet and single top production, while CC Z, W and  
4572 NC Z contributions are small. The background due to multijets from photoproduction, where  
4573  $Q^2 \sim 0$ , can be reduced considerably due to the tagging of the small angle scattered electron  
4574 with an electron tagger. The result of a cut-based analysis is shown in Fig. 7.5 where clear Z  
4575 and  $H \rightarrow b\bar{b}$  peaks are seen. Assuming that the photoproduction background is vetoed with a  
4576 90 % efficiency, the resulting signal is shown in Fig. 7.5 corresponding to a SM  $H \rightarrow b\bar{b}$  signal  
4577 strength  $\delta\mu/\mu$  of 2 % for an integrated luminosity of  $1000 \text{ fb}^{-1}$  and  $P_e = -0.8$ . This result is  
4578 consistent with earlier analysis and robust w.r.t. the update of the Higgs mass from 120 to  
4579 125 GeV confirming the high  $S/B > 1$  (see also Ref. [580] where an alternative approach to  
4580 estimate the multijet photoproduction background gives a similar signal strength uncertainty).  
4581 The result illustrates that even with harsh kinematic requirements and already a small luminosity  
4582 of  $100 \text{ fb}^{-1}$ , this important decay channel could be measured to an uncertainty of about 6 %.

4583 The stability of the cut-based results has been further shown for different hadronic calorimeter  
4584 resolution setups

$$\frac{\sigma}{E} = \frac{a}{\sqrt{E}} \oplus b \quad \text{for } |\eta| < |\eta_{\text{min}}|, \quad (7.2)$$

$$\frac{\sigma}{E} = \frac{c}{\sqrt{E}} \oplus d \quad \text{for } |\eta_{\text{min}}| < |\eta| < 5, \quad (7.3)$$

---

<sup>2</sup>The hadronic showering is not expected to change the kinematics of the DIS scattered lepton. This has been shown, see page 11 of Ref. [588], with the very good level of agreement of NC DIS electron kinematics with and without the ep-customized Pythia showering. Specifically, for 99.8 % of events the kinematics in the momentum vector components and for 98 % of the events the energy of the scattered electron remain unchanged.



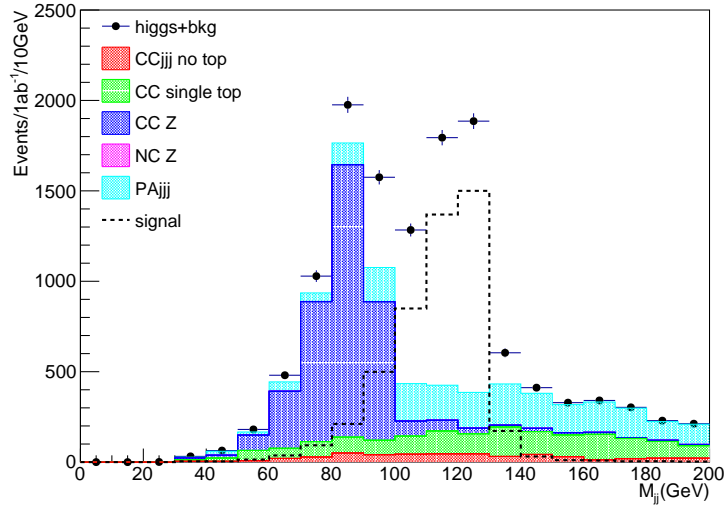


**Figure 7.5:** Invariant dijet mass distribution at DELPHES detector-level expected for  $1 \text{ ab}^{-1}$  and  $-80\%$  electron polarisation at LHeC. The  $S/B$  is about 2.9 for the events in the Higgs mass range of 100 to 130 GeV. Events are generated with MadGraph using  $M_H = 125 \text{ GeV}$  and showered with PYTHIA 6.4, and subject to cut-based event selection criteria, see text for further details. Note that samples are generated with a minimum dijet mass cut of 60 GeV.

4585 where for  $\eta_{\min} = 3$  the parameter  $b$  ( $d$ ) is varied within 1 (3) and 7 (9) % for two resolution  
 4586 parameters  $a$  ( $c$ ) of either 30 (60) and 35 (45) %. Alternatively, the central range was restricted  
 4587 to  $\eta_{\min} = 2$  with parameter  $b$  ( $d$ ) of 3 (5) % for resolution parameters  $a$  ( $c$ ) of 35 (45) %. While  
 4588 using the same analysis cuts, the signal yields varied within 34 %, it could be shown that with  
 4589 adjusted set of cuts (notably the choices of cuts for Higgs mass range,  $\Delta\phi_{b, MET}$ , and forward  
 4590  $\eta$ ) the SM  $H \rightarrow b\bar{b}$  signal strength  $\delta\mu/\mu$  varied with a fractional uncertainty of at most 7 %.

4591 The cut-based  $H \rightarrow b\bar{b}$  signal strength analyses are suffering from rather low acceptance times  
 4592 selection efficiencies in the range of 3 to 4 % only. Modern state-of-the-art analysis techniques,  
 4593 e.g. as performed for finding  $H \rightarrow b\bar{b}$  at the LHC regardless of the overwhelming QCD jet  
 4594 background, are based on neural networks in the heavy flavour tagging as well as in the analysis.

4595 Boosted Decision Tree (BDT)  $H \rightarrow b\bar{b}$  and  $H \rightarrow c\bar{c}$  analyses using the Toolkit for Multivariate  
 4596 Data Analysis with ROOT (TMVA) [590] are performed using independently produced signal  
 4597 and background samples based on the same setup as for the cut-based analyses, see Fig. 7.5.  
 4598 Those analyses start with loose preselections of at least three anti-kt jets with  $p_T > 15 \text{ GeV}$   
 4599 without any further heavy flavour tagging in addition to the CC DIS kinematic cuts of  $Q_h^2 > 400$   
 4600  $\text{GeV}^2$ ,  $y_h < 0.9$ , and missing energy  $E_T^{\text{miss}} > 20 \text{ GeV}$ . The invariant mass distributions using  
 4601 anti-kt  $R = 0.5$  jets are illustrated in Fig. 7.6, where the mass distributions in the upper plots  
 4602 illustrate in particular the single top contributions and the subsequent significant Higgs signal  
 4603 loss if simple anti-top cuts would be applied. In the lower plot of Fig. 7.6 the invariant dijet  
 4604 mass distribution of untagged Higgs signal candidates is seen clearly above the background  
 4605 contributions in the expected mass range of 100 to 130 GeV. It is observed that the remaining  
 4606 background is dominated by CC multi-jets. The quantities represented in the three distributions  
 4607 of Fig. 7.6 are important inputs for the BDT neural network in addition to further variables  
 4608 describing e.g. the pseudorapidities of the Higgs and forward jet candidates including jet and  
 4609 track heavy flavour probabilities, see details below and further in Ref. [583].

4610 As a novel element in these analyses, heavy flavour tagging based on track and jet probabilities

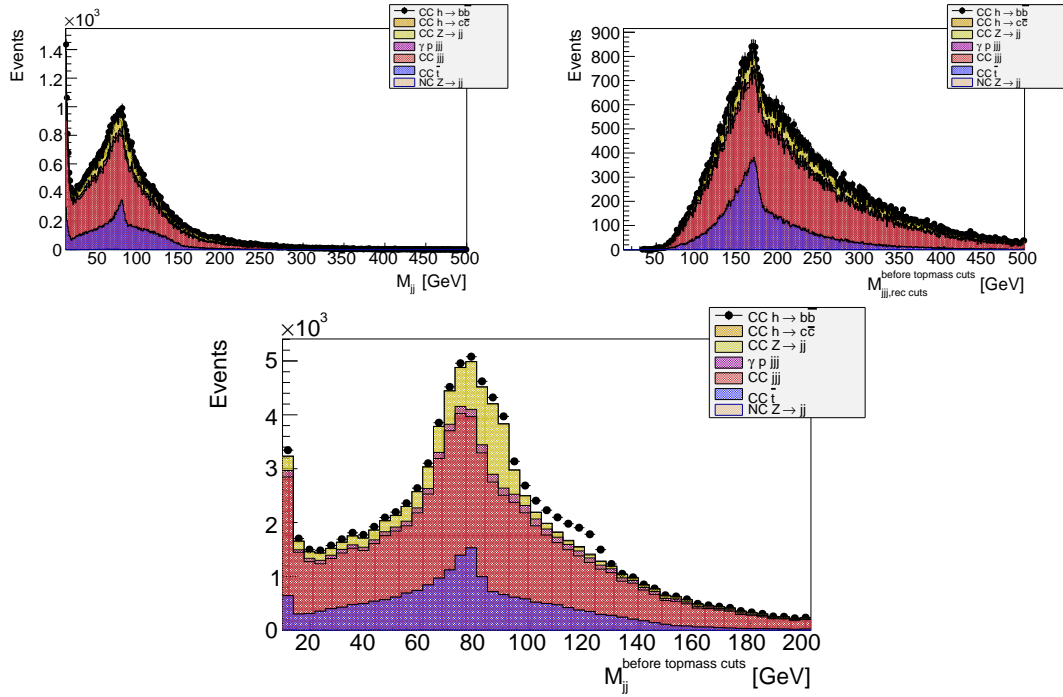


**Figure 7.6:** Invariant mass distributions at DELPHES detector level for an integrated luminosity of  $100 \text{ fb}^{-1}$  and  $-80\%$  electron polarisation. Events passed preselection cuts of  $Q_h^2 > 400 \text{ GeV}^2$ ,  $y_h < 0.9$ ,  $E_T^{\text{miss}} > 20 \text{ GeV}$  and at least three, flavour-untagged anti-kt  $R = 0.5$  jets with  $p_T > 15 \text{ GeV}$ . The different colours show the contributions per process, the photoproduction background ( $\gamma p \text{ jjj}$ ) is assumed to be vetoed with  $90\%$ . Note that samples are generated with a minimum dijet mass cut of  $60 \text{ GeV}$ . Upper left: Invariant dijet mass, showing  $W$  candidates from single top production (blue), based on combining jets with second and third lowest  $|\eta|$  values per event. Upper right: Invariant mass distribution combining the three highest  $p_T$  jets per event showing single top mass candidates (blue). Lower middle: Invariant dijet mass, showing Higgs candidates (black dots, including background), combining jets with the two lowest  $|\eta|$  values per event.

4611 has been implemented into the DELPHES detector analysis following the Tevatron D0 experi-  
 4612 mental ansatz described e.g. in Ref. [591]. The resulting  $b$  and  $c$ -jet efficiency versus the light jet  
 4613 misidentification efficiencies are illustrated in Fig. 7.7 for assumed nominal impact parameter  
 4614 resolution of  $10$  ( $5$ )  $\mu\text{m}$  for tracks with  $0.5 < p_T < 5$  ( $> 5$ )  $\text{GeV}$  and three choices of distance  
 4615 parameter  $R = 0.5, 0.7, 0.9$  for the anti-kt jets. In particular for the charm tagging, impact  
 4616 parameters are studied with resolutions of  $5$  ( $2.5$ )  $\mu\text{m}$  (Half Vertex Resolution),  $20$  ( $10$ )  $\mu\text{m}$   
 4617 (Double Vertex Resolution) for tracks with  $0.5 < p_T < 5$  ( $> 5$ )  $\text{GeV}$  within  $|\eta| < 3.5$ . For a  
 4618 conservative light jet efficiency of  $5\%$ , the  $b$ -jet tagging efficiency is rather robust around  $60\%$   
 4619 for the considered nominal impact parameter performance and the three considered anti-kt dis-  
 4620 tance parameters, in slight favour of the anti-kt  $R = 0.5$  choice. For the expected charm tagging,  
 4621 however, an excellent impact parameter resolution and  $R = 0.5$  jets give the best tagging effi-  
 4622 ciency of around  $30\%$ . This means a significant improvement e.g. w.r.t. a  $23\%$  charm tagging  
 4623 efficiency for  $R = 0.9$  jets at a nominal impact parameter resolution. These tagging efficiencies  
 4624 can be considered as realistic but rather conservative in particular for the remaining light jet  
 4625 efficiency which is expected to be about  $0.1\%$  at a  $b$ -jet efficiency of  $60\%$  using LHC-style neural  
 4626 network based taggers.

4627 A series of BDT score tests has been performed using the preselected signal samples and CC  
 4628 multi-jet as the main background sample to determine the optimal combination of the impact  
 4629 resolution parameters while resolving the two jets from the Higgs decay in dependence of  $R$ .

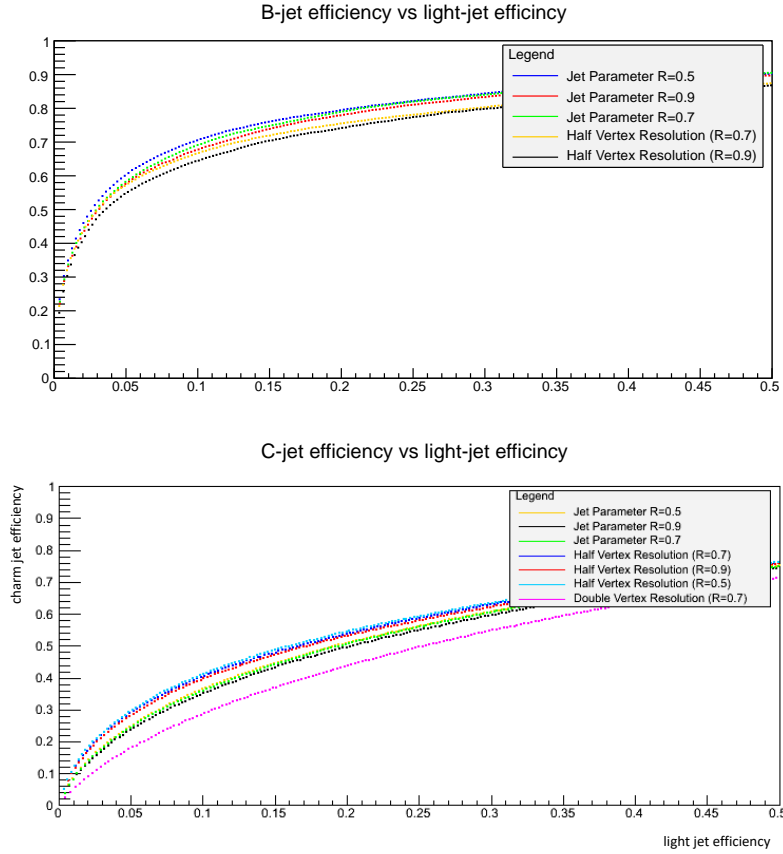


**Figure 7.7:** Expected average efficiency to tag a  $b$ -jet (upper plot) and charm-jet (lower plot) versus the light-jet efficiency ( $x$ -axis) based on Tevatron-style jet tagging [591]. Events are selected at DELPHES detector level using a CC multi-jet sample and for an integrated luminosity of  $100 \text{ fb}^{-1}$ . The coloured lines correspond to the choice of the anti-kt distance parameter  $R$  and different assumptions in the impact parameter resolution of 10 (5)  $\mu\text{m}$  (nominal, no text added in legend), 5 (2.5)  $\mu\text{m}$  (Half Vertex Resolution), 20 (10)  $\mu\text{m}$  (Double Vertex Resolution) for tracks with  $0.5 < p_T < 5$  ( $> 5$ ) GeV within  $|\eta| < 3.5$ .

4630 The resulting number of  $H \rightarrow b\bar{b}(c\bar{c})$  signal events versus the BDT score is illustrated in Fig. 7.8,  
 4631 which shows the evident interplay between detector performance and the choice of jet parameters  
 4632  $R$ , where the  $R = 0.9$  anti-kt jets show the worst performance. At a score of BDT=0, the highest  
 4633 number of signal events are achieved for  $R = 0.5$  anti-kt jets for both charm and beauty decays,  
 4634 where the effect of the impact resolution is much more stringent for the charm than for the beauty  
 4635 tagging. Following Fig. 7.8, the complete BDT-based  $H \rightarrow b\bar{b}(c\bar{c})$  analyses are performed for  
 4636 anti-kt  $R = 0.5$  jets and impact parameter resolution of 5 (2.5)  $\mu\text{m}$  (Half Vertex Resolution) for  
 4637 tracks with  $0.5 < p_T < 5$  ( $> 5$ ) GeV within  $|\eta| < 3.5$ . The acceptance times efficiency values are  
 4638 about 28% for the  $H \rightarrow b\bar{b}$  and about 11% for the  $H \rightarrow c\bar{c}$  channel at BDT=0.

4639 The results of the BDT  $H \rightarrow b\bar{b}$  and  $H \rightarrow c\bar{c}$  analyses, assuming that each background contri-  
 4640 bution is understood at the 2% level via control regions and negligible statistical Monte Carlo  
 4641 uncertainties for the background predictions for the signal region, are shown in Fig.7.9. Us-  
 4642 ing these assumptions, the resulting signal strengths are 0.8% for the  $H \rightarrow b\bar{b}$  and 7.4% for  
 4643 the  $H \rightarrow c\bar{c}$  channel. For the latter, the SM Higgs decays, in particular  $H \rightarrow b\bar{b}$ , represent  
 4644 also a part of the  $cc$  background contribution but can be controlled by the high precision of  
 4645 the genuine  $bb$  result. Advanced analysis strategies to distinguish  $bb$  and  $cc$  SM Higgs decays

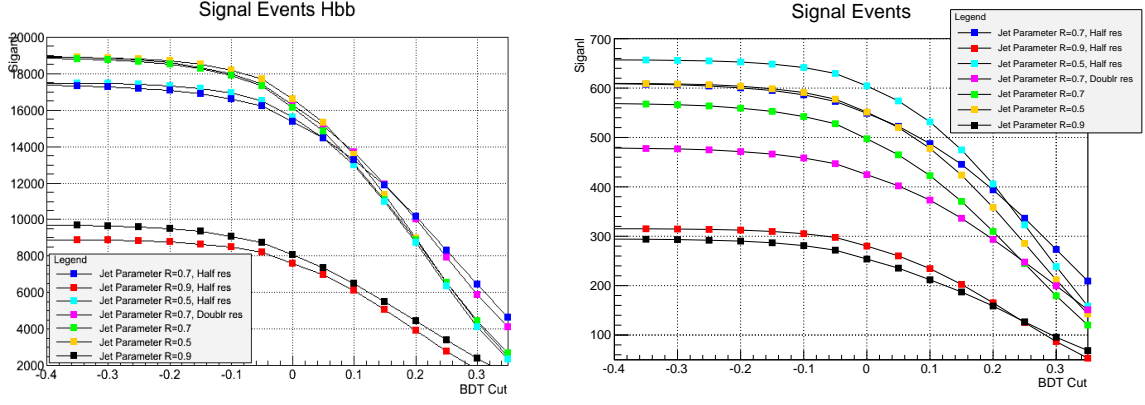


**Figure 7.8:** Expected  $H \rightarrow b\bar{b}$  (left) and  $H \rightarrow c\bar{c}$  (right) signal events as a function of the BDT score. Events are selected at DELPHES detector level for an integrated luminosity of  $1 \text{ ab}^{-1}$  and  $-80\%$  electron polarisation. The symbols correspond to the choice of the anti-kt distance parameter  $R$  and different assumptions in the impact parameter resolution of  $10$  ( $5$ )  $\mu\text{m}$  (nominal, no further text in legend added),  $20$  ( $10$ )  $\mu\text{m}$  (Doubl res),  $5$  ( $2.5$ )  $\mu\text{m}$  (Half res) for tracks with  $0.5 < p_T < 5$  ( $> 5$ )  $\text{GeV}$  within  $|\eta| < 3.5$ .

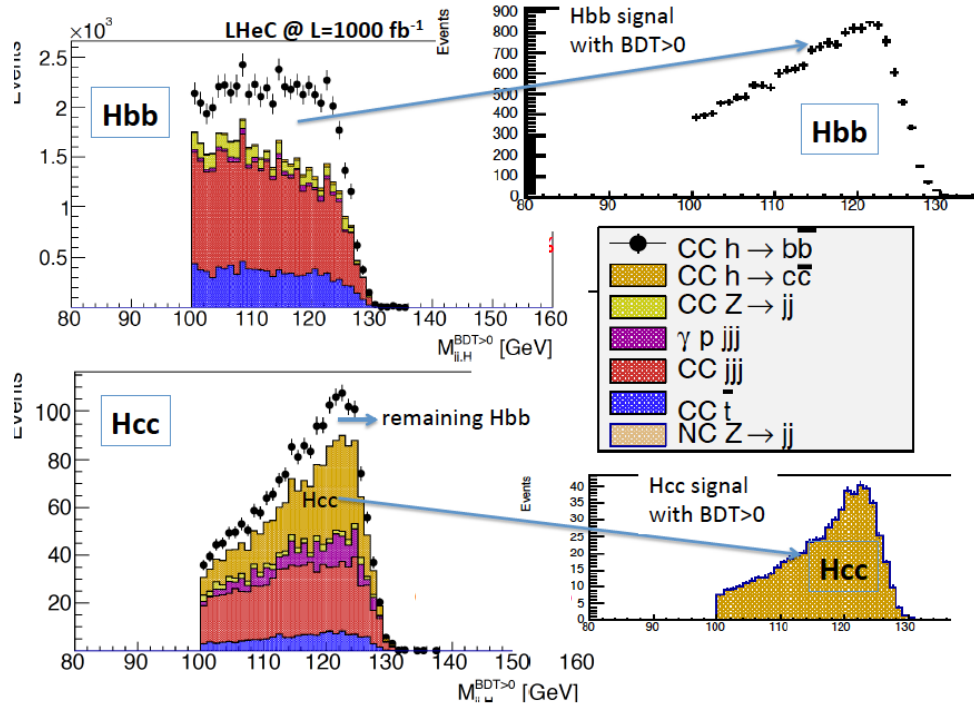


**Figure 7.9:** Result of the joint  $H \rightarrow b\bar{b}$  and  $H \rightarrow c\bar{c}$  analysis for an integrated luminosity of  $1 \text{ ab}^{-1}$  and  $-80\%$  electron polarisation at the LHeC. Left: Invariant mass distributions for the two channels with signal and background, see text. Right: Expected Higgs signal distributions after background subtraction. The background is assumed to be at the  $2\%$  level via control region measurements.

4646 via several layers of neural networks are discussed e.g. in Ref. [592] for an  $250 \text{ GeV}$  ILC and  
 4647  $M_H = 120 \text{ GeV}$ , where the expected  $H \rightarrow c\bar{c}$  cross section is  $6.9 \text{ fb}$  for  $M_H = 120 \text{ GeV}$  yields a  
 4648 signal strength uncertainty of  $8.8\%$  in the  $ZH$  all hadronic channel ( $Z \rightarrow q\bar{q}$ ) at an integrated  
 4649 luminosity of  $250 \text{ fb}^{-1}$ . The ILC charm cross section is quite similar to the  $5.7 \text{ fb}$  cross section for  
 4650  $M_H = 125 \text{ GeV}$  at LHeC. The number of preselected charm events and SM Higgs contributions  
 4651 for the ILC analysis are at a similar level as in this analysis, while the non-Higgs background at

4652 ILC is by a factor 6.8 larger than for the LHeC preselected events. Comparing the two results  
 4653 gives confidence into the expected  $H \rightarrow c\bar{c}$  signal strength results at LHeC using the before  
 4654 mentioned assumptions.

4655 In conclusion, Higgs to heavy flavour signal strength measurements require an excellent state-of-  
 4656 the-art calorimetry with high acceptance and excellent resolution as well as an impact parameter  
 4657 resolution as achieved e.g. with ATLAS inner b-layer. In addition, the details of the analysis  
 4658 strategy utilising neural network and advanced statistical methods (e.g. via RooStats/RooFit,  
 4659 see e.g. complex analysis methods using constraints via well measured control regions in signal  
 4660 fits [593]) will be important to control a high signal at low background yields where the latter  
 4661 is expected to be constrained via control regions to better than a few %.

### 4662 7.3.2 Higgs Decay into WW

4663 Inclusive charged current scattering, the CC production of the Higgs boson with a  $WW$  decay  
 4664 and the main backgrounds are illustrated in Fig. 7.10. The  $ep \rightarrow \nu H X \rightarrow \nu W^* W X$  process  
 4665 with hadronic  $W$  decays, see Fig. 7.10 a, causes a final state which to lowest order comprises  
 4666 4 + 1 jets and the escaping neutrino identified via missing energy (MET). The pure hadronic  
 4667  $WW$  Higgs decay has a branching ratio of about 45 %. Using MadGraph (MG5) and a version  
 4668 of PYTHIA, customised for  $ep$  DIS, events have been generated and analysed after passing a  
 4669 DELPHES description of the FCC-eh detector. The present study has been performed for the  
 4670 most asymmetric beam configuration of  $E_e = 60$  GeV and  $E_p = 50$  TeV yielding  $\sqrt{s} = 3.5$  TeV.

4671 The analysis has been focussed on requiring four fully resolved jets from the Higgs decay and at  
 4672 least one forward jet, where the jets are reconstructed using the anti- $k_T$  algorithm with  $R = 0.7$ .  
 4673 Further event categories where the jets from the Higgs decay products may merge and yield  
 4674 either three or only two large- $R$  jets in the final state have been not considered yet. However,  
 4675 as shown from state-of-the art LHC-style studies, those event categories and the use of e.g.  
 4676 dedicated top and W-tagging based on large- $R$  jet substructures may give additional access to  
 measure Higgs signal strengths.

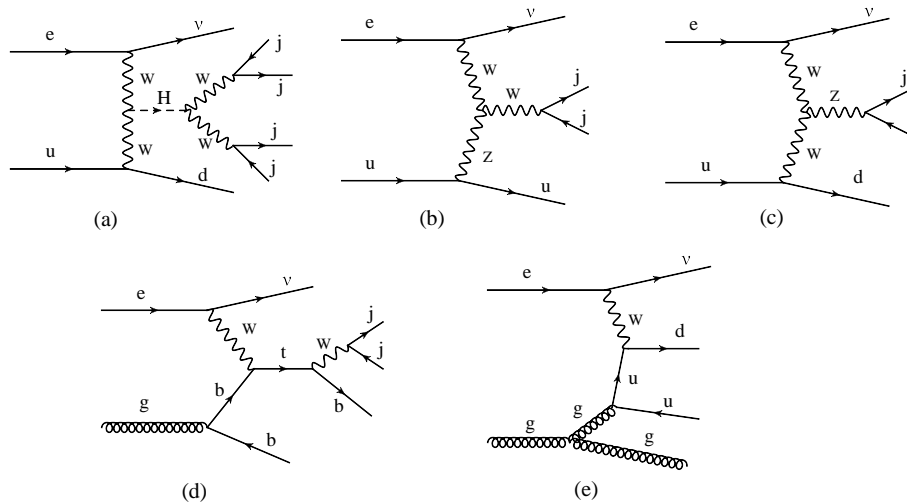


**Figure 7.10:** Typical lepton-parton diagrams relevant to the  $H \rightarrow W^*W$  analysis: a) signal: CC DIS with a Higgs produced in the t-channel and its decay into a pair of  $W$  bosons which generates a four-jet final state, besides the forward jet. The other diagrams are examples to illustrate background channels which at higher orders, with extra emissions, may mimic the signal configuration: b) single  $W$ -boson production; c) single  $Z$ -boson production; d) single top-quark production; e) QCD multi-jet production.

4677

4678 The analysis requiring fully resolved jets from the  $H \rightarrow W^*W \rightarrow 4j$  decay and at least one  
 4679 forward jet proceeds in the following steps:

- 4680 • Study of the reconstructed event configuration and recognition of its characteristics for  
 4681 defining a set of loose cuts. These are: the  $p_T$  of any jet has to be larger than 6 GeV, the  
 4682 rapidity difference between the forward jet and the reconstructed 4-jet Higgs candidate  
 4683 to be larger than 1.5, the azimuthal difference between that Higgs candidate and either  
 4684 the forward jet or the scattered lepton (MET) to be larger than 1, two-jet masses of the  
 4685 virtual and the real  $W$  boson candidate to be larger than 12 GeV and below 90 GeV ( $Z$   
 4686 mass).
- 4687 • Verification of truth matching to check that the combinatorial association of jets reproduces  
 4688 the Higgs candidate (four jets) and its  $W$  (two jets) decays (see Fig. 7.11 and text).
- 4689 • Application of this algorithm to the simulated background samples. The MadGraph single  
 4690  $W$ , top and  $Z$  production samples are turned to multi-jet background through PYTHIA.  
 4691 The cross sections are reliably calculated as there is a hard scale available. The initial  
 4692 cuts reduce this background to about 3% for single vector boson production and to 9%  
 4693 for top.
- 4694 • Due to the size of the  $Hb\bar{b}$  decay and jet radiation, there occurs a residual background  
 4695 from the Higgs itself which is also reduced to 3% through the cuts.
- 4696 • The final background is due to multi-jets. The MadGraph cross section for a 4+1 jet  
 4697 CC configuration is considered much too large in view of the cross section measurement  
 4698 results as a function of the jet number, both at HERA and the LHC, see for example [594].  
 4699 The sample was thus scaled using a conservative  $\alpha_s$  renormalisation to the inclusive cross  
 4700 section. The initial cuts reduce the multi-jet background to about 13%.
- 4701 • Following a detailed training study, a BDT analysis was used. This determined a final  
 4702 event number of about 12k for to a signal-to-background ratio of 0.23.

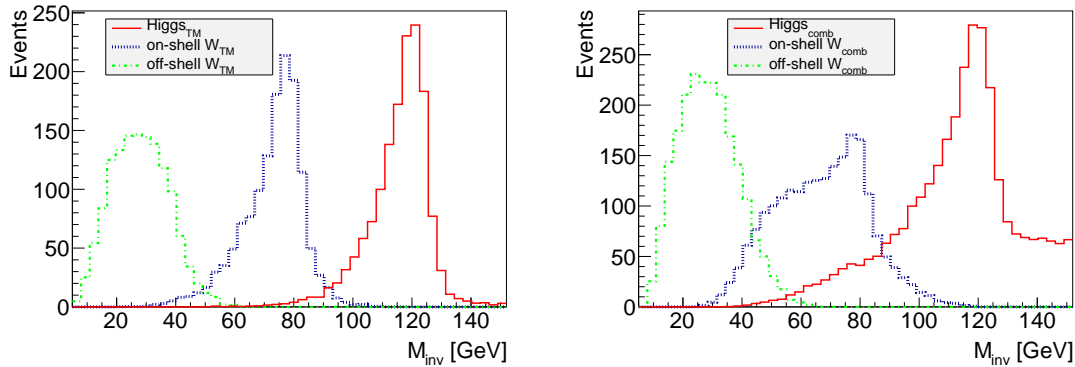


**Figure 7.11:** Reconstructed signal mass distributions (at DELPHES detector level) of truth matched events (left) and after the just combinatorial association of jets to the two  $W$  bosons forming Higgs candidates (right). Green: virtual  $W^*$  boson; blue:  $W$  boson; red: Higgs signal from  $W^*W$  reconstruction. It is observed that the combination causes some background while the respective signal peaks are clearly preserved with a purity of 68% that the correct forward jet is identified.

4703 The result of this analysis translates to an estimated uncertainty on  $\mu_{WW}$  of 1.9% at FCC-  
 4704 eh. The 4-jet mass distribution after the BDT requirement exhibits a clear  $WW$  Higgs peak  
 4705 (see Fig. 7.11) which illustrates the suitability to use the electron-proton environment for Higgs  
 4706 measurements in indeed challenging final state configurations.

### 4707 7.3.3 Accessing Further Decay Channels

4708 Following the detailed studies of the  $b\bar{b}$  and  $c\bar{c}$  decay channels, presented above, a coarser anal-  
 4709 ysis was established for other frequent decay channels both in NC and CC. Here acceptances  
 4710 and backgrounds were estimated with MadGraph, and efficiencies, distinguishing leptonic and  
 4711 hadronic decay channels for  $W$ ,  $Z$ , and  $\tau$ , were taken from prospective studies on Higgs cou-  
 4712 pling measurements at the LHC [595]. This provided a systematic scale factor,  $f$ , on the pure  
 4713 statistical error  $\delta_s$ , which comprised the signal-to-background ratio,  $S/B$ , and the product of  
 4714 acceptance,  $A$ , and extra reconstruction efficiency  $\epsilon$ , according to

$$f = \sqrt{\frac{1 + \frac{B}{S}}{A \cdot \epsilon}} \quad (7.4)$$

4715 The error on the signal strength  $\mu_i$  for each of the Higgs decay channels  $i$  is determined as  
 4716  $\delta\mu_i/\mu_i = f_i \cdot \delta_s$ .

Parameter	$b\bar{b}$	WW	gg	$\tau\tau$	cc	ZZ	$\gamma\gamma$
Branching fraction	0.581	0.215	0.082	0.063	0.029	0.026	0.0023
Statistical error ( $\delta_s$ ) [%]	0.09	0.15	0.24	0.28	0.41	0.43	1.41
Acceptance ( $A$ )	0.14	0.10	0.40	0.40	0.11	0.10	0.40
Signal/background ( $S/B$ )	9	0.2	0.1	0.2	0.43	0.33	0.5
Extra efficiency ( $\epsilon$ )	1	0.3	0.5	0.43	1	0.5	0.7
Scale factor $f$	2.8	16	7.4	5.9	5.5	9.0	3.3

**Table 7.3:** Statistical uncertainty for the seven most abundant Higgs decay channels, for the charged current Higgs measurement prospects with the FCC-eh, together with their systematic scale factor  $f$ , Eq. 7.4, resulting from acceptance, background and efficiency effects as given. Note that the results for  $b\bar{b}$  and  $c\bar{c}$  are taken from the BDT analysis (Sect. 7.3.1) with efficiency 1. The  $WW$  result is replaced by the BDT analysis (Sect. 7.3.2) for quoting the expected signal strength uncertainty.

4717 To good approximation these factors apply to LHeC, HE-LHeC and FCC-eh because the de-  
 4718 tector dimensions and acceptances scale with the proton energy, conceptually using the same  
 4719 technology and very similar resolution assumptions. Therefore there is one main matrix used  
 4720 for the subsequent experimental deterioration of the pure statistics precision, both for CC and  
 4721 NC. Future detailed analyses will lead to refining this expectation which for the current purpose  
 4722 was beyond the scope of the study. The results of the analysis of uncertainties are summarised  
 in Tab. 7.3 for the CC channel at the FCC-eh. The resulting signal strength uncertainty values

Setup	$b\bar{b}$	$b\bar{b} \oplus \text{Thy}$	WW	gg	$\tau\tau$	cc	ZZ	$\gamma\gamma$
LHeC NC	2.3	2.4	17	16	15	20	35	42
LHeC CC	0.80	0.94	6.2	5.8	5.2	7.1	12	15
HE-LHeC NC	1.15	1.25	8.9	8.3	7.5	10	17	21
HE-LHeC CC	0.41	0.65	3.2	3.0	2.7	3.6	6.2	7.7
FCC-eh NC	0.65	0.82	5.0	4.7	4.2	5.8	10	12
FCC-eh CC	0.25	0.56	1.9	1.8	1.6	2.2	3.8	4.6

**Table 7.4:** Summary of estimates on the experimental uncertainty of the signal strength  $\mu$ , in per cent, for the seven most abundant Higgs decay channels, in charged and neutral currents for the LHeC, the HE-LHeC and the FCC-eh. The  $b\bar{b}$  channel is the one which is most sensitive to theoretical uncertainties and for illustration is given two corresponding columns, see Sect. 7.3.4.

4723 are provided in Tab. 7.4. Note that for the beauty, charm and  $WW$  channels the table contains  
 4724

4725 the BDT analysis <sup>3</sup> results of Sect. 7.3.1 and Sect. 7.3.2, resp. The beauty and charm CC results  
4726 stem from the BDT analysis for LHeC and are applied to FCC-eh with a factor of about 1/3.  
4727 The CC  $WW$  results are due to the FCC-eh BDT analysis and are used for LHeC, enlarged by  
4728 a factor of 3.2, determined by the different cross sections and luminosities. For HE-LHC, the  
4729 values are about twice as precise as the LHeC values because the cross section is enlarged by  
4730 about a factor of two, see Tab. 7.1, and the integrated luminosity with  $2 \text{ ab}^{-1}$  twice that of the  
4731 LHeC. All signal strength uncertainties, in both CC and NC, for the three collider configurations  
are shown in Fig. 7.12.

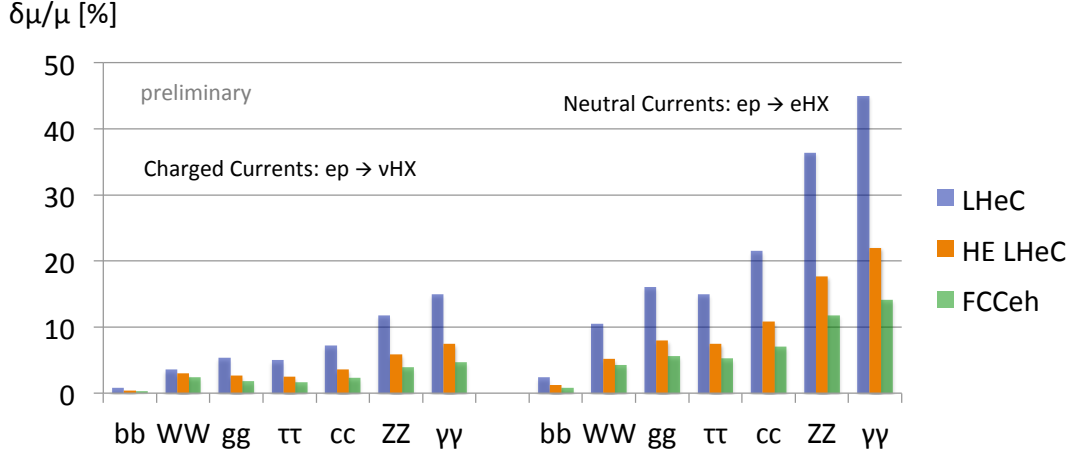


**Figure 7.12:** Uncertainties of signal strength determinations in the seven most abundant SM Higgs decay channels for the FCC-eh (green,  $2 \text{ ab}^{-1}$ ), the HE LHeC (brown,  $2 \text{ ab}^{-1}$ ) and LHeC (blue,  $1 \text{ ab}^{-1}$ ), in charged and neutral current DIS production.

4732

### 4733 7.3.4 Systematic and Theoretical Errors

4734 The signal strength is expressed relatively to a theoretical calculation of the charged current  
4735 Higgs cross section, including its decay into a chosen channel, according to

$$\mu = \frac{\sigma_{exp}}{\sigma_{thy}} = \frac{\sigma_{exp}}{\sigma_{Hty} \cdot br}. \quad (7.5)$$

4736 Consequently one can decompose the (relative) error of  $\mu$  into the genuine measurement error,  
4737 denoted as  $\delta\sigma_{exp}$ , including a possible systematic error contribution,  $E$ , and two further  
4738 components

$$\frac{\delta\mu}{\mu} = \left\{ \left( \frac{\delta\sigma_{exp}}{\sigma_{exp}} \right)^2 \cdot (1 \oplus E) + \left( \frac{\delta\sigma_{Hty}}{\sigma_{Hty}} \right)^2 + \left( \frac{\delta br}{br} \right)^2 \right\}^{1/2}, \quad (7.6)$$

4739 which are due to imperfections to theoretically model the Higgs production cross section,  $\sigma_{Hty}$ ,  
4740 and uncertainties on the branching ratio,  $br$ , in the channel under study. Note, that the experi-  
4741 mental uncertainty takes into account possible variations of the backgrounds which are estimated  
4742 conservatively and thus represent more than genuine statistics.

4743 The channel dependent signal strength uncertainties quoted in Tab. 7.4 are estimates of the  
4744 first, experimental term in Eq. 7.6 neglecting extra systematic error effects. They are derived as  
4745 stated above from the purely statistical error ( $\delta_s = 1/\sqrt{N}$ ), its increase due to acceptance ( $A$ )

<sup>3</sup>This is in very good agreement with the scale factor method: for example, the  $WW$  result in Tab. 7.3 leads to a value of 2.1% slightly worse than the BDT analysis.



4746 and efficiency ( $\epsilon$ ) effects and, further, the modulation caused by the background-to-signal ratio  
 4747 ( $B/S$ ). These factors are all involved in the BDT analysis but the scale factor equation, Eq. 7.4,  
 4748 may be used to estimate further systematic effects for any channel. From the relation

$$\frac{\delta\sigma_{exp}}{\sigma_{exp}} = \delta_s \cdot \sqrt{\frac{1 + B/S}{A \cdot \epsilon}} \quad (7.7)$$

4749 the combined systematic error contribution,  $E$ , caused by variations  $\Delta$  of  $A$ ,  $\epsilon$  and the back-  
 4750 ground  $B$  can be estimated as

$$E = \frac{1}{2} \left\{ \left( \frac{\Delta A}{A} \right)^2 + \left( \frac{\Delta \epsilon}{\epsilon} \right)^2 + \left( \frac{\Delta B}{B} \cdot \frac{B/S}{1 + B/S} \right)^2 \right\}^{1/2}. \quad (7.8)$$

4751 The formula shows that if the background-to-signal ratio is very small, then the background  
 4752 effect is suppressed  $\propto B/S$ . If it is larger than 1, the relative uncertainty of the background  
 4753 enters as an additional component of the signal strength error.

4754 Given the fact that the experimental  $H \rightarrow b\bar{b}$  result in the CC reaction is especially precise,  
 4755 compare Tab. 7.4, an estimate was performed of the systematic error in this channel. The  
 4756 following effects were included: a variation of the light-quark misidentification by a factor 3, a  
 4757 variation of the reduction of the photo-production via tagging between 2% and 10%, a variation  
 4758 of the combined acceptance times efficiency effect by 10% and a variation of the hadronic energy  
 4759 resolution, studied in Ref. [578], leading to a 7% signal variation. The overall effect of these  
 4760 contributions determines a systematic error of about 10% on  $\mu_{bb}$ , i.e.  $\delta\mu/\mu = 0.80 \pm 0.09$  for  
 4761  $H \rightarrow b\bar{b}$  at the LHeC in the CC channel. Similar levels of uncertainty are expected to occur for  
 4762 other channels but have not been estimated to such detail as those channels are measured less  
 4763 precisely.

4764 A separate effect arises from the measurement of the luminosity. While that will be measured  
 4765 about as accurate as 0.5%, based on Bethe-Heitler scattering and its accurate description to  
 4766 higher-order QEDC [1], additionally it will be negligible to a good approximation: the LHeC,  
 4767 and its successors, will provide a very precise, determination of all parton distributions from  
 4768 the  $ep$  data alone. Any systematic mistake in the normalisation will therefore affect both the  
 4769 measured and the calculated cross section and drop out in their ratio  $\mu$ .

4770 A next uncertainty on the signal strength arises from the theoretical description of  $\sigma_{CCH}$  to which  
 4771 the measured cross section is normalised. From a simulation of the systematic uncertainties  
 4772 due to imperfect calibrations and extra efficiencies one may expect the cross section to be  
 4773 known to better than 1%. The prediction will be available to N<sup>3</sup>LO,  $\alpha_s$  be determined to  
 4774 0.1 – 0.2% precision, and it can be gauged with the inclusive cross section measurement. This  
 4775 uncertainty, following Eq. 7.8, enters directly as a contribution to the  $\mu$  measurement result. A  
 4776 0.5% uncertainty, as can be seen in Tab. 7.4, becomes noticeable in most of the  $b\bar{b}$  results but  
 4777 is negligible for all other channels. In the present analysis values of 0.5% and 1% uncertainty  
 4778 have been considered and their effect on the  $\kappa$  result been evaluated, see Sect. 7.4.

4779 A final uncertainty is caused by the branching fractions and their uncertainty. A recent un-  
 4780 certainty estimate [573] quotes on the here most relevant  $H \rightarrow b\bar{b}$  branching ratio a theory  
 4781 contribution due to missing higher orders of 0.65%, a parameterisation uncertainty depending  
 4782 on the quark masses of 0.73%, and an  $\alpha_s$  induced part of 0.78%. The LHeC, or similarly the  
 4783 higher energy  $ep$  colliders, will determine the  $b$  mass (in DIS) to about 10 MeV and  $\alpha_s$  to per  
 4784 mille precision [1] which would render corresponding uncertainty contributions to  $br_{bb}$  negligible.  
 4785 The genuine theoretical uncertainty would also be largely reduced with an extra order pQCD.

4786 In the subsequent study the contribution from the branching fraction uncertainty has been ne-  
 4787 glected. This may also be justified by the programme here sketched, and similarly for other  
 4788 future colliders: the  $ep$  colliders will measure the couplings, especially of the  $WW$ ,  $bb$  and  $ZZ$   
 4789 very precisely, which will enable an iterative treatment of the branching ratio uncertainties.

4790 It may be noticed [573] that the  $\alpha_s$  contribution to the  $H \rightarrow gg$  branching fraction uncertainty  
 4791 is about 3.7%, i.e. twice as large as the estimated signal strength measurement uncertainty of  
 4792 this channel at the FCC-eh. There arises another important benefit of the future  $ep$  colliders  
 4793 and their high precision DIS programme for precision Higgs physics at the combined  $ep$  &  $pp$   
 4794 facilities.

## 4795 7.4 Higgs Coupling Analyses

4796 In order to quantify possible deviations from the SM expectation one may use the  $\kappa$  parameter-  
 4797 isation framework, introduced in Ref. [596], which enables easy comparisons between different  
 4798 collider configurations independently of their ability to access the total Higgs decay width. It  
 4799 should be noted that there are differences between the results in the EFT and in the  $\kappa$  formal-  
 4800 ism [597]. Therefore, it would be very interesting to go beyond the  $\kappa$  framework also for the  
 4801  $ep$  colliders here presented because out of the 2499 dimension-6 Wilson coefficients altogether  
 4802  $13 \cdot n_g^4 = 1053$  involve leptons and quarks [598], for  $n_g = 3$  generations. This, however, has been  
 4803 beyond the scope of this study. In the following results are presented for the various  $ep$  collider  
 4804 configurations (Sect. 7.2.2).

4805 The  $\kappa$  parameters are factors to the various Higgs couplings, equal to one in the SM, which scale  
 4806  $\sigma_{NC/CC}$  with  $\kappa_{Z/W}^2$ , the width  $\Gamma^i$  for a channel  $i$  with  $\kappa_i^2$  and lead to replacing  $\Gamma_H$  by the sum  
 4807  $\sum_j \kappa_j \Gamma^j$ , where we have assumed no non-SM H decays. This defines the following modifications  
 4808 of the cross sections (Eq. 7.1)

$$\sigma_{CC}^i = \sigma_{CC} br_i \cdot \kappa_W^2 \kappa_i^2 \frac{1}{\sum_j \kappa_j^2 br_j} \quad \text{and} \quad \sigma_{NC}^i = \sigma_{NC} br_i \cdot \kappa_Z^2 \kappa_i^2 \frac{1}{\sum_j \kappa_j^2 br_j}. \quad (7.9)$$

4809 Dividing these expressions by the SM cross section predictions one obtains the variations of the  
 4810 relative signal strengths,  $\mu^i$ , for charged and neutral currents and their  $\kappa$  dependence

$$\mu_{CC}^i = \kappa_W^2 \kappa_i^2 \frac{1}{\sum_j \kappa_j^2 br_j} \quad \text{and} \quad \mu_{NC}^i = \kappa_Z^2 \kappa_i^2 \frac{1}{\sum_j \kappa_j^2 br_j}. \quad (7.10)$$

4811 With seven decay channels considered in CC and NC, one finds that for each of the  $ep$  collider  
 4812 configurations there exist eight constraints on  $\kappa_W$  and  $\kappa_Z$  and two on the other five  $\kappa$  parameters.  
 4813 Using the signal strength uncertainties as listed in Tab. 7.4 fits to all seven channels, in NC and  
 4814 CC, are performed in a minimisation procedure to determine the resulting uncertainties for  
 4815 the  $\kappa$  parameters. These are done separately for each of the  $ep$  collider configurations with  
 4816 results listed in Tab. 7.5. A naive expectation would have been that  $\delta\kappa \simeq \delta\mu/2$ . Comparing the  
 4817 results, for example for LHeC (top rows), of the signal strengths (Tab. 7.4) with the  $\kappa$  fit results  
 4818 (Tab. 7.5) one observes that this relation holds approximately for the  $gg$ ,  $\tau\tau$ ,  $c\bar{c}$ ,  $\gamma\gamma$  channels.  
 4819 However, due to the dominance of  $H \rightarrow b\bar{b}$  in the total H width and owing to the presence of the  
 4820  $WWH$  and  $ZZH$  couplings in the initial state, there occurs a reshuffling of the precisions in the  
 4821 joint fit:  $\kappa_b$  is relatively less precise than  $\mu_{bb}$  while both  $\kappa_W$  and  $\kappa_Z$  become more precise than  
 4822 naively estimated, even when one takes into account that the  $H \rightarrow WW$  decay in CC measures  
 4823  $\kappa_W^4$ . The seven channel results are displayed in Fig. 7.13.

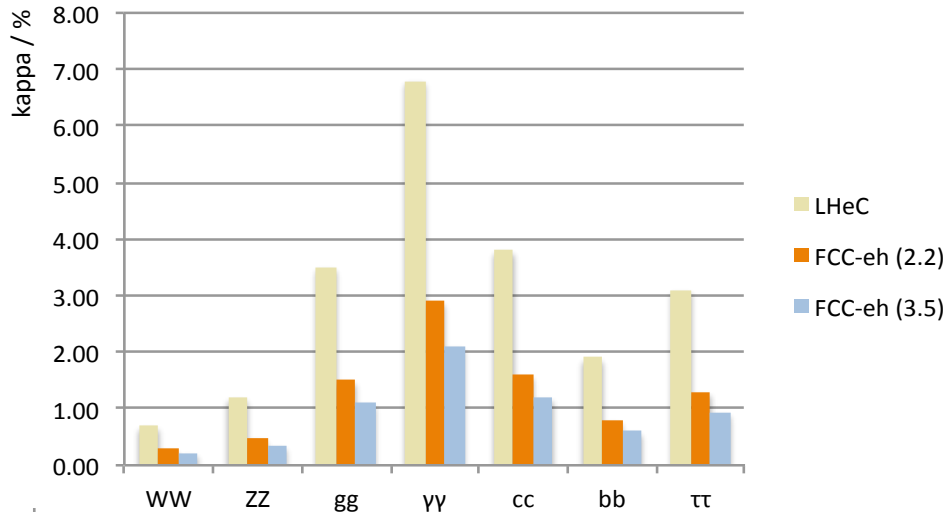


**Figure 7.13:** Summary of uncertainties of Higgs couplings from  $ep$  for the seven most abundant decay channels, for LHeC (gold), FCC-eh at 20 TeV proton energy (brown) and for  $E_p = 50$  TeV (blue).

Setup	$b\bar{b}$	WW	gg	$\tau\tau$	cc	ZZ	$\gamma\gamma$
LHeC	1.9	0.70	3.5	3.1	3.8	1.2	6.8
HE-LHeC	1.0	0.38	1.8	1.6	1.9	0.6	3.5
FCC-eh	0.60	0.22	1.1	0.93	1.2	0.35	2.1

**Table 7.5:** Summary of  $\kappa$  uncertainty values as obtained from separate fits to the signal strength uncertainty estimates for the seven most abundant Higgs decay channels, in charged and neutral currents for the LHeC, the HE-LHeC and the FCC-eh, see text.

4824 In the electroweak theory there is an interesting relation between the ratio of the  $W$  and  $Z$   
4825 couplings and the mixing angle,

$$\frac{\sigma(WW \rightarrow H \rightarrow AA)}{\sigma(ZZ \rightarrow H \rightarrow AA)} = \frac{\kappa_W^2}{\kappa_Z^2} = (1 - \sin^2 \theta_W)^2 \quad (7.11)$$

4826 This relation can be particularly well tested with the  $ep$  colliders as they measure both  $WWH$   
4827 and  $ZZH$  in one experiment and common theoretical environment. If one assumes the  $WW$   
4828 and  $ZZ$  measurements to be independent, the resulting error on  $\sin^2 \theta_W \simeq 0.23$  is 0.003 for the  
4829 LHeC and 0.001 for FCC-eh. However, this probably is smaller because there exist correlations  
4830 in the measurements which a genuine data based analysis would have to evaluate and take into  
4831 account.

4832 The effect of the theory uncertainties has been studied for the FCC-eh where the experimental  
4833 precision is highest. Tab. 7.6 presents the results of a  $\kappa$  analysis using the CC and NC FCC-  
4834 eh signal strength input (Tab. 7.4) neglecting the theoretical uncertainty and adding 0.5% or  
4835 1% in quadrature, to only  $\mu_{bb}$  where it matters. This results in an about linear increase of  
4836 the uncertainty for  $bb$  (by a factor of 1.5),  $WW$  (by 1.7) and  $ZZ$  (by 1.5), while all other  $\kappa$   
4837 uncertainties only slightly deteriorate. The effect of such uncertainties for LHeC is much smaller  
4838 as the  $\mu$  uncertainties are three times those of FCC-eh, see Tab. 7.4. Therefore, in the LHeC  
4839 case, the theory uncertainties are neglected.

Setup	$b\bar{b}$	WW	gg	$\tau\tau$	cc	ZZ	$\gamma\gamma$
FCC-eh (no thy)	0.60	0.22	1.1	0.93	1.2	0.35	2.1
FCC-eh (0.5% thy)	0.72	0.28	1.1	1.0	1.2	0.41	2.2
FCC-eh (1.0% thy)	0.91	0.37	1.1	1.0	1.3	0.53	2.3

**Table 7.6:** Summary of  $\kappa$  uncertainty values as obtained from separate fits to the signal strength uncertainty estimates for the seven most abundant Higgs decay channels, in charged and neutral currents for the FCC-eh, with no theoretical uncertainty, half a per cent and one per cent uncertainty added.

4840 An interesting question regards the role of the electron beam polarisation. Assuming a maximum  
4841 polarisation of  $P = -0.8$ , the CC (NC) Higgs cross section is calculated to be 1.8 (1.09) times  
4842 larger than that in unpolarised scattering. Therefore the signal CC and NC strength uncertain-  
4843 ties scale like 1.34 and 1.09, respectively. This is studied for the LHeC. If the default fit is made,  
4844 then the  $\kappa$  uncertainties quoted in Tab. 7.5 for  $bb$ ,  $WW$ ,  $gg$ ,  $\tau\tau$  and  $cc$  are enhanced by a factor  
4845 of 1.28. This is due to the combined effect of CC and NC which diminishes the deterioration a  
4846 bit, from 1.34 to 1.28. Thus, for example, the  $\kappa_W$  uncertainty moves from 0.7 to 0.9% in the  
4847 unpolarised case. The uncertainty on  $\kappa_Z$  is enhanced only by a factor of 1.14, becoming 1.38  
4848 instead of 1.21 because the NC channel has a particularly strong effect on the  $ZZH$  coupling.  
4849 Since the prospect to detect the  $\gamma\gamma$  channel in NC is very poor, the  $\kappa_\gamma$  uncertainty is enlarged  
4850 by the full CC factor of 1.34. It is for maximum precision very desirable to have the beam  
4851 polarised. This, together with electroweak physics, represents an important reason to continue  
4852 to develop high current polarised electron sources.

## 4853 7.5 Measuring the Top-quark–Higgs Yukawa Coupling

4854 Electron-proton collisions at high energy are known to provide a unique window of opportunity  
4855 to perform precision measurements in the top sector [458]. This is due to the large cross-sections  
4856 of the production of single top, which amounts to about 2 pb for  $E_e = 60$  GeV and  $E_p = 7$  TeV,  
4857 where clean signatures are provided without the challenges posed by pile-up. As a result, the  
4858 cross-section of the SM in association with a single top in  $e^-p$  collisions is large enough to  
4859 perform competitive measurements. This includes the measurement of the absolute value of the  
4860 Top Yukawa coupling and, most prominently, its CP-phase [469].

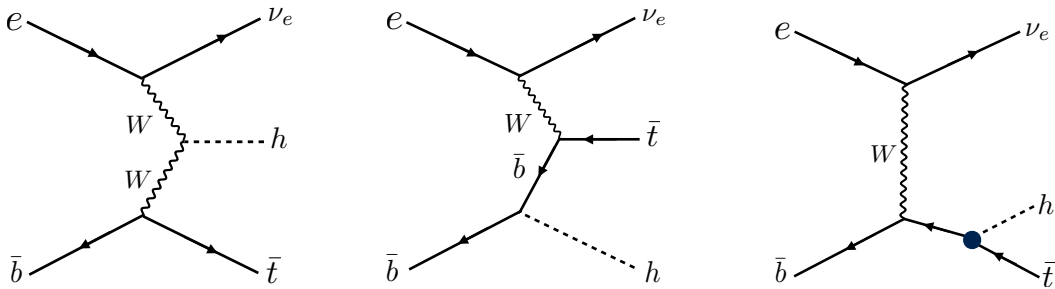


**Figure 7.14:** Leading order Feynman diagrams contributing to the process  $pe^- \rightarrow \bar{t} h \nu_e$  in high energy  $e^-p$  collisions. The black dot in the Feynman diagram on the right denotes the top-quark–Higgs coupling of interest in this section.

4861 In the SM, the Yukawa coupling of the third generation of quarks can be written down as:

$$\mathcal{L}_Y = -\frac{m_t}{v} \bar{t} t h - \frac{m_b}{v} \bar{b} b h, \quad (7.12)$$

where  $v \equiv (\sqrt{2}G_F)^{-1/2} = 2m_W/g \simeq 246$  GeV, and  $m_t$  ( $m_b$ ) is the mass of the top (bottom) quark. Due to the pure scalar nature of the Higgs boson in the SM, the top- and bottom-Higgs couplings are completely CP-even. To investigate any BSM contributions in terms of mixtures of CP-even and CP-odd states, we write a CP-phase dependent generalised Lagrangian as follows [599]:

$$\begin{aligned} \mathcal{L} = & -\frac{m_t}{v}\bar{t} [\kappa \cos \zeta_t + i\gamma_5 \sin \zeta_t]t h \\ & -\frac{m_b}{v}\bar{b} [\cos \zeta_b + i\gamma_5 \sin \zeta_b]b h. \end{aligned} \quad (7.13)$$

4862 Here,  $\zeta_t$  and  $\zeta_b$  are the phases of the top-Higgs and bottom-Higgs couplings, respectively. It is  
 4863 clear from the Lagrangian in Eq. (7.13) that  $\zeta_{t,b} = 0$  or  $\zeta_{t,b} = \pi$  correspond to a pure scalar state  
 4864 while  $\zeta_{t,b} = \frac{\pi}{2}$  to a pure pseudo scalar state. Thus, the ranges  $0 < \zeta_{t,b} < \pi/2$  or  $\pi/2 < \zeta_{t,b} < \pi$   
 4865 represent a mixture of the different CP-states. The case  $\kappa = 1$ ,  $\zeta_t = 0$  corresponds to the SM.

4866 In  $e^-p$  collisions, the top-Higgs couplings can be probed via associated production of the Higgs  
 4867 boson with an anti-top quark  $e^-p \rightarrow \bar{t}h\nu_e$ . It is necessary to consider a 5-flavour proton including  
 4868 the  $b$ -quark parton distribution. The Feynman diagrams for the process under investigation are  
 4869 shown in Fig. 7.14. It is important to note that three important couplings are involved, namely  
 4870  $hWW$ ,  $Wtb$  and the top-Higgs ( $tth$ ). A detailed study of  $hWW$  and  $Wtb$  couplings at the  $e^-p$   
 4871 collider have been performed in Refs. [458,600], respectively. For our studies we do not consider  
 4872 the BSM bottom-Higgs coupling since the effect of the phase  $\zeta_b$  on the total production cross  
 4873 section or kinematics of top-Higgs production at the LHeC are negligible. Thus in what follows,  
 4874 we simply set  $\zeta_b = 0$ .

4875 In the context of the LHC, quantitatively an interesting feature can be observed: in the pure SM  
 4876 case there is constructive interference between the diagrams shown in Fig. 7.14, left and middle,  
 4877 for  $\zeta_t > \pi/2$  resulting in an enhancement in the total production cross section of associated  
 4878 top-Higgs significantly. This is also true for  $\zeta_t < \pi/2$  - however the degree of enhancement is  
 4879 much smaller owing to the flipped sign of the CP-even part of the coupling.

4880 We probe the sensitivity of the top-Higgs couplings in terms of  $\zeta_t$  by building a model file for  
 4881 the Lagrangian in Eq. (7.13) using FeynRules [601], and then simulating the charged current  
 4882 associated top-Higgs production channel  $pe^- \rightarrow \bar{t}h\nu_e$  (see Fig. 7.14), with  $h$  further decaying  
 4883 into a  $b\bar{b}$  pair and the  $\bar{t}$  decaying leptonically in the LHeC set-up with centre of mass energy  
 4884 of  $\sqrt{s} \approx 1.3$  TeV. Here we perform the analysis at parton level only where for signal and  
 4885 background event generation we use the Monte Carlo event generator package MadGraph5 [361].  
 4886 We use NNPDF23\_lo\_as\_0130\_qed [602] parton distribution functions for all event generations.  
 4887 The factorisation and renormalisation scales for the signal simulation are fixed at  $\mu_F = \mu_R =$   
 4888  $(m_t + m_h)/4$  while background simulations are done with the default MadGraph5 [361] dynamic  
 4889 scales. The  $e^-$  polarisation is assumed to be  $-80\%$ . We now list and explain various kinematic  
 4890 observables that can serve as possible discriminants of a CP-odd  $t\bar{t}h$  coupling.

4891 In Fig. 7.15 we present the variation of the total cross section against the electron beam energy  
 4892 for the signal process  $pe^- \rightarrow \bar{t}h\nu_e$ , by considering un-polarised and polarised  $e^-$  beam. Also,  
 4893 the effect of branchings of  $h \rightarrow b\bar{b}$  and the  $\bar{t}$  decay for both leptonic and hadronic modes are  
 4894 shown. Possible background events typically arise from  $W+$  multi-jet events,  $Wb\bar{b}\bar{b}$  with missing  
 4895 energy which comes by considering only top-line, only Higgs-line, and without top- nor Higgs-  
 4896 line, in charged and neutral current deep-inelastic scattering and in photo-production by further  
 4897 decaying  $W$  into leptonic mode. We have estimated the cross sections for signal and all possible  
 4898 backgrounds imposing only basic cuts on rapidity  $|\eta| \leq 10$  for light-jets, leptons and  $b$ -jets, the  
 4899 transverse momentum cut  $p_T \geq 10$  GeV and  $\Delta R_{\min}=0.4$  for all particles.

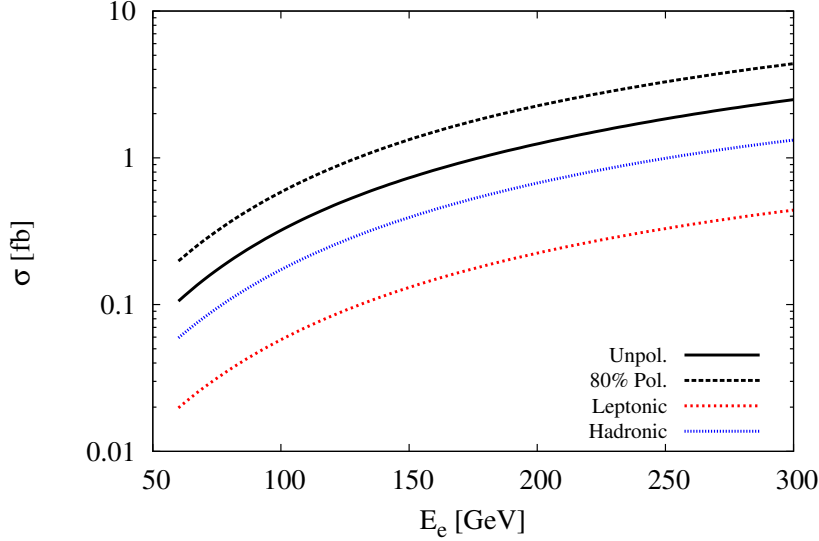


**Figure 7.15:** Cross-sections of the Higgs boson produced in association with a top quark in  $e^-p$  collisions with  $E_p = 7$  TeV. for different electron beam energies The dotted and solid *black* lines correspond to  $p e^- \rightarrow \bar{t} h \nu_e$  with and without longitudinal polarisation of the electron beam, respectively. The dotted *red* and *blue* lines correspond to  $\sigma \times \text{BR}$  for the leptonic and hadronic decay modes of  $\bar{t}$  where for this estimation we use basic cuts (see text).

4900 We now estimate the sensitivity of the associated top-Higgs production cross-section,  $\sigma(\zeta_t)$ , as  
 4901 a function of the CP phase of the  $tth$ -coupling as shown in Fig. 7.16 by considering  $E_e = 60$   
 4902 and with fixed  $E_p = 7$  TeV. The scale uncertainties are taken as  $(m_t + m_h)/8 \leq \mu_F = \mu_R \leq$   
 4903  $(m_t + m_h)/2$ . Here  $\sigma(\zeta_t = 0)$  corresponds to the SM cross section. We notice that the cross section  
 4904 is very sensitive to  $\zeta_t$  in the region  $\zeta_t > \frac{\pi}{2}$  where the interference between the diagrams becomes  
 4905 constructive. Below  $\zeta_t = \frac{\pi}{2}$  the interference is still constructive though its degree decreases  
 4906 with  $\zeta_t$ , thus increasing the cross section by around 5 times at  $\zeta_t = \frac{\pi}{2}$  which corresponds to  
 4907 the pure CP-odd case. On the other hand, for pure CP-even case  $\zeta_t = \pi$  with opposite-sign of  
 4908  $tth$ -coupling the cross section can be enhanced by up to 24 times for  $E_e = 60$  GeV. The scale  
 4909 uncertainty on an average is approximately 7% for  $E_e = 60$  GeV in the whole range of  $\zeta_t$ .

4910 In order to evaluate sensitivity to the measurement of the top Yukawa coupling and its P-phase,  
 4911 we implement the following criteria to select events, referred to as the fiducial selection:

- 4912 •  $p_T \geq 20$  GeV for  $b$ -tagged jets and light-jets, and  $p_T \geq 10$  GeV for leptons.
- 4913 • Since the LHeC collider is asymmetric, event statistics of final state particles are mostly  
 4914 accumulated on the left or right sides of the transverse plane  $\eta = 0$  (depending on the  
 4915 initial direction of  $p$  and  $e^-$ ) - we select events within  $-2 \leq \eta \leq 5$  for  $b$ -tagged jets while  
 4916  $2 \leq \eta \leq 5$  for leptons and light-jets,
- 4917 • The separation distance of all final state particles are taken to be  $\Delta R > 0.4$ .
- 4918 • Missing transverse energy  $\cancel{E}_T > 10$  GeV to select the top events.
- 4919 • Invariant mass windows for the Higgs through  $b$ -tagged jets and the top are required to  
 4920 be  $115 < m_{bb} < 130$  GeV and  $160 < m_t < 177$  GeV, respectively, which are important to  
 4921 reduce the background events substantially.

4922 In these selections the  $b$ -tagging efficiency is assumed to be 70%, with fake rates from  $c$ -initiated

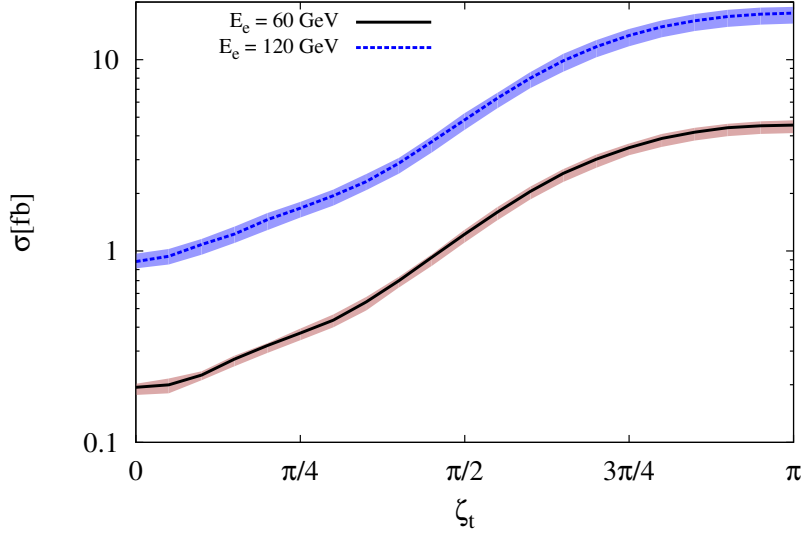


**Figure 7.16:** Total cross section of the Higgs boson produced in association with a single top as a function of  $\zeta_t$ , including scale uncertainties. The *black* solid and *blue* dotted lines correspond to  $E_e = 60$  and  $120$  GeV, respectively. These are obtained for fixed  $E_p = 7$  TeV and scales  $\mu_F = \mu_R = (m_t + m_h)/4$ .

4923 jets and light jets to the  $b$ -jets to be 10% and 1%, respectively.

4924 We estimated the exclusion regions of  $\zeta_t$  as a function of  $L$  in  $\text{fb}^{-1}$ . The exclusion is based  
 4925 on significance using the Poisson formula, where  $S$  and  $B$  are the number of expected signal  
 4926 and background events at a particular luminosity, respectively. Here we used 10% systematic  
 4927 uncertainty for background yields only. In Fig. 7.17, we present exclusion contours at various  
 4928 confidence levels for  $E_e = 60$  GeV – understandably, higher  $\sigma$ -contours demand larger luminosities.  
 4929 It is also seen that there is a kink around  $\zeta_t = \pi/2$  such that for the region  $0 < \zeta_t < \pi/2$ , we  
 4930 need larger luminosities for exclusion. This is in keeping with the feature exhibited in Fig. 7.16  
 4931 where the constructive interference between the signal diagrams enhances the cross-section over  
 4932 the SM value much more for  $\zeta_t > \pi/2$  thus requiring less luminosity to probe that region. For  
 4933  $L = 100 \text{ fb}^{-1}$ , regions above  $\pi/5 < \zeta_t \leq \pi$  and  $3\pi/10 < \zeta_t \leq \pi$  are excluded at  $2\sigma$  and  $3\sigma$  C.L.  
 4934 While around  $L = 400 \text{ fb}^{-1}$ , regions above  $\pi/6 < \zeta_t \leq \pi$  and  $\pi/4 < \zeta_t \leq \pi$  are excluded at  $4\sigma$   
 4935 and  $5\sigma$  C.L., respectively.

4936 As a measure of comparison, that asymmetry studies at the HL-LHC [599] help probe up to  
 4937  $\zeta_t = \pi/6$  for a total integrated luminosity of  $3 \text{ ab}^{-1}$ . Thus, it is clear that the LHeC provides a  
 4938 better environment to test the CP nature of Higgs boson couplings.

4939 For the integrated luminosity  $L = 1 \text{ ab}^{-1}$ , almost all values of  $\zeta_t$  can be excluded up to  $4\sigma$   
 4940 C.L. While investigating the overall sensitivity of  $\zeta_t$  by applying these two observables, it is also  
 4941 important to measure the accuracy of SM  $tth$  coupling  $\kappa$  at the LHeC energies. To measure the  
 4942 accuracy of  $\kappa$  by using signal and background yields we use the formula  $\sqrt{(S+B)/(2S)}$  at a  
 4943 particular luminosity. And for  $E_e = 60$  GeV, the measured accuracy at the design luminosity  
 4944  $L = 1 \text{ ab}^{-1}$  is given to be  $\kappa = 1.00 \pm 0.17$  of its expected SM value, where a 10% systematic  
 4945 uncertainty is been taken in background yields only.

4946 These results are obtained based on the evaluation of the fiducial cross-sections alone. As  
 4947 pointed out in Ref. [469], a number of other observables carry sensitivity to the structure of the  
 4948 top-Higgs Yukawa coupling, such as the rapidity difference between the top quark and the Higgs  
 4949 boson and a number of angular variables. While the fiducial rate studied here is the single most

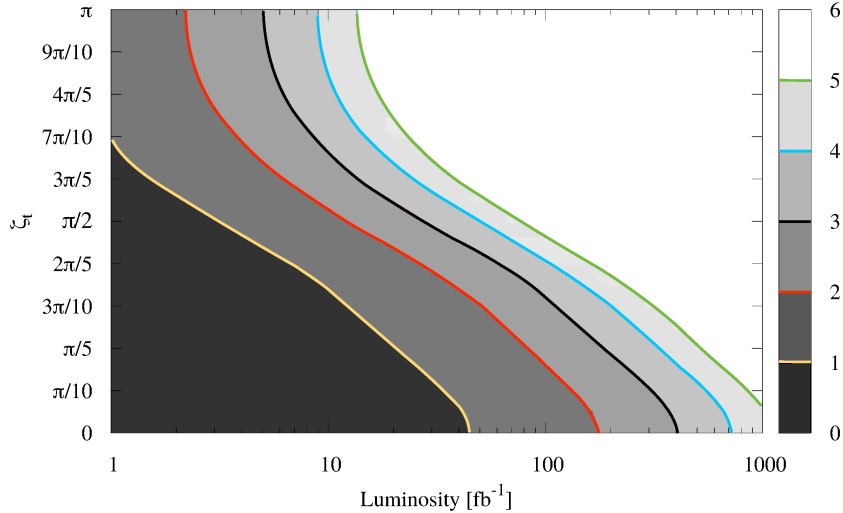


**Figure 7.17:** Exclusion contours for  $\zeta_t$  as a function of integrated luminosity for  $E_e = 60$  GeV and  $E_p = 7$  TeV. The regions beyond each contours are excluded for the particular luminosity, *black* and *red* solid lines correspond to  $3\sigma$  and  $2\sigma$  regions. Results are obtained based on fiducial cross-sections (see text).

4950 sensitive observable, it is evident that a multi-variate approach will significantly enhance the  
 4951 sensitivity reported here.

## 4952 7.6 Higgs Decay into Invisible Particles

4953 The Higgs decay into invisible particles could be a key to BSM physics. The SM branching  
 4954 ratio of  $H \rightarrow ZZ \rightarrow 4\nu$  is only 0.1%. Any sizable decay rate into invisible particles would  
 4955 thus indicate an exotic decay, for example to dark matter particles. Its non-observation would  
 4956 give the SM cross section measurement, reconstructing more than 99% of the ordinary decays  
 4957 a higher meaning for constraining the total Higgs decay width.

4958 For the LHeC at a luminosity of  $1 \text{ ab}^{-1}$ , initial parton-level studies of this decay were presented  
 4959 in Ref. [603], with the estimate of a two  $\sigma$  sensitivity to a branching fraction of 6%. For this  
 4960 study, NC production via  $ZZ$  fusion  $eq \rightarrow eqZZ \rightarrow eqH$  was used, which has a cross section  
 4961 of about 25 fb at the LHeC. The CC production via  $WW$  fusion has a larger cross section,  
 4962 but entails a missing energy signal by itself which requires further study of potentially quite  
 4963 some gain in precision. This channel, when employed for the invisible decay study, results in a  
 4964 mono-jet signature which is hard to separate from the SM DIS CC background.

4965 The neutral current study has been repeated using the LHeC Higgs WG analysis tools, intro-  
 4966 duced above: MadGraph, Pythia and Delphes. Similar to [603], an electron beam of 60 GeV  
 4967 with a polarization of -80% is assumed. The basic event topology contains the scattered electron,  
 4968 jet and missing transverse energy. Its main background results from SM  $W$  and  $Z$  productions  
 4969 (followed by  $W \rightarrow \ell\nu$  and  $Z \rightarrow \nu\bar{\nu}$ ). In the study NC and CC  $W$  production and NC  $Z$  produc-  
 4970 tion are considered, while single-top, NC multijets and  $W$  photoproduction were all found to be  
 4971 negligible. Requiring missing transverse energy of 60 GeV, exactly one electron and one jet, and  
 4972 no other leptons (including  $\tau$ ), as well as imposing several selection criteria on the kinematics of  
 4973 electron, jet and missing transverse momentum, we get a two  $\sigma$  sensitivity to a branching ratio  
 4974 of 7.2%, which is similar to the earlier result [603]. Fig. 7.18 shows the electron-jet invariant  
 4975 mass distribution after the selection for the signal (normalized to a 100% branching ratio) and



the background.

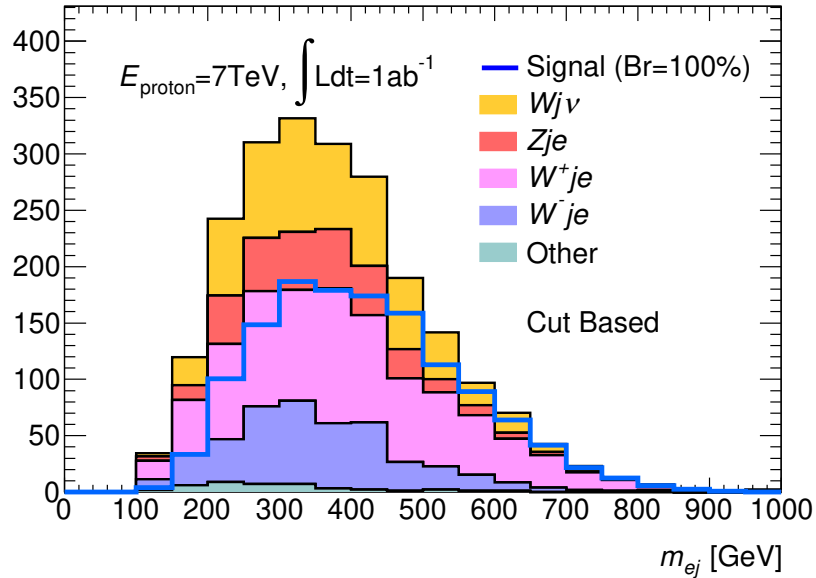


**Figure 7.18:** Electron-jet invariant mass distribution for the Higgs to invisible decay signal (normalized to 100% branching ratio) and the stacked backgrounds for an integrated luminosity of  $1 \text{ ab}^{-1}$  at the LHeC after all selection cuts.

4976

4977 The analysis has been further refined with a usage of multivariate analysis (Boosted Decision  
 4978 Tree in TVMA package). Basically the set of selection variables used in the cut-based analysis  
 4979 above was used as inputs to the multivariate analysis, tuned to yield the best output score to  
 4980 discriminate the signal from backgrounds. Fig. 7.19 shows the distribution of the discriminant  
 4981 variable for the signal and background (both area normalised). An optimization on the statistical  
 4982 significance is found at the BDT score  $> 0.25$ , and the resulting mass distribution is shown  
 4983 in Fig. 7.20. With  $1 \text{ ab}^{-1}$  of integrated luminosity, a two  $\sigma$  sensitivity of 5.5% is obtained  
 4984 consistent with the previous results. For a comparison, an estimate of 3.5% is given for a HL-  
 4985 LHC sensitivity study on this channel [604]. The result on the LHeC may be further improved  
 4986 in the future with a refined BDT analysis when one introduces extra parameters, beyond those  
 4987 initially introduced with the cut based analysis.

4988 In these initial studies no systematic uncertainties were considered. This may be justified with  
 4989 the very a clean environment of electron-hadron collider, in which precise measurements of  $W$   
 4990 and  $Z$  production will be made, for example in their decays to muons, for accurately controlling  
 4991 the systematics in the background prediction to a negligible level.

4992 The BDT analysis was repeated for higher proton energies. At the HE-LHeC ( $E_p=13.5 \text{ TeV}$ )  
 4993 the NC production cross section increases to 45 fb and the branching ratio sensitivity improves  
 4994 to 3.4% because the luminosity is doubled in the configurations here assumed. At the FCC-eh,  
 4995 the cross section rises to 120 fb and the sensitivity of the branching ratio reaches about 1.7%.

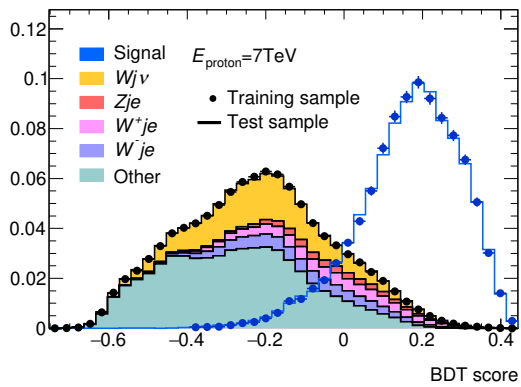


**Figure 7.19:** BDT output score distribution for the Higgs to invisible decay signal and the stacked backgrounds (both area normalized) at the LHeC.

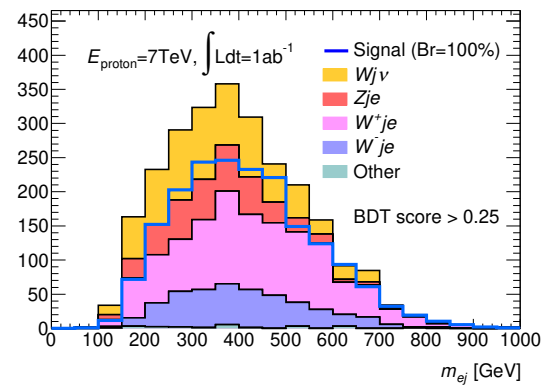


**Figure 7.20:** Electron-jet invariant mass distribution for the Higgs to invisible decay signal (normalized to 100% branching ratio) and the stacked backgrounds for an integrated luminosity of  $1 \text{ ab}^{-1}$  at the LHeC after the BDT score cut of 0.25.

## Chapter 8

# Searches for Physics Beyond the Standard Model

### 8.1 Introduction

The LHC was originally envisioned as the ultimate machine to search for physics beyond the Standard Model at the TeV scale. Since electrons and quarks share only electroweak interactions, an electron-proton collider could allow to measure the same phenomena in a different environment with generally higher precision. It could add complementary search channels or lead to the discovery of a weak signal. The possibility of undiscovered New Physics (NP) below the TeV scale could thus be also addressed by the LHeC, which is projected to operate when the LHC will be in its high luminosity phase, in spite of the lower centre-of-mass energy. Exotic phenomena that can be studied at  $ep$  colliders have been reviewed, for example, in [605]. More recently, but when the LHC was only beginning to yield data in Run I, an overview of the potential of the LHeC for probing physics beyond the Standard Model has been given in the Conceptual Design Report [1]. Since then, stringent constraints on NP phenomena have been obtained from the LHC and the absence of hints from NP to date is presently changing this paradigm to two alternative scenarios: NP may actually reside at an even larger energy scale; NP may be at or below the TeV scale, but more weakly coupled, and thus hidden in the SM backgrounds [606].

A similar  $pp$ - $ep$  synergy could be envisaged with higher proton beam energies at the FCC 100 km tunnel. With an electron beam of 60 GeV, the expected centre-of-mass energies for  $ep$  could be 2.9 TeV for  $E_p = 19$  TeV (Low-Energy FCC) and 3.5 TeV for  $E_p = 50$  TeV (FCC). Below we list recent developments which discuss new physics opportunities at the LHeC and its potential future high-energy upgrades.

### 8.2 Extensions of the SM Higgs Sector

Presently, given the precision of measurements in the Higgs sector, it appears that the discovered 125 GeV scalar is indeed the SM Higgs boson. The question remains, however, if the scalar potential is truly that of the SM or if it should be extended, possibly with additional degrees of freedom. Several extensions of the Higgs sector have been proposed and can be studied at the  $ep$  colliders with results often complementary to those of  $pp$  colliders and other future facilities.

### 8.2.1 Modifications of the Top-Higgs interaction

In electron-proton collisions the heavy top-quarks can be produced in association with a Higgs boson, which allows us to study the sensitivity of the LHeC or the FCC-eh to the top-Higgs ( $tH$ ) interaction. In Ref. [469] the sensitivity of the process  $pe^- \rightarrow \bar{t}H\nu_e$  to the CP nature of the  $tH$  coupling is investigated by considering a CP phase  $\zeta_t$  at the  $ttH$  and  $bbH$  vertices. The authors conclude, based on several observables and with appropriate error fitting methodology, that better limits on  $\zeta_t$  are obtained at the LHeC than at the HL-LHC. At the design luminosity of  $1 \text{ ab}^{-1}$ , almost all values of  $\zeta_t$  are excluded up to  $4\sigma$  C.L. and the SM top-Higgs coupling could be measured relative to its SM value with a precision of  $\kappa = 1.00 \pm 0.17$ .

Flavour changing neutral currents (FCNC) are completely absent at tree-level in the SM and strongly constrained, especially by low energy experiments. Anomalous flavour changing neutral current Yukawa interactions between the top quark, the Higgs boson, and either an up or charm quark are documented in Chapter 3, Sec. 5.3.6. Among other studies, in Ref. [607] the authors consider the Higgs decay modes  $H \rightarrow \gamma\gamma, bb$  and  $\tau\tau$  and  $E_e = 150 \text{ GeV}$ . The results are updated in Ref. [477] for  $E_e = 60 \text{ GeV}$ , including estimates for lower electron beam energies, and the  $2\sigma$  sensitivity on the branching ratio  $\text{Br}(t \rightarrow uh)$  is found to be  $0.15 \times 10^{-2}$ . Making use of the polarisation of the electron beam and multivariate techniques, Ref. [608] shows that limits on the branching ratio  $\text{Br}(t \rightarrow uh)$  of  $\mathcal{O}(0.1)\%$  can be obtained, an improvement over present LHC limits of  $0.19\%$  [609, 610]. These results vary with  $E_e$  and  $E_p$ .

### 8.2.2 Charged scalars

The prospects to observe a light charged Higgs boson through the decay  $H^+ \rightarrow \bar{c}b$  are investigated within the framework of the Two Higgs Doublet Model (2HDM) Type III, assuming a four-zero texture in the Yukawa matrices and a general Higgs potential [611]. The charged current production processes  $e^-p \rightarrow \nu H^+ q$  are considered. The analysed signature stems from the subsequent decay  $H^+ \rightarrow \bar{c}b$ . The parton level analysis accounts for irreducible SM backgrounds and considers scenarios up to a mass of  $200 \text{ GeV}$ , consistent with present limits from Higgs and flavour physics. The authors show that for  $L = 100 \text{ fb}^{-1}$  a charged Higgs boson could be observed with about  $3 - 4\sigma$  significance. This is to be compared with results from present LHC searches in which strong limits are set on the branching fraction  $B(t \rightarrow H^+ b)$ , assuming  $B(H^+ \rightarrow \bar{c}b) = 1.0$  or  $B(H^+ \rightarrow c\bar{s}) = 1.0$  for the charged Higgs boson mass range  $\sim 90 - 160 \text{ GeV}$  [612, 613].

A similar study,  $H^\pm \rightarrow sc + su$ , for the FCC-eh (with  $\sqrt{s} \approx 3.5 \text{ TeV}$ ) is presented in Ref. [614], in the context of a next-to-minimal supersymmetric model (NMSSM). Using dedicated optimisation techniques, the authors show that a light charged boson  $H^\pm$  can be observed with maximal significance of  $4.4 (2.2)\sigma$  provided its mass is at most  $m_{H^\pm} = 114(121) \text{ GeV}$ , for the total luminosity of  $1 \text{ ab}^{-1}$ .

The Georgi-Machacek (GM) model extends the Higgs sector by including higher multiplet states while preserving custodial symmetry. The physical states include, besides the SM Higgs, a heavier singlet  $H$ , a triplet  $(H_3^+, H_3^0, H_3^-)$  and a quintuplet  $(H_5^{++}, H_5^+, H_5^0, H_5^-, H_5^{--})$ . The  $H_5$  scalars do not couple to fermions and can therefore only be produced by vector boson fusion. An analysis for the prospects to discover the doubly charged Higgs bosons in the GM model at the LHeC and the FCC-eh is presented in Ref. [615]. Therein the production of a doubly-charged member of five-plet Higgs-bosons ( $H_5^{\pm\pm}$ ), produced from  $W^\pm W^\pm$  fusion is studied. The authors find that  $2$  to  $3\sigma$  limits can be obtained for mixings  $\sin(\theta_H)$  as low as  $0.2$ , for  $M(H_5) < 300 \text{ GeV}$ . The prospects can be improved at the FCC-eh collider, where doubly charged Higgs bosons can be tested for masses  $M_{H_5} < 400 \text{ GeV}$ , also for small scalar mixing angles (Fig. 8.1 (left)).

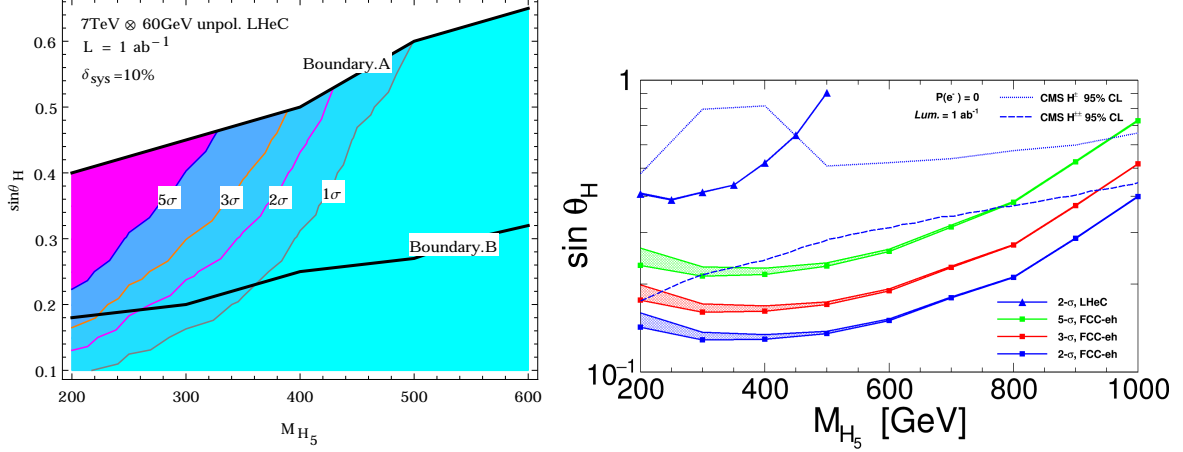


**Figure 8.1:** *Left:* Discovery contour with respect to  $\sin \theta_H$  and  $M(H_5^{++/--})$  at LHeC with unpolarized beam; *Right:* Limit Contours for the case of singly charged Higgs for FCC-eh and LHeC. The blue dotted curve and the blue dashed curves give the 95% CL limit from CMS for  $H_5^{+/-}$  and for  $H^{++/--}$  respectively [617, 618]. An unpolarized beam of integrated luminosity of  $1 \text{ ab}^{-1}$  and a 10% systematic uncertainty for background yields is assumed in both plots.

5072 The discovery prospects for the singly charged Higgs,  $H_5^\pm$  of the Georgi-Machacek model, pro-  
 5073 duced in  $W^\pm Z$  fusion, are evaluated in Ref. [616]. The authors perform a multivariate analysis,  
 5074 including a fast detector simulation, and consider the LHeC and the FCC-eh for a mass range  
 5075 from 200–1000 GeV. They find that the LHeC can improve over current LHC limits on  $H_5^\pm$  for  
 5076 masses up to about 400 GeV and scalar mixing angles  $\sin \theta_H \sim 0.5$  (Fig. 8.1 (right)).

### 5077 8.2.3 Neutral scalars

5078 Neutral scalar bosons generally appear in many extensions of the scalar sector. They can be  
 5079 added directly, as  $SU(1)$  singlets, or be part of higher representation  $SU(2)$  multiplets. They  
 5080 generally mix with the SM Higgs boson, from which they inherit a Higgs-like phenomenology.

5081 The potential of testing the heavier CP-even scalar that is contained in the 2HDM Type-I is  
 5082 presented in Ref. [619]. Therein, the lighter scalar particle is considered to be a SM-like Higgs  
 5083 boson and the properties of a heavy scalar, assumed to have the specific mass 270 GeV, is  
 5084 discussed. The authors state that the final state  $H \rightarrow Sh$ , where  $S$  is a scalar singlet with a  
 5085 mass around 100 GeV, is of particular interest, as it connects to the findings in Ref. [606].

5086 The prospects to search for a generic heavy neutral scalar particle are presented in detail  
 5087 Ref. [620]. The model is a minimal extension of the SM with one additional complex scalar  
 5088 singlet that mixes with the SM Higgs doublet, which governs its production and decay mode.  
 5089 The heavy scalar is produced via vector-boson fusion and decays into two vector bosons. A mul-  
 5090 tivariate analysis is performed and detector simulation is taken into account. Masses between  
 5091 200 and 800 GeV and scalar mixings as small as  $\sin^2 \alpha \sim 10^{-3}$  are considered. The resulting  
 5092 sensitivity for a total luminosity of  $1 \text{ ab}^{-1}$  is shown in Fig. 8.2, including existing bounds from  
 5093 the LHC and future HL-LHC projections. A significant improvement over existing LHC limits  
 5094 is found, with the LHeC probing scalar boson masses below  $\sim 500$  GeV, a region which remains  
 5095 difficult at the HL-LHC.

5096 The scalar bosons from the 2HDM Type-III framework may give rise to flavour violating signa-  
 5097 tures, as discussed in Ref. [623]. The prospects to observe the light and heavy CP-even neutral  
 5098 Higgs bosons via their decays into flavour violating  $b\bar{s}$  channels were studied with specific Yukawa

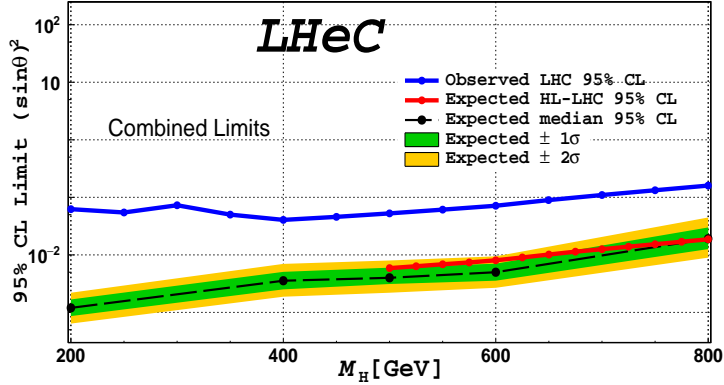


**Figure 8.2:** Expected exclusion limits (green and yellow bnds) for a heavy scalar search at the LHeC, assuming a systematic uncertainty on the SM background of 2% (from Ref. [620]). The blue line represents the current LHC limit at 95% CL as extracted from [621], the red line the forecast of the HL-LHC sensitivity via  $h_2 \rightarrow ZZ$  searches from Ref. [622]. The LHeC results correspond to an integrated luminosity of  $1 \text{ ab}^{-1}$ .

5099 textures and a general Higgs potential. The signature consists of one jet originating from b-  
5100 hadron fragmentation (b-tagged jets) and one light-flavour jet in the central rapidity region, with  
5101 a remaining jet in the forward region. Relevant SM backgrounds were considered and it is found  
5102 that flavour violating decays of the SM-like Higgs boson would be accessible with  $L = 100 \text{ fb}^{-1}$   
5103 at  $ep$  colliders.

5104 The prospects of observing the light CP-even neutral Higgs bosons of the NMSSM framework,  
5105 the MSSM with an additional singlet superfield, via their decays into b-quarks and in the neutral  
5106 and charged current production processes, are studied in Ref. [624]. In this work the following  
5107 constraints are incorporated into the spectrum: neutralino relic density corresponding to the  
5108 observed dark matter relic density; direct and indirect mass bounds from searches for specific  
5109 sparticles; the SM-like Higgs boson has a mass around 126 GeV and an invisible branching ratio  
5110 below 0.25. The signal is given by three jets plus an electron or missing transverse momentum  
5111 ( $E_T^{miss}$ ) arising from the neutral (charged) current interaction, where two jets are required to be  
5112 originating from a b-quark and the remaining jet is required to be in the forward region. For the  
5113 cut-based analysis a number of reducible and irreducible SM backgrounds, generated with a fast  
5114 detector simulation with an adaptation of the LHeC detector, are considered. It is found that  
5115 the boson  $h_1$  could be observable for some of the NMSSM benchmark points, at up to  $2.5\sigma$  level  
5116 in the  $e + 3j$  channel up to masses of 75 GeV; in the  $3j + E_T^{miss}$  channel  $h_1$  could be discovered  
5117 at  $2.4\sigma$  level up to masses of 88 GeV with  $L = 100 \text{ fb}^{-1}$ , and a  $5\sigma$  observation is possible with  
5118  $\mathcal{L} = 1 \text{ ab}^{-1}$  for masses up to 90 GeV.

#### 5119 8.2.4 Modifications of Higgs self-couplings

5120 As in the chapter on Higgs physics above, the  $e^-p$  collisions are a very convenient environment  
5121 to study the property of the SM Higgs boson itself. The latter is produced through vector-boson  
5122 fusion processes and the precise measurement of its properties provides a unique opportunity  
5123 to probe the interaction  $HVV$ , ( $V = W^\pm, Z$ ). These interactions are in general sensitive to  
5124 certain classes of beyond the SM physics, which can be parameterized, for instance, via higher  
5125 dimensional operators and their coefficients, cf. Refs. [571, 600, 625–627].

5126 The prospects of inferring the strengths of the two couplings  $HWW$  and  $HZZ$  were studied in  
5127 Refs. [600, 626] in the context of electron-proton collisions. The authors find that the higher-

5128 dimensional operator coefficients can be tested for values around  $\mathcal{O}(10^{-1})$  at the LHeC. This  
5129 sensitivity is improved at the FCC-eh due to larger centre-of-mass energies, which in general  
5130 enhance the vector-boson fusion cross sections.

5131 The Higgs self-coupling itself  $HHH$  can be tested through the measurement of the di-Higgs  
5132 production cross section as was shown in Ref. [571]. With appropriate error fitting methodology  
5133 this study illustrates that the Higgs boson self-coupling could be measured with an accuracy of  
5134  $g_{HHH}^{(1)} = 1.00_{-0.17(0.12)}^{+0.24(0.14)}$  of its expected SM value at  $\sqrt{s} = 3.5(5.0)$  TeV, considering an ultimate  
5135  $10 \text{ ab}^{-1}$  of integrated luminosity.

5136 An analysis presented in Ref. [627] evaluates the LHeC sensitivity to dimension-six operators.  
5137 The authors employ jet substructure techniques to reconstruct the boosted Higgs boson in the  
5138 final state. A shape analysis on the differential cross sections shows in some cases improvements  
5139 with respect to the high-luminosity LHC forecasts.

### 5140 8.2.5 Exotic Higgs boson decays

5141 The LHeC sensitivity to an invisibly decaying Higgs boson was investigated in Ref. [603]. Therein  
5142 the focus is on the neutral current production channel due to the enhanced number of observ-  
5143 ables compared to the charged current counterpart. The signal contains one electron, one jet  
5144 and large missing energy. A cut-based parton level analysis yields the estimated sensitivity of  
5145  $\text{Br}(h \rightarrow \text{invisible}) = 6 \%$  at  $2\sigma$  level. Exotic decays of the Higgs boson into a pair of light spin-0  
5146 particles referred to as  $\Phi$  was discussed in Ref. [628]. The studied signature is a final state with  
5147 4 b-quarks, which is well motivated in models where the scalars can mix with the Higgs doublet,  
5148 and suffers from multiple backgrounds at the LHC. The analysis is carried out at the parton  
5149 level, where simple selection requirements render the signature nearly free of SM background  
5150 and makes  $\Phi$  with masses in the range [20, 60] GeV testable for a  $hVV$  ( $V = W, Z$ ) coupling  
5151 strength relative to the SM at a few per-mille level and at 95 % confidence level.

5152 The prospects of testing exotic Higgs decays into pairs of light long-lived particles at the LHeC  
5153 were studied in Ref. [629] where it was shown that proper lifetimes as small as  $\mu\text{m}$  could be  
5154 tested, which is significantly better compared to the LHC. This is shown in Fig. 8.3 (left). This  
5155 information can be interpreted in a model where the long-lived particles are light scalars that mix  
5156 with the Higgs doublet, where both, production and decay, are governed by this scalar mixing  
5157 angle. The area in the mass-mixing parameter space that give rise to at least 3 observable  
5158 events with a displaced vertex are shown in Fig. 8.3. It is apparent that mixings as small as  
5159  $\sin^2 \alpha \sim 10^{-7}$  can be tested at the LHeC for scalar masses between 5 and 15 GeV [629].

## 5160 8.3 Searches for supersymmetry

5161 Several SUSY scenarios might remain still elusive in searches performed at  $pp$  colliders. While  
5162 the null results from current searches by the LHC experiments have produced impressive con-  
5163 straints on the SUSY coloured sector (squarks and gluinos) because of their large production  
5164 cross sections in strong interactions, less stringent constraints have been placed on weakly-  
5165 produced SUSY particles, namely neutralinos  $\tilde{\chi}^0$ , charginos  $\tilde{\chi}^\pm$ , and sleptons  $\tilde{\ell}^\pm$ . Some of these  
5166 scenarios where  $ep$  colliders might have discovery potential complementary to that of the HL-  
5167 LHC are discussed below. These include R-parity conserving SUSY models, e.g. motivated by  
5168 dark matter, or R-parity violating SUSY models, e.g. including single production of bottom and  
5169 top squarks and low mass gluinos.

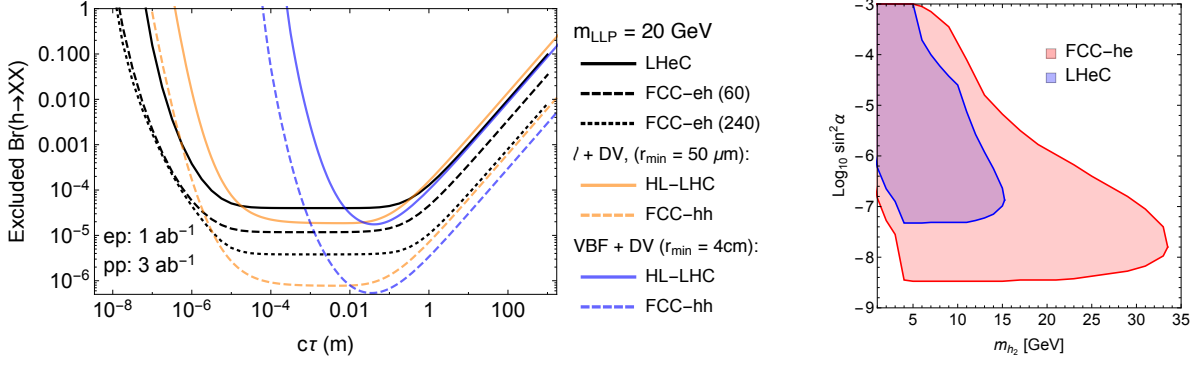


**Figure 8.3:** Sensitivity contours for displaced vertex searches for Higgs decays into long-lived scalar particles (LLP), which are pair produced from decays of the Higgs boson, and which themselves decay via scalar mixing into fully visible final states. Left: As a function of the LLP lifetime for a fixed mass from Ref. [629]. Right: For a specific model, where lifetime and production rate of the LLP are governed by the scalar mixing angle. The contours are for 3 events and consider displacements larger than  $50 \mu\text{m}$  to be free of background.

### 8.3.1 Search for the SUSY Electroweak Sector: prompt signatures

5170

5171 Electroweakino scenarios where charginos, neutralinos, and sleptons are close in mass can be  
 5172 characterised by the neutralino mass  $m$  and the mass splitting between charginos and neutralinos  
 5173  $\Delta m$ . We here refer to scenarios with  $\Delta m < 50 \text{ GeV}$  as *compressed*. A subtlety arises for  
 5174  $\Delta m \leq 1 \text{ GeV}$ , when the  $\tilde{\chi}_1^\pm / \tilde{\chi}_2^0$  becomes long lived and its decays are displaced. For  $\Delta m > 1 \text{ GeV}$   
 5175 the decays are prompt, the visible decay products from  $\tilde{\ell}$  and  $\tilde{\chi}_1^\pm / \tilde{\chi}_2^0$  have very soft transverse  
 5176 momenta ( $p_T$ ) and the SM backgrounds are kinematically similar to the signal. The analyses  
 5177 therefore become challenging and sensitivities decrease substantially. Two SUSY scenarios are  
 5178 considered in Ref. [630] and depicted in Fig. 8.4 where the LSP  $\tilde{\chi}_1^0$  is Bino-like,  $\tilde{\chi}_1^\pm$  and  $\tilde{\chi}_2^0$   
 5179 are Wino-like with almost degenerate masses, and the mass difference between  $\tilde{\chi}_1^0$  and  $\tilde{\chi}_1^\pm$  is  
 small. The signal is produced via the process “ $pe^- \rightarrow je^- \tilde{\chi} \tilde{\chi}$ ”, where  $\tilde{\chi} = \tilde{\chi}_1^0, \tilde{\chi}_1^\pm$  or  $\tilde{\chi}_2^0$ .

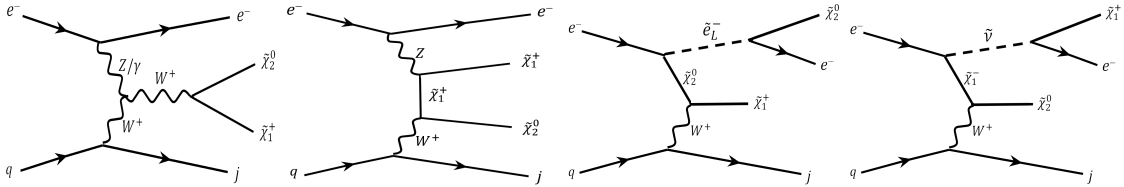


**Figure 8.4:** Representative production diagrams for the signal processes considered in Ref. [630]. The *decoupled-slepton* scenario includes only the first two diagrams, while the *compressed-slepton* scenario includes all four diagrams.

5180

5181 Conservative leading order cross sections are considered for the SUSY signal models. The  
 5182 kinematic observables are input to the TMVA package to perform a multivariate analysis at the  
 5183 detector level.

5184 In the compressed-slepton scenario, the case where the left-handed slepton  $\tilde{\ell}_L$  and sneutrino  
 5185  $\tilde{\nu}$  are slightly heavier than  $\tilde{\chi}_1^\pm$  or  $\tilde{\chi}_2^0$  is considered. When fixing the mass difference  $\Delta m =$   
 5186  $m_{\tilde{\ell}} - m_{\tilde{\chi}_1^\pm, \tilde{\chi}_2^0} = 35 \text{ GeV}$  and ignoring the systematic uncertainty on the background, the analysis  
 5187 indicates that the  $2$  ( $5$ ) $\sigma$  limits on the  $\tilde{\chi}_1^\pm, \tilde{\chi}_2^0$  mass are  $616$  ( $517$ )  $\text{GeV}$  for  $2.5 \text{ ab}^{-1}$  luminosity at  
 5188 the FCC-eh, and  $266$  ( $227$ )  $\text{GeV}$  for  $1 \text{ ab}^{-1}$  luminosity at the LHeC, respectively. An illustration  
 5189 of the model assumptions in terms of sleptons and neutralino masses and the current constraints  
 5190 at the LHC is presented in Fig. 8.5 (left). Results are illustrated in Fig. 8.5 (right). The effects



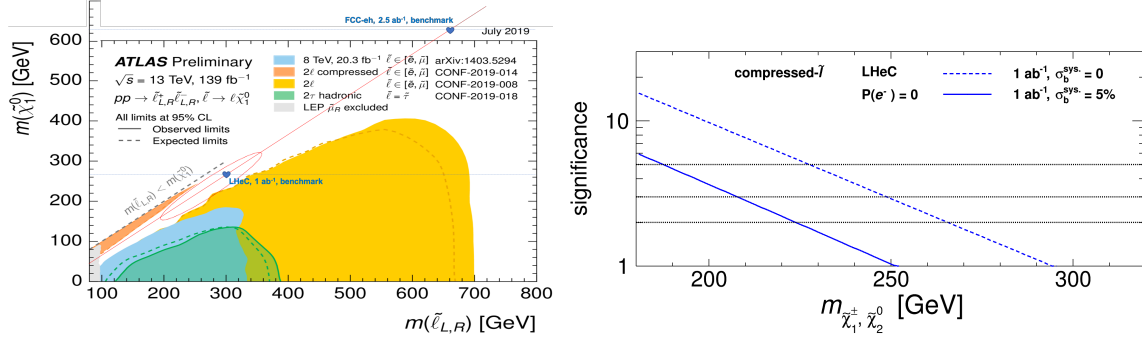


**Figure 8.5:** *Left:* Benchmark assumption on slepton masses and 2019 reach of current ATLAS searches for sleptons (Ref. ATLAS public twiki). *Right:* Significances as varying the masses of  $\tilde{\chi}_1^\pm$  and  $\tilde{\chi}_2^0$  for the compressed-slepton scenario at the LHeC with unpolarised beams and  $1 \text{ ab}^{-1}$  luminosity. For dashed (solid) curve, a systematic uncertainty of 0% (5%) on the background is considered. The figure is from Ref. [630].

5191 of varying  $\Delta m$  are investigated: fixing  $m_{\tilde{\chi}_1^\pm, \tilde{\chi}_2^0}$  to be 400 GeV, it is found that at the FCC-eh  
 5192 the significance is maximal when  $\Delta m$  is around 20 GeV.

5193 In the decoupled-slepton scenarios where only  $\tilde{\chi}_1^0$ ,  $\tilde{\chi}_1^\pm$  and  $\tilde{\chi}_2^0$  are light and other SUSY particles  
 5194 are heavy and decoupled, the  $2\sigma$  limits obtained on the  $\tilde{\chi}_1^\pm$ ,  $\tilde{\chi}_2^0$  mass are 230 GeV for  $2.5 \text{ ab}^{-1}$   
 5195 luminosity at the FCC-eh when neglecting the systematic uncertainty on the background. Large  
 5196 systematic uncertainties on the SM background processes can substantially affect the sensitivity,  
 5197 hence good control of experimental and theoretical sources of uncertainties is very important.

5198 Finally, it is also found that the possibility of having a negatively polarised electron beam  
 5199 ( $P_e = 80\%$ ) could potentially extend the sensitivity to electroweakinos by up to 40%.

5200 Overall, since the sensitivity to the electroweak SUSY sector depends on the mass hierarchy  
 5201 of  $\tilde{\chi}_1^\pm$ ,  $\tilde{\chi}_1^0$ ,  $\tilde{\chi}_2^0$  and sleptons, and given the difficulty to probe efficiently small  $\Delta m$  regions at  
 5202 the current LHC and possibly at the HL-LHC, measurements at  $ep$  colliders may prove to offer  
 5203 complementary or additional reaches, in particular for the compressed scenarios.

### 5204 8.3.2 Search for the SUSY Electroweak Sector: long-lived particles

5205 Studies on Higgsinos ( $\chi$ ) with masses  $\mathcal{O}(100)$  GeV are motivated by natural SUSY theories and  
 5206 help to avoid large fine-tuning on the Higgs boson mass. In these scenarios the low energy  
 5207 charginos ( $\chi^\pm$ )/neutralinos ( $\chi^0$ ) are all Higgsino-like and their masses are nearly degenerate,  
 5208 only slightly above the neutralino.

5209 As mentioned above, a compressed spectrum with nearly degenerate masses results in a kinematic  
 5210 suppression of the heavier  $\chi^\pm$  decays into  $W^\pm \chi^0$ , which has twofold consequences: it yields final  
 5211 states without hard leptons; it enhances the  $\chi^\pm$  lifetime up to  $\mathcal{O}(1)$  mm. At the LHC the absence  
 5212 of hard leptons with sizable transverse momentum makes this signature difficult to investigate.  
 5213 One possibility is to search for the tracks from  $\chi^\pm$ , which effectively disappear once it decays  
 5214 and are thus called *disappearing tracks*.

5215 The discovery prospects for prompt signatures of electroweakino decays in electron-proton col-  
 5216 lisions are presented in Ref. [631]. The light  $\chi^\pm$  (and  $\chi^0$ ) can be produced in pairs via in vector  
 5217 boson fusion of the charged or neutral currents. A cut-based analysis of these processes at the  
 5218 LHeC, assuming prompt  $\chi^\pm$  decays, yields  $2\sigma$  discovery prospects for masses up to 120 GeV.

5219 Taking into account the finite lifetime of the charginos, two comments are in order: first, the

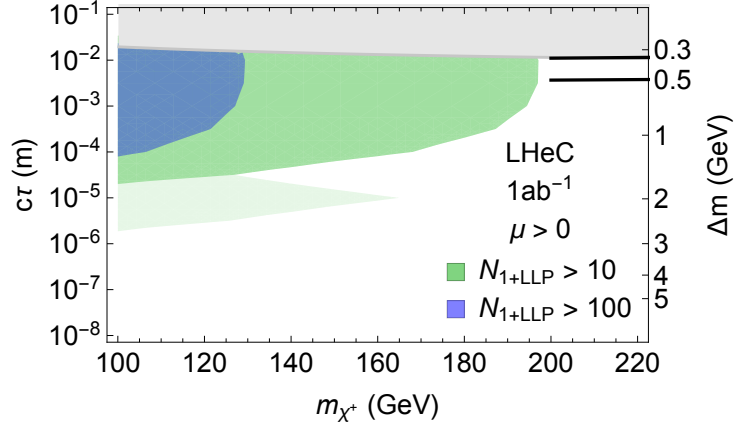


**Figure 8.6:** Exclusion limits on Higgsino masses as a function of their lifetime from Ref. [629]. Coloured regions denote where 10 or 100 events with at least one LLP decay are observed. Light shading indicates the uncertainty in the predicted number of events due to different hadronisation and LLP reconstruction assumptions. The black curves are the optimistic and pessimistic projected bounds from HL-LHC disappearing track searches.

5220 lifetimes and boosts of the  $\chi^+$  are in general too small to resolve a disappearing track; second,  
 5221 the soft final state is not a problem per se and can in principle be observed.

5222 Instead of searching for a disappearing track, the long lifetimes of the  $\chi^+$  can be exploited  
 5223 via the measurement of the impact parameter of the soft hadronic final, as is discussed in  
 5224 Ref. [629]. The crucial machine performance parameters are the tracking resolution, which is  
 5225 as good as  $\mathcal{O}(10)\mu\text{m}$ , and the absence of pile up, which allows to identify and measure a single  
 5226 soft pion’s impact parameter. In this way the LHeC can test  $\chi$  with masses up to 200 GeV. The  
 5227 corresponding sensitivity is shown in Fig. 8.6, and the bounds on disappearing track searches  
 5228 at the HL-LHC are shown as black lines in the figure. By considering non-prompt decays  
 5229 of Higgsinos, the discovery prospects compared to the prompt analysis is thus significantly  
 5230 improved. Further means of improving the prospects is an increased centre-of-mass energy,  
 5231 which enhances the production rate of the Higgsinos.

### 5232 8.3.3 R-parity violating signatures

5233 Supersymmetry typically evokes the so-called R-parity, which implies that each fundamental  
 5234 vertex contains an even number of sparticles and helps preventing rapid proton decays. In  
 5235 general, R-parity need not be an exact symmetry of the theory, such that interactions can be  
 5236 present that allow for sparticles to decay into SM particles and include the possibility to violate  
 5237 lepton and/or baryon number.

5238 R-parity violating interactions are particularly interesting in electron-proton collisions, where  
 5239 single superpartners might be produced resonantly, and detected via the corresponding  $2 \rightarrow 2$   
 5240 process. This is discussed in Refs. [632, 633] for the case of the *sbottom*, showing that a good  
 5241 level of precision could be achieved at LHeC compared with all the knowledge derived from  
 5242 indirect measurements.

5243 Single (anti-)top quark production associated with a lightest neutralino in the MSSM with R-  
 5244 parity breaking coupling is investigated in Ref. [634] for the LHeC. The study, which includes  
 5245 calculations of QCD contributions at NLO, concludes that the available constraints would allow  
 5246 a notable production rate.

5247 Certain SUSY scenarios might produce prompt signals of multiple soft jets, which generally  
5248 resemble QCD backgrounds at the LHC and are thus notoriously difficult to test. The largely  
5249 QCD-free environment of electron-proton collisions allows to test this class of signatures. One  
5250 example of this signal can come from gluinos, which are tested at the LHC via signatures that  
5251 involve large amounts of missing energy. If the gluino has an all-hadronic decay – as in R-parity  
5252 violating scenarios or Stealth SUSY models – the current experimental searches have a gap in  
5253 sensitivity for masses between about 50 to 70 GeV [635]. Gluinos within this gap can be tested at  
5254 the LHeC [636], where a three sigma exclusion sensitivity was demonstrated with simple signal  
5255 selection cuts.

## 5256 8.4 Feebly Interacting Particles

5257 New physics may interact with the SM via the so-called portal operators, including the vector,  
5258 scalar, pseudoscalar, or neutrino portal. In these scenarios, the SM is often extended by an  
5259 entire sector of new physics, comprising new forces and several particle species, which may be  
5260 connected to the big open questions of Dark Matter or the origin of neutrino mass.

5261 These hypothetical new sectors derive their typically very feeble interaction strength with the  
5262 known particles from mass mixing with a SM particle that shares their quantum numbers. Some  
5263 examples are being discussed below.

### 5264 8.4.1 Searches for heavy neutrinos

5265 The observation of neutrino oscillations requires physics beyond the SM that gives rise to the light  
5266 neutrino masses. One well-motivated class of models for this purpose is the so-called symmetry  
5267 protected type I seesaw scenario, which features heavy neutrinos with signatures that are in  
5268 principle observable at colliders, cf. Ref. [637] and references therein. A comprehensive overview  
5269 over collider searches for the heavy and mostly sterile neutrinos can be found in Ref. [638], where  
5270 the promising signatures for such searches at electron-proton colliders have been identified.

5271 In electron-proton collisions heavy neutrinos can be produced via the charged current (see the  
5272 left panel of Fig. 8.7). The heavy neutrino production cross section is dependent on the active-  
5273 sterile neutrino mixing with the electron flavour called  $|\theta_e|^2$ . The most promising searches at  
5274 the LHeC are given by processes with lepton flavour violating final states and displaced vertices,  
5275 the prospects of which are evaluated in Ref. [639] and are shown in the right panel of Fig. 8.7. It  
5276 is remarkable, that the prospects to detect heavy neutrinos with masses above about 100 GeV  
5277 are much better in electron-proton collisions compared to proton-proton or electron-positron,  
5278 due to the much smaller reducible backgrounds.

5279 The prospects of heavy neutrino detection can be further enhanced with jet substructure tech-  
5280 niques when the  $W$  boson in the decay  $N \rightarrow eW$ ,  $W \rightarrow jj$  is highly boosted. Ref. [640] shows  
5281 that these techniques can help to distinguish the heavy neutrino signal from the few SM back-  
5282 grounds. A considerable improvement in the bounds of  $|V_{eN}|^2$  over present limits from LHC,  
5283  $0\nu 2\beta$  experiments and from electroweak precision data is obtained with  $1 \text{ ab}^{-1}$  of integrated  
5284 luminosity at the LHeC.

5285 An alternative approach is employed in Ref. [645] where the dominant sterile neutrino inter-  
5286 actions with the SM are taken to be higher dimension effective operators (parameterizing a  
5287 wide variety of UV-complete new physics models) while contributions from neutrino mixing is  
5288 neglected. The study shows prospects of Majorana neutrino detection for masses lower than  
5289 700 and 1300 GeV can be discovered at the LHeC with  $E_e = 50$  and 150 GeV, respectively, for

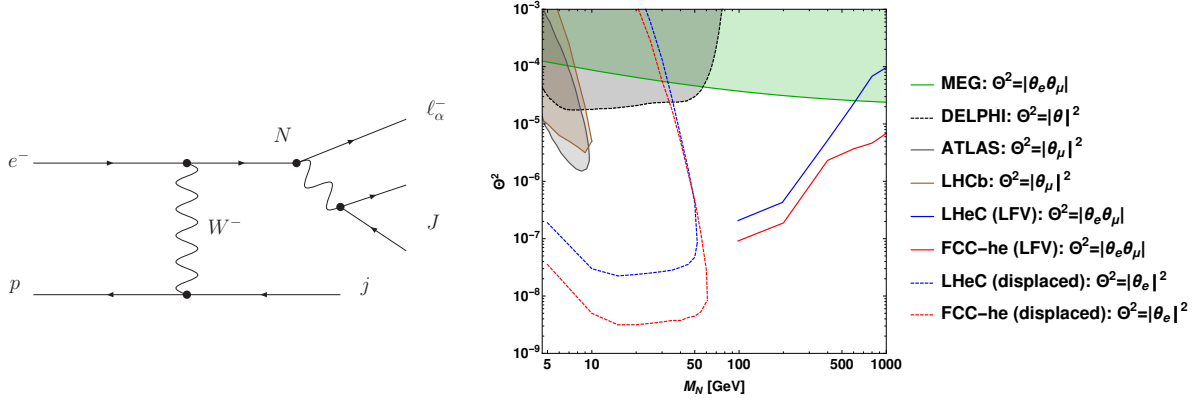


**Figure 8.7:** Left: Dominant tree-level production mechanism for sterile neutrinos at the LHeC. The sterile neutrino decay via the charged current gives rise to the so-called lepton flavor violating lepton-trijet signature. Right: Sensitivity of the LFV lepton-trijet searches (at 95 % C.L.) and the displaced vertex searches (at 95 % C.L.) from Ref. [639] compared to the current exclusion limits from ATLAS [641], LHCb [642], LEP [643], and MEG [644].

5290  $E_p = 7$  TeV. Recently the influence of vector and scalar operators on the angular distribution of  
 5291 the final anti-lepton was investigated. The forward-backward asymmetry is studied in Ref. [646],  
 5292 wherein, in particular, the feasibility of initial electron polarisation as a discriminator between  
 5293 different effective operators is studied.

5294 Prospects of testing left-right symmetric models, featuring additional charged and neutral gauge  
 5295 bosons and heavy neutrinos, were studied in the context of electron-proton collisions in Refs. [647,  
 5296 648]. The authors show that the production of heavy right-handed neutrinos of mass  $\mathcal{O}(10^2-$   
 5297  $10^3)$  GeV at the LHeC, with a lepton number violating final state, can yield information on  
 5298 the parity breaking scale in left-right symmetric theories. Heavy neutrinos of sub-TeV mass in  
 5299 inverse see-saw model with Yukawa coupling of  $\mathcal{O}(0.1)$  are investigated for the LHeC in Ref. [649].

#### 5300 8.4.2 Fermion triplets in type III seesaw

5301 Another technically natural way of generating the light neutrino masses is the so-called Type  
 5302 III seesaw mechanism, which extends the SM with a fermion  $SU(2)$  triplet. In minimal versions  
 5303 of these models the neutral and charged triplet fermions have almost degenerate masses around  
 5304 the TeV scale.

5305 In the three generation triplet extension of the type-III seesaw, the role of mixings between  
 5306 active neutrinos and neutral triplet fermions has been investigated in Ref. [650]. Depending  
 5307 upon the choices of Dirac Yukawa coupling, the mixing angles can take many possible values,  
 5308 from very small to large. With very small mixings, decay length of the triplet fermion can be  
 5309 very large. It can show a displaced decay inside the detector or outside the detector of the  
 5310 high energy colliders. The proper decay length as a function of the lightest light neutrino mass  
 5311  $m_1(m_3)$  for the Normal (Inverted) hierarchy case are shown in Fig. 8.8.

5312 The prospects of probing this mechanism via searches for the new fermions are evaluated in  
 5313 Ref. [652], wherein signatures from long-lived particles at various experiments were considered.  
 5314 The triplet fermions are primarily produced through their gauge interactions, as shown in the  
 5315 left panel of Fig. 8.9, and can be observed via displaced vertices and disappearing track searches  
 5316 for masses of a few hundred GeV. The authors find that the LHeC can observe displaced vertices  
 5317 from the decays of the charged fermion triplet components via the soft pion impact param-  
 5318 eters for triplet masses up to about 220 GeV and has a complementary sensitivity to the light

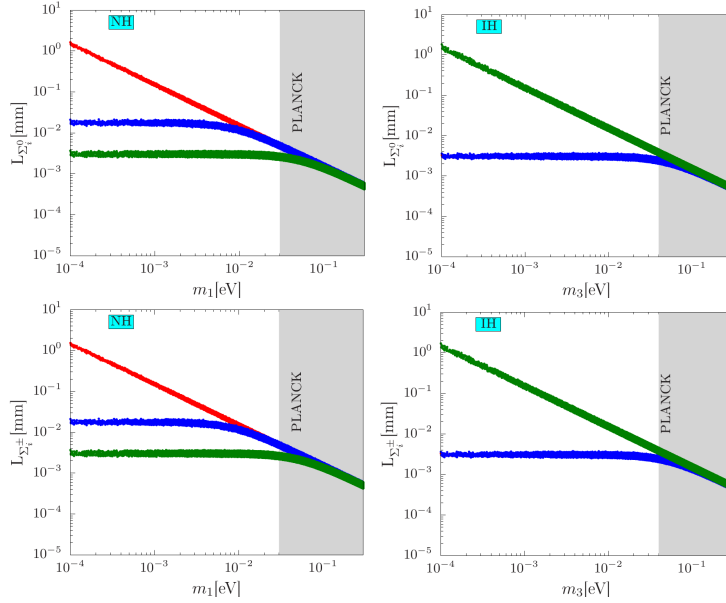


**Figure 8.8:** Proper decay length of  $\Sigma_i^0$  ( $\Sigma_i^\pm$ ) with respect to the lightest light neutrino mass in the upper (lower) panel for 1 TeV triplet. The Normal (Inverted) hierarchy case is shown in the left (right) panel. The first generation triplet is represented by the red band, the second generation is represented by the blue band and the third generation is represented by the green band respectively. The shaded region is excluded by the PLANCK data [651].

5319 neutrino mass scale, which governs the lifetime of the neutral fermion, compared the LHC and  
 5320 MATHUSLA. The final results from Ref. [652] for the LHeC are shown in the right panel of  
 5321 Fig. 8.9.

5322 If the mixing becomes sufficiently large, and/or if the masses are  $\mathcal{O}(100)$  GeV, the triplet fermions  
 5323 decay promptly. Also in this case, the heavy triplets can show a variety of interesting collider  
 5324 signatures including fat jets. The latter have been studied for FCC-he in Ref. [653].

### 5325 8.4.3 Dark photons

5326 Minimal extensions of the SM often involve additional gauge factors. In particular the  $U(1)_X$  ex-  
 5327 tensions are interesting, because they are often connected to a dark charge that can be associated  
 5328 with the dark matter.

5329 An SM-extending  $U(1)_X$  predicts an additional gauge boson that naturally mixes with the  $U(1)_Y$   
 5330 factor of the SM kinetically [654]. This kinetic mixing lets the SM photon couple to fermions that  
 5331 carry the dark charge  $X$ , and the other gauge boson to the electric charge. Both interactions  
 5332 are suppressed by the mixing parameter  $\epsilon$ . In most models the additional gauge boson also  
 5333 receives a mass, possibly from spontaneous breaking of the  $U(1)_X$ , and the corresponding mass  
 5334 eigenstate is called a dark photon. Dark photons typically have masses around the GeV scale  
 5335 and their interactions are QED-like, scaled with the small mixing parameter  $\epsilon$ . It can decay to  
 5336 pairs of leptons, hadrons, or quarks, which can give rise to a displaced vertex signal due to its  
 5337 long lifetime.

5338 The prospects for the dark photon searches via their displaced decays in  $ep$  collisions are pre-  
 5339 sented in Ref. [655]. The dark photon production process targeted in this search is depicted in  
 5340 Fig. 8.10. The signal is given by the process  $e^-p \rightarrow e^-X\gamma'$ , where  $X$  denotes the final state  
 5341 hadrons, and the dark photon  $\gamma'$  decays into two charged fermions or mesons.

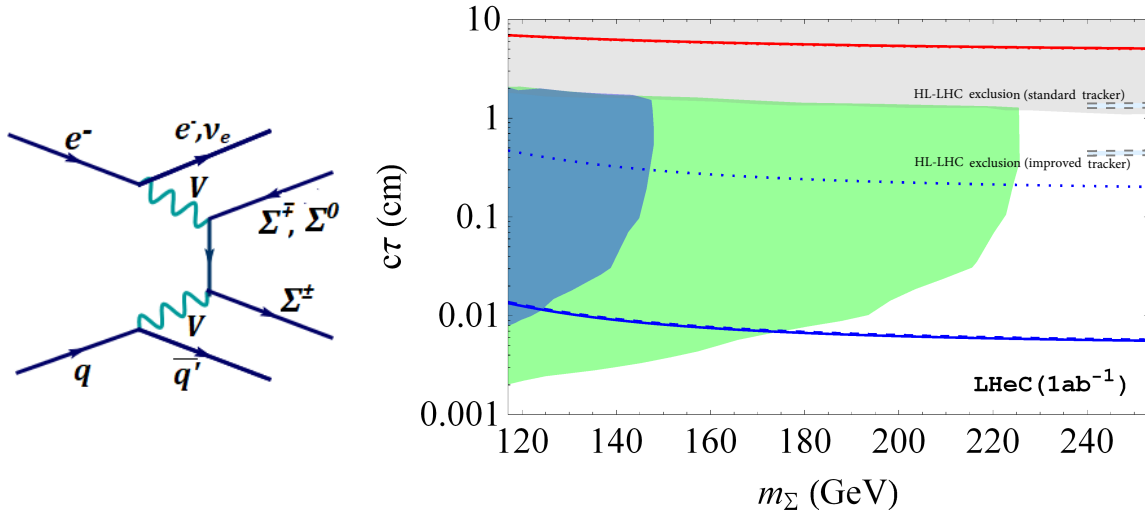


**Figure 8.9:** Left: Dominant production diagram of triplet fermion pairs via their gauge interactions. Right: Prospects of displaced vertex searches from charged fermion triplet  $\Sigma^{\pm}$ . The blue and green shaded regions denote the expected observability of 10 (100) events, dashed lines denote HL-LHC exclusion sensitivity, and the red line is connected to the light neutrino properties. For details, see text and Ref. [652].

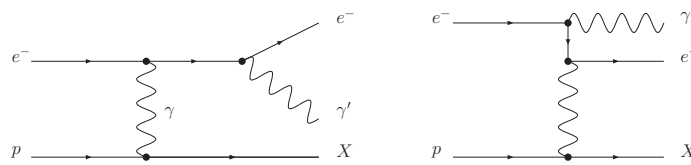


**Figure 8.10:** Feynman diagrams for the dark photon production processes in electron-proton collisions. Here  $X$  denotes the final state hadrons after the scattering process.

5342 The most relevant performance characteristics of the LHeC are the very good tracking resolution  
 5343 and the very low level of background, which allow the detection of a secondary vertex with a  
 5344 displacement of  $\mathcal{O}(0.1)$  mm.

5345 The resulting sensitivity contours in the mass-mixing parameter space are shown in Fig. 8.11,  
 5346 where the different colours correspond to different assumptions on the irreducible background  
 5347 and the solid and dashed lines consider different signal reconstruction efficiencies. Also shown  
 5348 for comparison are existing exclusion limits from different experiments, and the region that is  
 5349 currently investigated by the LHCb collaboration [656].

5350 The domain in parameter space tested in electron-proton collisions is complementary to other  
 5351 present and planned experiments. In particular for masses below the di-muon threshold, searches  
 5352 at the LHC are practically impossible. It is remarkable that dark photons in this mass range can  
 5353 be part of a dark sector that explains the observed Dark Matter in the Universe via a freeze-in  
 5354 mechanism, cf. e.g. Ref. [657].

#### 5355 8.4.4 Axion-like particles

5356 The axion is the Goldstone boson related to a global  $U(1)$  symmetry, which is spontaneously  
 5357 broken at the so-called Peccei-Quinn scale, assumed to be around the GUT scale. Its mass,  
 5358 being inversely proportional to the Peccei-Quinn scale, is therefore usually in the sub-eV regime  
 5359 and the axion provides a dynamical solution to the strong CP problem of the standard model.

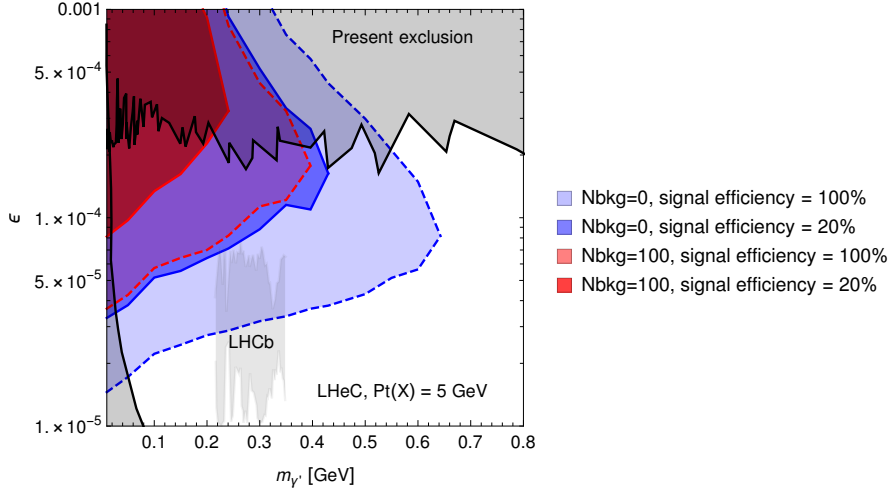


**Figure 8.11:** Projected sensitivity of dark photon searches at the LHeC via displaced dark photon decays from Ref. [655]. The sensitivity contour lines are at the 90 % confidence level after a transverse momentum cut on the final state hadrons of 5 GeV. The blue and red areas denote the assumption of zero and 100 background events, respectively, the solid and dashed lines correspond to a reconstruction efficiency of 100 % and 20 %, respectively. See Ref. [655] for details.

5360 Axions are a very attractive candidate for *cold* dark matter, despite their tiny mass.

5361 Axion-like particles (ALP) are motivated by the original idea of the QCD axion and similarly,  
 5362 they are good dark matter candidates. ALPs are pseudoscalar particles that are usually assumed  
 5363 to be relatively light (i.e. with masses around and below one GeV) and couple to the QCD field  
 5364 strength. In addition, they may have a number of further interactions, for instance they can  
 5365 interact with the other fields of the SM and also mix with the pion. Particularly interesting is  
 5366 the possibility to produce ALPs via vector boson fusion processes.

5367 A recent study [658] has evaluated the prospects of detecting ALPs at the LHeC via the process  
 5368  $e^- \gamma \rightarrow e^- a$ , as shown in the left panel of Fig. 8.12, in a model independent fashion. The  
 5369 investigated signature is the decay  $a \rightarrow \gamma \gamma$ , which allows to test the effective ALP-photon  
 5370 coupling for ALPs with masses in the range of  $10 \text{ GeV} < m_a < 3 \text{ TeV}$ . It was found that  
 5371 sensitivities can improve current LHC bounds considerably, especially for ALP masses below  
 5372 100 GeV, as shown in the right panel of Fig. 8.12. The authors state that ALP searches at  $ep$   
 5373 colliders might become an important handle on this class of new physics scenarios [658].

## 5374 8.5 Anomalous Gauge Couplings

5375 New physics beyond the SM can modify SM interactions, for instance at the loop level. Such  
 5376 contributions could either modify the interaction strength of SM particles or introduce additional  
 5377 interactions that are not present in the SM, like flavour changing neutral couplings.

5378 Searches for anomalous couplings of top quarks are summarised in Section 5.3. They are  
 5379 parametrised via an effective Lagrangian and are studied by analysing specific processes. For  
 5380 example, anomalous  $Wtb$  couplings are studied in  $e^- p \rightarrow \nu_e \bar{t}$ , and anomalous  $t\bar{t}\gamma$  and  $t\bar{t}Z$   
 5381 couplings are studied in top quark pair production. In addition FCNC  $tu\gamma$  and  $tuZ$  couplings are  
 5382 analysed in NC DIS single top quark production, and FCNC  $tHu$  couplings are investigated in  
 5383 CC DIS single top quark production. Limits on the corresponding FCNC branching ratios are  
 5384 discussed in Section 5.3.6 and summarised and compared to different colliders in Fig. 5.18.

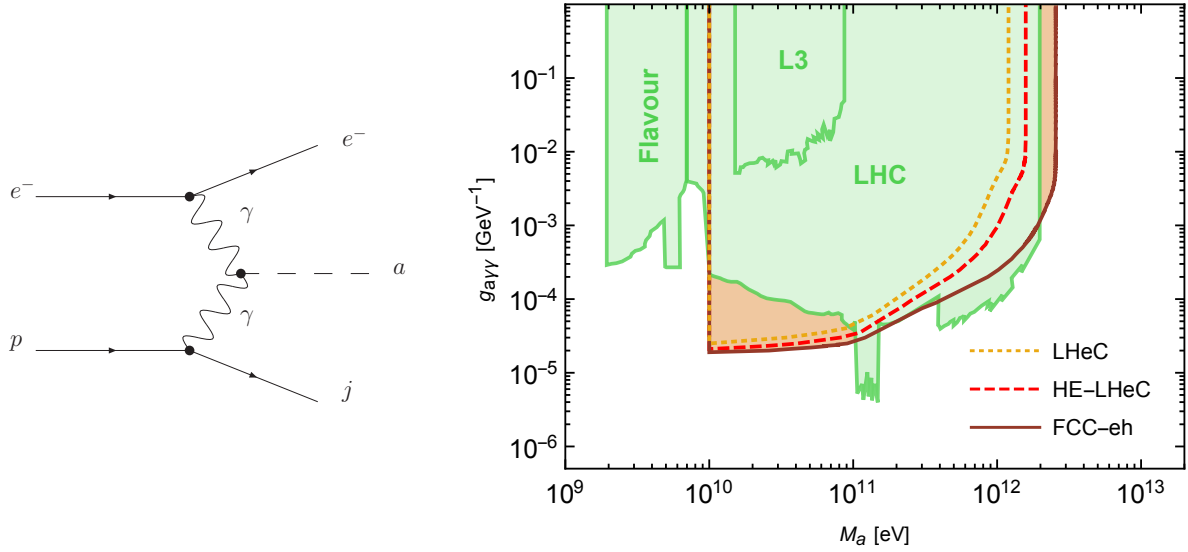


**Figure 8.12:** Left: Production of axion-like particles (ALPs) via photon fusion. Right: Projected sensitivity of the LHeC to ALPs coupling with photons at 95% CL. The existing exclusion limits are shown with the green regions. See Ref. [658] for details.

5385 Triple gauge boson couplings (TGC)  $W^+W^-V$ ,  $V = \gamma, Z$  are precisely defined in the SM and any  
 5386 significant deviation from the predicted values could indicate new physics. Present constraints  
 5387 on anomalous triple vector boson couplings are dominated by LEP (but they are not free of  
 5388 assumptions) and the  $WWZ$  and  $WW\gamma$  vertices can be tested at LHeC in great detail.

5389 The search for anomalous  $WW\gamma$  and  $WWZ$  couplings with polarised electron beam were studied  
 5390 in Ref. [451] via the processes  $ep \rightarrow \nu q\gamma X$  and  $ep \rightarrow \nu qZX$ . It was found that the LHeC  
 5391 sensitivity with  $E_e = 60$  GeV and  $L = 100/\text{fb}$  is comparable with existing experimental limits  
 5392 from lepton and hadron colliders, and that the sensitivity to anomalous  $Z$  couplings might  
 5393 be better, reaching  $(\Delta\kappa_{\gamma,Z}, \lambda_{\gamma,Z})$  as small as  $\mathcal{O}(10^{-1}, 10^{-2})$ . In general, beam polarisation  
 5394 and larger electron beam energies improve the sensitivity, and the LHeC was found to give  
 5395 complementary information on the anomalous couplings compared to the LHC.

5396 The prospects of testing anomalous triple gauge couplings are also investigated in Ref. [450].  
 5397 Therein the authors study the kinematics of an isolated hard photon and a single jet with a  
 5398 substantial amount of missing transverse momentum. They show that the LHeC is sensitive  
 5399 to anomalous triple gauge couplings via the azimuthal angle differences in the considered final  
 5400 state. It is pointed out that, in such an analysis, it is possible to probe the  $WW\gamma$  vertex  
 5401 separately with no contamination from possible BSM contributions to the  $WWZ$  coupling. The  
 5402 estimations consider  $E_e = 100, 140, 200$  GeV and it is claimed that, while higher energies yield  
 5403 better sensitivities, the differences are not very large. For an integrated luminosity of  $200 \text{ fb}^{-1}$   
 5404 and  $E_e = 140$  GeV the exclusion power of the LHeC is superior to all existing bounds, including  
 5405 those from LEP.

5406 The process  $e^-p \rightarrow e^- \mu^+ \nu j$  is investigated in Ref. [452]. The analysis is carried out at the parton  
 5407 level and includes the cross section measurement and a shape analysis of angular variables, in  
 5408 particular of the distribution of the azimuthal angle between the final state forward electron and  
 5409 jet. It is shown that the full reconstruction of leptonic  $W$  decay can be used for  $W$  polarization  
 5410 which is another probe of anomalous triple gauge couplings. The results show that the LHeC  
 5411 could reach a sensitivity to  $\lambda_\gamma$  and  $\Delta k_\gamma$  as small as  $\mathcal{O}(10^{-3})$  for  $L = 2 - 3/\text{ab}$ .



### 5412 8.5.1 Radiation Amplitude Zero

5413 The LHeC is ideal for testing a novel feature of the Standard Model: the *radiation amplitude*  
 5414 *zero* [659–662] of the amplitude  $\gamma W^- \rightarrow c\bar{b}$  and related amplitudes, see Fig. 8.13. The Born  
 5415 amplitude is predicted to vanish and change sign at  $\cos\theta_{CM} = \frac{e_{\bar{b}}}{e_W} = -1/3$ . This LHeC mea-  
 5416 surement tests the compositeness of the  $W$  boson and its zero anomalous magnetic moment at  
 5417 leading order, where one has  $g_W = 2$ ,  $\kappa_W = 1$ , as well as  $g_q = 2$  for the quarks. More gener-  
 5418 ally, one can also test the radiation amplitude zero for the top quark from measurements of the  
 process  $\gamma b \rightarrow W^- t$ .

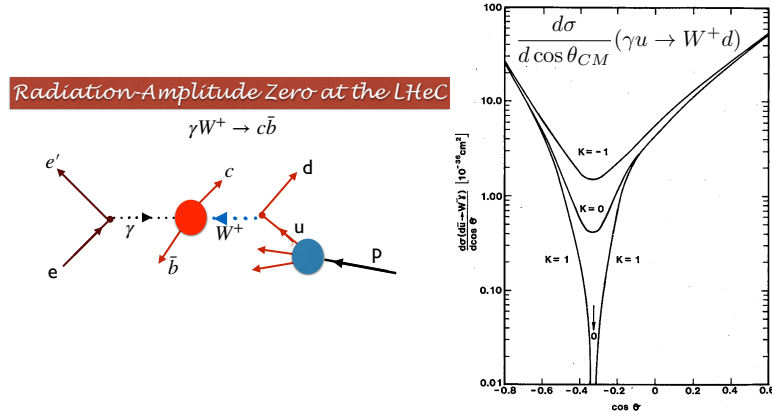


**Figure 8.13:** The radiation amplitude zero of the Standard Model in  $\gamma W^+ \rightarrow c\bar{b}$  and  $\gamma u \rightarrow W^+ d$ . The prediction for the angular distribution  $\frac{d\sigma}{d\cos(\theta_{CM})}(\gamma u \rightarrow W^+ d)$  is from Ref. [662].

5419

## 5420 8.6 Theories with heavy resonances and contact interaction

5421 In many other BSM scenarios, new physics will manifest itself by the presence of new reso-  
 5422 nances. Although the high centre-of-mass energy of  $pp$  colliders allow for a better reach in most  
 5423 of these scenarios, the LHeC and FCC-eh, thanks to the clean collision environment and the  
 5424 virtual absence of pileup, can complement the LHC in the search for these new phenomena.  
 5425 Deviations from Standard Model predictions could signal new physics even if it is at an energy  
 5426 scale beyond the centre-of-mass energy of the collider. In this case, the effective four-fermion  
 5427 contact interaction could be explained by the exchange of a virtual heavy particle, such as a  
 5428 leptoquark, a heavy boson or elementary constituents of quarks and leptons in composite mod-  
 5429 els. The effective contact interaction scale then represents the typical mass scale of the new  
 5430 particles. Relevant studies on various topics including scalar and vector leptoquarks and excited  
 5431 leptons, are collected in this section.

### 5432 8.6.1 Leptoquarks

5433 In recent years the experiments that study heavy flavoured mesons have revealed intriguing hints  
 5434 for new physics in semileptonic decays of  $B$  mesons. A violation of lepton flavour universality  
 5435 at the level of 3 to  $5\sigma$  is apparent in both the charged current and neutral current mediated  
 5436 processes [663]. In this context BSM theories involving leptoquarks (LQs) have gained renewed  
 5437 interest as they can give rise to lepton universality violating decays of heavy mesons at tree level,  
 5438 provided they couple to the second and third generation of quarks. Leptoquarks first appeared

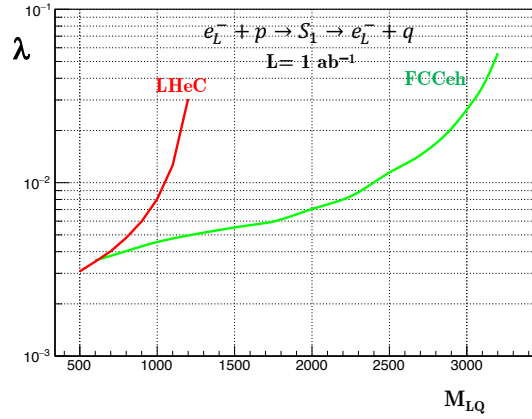


**Figure 8.14:** Estimated  $2\sigma$  significance for the coupling  $\lambda$  at LHeC and FCC-eh for the scalar lepto-quark  $S_1$  as a function of its mass, assuming  $1 \text{ ab}^{-1}$  luminosity and no systematic uncertainty.

5439 in Ref. [664] in Pati and Salam’s  $SU(4)$  model, where lepton number was considered to be the  
 5440 fourth colour. They also appear in Grand Unified theories, extended technicolor models and  
 5441 compositeness models. The nomenclature and classification are based on their transformation  
 5442 properties under the SM gauge groups [665, 666].

5443 In  $ep$  collisions LQs can be produced in an s-channel resonance via their coupling to the first  
 5444 generation of quarks, the signature being a peak in the invariant mass of the outgoing  $\ell q$  system.  
 5445 Contrary to what is achievable in the LHC environment, it has been shown that at the LHeC  
 5446 many properties of the LQs can be measured with high precision [1].

5447 The search for LQs at the LHC is essentially insensitive to the coupling LQ-e-q, characterized  
 5448 by the parameter  $\lambda$ , since the dominant process is pair production via the strong interaction.  
 5449 Recent searches have therefore been able to exclude LQs of the first generation of mass up to 1.4  
 5450 TeV, assuming a branching ratio to charged leptons = 1.0. For other generations, the bounds  
 5451 are  $\sim 1$  TeV. (for the latest results, see, for example Ref. [667, 668]). Under the assumption  
 5452 that the LQ has  $O(0.1)$  branching ratios to a number of tested final states, there remains some  
 5453 parameter space where the LHeC can make a significant contribution in the search for LQs.

5454 For LQs with masses below the centre-of-mass energy of the collider, suitable searches promise  
 5455 a sensitivity to  $\lambda$  as small as  $O(10^{-3})$ . As shown in [669], production of the first generation  
 5456 scalar leptoquarks at LHeC can have a much higher cross section than at the LHC. The authors  
 5457 also show that a sensitivity to the Yukawa coupling, for the LQs called  $R_2^{5/3} \sim (\mathbf{3}, \mathbf{2}, 7/6)$  and  
 5458  $\tilde{R}_2^{2/3} \sim (\mathbf{3}, \mathbf{2}, 1/6)$ , better than the electromagnetic strength ( $\sim 0.3$ ) of  $5\sigma$  can be reached up to a  
 5459 mass of 1.2 TeV.

5460 For the  $S_1$  scalar leptoquark  $(\bar{\mathbf{3}}, \mathbf{1}, 1/3)$ , an estimate of the sensitivity of the LHeC and the FCC-  
 5461 eh as a function of the LQ mass and LL Yukawa coupling is shown in Fig. 8.14, assuming  $1 \text{ ab}^{-1}$   
 5462 of integrated luminosity. Here, the signal was generated at leading order using MadGraph with  
 5463 the model files from Ref. [670], with hadronisation performed by Herwig7 [362, 671] and detector  
 5464 simulation with Delphes [460]. The SM background  $e^- p \rightarrow e^- j$  was also generated at leading  
 5465 order. A simple set of cuts on the  $p_T$  of the leading electron and jet and a window on the  
 5466 invariant mass of the  $e$ -jet system was applied.

5467 The  $\tilde{R}_2^{2/3}$  scalar LQ allows for coupling to right-handed neutrinos, providing interesting search  
 5468 channels. Its signatures at  $ep$  colliders have been investigated recently [672, 673]. In the lepton +  
 5469 jet final state, it is found that LHeC can probe up to 1.2 TeV at  $3\sigma$  significance with an  $e^-$  beam,

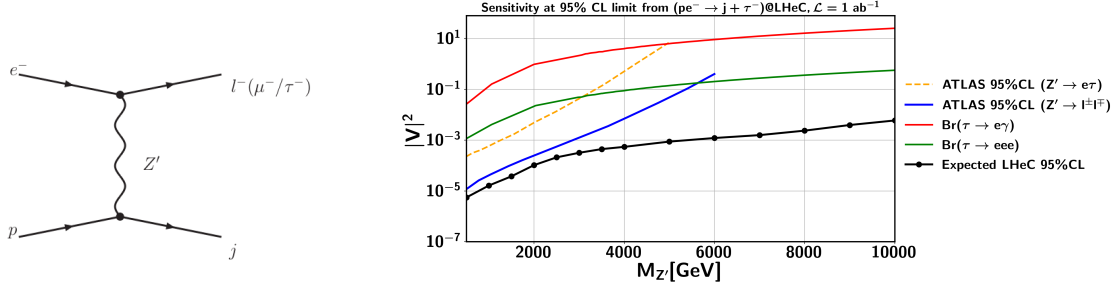


**Figure 8.15:** Left: Feynman diagram for the  $e$ - $\tau$  (and  $e$ - $\mu$ ) conversion processes  $pe^- \rightarrow \tau^- + j$  (and  $pe^- \rightarrow \mu^- + j$ ) mediated by a  $Z'$  with flavour-violating couplings to charged leptons at the LHeC. Right: Limits on the coupling parameter  $|V|^2$  for signal hypothesis compared with the existing limits from experimental constraints on the relevant flavour conserving and flavour violating processes. The black line is the LHeC sensitivity for the process  $pe^- \rightarrow \tau j$ . For the other limits, see text.

5470 and at  $5\sigma$  discovery with an  $e^+$  beam and  $1 \text{ ab}^{-1}$  of integrated luminosity. At FCC-eh, a  $5\sigma$   
 5471 discovery can be reached with an  $e^-$  beam up to  $\sim 2.3 \text{ TeV}$  and  $1 \text{ ab}^{-1}$  of integrated luminosity.

### 5472 8.6.2 $Z'$ mediated charged lepton flavour violation

5473 Charged lepton flavour violating signatures are well tested involving electrons and muons, but  
 5474 less so when they involve tau leptons. Interestingly, in many extensions of the SM lepton flavour  
 5475 is much more strongly violated in the tau sector whilst weaker experimental constraints at low  
 5476 energy exist. In Ref. [674] the  $Z'$  mediated  $e - \tau$  (and  $e - \mu$ ) conversion processes are studied  
 5477 at the LHeC, considering the lepton flavour violating processes  $pe^- \rightarrow \tau^- j$  (and  $pe^- \rightarrow \mu^- j$ ).

5478 For this LHeC study, a 60-GeV electron beam with up to 80% polarization is considered, to  
 5479 achieve a centre-of-mass energy close to 1.3 TeV with a total of  $1 \text{ ab}^{-1}$  integrated luminosity.  
 5480 Several backgrounds featuring tau leptons are considered, a parameterised reconstruction effi-  
 5481 ciency and mis-identification for tau jets is included in the analysis. To distinguish between the  
 5482 signal events and all relevant backgrounds, 31 kinematic variables (at the reconstruction level  
 5483 after the detector simulation) are used as input to a tool for Multi-Variate Analysis (TMVA).  
 5484 A BDT algorithm is used to separate the signal events from the background events. Systematic  
 5485 uncertainties are evaluated and are found to be around 2%.

5486 Assuming equal couplings  $|V_R^{ij}| = |V_L^{ij}| \equiv |V|$  of the  $Z'$  to quark-quark or lepton-lepton flavours  
 5487  $i, j$ , the LHeC is found to be sensitive to  $Z'$  masses up to  $\mathcal{O}(10)$  TeV, as depicted in Fig. 8.15 by  
 5488 the black line. Included in the Figure are also the existing limits from ATLAS searches for  $Z'$   
 5489 decays into  $e\tau$  [675] and the search for same flavour final states [676]. The experimental limits  
 5490 based on the branching ratio  $\text{BR}(\tau \rightarrow e\gamma)$  [677] and  $\text{BR}(\tau \rightarrow eee)$  [678] are also reported.

5491 Overall, lepton flavour violation in the tau sector can be tested extremely well at the LHeC,  
 5492 surpassing the sensitivity of the LHC and low energy experiments in the whole considered mass  
 5493 range by more than two orders of magnitude. This is particularly interesting for very heavy  $Z'$   
 5494 that are not accessible for direct production, where the LHeC provides an exciting new discovery  
 5495 channel for this kind of lepton flavour violating processes.

### 5496 8.6.3 Vector-like quarks

5497 In composite Higgs models, new vector-like quarks are introduced. The third generation is  
 5498 favored, in particular the top-partner ( $T$ ) with charge  $2/3$ . The prospects of detecting  $T$  at the  
 5499 LHeC are discussed in Ref. [679]. For this search a simplified model is considered where  $T$  is

5500 produced from positron proton scattering via intergenerational mixing and decays as  $T \rightarrow tZ$ ,  
 5501 with the final state  $\nu_e \ell^+ \ell^- b j j'$ , considering  $E_e = 140$  GeV. The authors find that for  $L = 1/\text{ab}$   
 5502 masses for the top partner  $T$  around 800 GeV can be tested when the model-related coupling  
 5503 constants are  $\mathcal{O}(0.1)$  and that mixing between  $T$  and the first generation quarks can significantly  
 5504 enhance the LHeC sensitivity.

5505 Another search strategy for singly produced top partners is given by their decays  $T \rightarrow Wb$  and  
 5506  $T \rightarrow th$ , which is presented in Ref. [680]. The analysis is based on a simplified model where  
 5507 the top partner is an  $SU_L(2)$  singlet and interacts only with the third generation of quarks. It  
 5508 considers collisions of positrons and protons with  $E_e = 140$  GeV. The analysis, carried out at  
 5509 the parton level, investigates the kinematic distributions of the final states. Useful kinematic  
 5510 variables for the  $bW$  final state were found to be the transverse momentum of the lepton,  $b$ -jet  
 5511 missing energy, while for the  $th$  final state the most useful observable is the transverse hadronic  
 5512 energy. For masses of  $\mathcal{O}(1)$  TeV the LHeC is found to be sensitive to the new interactions when  
 5513 they are  $\mathcal{O}(0.1)$  for  $L = 1/\text{ab}$ , in agreement with [679]. A very similar analysis was performed  
 5514 for the  $T \rightarrow Wb$  signal channel with comparable results [681].

#### 5515 8.6.4 Excited fermions ( $\nu^*$ , $e^*$ , $u^*$ )

5516 The potential of searches for excited spin-1/2 and spin-3/2 neutrinos are discussed in Ref. [682].  
 5517 For the analysis the authors consider effective currents that describe the interactions between  
 5518 excited fermions, gauge bosons, and SM leptons. For the signature, the production of the excited  
 5519 electron neutrino  $\nu^*$  and its subsequent decay  $\nu^* \rightarrow We$  with  $W \rightarrow jj$  was chosen. The analysis,  
 5520 carried out at the parton level, considers  $E_e = 60$  GeV, and consists in a study of the kinematic  
 5521 distributions of the final states. It is concluded that the signature can be well distinguished  
 5522 from backgrounds, and that other lepton-hadron colliders would be required to test the excited  
 5523 neutrinos of different flavours.

5524 Analyses in similar models, considering electron-proton collisions at energies of the FCC-eh and  
 5525 beyond, were carried out for excited electron neutrinos and are presented in Ref. [683]. An  
 5526 analysis for the reach for testing excited electrons is discussed in Ref. [684], and for excited  
 5527 quarks in a composite model framework in Ref. [685].

#### 5528 8.6.5 Colour octet leptons

5529 Unresolved issues of the SM, like family replication and quark-lepton symmetry, can be addressed  
 5530 by composite models, where quarks, leptons, and gauge bosons are composite particles made up  
 5531 of more basic constituents. One general class of particles, predicted in most composite models,  
 5532 are colour octet leptons, which are bound states of a heavy fermion and a heavy scalar particle  
 5533 that is assumed to be colour-charged. In this scenario each SM lepton is accompanied by a colour  
 5534 octet lepton, which may have spin 1/2 or 3/2. Since they are unobserved, the compositeness  
 5535 scale is expected to be at least  $\mathcal{O}(1)$  TeV.

5536 At the LHeC, the colour octet partner of the electron  $e_8$  can be produced through the process  
 5537  $e^- p \rightarrow e_8 g + X$  and studied via its decays products. An analysis including the study of kinematic  
 5538 distributions that were obtained at the parton level is presented in Ref. [686]. It was shown that  
 5539 discovery prospects exist for masses of  $\mathcal{O}(\text{TeV})$ . A similar analysis is performed for the FCC-eh  
 5540 at much higher energies in Ref. [687].

5541 **8.6.6 Quark substructure and Contact interactions**

5542 Several long-standing questions arise in the SM, such as those enumerated in Section 1.1. Perhaps  
 5543 most seriously, the SM does not appear to provide a clear, dynamical *raison d'être* for the  
 5544 existence of quarks. Leptons and quarks appear in the Standard Model in a symmetric way,  
 5545 sharing electromagnetic interaction with the same charge quantization and with a cancellation of  
 5546 anomaly in the family structure. This strongly suggests that they may be composed of the same  
 5547 fundamental constituents, or that they form a representation of an extended gauge symmetry  
 5548 group of a Grand Unified Theory.

5549 Assuming that the electron is a point-like particle, the quark substructure can be investigated  
 5550 by introducing a form factor  $f_q(Q^2)$  to describe deviations of the  $ep$  scattering cross section:

$$\frac{d\sigma}{dQ^2} = \frac{d\sigma^{SM}}{dQ^2} f_q^2(Q^2) \quad (8.1)$$

$$f_q^2(Q^2) \simeq 1 - \frac{R^2}{6} Q^2 \quad (8.2)$$

5551 Here,  $R$  is the rms electric charge quark radius. The present limit from HERA is  $4.3 \times 10^{-19}$   
 5552 m [688] while it is estimated that LHeC will be sensitive up to  $\sim 10^{-19}$  m [689].

5553 An electric precursor to QCD was formulated in 1969 that assumed that hadron constituents  
 5554 are highly electrically charged and where the strong attraction between positive and negative  
 5555 constituents was assumed to bind them together [690]. Neither the electric model nor Schwinger's  
 5556 comparable model of monopoles [691] reproduce the observed particle spectrum of hadrons, or  
 5557 the observed pattern of weak interactions. The ATLAS Collaboration has recently reported  
 5558 searches for free magnetic monopoles and free highly electrically charged particles produced in  
 5559  $pp$  collisions at 13 TeV [692]. No candidates were detected with one or two Dirac magnetic  
 5560 charges or with electric charges  $20e < |z| < 100e$ . This extends the results of previous searches  
 5561 made at lower energies and in cosmic rays or bulk matter. A simple picture of what might emerge  
 5562 with highly electrically charged constituents is obtained by modeling the proton's substructure  
 5563 by a charge of (say)  $21|e|$  smeared uniformly over a region of radius  $10^{-19}$  m, and two charges  
 5564 of  $-10|e|$  smeared over a larger region of radius  $2 \times 10^{-19}$  m. The model II by Hofstadter [693]  
 5565 predicts the form factor results shown in Fig. 8.16, consistent the HERA upper limit.

5566 More generally [694], contact interactions can be parameterized in the Lagrangian by coupling  
 5567 coefficients  $\eta_{ij}^q$  where the indices  $i, j$  indicate the left-handed or right-handed fermion helicities  
 5568 and  $q$  the quark flavor. The interaction can be of a scalar, vector or tensor nature and the  
 5569 interference with SM currents can be constructive or destructive. It has been estimated that  
 5570 the LHeC can be sensitive to a scale of contact interaction of  $\sim 40 - 60$  TeV with  $100 \text{ fb}^{-1}$  of  
 5571 integrated luminosity [689] while the present LHC limits are between 20 and 40 TeV, depending  
 5572 on the sign of the interference [695, 696].

5573 **8.7 Summary and conclusion**

5574 The lack of new physics at the LHC to date forces the community to develop new theoretical  
 5575 ideas as well as to explore the complementarities of  $pp$  machines with other possible future  
 5576 facilities. In the context of  $ep$  colliders, several studies are being carried out to understand the  
 5577 potential to search for new physics, considering that many interactions can be tested at high  
 5578 precision that are otherwise not easily accessible.

5579 At  $ep$  colliders, most BSM physics is accessed via vector-boson fusion, which suppresses the  
 5580 production cross section quickly with increasing mass. Nonetheless, scalar extensions of the SM

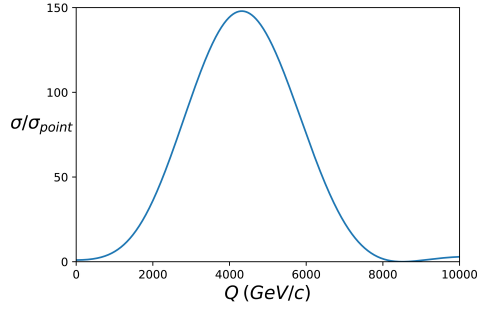


**Figure 8.16:** Form factor effect in the e-p interaction produced by substructure according to Model II of Hofstadter [693] with the model parameters given in the text.

5581 as well as neutrino-mass related BSM physics can be well tested at  $ep$  due to the smallness and  
 5582 reducibility of the SM backgrounds. The absence of pile up and complicated triggering makes  
 5583 searches for soft-momenta final state particles feasible, so that results for BSM theories for  
 5584 example characterised by the presence of non-prompt, long-lived particles are complementary to  
 5585 those at the LHC. Additionally, the excellent angular acceptance and resolution of the detector  
 5586 also renders the LHeC a very suitable environment for displaced vertex searches. An increase  
 5587 in the centre-of-mass energy as high as the one foreseen at the FCC would naturally boost the  
 5588 reach in most scenarios considerably.

5589 Finally, it is worth noting that the LHeC can offer different or indirect ways to search for  
 5590 new physics. It was shown recently that Lorentz invariance violation in the weak vector-boson  
 5591 sector can be studied in electron-proton scattering [697] via a Fourier-analysis of the parity  
 5592 violating asymmetry in deep inelastic scattering. Moreover, New Physics could be related to  
 5593 nucleon, nuclear, and top structure functions as discussed in Refs. [39, 698, 699]. Investigating  
 5594 of the  $B_c^{(*)}$  meson and doubly heavy baryon also was shown to have discovery potential for New  
 5595 Physics [700–702].

## Chapter 9

# Influence of the LHeC on Physics at the HL-LHC

After almost 10 years of scientific exploitation of the LHC and about  $175 \text{ fb}^{-1}$  of proton-proton collision data delivered to each of the ATLAS and CMS experiments, the sensitivity of a significant fraction of leading measurements and searches becomes limited by systematic uncertainties. Uncertainties induced by the strong interaction, in particular related to the proton structure, play a prominent role and tend to saturate the physics reach of the experiments. This context will only become more evident when the LHC enters its high-luminosity era.

With high precision PDFs measured independently from the other LHC experiments, the LHeC project can resolve this situation. It allows a clean study of the pure QCD effects it aims at measuring, resolving the ambiguity between new physics effects at high mass and PDF uncertainties that intrinsically affects the interpretation of proton-proton data alone. At the weak scale, improved PDFs provide a significant boost to the achievable precision of measurements of the Higgs boson properties and of fundamental electroweak parameters. The LHeC is thus a perfect companion machine for the HL-LHC, allowing a full exploitation of the data and significantly extending its reach.

The present chapter illustrates this with a few selected examples in the domain of precision measurements of the  $W$ -,  $Z$ - and Higgs boson properties. The impact of precise PDFs on searches for TeV-scale new physics is also illustrated. Besides, the complementarity of PDF studies at the LHeC and the HL-LHC and the impact of new QCD dynamics at small  $x$  on measurements at hadronic colliders, as well as the impact of electron-nucleus scattering data on heavy-ion physics at the LHC, are presented.

## 9.1 Precision Electroweak Measurements at the HL-LHC

### 9.1.1 The effective weak mixing angle

Prospective studies for the measurement of the effective weak mixing angle using the forward-backward asymmetry,  $A_{\text{FB}}$ , in Drell-Yan di-lepton events at the HL-LHC were performed at ATLAS [703], CMS [704] and LHCb [705] and reported in the CERN report on Standard Model physics at the HL-LHC [184]. A brief summary is given here, focusing on the impact of the LHeC on this measurement.

At leading order, lepton pairs are produced through the annihilation of a quark and antiquark

5627 via the exchange of a  $Z$  boson or a virtual photon. The definition of  $A_{\text{FB}}$  is based on the angle  
 5628  $\theta^*$  between the initial- and final-state fermions:

$$A_{\text{FB}} = \frac{\sigma_{\text{F}} - \sigma_{\text{B}}}{\sigma_{\text{F}} + \sigma_{\text{B}}}, \quad (9.1)$$

5629 where  $\sigma_{\text{F}}$  and  $\sigma_{\text{B}}$  are the cross sections in the forward ( $\cos \theta^* > 0$ ) and backward ( $\cos \theta^* < 0$ )  
 5630 hemispheres, respectively.

5631 A non-zero  $A_{\text{FB}}$  in dilepton events arises from the vector and axial-vector couplings of elec-  
 5632 troweak bosons to fermions. At tree level, the vector and axial-vector couplings of the  $Z$  boson  
 5633 to a fermion  $f$  are

$$g_V^f = T_3^f - 2Q_f \sin^2 \theta_W, \quad g_A^f = T_3^f. \quad (9.2)$$

5634 The coupling ratio,  $g_V^f/g_A^f = 1 - 4|Q_f| \sin^2 \theta_W$ , generates the asymmetry. Defining

$$\mathcal{A}_f = 2 \frac{g_V^f/g_A^f}{1 + (g_V^f/g_A^f)^2} \quad (9.3)$$

5635 one finds, for a given sub-process  $q\bar{q} \rightarrow Z \rightarrow \ell^+\ell^-$ ,

$$A_{\text{FB}} = \frac{3}{4} \mathcal{A}_q \mathcal{A}_\ell. \quad (9.4)$$

5636 As discussed in Sects. 5.1 and 9.1.3 below, Eq. (9.2) is subject to radiative corrections introducing  
 5637 the effective weak mixing angle  $\sin^2 \theta_{\text{eff}}^\ell$  in replacement of the leading order observable  $\sin^2 \theta_W$ .  
 5638 The asymmetry definitions downstream are however unchanged.

5639 The angle  $\theta^*$  is uniquely defined in  $e^+e^-$  collisions, where the directions of the  $e^+$  and  $e^-$   
 5640 beams are known. In proton-antiproton collisions, at the Tevatron, the incoming quarks and  
 5641 anti-quarks also have preferred directions, and a non-zero asymmetry exists for all lepton-pair  
 5642 rapidities. At the LHC the beams are symmetric, and a non-zero asymmetry only appears for  
 5643 high-rapidity events, as the direction of the longitudinal boost reflects, on average, the direction  
 5644 of the incoming valence quark. While the expected  $Z$ -boson statistics are very large, with  
 5645  $\mathcal{O}(3 \times 10^9)$  events expected in ATLAS and CMS, the measurement is thus highly affected by  
 5646 PDF uncertainties, and in particular by the  $u$  and  $d$  valence and sea distributions.

5647 Prospective studies were performed by ATLAS, CMS and LHCb, including a discussion of  
 5648 expected PDF uncertainties. The impact of LHeC PDFs was evaluated by ATLAS and is  
 5649 discussed further. Tab. 9.1 compares the published ATLAS result [433] with the prospects for  
 5650  $3 \text{ ab}^{-1}$ , for a variety of PDF sets. The statistical uncertainty is at the level of  $3 \times 10^{-5}$  with this  
 5651 sample, and the experimental systematic uncertainties are improved by 10 – 25% depending on  
 5652 the PDF scenario considered. While MMHT2014 [706] and CT14 [65] claim comparable PDF  
 5653 uncertainties, the size of the PDF uncertainty is reduced at the HL-LHC thanks to the increased  
 5654 sample size, which helps constraining this component *in situ*. The HL-LHC PDF set [255], which  
 5655 incorporates the expected constraints from present and future LHC data, further decreases the  
 5656 associated uncertainty by about 20%. The LHeC projection [53] results from a QCD fit to  
 5657  $1 \text{ ab}^{-1}$  of  $ep$  scattering pseudodata, with  $E_e = 60 \text{ GeV}$  and  $E_p = 7 \text{ TeV}$ ; in this case, the PDF  
 5658 uncertainty is subleading compared to the experimental systematics.

5659 Fig. 9.1 compares the ATLAS sensitivity studies of  $\sin^2 \theta_{\text{eff}}^\ell$  to previous measurements from the  
 5660 LHC experiments [432–434, 707], and to the legacy measurements by the experiments at LEP  
 5661 and SLC [429] and the Tevatron [431]. The precision of the measurement of the weak mixing  
 5662 angle in  $Z$ -boson events, using  $3000 \text{ fb}^{-1}$  of  $pp$  collision data at  $\sqrt{s} = 14 \text{ TeV}$ , exceeds the  
 5663 precision achieved in all previous single-experiments to date. The LHeC is thus essential in  
 5664 exploiting the full potential of the HL-LHC data for this measurement.



Parameter	Unit	ATLAS (Ref. [433])		HL-LHC projection	
		MMHT2014	CT14	HL-LHC PDF	LHeC PDF
Centre-of-mass energy, $\sqrt{s}$	TeV	8	14	14	14
Int. luminosity, $\mathcal{L}$	$\text{fb}^{-1}$	20	3000	3000	3000
Experimental uncert.	$10^{-5}$	$\pm 23$	$\pm 9$	$\pm 7$	$\pm 7$
PDF uncert.	$10^{-5}$	$\pm 24$	$\pm 16$	$\pm 13$	$\pm 3$
Other syst. uncert.	$10^{-5}$	$\pm 13$	–	–	–
Total uncert., $\Delta \sin^2\theta_W$	$10^{-5}$	$\pm 36$	$\pm 18$	$\pm 15$	$\pm 8$

**Table 9.1:** The breakdown of uncertainties of  $\sin^2\theta_W$  from the ATLAS preliminary results at  $\sqrt{s} = 8$  TeV with  $20 \text{ fb}^{-1}$  [433] is compared to the projected measurements with  $3000 \text{ fb}^{-1}$  of data at  $\sqrt{s} = 14$  TeV for two PDF sets considered in this note. All uncertainties are given in units of  $10^{-5}$ . Other sources of systematic uncertainties, such as the impact of the MC statistical uncertainty, evaluated in Ref. [433] are not considered in the HL-LHC prospect analysis.

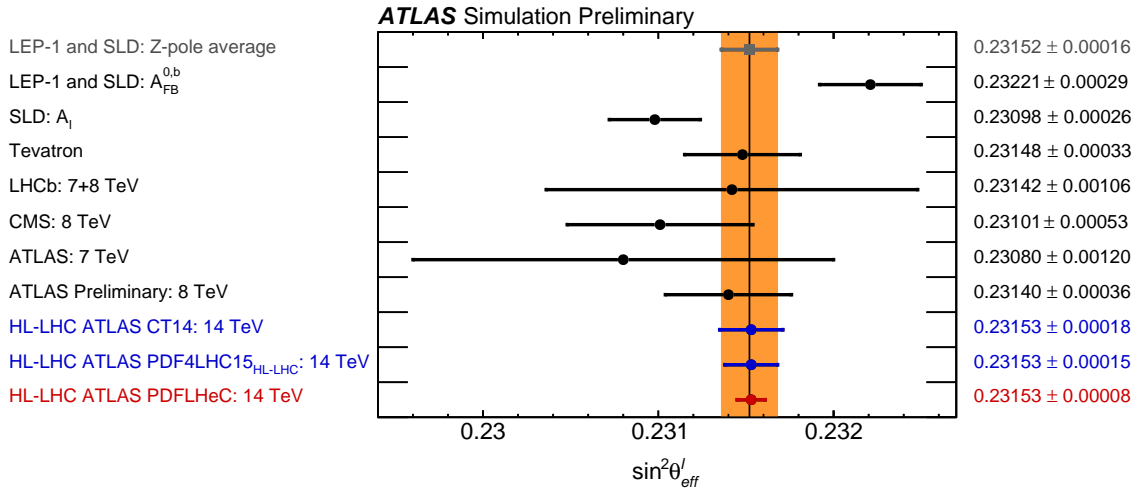


**Figure 9.1:** Comparison of measurements or combinations of  $\sin^2\theta_{\text{eff}}^{\ell}$  with the world average value (orange band) and the projected uncertainties of measurements at the HL-LHC. For the HL-LHC the central values are set to the world average value and uncertainties are displayed for different assumptions of the available PDF sets, similar to Tab. 9.1.

### 5665 9.1.2 The $W$ -boson mass

5666 This section summarises a study describing prospects for the measurement of  $m_W$  with the  
5667 upgraded ATLAS detector, using low pile-up data collected during the HL-LHC period [708].  
5668 Similar features and performance are expected for CMS.

5669 Proton-proton collision data at low pile-up are of large interest for  $W$  boson physics, as the low  
5670 detector occupancy allows an optimal reconstruction of missing transverse momentum, and the  
5671  $W$  production cross section is large enough to achieve small statistical uncertainties in a moderate  
5672 running time. At  $\sqrt{s} = 14$  TeV and for an instantaneous luminosity of  $\mathcal{L} \sim 5 \times 10^{32} \text{ cm}^{-2}\text{s}^{-1}$ ,  
5673 corresponding to two collisions per bunch crossing on average at the LHC, about  $\times 10^7$   $W$  boson  
5674 events can be collected in one month. Such a sample provides a statistical sensitivity at the  
5675 permille level for cross section measurements, at the percent level for measurements of the  $W$   
5676 boson transverse momentum distribution, and below 4 MeV for a measurement of  $m_W$ .

5677 Additional potential is provided by the upgraded tracking detector, the ITk, which extends the

5678 coverage in pseudorapidity beyond  $|\eta| < 2.5$  to  $|\eta| < 4$ . The increased acceptance allows  $W$ -  
5679 boson measurements to probe a new region in Bjorken  $x$  at  $Q^2 \sim m_W^2$ . This will in turn allow  
5680 further constraints on the parton density functions (PDFs) from cross section measurements,  
5681 and reduce PDF uncertainties in the measurement of  $m_W$ . A possible increase of the LHC  
5682 centre-of-mass energy, such as the HE-LHC program with  $\sqrt{s} = 27$  TeV [709], could play a  
5683 similar role on a longer timescale.

5684 Leptonic  $W$  boson decays are characterised by an energetic, isolated electron or muon, and sig-  
5685 nificant missing transverse momentum reflecting the decay neutrino. The hadronic recoil,  $u_T$ , is  
5686 defined from the vector sum of the transverse momenta of all reconstructed particles in the event  
5687 excluding the charged lepton, and provides a measure of the  $W$  boson transverse momentum.  
5688 Lepton transverse momentum,  $p_T^\ell$ , missing transverse momentum,  $E_T^{\text{miss}}$ , and the hadronic recoil  
5689 are related through  $\vec{E}_T^{\text{miss}} = -(\vec{p}_T^\ell + \vec{u}_T)$ . The  $p_T^\ell$  and  $E_T^{\text{miss}}$  distributions have sharp peaks at  
5690  $p_T^\ell \sim E_T^{\text{miss}} \sim m_W/2$ . The transverse mass  $m_T$ , defined as  $m_T = \sqrt{2p_T^\ell E_T^{\text{miss}} \cos(\phi_\ell - \phi_{\text{miss}})}$ ,  
5691 peaks at  $m_T \sim m_W$ .

5692 Events are selected applying the following cuts to the object kinematics, after resolution correc-  
5693 tions:

- 5694 •  $p_T^\ell > 25$  GeV,  $E_T^{\text{miss}} > 25$  GeV,  $m_T > 50$  GeV and  $u_T < 15$  GeV;
- 5695 •  $|\eta_\ell| < 2.4$  or  $2.4 < |\eta_\ell| < 4$ .

5696 The first set of cuts select the range of the kinematic peaks of the  $W$  boson decay products,  
5697 restricting to the region of small  $p_T^W$  to maximise the sensitivity of the distributions to  $m_W$ .  
5698 Two pseudorapidity ranges are considered, corresponding to the central region accessible with  
5699 the current ATLAS detector, and to the forward region accessible in the electron channel with  
5700 the ITk.

5701 The  $W$ -boson mass is determined comparing the final state kinematic peaks in the simulation  
5702 to those observed in the data, and adjusting the value of  $m_W$  assumed in the former to optimise  
5703 the agreement. The shift in the measured value of  $m_W$  resulting from a change in the assumed  
5704 PDF set is estimated using a set of template distributions obtained for different values of  $m_W$   
5705 and a given reference PDF set, and “pseudo-data” distributions obtained for an alternate set  
5706 representing, for example, uncertainty variations with respect to the reference set. The PDF  
5707 uncertainty for a given set is calculated by summing the shifts obtained for all uncertainty  
5708 variations in quadrature.

5709 The PDF uncertainty is calculated for the CT14 [65], MMHT2014 [706], HL-LHC [255] and  
5710 LHeC [53] PDF sets and their associated uncertainties. Compared to current sets such as  
5711 CT14 and MMHT2014, the HL-LHC set incorporates the expected constraints from present and  
5712 future LHC data; it starts from the PDF4LHC convention [251] and comes in three scenarios  
5713 corresponding to more or less optimistic projections of the experimental uncertainties.

5714 The expected statistical and PDF uncertainties are illustrated in Tab.9.2 and Fig.9.2. The  
5715 CT10 and CT14 sets yield comparable uncertainties. The MMHT2014 uncertainties are about  
5716 30 % lower. The three projected HL-LHC PDF sets give very similar uncertainties; scenario 2  
5717 is the most conservative and shown here. Compared to CT10 and CT14, a reduction in PDF  
5718 uncertainty of about a factor of two is obtained in this case.

5719 The LHeC sample can be collected in about three years, synchronously with the HL-LHC op-  
5720 eration. In this configuration, the neutral- and charged-current DIS samples are sufficient to  
5721 disentangle the first ( $d, u$ ) and second ( $s, c$ ) generation parton densities without ambiguity, and

5722 reduce the PDF uncertainty below 2 MeV, a factor 5–6 compared to present knowledge. Also  
5723 in this case the  $m_W$  measurement will benefit from the large  $W$  boson samples collected at the  
5724 LHC, and from the combination of the central and forward categories. In this context, PDF  
5725 uncertainties would be sub-leading even with  $1 \text{ fb}^{-1}$  of low pile-up LHC data.

Parameter	Unit	ATLAS (Ref. [424])		HL-LHC projection		
		CT10	CT14	HL-LHC	LHeC	LHeC
Centre-of-mass energy, $\sqrt{s}$	TeV	7	14	14	14	14
Int. luminosity, $\mathcal{L}$	$\text{fb}^{-1}$	5	1	1	1	1
Acceptance		$ \eta  < 2.4$	$ \eta  < 2.4$	$ \eta  < 2.4$	$ \eta  < 2.4$	$ \eta  < 4$
Statistical uncert.	MeV	$\pm 7$	$\pm 5$	$\pm 4.5$	$\pm 4.5$	$\pm 3.7$
PDF uncert.	MeV	$\pm 9$	$\pm 12$	$\pm 5.8$	$\pm 2.2$	$\pm 1.6$
Other syst. uncert.	MeV	$\pm 13$	-	-	-	-
Total uncert. $\Delta m_W$	MeV	$\pm 19$	13	7.3	5.0	4.1

**Table 9.2:** Measurement uncertainty of the  $W$ -boson mass at the HL-LHC for different PDF sets (CT14, HL-LHC PDF and LHeC PDF) and lepton acceptance regions in comparison with a measurement by ATLAS [424]. The HL-LHC projections are obtained from a combined fit to the simulated  $p_T^\ell$  and  $m_T$  distributions.

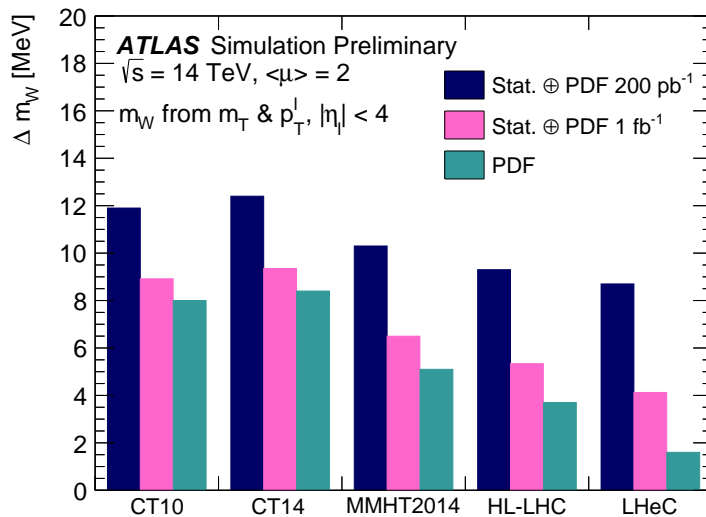


**Figure 9.2:** Measurement uncertainty of  $m_W$  at the HL-LHC with  $200 \text{ pb}^{-1}$  (dark blue) and  $1 \text{ fb}^{-1}$  (pink) of collected low pile-up data for different present and future PDF sets. The green area indicates the PDF uncertainty from those sets alone. The projections are obtained from a combined fit to the simulated  $p_T^\ell$  and  $m_T$  distributions in the acceptance  $|\eta| < 4$ .

### 5726 9.1.3 Impact on electroweak precision tests

5727 The theoretical expressions for the electroweak parameters discussed above are functions of the  
5728 other fundamental constants of the theory. In the Standard Model, an approximate expression  
5729 for  $m_W$ , valid at one loop for  $m_H > m_W$ , is [429]

$$m_W^2 = \frac{m_Z^2}{2} \left( 1 + \sqrt{1 - \frac{\sqrt{8}\pi\alpha_{em}}{G_F m_Z^2} \frac{1}{1 - \Delta r}} \right), \quad (9.5)$$

$$\Delta r = \Delta\alpha_{em} - \frac{\cos^2\theta_W}{\sin^2\theta_W} \Delta\rho, \quad (9.6)$$

$$\Delta\rho = \frac{3G_F m_W^2}{8\sqrt{2}\pi^2} \left[ \frac{m_{\text{top}}^2}{m_W^2} - \frac{\sin^2\theta_W}{\cos^2\theta_W} \left( \ln \frac{m_H^2}{m_W^2} - \frac{5}{6} \right) + \dots \right]. \quad (9.7)$$

5730  $\Delta r$  includes all radiative corrections to  $m_W$ ,  $\Delta\alpha_{em}$  is the difference between the electromagnetic  
 5731 coupling constant evaluated at  $q^2 = 0$  and  $q^2 = m_Z^2$ , and  $\Delta\rho$  is the quantum correction to the  
 5732 tree-level relation  $\rho \equiv m_W^2/(m_Z^2 \cos^2\theta_W) = 1$ , defined as  $\rho = 1 + \Delta\rho$ .

5733 Similarly, approximate one-loop expressions for the vector and axial-vector couplings between  
 5734 the  $Z$  boson and the fermions,  $g_V$  and  $g_A$ , are

$$g_V = \sqrt{1 + \Delta\rho} (T_3 - 2Q(1 + \Delta\kappa) \sin^2\theta_W), \quad (9.8)$$

$$g_A = \sqrt{1 + \Delta\rho} T_3, \quad (9.9)$$

5735 where

$$\Delta\kappa = \frac{3G_F m_W^2}{8\sqrt{2}\pi^2} \left[ \frac{\cos^2\theta_W}{\sin^2\theta_W} \frac{m_{\text{top}}^2}{m_W^2} - \frac{10}{9} \left( \ln \frac{m_H^2}{m_W^2} - \frac{5}{6} \right) + \dots \right]. \quad (9.10)$$

5736 At two loops, also the strong coupling constant enters.

5737 A large class of theories beyond the SM predict particles that contribute to the  $W$ - and  $Z$ -boson  
 5738 self-energies, modifying the above expressions. From the point of view of on-shell observables  
 5739 of the  $W$  and  $Z$ , these modifications are usually parameterized using the so-called *oblique*  
 5740 parameters, called  $S$ ,  $T$  and  $U$  [710]. Their values are by definition 0 in the SM and, for  
 5741 example, a significant violation of the relation between  $m_W$ ,  $m_H$  and  $m_{\text{top}}$  would translate into  
 5742 non-zero values for  $S$  and  $T$ .

5743 A typical application of this formalism consists in using the measured properties of the  $W$   
 5744 and  $Z$  bosons, the top quark mass, and the values of coupling constants, to derive an indirect  
 5745 determination of the Higgs boson mass in the SM and compare the latter to the measured value.  
 5746 Beyond the SM, the measured values can be used to derive allowed contours in the  $(S, T)$  plane.

5747 Present and future measurement uncertainties for the most relevant electroweak parameters are  
 5748 summarised in Tab.9.3, and are used to evaluate the impact of the improved measurements on  
 5749 electroweak precision tests. Specifically, we consider the effect of improved measurements of  $m_W$   
 5750 and  $\sin^2\theta_{\text{eff}}^\ell$  discussed in this chapter, and of the improved precision of  $\alpha_s$  discussed in Chapter 4.  
 5751 In addition, we consider an ultimate precision of 300 MeV for the top quark mass measured at  
 5752 the LHC.

5753 The results are illustrated in Figs.9.3 and 9.4. The former results from a fit performed using  
 5754 the GFitter framework [426], and compares the indirect determinations of the Higgs boson mass  
 5755 for the present and expected measurement precisions. The indirect uncertainty in  $m_H$  reduces  
 5756 from about 20% to 10%.

5757 Fig.9.4 was performed using HEPfit [711], and compares allowed contours for the  $S$  and  $T$   
 5758 parameters. Here also, the allowed region is reduced by a factor of about two from the improved  
 5759 measurements of  $m_W$ ,  $\sin^2\theta_{\text{eff}}^\ell$ ,  $m_{\text{top}}$  and  $\alpha_s$ . Improved theoretical calculations in the SM will  
 5760 provide an additional reduction of 10-15%.

Parameter	Unit	Value	Uncertainty	
			Present	Expected
$m_Z$	MeV	91187.6	2.1	2.1
$m_W$	MeV	80385	15	5
$\sin^2\theta_{\text{eff}}^\ell$		0.23152	0.00016	0.00008
$m_{\text{top}}$	GeV	173.1	0.7	0.3
$\alpha_s(M_Z)$		0.1179	0.0010	0.0001

**Table 9.3:** Present uncertainties for the relevant EW precision observables [133, 180, 429], and their expected precision in the LHeC and HL-LHC era.

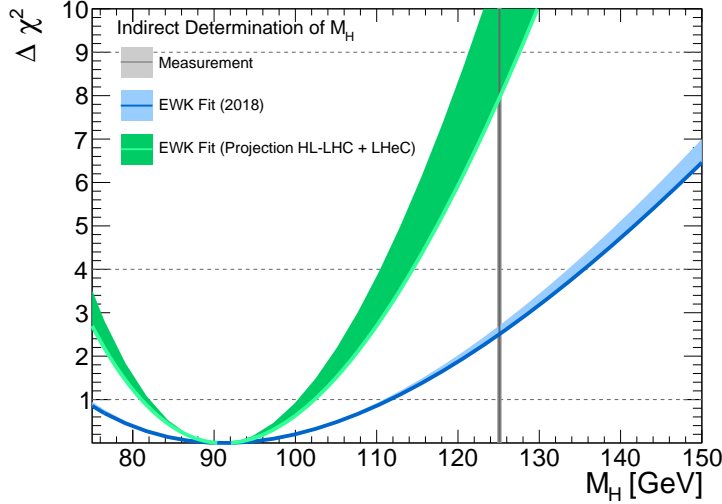


**Figure 9.3:** Comparisons of  $\chi^2$  distributions for different Higgs boson mass values, using present and future experimental uncertainties. The theoretical uncertainties are indicated by the filled areas. The Gfitter program [426] was used for this analysis.

5761 In summary, the LHeC data promises significant improvements in the measurement precision  
5762 of fundamental electroweak parameters such as  $m_W$  and  $\sin^2\theta_{\text{eff}}^\ell$ . The improved measurements  
5763 enhance the sensitivity of electroweak tests by a factor of two or more.

## 5764 9.2 Higgs Physics

### 5765 9.2.1 Impact of LHeC data on Higgs cross section predictions at the LHC

5766 A detailed analysis of Higgs boson production cross sections was given in the report on Higgs  
5767 Physics at the HL-LHC and HE-LHC [712]. Central values at  $\sqrt{s} = 14\text{ TeV}$  and the corre-  
5768 sponding uncertainties are reported in Tab. 9.4. Perturbative uncertainties (labelled  $\Delta\sigma_{\text{scales}}$  in  
5769 Tab. 9.4) generally dominate compared to the contributions of  $\alpha_s$  and the PDFs. This is espe-  
5770 cially true for gluon fusion, where the residual theoretical uncertainties correspond to missing  
5771 corrections beyond N<sup>3</sup>LO in QCD, and for  $t\bar{t}H$  production which is known to NLO QCD+EW  
5772 accuracy. The weak boson fusion,  $WH$  and  $ZH$  cross sections are known to NNLO QCD + NLO  
5773 EW accuracy; residual theoretical uncertainties are smaller for these weak interaction processes.

5774 In Ref. [712],  $\alpha_s$ -related uncertainties are propagated assuming  $\alpha_s = 0.118 \pm 0.0015$ , and the  
5775 assumed PDF uncertainties reflect the HL-LHC prospects [255]. They are in excess of 3% for  
5776 gluon fusion and  $t\bar{t}H$ , below 2% for  $WH$  and  $ZH$ , and 0.4% for weak boson fusion. The LHeC

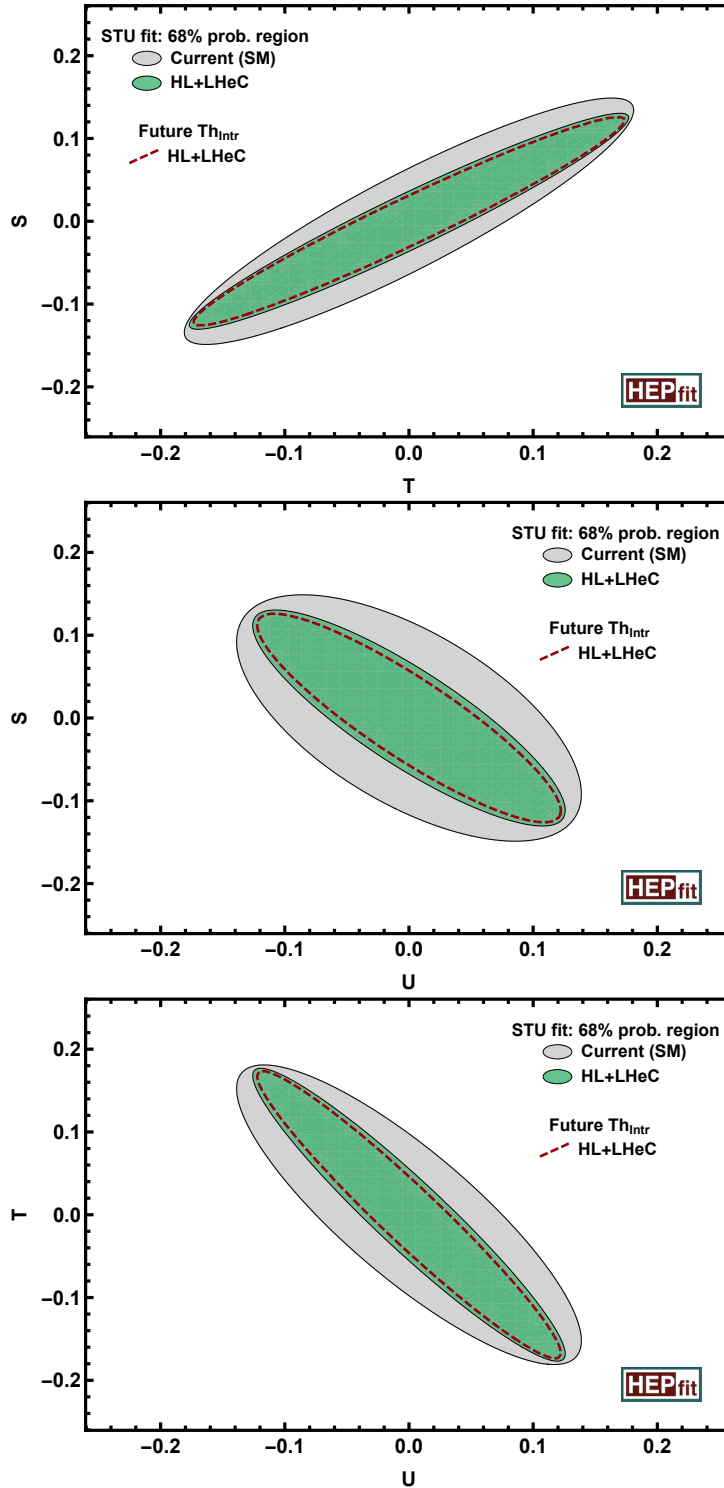


**Figure 9.4:** Allowed regions in the  $(S, T, U)$  plane showing all three combinations:  $S$  vs  $T$  (top),  $S$  vs  $U$  (middle),  $T$  vs  $U$  (bottom). The grey and green areas indicate the currently allowed region and the LHeC projection, respectively. The dashed line indicates the effect of expected theoretical improvements. The HEPfit program [711] was used for this analysis.

5777 uncertainties in Tab. 9.4 are calculated using MCFM [713], interfaced to PDFs determined from  
 5778 LHeC pseudodata as described in Chapter 3. Assuming the prospects for  $\alpha_s$  and PDFs described

5779 in Chapters 3 and 4, and with the exception of weak-boson fusion production, the corresponding  
 5780 uncertainties decrease by a factor 5 to 10.

Process	$\sigma_H$ [pb]	$\Delta\sigma_{\text{scales}}$	$\Delta\sigma_{\text{PDF}+\alpha_s}$	
			HL-LHC PDF	LHeC PDF
Gluon-fusion	54.7	5.4 %	3.1 %	0.4 %
Vector-boson-fusion	4.3	2.1 %	0.4 %	0.3 %
$pp \rightarrow WH$	1.5	0.5 %	1.4 %	0.2 %
$pp \rightarrow ZH$	1.0	3.5 %	1.9 %	0.3 %
$pp \rightarrow t\bar{t}H$	0.6	7.5 %	3.5 %	0.4 %

**Table 9.4:** Predictions for Higgs boson production cross sections at the HL-LHC at  $\sqrt{s} = 14$  TeV and its associated relative uncertainties from scale variations and two PDF projections, HL-LHC and LHeC PDFs,  $\Delta\sigma$ . The PDF uncertainties include uncertainties of  $\alpha_s$ .

5781 The important, beneficial role of  $ep$  PDF information for LHC Higgs physics can also be illus-  
 5782 trated using the predictions for the total cross section,  $pp \rightarrow HX$  at the LHC. This has recently  
 5783 been calculated [714] to N<sup>3</sup>LO pQCD. In Fig. 9.5 calculations of this cross section are shown  
 5784 for several recent sets of parton distributions, calculated with the iHix code [715], including the  
 5785 LHeC set.

5786 The effect of these improvements on Higgs boson coupling determination at the HL-LHC is at  
 5787 present modest, due to the combined effect of still significant perturbative uncertainties and  
 5788 of the expected experimental systematic uncertainties. The influence of the LHeC on these  
 5789 measurements is further discussed in the next section.

## 5790 9.2.2 Higgs Couplings from a simultaneous analysis of $pp$ and $ep$ collision 5791 data

5792 The LHC data collected during the Runs I and II have provided a first exploration of the  
 5793 properties of the Higgs boson. The so-called  $\kappa$  framework [716] – which allows modifications  
 5794 of the SM-like couplings of the Higgs boson to each SM particle  $i$ , parameterised by coupling  
 5795 modifiers  $\kappa_i$  – has been widely used for the interpretation of these measurements. With current  
 5796 data, the  $\kappa$  parameters associated to the main couplings of the Higgs can be determined to  
 5797 a precision of roughly 10-20 %, see e.g. [717].<sup>1</sup> This knowledge will be further improved at  
 5798 the high-luminosity phase of the LHC, reaching a precision in many cases well below the 10 %  
 5799 level [712]. Even at the HL-LHC it will however, be difficult to obtain sensible measurements of  
 5800 certain Higgs interactions, especially the coupling to charm quarks. Such gap would be covered  
 5801 by the precise measurements of that channel at the LHeC, as described in Sect. 7. Channels  
 5802 measured to a few percent accuracy at both HL-LHC and LHeC would provide important cross  
 5803 checks and additional physics information because of the different dominant Higgs production  
 5804 mechanisms,  $gg \rightarrow H$  in  $pp$  and  $WW \rightarrow H$  in  $ep$ . There follows a remarkable complementarity  
 5805 between the measurements from both machines and a joint precision that is comparable to that  
 5806 at ILC or CLIC [718], which yet have the important possibility to determine the total cross  
 5807 section through the  $e^+e^- \rightarrow Z^* \rightarrow ZH$  reaction. Furthermore, as also explained in Sect. 7,  
 5808 the LHeC environment allows very precise determinations of certain interactions, well beyond  
 5809 of what will be possible at the high-luminosity  $pp$  collider. In this subsection we briefly describe  
 5810 the complementarity between the Higgs measurements at the  $pp$  and  $ep$  colliders, illustrated via  
 5811 a combined fit to the HL-LHC and LHeC projections in the  $\kappa$  framework.

<sup>1</sup>Note that at the LHC one can only determine coupling ratios.

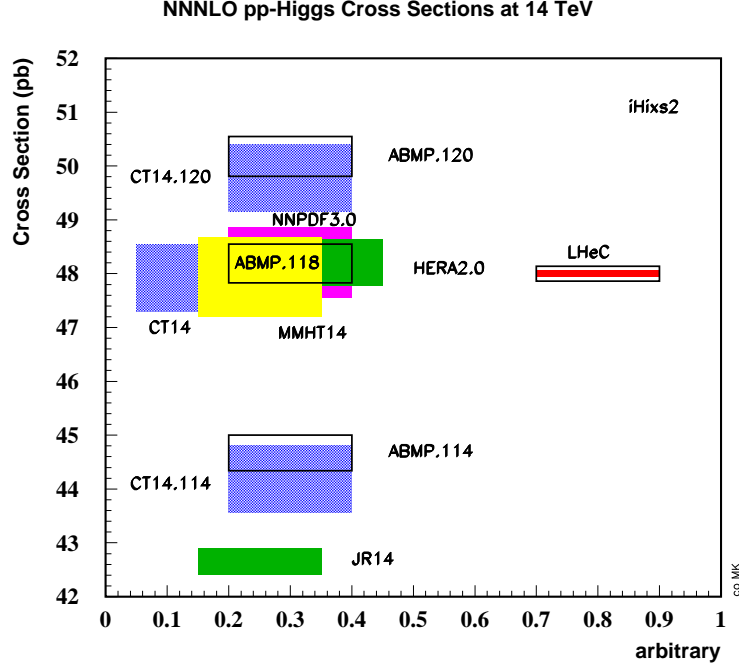


**Figure 9.5:** Cross sections of Higgs production calculated to  $N^3$ LO using the iHix program [715] for existing PDF parameterisation sets (left side) and for the LHeC PDFs (right side). The widths of the areas correspond to the uncertainties as quoted by the various sets, having rescaled the CT14 uncertainties from 90 to 68 % C.L. Results (left) are included also for different values of the strong coupling constant  $\alpha_s(M_Z^2)$ , from 0.114 to 0.120. The inner LHeC uncertainty band (red) includes the expected systematic uncertainty due to the PDFs while the outer box illustrates the expected uncertainty resulting from the determination of  $\alpha_s$  with the LHeC.

5812 For a detailed description of the Higgs physics program at the LHeC we refer to Chapter 7. The  
5813 only information not included in the fit presented in this section is that of the determination  
5814 of the top Yukawa coupling, since projections from that study are performed assuming any  
5815 coupling other than  $\kappa_t$  to be SM like. Comments in this regard will be made, when necessary,  
5816 below.

5817 For the HL-LHC inputs of the combined fit we rely on the projections presented in Ref. [712],  
5818 as used in the comparative study in Ref. [718]. These HL-LHC inputs include projections for  
5819 the total rates in the main production (ggF, VBF,  $VH$  and  $ttH$ ) and decay channels ( $H \rightarrow$   
5820  $bb$ ,  $\tau\tau$ ,  $\mu\mu$ ,  $ZZ^*$ ,  $WW^*$ ,  $\gamma\gamma$ ,  $Z\gamma$ ). They are available both for ATLAS and CMS. Regarding  
5821 the theory systematics in these projections, we assume the scenario S2 described in [712], where  
5822 the SM theory uncertainties are reduced by roughly a factor of two with respect to their current  
5823 values, a reduction to which LHeC would contribute by eliminating the PDF and  $\alpha_s$  parts of  
5824 the uncertainty, see Fig.9.5. Theory systematics are assumed to be fully correlated between  
5825 ATLAS and CMS. These projections are combined with LHeC ones, where, as in Ref. [718],  
5826 we use the future projections for the SM theory uncertainties in the different production cross  
5827 sections and decay widths. In the  $\kappa$  fit performed here we assume: (1) no Higgs decays into  
5828 particles other than the SM ones; (2) heavy particles are allowed to modify the SM loops, so we  
5829 use effective  $\kappa$  parameters to describe the SM loop-induced processes, i.e. we use  $\kappa_g, \kappa_\gamma, \kappa_{Z\gamma}$  as



5830 free parameters. The total list of free parameters considered for this combined HL-LHC+LHeC  
 5831  $\kappa$  fit is, therefore,

$$\{\kappa_b, \kappa_t, \kappa_\tau, \kappa_c, \kappa_\mu, \kappa_Z, \kappa_W, \kappa_g, \kappa_\gamma, \kappa_{Z\gamma}\}, \quad (9.11)$$

5832 for a total of 10 degrees of freedom. Coupling modifiers associated to any other SM particles  
 5833 are assumed to be SM-like,  $\kappa_i = 1$ .

Parameter	Uncertainty		
	HL-LHC	LHeC	HL-LHC+LHeC
$\kappa_W$	1.7	0.75	0.50
$\kappa_Z$	1.5	1.2	0.82
$\kappa_g$	2.3	3.6	1.6
$\kappa_\gamma$	1.9	7.6	1.4
$\kappa_{Z\gamma}$	10	–	10
$\kappa_c$	–	4.1	3.6
$\kappa_t$	3.3	–	3.1
$\kappa_b$	3.6	2.1	1.1
$\kappa_\mu$	4.6	–	4.4
$\kappa_\tau$	1.9	3.3	1.3

**Table 9.5:** Results of the combined HL-LHC + LHeC  $\kappa$  fit. The output of the fit is compared with the results of the HL-LHC and LHeC stand-alone fits. The uncertainties of the  $\kappa$  values are given in per cent.

5834 The results of the HL-LHC+LHeC fit, which has been performed using the HEPfit code [711],  
 5835 are shown in Tab. 9.5 and Fig. 9.6<sup>2</sup>. The increment in constraining power after adding the LHeC  
 5836 measurements is especially apparent for the couplings to  $W$  bosons and  $b$  quarks, bringing an  
 5837 improvement with respect to the HL-LHC result of a factor  $\simeq 3$ . As explained at the beginning  
 5838 of this section, the LHeC measurements also bring the possibility of setting sensible constraints  
 5839 on the Higgs interactions with charm quarks, with a precision of roughly 4%. The HL-LHC  
 5840 measurements, in turn, fill some of the *gaps* in the fit at the LHeC, where there is little sensitivity  
 5841 to the couplings involved in rare Higgs decays, e.g.  $H \rightarrow \mu\mu$  and  $H \rightarrow Z\gamma$ . This makes apparent  
 5842 the complementarity between the measurements at  $ep$  and  $pp$  machines, with the former leading  
 5843 in terms of precision in the largest Higgs couplings, while the high-luminosity of the latter brings  
 5844 sensitivity to the smaller interactions.

5845 Finally, as mentioned at the beginning, we did not include in this combined  $ep+pp$  fit the  
 5846 projections for top Yukawa interactions at the LHeC from Section 7.5, as these were not derived  
 5847 in a global setup, but rather setting all other interactions involved in  $\bar{t}H\nu_e$  product to their SM  
 5848 values. However, the main uncertainty from the other  $\kappa$  parameters is expected to come from  
 5849 the  $W$  and  $b$  couplings,  $\kappa_W$  and  $\kappa_b$ , which are determined with an overall precision of  $\sim 0.8\%$   
 5850 and  $2\%$ . Therefore one expects the LHeC result,  $\delta\kappa_t \sim 17\%$  for  $L = 1 \text{ ab}^{-1}$ , to be minimally  
 5851 affected. This number is to be compared with the HL-LHC projection of  $\sim 4\%$ , which is expected  
 5852 to dominate in a combined result.

### 5853 9.3 Further precision SM measurements at the HL-LHC

5854 The LHeC measurements and the results from their phenomenological interpretations will have  
 5855 an important impact on many areas of the HL-LHC physics programme. This goes far beyond  
 5856 the precision electroweak and the Higgs physics, as discussed at hand of dedicated analyses in

<sup>2</sup>The  $\kappa$  analysis of the LHeC has been performed independently using a MINUIT based fit program leading to perfect agreement with the HEPfit result.

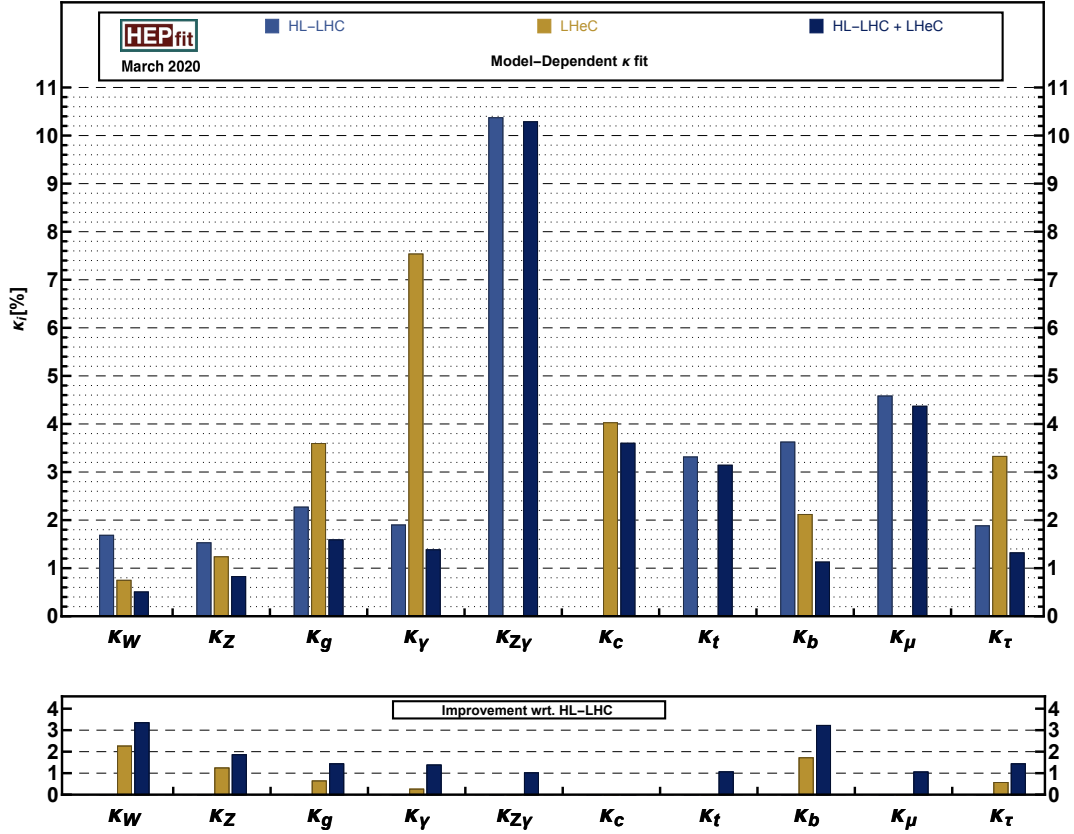


**Figure 9.6:** Top: Uncertainty of the determination of the scale factor  $\kappa$  in the determination of the Higgs couplings, in per cent. Results are given of the combined HL-LHC + LHeC  $\kappa$  fit (dark blue) and of the HL-LHC (blue) and LHeC (gold) stand-alone fits. There is no accurate measurement expected of  $\kappa_c$  at the LHC. Likewise the precision of the rare channels  $Z\gamma$ ,  $t\bar{t}$  and  $\mu\mu$  will be very limited at the LHeC. Bottom: Improvement of the  $\kappa$  determinations through the addition of the  $ep$  information (gold) and by the combined  $ep + pp$  analysis (dark blue), calculated with respect to the HL-LHC prospects. Strong improvements are seen for the  $W$ ,  $Z$  and  $b$  couplings, while that for charm cannot be illustrated here as  $\kappa_c$  is considered to be not measurable at the HL-LHC.

5857 the previous sections, and BSM or  $eA$  physics as discussed in the subsequent sections. In this  
 5858 section a few further selected topics of the Standard Model (SM) physics programme at the LHC  
 5859 and HL-LHC are discussed, where substantial improvements due to the LHeC can be expected.

5860 In general, two distinct aspects can be considered for any SM measurement in that respect <sup>3</sup>:

- 5861 • improvements of the analysis of the recorded event data, and  
 5862 • improvements of the phenomenological interpretation of the measurements.

5863 In order to assess the impact of the LHeC for the first bullet, one must recollect that an essential  
 5864 key ingredient of the analysis of any hadron collider data is the utilisation of phenomenological  
 5865 models, and commonly QCD inspired Monte Carlo (MC) event generators are employed. These  
 5866 are used for calibration, corrections of limited acceptance and resolution effects (*unfolding*),  
 5867 training of machine learning algorithms for event or object classification, extrapolations from

<sup>3</sup>In some cases, a model- or physics parameter is directly extracted from the experiment data and the two applications are merged into a single analysis workflow, for instance in many LHC top-quark mass analyses. Additionally to these two aspects, of course, the complementarity of the physics case of  $ep$  collisions enhances our understanding of the fundamental laws of physics.

5868 the *fiducial* to the *full* phase space, estimates of different background sources and also signal  
5869 extraction. Although the implemented models are derived from more fundamental equations like  
5870 the QCD Lagrangian, a number of model parameters remain poorly known and have to be *tuned*  
5871 with data. Also, since most models involve approximations and may be numerically limited, any  
5872 model needs to be validated, or invalidated, with independent measurements prior to its usage,  
5873 of course. With more and more data being recorded at the (HL-)LHC, statistical uncertainties  
5874 become very small and systematic uncertainties are reduced due to improved calibration and  
5875 analysis algorithms, so that uncertainties associated to the MC event models become important  
5876 and are limiting the accuracy of the HL-LHC measurements. It must be noted, that the MC  
5877 parameters should be tuned with data from another experiment in order to avoid a potential  
5878 bias of the actual measurement due to experimental correlations.

5879 For the second bullet, the phenomenological interpretation of hadron collider measurements, like  
5880 for instance tests of pQCD or the determination of SM parameters (e.g.  $\alpha_s(M_Z)$ ,  $\sin^2\theta_{\text{eff}}^\ell$ ,  $m_W$ ,  
5881 the  $\kappa$  parameters, ...), the proton PDFs and SM parameter which are input to the prediction  
5882 must be known with high accuracy, most noteworthy the value of  $\alpha_s(M_Z)$ .

5883 The most important inputs of the LHeC to the HL-LHC measurements are of course the precise  
5884 determination of the PDFs and  $\alpha_s(M_Z)$ , see Chapter 3. These will improve both, the data  
5885 analysis and its interpretation. Beyond that, the measurements of charged particle spectra, jet  
5886 shape and jet substructure observables, jet cross sections and event shape observables or heavy  
5887 flavor cross sections will help to improve MC models further, for instance with the determination  
5888 of charm and bottom-quark masses, heavy quark ( $c$ ,  $b$ ) fragmentation functions and fragmen-  
5889 tation fractions, finding optimal choices for all scales involved in a MC model, or determining  
5890 the optimal parameters for the parton shower. Such measurements can be performed with high  
5891 precision at the LHeC, since DIS represents a superior QCD laboratory. This is because in the  
5892 final state there is always a lepton, which is used for trigger and vertexing, and simultaneously  
5893 a hadronic system which is then subject of interest. In addition, the overconstrained kinematic  
5894 system allows for the precise calibration of hadronic final state objects, and furthermore limiting  
5895 effects like minimum bias definition or pile-up are absent.

5896 In the following, a few selected subjects are discussed at hand of LHC analyses performed with  
5897 Run-I data at  $\sqrt{s} = 8$  or 13 TeV, and thus giving a tangible indication about challenges at future  
5898 HL-LHC measurements:

- 5899 • The measurement of the integrated top-quark pair cross section represents an outstand-  
5900 ing benchmark quantity for the entire field of top-quark physics. Its measurement for  
5901 top-transverse momenta  $p_T^t > 400$  GeV in the *lepton+jets* decay channel yields a high  
5902 experimental precision with both, small statistical and systematic uncertainties. However,  
5903 its measurement precision is limited by theoretical uncertainties (also called *modelling* un-  
5904 certainties), and the largest individual source stems from the PDFs [180, 720]. A related  
5905 study of PDF effects on the acceptance correction for the integrated top-pair production  
5906 cross section and single-top production  $Wt$  is displayed in Fig. 9.7. The acceptance correc-  
5907 tion changes by up to 0.5–1 % for different PDF sets, and can become as large as 2.5 % for  
5908 different PDF sets and eigenvectors. Another very important uncertainty for top-quark  
5909 measurements is from the modelling of the parton shower. Both uncertainties from the  
5910 PDFs and from parton shower modelling, are expected to be significantly reduced with  
5911 LHeC data.
- 5912 • The determination of the top-quark mass  $m_t$  from LHC data requires the precise modelling  
5913 of the physics and all background processes with suitable MC models. Today, the value  
5914 of  $m_t$  is determined most precisely from a combination of such individual analyses, and

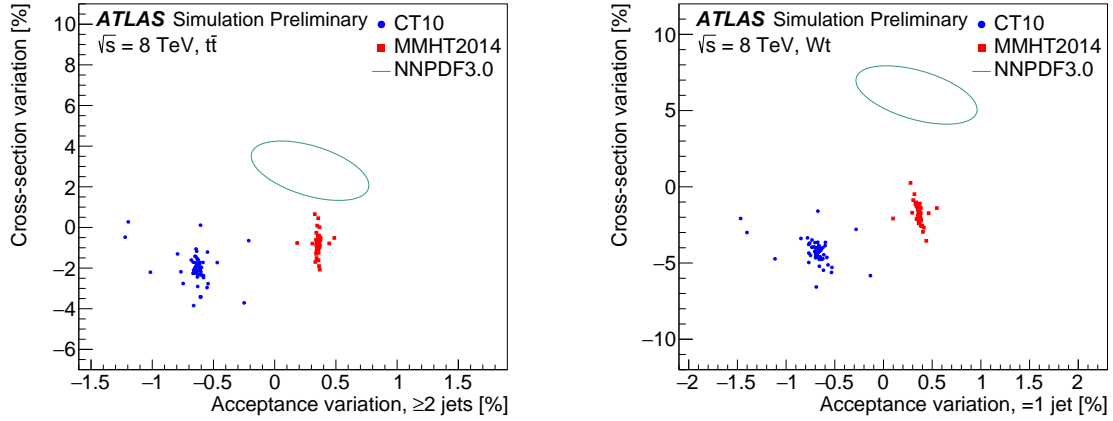


**Figure 9.7:** Impact of PDF uncertainty from CT10 and MMHT2014 eigenvectors or NNPDF3.0 replicas, on the cross section and the acceptance correction for top pair production  $t\bar{t}$  (left) and single top production  $Wt$  (right) (taken from Ref. [719]). Events are selected with at least two jets or with exactly one jet, respectively. Depending on the PDF set and eigenvector employed, the cross sections varies by up to 5–7% for top-pair and more than 10% for single-top production. Also the acceptance correction varies by about 0.5–1% for different PDF sets, and can become as large as 2.5% for different PDF sets and eigenvectors. Since the acceptance correction has to be imposed for the measurement, the limited knowledge of the PDFs introduces a sizeable modelling uncertainty on the measurement.

5915 uncertainties of 0.4–0.8 GeV are reported [180, 721–725]. Any of these individual precision  
 5916 determinations are limited by model uncertainties, and therefore improvements at the  
 5917 HL-LHC cannot be obtained with more data, but only with improved models. Some of  
 5918 the model uncertainties, e.g. PDF, parton shower, hadronisation or fragmentation related  
 5919 uncertainties can be expected to be reduced with LHeC data.

5920 • At the HL-LHC also rare decay channels can be exploited for precision measurements. For  
 5921 example, the top-quark mass can be determined from top-quark pair production with a sub-  
 5922 sequent decay, where one  $b$ -quark hadronises into a  $B$ -hadron which then decays through  
 5923 a  $J/\psi$ -meson into a pair of muons,  $t\bar{t} \rightarrow W^+bW^-b \rightarrow \ell\nu_\ell J/\psi (\rightarrow \mu^+\mu^-) Xqq'b$  [726]. Such  
 5924 a measurement requires the precise knowledge of  $b$ -quark fragmentation, which can be well  
 5925 measured at the LHeC, and will thus improve the HL-LHC measurement.

5926 • The value of the strong coupling constant  $\alpha_s(M_Z)$  is one of the least known fundamental  
 5927 parameters in physics and an improved determination with new measurement constitutes  
 5928 a real challenge for LHC and HL-LHC experiments. A large number of observables at the  
 5929 LHC are *per-se* sensitive to  $\alpha_s(M_Z)$ , and its value was determined in the past from var-  
 5930 ious definitions of jet cross section observables (see e.g. [155, 156, 727, 728]) or transverse  
 5931 energy-energy correlations [729],  $Z$ +jet cross sections [730], integrated [731] or differen-  
 5932 tial top-quark cross sections [732], inclusive  $W$  or  $Z$  production [733, 734], prompt photon  
 5933 data [735], and many other observables (see Ref. [180] for a review). Although the harsh en-  
 5934 vironment in high-luminosity hadron-hadron collisions requires sophisticated analysis tech-  
 5935 niques and dedicated measurements, small experimental uncertainties for  $\alpha_s(M_Z)$  could be  
 5936 achieved. Hence,  $\alpha_s$  determinations are nowadays limited due to theoretical uncertainties  
 5937 and the dominant uncertainties are most commonly PDF related [730, 731, 733, 734] (only  
 5938 for observables where NNLO predictions are not yet applicable, the scale uncertainties  
 5939 may overshoot the PDF uncertainties). Therefore, already today the knowledge of the  
 5940 PDFs represent the limiting factor, and a significant reduction of the total uncertainty for  
 5941  $\alpha_s(M_Z)$  can (only) be achieved with PDFs determined at the LHeC.

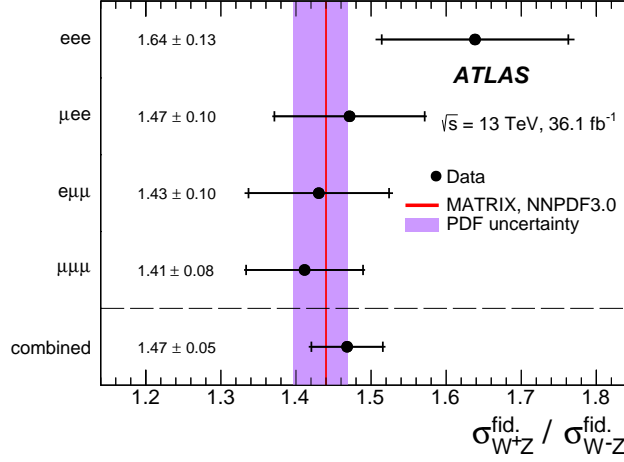


**Figure 9.8:** Measurement of the ratio of di-boson  $\sigma(W^+Z)/\sigma(W^-Z)$  integrated cross sections in a fiducial phase space for four different decay channels and their combination at  $\sqrt{s} = 13$  TeV in comparison with NNLO predictions [736, 737] (taken from Ref. [738]). The total uncertainties of the data points are dominated by statistical uncertainties and will be reduced in the future. The shaded violet band indicates the size of the PDF uncertainties that limits the overall interpretation of the measurement.

5942  
5943  
5944  
5945  
5946  
5947  
5948  
5949  
5950  
5951  
5952  
5953  
5954

- The production of  $W^\pm Z$  pairs in  $pp$  collisions provides a crucial test of the electroweak sector of the SM, since di-boson production is sensitive to the gauge-boson self-interactions. Already small deviations in the observed distributions could provide indications for new physics. The process can be well measured in a high-pile up environment and can be well separated from its huge QCD background. However, due to the relatively small  $W^\pm Z$  cross sections high statistical precision can only be achieved with high luminosity. Recent measurement of  $W^\pm Z$  pairs at  $\sqrt{s} = 13$  TeV based on  $36 \text{ fb}^{-1}$  of integrated luminosity have been performed by ATLAS and CMS [738, 739]. In Fig. 9.8 the ratio of fiducial cross sections  $\sigma_{W^+Z}/\sigma_{W^-Z}$  is displayed. The largest individual uncertainty is the statistical uncertainty and therefore future measurements at the LHC and HL-LHC are of great importance in order to reach higher precision. Nonetheless, already today, the overall phenomenological interpretation is limited by PDF uncertainties, as visible from Fig. 9.8, and these can be improved best with PDFs from LHeC.

5955  
5956  
5957  
5958  
5959  
5960  
5961

In the situation of the absence of indications for new physics, an important goal of the future LHC and HL-LHC physics programme has to be devoted to precision measurements. From the examples discussed above ( $W$ -boson mass and Higgs measurements are discussed in previous sections), it becomes obvious that limiting factors of such measurements arise from the signal and MC modelling, where PDF uncertainties constitute a limiting factor, and also improved understandings of parton shower, hadronisation and fragmentation processes are of importance. These aspects can all be ameliorated with independent precision measurements at the LHeC.

5962  
5963  
5964  
5965  
5966

Similarly, the phenomenological interpretation of many processes is already today limited by PDF uncertainties, and as outlined,  $\alpha_s$  determinations, di-boson processes, top-mass or top-cross section measurements, and many other topics, require a higher precision for PDFs. In the HL-LHC era, where data and predictions are more precise, the detailed knowledge of the PDFs will become of even greater importance.

## 9.4 High Mass Searches at the LHC

### 9.4.1 Strongly-produced supersymmetric particles

The potential of the HL- and HE-LHC to discover supersymmetry was extensively discussed in Ref. [740]. Here we focus on searches for gluinos within MSSM scenarios. Gluino pairs are produced through the strong interaction, and their production cross section is relatively large; naturalness considerations indicate that gluino masses should not exceed a few TeV and lie not too far above the EW scale. Hence, they are certainly among the first particles that could be discovered at the HL-LHC.

In the following we assume that a simplified topology dominates the gluino decay chain, culminating in jets plus missing energy originating from a massless LSP,  $\tilde{\chi}_0$ . Ref. [740] evaluated the sensitivity of the HL- and HE-LHC to gluino pair production with gluinos decaying exclusively to  $q\bar{q}\tilde{\chi}_0$ , through off-shell first and second generation squarks, using a standard search for events with jets and missing transverse energy. Currently, the reach for this simplified model with  $36\text{ fb}^{-1}$  of 13 TeV data is roughly 2 TeV gluinos, for a massless LSP [741, 742]. Extrapolating to  $3\text{ ab}^{-1}$  at 14 TeV, the limit grows to 3.2 TeV. For  $15\text{ ab}^{-1}$  at 27 TeV, a limit of 5.7 TeV was found.

When deriving limits, an overall systematic uncertainty of 20% was assumed on the SM background contributions, and a generic 10% uncertainty was assumed on the signal normalisation, not taking into account PDF-related uncertainties which are as large as 50% for gluinos around 3 TeV. The effect of this additional source of uncertainty was found to induce a variation in the mass limit by  $\pm 200\text{ GeV}$  at the HL-LHC, and as much as  $\pm 500\text{ GeV}$  at the HE-LHC.

We can revert this argument, and claim that with present PDF knowledge, mass limits could be as low as 3.0 TeV and 5.3 TeV at the HL- and HE-LHC, respectively. Data from the LHeC would make this contribution negligible compared to other sources of uncertainty. Compared to the most conservative scenario, the increase in sensitivity would correspond to an increase in centre-of-mass energy by approximately 5 to 10%.

### 9.4.2 Contact interactions

New, high-mass gauge bosons are most often searched for in resonant final states. Peaks in the invariant-mass distributions of electron, muon or jet pairs directly reflect the presence of such new particles; the accessible mass range is limited by the available centre-of-mass energy.

Particles with a mass beyond the kinematic limit generally interfere with the  $Z$  boson and the photon, generating non-resonant deviations in the invariant mass distributions. Such models can be parameterised as contact interactions (CI) between two initial-state quarks and two final-state leptons of given chirality:

$$\mathcal{L}_{\text{CI}} = \frac{g^2}{\Lambda^2} \eta_{ij} (\bar{q}_i \gamma_\mu q_i) (\bar{\ell}_i \gamma^\mu \ell_i), \quad (9.12)$$

where  $i, j = \text{L or R}$  (for left- or right-handed chirality),  $g$  is a coupling constant set to be  $4\pi$  by convention, and  $\Lambda$  is the CI scale. The sign of  $\eta_{ij}$  determines whether the interference between the SM Drell–Yan (DY) process,  $q\bar{q} \rightarrow Z/\gamma^* \rightarrow \ell^+\ell^-$ , is constructive or destructive.

The size and sign of the observed deviation with respect to the SM probes the scale and interference pattern of the interaction. The sensitivity of the search is limited by experimental uncertainties (finite statistics and experimental systematic uncertainties) and by uncertainties in the theoretical modelling of the DY background.

6008 The most recent results of the ATLAS and CMS Collaborations [695, 696] are based on  $e^+e^-$   
6009 and  $\mu^+\mu^-$  final states in  $36\text{ fb}^{-1}$  of data, and probe CI's up to a typical scale of 25 TeV, de-  
6010 pending on the chirality and sign of the interaction coupling parameter. The limits derived by  
6011 ATLAS, summarised in Tab. 9.6, accounted for theoretical uncertainties induced by the PDFs  
6012 and by  $\alpha_s$ . The dominant PDF uncertainty was estimated from the 90% CL uncertainty in  
6013 the CT14nnlo PDF set, adding an envelope from the comparison of the CT14nnlo, MMHT2014  
6014 and NNPDF3.0 [743] central sets. The strong coupling constant uncertainty was propagated  
6015 assuming  $\alpha_s = 0.118 \pm 0.003$ , with a subleading effect.

6016 The present study evaluates the sensitivity of this search at the HL-LHC. The increase in  
6017 sensitivity is estimated using samples of Standard-Model like pseudo data, corresponding to the  
6018 integrated luminosity of  $3\text{ ab}^{-1}$ . In a first step, both the experimental and theoretical systematic  
6019 uncertainties are kept in the publication. In this regime, the extrapolated statistical uncertainty  
6020 is typically a factor 5 to 10 smaller than the theoretical uncertainty. Improvements from the  
6021 LHeC in  $\alpha_s$  and in the proton PDFs are incorporated in a second step. Assuming the prospects  
6022 described in Chapter 3,  $\alpha_s$  and PDF uncertainties are smaller than the statistical fluctuations  
6023 and can be neglected in a first approximation.

6024 The results are summarised in Tab. 9.6. Everything else equal, increasing the sample size from  
6025  $36\text{ fb}^{-1}$  to  $3\text{ ab}^{-1}$  enhances the CI reach by a typical factor of two. Accounting for the improve-  
6026 ment in the theoretical modelling of the DY process brought by the LHeC brings another factor  
6027 of 1.5–1.8 in the limits. In the last case, the limits reach well into range directly accessible with  
6028 proton-proton collisions at  $\sqrt{s} = 100\text{ TeV}$ , as envisioned at the FCC-hh.

Model	ATLAS (Ref. [695])	HL-LHC	
	$\mathcal{L} = 36\text{ fb}^{-1}$ (CT14nnlo)	$\mathcal{L} = 3\text{ ab}^{-1}$ (CT14nnlo)	$\mathcal{L} = 3\text{ ab}^{-1}$ (LHeC)
LL (constr.)	28 TeV	58 TeV	96 TeV
LL (destr.)	21 TeV	49 TeV	77 TeV
RR (constr.)	26 TeV	58 TeV	84 TeV
RR (destr.)	22 TeV	61 TeV	75 TeV
LR (constr.)	26 TeV	49 TeV	81 TeV
LR (destr.)	22 TeV	45 TeV	62 TeV

**Table 9.6:** Contact interaction limits from ATLAS based on  $36\text{ fb}^{-1}$  of data [695], and extrapolated to the full HL-LHC dataset ( $3\text{ ab}^{-1}$ ). The extrapolation is performed assuming the same PDF and  $\alpha_s$  uncertainties as in Ref. [695], and assuming the improved uncertainties as obtained from the LHeC.

## 6029 9.5 PDFs and the HL-LHC and the LHeC

6030 As discussed in the previous Sections, a precise determination of PDFs is an essential ingredient  
6031 for the success of the HL-LHC. Conversely, the HL-LHC itself offers a significant opportunity to  
6032 improve our understanding of proton structure. In this Section we will discuss the possibilities  
6033 that the combination of HL-LHC and LHeC measurements offer for the determination of PDFs  
6034 in the proton.

### 6035 9.5.1 PDF Prospects with the HL-LHC and the LHeC

6036 In Ref. [255] the HL-LHC potential to constrain PDFs was analysed in detail, focussing on SM  
6037 processes that are expected to have the most impact at higher  $x$ . In particular, projections for  
6038 the production of top quark pairs, inclusive jets, forward  $W$  + charm quark and direct photons,

6039 as well as forward and high-mass Drell-Yan and the  $Z$  boson  $p_{\perp}$  distribution were included. It  
 6040 was found that PDF uncertainties on LHC processes can be reduced by a factor between two  
 6041 and five, depending on the specific flavour combination and on the optimistic assumptions about  
 6042 the reduction of the (experimental) systematic uncertainties.

6043 It is of interest to compare these constraints with those expected to come from the LHeC itself, as  
 6044 well as potential improvements from a combined PDF fit to the HL-LHC and LHeC datasets; this  
 6045 was studied in [58]. The basic procedure consists in generating HL-LHC and LHeC pseudodata  
 6046 with the PDF4LHC15 set [251] and then applying Hessian PDF profiling [253, 744], in other  
 6047 words a simplified version of a full refit, to this baseline to assess the expected impact of the  
 6048 data. While the HL-LHC datasets are described above, the LHeC pseudodata correspond to  
 6049 the most recent publicly available official LHeC projections, see Section 3.2, for electron and  
 6050 positron neutral-current (NC) and charged-current (CC) scattering. As well as inclusive data  
 6051 at different beam energies ( $E_p = 1,7$  TeV), charm and bottom heavy quark NC and charm  
 6052 production in  $e^-p$  CC scattering are included.

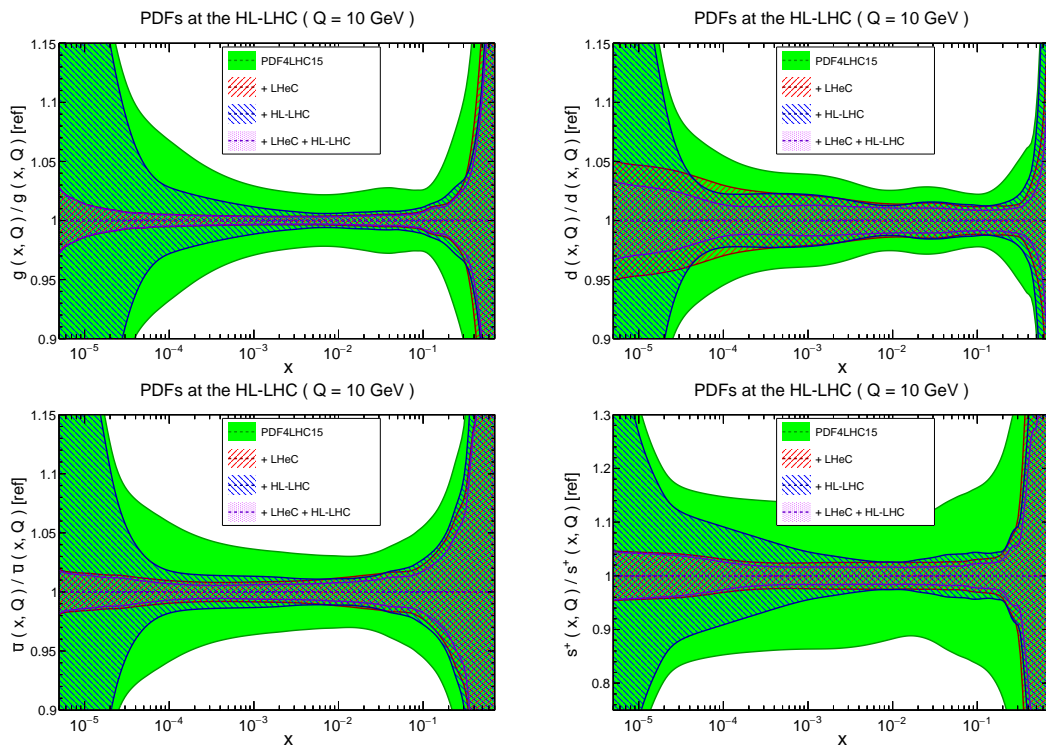


**Figure 9.9:** Impact of LHeC on the  $1\text{-}\sigma$  relative PDF uncertainties of the gluon, down quark, anti-up quark and strangeness distributions, with respect to the PDF4LHC15 baseline set (green band). Results for the LHeC (red), the HL-LHC (blue) and their combination (violet) are shown.

6053 The expected impact of the HL-LHC, LHeC and their combination on the PDF uncertainties of  
 6054 the gluon, down quark, anti-up quark and strangeness distributions are shown in Fig. 9.9. One  
 6055 observes that at low  $x$  the LHeC data place in general by far the strongest constraint, in partic-  
 6056 ular for the gluon, as expected from its greatly extended coverage at small  $x$ . At intermediate  
 6057  $x$  the impact of the HL-LHC and LHeC are more comparable in size, but nonetheless the LHeC  
 6058 is generally expected to have a larger impact. At higher  $x$  the constraints are again compar-  
 6059 able in size, with the HL-LHC resulting in a somewhat larger reduction in the gluon and strangeness  
 6060 uncertainty, while the LHeC has a somewhat larger impact for the down and anti-up quark  
 6061 distributions. Thus, the combination of both HL-LHC and LHeC pseudodata nicely illustrate



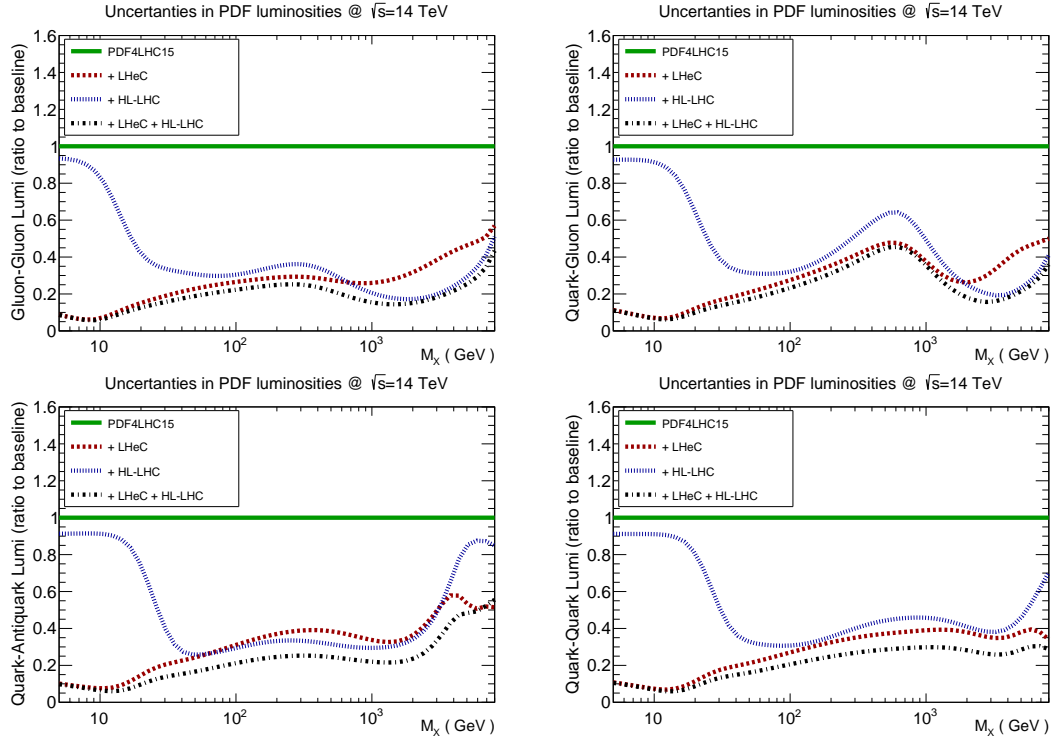


**Figure 9.10:** Impact of LHeC, HL-LHC and combined LHeC + HL-LHC pseudodata on the uncertainties of the gluon-gluon, quark-gluon, quark-antiquark and quark-quark luminosities, with respect to the PDF4LHC15 baseline set. In this comparison we display the relative reduction of the PDF uncertainty in the luminosities compared to the baseline.

6062 a clear and significant reduction in PDF uncertainties over a very wide range of  $x$ , improving  
 6063 upon the constraints from the individual datasets in a non-negligible way.

### 6064 9.5.2 Parton luminosities at the HL-LHC

6065 In Fig. 9.10 we show the impact on the gluon-gluon, quark-gluon, quark-antiquark and quark-  
 6066 quark partonic luminosities for a center-of-mass energy  $\sqrt{s} = 14$  TeV. Some clear trends are  
 6067 evident from this comparison, consistent with the results from the individual PDFs. We can  
 6068 in particular observe that at low mass the LHeC places the dominant constraint, while at  
 6069 intermediate masses the LHeC and HL-LHC constraints are comparable in size, and at high  
 6070 mass the stronger constraint on the gluon-gluon and quark-gluon luminosities comes from the  
 6071 HL-LHC, with the LHeC dominating for the quark-quark and quark-antiquark luminosities. As  
 6072 in the case of the PDFs, for the partonic luminosities the combination of the HL-LHC and LHeC  
 6073 constraints leads to a clear reduction in the PDF uncertainties in comparison to the individual  
 6074 cases, by up to an order of magnitude over a wide range of invariant masses,  $M_X$ , of the produced  
 6075 final state.

6076 In summary, these results demonstrate that while the HL-LHC alone is expected to have a size-  
 6077 able impact on PDF constraints, the LHeC can improve our current precision on PDFs signifi-  
 6078 cantly in comparison to this, in particular at low to intermediate  $x$ . Moreover, the combina-  
 6079 tion of both the LHeC and HL-LHC pseudodata leads to a significantly superior PDF error reduction  
 6080 in comparison to the two facilities individually. Further details, including LHeC-only studies as  
 6081 well as an investigation of the impact of the PDF baseline on the uncertainty projections, can  
 6082 be found in Ref. [58].

### 6083 9.5.3 PDF Sensitivity: Comparing HL-LHC and LHeC

6084 While the experimental reach of each facility in the  $\{x, Q^2\}$  kinematic plane provides a useful  
 6085 comparison, there are more factors to consider – especially when we are striving for ultra-high  
 6086 precision measurements. One measure that provides a dimension beyond the  $\{x, Q^2\}$  plane is the  
 6087 *sensitivity*; this is a combination of the correlation coefficient times a scaled residual [745, 746].  
 6088 This provides an extra dimension of information in comparison to a simple  $\{x, Q^2\}$  map and  
 6089 represents a measure of the impact of the data.

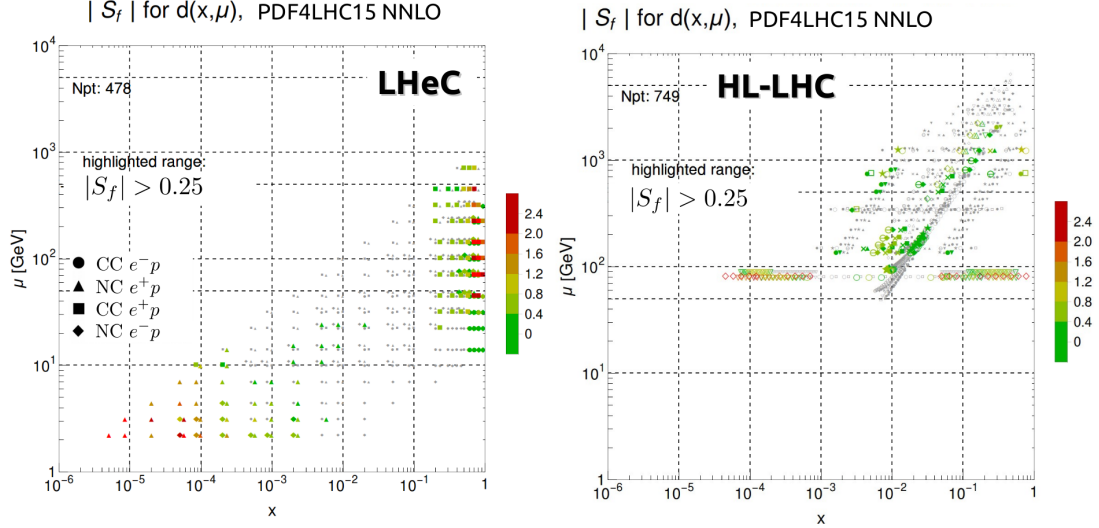


**Figure 9.11:** Sensitivity for a sample flavour  $\{d(x, Q)\}$  in the  $\{x, Q^2\}$  kinematic plane for the LHeC (left) and the HL-LHC (right) calculated with pseudodata [746]. We observe the LHeC is particularly sensitive in both the high and low  $x$  regions, and the HL-LHC covers the intermediate  $x$  region out to large  $Q$  scales.

6090 In Fig. 9.11 this PDF sensitivity for a sample PDF flavour is displayed for the LHeC and the  
 6091 HL-LHC pseudo-data. In particular, one observe that the LHeC provides strong sensitivity in  
 6092 the high- $x$  region, which is of great importance for BSM searches, and also in the low- $x$  region,  
 6093 which is relevant for QCD phenomena such as saturation. The HL-LHC provides constraints  
 6094 coming from  $W/Z$  production ( $Q \sim M_{W/Z}$ ) as well as from jets at high scales. The combination  
 6095 of these measurements will provide strongest constraints on the various PDF flavours across the  
 6096 broad  $\{x, Q^2\}$  kinematic plane.

## 6097 9.6 Impact of New Small- $x$ Dynamics on Hadron Collider Physics

6098 As discussed in Subsections 4.2.1 and 4.2.3, the presence of new dynamics at small  $x$  as claimed in  
 6099 Refs. [245, 249, 250] will have impact on hadronic observables. The impact is stronger for larger  
 6100 energies, therefore more important for the FCC-hh than for the LHC. But it may compete  
 6101 with other uncertainties and thus become crucial for precision studies even at LHC energies.  
 6102 Studies on the impact of non-linear dynamics at hadron colliders have been devoted mainly  
 6103 to photoproduction in UPCs, see e.g. [747–749] and Refs. therein for the case of gauge boson  
 6104 production. In this section we focus on the effect of resummation at small  $x$ .

6105 While hadronic data like jet, Drell-Yan or top production at existing energies do not have much  
 6106 constraining power at low  $x$  [245] and thus need not be included in the extraction of PDFs  
 6107 using resummed theoretical predictions, this fact does not automatically mean that the impact  
 6108 of resummation is not visible at large scales for large energies. Indeed the PDFs obtained with

6109 small- $x$  resummation may change at low energies in the region of  $x$  relevant for hadronic data,  
6110 thereby giving an effect also at higher energies after evolving to those scales. A consistent  
6111 inclusion of resummation effects on hadronic observables is thus crucial for achieving precision.  
6112 The difficulty for implementing resummation on different observables lies in the fact that not only  
6113 evolution equations should include it but also the computation of the relevant matrix elements  
6114 for the observable must be performed with matching accuracy.

6115 Until present, the only observable that has been examined in detail is Higgs production cross  
6116 section through gluon fusion [750]. Other observables like Drell-Yan [751] or heavy quark [752]  
6117 production are under study and they will become available in the near future.

6118 For  $gg \rightarrow H$ , the LL resummation of the matrix elements matched to fixed order at N<sup>3</sup>LO was  
6119 done in Refs. [270, 750] and the results are shown in Figs. 9.12 and 9.13. Fig. 9.12 shows the  
6120 increasing impact of resummation on the cross section with increasing energy. It also illustrates  
6121 the fact that the main effect of resummation comes through the modification of the extraction  
6122 of parton densities and their extrapolation, not through the modification of the matrix elements  
6123 or the details of the matching.

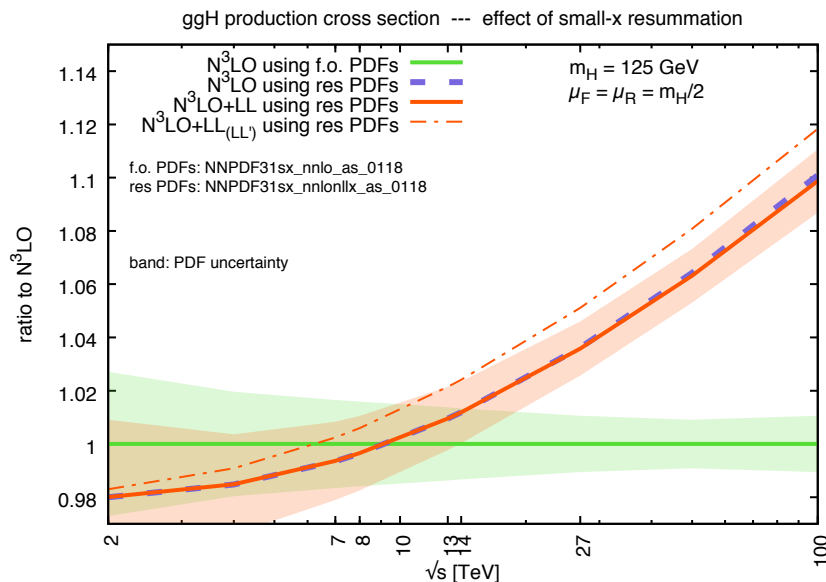


**Figure 9.12:** Ratio of the N<sup>3</sup>LO Higgs cross section with and without resummation to the N<sup>3</sup>LO fixed-order cross section, as a function of the collider centre-of-mass energy. “f.o.” denotes fixed order, “res” denotes resummed and “LL” a different anomalous dimension matching at leading logarithmic accuracy, see the legend on the plot and Ref. [750] for details. The PDFs used are from the global dataset of Ref. [249]. Figure taken from Ref. [750].

6124 Fig. 9.13 indicates the size of the different uncertainties on the absolute values of the cross section  
6125 with increasing accuracy of the perturbative expansion, at HL-LHC and FCC-hh energies. For  
6126 N<sup>3</sup>LO(+LL) it can be seen that while at the HL-LHC, the effect of resummation is of the same  
6127 order as other uncertainties like those coming scale variations, PDFs and subleading logarithms,  
6128 this is not the case for the FCC where it can be clearly seen that it will be the dominant one.  
6129 Resummation should also strongly affect the rapidity distributions, a key need for extrapolation  
6130 of observed to total cross sections. In particular, rapidity distributions are more directly sensitive  
6131 to PDFs at given values of momentum fraction  $x$ , and therefore in regions where this momentum  
6132 fraction is small (large rapidities) the effect of resummation may be sizeable also at lower collider  
6133 energies. These facts underline the need of understanding the dynamics at small  $x$  for any kind

6134 of precision physics measurements at future hadronic colliders, with increasing importance for  
 6135 increasing energies.

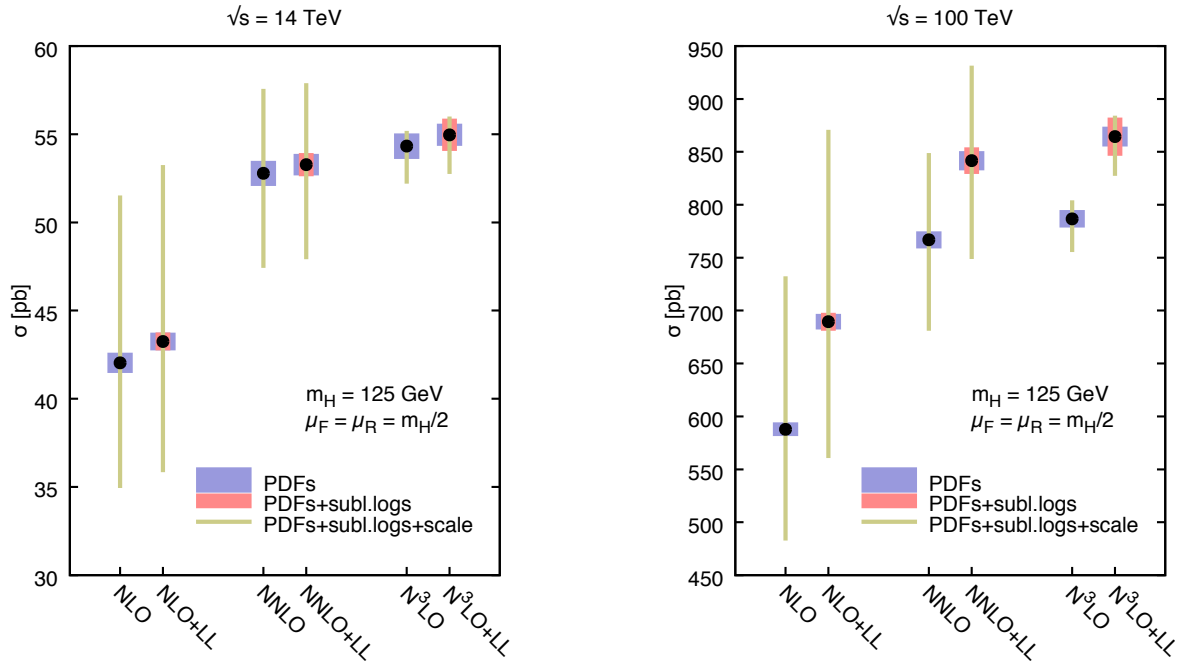


**Figure 9.13:** Perturbative progression of the Higgs cross section for two collider energies  $\sqrt{s} = \{14, 100\}$  TeV. In each plot the NLO, NLO+LL, NNLO, NNLO+LL,  $N^3\text{LO}$  and  $N^3\text{LO}+\text{LL}$  results are shown. The results are supplemented by uncertainty bands from PDF, subleading logarithms and scale uncertainties. Figure taken from Ref. [750].

6136 Finally, it should be mentioned that a different kind of factorisation, called transverse momentum  
 6137 (TMD) factorisation [37, 496, 753–756], may have an effect on large scale observables in hadronic  
 6138 colliders. The extension of the TMD evolution equations towards small  $x$  [757] and the relation of  
 6139 such factorisation with new dynamics at small  $x$ , either through high-energy factorisation [758–  
 6140 761] or with the CGC [492, 493], is under development [762].

## 6141 9.7 Heavy Ion Physics with $eA$ Input

6142 The study of hadronic collisions at RHIC and the LHC, proton-proton, proton-nucleus and  
 6143 nucleus-nucleus, has produced several observations of crucial importance for our understanding  
 6144 of QCD in complex systems where a large number of partons is involved [763, 764]. The different  
 6145 stages of a heavy ion collision, as we presently picture it, are schematically drawn in Fig 9.14.

6146 First, the hot and dense partonic medium created in heavy ion collisions, the quark-gluon plasma  
 6147 (QGP), experiences a collective behaviour of which azimuthal asymmetries and transverse spectra  
 6148 with a specific ordering in particle masses are the most prominent observables. This collec-  
 6149 tivity can be very well described by relativistic hydrodynamics [765]. For this description, the  
 6150 system has to undergo some dynamics leading to rough isotropisation in a short time,  $\lesssim 1$  fm/c,  
 6151 for which both strong and weak coupling explanations have been proposed [545].

6152 Second, collisions between smaller systems,  $pp$  and  $pA$ , show many of the features [542–544] that  
 6153 in heavy ion collisions are taken as indicative of the production of a dense hot partonic medium.  
 6154 The most celebrated of such features, the long rapidity range particle correlations collimated in

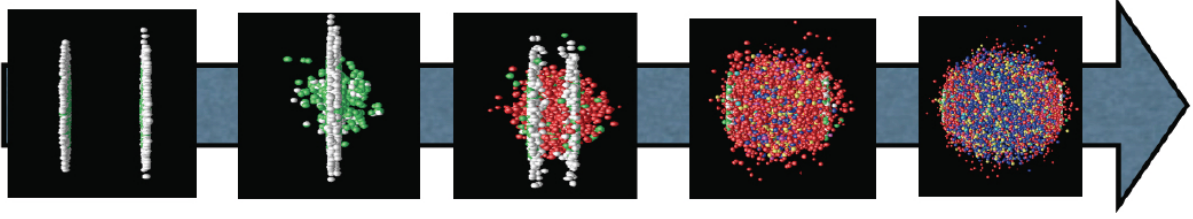


**Figure 9.14:** Sketch of a heavy ion collision with time running left to right, going from the approach of two ultrarelativistic Lorentz-contracted nuclei, the collision and parton creation in the central rapidity region, the beginning of expansion and formation of the QGP, the expansion of the QGP until hadronisation, and, finally, the expansion of the hadronic gas.

6155 azimuth, named the ridge (see Sect. 6.5), has been found in all collisions systems. The dynamics  
 6156 underlying this phenomena, either the formation of QGP and the existence of strong final state  
 6157 interactions, or some initial state dynamics that leaves imprint on the final observables, is under  
 6158 discussion [545].

6159 Finally, the QGP is extremely opaque to both highly energetic partons [766] and quarkonia [767]  
 6160 traversing it. These observables, whose production in  $pp$  can be addressed through perturba-  
 6161 tive methods, are called hard probes [768]. The quantification of the properties of the QGP  
 6162 extracted through hard probes is done by a comparison with predictions based on assuming a  
 6163 nuclear collision to be a superposition of collisions among free nucleons. Such predictions contain  
 6164 uncertainties coming both from nuclear effects other than those in QGP (named cold nuclear  
 6165 matter effects), and from uncertainties in the dynamics determining the interaction between the  
 6166 energetic parton or bound state and the medium. In the case of partons, this has motivated the  
 6167 development of sophisticated jet studies in heavy ion collisions [769].

6168  $eA$  collisions studied in the energy range relevant for the corresponding hadronic accelerator – the  
 6169 LHeC for the LHC – would substantially improve our knowledge on all these aspects and, indeed,  
 6170 on all stages of a heavy ion collisions depicted in Fig. 9.14. Besides, they can reduce sizeably the  
 6171 uncertainties in the extracted QGP parameters, the central goal of the heavy program for the  
 6172 understanding of the different phases of QCD. Here we provide three examples of such synergies:

- 6173 • Nuclear parton densities: The large lack of precision presently existing in the deter-  
 6174 mination of parton densities induce large uncertainties in the understanding of several  
 6175 signatures of the QGP. For example, for  $J/\psi$  suppression, its magnitude at midrapidity  
 6176 at the LHC is compatible with the sole effect of nuclear shadowing on nPDFs [767], see  
 6177 Fig. 9.15. While from data at lower energies and at forward and backward rapidities it is  
 6178 clear that this is not the only effect at work, only a reduction on the nPDF uncertainty  
 6179 as feasible at the LHeC, see Sect. 6.2, will make possible a precise quantification of the  
 6180 different mechanisms producing either suppression (screening, gluon dissociation, energy  
 6181 loss) or enhancement (recombination or coalescence), that play a role for this observable.
- 6182 • Initial conditions for the collective expansion and the small system problem: At present,  
 6183 the largest uncertainty in the determination of the transport coefficients of the partonic  
 6184 matter created in heavy ion collisions [771, 772] (see Fig. 9.16), required in hydrodynamic  
 6185 calculations, and in our understanding of the speed of the approach to isotropisation and  
 6186 of the dynamics prior to it [773], comes from our lack of knowledge of the nuclear wave  
 6187 function and of the mechanism of particle production at small to moderate scales – i.e. the  
 6188 soft and semihard regimes. Both aspects determine the initial conditions for the application  
 6189 of relativistic hydrodynamics. This is even more crucial in the discussion of small systems,

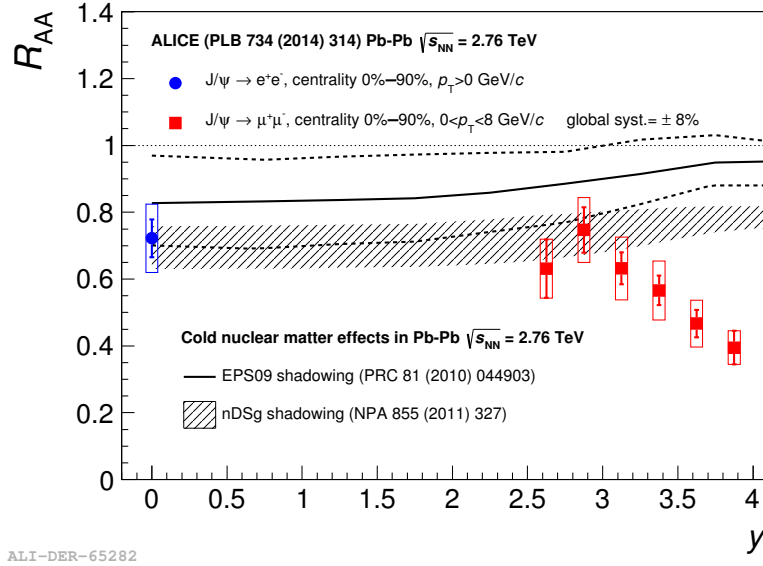


**Figure 9.15:** ALICE inclusive  $J/\psi$  nuclear modification factor versus rapidity [770], compared to nPDF calculations. Taken from [767].

6190  
6191  
6192  
6193  
6194  
6195  
6196  
6197  
6198

where details of the transverse structure of protons are key [774] not only to provide such initial conditions but also to establish the relative role of initial versus final state dynamics. For example, the description of azimuthal asymmetries in  $pp$  and  $pPb$  collisions at the LHC demands that the proton is modelled as a collection of constituent quarks or hot spots [765, 774].  $ep$  and  $eA$  collisions at the LHeC can constrain both aspects in the pertinent kinematic region, see Sects. 3.4 and 6.3. Besides, they can clarify the mechanisms of particle production and the possible relevance of initial state correlations on the final state observables as suggested e.g. by CGC calculations, see Sects. 4.2.1 and 6.4, whose importance for LHC energies can be established at the LHeC.

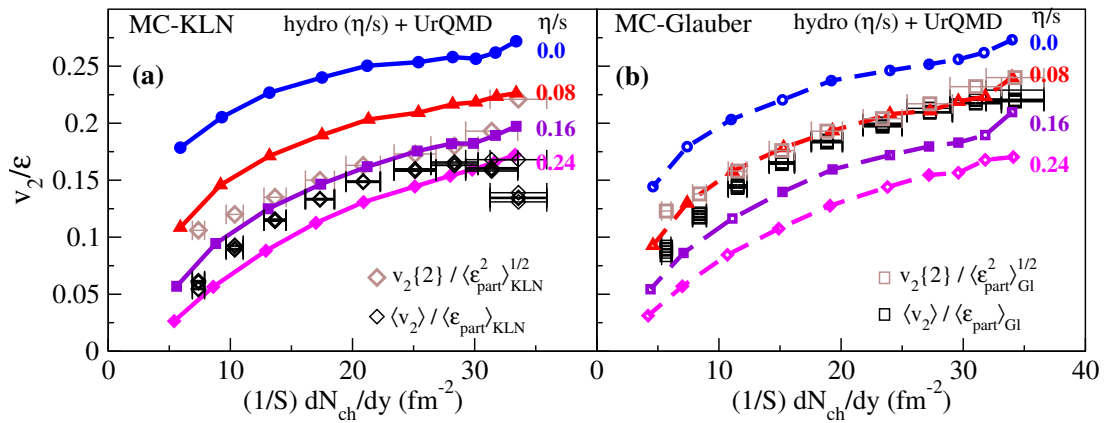


**Figure 9.16:** Comparison of the universal  $v_2(\eta/s)/\varepsilon$  vs.  $(1/S)(dN_{ch}/dy)$  curves with experimental data for  $\langle v_2 \rangle$  [775],  $v_2\{2\}$  [776], and  $dN_{ch}/dy$  [777] from the STAR Collaboration. The experimental data used in (a) and (b) are identical, but the normalisation factors  $\langle \varepsilon_{part} \rangle$  and  $S$  used on the vertical and horizontal axes, as well as the factor  $\langle \varepsilon_{part}^2 \rangle^{1/2}$  used to normalize the  $v_2\{2\}$  data, are taken from the MC-KLN model in (a) and from the MC-Glauber model in (b). Theoretical curves are from simulations with MC-KLN initial conditions in (a) and with MC-Glauber initial conditions in (b). Taken from [771].

6199

- Impact on hard probes: Besides the improvement in the determination of nPDFs that

6200 affects the quantification of hard probes, commented above,  $eA$  collisions can help to un-  
6201 derstand the dynamics of the probes by analysing the effects of the nuclear medium on  
6202 them. As two examples, the abundant yields of jets and large transverse momentum parti-  
6203 cles at the LHeC [1] will allow precise studies of the nuclear effects on jet observables and of  
6204 hadronisation inside the nuclear medium. These two aspects are of capital importance not  
6205 only in heavy ion collisions but also in small systems where the lack of jet modification is  
6206 the only QGP-like characteristics not observed in  $pPb$ . On the other hand, measurements  
6207 of exclusive quarkonium production at the LHeC [1] will provide a better understanding  
6208 of the cold nuclear matter effects on this probe, on top of which the effects of the QGP  
6209 will provide a quantitative characterisation of this new form of QCD matter.

6210 As discussed in Sect. 6.2,  $pPb$  and  $PbPb$  collisions at the LHC offer possibilities for constraining  
6211 nPDFs, through the measurement of EW vector boson production [778], dijets [508], D mesons at  
6212 forward rapidities [520] and exclusive charmonium and dijet photoproduction in ultraperipheral  
6213 collisions [779–781]. Specifically, dijets in UPCs could constrain nPDFs in the region  $10^{-3} \lesssim$   
6214  $x \lesssim 0.7$  and  $200 \lesssim Q^2 \lesssim 10^4 \text{ GeV}^2$ .  $eA$  collisions would provide more precise nPDFs, whose  
6215 compatibility with these mentioned observables would clearly establish the validity of collinear  
6216 factorisation and the mechanisms of particle production in collisions involving nuclei.

6217 Furthermore,  $eA$  offers another system where photon-photon collisions, recently measured in  
6218 UPCs at the LHC [782], can be studied. For example, the observed acoplanarity of the produced  
6219 muon pairs can be analysed in  $eA$  in order to clarify its possible origin and constrain the parton  
6220 densities in the photon.

6221 Finally, the possible existence of a new non-linear regime of QCD - saturation - at small  $x$  is  
6222 also under study at the LHC, for example using dijets in the forward rapidity region in  $pPb$   
6223 collisions [783]. As discussed in Sect. 6.5, the ridge phenomenon (two particle correlations peaked  
6224 at zero and  $\pi$  azimuthal angles and stretched along the full rapidity of the detector) observed in  
6225 all collision systems,  $pp$ ,  $pPb$  and  $PbPb$  at the LHC, has been measured in photoproduction on  
6226 Pb in UPCs at the LHC [546]. For the time being, its existence in smaller systems like  $e^+e^-$  [547]  
6227 at LEP and  $ep$  at HERA [548] has been scrutinised but the results are not conclusive. These  
6228 studies are fully complementary to those in  $ep$  and  $eA$ , where its search at the smallest possible  
6229 values of  $x$  at the LHeC would be most interesting. For example, the collision of the virtual  
6230 photon with the proton at the LHeC can be considered as a high energy collision of two jets or  
6231 “flux tubes”.

6232 In conclusion,  $ep$  and  $eA$  collisions as studied at the LHeC will have a large impact on the  
6233 heavy ion programme, as the comparison of the kinematic reach of DIS and hadronic machines  
6234 shown in Fig. 9.17 makes evident. It should be noted that there exist proposals for extending  
6235 such programme into Run 5 and 6 of the LHC [494], by running lighter ions and with detector  
6236 upgrades in ATLAS and CMS (starting in Run 4) and LHCb (Upgrade II [784]).

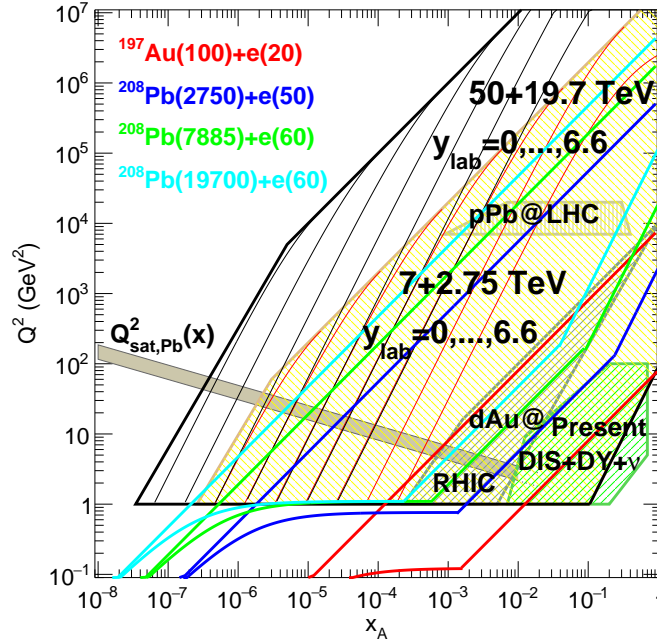


**Figure 9.17:** Kinematic regions in the  $x - Q^2$  plane explored by data sets (charged lepton and neutrino DIS, DY,  $dAu$  at RHIC and  $pPb$  at the LHC) used in present nPDF analyses [488], compared to the ones achievable at the EIC (red), the LHeC (ERL against the HL-LHC beams, dark blue) and two FCC-eh versions (with Pb beams corresponding to proton energies of 20 TeV - green and 50 TeV - light blue). Acceptance is taken to be  $1^\circ < \theta < 179^\circ$ , and  $0.01(0.001) < y < 1$  for the EIC (all other colliders). The areas delimited by thick brown and black lines show the regions accessible in  $pPb$  collisions at the LHC and the FCC-hh (50 TeV) respectively, while the thin lines represent constant rapidities from 0 (right) to 6.6 (left) for each case. The saturation scale  $Q_{sat}$  shown here for indicative purposes only, see also [489], has been drawn for a Pb nucleus considering an uncertainty  $\sim 2$  and a behaviour with energy following the model in [490]. Note that it only indicates a region where saturation effects are expected to be important but there is no sharp transition between the linear and non-linear regimes.



## Chapter 10

# The Electron Energy Recovery Linac

We studied different options for the electron accelerator for LHeC in Ref. [1], of which the Energy Recovery Linac (ERL) option is retained in this update of the CDR. This is due to the higher achievable luminosity of the Linac-Ring option, as compared to the Ring-Ring option, as well as the interference of the installation of an electron ring in the LHC tunnel with its operation [785]. The clear advantage of the ERL compared to its contenders in 2012 is the possibility to keep the overall energy consumption at bay, albeit, in its baseline configuration and size of the return arcs, operation is still limited to lepton energies below 70 GeV to avoid excessive synchrotron radiation losses. Since there is no fundamental beam loading in an ERL by its principle, higher average currents and thus higher luminosities would not lead to larger power consumption.

### 10.1 Introduction – Design Goals

The main guidelines for the design of the Electron ERL and the Interaction Region (IR) with the LHC are:

- electron-hadron operation in parallel with high luminosity hadron-hadron collisions in LHC/HL-LHC;
- centre-of-mass collision energy in the TeV scale;
- power consumption of the electron accelerator smaller than 100 MW;
- peak luminosity approaching  $10^{34} \text{ cm}^{-2}\text{s}^{-1}$ ;
- integrated luminosity exceeding by at least two orders of magnitude that achieved by HERA at DESY.

The electron energy  $E_e$  chosen in the previous version of the CDR [1] was 60 GeV. This could be achieved with an ERL circumference of 1/3 of that of the LHC. Cost considerations and machine-detector performance aspects, in particular the amount of synchrotron radiation losses in the IR, have led to define a new reference configuration with  $E_e = 49.2 \text{ GeV}$  and a circumference of  $\approx 5.4 \text{ km}$ , 1/5 of that of the LHC.

The ERL consists of two superconducting (SC) linacs operated in CW connected by at least three pairs of arcs to allow three accelerating and three decelerating passes (see Fig. 10.1). The length of the high energy return arc following the interaction point should be such as to provide a half RF period wavelength shift to allow the deceleration of the beam in the linac structures in three passes down to the injection energy and its safe disposal. SC Cavities with an unloaded

6268 quality factor  $Q_0$  exceeding  $10^{10}$  are required to minimise the requirements on the cryogenic  
 6269 cooling power and to allow an efficient ERL operation. The choice of having three accelerating  
 6270 and three decelerating passes implies that the circulating current in the linacs is six times the  
 6271 current colliding at the Interaction Point (IP) with the hadron beam.

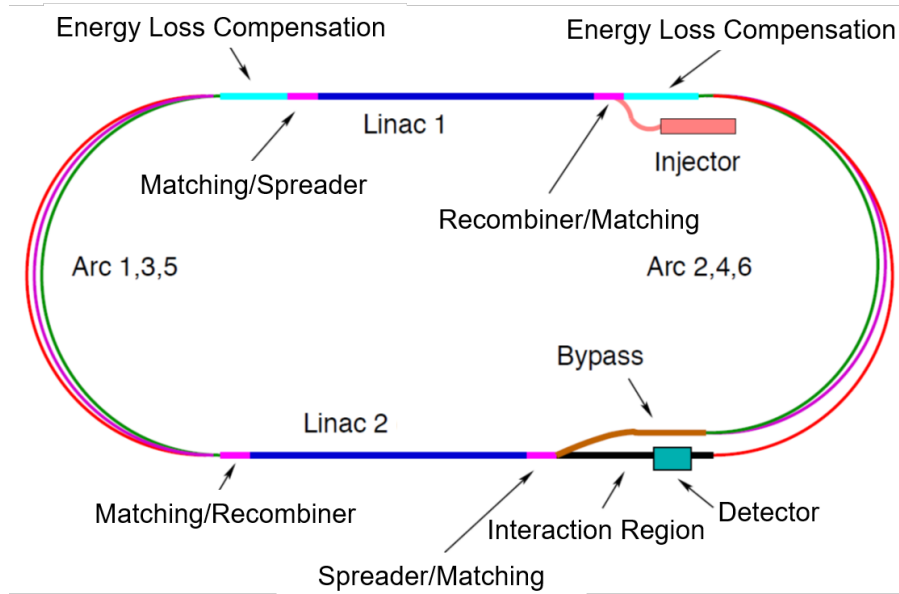


**Figure 10.1:** Schematic layout of the LHeC design based on an Energy Recovery Linac.

6272 The choice of an Energy Recovery Linac offers the advantage of a high brightness beam and it  
 6273 avoids performance limitations due to the beam-beam effect seen by the electron beam [786],  
 6274 which was a major performance limitation in many circular lepton colliders (e.g. LEP) and for  
 6275 the LHeC Ring-Ring option. The current of the ERL is limited by its source and an operational  
 6276 goal of  $I_e = 20$  mA has been set, corresponding to a bunch charge of 500 pC at a bunch frequency  
 6277 of 40 MHz. This implies operating the SRF cavities with the very high current of 120 mA for a  
 6278 virtual beam power (product of the beam current at the IP times the maximum beam energy) of  
 6279 1 GW. The validation of such performance in terms of source brightness and ERL 3-turn stable  
 6280 and efficient operation in the PERLE facility [9] is a key milestone for the LHeC design.

6281 A small beam size at the IP is required to maximize luminosity and approach peak luminosities  
 6282 of  $10^{34}$  cm<sup>-2</sup>s<sup>-1</sup> and integrated luminosities of 1 ab<sup>-1</sup> in the LHeC lifetime. In particular  $\beta^* <$   
 6283 10 cm needs to be achieved for the colliding proton beam compatibly with the optics constraints  
 6284 imposed by the operation in parallel to proton-proton physics in the other IPs during the HL-  
 6285 LHC era [3]. The peak luminosity values quoted above exceed those at HERA by 2-3 orders of  
 6286 magnitude. The operation of HERA in its first, extended running period 1992–2000, provided  
 6287 and integrated luminosity of about 0.1 fb<sup>-1</sup> for the H1 and ZEUS experiments, corresponding  
 6288 to the expected integrated luminosity collected over 1 day of LHeC operation.

## 6289 10.2 The ERL Configuration of the LHeC

6290 The main parameters of the LHeC ERL are listed in Tab. 10.1; their choices and optimisation  
 6291 criteria will be discussed in the following sections.

Parameter	Unit	Value
Injector energy	GeV	0.5
Total number of linacs		2
Number of acceleration passes		3
Maximum electron energy	GeV	49.19
Bunch charge	pC	499
Bunch spacing	ns	24.95
Electron current	mA	20
Transverse normalized emittance	$\mu\text{m}$	30
Total energy gain per linac	GeV	8.114
Frequency	MHz	801.58
Acceleration gradient	MV/m	19.73
Cavity iris diameter	mm	130
Number of cells per cavity		5
Cavity length (active/real estate)	m	0.918/1.5
Cavities per cryomodule		4
Cryomodule length	m	7
Length of 4-CM unit	m	29.6
Acceleration per cryomodule (4-CM unit)	MeV	289.8
Total number of cryomodules (4-CM units) per linac		112 (28)
Total linac length (with with spr/rec matching)	m	828.8 (980.8)
Return arc radius (length)	m	536.4 (1685.1)
Total ERL length	km	5.332

**Table 10.1:** Parameters of LHeC Energy Recovery Linac (ERL).

### 6292 10.2.1 Baseline Design – Lattice Architecture

6293 The ERL, as sketched in Fig. 10.1, is arranged in a racetrack configuration; hosting two su-  
6294 perconducting linacs in the parallel straights and three recirculating arcs on each side. The  
6295 linacs are 828.8 m long and the arcs have 536.4 m radius, additional space of 76 m is taken up by  
6296 utilities like Spreader/Recombiner (Spr/Rec), matching and energy loss compensating sections  
6297 adjacent to both ends of each linac (total of 4 sections) [787]. The total length of the racetrack  
6298 is 5.332 km:  $1/5$  of the LHC circumference  $2 \cdot (828.8 + 2 \cdot 76 + 536.4\pi)$  m. Each of the two linacs  
6299 provides 8.114 GV accelerating voltage, therefore a 49.19 GeV energy is achieved in three turns.  
6300 After the collision with the protons in the LHC, the beam is decelerated in the three subsequent  
6301 turns. The injection and dump energy has been chosen at 0.5 GeV.

6302 Injection into the first linac is done through a fixed field injection chicane, with its last magnet  
6303 (closing the chicane) being placed at the beginning of the linac. It closes the orbit *bump* at the  
6304 lowest energy, injection pass, but the magnet (physically located in the linac) will deflect the  
6305 beam on all subsequent linac passes. In order to close the resulting higher pass *bumps*, the so-  
6306 called re-injection chicane is instrumented, by placing two additional opposing bends in front of  
6307 the last chicane magnet. The chosen arrangement is such that, the re-injection chicane magnets  
6308 are only *visible* by the higher pass beams. The second linac in the racetrack is configured exactly  
6309 as a mirror image of the first one, with a replica of the re-injection chicane at its end, which  
6310 facilitates a fixed-field extraction of energy recovered beam to the dump.

### 6311 Linac Configuration and Multi-pass Optics

6312 Appropriate choice of the linac optics is of paramount importance for the transverse beam  
6313 dynamics in a multi-pass ERL. The focusing profile along the linac (quadrupole gradients) need

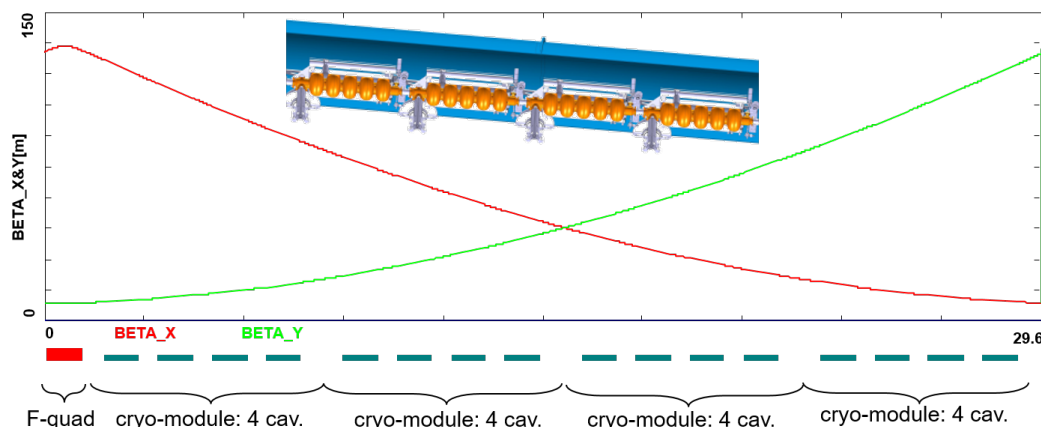


**Figure 10.2:** Layout of a half-cell composed out of four cryomodules (each hosting four, 5-cell cavities: top insert) and a focusing quad. Beta functions reflect  $130^\circ$  FODO optics.

6314 to be set (and they stay constant), so that multiple pass beams within a vast energy range may  
 6315 be transported efficiently. The chosen arrangement is such that adequate transverse focusing is  
 6316 provided for a given linac aperture. The linac optics is configured as a strongly focusing,  $130^\circ$   
 6317 FODO. In a basic FODO cell a quadrupole is placed every four cryomodules, so that the full cell  
 6318 contains two groups of 16 RF cavities and a pair of quads (F, D) as illustrated in Fig. 10.2. The  
 6319 entire linac is built out of 14 such cells. Energy recovery in a racetrack topology explicitly requires  
 6320 that both the accelerating and decelerating beams share the individual return arcs [788]. This  
 6321 in turn, imposes specific requirements for TWISS function at the linacs ends: TWISS functions  
 6322 have to be identical for both the accelerating and decelerating linac passes converging to the  
 6323 same energy and therefore entering the same arc. There is an alternative scheme, proposed by  
 6324 Peter Williams [789], who has argued that it would be beneficial to separate the accelerating and  
 6325 decelerating arcs. This would simplify energy compensation systems and linac-to-arc matching,  
 6326 but at an higher cost of the magnetic system of the arcs. However, doubling number of arcs is  
 6327 a very costly proposition. On the other hand, C-BETA experiment is pioneering a multi-pass  
 6328 arcs to transport a vast energy range through the same beam-line and it still intends to use  
 6329 them for energy recovery. Our approach, based on proven, CEBAF-like, RLA technology [790]  
 6330 is somewhere in the 'middle'.

6331 To visualize beta functions for multiple accelerating and decelerating passes through a given  
 6332 linac, it is convenient to reverse the linac direction for all decelerating passes and string them  
 6333 together with the interleaved accelerating passes, as illustrated in Fig. 10.3. This way, the  
 6334 corresponding accelerating and decelerating passes are joined together at the arc's entrance/exit.  
 6335 Therefore, the matching conditions are automatically built into the resulting multi-pass linac  
 6336 beamline. One can see that both linacs uniquely define the TWISS functions for the arcs: Linac  
 6337 1 fixes input to all odd arcs and output to all even arcs, while Linac 2 fixes input to all even  
 6338 arcs and output to all odd arcs. The optics of the two linacs are mirror-symmetric; They were  
 6339 optimised so that, Linac 1 is periodic for the first accelerating pass and Linac 2 has this feature  
 6340 for last decelerating one. In order to maximize the BBU threshold current [791], the optics is  
 6341 tuned so that the integral of  $\beta/E$  along the linac is minimised. The resulting phase advance per  
 6342 cell is close to  $130^\circ$ . Non-linear strength profiles and more refined merit functions were tested,  
 6343 but they only brought negligible improvements.

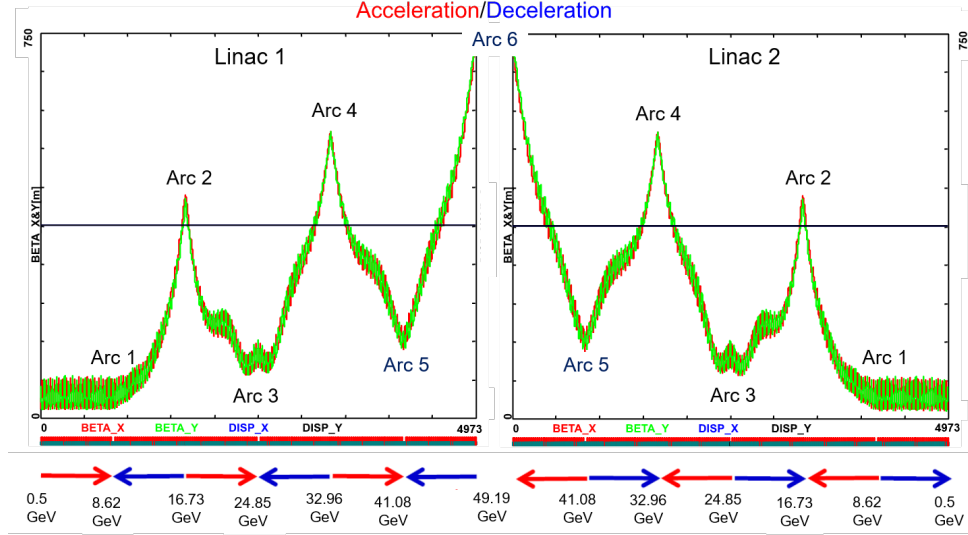


**Figure 10.3:** Beta function in the optimised multi-pass linacs (3 accelerating passes and 3 decelerating passes in each of two linacs). The matching conditions are automatically built into the resulting multi-pass linac beamline.

### 6344 Recirculating Arcs – Emittance Preserving Optics

6345 Synchrotron radiation effects on beam dynamics, such as the transverse emittance dilution  
 6346 induced by quantum excitations have a paramount impact on the collider luminosity. All six  
 6347 horizontal arcs are accommodated in a tunnel of 536.4m radius. The transverse emittance  
 6348 dilution accrued through a given arc is proportional to the emittance dispersion function,  $H$ ,  
 6349 averaged over all arc's bends [792]:

$$\Delta\epsilon = \frac{2\pi}{3} C_q r_0 \langle H \rangle \frac{\gamma^5}{\rho^2}, \quad (10.1)$$

6350 where

$$C_q = \frac{55}{32\sqrt{3}} \frac{\hbar}{mc} \quad (10.2)$$

6351 and  $r_0$  is the classical electron radius and  $\gamma$  is the Lorentz boost. Here,  $H = (1 + \alpha^2)/\beta \cdot$   
 6352  $D^2 + 2\alpha DD' + \beta \cdot D'^2$  where  $D, D'$  are the bending plane dispersion and its derivative, with  
 6353  $\langle \dots \rangle = \frac{1}{\pi} \int_{\text{bends}} \dots d\theta$ .

6354 Therefore, emittance dilution can be mitigated through appropriate choice of arc optics (values  
 6355 of  $\alpha, \beta, D, D'$  at the bends). In the presented design, the arcs are configured with a FMC  
 6356 (Flexible Momentum Compaction) optics to ease individual adjustment of,  $\langle H \rangle$ , in various  
 6357 energy arcs.

6358 Optics design of each arc takes into account the impact of synchrotron radiation at different  
 6359 energies. At the highest energy, it is crucial to minimise the emittance dilution due to quantum  
 6360 excitations; therefore, the cells are tuned to minimise the emittance dispersion,  $H$ , in the bending  
 6361 sections, as in the TME (Theoretical Minimum Emittance) lattice. On the other hand, at the  
 6362 lowest energy, it is beneficial to compensate for the bunch elongation with isochronous optics.  
 6363 The higher energy arcs (4,5 and 6) configured with the TME cells are still quasi-isochronous. To  
 6364 fully compensate remnant bunch elongation one could set higher pass linacs slightly off-crest to  
 6365 compress the bunches, since one has full control of gang-phases for individual linac passes. All  
 6366 styles of FMC lattice cells, as illustrated in Fig. 10.4, share the same footprint for each arc. This

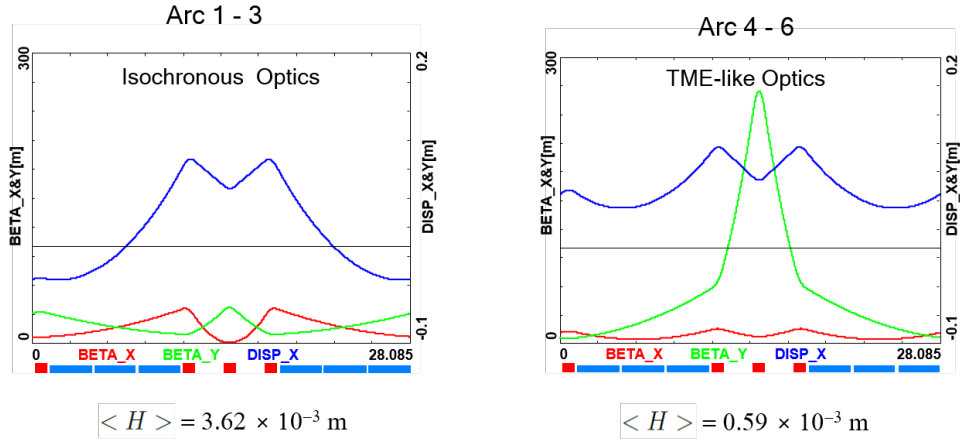


**Figure 10.4:** Two styles of FMC cells appropriate for different energy ranges. Left: lower energy arcs (Arc 1–3) configured with *Isochronous* cells, Right: higher energy arcs configured with *TME-like* cells. Corresponding values of the emittance dispersion averages,  $\langle H \rangle$ , are listed for both style cells.

6367 allows us to stack magnets on top of each other or to combine them in a single design. Here,  
 6368 we use substantially shorter than in the 60 GeV design, 28.1 m, FMC cell configured with six  
 6369 3 m bends, in groups of flanked by a quadrupole singlet and a triplet, as illustrated in Fig. 10.4.  
 6370 The dipole filling factor of each cell is 63 %; therefore, the effective bending radius  $\rho$  is 336.1 m.  
 6371 Each arc is followed by a matching section and a recombiner (mirror symmetric to spreader and  
 6372 matching section). Since the linacs are mirror-symmetric, the matching conditions described  
 6373 in the previous section, impose mirror-symmetric arc optics (identical betas and sign reversed  
 6374 alphas at the arc ends).

6375 Path-length adjusting chicanes were also foreseen to tune the beam time of flight in order to hit  
 6376 the proper phase at each linac injection. Later investigations proved them to be effective only  
 6377 with lower energy beams, as these chicanes trigger unbearable energy losses, if applied to the  
 6378 highest energy beams. A possible solution may consist in distributing the perturbation along  
 6379 the whole arc with small orbit excitations. This issue will be fully addressed in a subsequent  
 6380 section on 'Synchrotron Radiation Effects - Emittance Dilution'.

### 6381 Spreaders and Recombiners

6382 The spreaders are placed directly after each linac to separate beams of different energies and  
 6383 to route them to the corresponding arcs. The recombiners facilitate just the opposite: merging  
 6384 the beams of different energies into the same trajectory before entering the next linac. As  
 6385 illustrated in Fig. 10.5, each spreader starts with a vertical bending magnet, common for all  
 6386 three beams, that initiates the separation. The highest energy, at the bottom, is brought back  
 6387 to the horizontal plane with a chicane. The lower energies are captured with a two-step vertical  
 6388 bending adapted from the CEBAF design [790].

6389 Functional modularity of the lattice requires spreaders and recombiners to be achromats (both  
 6390 in the horizontal and vertical plane). To facilitate that, the vertical dispersion is suppressed by  
 6391 a pair of quadrupoles located in-between vertical steps; they naturally introduce strong vertical  
 6392 focusing, which needs to be compensated by the middle horizontally focusing quad. The overall  
 6393 spreader optics is illustrated in Fig. 10.6. Complete layout of two styles of switch-yard with  
 6394 different energy ratios is depicted in Fig. 10.5. Following the spreader, there are four matching  
 6395 quads to *bridge* the Twiss function between the spreader and the following 180° arc (two betas

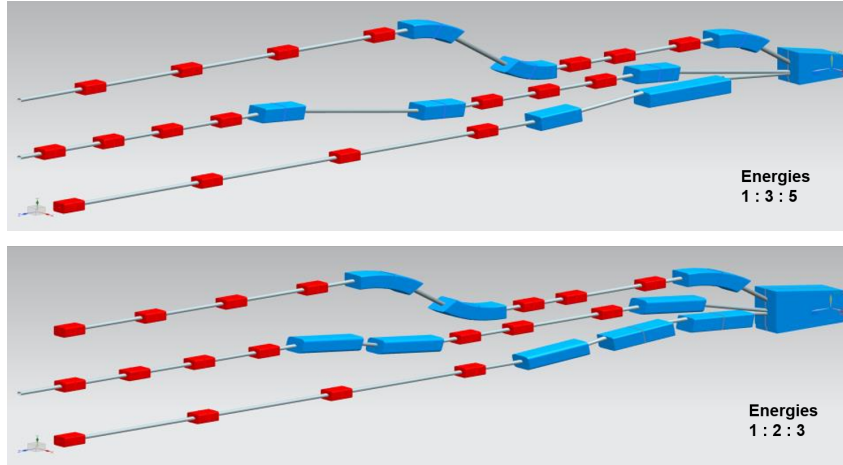


**Figure 10.5:** Layout of a three-beam switch-yard for different energy ratios: 1:3:5 and 1:2:3 corresponding to specific switch-yard geometries implemented on both sides of the racetrack

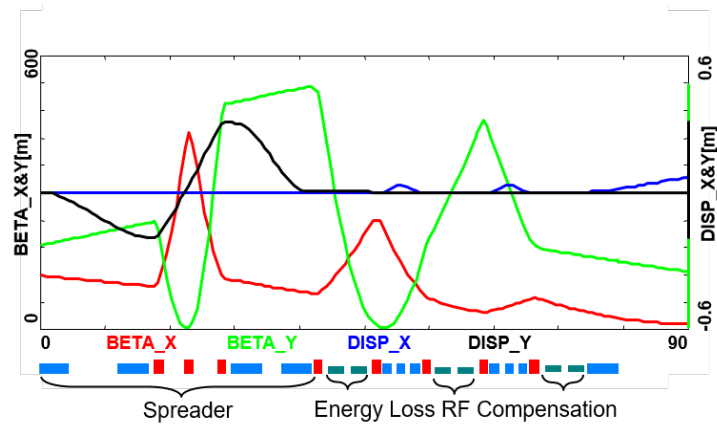


**Figure 10.6:** Spreader 3 (24.8 GeV) optics; featuring a vertical achromat with three dispersion suppressing quads in-between the two steps, a pair of path-length adjusting dogleg chicanes and four betatron matching quads, interleaved with three energy loss compensating sections (2-nd harmonic RF cavities marked in green).

6396 and two alphas). Combined spreader-arc-recombiner optics, features a high degree of modular  
 6397 functionality to facilitate momentum compaction management, as well as orthogonal tunability  
 6398 for both the beta functions and dispersion, as illustrated in Fig. 10.7.

### 6399 **Alternative design of the spreader/recombiner**

6400 The desire to reduce the number of elements included in the spreader led to the reduction of  
 6401 the number of steps required to separate vertically the different beams and route them into  
 6402 their specific arcs. In particular, this alternative spreader design uses a single vertical step  
 6403 instead of two. Although the concept has been briefly discussed in [1] it was not retained due  
 6404 to the superconducting technology needed for the quadrupoles that must be avoided in this  
 6405 highly radiative section. Nevertheless, recent studies have been pursuing a one step spreader  
 6406 version, based on normal conducting magnet technology. It assumes a pole tip field of less than  
 6407 1 T for an aperture radius of 30 mm, allowing the use of thin quadrupoles and thus minimise  
 6408 potential overlap with the other beamlines. With respect to the previous study, the use of normal  
 6409 conductors was made possible by increasing the overall spreader length and reducing the number

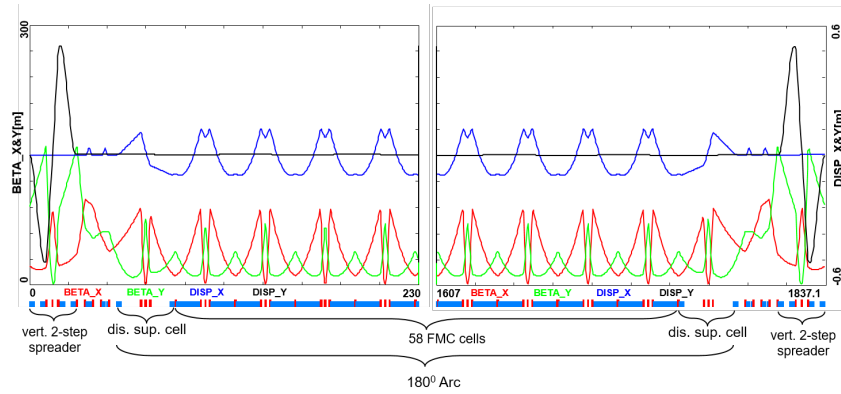


**Figure 10.7:** Complete Optics for Arc 3 (including switch-yard); featuring: low emittance 180° arc based on isochronous cells (30 cells flanked by dispersion suppression cell with missing dipoles on each side), spreaders and recombiners with matching sections and doglegs symmetrically placed on each side of the arc proper.

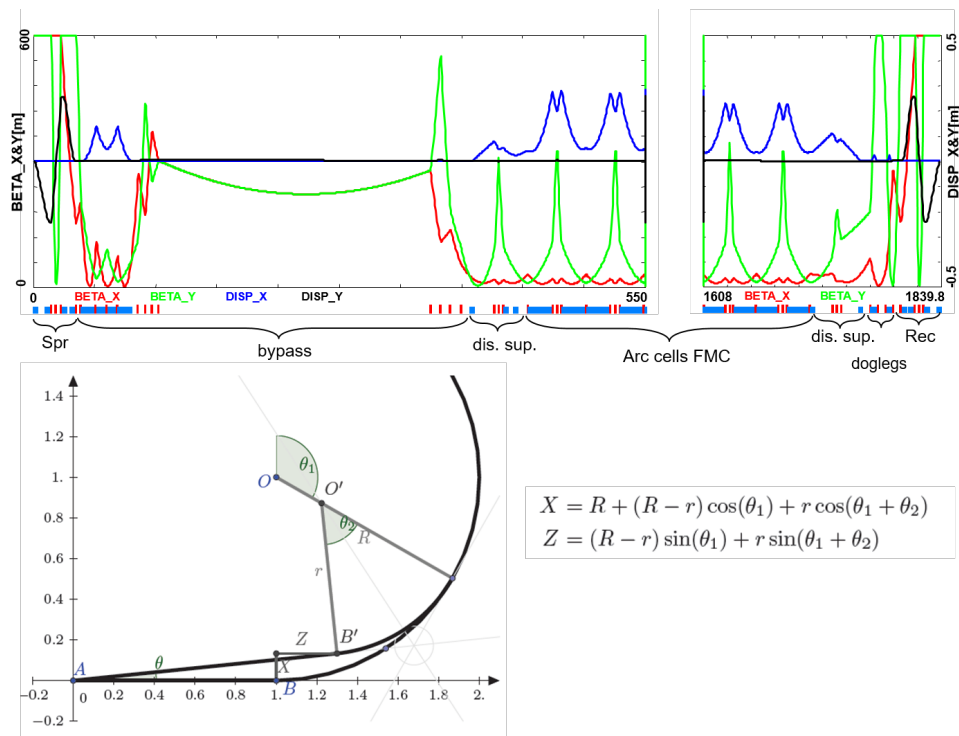


**Figure 10.8:** Optics and layout of Arc 4 including the detector bypass. The lattice (top insert) features a vertical spreader, an initial horizontal bending, a straight section, a modified dispersion suppressor, seven junction cells, and four regular cells. The bypass geometry (bottom insert), features a long IP line, AB, which for visual reasons has been purposely stretched, being actually about 1/5 of the arc radius. All geometric dependencies of the bypass parameters are summarized in the inserted formulae.



6410 of quadrupoles. In particular, the focusing magnets are limited to two outer quadrupoles for the  
 6411 achromatic function and one quadrupole in the middle, where the dispersion is zero, to control  
 6412 the beta function in the defocusing plane. Two visualisations are given Fig 10.9 and 10.10.

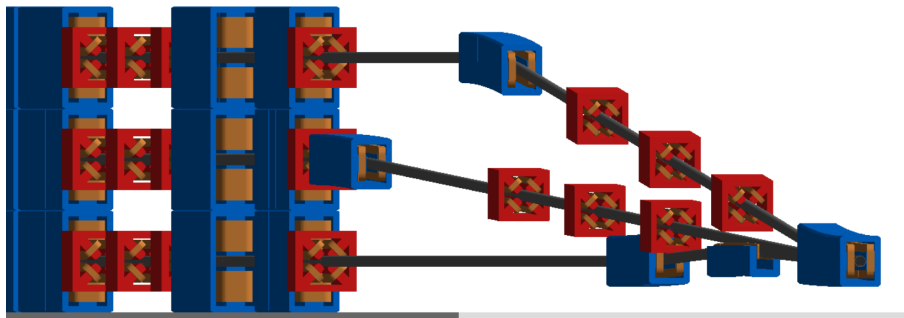


**Figure 10.9:** 3D visualisation of the spreader 1,3,5 inserted between the end of the linac and routing the different beamlines into their respective dispersion suppressors.

Both spreader types start with a first dipole that separates vertically the different beamlines in a 1-3-5 ratio for the odd number spreaders and in a 1-2-3 ratio for the even number spreaders. These ratios are defined by the beam energies of the corresponding turn. Therefore by fixing the length of the longest beamline for each spreaders (odd and even numbers) one obtains the required angle to get a 50 cm vertical offset between each beamlines. The equations below represent the required bending angle in the dipole and beamline lengths in order to meet the requirements,

$$\theta_3 = \frac{0.5}{l_3 - L} \quad l_1 = \frac{2E_1}{E_3}(l_3 - L) + L \quad (10.3)$$

$$\theta_2 = \frac{1}{l_2 - L} \quad l_4 = \frac{1E_4}{2E_2}(l_2 - L) + L \quad (10.4)$$

6413 where the index  $i$  corresponds to the beamline number associated to an energy  $E_i$ .  $L$  is the  
 6414 dipole length and  $l$  is the whole spreader beamline length.

6415 For the beam line 2 and 4 we obtain  $l_4 \approx l_2$  according to the energy ratio of 1.97. On the other  
 6416 hand,  $l_3$  will be longer than  $l_1$  because the energy ratio is 2.88. One can therefore tune the  
 6417 angle of the even number spreaders by defining  $l_2$  as it will be the longest. However the angle  
 6418 of the odd number spreaders will be determined by the length of  $l_3$ . Regarding the chicane  
 6419 used for the highest energy only a minimum separation between the highest energy and the  
 6420 intermediate energy allows the introduction of the opposite bending dipole. It constraints in  
 6421 return the placement of the quadrupoles of the intermediate energy. The location of the magnets  
 6422 is the main limitation towards a minimization of the spreader length: the shorter the lattice  
 6423 gets, the stronger the quadrupoles need to be in order to preserve the achromatic function.

6424 As a result, a one step spreader halves the number of dipoles present in the lattice and relaxes  
 6425 the constraint on magnets interference and overlap favorable for compactness. Dividing by two  
 6426 the number of dipoles has a noticeable effect on the synchrotron power radiated in the spreader  
 6427 which is, in addition, beneficial for the emittance growth. The dipole fields required, for a  
 6428 maximal length of 50 m, are 226 mT for the odd number spreaders and 326 mT for the even  
 6429 number spreaders. The multipass linac optics Fig. 10.3 shows that the even number spreaders  
 6430 ,*i.e.* 2, 4 and 6, have the highest beta functions at their entrance which is detrimental from the  
 6431 perspective of minimizing the emittance growth within the spreader lattice. A solution to solve  
 6432 this issue is to insert a doublet of quadrupoles at the exit of the linac. All three energies will

6433 go through the doublet and, therefore, a compromise has to be found for the gradients. Finally,  
 6434 the reduction of the  $\mathcal{H}$  function over the length of the spreader and specifically in the dipoles  
 6435 contributes to a further reduction of the emittance growth.

6436 The energy loss for spreader 1 is low due to the low beam energy; spreader 2 and 3 have similar  
 6437 values that are acceptable as well as the one of spreader 4. Spreader 5 and 6 have the highest  
 6438 beam energies and therefore the largest energy loss. In addition, the dipoles used to produce the  
 6439 chicane need double the field strength compared to the other dipoles for the same length, *i.e.*  
 6440 half the bending radius, in order to save space for the other elements in the other beamlines.  
 6441 The vertical emittance growth is well controlled just as in the even number spreaders. Only  
 6442 spreader 6 has an order of magnitude higher contribution but one has to keep in mind that  
 6443 the even number spreaders will only act as recombiner since there will be the horizontal bypass  
 6444 doing the separation with the detector and a vertical separation will only occur for arc 2 and 4.  
 6445 Consequently spreader 6 should not be taken into account for the emittance growth contribution  
 6446 until the interaction point.

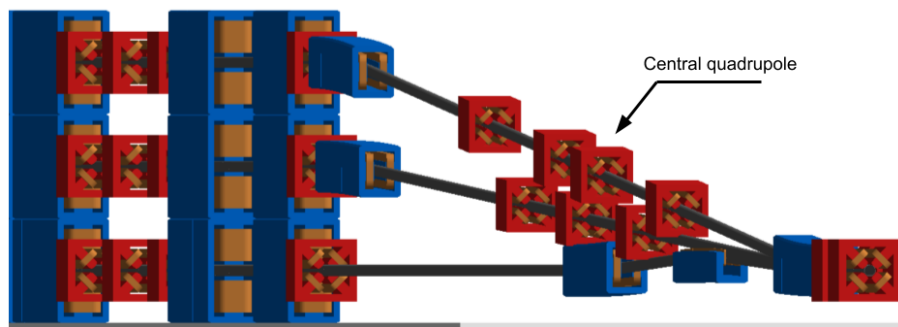


**Figure 10.10:** 3D visualisation of the spreader 2,4,6 inserted between the end of the linac and routing the different beamlines into their respective dispersion suppressors.

6447 The optics for the Spreader/Recombiner of arc 2 and 4 are presented Fig. 10.11, it shows the  
 6448 achromatic function supported by the outer quadrupoles while the control of the horizontal beta  
 6449 function is provided by the "middle" quadrupole. One sees that the lattice of the arc 2 requires  
 6450 to split the "middle" quadrupole in two, in order to avoid overlap with the other beamline (arc  
 6451 4), see Fig.10.10. These two optics are the most challenging as they have high beta functions at  
 6452 the entrance of their lattices, due to the multi pass linac optics as previously explained.

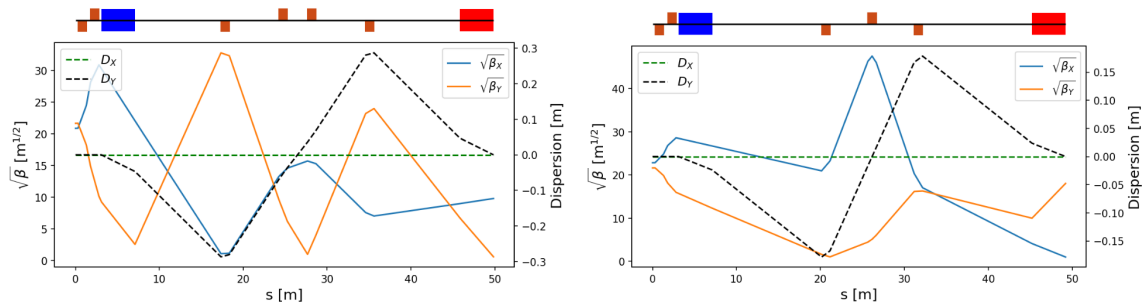


**Figure 10.11:** Left : Spreader/Recombiner optics of the arc 2 for the 16.73 GeV electron beam. Right : Spreader/Recombiner optics of the arc 4 for the 32.96 GeV electron beam.

6453 **IR Bypasses**

6454 After the last spreader the 49.19 GeV beam goes straight to the interaction region. However the  
 6455 lower energy beams; at 16.7 and 33.0 GeV, need to be further separated horizontally in order  
 6456 to avoid interference with the detector. Different design options for the bypass section were  
 6457 explored [793] and the one that minimises the extra bending has been chosen and implemented  
 6458 in the lattice.

6459 Ten arc-like dipoles are placed very close to the spreader, to provide an initial bending,  $\theta$ , which  
 6460 results in  $X = 10$  m separation from the detector located 120 m downstream. The straight  
 6461 section of the bypass is approximately 240 m long. After the bypass, in order to reconnect to  
 6462 the footprint of Arc 6, 7 of 30 standard cells in Arc 2 and Arc 4 are replaced with 7 higher field,  
 6463 junction cells. The number of junction cells is a compromise between the field strength increase  
 6464 and the length of additional bypass tunnel, as can be inferred from the scheme summarised in  
 6465 Fig. 10.8. The stronger bending in the junction cells creates a small mismatch, which is corrected  
 6466 by adjusting the strengths of the quadrupoles in the last junction cell and in the first regular  
 6467 cell.

6468 **Synchrotron Radiation Effects – Emittance Dilution**

6469 ERL efficiency as a source of multi-GeV electrons for a high luminosity collider is limited by the  
 6470 incoherent synchrotron radiation effects on beam dynamics; namely the transverse emittance  
 6471 dilution and the longitudinal momentum spread (induced by quantum excitations). The first  
 6472 effect, the transverse emittance increase, will have a paramount impact on the collider luminosity,  
 6473 due to stringent limits on the allowed emittance increase. The second one, accrued momentum  
 6474 spread, governs asymmetries of accelerated and decelerated beam profiles. These asymmetries  
 6475 substantially complicate multi-pass energy recovery and matching, and ultimately they limit the  
 6476 energy reach of the ERLs due to recirculating arc momentum acceptance.

6477 Arc optics was designed to ease individual adjustment of momentum compaction (needed for the  
 6478 longitudinal phase-space control, essential for operation with energy recovery) and the horizontal  
 6479 emittance dispersion,  $H$ , in each arc. Tab. 10.2 lists arc-by-arc dilution of the transverse,  $\Delta\epsilon$ , and  
 6480 longitudinal,  $\Delta\sigma_{\frac{\Delta E}{E}}$ , emittance due to quantum excitations calculated using analytic formulas,  
 6481 Eqs. (10.5), (10.6) and (10.7), introduced by M. Sands [792]:

$$\Delta E = \frac{2\pi}{3} r_0 m c^2 \frac{\gamma^4}{\rho} \quad (10.5)$$

6482

$$\Delta\epsilon_N = \frac{2\pi}{3} C_q r_0 \langle H \rangle \frac{\gamma^6}{\rho^2}, \quad (10.6)$$

6483

$$\frac{\Delta\epsilon_E^2}{E^2} = \frac{2\pi}{3} C_q r_0 \frac{\gamma^5}{\rho^2}, \quad (10.7)$$

6484 where  $C_q$  is given by Eq. (10.2). Here,  $\Delta\epsilon_E^2$  is an increment of energy square variance,  $r_0$  is  
 6485 the classical electron radius,  $\gamma$  is the Lorentz boost and  $C_q \approx 3.832 \cdot 10^{-13}$  m for electrons (or  
 6486 positrons).

6487 Apart from the horizontal 180° arcs, there are other sources of emittance dilution due to syn-  
 6488 chrotron radiation, namely vertical Spreaders and Recoiners, as well as horizontal 'Doglegs'  
 6489 used to compensate seasonal variation of path-length. To minimise their contribution to the ver-  
 6490 tical emittance dilution, special optics with small vertical  $\langle H \rangle$  has been introduced in Spr/Rec  
 6491 sections. The effects on vertical emittance dilution coming from these beamlines (Spr/Rec) are

Beamline	Beam energy [GeV]	$\Delta E$ [MeV]	$\Delta\epsilon_N^x$ [mm mrad]	$\Delta\sigma_{\frac{\Delta E}{E}}$ [%]
arc 1	8.62	0.7	0.0016	0.0005
arc 2	16.73	10	0.085	0.0027
arc 3	24.85	49	0.91	0.0072
arc 4	32.96	152	0.81	0.015
arc 5	41.08	368	3.03	0.026
arc 6	49.19	758	8.93	0.040

**Table 10.2:** Energy loss and emittance dilution (horizontal and longitudinal) due to synchrotron radiation generated by all six 180° arcs (not including Spreaders, Recombiners and Doglegs). Here,  $\Delta\sigma_{\frac{\Delta E}{E}} = \sqrt{\frac{\Delta\epsilon_E^2}{E^2}}$

Beamline	Beam energy [GeV]	$\Delta E$ [MeV]	$\Delta\epsilon_N^y$ [mm mrad]	$\Delta\sigma_{\frac{\Delta E}{E}}$ [%]
Spr/Rec 1	8.62	0.2	0.035	0.0008
Spr/Rec 2	16.73	3.0	0.540	0.0044
Spr/Rec 3	24.85	6.0	0.871	0.0066
Spr/Rec 4	32.96	21.6	5.549	0.0143
Spr/Rec 5	41.08	7.1	0.402	0.0062
Spr/Rec 6	49.19	39.2	3.92	0.0205

**Table 10.3:** Energy loss and emittance dilution (vertical and longitudinal) due to synchrotron radiation generated by the two step Spreader, or Recombiner design of a given arc. Here,  $\Delta\sigma_{\frac{\Delta E}{E}} = \sqrt{\frac{\Delta\epsilon_E^2}{E^2}}$

6492 summarized in Tab. 10.3 for the two-step spreaders and in Tab. 10.4 for the alternative version  
6493 of a one-step spreader.

	Beam Energy [GeV]	$\Delta E$ [MeV]	$\Delta\epsilon_N^y$ [mm.mrad]	$\Delta\sigma_{\frac{\Delta E}{E}}$ [%]
Spreader 1	8.62	0.04	0.004	0.0002
Spreader 2	16.73	0.31	0.004	0.0007
Spreader 3	24.85	0.32	0.012	0.0006
Spreader 4	32.96	1.18	0.112	0.0013
Spreader 5	41.08	2.64	0.083	0.0019
Spreader 6	49.19	7.92	1.060	0.0040

**Table 10.4:** Energy loss and emittance dilution (vertical and longitudinal) due to synchrotron radiation generated by a one-step Spreader, or Recombiner design of a given arc. Here,  $\Delta\sigma_{\frac{\Delta E}{E}} = \sqrt{\frac{\Delta\epsilon_E^2}{E^2}}$

6494 Similarly, the horizontal emittance dilution induced by the Doglegs (four dogleg chicanes per  
6495 arc) in various arcs is summarized in Tab. 10.5. Each dogleg chicane is configured with four 1  
6496 meter bends (1 Tesla each), so that they bend the lowest energy beam at 8.6 GeV by 2 degrees.  
6497 The corresponding path-lengths gained in the Doglegs of different arcs are also indicated.

6498 As indicated in Tab. 10.5, the Doglegs in the highest energy arcs, Arc 5 and Arc 6, provide only  
6499 sub mm path-length gain with large synchrotron radiation effects. They are not very effective  
6500 and generate strong, undesired emittance dilution. Therefore, it is reasonable to eliminate them  
6501 from both Arc 5 and 6. Instead, one could resort to an alternative path-length control via

Beamline	Beam energy [GeV]	$\Delta E$ [MeV]	$\Delta\epsilon_N^x$ [mm mrad]	$\Delta\sigma_{\frac{\Delta E}{E}}$ [%]	path-length [mm]
Doglegs 1	8.62	2	0.201	0.007	7.32
Doglegs 2	16.73	9	0.667	0.009	1.96
Doglegs 3	24.85	19	5.476	0.014	0.84
Doglegs 4	32.96	33	5.067	0.014	0.52
Doglegs 5	41.08	52	12.067	0.028	0.36
Doglegs 6	49.19	74	2.836	0.011	0.28

**Table 10.5:** Energy loss and emittance dilution (horizontal and longitudinal) due to synchrotron radiation generated by the Doglegs (four dogleg chicanes) of a given arc. Here,  $\Delta\sigma_{\frac{\Delta E}{E}} = \sqrt{\frac{\Delta\epsilon_E^2}{E^2}}$

6502 appropriate orbit steering with both horizontal and vertical correctors present at every girder  
6503 and distributed evenly throughout the arc.

6504 Combining all three contributions: (180° arc, Spreader, Recombiner and Doglegs (no Doglegs in  
6505 Arcs 5 and 6), the net cumulative emittance dilution is summarized in Tab. 10.6 for the case of  
6506 the two-step spreader.

Beamline	Beam energy [GeV]	$\Delta E$ [MeV]	$\Delta^{\text{cum}}\epsilon_N^x$ [mm mrad]	$\Delta^{\text{cum}}\epsilon_N^y$ [mm mrad]	$\Delta^{\text{cum}}\sigma_{\frac{\Delta E}{E}}$ [%]
Arc 1	8.62	3	0.2	0.1	0.01
Arc 2	16.73	25	1.0	1.2	0.03
Arc 3	24.85	80	7.3	2.9	0.06
Arc 4	32.96	229	13.2	14.0	0.12
Arc 5	41.08	383	16.2	14.8	0.16
<b>IR</b>	49.19	39	<b>16.2</b>	<b>18.7</b>	<b>0.18</b>
Arc 6	49.19	797	25.2	22.6	0.24
Arc 5	41.08	383	28.2	23.4	0.28
Arc 4	32.96	229	34.1	34.5	0.33
Arc 3	24.85	80	40.5	36.3	0.37
Arc 2	16.73	25	41.2	37.4	0.39
Arc 1	8.62	3	41.4	37.4	0.40
Dump	0.5		41.4	37.4	0.40

**Table 10.6:** Energy loss and cumulative emittance dilution (transverse and longitudinal) due to synchrotron radiation at the end of a given beam-line (complete Arc including: 180° arc, Spreader, Recombiner and Doglegs in arcs 1-4). The table covers the entire ER cycle: 3 passes 'up' + 3 passes 'down'. Cumulative emittance dilution values just before the IP (past Arc 5 and Spr 6), which are critical for the luminosity consideration are highlighted in 'bold'. That row accounts for contributions from Spr 6 (the last bending section before the IR) to energy loss, as well as the vertical and longitudinal emittance dilutions. Here,  $\Delta\sigma_{\frac{\Delta E}{E}} = \sqrt{\frac{\Delta\epsilon_E^2}{E^2}}$

6507 Tab. 10.6 shows, the LHeC luminosity requirement of total transverse emittance dilution in  
6508 either plane (normalized) at the IP (at the end of Arc 5), not to exceed 20 mm mrad (hor:  
6509 16.2 mm mrad and ver: 18.7 mm mrad) is met by-design, employing presented low emittance  
6510 lattices in both the arcs and switch-yards. In the case of the optimised one-step spreader design,  
6511 another reduction - mainly of the vertical emittance budget - is obtained, providing a comfortable  
6512 safety margin of the design.

6513 Finally, one can see from Eqs. (10.6) and (10.7) an underlying universal scaling of the transverse

6514 (unnormalized) and longitudinal emittance dilution with energy and arc radius; they are both  
6515 proportional to  $\gamma^5/\rho^2$ . This in turn, has a profound impact on arc size scalability with energy;  
6516 namely the arc radius should scale as  $\gamma^{5/2}$  in order to preserve both the transverse and longi-  
6517 tudinal emittance dilutions, which is a figure of merit for a synchrotron radiation dominated  
6518 ERL.

### 6519 10.2.2 30 GeV ERL Options

6520 One may think of an upgrade path from 30 to 50 GeV ERL, using the same 1/5 of the LHC  
6521 circumference (5.4 km), footprint. In this scenario, each linac straight (front end) would initially  
6522 be *loaded* with 18 cryomodules, forming two 5.21 GV linacs. One would also need to decrease  
6523 the injector energy by factor of 5.21/8.11. The top ERL energy, after three passes, would reach  
6524 31.3 GeV. Then for the upgrade to 50 GeV, one would fill the remaining space in the linacs  
6525 with additional 10 cryomodules each; 2.9 GV worth of RF in each linac. This way the energy  
6526 ratios would be preserved for both 30 and 50 GeV ERL options, so that the same switch-yard  
6527 geometry could be used. Finally, one would scale up the entire lattice; all magnets (dipoles and  
6528 quads) by 8.11/5.21 ratio. If one wanted to stop at the 30 GeV option with no upgrade path,  
6529 then the 1/12 of the LHC circumference (2.2 km) would be a viable footprint for the racetrack,  
6530 featuring: two linacs, 533 m each, (18 cryomodules) and arcs of 136 m radius. Again, assuming  
6531 0.32 GeV injection energy, the top ERL energy would reach 31.3 GeV.

### 6532 10.2.3 Component Summary

6533 This closing section will summarise active accelerator components: magnets (bends and quads)  
6534 and RF cavities for the 50 GeV baseline ERL. The bends (both horizontal and vertical) are  
6535 captured in Tab. 10.7, while the quadrupole magnets and RF cavities are collected in Tab. 10.8.

6536 One would like to use a combined aperture (3-in-one) arc magnet design with 50 cm vertical  
6537 separation between the three apertures, proposed by Attilio Milanese [794]. That would reduce  
6538 net arc bend count from 2112 to 704. As far as the Spr/Rec vertical bends are concerned, the  
6539 design was optimised to include an additional common bend separating the two highest passes.  
6540 So, there are a total of 8 trapezoid B-com magnets, with second face tilted by 3° and large 10 cm  
6541 vertical aperture, the rest are simple rectangular bends with specs from the summary Tab. 10.7.

Section	Arc dipoles (horiz.)				Spr/Rec dipoles (vert.)				<i>Dogleg</i> dipoles (horiz.)			
	<i>N</i>	<i>B</i> [T]	<i>g</i> /2[cm]	<i>L</i> [m]	<i>N</i>	<i>B</i> [T]	<i>g</i> /2[cm]	<i>L</i> [m]	<i>N</i>	<i>B</i> [T]	<i>g</i> /2[cm]	<i>L</i> [m]
Arc 1	352	0.087	1.5	3	8	0.678	2	3	16	1	1.5	1
Arc 2	352	0.174	1.5	3	8	0.989	2	3	16	1	1.5	1
Arc 3	352	0.261	1.5	3	6	1.222	2	3	16	1	1.5	1
Arc 4	352	0.348	1.5	3	6	1.633	2	3	16	1	1.5	1
Arc 5	352	0.435	1.5	3	4	1.022	2	3				
Arc 6	352	0.522	1.5	3	4	1.389	2	3				
Total	2112				36				64			

**Table 10.7:** 50 GeV ERL – Dipole magnet count along with basic magnet parameters: Magnetic field (*B*), Half-Gap (*g*/2), and Magnetic length (*L*).

Section	Quadrupoles				RF cavities			
	$N$	$G$ [T/m]	$a$ [cm]	$L$ [m]	$N$	$f$ [MHz]	cell	$G_{\text{RF}}$ [T/m]
Linac 1	29	1.93	3	1	448	802	5	20
Linac 2	29	1.93	3	1	448	802	5	20
Arc 1	255	9.25	2.5	1				
Arc 2	255	17.67	2.5	1				
Arc 3	255	24.25	2.5	1	6	1604	9	30
Arc 4	255	27.17	2.5	1	12	1604	9	30
Arc 5	249	33.92	2.5	1	18	1604	9	30
Arc 6	249	40.75	2.5	1	36	1604	9	30
Total	1576				968			

**Table 10.8:** 50 GeV ERL – Quadrupole magnet and RF cavities count along with basic magnet/RF parameters: Magnetic field gradient ( $G$ ), Aperture radius ( $a$ ), Magnetic length ( $L$ ), Frequency ( $f$ ), Number of cells in RF cavity (cell), and RF Gradient ( $G_{\text{RF}}$ ).

### 10.3 Electron-Ion Collisions

Besides colliding proton beams, the LHC also provides collisions of nuclear (fully-stripped ion) beams with each other (AA collisions) or with protons ( $pA$ ). Either of these operating modes offers the possibility of electron-ion ( $eA$ ) collisions in the LHeC configuration<sup>1</sup>

Here we summarise the considerations leading to the luminosity estimates given in Tab. 2.4 for collisions of electrons with  $^{208}\text{Pb}^{82+}$  nuclei, the nominal heavy ion species collided in the LHC. Other, lighter, nuclei are under consideration for future LHC operation [494] and could also be considered for electron-ion collisions.

The heavy ion beams that the CERN injector complex can provide to the LHC, the HE-LHC and the FCC provide a unique basis for high energy, high luminosity deep inelastic electron-ion scattering physics. Since HERA was restricted to protons only, the LHeC or FCC-eh would extend the kinematic range in  $Q^2$  and  $1/x$  by 4 or 5 orders of magnitude. This is a huge increase in coverage and would be set to radically change the understanding of parton dynamics in nuclei and of the formation of the quark gluon plasma.

An initial set of parameters in the maximum energy configurations was given in [34]. The Pb beam parameters are essentially those foreseen for operation of the LHC (or HL-LHC) in Run 3 and Run 4 (planned for the 2020s). These parameters have already been largely demonstrated [795] except for the major remaining step of implementing slip-stacking injection in the SPS which would reduce the basic bunch spacing from 100 to 50 ns [796]. With respect to the proton spacing of 25 ns, this allows the electron bunch intensity to be doubled while still respecting the limit on total electron current. In fact, without the slip-stacking in the SPS, the initial luminosity would be the same with a 100 ns Pb spacing (and quadrupled electron bunch intensity). However one must remember that the evolution of the Pb beam intensity will be dominated by luminosity burn-off by the concurrent PbPb collisions at the other interaction points and integrated luminosity for both PbPb and ePb collisions will be higher with the higher total Pb intensity. The details of this will depend on the operating scenarios, number of active experiments, etc, and are not considered further here. The time-evolution of eA luminosity will be determined by that of PbPb and pPb collisions, as discussed, for example, in Ref. [15,494,797].

<sup>1</sup>In  $pA$  operation of the LHC the beams may be reversed ( $Ap$ ) for some part of the operating time. Only one direction (ions in Beam 2) would provide  $eA$  collisions while the other would provide ep collisions at significantly reduced luminosity compared to the  $pp$  mode, since there would be fewer proton bunches of lower intensity.

6570 Combining these assumptions with the default 50 GeV electron ERL for LHeC and 60 GeV for  
 6571 FCC-eh, yields the updated parameter sets and initial luminosities given in Tab. 2.4, earlier in  
 6572 the present report.

6573 Radiation damping of Pb beams in the hadron rings is about twice as fast as for protons and can  
 6574 be fully exploited since it takes longer to approach the beam-beam limit at the PbPb collisions  
 6575 points. For the case of the FCC-hh [15], one can expect the emittance values in Tab. 2.4 to be  
 6576 reduced during fills [15, 494, 797].

6577 The Pb beam will be affected by ultraperipheral collision effects, mainly bound-free pair pro-  
 6578 duction and Coulomb dissociation of the nuclei, induced by the electromagnetic fields of the  
 6579 electrons, seen as pulses of virtual photons. The relevant cross-sections will be similar to those  
 6580 in pPb collisions which are down by a factor of  $Z^2$  compared to those in PbPb collisions and  
 6581 can be neglected in practice.

## 6582 10.4 Beam-Beam Interactions

6583 In the framework of the Large Hadron electron Collider, the concept of an Energy Recirculating  
 6584 Linac (ERL) allows to overcome the beam-beam limit that one would face in a storage ring. The  
 6585 electron beam can be heavily disturbed by the beam collision process, while the large acceptance  
 6586 of the ERL will still allow for a successful energy recovery during the deceleration of the beam  
 6587 so that the power consumption is minimised. In order to compare the relevant beam-beam  
 6588 parameters and put them into the context of other colliders, two tables are shown highlighting,  
 6589 on the one hand, the parameters from LEP and LHC runs in Tab. 10.9, and on the other hand,  
 6590 the parameters planned for LHeC at HL-LHC in Tab. 10.10.

Parameter	Unit	LEP	LHC
Beam sizes $\sigma_x / \sigma_y$	$\mu\text{m}$	180 / 7	16.6 / 16.6
Intensity	$10^{11}$ particles/bunch	4.00	1.15
Energy	GeV	100	7000
$\beta_x^* / \beta_y^*$	cm	125/5	55/55
Crossing angle	$\mu\text{rad}$	0	0/285
Beam-beam tune shift $\Delta Q_x / \Delta Q_y$		0.0400/0.0400	0.0037/0.0034
Beam-beam parameter $\xi$		0.0700	0.0037

**Table 10.9:** Comparison of parameters for the LEP collider and LHC. Taken from CDR 2012, p.286.

Beam parameter	Unit	LHeC at HL-LHC	
		Proton beam	Electron beam
Energy	GeV	7000	49.19
Normalized emittance	mm·mrad	2.5	50
Beam sizes $\sigma_{x,y}$	$\mu\text{m}$	5.8	5.8
Intensity	$10^9$ particles/bunch	220.00	3.12
Bunch length $\sigma_s$	mm	75.5	0.6
$\beta_{x,y}^*$	cm	10.00	6.45
Disruption factor		$1.2 \times 10^{-5}$	14.5
Beam-beam parameter $\xi$		$1.52 \times 10^{-4}$	0.99

**Table 10.10:** Comparison of parameters for the LHeC at HL-LHC. The parameters presented correspond to the default design.



6591 In the case of LHeC, the  $\beta$ -functions at the interaction point are chosen such that the transverse  
6592 beam sizes of the  $e^-$  and  $p^-$  beams are equal in both transverse planes. Although the proton and  
6593 electron emittances are different, the beta functions at the interaction point are set accordingly  
6594 so that the two beams conserve  $\sigma_x^e = \sigma_x^p$  and  $\sigma_y^e = \sigma_y^p$ .

#### 6595 10.4.1 Effect on the electron beam

6596 The disruption parameter for the electron beam is of the order of 14.5 which corresponds, in  
6597 linear approximation, to almost 2 oscillations of the beam envelope within the proton bunch.  
6598 The non linearity of the interaction creates a distortion of the phase space and a mismatch from  
6599 the design optics (see Fig. 10.12). The mismatch and distortion can be minimized by tuning the  
6600 Twiss parameters ( $\alpha^*$ ,  $\beta^*$ ) at the interaction point.

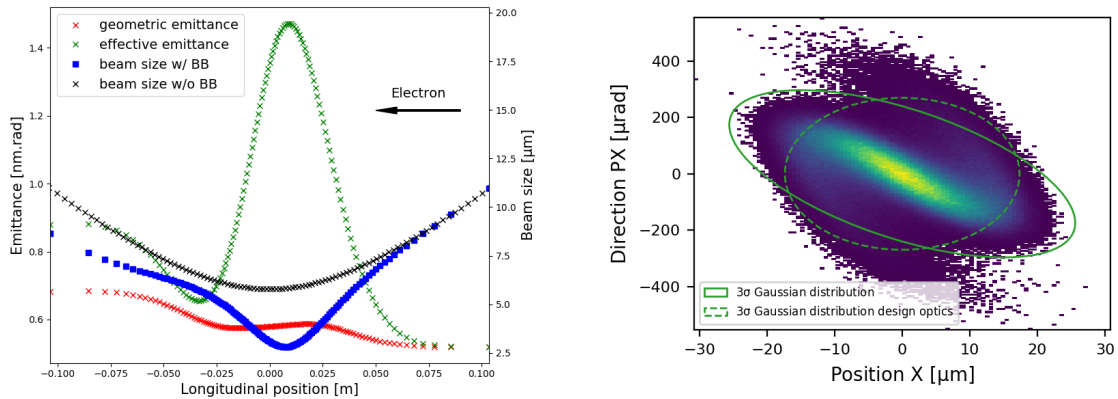


**Figure 10.12:** Left: Electron beam sizes with (blue) and without (black) the beam-beam forces exerted on the electron beam. The geometric emittance is represented in red and the effective emittance that takes into account the mismatch from the original optics is illustrated in green. Right: The horizontal phase space of the spent electron distribution backtracked to the interaction point.  $3\sigma$  Gaussian distribution are highlighted for the post-collided distribution (solid line) and the design optics (dashed line).

6601 In a series of studies the optics parameters of the electron beam were tracked back to the  
6602 interaction point in presence of the beam-beam forces in order to show the impact of the beam-  
6603 beam effect for different values of the electron Twiss parameters at the IP. In addition, the  
6604 influence of a waist shift from the IP (proportional to  $\alpha^*$ ), similar to changing the foci of the  
6605 interacting beams, has been studied and allows to keep the electron beam for a longer time  
6606 within the proton bunch, thus optimizing the luminosity. The modification of the electron  
6607 beta function ( $\beta^*$ ) leads to more freedom and gives access, among all the possibilities, to two  
6608 different optima regarding the luminosity and the mismatch from the design optics. The results  
6609 are summarized in the contour plots of Fig. 10.13.

6610 As a consequence, the Twiss parameters at the interaction point can be set in a way, to minimize  
6611 the mismatch of the optics (i.e. the effective emittance) or to maximize the luminosity. In case  
6612 the optimization of the luminosity is chosen (see the circle marker in Fig. 10.13), a modified  
6613 capture optics in the beam transfer to the arc structure will be needed to re-match the modified  
6614 Twiss functions perturbed by the non-linear beam-beam effects.

6615 The effect of possible offsets between the two colliding beams has been characterized in previous  
6616 beam-beam studies [798], and – if uncorrected – might lead to an electron beam emittance  
6617 growth. The parameters for these studies have been updated and the results are presented in  
6618 Fig. 10.14. As any offset between the two beams is amplified, it results in a larger increase of the  
6619 beam envelope. As a solution, a fast feed-forward system is proposed, across the Arc 6, which

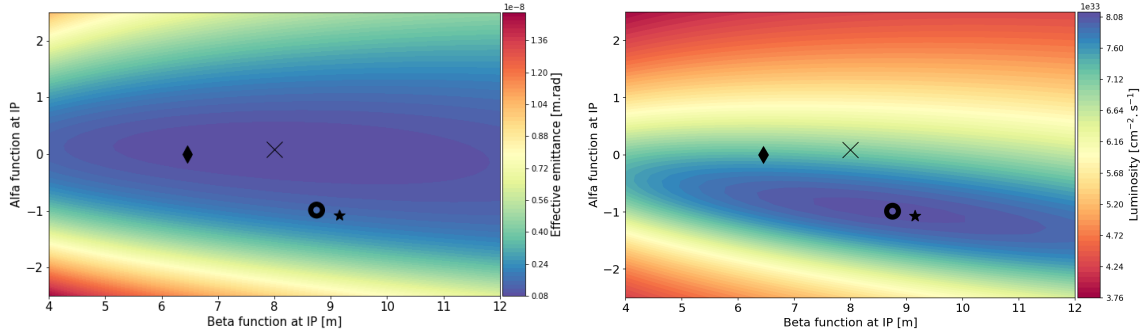


**Figure 10.13:** Left : Contour plot describing the effective emittance post collision as a function of the alfa and beta functions at IP. Right : Contour plot describing the luminosity as a function of the alfa and beta functions at the IP. The diamond marker represents the initial Twiss parameters, the circle shows the luminosity optimum, the cross symbolizes the smallest mismatch from the original optics and the star illustrates the minimal geometric emittance growth.

6620 would aim at damping the transverse motion so that the beam emittance can be recovered.  
 6621 Using two sets of kickers placed at the center and at the end of the arc, an offset of  $0.16\sigma$  can be  
 6622 damped. A single set cutting across the whole arc can correct a  $1\sigma$  offset with approximately  
 4.4 kV.

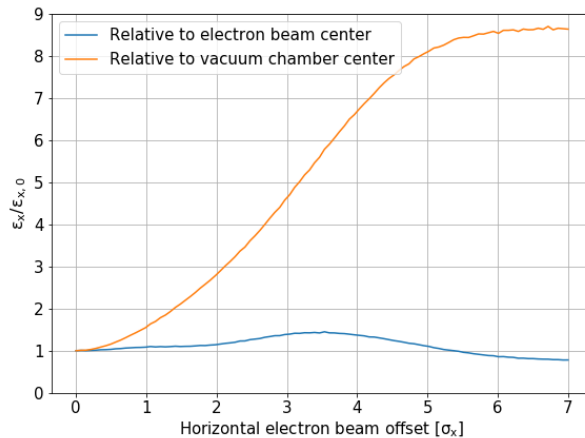


**Figure 10.14:** Electron beam emittance relative change with respect to its centroid (blue) and with respect to the vacuum chamber center (orange).

6623

6624 Additionally, the coupling of the beam-beam effect with long range wakefields has been ad-  
 6625 dressed [798]. Assuming a misaligned bunch injected among a train of nominal bunches, the  
 6626 coupling of the beam-beam effect with the wakefields leads to a reduction of the damping of  
 6627 the excitation created by the misaligned bunch. Nevertheless it can be shown that the beam  
 6628 stability is conserved and the total amplification remains acceptable with respect to the study  
 6629 that was not considering the coupling.

#### 6630 10.4.2 Effect on the proton beam

6631 The beam-beam interaction between the electron and proton beams is asymmetric in terms of  
 6632 beam rigidities. Although the less energetic 49.19 GeV electron beam is heavily distorted by the  
 6633 strong 7 TeV proton beam, the proton beam will suffer from an emittance growth adding up  
 6634 turn by turn [798] due to the build up of the tiny disruption created by the offset between the

6635 beams. In fact, the previous studies gave a growth rate of around 0.01 %/s for a jitter of  $0.2 \sigma_x$ .  
 6636 As long as an adequate control of the bunches is preserved, this effect should lie in the shadow  
 6637 of other effects leading to emittance blow-up in the LHC (e.g. IBS). Since the electron beam  
 6638 energy decreased from 60 GeV to 49.19 GeV this study needs to be updated and the results  
 6639 should remain in agreement with the previous statement.

## 6640 10.5 Arc Magnets

6641 In this section, a conceptual design of the main magnets needed for the Linac-Ring (LR) ac-  
 6642 celerator at 50 GeV is described. The number and types of magnets is listed in Tabs. 10.7  
 6643 and 10.8.

### 6644 10.5.1 Dipole magnets

6645 The bending magnets are used in the arcs of the recirculator. Each of the six arcs needs 352  
 6646 horizontal bending dipoles. Additional dipoles are needed in the straight sections: 36 vertical  
 6647 bending dipoles in the spreader/recombiner and 64 horizontal bending dipoles for the “dogleg”.  
 6648 These magnets are not considered at the moment.

6649 In the CDR issued in 2012 for a 60 GeV lepton ring (LR) , a design based on three independent  
 6650 dipoles stacked on top of each other was proposed. A post-CDR design with three apertures  
 6651 dipoles was introduced in 2014 [794]. This solution allows reducing the Ampere-turns and the  
 6652 production cost of the dipoles. For a 50 GeV LR, the three apertures dipole design is adapted  
 6653 to fulfil new magnetic field requirements.

6654 The 352 horizontal bending dipoles needed for each arc, combined in three apertures dipoles re-  
 6655 sult in a total of 704 units. These magnets are 3 m long and provide a field in the 30 mm aperture  
 6656 ranging from 0.087 T to 0.522 T depending on the arc energy, from 8.62 GeV to 49.19 GeV.

Parameter	Unit	Value
Beam energy	GeV	8.62 to 49.19
Magnetic field	T	0.087 to 0.522
Magnetic length	m	3
Vertical aperture	mm	30
Pole width	mm	90
Number of apertures		3
Distance between apertures	mm	500
Mass	8000	kg
Number of magnets		704
Current	A	4250
Number of turns per magnet		4
Current density	A/mm <sup>2</sup>	1
Conductor material		aluminum
Magnet resistance	mΩ	0.17
Power	kW	3
Total power consumption six arcs	MW	2.1
Cooling		air

**Table 10.11:** 50 GeV ERL – Main parameters of the three apertures bending magnets.

6657 In the proposed design, the three apertures are stacked vertically but offset transversely. This  
 6658 allows recycling the Ampere-turns from one aperture to the other. The coils are centrally located

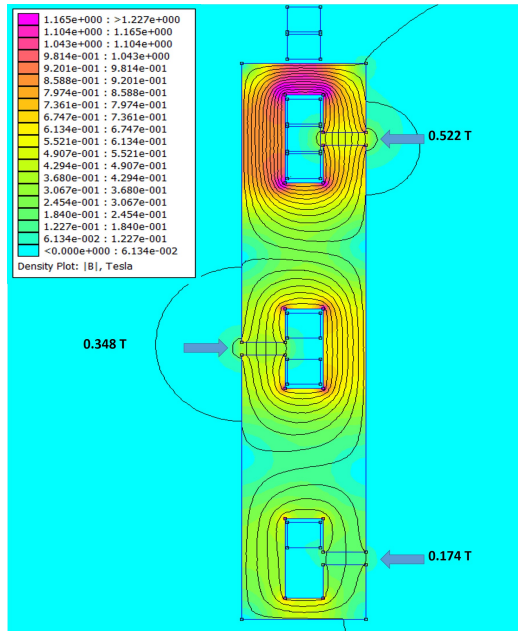


**Figure 10.15:** 50 GeV ERL - Cross section of the three apertures bending magnet, arc 2, 4 and 6 with 500 mm between consecutive arcs - Finite Element Method (FEM).

6659 on the yoke and are made of simple aluminium bus-bars all powered in series. A current density  
 6660 of  $1 \text{ A/mm}^2$  in the coils is sufficiently low to not have water-cooling but in order to limit the  
 6661 temperature in the tunnel it may be required. Trim coils can be added on two of the apertures  
 6662 to provide some tuning. Alternatively, each stage could be powered separately. The dipole yokes  
 6663 are made of low carbon steel plates. The relevant parameters are summarised in Tab. 10.11 and  
 6664 the cross section is illustrated in Fig. 10.15 for 500 mm between consecutive arcs.

## 6665 10.5.2 Quadrupole magnets

### 6666 Quadrupoles for recirculator arcs

6667 In total 1518 quadrupoles are needed for the recirculator arcs: 255 for each of the arcs one to four  
 6668 and 249 for each of the arcs five and six. The required integrated gradients, comprised between  
 6669 9.25 T and 40.75 T, can be achieved using one type of quadrupole one meter long. However,  
 6670 instead of operating the magnets at low current for lower arcs energy, it can be considered to  
 6671 have a shorter model 0.6 meter long for arcs one to three. These quadrupoles require water-  
 6672 cooling for the coils. The relevant parameters are summarised in Tab. 10.12 and the cross section  
 6673 is illustrated in Fig. 10.16 (left).

6674 In order to reduce the power consumption, it could be envisaged to use a hybrid configuration  
 6675 for the quadrupoles, with most of the excitation given by permanent magnets. The gradient  
 6676 strength could be varied by trim coils or by mechanical methods.

### 6677 Quadrupoles for the two 8.1 GeV linacs

6678 In the two 8.1 GeV linacs, 29 + 29 quadrupoles, each providing 1.93 T integrated strength are  
 6679 required. The present design solution considers 30 mm aperture radius magnets. The relevant  
 6680 parameters are summarised in Tab. 10.13 and the cross section is illustrated in Fig. 10.16 (right).

Parameter	Unit	Value
Beam energy	GeV	8.62 to 49.19
Field gradient	T/m	9.25 to 40.75
Magnetic length	m	1
Aperture radius	mm	25
Mass	kg	550
Number of magnets		1518
Current at 40.75 T/m	A	560
Number of turns per pole		17
Current density at 40.75 T/m	A/mm <sup>2</sup>	6.7
Conductor material		copper
Magnet resistance	mΩ	33
Power at 8.62 GeV	kW	0.5
Power at 16.73 GeV	kW	1.9
Power at 24.85 GeV	kW	3.7
Power at 32.96 GeV	kW	4.6
Power at 41.08 GeV	kW	7.2
Power at 49.19 GeV	kW	10.3
Total power consumption six arcs	MW	7.1
Cooling		water

**Table 10.12:** 50 GeV ERL – Main parameters of the arc quadrupoles.

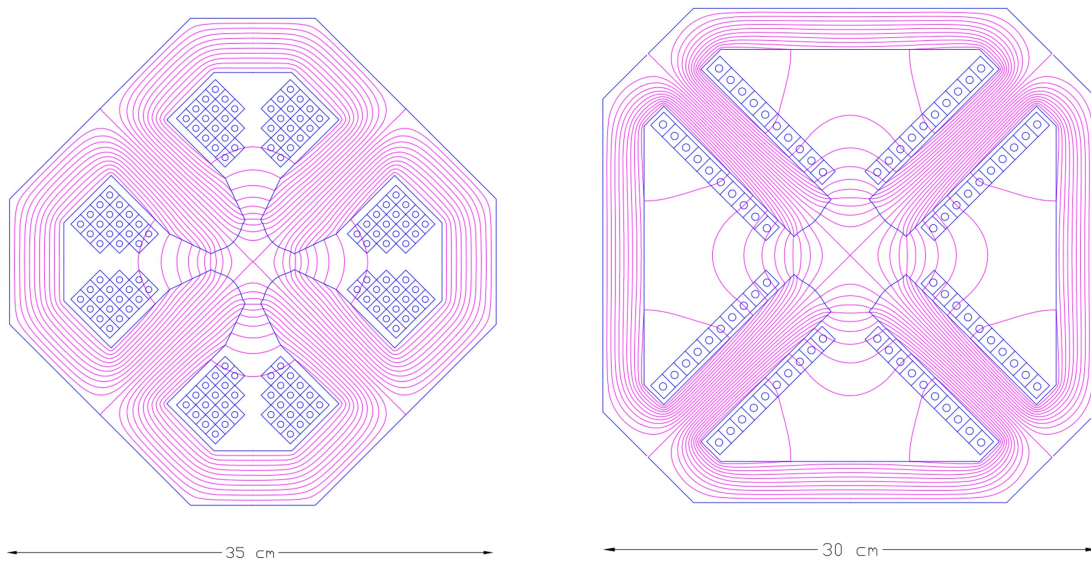


**Figure 10.16:** 50 GeV ERL. Left: Cross section of the arc quadrupole magnets. Right: Cross section of the linac quadrupole magnets.

## 6681 10.6 LINAC and SRF

6682 Each of the two main linacs has an overall length of 828.8 m and provides an acceleration of  
6683 8.114 GV. Each linac consists of 112 cryomodules, arranged in 28 units of 4 cryomodules with  
6684 their focussing elements – each cryomodule contains four 5-cell cavities, optimised to operate with  
6685 large beam current (up to 120 mA at the High Order Mode – HOM – frequencies). The operating  
6686 temperature is 2 K; the cavities are based on modern SRF technology and are fabricated from  
6687 bulk Nb sheets; they are described in detail in section 10.6.2 below. The nominal acceleration

Parameter	Unit	Value
Beam energy	GeV	8.62 to 49.19
Field gradient	T/m	7.7
Magnetic length	m	0.25
Aperture radius	mm	30
Mass	kg	110
Number of magnets		56
Current at 7.7 T/m	A	285
Number of turns per pole		10
Current density at 7.7 T/m	A/mm <sup>2</sup>	3
Conductor material		copper
Magnet resistance	mΩ	6
Power at 8.1 GeV	kW	0.5
Total power consumption 2 linacs	MW	0.03
Cooling		water

**Table 10.13:** 50 GeV ERL – Main parameters of the linac quadrupoles.

6688 gradient is 19.73 MV/m.

6689 In addition to the main linacs, the synchrotron losses in the arcs will make additional linacs  
6690 necessary, referred to here as the *loss compensation linacs*. These will have to provide different  
6691 accelerations in the different arcs, depending on the energy of the beams as shown in Tab. 10.14.  
6692 The quoted beam energies are at entry into the arc. Their natural placement would be at the  
6693 end of the arcs just before the combiner, where the different energy beams are still separate.  
6694 The largest of these linacs would have to compensate the SR losses at the highest energy,  
6695 requiring a total acceleration of about 700 MV. The loss compensation linacs will be detailed in  
section 10.6.6 below.

Section	Beam energy [GeV]	$\Delta E$ [MeV]
Arc 1	8.62	3
Arc 2	16.73	25
Arc 3	24.85	80
Arc 4	32.96	229
Arc 5	41.08	383
Arc 6	49.19	836

**Table 10.14:** Synchrotron radiation losses for the different arc energies

6696

6697 Through all arcs but Arc 6, the beam passes twice, once while accelerated and once while decel-  
6698 erated. It is planned to operate these additional *loss compensation linacs* at 1603.2 MHz, which  
6699 allows energy compensation of both the accelerated and the decelerated beam simultaneously.  
6700 This subject will be discussed in detail in a subsequent section 10.6.6.

### 6701 10.6.1 Choice of Frequency

6702 The RF frequency choice primarily takes into account the constraints of the LHC bunch repeti-  
6703 tion frequency,  $f_0$ , of 40.079 MHz, while allowing for a sufficiently high harmonic,  $h$ , for a flexible  
6704 system. For an ERL with  $n_{pass} = 3$  recirculating passes and in order to enable equal bunch  
6705 spacing for the 3 bunches – though not mandatory – it was originally considered to suppress all  
6706 harmonics that are not a multiple of  $n_{pass} \cdot f_0 = 120.237$  MHz. Initial choices for instance were

6707 721.42 MHz ( $h = 18$ ) and 1322.61 MHz ( $h = 33$ ) in consideration of the proximity to the frequen-  
 6708 cies used for state-of-the-art SRF system developments worldwide [799]. In synergy with other  
 6709 RF system developments at CERN though, the final choice was 801.58 MHz ( $h = 20$ ), where  
 6710 the bunching between the 3 recirculating bunches can be made similar but not exactly equal.  
 6711 Note that this frequency is also very close to the 805 MHz SRF proton cavities operating at the  
 6712 Spallation Neutron Source (SNS) at ORNL, so that one could leverage from the experience in  
 6713 regard to cryomodule and component design at this frequency.

6714 Furthermore, in the frame of an independent study for a 1 GeV CW proton linac, a capital  
 6715 plus operational cost optimisation was conducted [800]. This optimisation took into account  
 6716 the expenditures for cavities, cryomodules, the linac tunnel as well as the helium refrigerator  
 6717 expenses as a function of frequency and thus component sizes. Labor costs were included based  
 6718 on the existing SNS linac facility work breakdown structure. It was shown that capital plus  
 6719 operating costs could be minimised with a cavity frequency between 800 MHz and 850 MHz,  
 6720 depending also on the choice of the operating He bath temperature (1.8 K to 2.1 K). Clear benefit  
 6721 of operating in this frequency regime are the comparably small dynamic RF losses per installation  
 6722 length due to a relatively small BCS surface resistance as well as low residual resistance of  
 6723 the niobium at the operating temperature. This could be principally verified as part of the  
 6724 prototyping effort detailed in the next sub-section. Note that the cost optimum also favors  
 6725 cavities operating at rather moderate field levels ( $< 20$  MV/m). This comes as a benefit in  
 6726 concern of field emission and associated potential performance degradations.

## 6727 10.6.2 Cavity Prototype

6728 Given the RF frequency of 801.58 MHz, JLab has collaborated with CERN, and consequently  
 6729 proposed a five-cell cavity design that was accepted for prototyping, see Fig. 10.17. The cavity  
 shape has also been adopted for PERLE. Tab. 10.15 summarises the relevant cavity parameters.

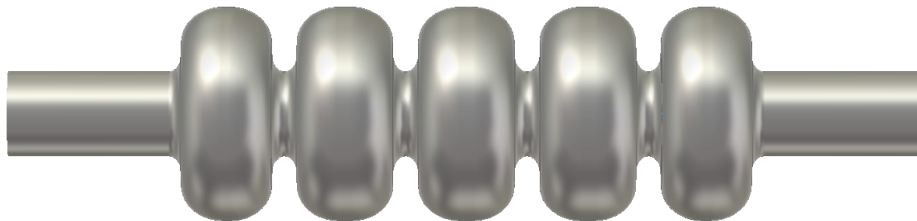


**Figure 10.17:** Bare 802 MHz five-cell cavity design (RF vacuum) with a 130 mm iris and beam tube aperture.

6730

6731 The cavity exhibits a rather large iris and beam tube aperture (130 mm) to consider beam-  
 6732 dynamical aspects such as HOM-driven multi-bunch instabilities. Despite the comparably large  
 6733 aperture, the ratio of the peak surface electric field,  $E_{pk}$ , respectively the peak surface magnetic  
 6734 field,  $B_{pk}$ , and the accelerating field,  $E_{acc}$ , are reasonably low, while the factor  $R/Q \cdot G$  is  
 6735 kept reasonably high, concurrently to limit cryogenic losses. This is considered as a generically  
 6736 well *balanced* cavity design [801]. The cavity cell shape also avoids that crucial HOMs will  
 6737 coincide with the main spectral lines (multiples of 801.58 MHz), while the specific HOM coupler  
 6738 development is pending.

6739 Furthermore, as shown in Fig. 10.18 for the case of the bunch recombination pattern considered  
 6740 for PERLE originally, the much denser intermediate beam current lines (green) are not coinciding  
 6741 with cavity HOMs. Here the figure plots the real part of the beam-excited cavity monopole

Parameter	Unit	Value
Frequency	MHz	801.58
Number of cells		5
active length $l_{act}$	mm	917.9
loss factor	V pC <sup>-1</sup>	2.742
$R/Q$ (linac convention)	$\Omega$	523.9
$R/Q \cdot G$ per cell	$\Omega^2$	28788
Cavity equator diameter	mm	327.95
Cavity iris diameter	mm	130
Beam tube inner diameter	mm	130
diameter ratio equator/iris		2.52
$E_{peak}/E_{acc}$		2.26
$B_{peak}/E_{acc}$	mT/(MV/m)	4.2
cell-to-cell coupling factor $k_{cc}$	%	3.21
TE <sub>11</sub> cutoff frequency	GHz	1.35
TM <sub>01</sub> cutoff frequency	GHz	1.77

**Table 10.15:** Parameter table of the 802 MHz prototype five-cell cavity.

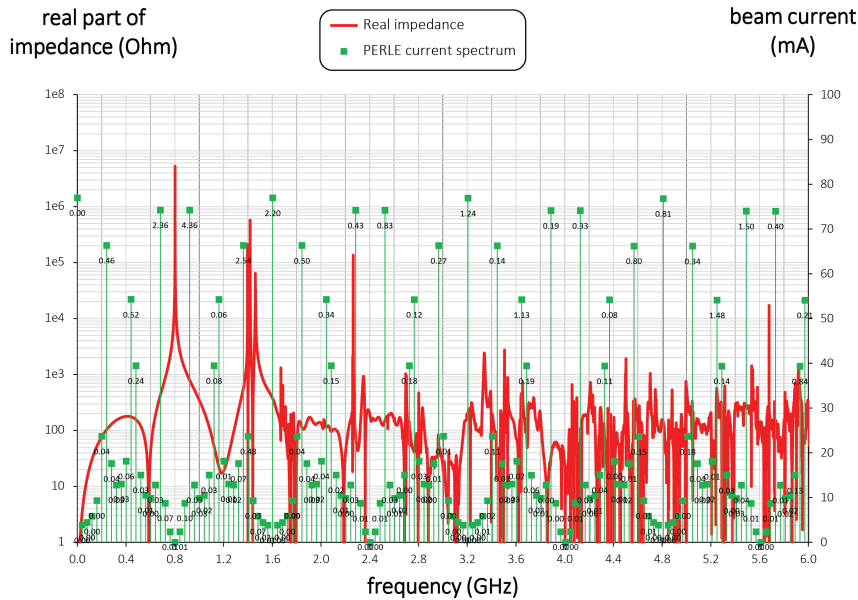


**Figure 10.18:** Real monopole impedance spectrum of the five-cell 802 MHz cavity prototype (red) together with the considered beam current lines (green) for the 3-pass PERLE machine (25 mA injected current). The numbers associated with the spectral lines denote the power dissipation (in Watt).

6742 impedance spectrum up to 6 GHz, and denotes the power deposited at each spectral line (in  
6743 Watt) for an injected beam current of 25 mA. For instance, the summation of the power in  
6744 this spectral range results in a moderate 30 W. This covers the monopole modes with the  
6745 highest impedances residing below the beam tube cutoff frequency. The HOM-induced heat has  
6746 to be extracted from the cavity and shared among the HOM couplers attached to the cavity  
6747 beam tubes. The fraction of the power escaping through the beam tubes above cutoff can be  
6748 intercepted by beam line absorbers.

6749 Note that for Fig. 10.18 a single HOM-coupler end-group consisting of three scaled TESLA-  
6750 type coaxial couplers was assumed to provide damping. Instead of coaxial couplers, waveguide  
6751 couplers could be utilized, which for instance have been developed at JLab in the past for high



6752 current machines. These are naturally broadband and designed for high power capability, though  
6753 some penalty is introduced as this will increase the complexity of the cryomodule. Ultimately,  
6754 the aim is to efficiently damp the most parasitic longitudinal and transverse modes (each polar-  
6755 ization). The evaluation of the total power deposition is important for LHeC to decide which  
6756 HOM coupler technology is most appropriate to cope with the dissipated heat and whether  
6757 active cooling of the couplers is a requirement.

6758 Though the prototype efforts focused on the five-cell cavity development, JLab also produced  
6759 single-cell cavities, i.e. one further Nb cavity and two OFE copper cavities. The former has been  
6760 shipped to FNAL for N-doping/infusion studies, whereas the latter were delivered to CERN for  
6761 Nb thin-film coating as a possible alternative to bulk Nb cavities. In addition, a copper cavity  
6762 was built for low power bench measurements, for which multiple half-cells can be mechanically  
6763 clamped together. Presently, a mock-up can be created with up to two full cells. This cavity  
6764 has been produced in support of the pending HOM coupler development. The ensemble of  
6765 manufactured cavities resonating at 802 MHz is shown in Fig. 10.19.

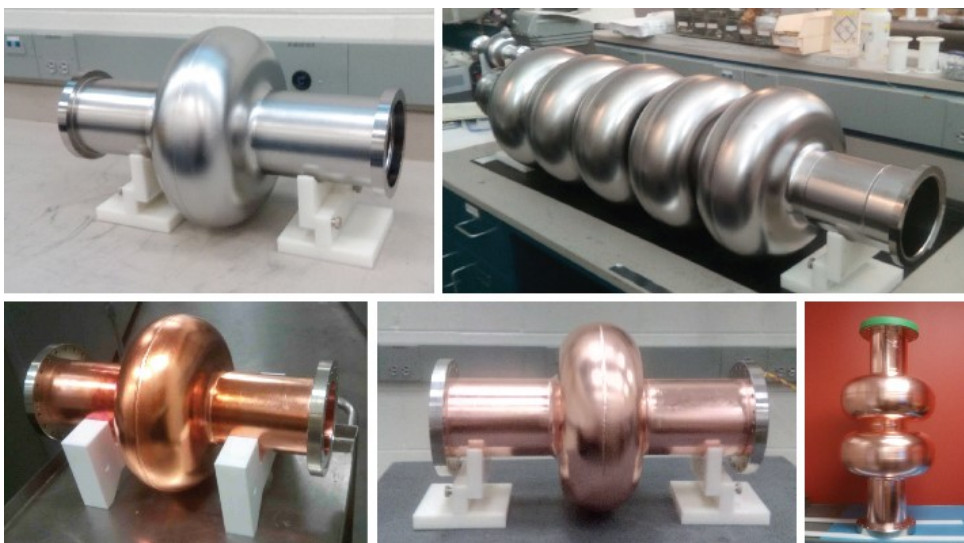


**Figure 10.19:** Ensemble of 802 MHz cavities designed and built at JLab for CERN. The Nb cavities have been tested vertically at 2 Kelvin in JLab’s vertical test area.

6766 Results for the Nb cavities - made from fine grain high-RRR Nb - were encouraging since both  
6767 cavities reached accelerating fields,  $E_{\text{acc}}$ , slightly above 30 MV/m ultimately limited by thermal  
6768 breakdown (quench). Moreover, the RF losses were rather small as a benefit of the relatively  
6769 low RF frequency as anticipated. The residual resistance extracted from the measurement data  
6770 upon cooldown of the cavity was  $3.2 \Omega \pm 0.8 \Omega$ . This resulted in unloaded quality factors,  
6771  $Q_0$ , well above  $4 \times 10^{10}$  at 2 K at low field levels, while  $Q_0$ -values beyond  $3 \times 10^{10}$  could be  
6772 maintained for the five-cell cavity up to  $\sim 27$  MV/m (see Fig. 10.20). Only standard interior  
6773 surface post-processing methods were applied including bulk buffered chemical polishing, high  
6774 temperature vacuum annealing, light electropolishing, ultrapure high-pressure water rinsing,  
6775 and a low temperature bake-out. While the vertical test results indicate generous headroom for  
6776 a potential performance reduction once a cavity is equipped with all the ancillary components  
6777 and installed in a cryomodule, clean cavity assembly procedure protocols must be established  
6778 for the cryomodules to minimise the chance of introducing field-emitting particulates.

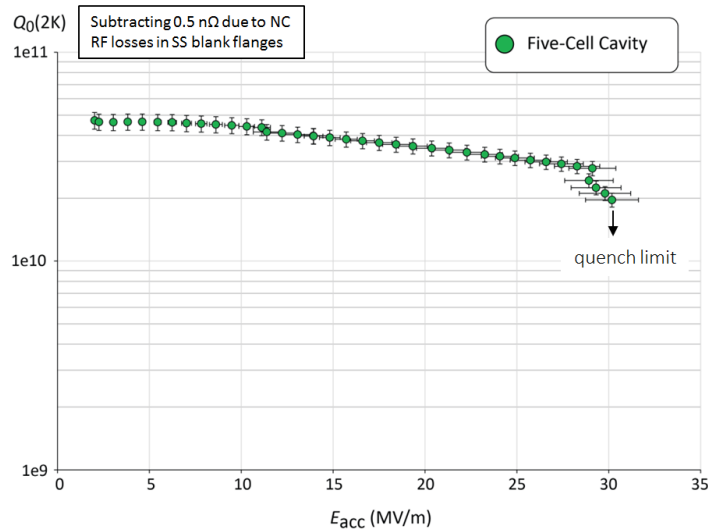


Figure 10.20: Vertical test result of the five-cell 802 MHz niobium cavity prototype.

### 6779 10.6.3 Cavity-Cryomodule

6780 The ERL cryomodules hosting the superconducting RF cavities are a key component of the  
 6781 accelerator. They should provide the proper mechanical, vacuum and cryogenic environment to  
 6782 the SRF cavities equipped with their ancillaries systems: helium tank, power coupler and HOM  
 6783 couplers. Each cryomodule is containing 4 superconducting 801.58 MHz 5-cells elliptical cavities  
 6784 described in the previous chapters.

6785 Recently, several projects worldwide have designed cryomodules for elliptical cavities with a  
 6786 cavity configuration (number, length and diameter) quite close to the one required by LHeC  
 6787 ERL:

- 6788 • SNS [802]: two different sized cryomodules host either 4 elliptical 6-cells 805 MHz cavities  
 6789 of  $\beta = 0.81$  or 4 elliptical 6-cells 805 MHz of  $\beta = 0.61$ ;
- 6790 • SPL [803]: the cryomodule is designed to integrate 4 elliptical 5-cells 704 MHz cavities of  
 6791  $\beta = 1$ ;
- 6792 • ESS [804]: two cryomodules of the same length can host either 4 elliptical 6-cells 704 MHz  
 6793 cavities of  $\beta = 0.67$  or 4 elliptical 5-cells 704 MHz cavities of  $\beta = 0.85$ .

6794 These three cryomodule designs are based on two completely different concepts for the cavity  
 6795 string support structure. SNS and ESS cryomodules are based on an intermediate support  
 6796 system, called the spaceframe, which is horizontally translated inside the cryomodule vacuum  
 6797 vessel. The low pressure cryogenic line is located above the cavities string and connected to the  
 6798 cryogenic transfer line by a double angled connection, the jumper. RF waveguides are connected  
 6799 underneath the cryomodule, using door-knob transition to the couplers. All the hanging and  
 6800 alignment operations of the cavities string and shielding are implemented outside the vacuum  
 6801 tank, using the spaceframe. In the ESS case, each cavity is hanged by 2 sets of 4 cross rods. The  
 6802 thermal shield is also hanged to these rods by the mean of an aluminium “elastic boxes” that  
 6803 allow the thermal shrinkage while maintaining the transverse stability. The thermal shield is  
 6804 made of 2.5 mm thick aluminium and wrapped with multi-layer insulation. It is fastened directly  
 6805 to the support rods of the cavities string.

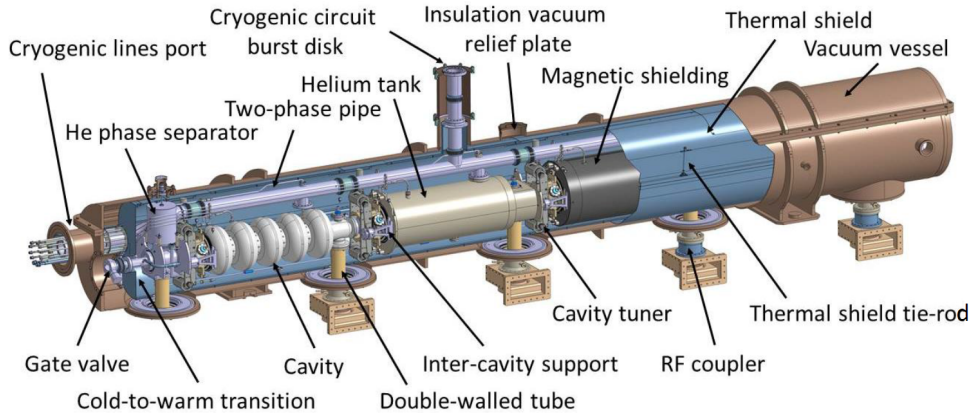


**Figure 10.21:** SPL cryomodule general assembly view

6806 In the SPL cryomodule, the cavity string is directly supported by the power coupler and with  
 6807 dedicated inter-cavity support features. Moreover, the SPL cryomodule integrates a full length  
 6808 demountable top lid, enabling the cavity string assembly from the cryomodule top (Fig. 10.21).  
 6809 The thermal shield is made of rolled aluminium sheets, and is composed of four main parts  
 6810 assembled before the vertical insertion of the string of cavities. The shield, wrapped with multi-  
 6811 layer insulation, is suspended to the vacuum vessel via adjustable tie rods in titanium alloy which  
 6812 also cope, by angular movements, with its thermal contractions. The cavity stainless steel helium  
 6813 tanks are connected by a 100-mm-diameter two-phase pipe placed above the cavities. This pipe  
 6814 ensures liquid feeding to the cavities by gravity, and is also used as a pumping line for gaseous  
 6815 helium.

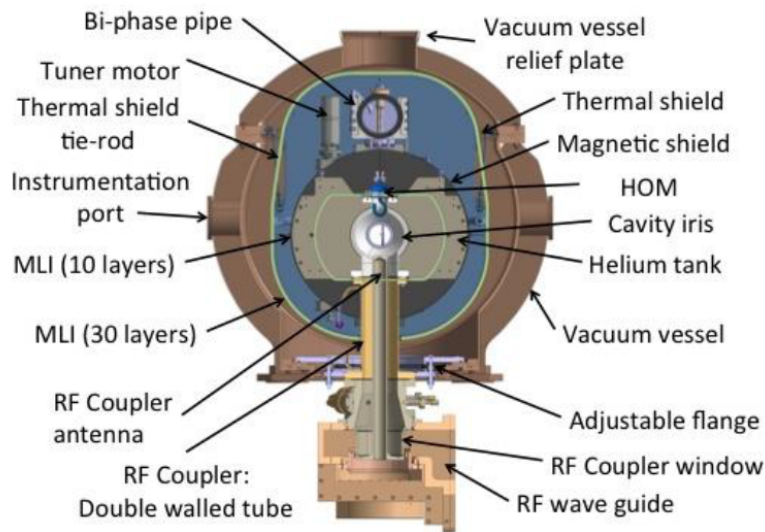


**Figure 10.22:** Cross-view of the SPL cryomodule

6816 With the aim of minimizing static heat loads from room temperature to 2 K by solid thermal  
 6817 conduction, the number of mechanical elements between the two extreme temperatures is re-  
 6818 duced to the strict minimum: the cavities are supported directly via the external conductor of  
 6819 the RF coupler (Fig. 10.22), the double-walled tube (DWT). The latter is made out of a stain-  
 6820 less steel tube with an internal diameter of 100 mm, which is actively cooled by gaseous helium  
 6821 circulating inside a double-walled envelope in order to improve its thermal efficiency.

6822 An additional supporting point to keep cavity straightness and alignment stability within re-  
6823 quirements is obtained by supporting each cavity on the adjacent one via the inter-cavity support,  
6824 which is composed of a stem sliding inside a spherical bearing. As a result, a pure vertical sup-  
6825 porting force is exchanged by adjacent cavities whereas all other degrees of freedom remain unre-  
6826 strained allowing thermal contraction movements to occur unhindered. The thermo-mechanical  
6827 behaviour of this supporting system has been extensively studied on a dedicated test bench at  
6828 CERN, proving its efficiency and reliability.

6829 There are some specific additional constraints or requirements for a cryomodule to be used in  
6830 an ERL, and some of them are quite challenging, The first set of constraints is linked to the CW  
6831 operation of the cryomodules (contrary to SNS, SPL and ESS which are pulsed accelerators),  
6832 where dynamic heat loads are much larger than the static ones. Thus, reaching high  $Q_0$  (low  
6833 cryogenic losses) is a main objective in these machines and beside specific optimization on cavity  
6834 design and preparation (such as N-doping), magnetic shielding should be carefully studied:  
6835 material, operating temperature, numbers of layers, active and/or passive shielding. Another  
6836 important constraint is linked to relative high power to be extracted by the HOM couplers:  
6837 thermal analysis should be carefully performed to have an optimized evacuation of the HOM  
6838 thermal load not to degrade the cryogenic performances of the cryomodule.

6839 We recently decided to push further away the analysis to use the SPL cryomodule for the LHeC  
6840 ERL, thanks to its geometrical compatibility with the LHeC ERL superconducting cavities,  
6841 but also because it fits quite well the overall ERL requirements. One of the clear advantages  
6842 of the SPL configuration is a much simplified assembly procedure (Fig. 10.23), with its top-lid  
configuration which also allows an easier maintenance.

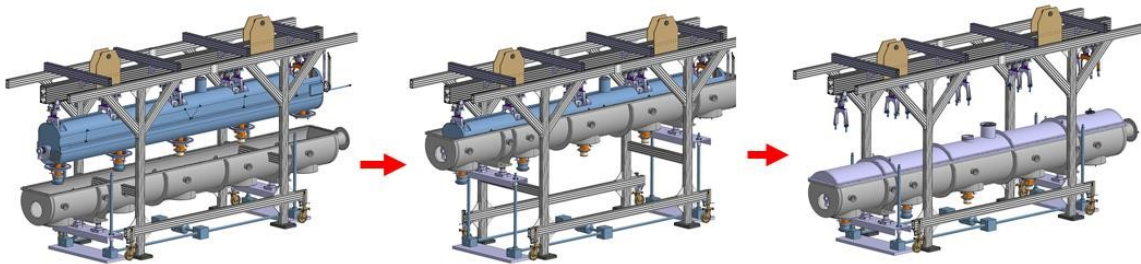


Figure 10.23: Cryomodule assembly procedure main steps

6843

6844 The first study performed was to analyse the possibility to integrate the ERL cavities instead  
6845 of the SPL ones. The 802 MHz cavities are a little bit shorter than the SPL ones and the cells  
6846 are also smaller in diameter. The beam port internal diameter is about the same, as well as  
6847 the power coupler port. As a result, the SPL cryomodule is well fitted to the ERL 802 MHz  
6848 superconducting cavities from the geometrical point of view, and they could be easily integrated  
6849 providing minor mechanical features adaptations.

6850 The second analysed point is the beam vacuum. As the SPL cryomodule existing design was  
6851 done for a prototype, intended for RF and cryogenic test only, without beam, the vacuum valve  
6852 is a VAT CF63 “vatterfly” valve with viton seal and manual actuator, which is not adapted for a  
6853 real operating cryomodule. Integration of an all-metal gate valve instead is not an issue and we  
6854 also designed a specific solution based on a two stages valves (Fig. 10.24) to adapt the already  
6855 fabricated SPL prototype cryomodule in order to be able to integrate the 802 MHz cavities.

6856 The third study performed is the compatibility of the SPL cryogenic features with the ERL  
6857 requirements. SPL was designed to operate 702 MHz cavities at 25 MV/m with a  $Q_0$  of  $5 \times 10^9$

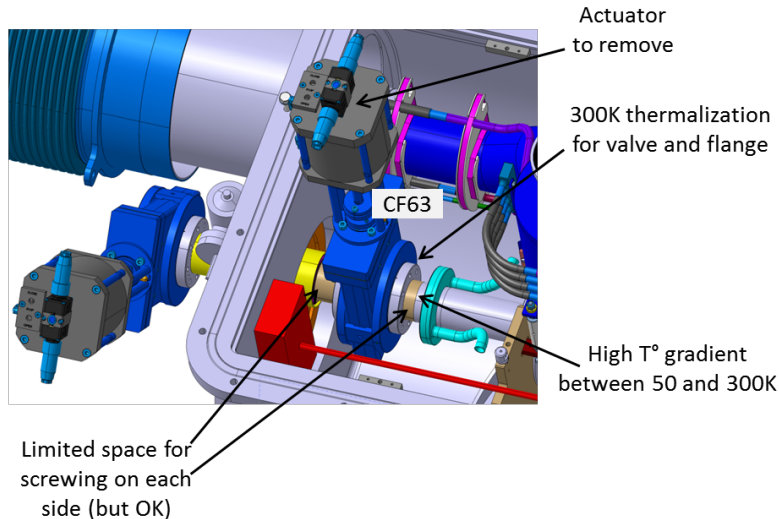


**Figure 10.24:** The two stages vacuum valve solution for adapting the SPL cryomodule prototype to the 802 MHz cavities of the LHeC ERL.

6858 with a 8.2 % duty cycle. The LHeC ERL will operate SRF cavities in CW regime, but at a lower  
 6859 field (20 MV/m) and with a higher expected  $Q_0$  at the nominal gradient (about  $1.5 \times 10^{10}$ ).  
 6860 As a result, and despite the different duty cycle, the dynamic cryogenic losses are estimated to  
 6861 be only about 30 % more in the ERL case. The overall cryogenic dimensioning is then fully  
 6862 compatible, providing some unavoidable adaptation of a few internal cryogenic piping. The  
 6863 main issue still to address is the need and consequences of the HOM coupler cooling. Even if  
 6864 the present engineering analysis showed that this point will not be a showstopper, it might have  
 6865 an impact on some cryogenic piping and cooling circuit.

6866 Detailed engineering studies are being pursued to transform the SPL cryomodule prototype into  
 6867 an ERL LHeC cryomodule prototype. We are taking benefit of all the design and fabrication  
 6868 work previously performed on the SPL, and also on the fact some parts, such as the thermal and  
 6869 magnetic shielding, are not yet fabricated and could be exactly adapted to the ERL requirements.  
 6870 This will give the possibility to have an earlier full prototype cryomodule RF and cryogenic test as  
 6871 compared to a standard experimental plan where the complete study and fabrication is starting  
 6872 from scratch.

#### 6873 10.6.4 Electron sources and injectors

##### 6874 Specification of electron sources

6875 Operation of the LHeC with an electron beam, delivered by a full energy ERL imposes specific  
 6876 requirements on the electron source. It should deliver a beam with the charge and temporal  
 6877 structure required at the Interaction Point. Additionally as during acceleration in a high energy  
 6878 ERL both longitudinal and transverse emittances of the beam are increased due to Synchrotron  
 6879 Radiation (SR), the 6D emittance of the beam delivered by electron source should be small  
 6880 enough to mitigate this effect. The general specification of the electron source are shown in  
 6881 Tab. 10.16. Some parameters in this table such as RMS bunch length, uncorrelated energy  
 6882 spread and normalised transverse emittance are given on the basis of the requirements for the  
 6883 acceleration in ERL and to pre-compensate the effects of SR. The most difficult of the parameters  
 6884 to specify is injector energy. It should be as low as possible to reduce the unrecoverable power  
 6885 used to accelerate the beam before injection into the ERL while still being high enough to deliver

6886 short electron bunches with high peak current. Another constraint on the injection energy is  
6887 the average energy and energy spread of the returned beam. The average energy cannot be  
6888 less than the energy of electron source, but the maximum energy in the spectrum should not  
6889 exceed 10 MeV the neutron activation threshold. An injection energy of 7 MeV is a reasonable  
compromise to meet this constraint.

Parameter	Unit	Value
Booster energy	MeV	7*
Bunch repetition rate	MHz	40.1
Average beam current	mA	20
Bunch charge	pC	500
RMS bunch length	mm	3
Normalised transverse emittance	$\pi \cdot \text{mm} \cdot \text{mrad}$	<6
Uncorrelated energy spread	keV	10
Beam polarisation		Unpolarised/Polarised

**Table 10.16:** General specification of the LHeC ERL electron source.

6890

6891 The required temporal structure of the beam and the stringent requirements for beam emittance  
6892 do not allow the use of conventional thermionic electron sources for the LHeC ERL without using  
6893 a bunching process involving beam losses. While this option cannot completely be excluded as a  
6894 source of unpolarised electrons. The additional requirement to deliver polarised beam can only  
6895 be met with photoemission based electron sources.

6896 There are now four possible designs of electron sources for delivering unpolarised beams and  
6897 (potentially) three for delivering polarised beams:

- 6898 1. A thermionic electron source with RF modulated grid or gate electrode with following  
6899 (multi)stage compression and acceleration. The electron source could be either a DC  
6900 electron gun or an RF electron source in this case. Although these sources are widely used  
6901 in the injectors of Infra-Red FELs [805] their emittance is not good enough to meet the  
6902 specification of the LHeC injector. Moreover, thermionic sources cannot deliver polarised  
6903 electrons.
- 6904 2. A VHF photoemission source. This is a type of normal conducting RF source which  
6905 operates in the frequency range 160 MHz – 200 MHz. The relatively low frequency of these  
6906 sources means that they are large enough that sufficient cooling should be provided to  
6907 permit CW operation. This type of source has been developed for the new generation  
6908 of CW FELs such as LCLS-II [806], SHINE [807] and a back-up option of the European  
6909 XFEL upgrade [808], but they have not yet demonstrated the average current required  
6910 for the LHeC injector. The possibility of generating polarised electrons with this type of  
6911 source has not investigated yet.
- 6912 3. A superconducting RF photoemission source. This type of sources are under development  
6913 for different applications such as CW FEL's (ELBE FEL [809], SRF option of LCLS-II  
6914 injector [810], European XFEL upgrade [811]), as a basis of injectors for ERL's (bERLin-  
6915 Pro [812]) and for electron cooling (BNL [813]). Though this type of sources has already  
6916 demonstrated the possibility of delivering the average current, required for the LHeC with  
6917 unpolarised beams (BNL), and has the potential for operation with GaAs type photocath-  
6918 odes (HZDR) which are required for delivery of polarised beams, the current technology  
6919 of SRF photoelectron source cannot be considered as mature enough for use in the LHeC.

6920  
6921  
6922  
6923  
6924  
6925  
6926  
6927  
6928  
6929  
6930  
6931

4. A DC photoemission source. In this type of source the electrons are accelerated immediately after emission by a potential difference between the source cathode and anode. This type of source is the most common for use in ERL injectors. It has been used in the projects which are already completed (JLAB [814], DL [815]), is being used for ongoing projects (KEK [816], Cornell/CBeta [817]) and is planned to be used in new projects such as the LHeC prototype PERLE [818]. The technology of DC photoemission sources is well-developed and has demonstrated the average current and beam emittance required for the LHeC ERL (Cornell). Another advantage of the photoelectron source with DC acceleration is the possibility of operation with GaAs based photocathodes for delivering of polarised beam. Currently it's the only source, which can deliver highly polarised electron beams with the current of several mA's which is already in the range of LHeC specifications (JLab [819]).

6932  
6933  
6934

Based on this analysis at CDR stage we consider the use of DC photoemission source as a basic option, keeping in mind that in the course of the injector development other types of electron sources may be considered, especially for providing of unpolarised beam.

### 6935 The LHeC unpolarised injector

The injector layout follows the scheme depicted in Fig. 10.25. Its design will be similar to the

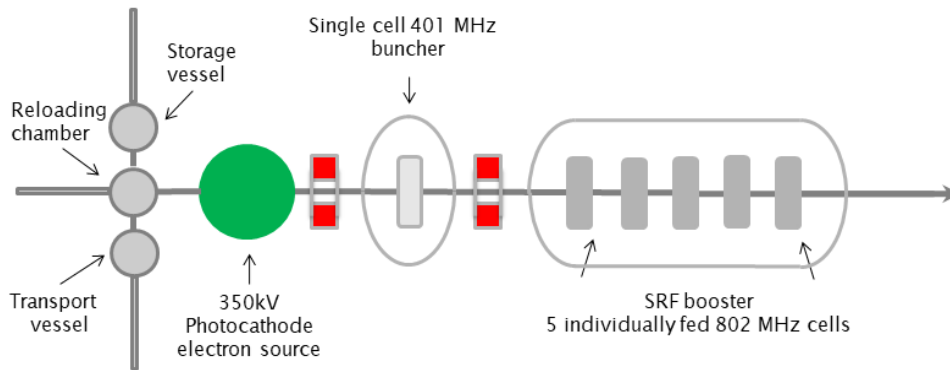


**Figure 10.25:** The layout of the unpolarised injector.

6936  
6937  
6938  
6939  
6940  
6941  
6942  
6943  
6944  
6945  
6946

unpolarised variant of the PERLE injector [818]. The electron source with DC acceleration delivers a CW beam with the required bunch charge and temporal structure. Immediately after the source is a focusing and bunching section consisting of two solenoids with a normal conducting buncher placed between them. The solenoids have two purposes. Firstly to control the transverse size of the space charge dominated beam which will otherwise rapidly expand transversely. This ensures that the beam will fit through all of the apertures in the injector beamline. Secondly the solenoids are used for emittance compensation to counter the space charge induced growth in the projected emittance. This is then followed by a superconducting booster linac. This accelerates the beam up to its injection energy, provides further longitudinal bunch compression and continues the emittance compensation process.

6947  
6948  
6949  
6950  
6951  
6952

The DC electron source will have an accelerating voltage of 350 kV using a high quantum efficiency antimonide based photocathode such as Cs<sub>2</sub>KSb. The photoinjector laser required for this cathode type will be a 532 nm green laser. There will be a load lock system to allow photocathodes to be replaced without breaking the source vacuum. This significantly reduces the down time required for each replacement which is a major advantage in a user facility such as the LHeC where maximising uptime is very important. The cathode electrode will be mounted

6953 from above similar to the Cornell [820] and KEK [821] sources. This electrode geometry makes  
 6954 the addition of a photocathode exchange mechanism much easier as the photocathode can be  
 6955 exchanged through the back of the cathode electrode. In addition the cathode electrode will be  
 6956 shaped to provide beam focusing. The operational voltage of 350 kV for the source was chosen  
 6957 as practical estimate of what is achievable. A higher voltage would produce better performance  
 6958 but would be challenging to achieve in practice. The highest operational voltage successfully  
 6959 achieved is 500 kV by the DC electron source that is used for the cERL injector [822]. However  
 6960 350 kV is sufficient to achieve the required beam quality [818].

### 6961 **Polarised electron source for ERL**

6962 Providing polarised electrons has always been a challenging process, especially at relatively high  
 6963 average current as required for the LHeC. The only practically usable production mechanism  
 6964 of polarised electrons is the illumination of activated to Negative Electron Affinity (NEA) state  
 6965 GaAs based photocathodes with circularly polarised laser light. The vacuum requirements for  
 6966 these cathodes mean that this must be done in a DC electron source only. In the course of the  
 6967 last 30 years significant progress has been achieved in improving the performance of polarised  
 6968 electron sources. The maximum achievable polarisation has reached 90 % and the maximum  
 6969 Quantum Efficiency (QE) of the photocathode at the laser wavelength of maximum polarisation  
 6970 has reached 6 %. Meanwhile the implementation of a polarised electron source into the LHeC  
 6971 remains a challenge as the practical operational charge lifetime of the GaAs based photocathode  
 6972 does not exceed hundreds Coulombs (JLAB [823]) at an operational current in mA range.

In Fig. 10.26 a preliminary design of the LHeC polarised injector is shown. In general, the design

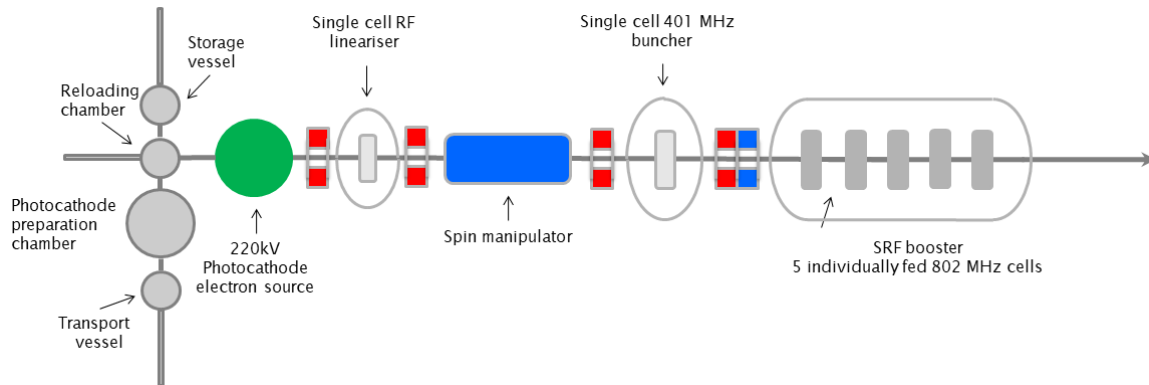


**Figure 10.26:** The layout of the polarised injector.

6973 of the polarised electrons injector is close to that of the unpolarised injector and is based on a  
 6974 DC electron source where a photocathode is illuminated by a pulsed laser beam. The choice of a  
 6975 DC source is dictated by the necessity of achieving extra high vacuum, with a pressure at a level  
 6976 of  $10^{-12}$  mbar, in the photocathode area. This level of vacuum is necessary for providing long  
 6977 lifetime of the photocathode. In order to reduce photocathode degradation caused by electron  
 6978 stimulated gas desorption, the accelerating voltage in the source is reduced to 220 kV. The main  
 6979 differences with unpolarised injector are the presence of a photocathode preparation system,  
 6980 permanently attached to the source, and a Wien filter based spin manipulator between the source  
 6981 and the buncher. In order to reduce depolarisation of the beam in the spin manipulator, caused  
 6982 by the space charge induced energy spread of the beam, an RF dechirper is installed between  
 6983 the source and the spin manipulator. The injector is also equipped with a Mott polarimeter to  
 6984 characterise the polarisation of the beam delivered by the source.  
 6985



6986 An important consideration of the operation with interchangeable photocathodes is minimisation  
6987 of the down time required for the photocathode exchange. It typically takes few hours to replace  
6988 the photocathode and to characterise polarisation of the beam. For large facility like LHeC this  
6989 is unacceptable. A practical solution could be operation with 2 or more electron sources which  
6990 operate in rotation similar to the way which was proposed at BNL [824]. Another motivation  
6991 for using multi-source injector is the nonlinear dependence of photocathode charge lifetime on  
6992 average beam current (JLAB [819]), which reduces with increasing of the average current. For  
6993 example in case of 3 electron sources 2 of them can be operated with half operation frequency  
6994 20.05 MHz in opposite phase delivering average current of 10 mA each, while the third is in stand  
6995 by regime with freshly activated photocathode. The only time which is necessary to switch it  
6996 on is the time required for rising the high voltage. Another advantage of using a multi-source  
6997 scheme is the reduction of the average laser power deposited on the photocathode and as result  
6998 relaxing requirements for the photocathode cooling. In order to implement the multi-source  
6999 polarised electron injector, development of a deflection system which is able to merge the beams  
7000 from different sources before the spin rotator is required.

### 7001 Lasers for electron sources

7002 In the proposed design of the LHeC injection system at least 2 lasers must be used. In the  
7003 unpolarised electron injector, which is going to operate with antimionide-based photocathode,  
7004 a laser with a wavelength of 532 nm is required. Typical initial QE of these photocathodes is  
7005 10% and for practical application reduction of QE up to 1% may be expected. For polarised  
7006 electron source typical QE varies from 1% down to 0.1% and laser with a wavelength of 780 nm  
7007 is required. The optimised parameters of the required lasers are summarised in Tab. 10.17. Laser  
7008 temporal profile and spot size on the photocathode are given on the basis of source optimisation  
for operation at 350 kV for unpolarised regime and 220 kV for polarised.

Laser beam parameter	Unit	Unpolarised mode	Polarised mode
Laser wavelength	nm	532	780
Laser pulse repetition rate	MHz	40.1	40.1
Energy in the single pulse at photocathode QE=1%	$\mu$ J	0.12	
Average laser power at photocathode QE=1%	W	4.7*	
Energy in the single pulse at photocathode QE=0.1%	$\mu$ J		0.79
Average laser power at photocathode Qe=0.1%	W		32*
Laser pulse duration	ps FWHM	118	80
Laser pulse rise time	ps	3.2	3.2
Laser pulse fall time	ps	3.2	3.2
Spot diameter on the photocathode surface	mm	6.4	8
Laser spot shape on the photocathode surface		Flat top	

Table 10.17: Parameters of the electron source drive laser.

7009

## 7010 10.6.5 Positrons - INCOMPLETE Being edited

### 7011 Possible positron sources

7012 The possibility to use positrons for LHeC collisions is discussed. Several positron sources, for  
7013 high-energy colliders, have been studied. The SLC  $e^+$  source is the only high energy linear  
7014 collider constructed up to now and dismantled in the year 1998. Today several future high-  
7015 energy colliders are considering a positron source. All these projects need to deliver intense high

7016 quality positron beams for the colliders. 10.18 shows the SLC parameters and those related  
7017 to the CLIC, ILC, FCChe and FCC ERL studies regarding the  $e^+$  flux. The last column is a  
proposal discussed in the next paragraph.

Parameter	SLC	CLIC (3 TeV)	ILC (500 GeV)	FCC he (Pulsed)	FCC he (ERL)	LHeC CLIC based
Energy ( AT IP ) [GeV]						
$e^+$ /bunch (At IP) [ $10^9$ ]						
$e^+$ /bunch (At IP) [GeV]						
Norm. emittance [mm.mrad]	30 (H)					
	2 (V)	0.02 (V)				
Norm. emittance [eV.m]						
Bunches / macropulse						
Repetition rate [Hz]						
Bunches / s						
$e^+$ flux [ $10^{14} e^+$ /s]	0.06	1.1	3.9	18	440	1.1

**Table 10.18:** Positrons flux for various collider.

7018

7019 A conventional positron source uses only a single amorphous target. An electron beam hits the  
7020 target where Bremstrahlung and pair-production take place. Downstream the target, particular  
7021 devices (Quarter Wave Transformer QWT or Adiabatic Matching Device AMD) allow capturing  
7022 as much as possible positrons that have a large emittance. The CLIC  $e^+$  source [1]Fix Ref.  
7023 takes advantage of a hybrid target design. A thin crystal target allows reducing the peak power  
7024 deposition and enhances photon production via a channelling process. An amorphous target  
7025 converting the photons into positrons follows it. In between, a magnet sweeps out charged  
7026 particles. The ILC  $e^+$  source [2]Fix Ref. takes advantage of a long helical undulator using the  
7027 high-energy electron beam of the collider. The electron beam passing through the undulator  
7028 produces polarised photons impinging on a moving target. The later converts photons into  
7029 positrons. The initial LHeC  $e^+$  source [3]Fix Ref. proposes using 10 hybrid targets in parallel  
7030 to overcome the requested important  $e^+$  flux for the pulsed operation at 140 GeV (Figure 1)Fix  
7031 Ref.. To evaluate the performance of  $e^+$  sources, one defines a *positron yield* parameter. This  
7032 parameter is the number of positrons, at a given place along the production channel, per electron  
7033 impinging onto the target. It is crucial to improve the positron yield in order to reduce the peak  
7034 energy density deposition PEDD and the shockwave into the target. The target lifetime suffers  
7035 from the cyclic thermal loads and stresses from the beam pulses. The evacuation of the average  
7036 power (kW to MW) from the target is challenging and should be investigated for the reliability  
7037 of the target. Heat dissipation in the amorphous target may be improved by replacing it with  
7038 a granular target (experiment at KEK). The capture and accelerating sections should also be  
7039 optimised. Peak magnetic field and its shape, aperture and accelerating gradient of the RF  
7040 structures are important parameters. Given the large emittance of the  $e^+$  beam, a damping ring  
7041 is mandatory. Due to the high requested  $e^+$  flux, an accumulation process should be considered.  
7042 The  $e^+$  flux is

$$\frac{dN^+}{dt} = a \cdot y \cdot N^- \cdot E^- \cdot f, \quad (10.8)$$

7043 where  $a$  is the accumulation efficiency and is a function of the damping time,  $y$  is the yield as  
7044 defined above,  $N^-$  is the number of electron impinging on the target,  $E^-$  is the electron beam  
7045 energy on the target, and  $f$  the linac repetition rate.

7046 **Challenges for the high positron flux**

7047 The present LHeC parameters would request a positron flux 21 000 times the SLC flux, see  
7048 Tab. 10.19.

Parameter	Unit	Value
Bunch spacing	ns	25
Current	mA	20
Charge	nC / bunch	0.5
Flux	$10^{14} e^+/s$	1240

**Table 10.19:** Challenging LHeC  $e^+$  beam in CW mode.

7049 The CDR [1] describes several mitigation schemes to cope with the LHeC ERL requirements.  
7050 The parameters were the following: a positron current of 6 mA with a positron flux of  $4.4 \times$   
7051  $10^{16} e^+/s$ . The normalized transverse emittances of 50 mm.mrad and the longitudinal emittance  
7052 5 MeV.mm. As mentioned at this time, a serious and concerted R&D effort is required to develop  
7053 and evaluate a baseline design. Today, the LEMMA project [4]Fix Ref. assumes 1500 bunches  
7054 with  $5 \times 10^{11} e^+/bunch$  and 10 Hz repetition rate. This corresponds to a flux of  $7.5 \times 10^{15} e^+$   
7055 /s. The study refers to the LHeC flux [1] and indicates clearly this as a key issue for the study.

7056 **A new approach for the LHeC  $e^+$  flux**

7057 According to the very challenging parameters, a change of paradigm is proposed. The idea is  
7058 using the CLIC  $e^+$  flux,  $1 \times 10^{14} e^+/s$ , which is already challenging. However, the CLIC positron  
7059 source has been studied in details and many simulations have been performed [5]Fix Ref.. We  
7060 propose to consider three possible options, all based of the CLIC  $e^+$  flux:

- 7061 • Option 1: Keep the CW mode and the bunch spacing of 25 ns. This implies a bunch  
7062 charge of  $2.5 \times 10^6 e^+/bunch$  and a current of 16  $\mu$ A.
- 7063 • Option 2:  
7064 Keep the CW mode with a bunch charge of  $2.5 \times 10^9 e^+/bunch$ . This implies a bunch  
7065 spacing of 25  $\mu$ s and a current of 16  $\mu$ A.
- 7066 • Option 3: Keep the bunch spacing of 25 ns with a bunch charge of  $1 \times 10^9 e^+/bunch$ . This  
7067 implies a pulsed mode with a repetition rate of 50 Hz. The beam current is now 6.4 mA.

7068 The last column of 10.18 gives the parameters corresponding to this option. Figure 3Fix Ref.  
7069 gives a pattern of the beam structure. According to the consequences on the LHeC luminosity,  
7070 one of these options will be studied accordingly.

7071 **10.6.6 Compensation of Synchrotron Radiation Losses**

7072 Depending on energy, each arc exhibits fractional energy loss due to the synchrotron radiation,  
7073 which scales as  $\gamma^4/\rho$  (see Eq. (10.5)). Arc-by-arc energy loss was previously summarised in  
7074 Tab. 10.14. That energy loss has to be replenished back to the beam, so that at the entrance of  
7075 each arc the accelerated and decelerated beams have the same energy, unless separate arcs are  
7076 used for the accelerated and decelerated beams. Before or after each arc, a matching section  
7077 adjusts the optics from and to the linac. Adjacent to these, additional cells are placed, hosting  
7078 the RF compensating sections. The compensation makes use of a second harmonic RF at  
7079 1603.2 MHz to replenish the energy loss for both the accelerated and the decelerated beams,

7080 therefore allowing them to have the same energy at the entrance of each arc, as shown in  
 7081 Fig. 10.27.

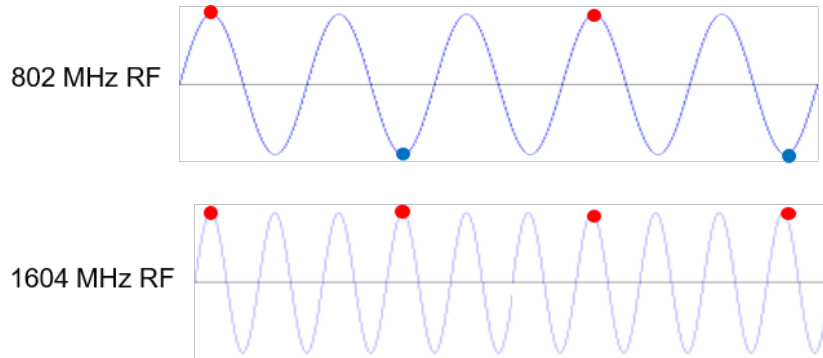


**Figure 10.27:** The second-harmonic RF restores the energy loss in both the accelerating and decelerating passes.

7081

7082 Parameters of the RF compensation cryomodules, shown in Table 10.20, have been extrapolated  
 7083 from the ILC cavity design, expecting that the higher frequency and lower gradient would  
 support continuous operation.

Parameter	Unit	Value
Frequency	MHz	1603.2
Gradient	MV/m	30
Design		Nine cells
Cells length	mm	841
Structure length	m	1
Cavity per cryomodule		6
Cryomodule length	m	6
Cryomodule voltage	MV	150

**Table 10.20:** A tentative list of parameter for the compensating RF cryomodules extrapolated from the ILC design.

7084

7085 As illustrated schematically in Fig. 10.27, there are two beams in each arcs (with exception  
 7086 of Arc 6) one needs to replenish energy loss for: the accelerated and the decelerated beams.  
 7087 Assuming nominal beam current of 20 mA, the net current for two beams doubles. Therefore,  
 7088 40 mA current in Arcs 1-5, was used to evaluated power required to compensate energy loss by  
 7089 2-nd harmonic RF system, as summarized in Table 10.21.

Section	$\Delta E$ [MeV]	$P$ [MW]	Cryomodules
Arc 1	3	0.12	0
Arc 2	25	1.0	0
Arc 3	80	3.2	1
Arc 4	229	9.16	2
Arc 5	383	15.32	3
Arc 6	836	16.7	6

**Table 10.21:** Arc-by-arc synchrotron radiated power for both the accelerated and decelerated beams (only one beam in Arc 6) along with a number of 2-nd harmonic RF cryomodules required to compensate energy loss.

7090 The compensating cryomodules are placed into Linac 1 side of the racetrack, before the bending  
7091 section of Arc 1, Arc 3, and Arc 5 and after the bending section of Arc 2, Arc 4, and Arc 6.  
7092 This saves space on Linac 2 side to better fit the IP line and the bypasses. Note that with the  
7093 current vertical separation of 0.5 m it will not be possible to stack the cryomodules on top of  
7094 each other; therefore, they will occupy 36 m on the Arc 4 and Arc 6 side and 18 m on the Arc 3  
7095 and Arc 5 side of the racetrack. Each of the compensating cavities in Arc 5 needs to transfer  
7096 up to 1 MW to the beam. Although a 1 MW continuous wave klystron are available [825], the  
7097 cryomodule integration and protection system will require a careful design. Tab. 10.21 shows the  
7098 energy loss for each arc and the corresponding synchrotron radiated power, along with number  
7099 of cryomodules at 1603.2 MHz RF frequency required to replenish the energy loss.

### 7100 **10.6.7 LINAC Configuration and Infrastructure**

7101 Since the power supplied to the beam in the main linacs will be recovered, the average RF power  
7102 requirements at 802 MHz are relatively small and determined by the needs to handle transients  
7103 and microphonics.

7104 The RF power required for the second-harmonic RF system however is substantial – it can be  
7105 estimated from Tab. 10.14 with the nominal current of 20 mA. Tab. 10.21 above summarizes  
7106 the estimated power lost in each arc depending on beam energy; these power values must be  
7107 supplied by the 6 2-nd harmonic RF systems.

7108 The RF infrastructure required at 802 MHz

## 7109 **10.7 Interaction Region**

7110 The design of the LHeC Interaction region has been revised with respect to the LHeC CDR to  
7111 take into account the reduction of the electron energy from 60 GeV to 50 GeV and the latest  
7112 design of the HL-LHC optics and it has been optimized to minimize synchrotron radiation power  
7113 and critical energy at the IP.

### 7114 **10.7.1 Layout**

7115 The basic principle of the Linac-Ring IR design remains unchanged and it is shown in Fig. 10.28:  
7116 the two proton beams are brought onto intersecting orbits by strong separation and recombina-  
7117 tion dipoles. A collision of the proton beams at the IP is avoided by selecting appropriately its  
7118 location, i.e. by displacing it longitudinally with respect to the point where the two counter-  
7119 rotating proton beams would collide. The large crossing angle keeps the long range beam-beam  
7120 effect small and separates the beams enough to allow septum quadrupoles to focus only the  
7121 colliding beam (the anti-clockwise rotating LHC beam – Beam 2). The non-colliding beam (the  
7122 clockwise rotating LHC beam – Beam 1) is unfocused and passes the septum quadrupoles in a  
7123 field free aperture. The electron beam is brought in with an even larger angle, partly sharing  
7124 the field free aperture of the septum quadrupoles with the non-colliding beam. A weak dipole  
7125 in the detector region bends the electron beam into head-on collisions with the colliding proton  
7126 beam. The two proton beams are also exposed to the dipole field but, due to the large beam  
7127 rigidity, they are barely affected. After the interaction point a dipole with opposite polarity  
7128 separates the orbits of the electron and proton beam.

7129 The high electron current (cf. Tab. 10.1) required to approach the goal peak luminosity of  
7130  $10^{34} \text{cm}^{-2} \text{s}^{-1}$  poses a potential problem for the interaction region (IR) as it increases the already  
7131 high synchrotron radiation.

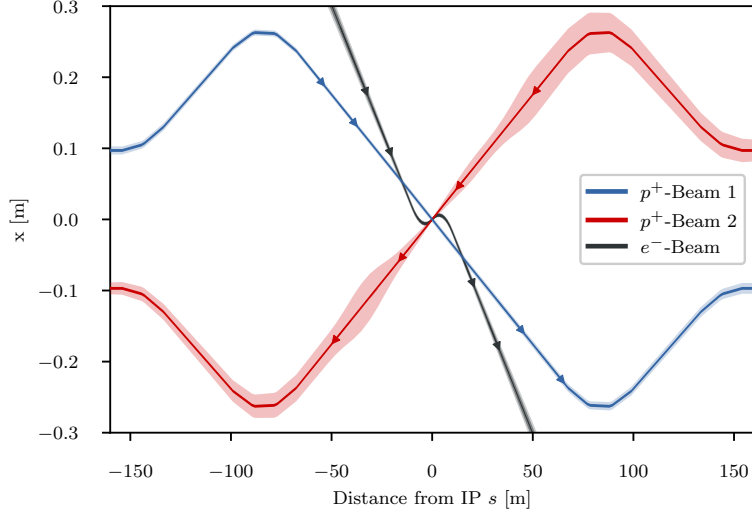


**Figure 10.28:** Geometry of the interaction region with  $10\sigma$  envelopes. The electron beam is colliding with the focussed anti-clockwise rotating LHC beam (Beam 2) while the clockwise rotating LHC beam is unfocussed and passes the Interaction Region without interacting with the other two beams

Magnet	Gradient [T/m]	Length [m]	Free aperture radius [mm]
Q1A	252	3.5	20
Q1B	164	3.0	32
Q2 type	186	3.7	40
Q3 type	175	3.5	45

**Table 10.22:** Parameters of the final focus quadrupole septa. The parameters of Q1A/B and Q2 are compatible with the Nb<sub>3</sub>Sn based designs from [827] assuming the inner protective layer of Q2 can be reduced to 5 mm thickness.

7132 The ERL parameters are not the only major change the new IR design has to account for.  
7133 The first design of the quadrupole septa featured a separation of 68 mm for the two proton  
7134 beams. However, this design focused strongly on providing a field free region for the non-  
7135 colliding beam. Unfortunately, this lead to a poor field quality for the strongly focused colliding  
7136 beam. The first quadrupole Q1 was a half quadrupole design effectively acting as a combined  
7137 function magnet with a dipole component of 4.45 T [826]. The sextupole field component was  
7138 also prohibitively high. Consequently, a new design approach focusing on the field quality in the  
7139 quadrupole aperture was necessary. The parameters relevant for the interaction region design  
7140 are summarised in Tab. 10.22.

7141 It is noteworthy that the minimum separation of the two beams at the entrance of the first  
7142 quadrupole Q1A increased from 68 mm to 106 mm requiring a stronger bending of the electron  
7143 beam. This would increase the already high synchrotron radiation in the detector region even  
7144 more. In order to compensate this increase, it was decided to increase  $L^*$  (i.e. the distance from  
7145 the IP to the first superconducting septum quadrupole focussing Beam 2) to 15 m, an approach  
7146 that was shown to have a strong leverage on the emitted power [828].

7147 The increased separation of the two proton beams, the longer  $L^*$  and the overall longer final  
7148 focus triplet make longer and stronger separation and recombination dipoles necessary. The  
7149 dipoles differ from the arc dipoles in that the magnetic field in both apertures has the same  
7150 direction. Consequently the cross talk between both apertures is significant and the maximum

Magnet	Field strength [T]	Interbeam distance [mm]	Length [m]	Number
D1	5.6	$\geq 496$ mm	9.45	6
D2	4.0	$\geq 194$ mm	9.45	4
IP Dipole	0.21	-	10	-

**Table 10.23:** Parameters of the separation and recombination dipoles. The respective interbeam distances are given for the magnet with the lowest value.

7151 reachable field is lower. The new geometry keeps the required field below 5.6 T. The required  
7152 lengths and strength of these dipoles are listed in Tab. 10.23. It should be noted that the inter-  
7153 beam distance is different for each of the five magnets per side, so each magnet will likely require  
7154 an individual design. The design of the D1 dipoles is further complicated by the fact that an  
7155 escape line for neutral collision debris traveling down the beam pipe will be necessary [1], as well  
7156 as a small angle electron tagger. These issues have not been addressed so far, further studies  
7157 will require detailed dipole designs.

7158 The first design of the LHeC interaction region featured detector dipoles occupying almost the  
7159 entire drift space between the interaction point and first quadrupole. The approach was to have  
7160 the softest synchrotron radiation possible to minimise the power. However, since the purpose  
7161 of the dipoles is to create a spacial separation at the entrance of the first quadrupole, it is  
7162 possible to make use of a short drift between dipole and quadrupole to increase the separation  
7163 without increasing the synchrotron radiation power. A dipole length of  $\frac{2}{3}L^*$  is the optimum in  
7164 terms of synchrotron radiation power [829]. Compared to the full length dipole it reduces the  
7165 power by 15.6 % at the cost of a 12.5 % higher critical energy. With an  $L^*$  of 15 m the optimum  
7166 length of the detector dipoles is 10 m. A magnetic field of 0.21 T is sufficient to separate the  
7167 electron and proton beams by 106 mm at the entrance of the first quadrupole. With these  
7168 dipoles and an electron beam current of 20 mA at 49.19 GeV the total synchrotron radiation  
7169 power is 38 kW with a critical energy of 283 keV to be compared with a power of 83 kW and a  
7170 critical energy of 513 keV for the electron beam energy of 60 GeV. More detailed studies on the  
7171 synchrotron radiation for different options and including a beam envelope for the electron beam  
7172 are summarised in Tab. 10.26 below.

7173 A schematic layout of the LHeC interaction region with the dipoles discussed above is shown in  
7174 Fig. 10.29. The corresponding beam optics will be discussed in the following sections.

## 7175 10.7.2 Proton Optics

7176 As discussed above, the  $L^*$  was increased to 15 m in order to compensate the increased syn-  
7177 chrotron radiation due to the larger separation. The final focus system is a triplet consisting  
7178 of the quadrupoles Q1A and Q1B (see Tab. 10.22), three elements of the Q2 type and two of  
7179 the Q3 type. Between the elements a drift space of 0.5 m was left to account for the magnet  
7180 interconnects in a single cryostat. Between Q1 and Q2 as well as Q2 and Q3 a longer drift of  
7181 5 m is left for cold-warm transitions, Beam Position Monitors (BPMs) and vacuum equipment.  
7182 Behind Q3, but before the first element of the recombination dipole D1, another 16 m of drift  
7183 space are left to allow for the installation of non-linear correctors in case the need arises, as well  
7184 as a local protection of the triplet magnets from asynchronous beam dumps caused by failures  
7185 of the beam dump kickers (MKD) as discussed below.

7186 As the recombination dipoles D1 and D2 for the LHeC interaction region require more space  
7187 than the current ALICE interaction region, the quadrupoles Q4 and Q5 had to be moved further  
7188 away from the IP. The position of Q6 is mostly unchanged but due to a need for more focusing

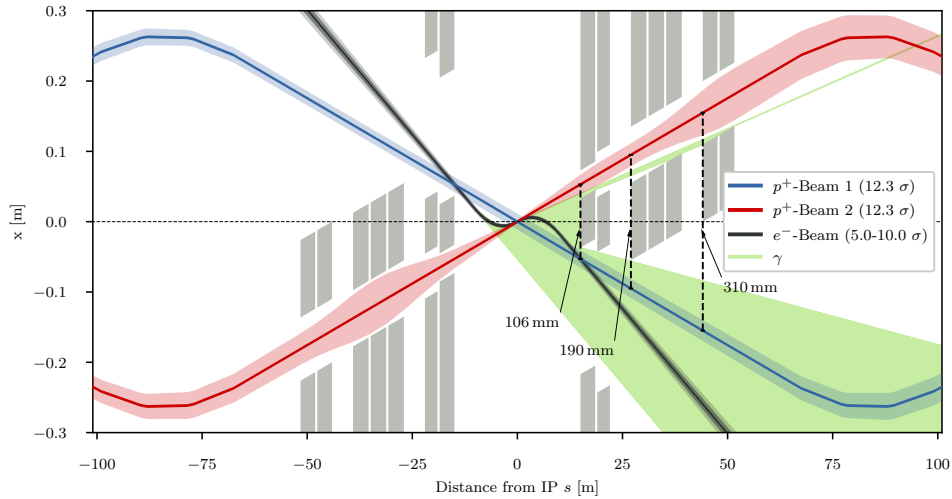


**Figure 10.29:** Schematic layout of the LHeC interaction region. The colliding proton beam and the electron beam are shown at collision energy while the non-colliding beam is shown at injection energy when its emittance is the largest.

7189 the length was increased by replacing it with two elements of the MQM magnet class of LHC.  
 7190 With the triplet quadrupole parameters provided in Tab. 10.22 we were able to match optics with  
 7191 a minimum  $\beta^*$  of 10 cm. The corresponding optics are shown in Fig. 10.30 and feature maximum  $\beta$  functions in the triplet in the order of 20 km. With these large  $\beta$  functions, the free apertures

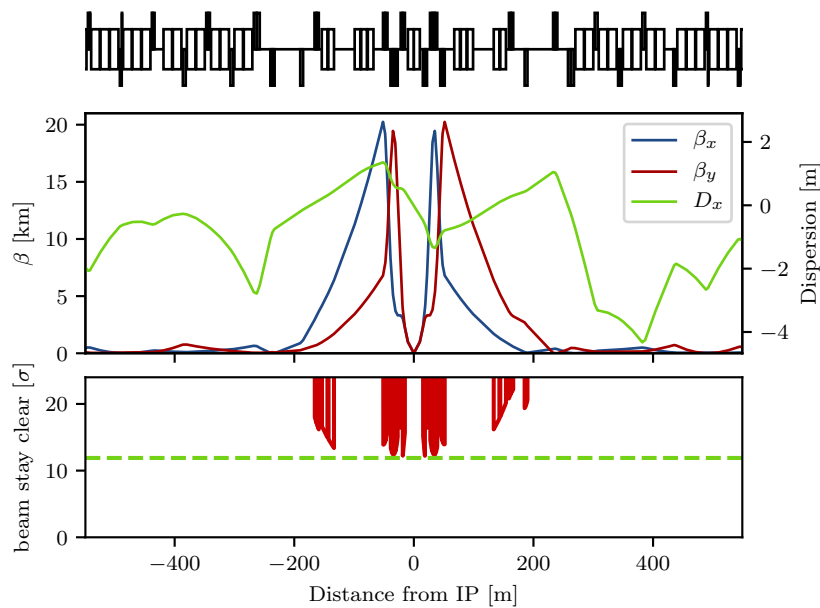


**Figure 10.30:** Optics (top) and beam stay clear (bottom) of the colliding beam with  $\beta^* = 10$  cm.

7192 of the quadrupoles leave just enough space for a beam stay clear of  $12.3\sigma$ , the specification of the  
 7193 LHC. This is illustrated in Fig 10.30. However, since the LHeC is supposed to be incorporated  
 7194 in the HL-LHC lattice, this minimum beam stay clear requires specific phase advances from the  
 7195 MKD kicker to the protected aperture as detailed later. The large  $\beta$  functions not only drive  
 7196 the aperture need in the final focus system, but also the required chromaticity correction in  
 7197



7198 the adjacent arcs. To increase the leverage of the arc sextupoles, the Achromatic Telescopic  
 7199 Squeezing scheme (ATS) developed for HL-LHC [830] was extended to the arc upstream of  
 7200 IP2 for the colliding beam (Beam 2) (see Fig. 10.31). This limited the optical flexibility in  
 7201 the matching sections of IR2, specifically of the phase advances between arc and IP2. As a  
 7202 consequence, the optical solution that has been found (Fig. 10.30) still has a residual dispersion  
 7203 of 15 cm at the IP and the polarities of the quadrupoles Q4 and Q5 on the left side of the  
 7204 IP break up the usual sequence of focusing and defocusing magnets. It needs to be studied  
 7205 whether this is compatible with the injection optics. The latest optics designs can be found at  
 the webpage [831].

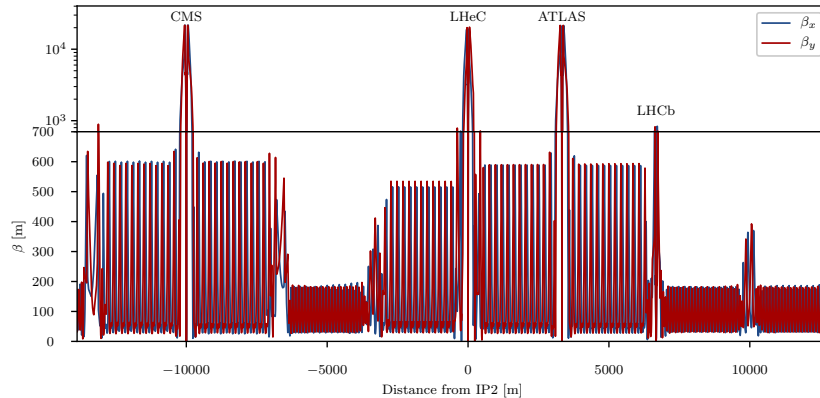


**Figure 10.31:** Optics of full ring of the colliding LHC proton beam (Beam 2).

7206

7207 The free apertures given in Tab. 10.22 include a 10 mm thick shielding layer in Q1 and 5 mm in  
 7208 Q2 and Q3. This is necessary to protect the superconducting coils from synchrotron radiation  
 7209 entering the magnets as can be seen in Fig. 10.29. The absorber must also protect the magnets  
 7210 from collision debris. Simulations of both synchrotron radiation and collision debris are yet to  
 7211 be conducted in order to confirm the feasibility of this design.

7212 A separation between the two proton beams in time is currently foreseen, i.e. while the orbits  
 7213 of the two proton beams do cross, the bunches do not pass through the IP at the same time.  
 7214 This approach is complicated by the fact that the timing of the bunches in the other three  
 7215 interaction points should not be affected. The easiest way to accomplish this is by shifting the  
 7216 interaction point of LHeC by a quarter of a bunch separation, i.e.  $6.25 \text{ ns} \times c \approx 1.87 \text{ m}$  upstream  
 7217 or downstream of the current ALICE IP, similar to what has been done for the LHCb detector  
 7218 in Point 8 of the LHC. This will of course have an impact in the integration of the detector in  
 7219 the underground cavern [832], however it seems feasible [833].

7220 The LHC protected aperture in the event of an asynchronous beam dump significantly depends  
 7221 on the phase advance between the MKD kicker and the local aperture protection [834]. This  
 7222 is due to the oscillation trajectory of bunches deflected during the kicker rise time. With a  
 7223 phase advance of  $0^\circ$  or  $180^\circ$  from the kicker to the protected aperture, a direct hit should be  
 7224 unlikely, so aperture bottlenecks should be close to that. For a beam stay clear of  $12.3\sigma$  a phase  
 7225 advance of less than  $30^\circ$  from either  $0^\circ$  or  $180^\circ$  was calculated to be acceptable [834]. The major  
 7226 complication comes from the fact that not only the final focus system of LHeC, but also of the  
 7227 two main experiments ATLAS and CMS need to have to correct phase advances and since the  
 7228 phase advances between IP2 (LHeC) and IP1 (ATLAS) are locked in the achromatic telescopic  
 7229 squeezing scheme there are few degrees of freedom to make adaptations.

7230 The Achromatic Telescopic Squeezing (ATS) scheme [830] is a novel optical solution proposed

7231 for the HL-LHC to strongly reduce the  $\beta^*$  while controlling the chromatic aberrations induced,  
7232 among other benefits.

7233 The principles of the ATS as implemented for the HL-LHC are as follows: first, in the presqueeze  
7234 stage, a standard matching procedure is performed in the interaction regions to obtain a value of  
7235  $\beta^*$  which is achievable in terms of quadrupole strengths and chromaticity correction efficiency,  
7236 in the case of HL-LHC this corresponds to IR1 and IR5. A further constraint at this point is  
7237 to match the arc cell phase advance on the regions adjacent to the low  $\beta^*$  interaction regions to  
7238 exactly  $\pi/2$ . Later, at the collision stage, the low  $\beta^*$  insertions remain unchanged and instead  
7239 the adjacent interaction regions contribute to the reduction of  $\beta^*$ , that is IR8 and IR2 for IR1,  
7240 and IR4 and IR6 for IR5. The  $\pi/2$  phase advance allows the propagation of  $\beta$ -waves in the  
7241 arc. If phased correctly with the IP, these  $\beta$ -waves will reach their maximum at every other  
7242 sextupoles, increasing the  $\beta$  function at their location at the same rate that the decrease in  $\beta^*$ .  
7243 The increase of the  $\beta$  function at the location of the sextupoles will result in an increase of their  
7244 efficiency, allowing the system to correct the high chromaticity produced by the high- $\beta$  function  
7245 in the inner triplet. This way, the ATS allows a further reduction of the  $\beta^*$  at the same time  
7246 that correcting the chromaticity aberrations produced in the low  $\beta$  insertions.

7247 Following the experience for HL-LHC, the ATS scheme was proposed for the LHeC project to  
7248 overcome some of the challenges of this design in terms of limits in the quadrupole strengths of  
7249 the interaction region and in the chromaticity correction.

7250 A first integration of the LHeC IR into the HL-LHC lattice using the ATS scheme for the  
7251 previous nominal case with  $\beta^* = 10$  cm and  $L^* = 10$  m was presented by extending the  $\beta$  wave  
7252 into the arc 23 [828]. The flexibility of this design was later explored to study the feasibility  
7253 of minimising  $\beta^*$ , to increase the luminosity, and increasing  $L^*$ , to minimise the synchrotron  
7254 radiation. It was found that increasing  $L^*$  to 15 m provided a good compromise but keeping the  
7255  $\beta^*$  to 10 cm.

7256 The changes made to the HLLHCV1.3 lattice [835] to obtain the LHeC lattice and the detailed  
7257 matching procedure are described in Ref. [836]. At the end of this process a lattice for the  
7258 required collision optics in all IRs ( $\beta^*=15$  cm for IR1 and IR5 and  $\beta^*=10$  cm for IR2) has  
7259 been obtained, with the appropriate corrections (crossing, dispersion, tune and chromaticity).  
7260 The phases between the MKD kicker in IR6 and the different low  $\beta^*$  triplets were also checked,  
7261 resulting in  $15^\circ$  from the horizontal for IR1,  $22^\circ$  for IR2 and  $26^\circ$  for IR5, therefore fulfilling the  
7262  $< 30^\circ$  requirement for all three IRs.

7263 Similarly the chromaticity correction for the LHeC lattice further develops from the HL-LHC  
7264 chromaticity correction scheme [836] allowing to correct the chromaticity for the case with  
7265  $\beta^* = 10$  cm in IP2 within the available main sextupole strength. Lattices with  $\beta^* = 7, 8$  and  
7266  $9$  cm and  $L^* = 15$  m were also successfully matched in terms of both the  $\beta^*$  and the chromaticity  
7267 correction. It must be noted however that these cases require a larger aperture in the inner  
7268 triplet.

7269 Dynamic aperture (DA) studies were performed to analyze the stability of the lattice designs  
7270 using SixTrack [837] on a thin-lens version of the LHeC lattice at collision ( $\beta^* = 0.15$  m in  
7271 IP1 and IP5,  $\beta^* = 10$  cm in IP2) over  $10^5$  turns with crossing angles on, 30 particles pairs per  
7272 amplitude step of  $2\sigma$ , 5 angles in the transverse plane and a momentum offset of  $2.7 \times 10^{-4}$ .  
7273 The energy was set to 7 TeV and the normalised emittance of the proton beam to  $\epsilon = 2.5 \mu\text{m}$ .  
7274 No beam-beam effects were included in this study.

7275 Previous DA studies had been performed for an earlier version of the LHeC lattice [828]. These  
7276 studies did not include triplet errors of either of the low- $\beta$  interaction regions, as these errors

were not available at that stage. These studies were updated for the newer version of the LHeC lattice described in the previous sections and included errors on the triplets of IR1 and IR5. For the case of IR2 errors tables for the new triplet are not yet available but it was estimated that the same field quality than the triplets for the HL-LHC IR can be achieved for these magnets, and therefore the same field errors were applied but adjusted to the LHeC triplet apertures.

The initial DA resulted in  $7\sigma$  but following the example of HL-LHC and FCC studies [838] two further corrections were implemented: the use of non-linear correctors to compensate for the non linear errors in the LHeC IR, and the optimisation of the phase advance between IP1 and IP5. With these corrections the DA was increased to  $10.2\sigma$ , above the target of  $10\sigma$ . The case for lower  $\beta^*$ , particularly for the case of interest with  $\beta^* = 7\text{ cm}$  proved to be more challenging, as expected, when adding errors on the LHeC IR; however with the use of the latest corrections a DA of  $9.6\sigma$  was achieved, that is not far off from the target. The DA versus angle for both these cases are shown in Fig. 10.32. It is important to point out that the challenge for the  $\beta^*=7\text{ cm}$  case comes instead from the quadrupole aperture and gradient requirements, particularly in the first magnet.

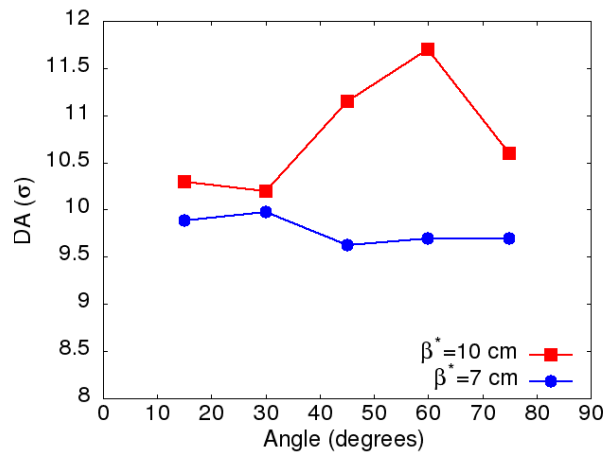


**Figure 10.32:** Dynamic aperture vs angle for 60 seeds for the LHeC lattice at collision for the cases  $\beta^* = 10\text{ cm}$  (red) and  $\beta^* = 5\text{ cm}$  in IP2.

7291

$\beta^*$  values lower than  $10\text{ cm}$  require a completely different final focus system as the lower  $\beta^*$  means the beam size in the triplet will become larger. Larger apertures are required and consequently the gradients in the quadrupoles will decrease. However similar integrated focusing strengths will be required so the overall length of the triplet will increase. As this will in turn increase the  $\beta$  functions in the triplet further it is imperative to optimise the use of the available space. An example of available space is the drift between the detector region dipoles and the triplet magnets as shown in Fig. 10.33. The optimum dipole lengths in terms of synchrotron radiation power was determined to be  $2/3 \cdot L^*$  so a drift of  $5\text{ m}$  is left. Now it is immediately clear that this region cannot be occupied by a superconducting quadrupole septum as that would effectively decrease  $L^*$  and thus increase the synchrotron radiation power as a stronger separation is necessary. Instead it is thinkable that a normal conducting quadrupole septum can be built that either does not require a yoke or similar structure between the beams or has a very thin yoke, or a septum that has a very limited and controlled field in the region of the electron beam trajectory. In the later case it might even be used as part of the final focus system of the electron beam. Either way, it is clear that such a normal conducting septum must have a pole tip field way below the saturation limit of iron. The section on electron optics shows that a normal quadrupole of this kind can also have benefits in terms of synchrotron radiation, but studies remained to be

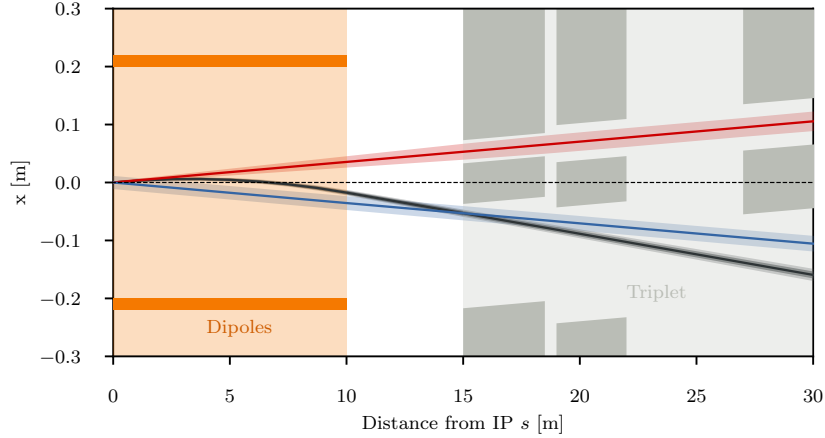


**Figure 10.33:** Empty space between the detector dipole and the superconducting quadrupoles of the final focus triplet.

7309 done to make sure the parameters work for both cases. For our calculation a pole tip field of  
 7310 1 T was assumed. For  $\beta^* = 5$  cm an aperture radius of 20 mm is required at a distance of 14 m  
 7311 from the IP, resulting in a pole tip field of 50 T/m for the normal conducting septum called Q0.  
 7312 Possible ratios of apertures and gradients for the remaining triplet magnets were approximately  
 7313 based on the quadrupole parameters shown in Tab. 10.22, however these parameters would  
 7314 require a magnet design for confirmation. With the quadrupole parameters shown in Tab. 10.24  
 7315 we were able to obtain triplet optics that can accommodate a beam with a minimum  $\beta^*$  of 5 cm.

Magnet	Gradient [T/m]	Length [m]	Aperture radius [mm]
Q0 (nc)	50	3.0	20
Q1A	110	3.5	27
Q1B	162	5.0	37
Q2	123	5.0	62
Q3	123	4.5	62

**Table 10.24:** Parameters of the final focus quadrupole septa required to accommodate a  $\beta^*$  of 5 cm. The normal conducting quadrupole is called Q0 although it has the same polarity as Q1A/B.

7316

7317 The corresponding optics are shown in Fig. 10.34. So from the triplet point of view it appears  
 7318 possible to reach lower  $\beta^*$ , however many assumptions need verification: First the magnetic  
 7319 design for the normal conducting quadrupole septum must be shown to be possible. If there  
 7320 is a residual field in the space of the electron beam trajectory, the impact on the electron  
 7321 beam and the synchrotron radiation power must be evaluated. The parameters of the modified  
 7322 superconducting triplet quadrupole septa, although scaled conservatively, must be confirmed.  
 7323 Furthermore the larger aperture radius of Q1 might require a larger separation at the entrance of  
 7324 Q1, increasing the synchrotron power that is already critical. Thus a full design of such magnets  
 7325 is required. Lastly, the interaction region must be integrated into the full ring to verify that  
 7326 chromaticity correction is possible. Studies in Ref. [836] that were conducted on the normal  
 7327 triplet without regard for aperture constraints suggest that a chromaticity correction is only  
 7328 possible for a  $\beta^*$  down to around 7 cm.

7329 So far, the optics of the final focus system featured asymmetrically powered triplets on the two

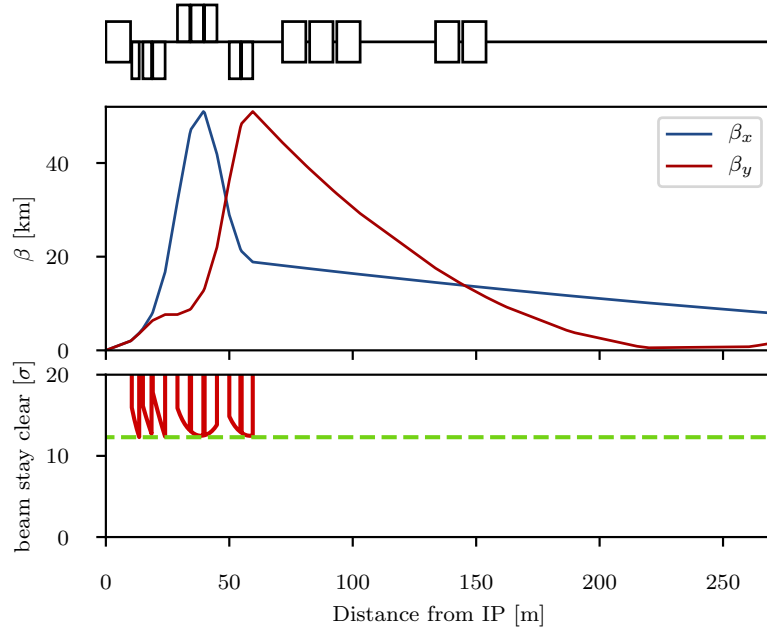


**Figure 10.34:** Optics (top) and beam stay clear (bottom) in the triplet region of colliding beam with  $B^* = 5$  cm.

7330 sides of the IP. This is inherited from the ALICE final focus system where the aperture is shared  
7331 and the antisymmetry guarantees the same optics for both beams and similar chromaticities in  
7332 both horizontal and vertical planes. In the LHeC final focus system however, the apertures of the  
7333 quadrupoles are not shared between both beams, so the antisymmetry is not strictly necessary,  
7334 although it eases the integration in the full ring. An alternative approach that is worth studying  
7335 is a symmetric doublet. Doublets feature a large  $\beta$  function in one plane and a relatively low one  
7336 in the other plane for equal  $\beta$  functions at the IP. Since the non-colliding proton beam is of no  
7337 concern for LHeC it makes sense to create doublets on each side of the IP that have the peak  $\beta$   
7338 function in the horizontal plane as the chromaticity correction was limited in the vertical plane.  
7339 Furthermore, in a doublet the integrated focusing strength needed is lower as fewer quadrupoles  
7340 act against each other. This further reduces the chromaticity and should also reduce the overall  
7341 length of the final focus system. With the space saved by the doublet it is possible to either shift  
7342 the recombination dipoles D1 and D2 closer to the IP, reducing the needed integrated strengths,  
7343 or even to increase  $L^*$  to further reduce the synchrotron radiation power and critical energy.  
7344 In order to make best use of the available doublet quadrupole aperture, it is also thinkable to  
7345 collide with flat beams. The main disadvantage of symmetric doublets is the breaking of the  
7346 sequence of focusing and defocusing quadrupoles. As no changes should be made to the arcs,  
7347 the left-right symmetry needs to be broken up again in one of the matching sections, either by  
7348 introducing another quadrupole on one side of the IP, or by overfocusing the beam.

7349 At collision energy the non-colliding beam has no optics specification within the straight section.  
7350 Consequently the optics should transfer the beam from the left arc to the right arc without hitting  
7351 the aperture and at a specific phase advance. The same is true at injection energy, but with a  
7352 larger emittance, making the satisfaction of the aperture constraint more difficult. Thus it is  
7353 sufficient to find working injection optics, as no squeeze will be required for this beam. This  
7354 approach of course will require some tuning as at least one arc will apply the ATS scheme at  
7355 collision, but as the aperture constraint is less tight at higher energy there should be enough

7356 degrees of freedom available.

7357 Finding injection optics appears trivial at first but is complicated by the fact that the distance  
 7358 between the IP and the first quadrupole magnet Q4 is larger than 159 m. A total distance  
 7359 of 318 m needs to be bridged without any focusing available. A solution has been found with  
 7360  $\beta^* = 92$  m and  $\alpha^* = \pm 0.57$  with the required beam size in the quadrupole septa and Q4 [836].  
 The corresponding optics are shown in Fig. 10.35. For the magnets Q4 and Q5 LHC quadrupoles

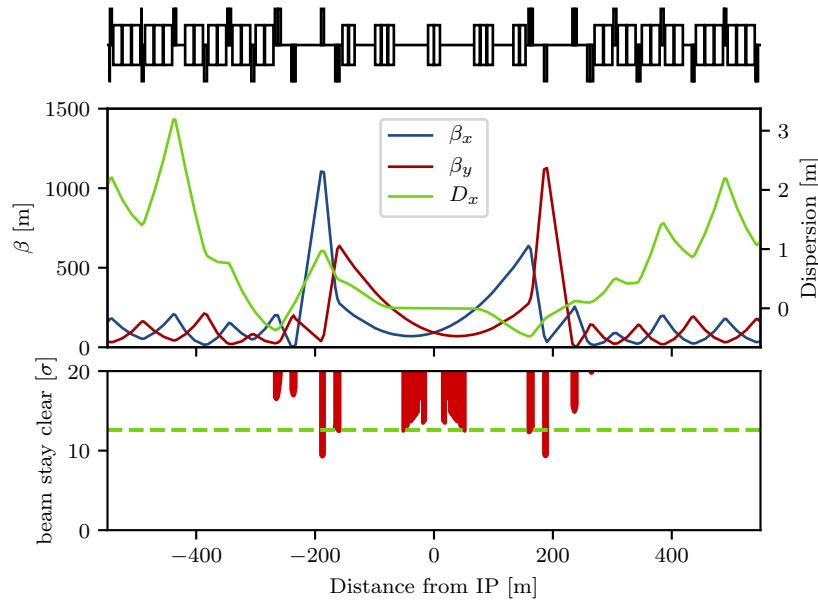


**Figure 10.35:** Optics (top) and beam stay clear of the non-colliding beam at injection energy. The Q5 quadrupole magnets on either side of the IP currently are aperture bottlenecks. It should be possible to mitigate this problem by replacing the magnets with longer, larger aperture magnets.

7361  
 7362 of the large aperture MQY type with 70 mm aperture diameter and a 160 T/m gradient were  
 7363 assumed. As can be seen in the aperture plot, the triplet quadrupole septa and Q4 are just below  
 7364 the minimum beam stay clear at injection of  $12.6\sigma$  but it is expected that nominal aperture can  
 7365 be achieved With some minor optimisation. However the Q5 magnets only have a beam stay  
 7366 clear of about  $9.2\sigma$  with little chance of decreasing the beam size without increasing it both  
 7367 in Q4 and in the quadrupole septa. Consequently it will be necessary to use quadrupoles with  
 7368 apertures larger than 106 mm and make up for the lower gradient by increasing the length or by  
 7369 using Nb<sub>3</sub>Sn technology. At injection energy the remaining magnets in the IR have strengths  
 7370 according to the HL-LHC specification and thus do not pose any problems. However the injection  
 7371 optics shown in Fig. 10.35 will require some changes during the ramp as Q4, Q5 and Q6 would  
 7372 become too strong at collision energy. This is not considered a problem though, as the emittance  
 7373 shrinking will ease the aperture requirements.

7374 The non-colliding proton beam does not need to be focused and consequently passes the quadrupole  
 7375 septa of the colliding beam in the field free region.

7376 The large angle of 7200  $\mu$ rad between the two beams (compared to 590  $\mu$ rad in the high lumi-  
 7377 nosity IPs) should suffice to mitigate long range beam-beam effects, considering that the shared  
 7378 aperture is only 30 m long as opposed to the main experiments where the shared aperture exceeds  
 7379 a length of 70 m.

7380 **10.7.3 Electron Optics**

7381 First ideas of a possible layout and design of the LHeC IR have already been presented in Ref. [1].  
 7382 Based on the principles explained there, a further optimisation of the beam separation scheme  
 7383 has been established, with the ultimate goal of lowest synchrotron radiation power and critical  
 7384 energy in the direct environment of the particle detector. Depending on the requests from the  
 7385 actual detector geometry and shielding, the flexibility of the new IR layout allows to optimise  
 7386 for either side.

7387 The basic principle is – as before – based on the large ratio (approximately 140) of the proton  
 7388 to electron beam momentum (or beam rigidity,  $B\rho = p/e$ ) that makes a magnetic field based  
 7389 separation scheme the straightforward solution to the problem, using effective dipole fields.

7390 Boundary conditions are set however due to the limited longitudinal space, resulting from the  
 7391 distance of the first focusing elements of the proton lattice, located at  $L^* = 15$  m, and the need for  
 7392 sufficient transverse separation, defined by the technical design of this first proton quadrupole.  
 7393 The size of the two beams and – clear enough – the power of the emitted synchrotron radiation  
 7394  $P_{\text{syn}}$  and the critical energy  $E_{\text{crit}}$  have to be taken into account in addition. The well known  
 7395 dependencies of these two parameters on the beam energy  $E_e = m_e c^2 \gamma$  and bending radius  $\rho$   
 7396 are given by

$$P_{\text{syn}} = \frac{e^2 c}{6\pi\epsilon_0} \frac{\gamma^4}{\rho^2} \quad \text{and} \quad E_{\text{crit}} = \frac{3 \hbar c \gamma^3}{2 \rho}. \quad (10.9)$$

7397 The schematic layout of the original design of the electron interaction region shown in Fig. 10.29  
 is reproduced in Fig. 10.36 (a). The long dipole magnet B, used to deflect the electron beam, is

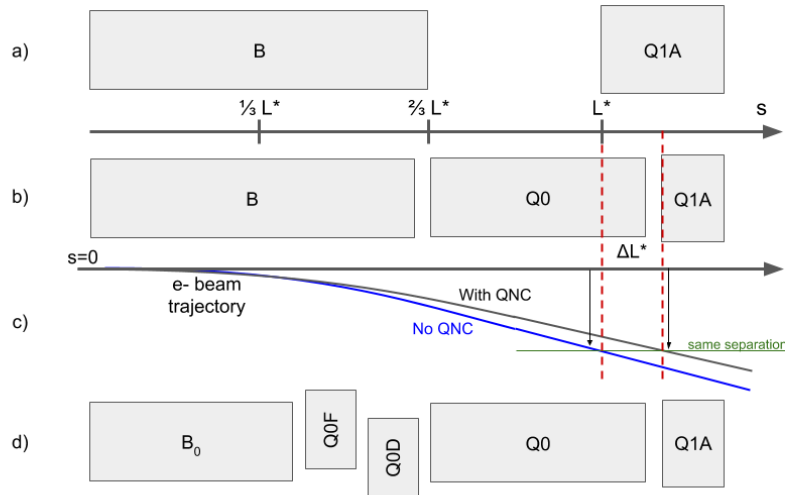


**Figure 10.36:** Separation scheme based on a long dipole magnet B (a) and improved layout using Q0, a normal conducting half-quadrupole as first focusing element of the proton beam (b). The last design features a doublet of off-centered quadrupoles to minimise the electron beam size at the entrance of Q1A (d).

7398 embedded inside the detector structure which is ranging from  $-6$  m to  $4$  m around the interaction  
 7399 point, extended by  $\pm 1.65$  m of muon chamber. Basic interaction region designs with and without  
 7400 chromaticity correction were presented [839, 840] but were not fully integrated in the ERL. The  
 7401 electron final quadrupoles were placed at  $30$  m from the IP [841], compatible with the proton  
 7402 layout described above. While this approach is straightforward, the only parameter that can be  
 7403

7404 used to minimise the power of the emitted synchrotron radiation is the length of the separator-  
7405 dipole field [829]. In addition, the installation of the first focusing elements of the electron beam  
7406 downstream of the triplet focussing the colliding proton beam leads to a considerable increase  
7407 of the electron beam size in the separation plane.

7408 Lattices including chromaticity correction had a significant length of 150 m. However, the whole  
7409 straight section between Linac and arc is only 290 m long [1] and the IR design did not include a  
7410 matching and splitting section or a focus system for the spent, outgoing electron beam. Without  
7411 chromaticity correction in the electron final focus, aberrations at the IP decrease luminosity by  
7412 about 20% [842].

7413 Investigations have been launched to minimise critical energy and emitted synchrotron radiation  
7414 power by reducing the separation in two main steps:

7415 • introduce a compact mirror-plate half quadrupole (QNC) in front of Q1A (on the IP side)  
7416 to focus the colliding proton beam and provide a field free region for the electron and non-  
7417 interacting proton beam. This reduces the required bending field of the separation dipole  
7418 B for the same separation at Q1A. In addition, the normal conducting magnet QNC will  
7419 act as shielding of the superconducting triplet magnets that would otherwise be subject to  
7420 direct synchrotron radiation. Additional shielding is foreseen, to protect the SC magnets  
7421 and avoid as much as possible backshining to the detector. In addition, sufficient space  
7422 will be provided to correct the vertical orbit and coupling of the electrons coming from  
7423 the solenoid.

7424 • reduce the beam size of the electron beam by a very early focusing of the beam. As positive  
7425 side effect this leads to a considerable reduction of the chromaticity of the electron lattice.

7426 The first step is sketched in Fig. 10.36 (b) and the corresponding electron beam trajectory is  
7427 shown in Fig. 10.36 (c).

7428 The introduction of the mirror plate half quadrupole QNC allows to reduce the length of the  
7429 Q1A quadrupole while conserving the total integrated gradient, therefore leaving the overall  
7430 focusing properties of the proton lattice quasi untouched. The entry of Q1A is therefore moved  
7431 away from the IP to relax the separation fields.

7432 Scanning the Q1A entry position leads to either an optimum of the critical energy or to a  
7433 minimum of the emitted synchrotron power. Both cases are shown in Fig. 10.37 and for each  
7434 of them the new Q1A entry position has been determined. The power of the emitted radiation  
7435 is reduced by up to 28%. The colliding proton beam, passing through this half quadrupole  
7436 with a certain offset to guarantee sufficient beam stay clear, will receive a deflecting kick in the  
7437 horizontal plane of about  $90\ \mu\text{rad}$ . It supports the dipole based beam separation, provided by  
7438 the so-called D1 / D2 magnets in LHC, and will be integral part of the LHC design orbit.

7439 The resulting beam optics of the protons differs only marginally from the original version and  
7440 only a slight re-match is needed. However by carefully choosing the gradient of the new magnet  
7441 the parameters of the superconducting proton quadrupoles are untouched and the phase advance  
7442 at the end of the interaction region lattice is conserved in both planes.

### 7443 **Improved Electron lattice**

7444 A further improvement of the emitted synchrotron power and critical energy is obtained by  
7445 introducing an early focusing scheme of the electrons, which leads to a reduced electron beam  
7446 size and thus to softer separation requirements.



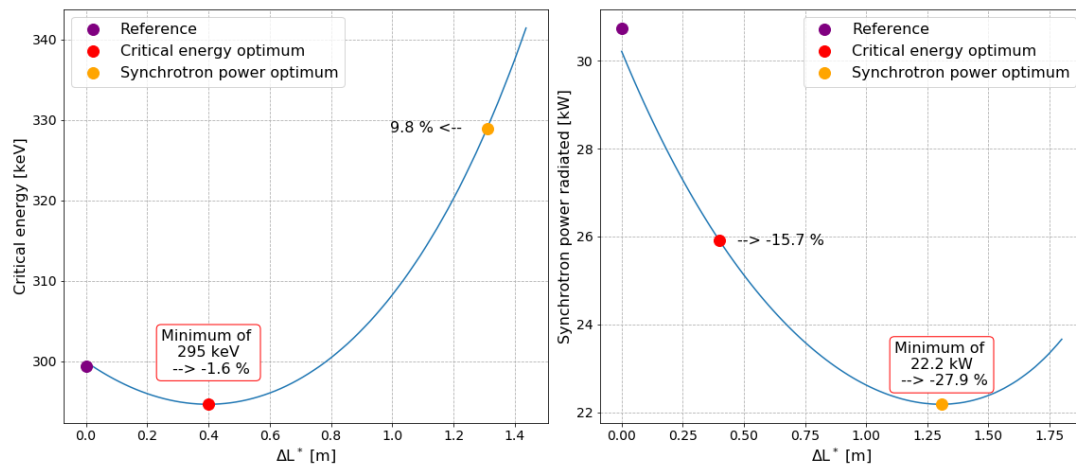


**Figure 10.37:** Improved critical energy and power of the synchrotron radiation for the half quadrupole based proton lattice. Left side: critical energy, right side: synchrotron radiation power. The horizontal axis refers to the shift  $\Delta L^*$  of the position of the first proton superconducting magnet Q1A.

7447 The reduction of the electron beam size is obtained by installing a quadrupole doublet in the  
7448 electron lattice between the separation dipole and the QNC (half-) quadrupole. A carefully  
7449 matched focusing strength of this doublet will minimise the  $\beta$  function of the electrons at the  
7450 location of Q1A. At the same time an effective dipole field, that is needed to maintain the  
7451 separation of proton and electron beams, is provided by shifting the magnet centres of the  
7452 doublet lenses off axis. The horizontal offset of these quadrupoles has been chosen to provide  
7453 the same bending radius as the separation dipole, thus leading in first order to the same critical  
7454 energy of the emitted light in all separation fields. A detailed calculation of the divergence of the  
7455 photons, the geometry of the radiation fan and the position of the absorbers and collimators will  
7456 be one of the essential next steps within the so-called machine-detector-interface considerations.

7457 Fig. 10.36 (d) shows the new layout – compared to the previous version. The doublet providing  
7458 the early focusing of the electron beam is embedded in the separator dipole, i.e. it is positioned  
7459 at  $s = 6.3$  m and acts in combination with the separation dipole. The quadrupole gradients have  
7460 been chosen for optimum matching conditions of the electron beam and the transverse shift of  
7461 the field centres provide the same separation dipole effect as used in the long dipole.

7462 The early focusing of the electron beam allows for a softer separation of the beams, and leads  
7463 therefore directly to a reduced critical energy  $E_{\text{crit}}$  and power  $P_{\text{syn}}$  of the emitted radiation.  
7464 Fig. 10.38 shows the dependence of  $E_{\text{crit}}$  and  $P_{\text{syn}}$  on the  $\beta$ -function at  $s = L^*$  for the electron  
7465 optics for different values of the required electron beam stay-clear expressed in units of the  
7466 electron beam size  $\sigma$ . The beam separation has been re-calculated and the critical energy  
7467 and radiation power are plotted. The graphs include different assumptions for the beam size  
7468 considered. Including orbit tolerances, a beam stay-clear of  $20 \sigma$  is considered as the most  
7469 relevant case, which refers to the red curve in the graph.

7470 In order to provide a complete study with the lattice featuring the off-centered quadrupoles, the  
7471 new interaction region has been embedded in between the high energy end of the acceleration  
7472 part of the linac and the *Arc 6* of the ERL, which marks the start of the energy recovery lattice.  
7473 An optimum has been found for a beam optics with a beta function in the plane of the beam  
7474 separation (i.e. horizontal) of  $\beta_x = 90$  m at  $L^* \approx 15$  m

7475 An improvement of about 9% for the critical energy and close to 25% of the radiated power is

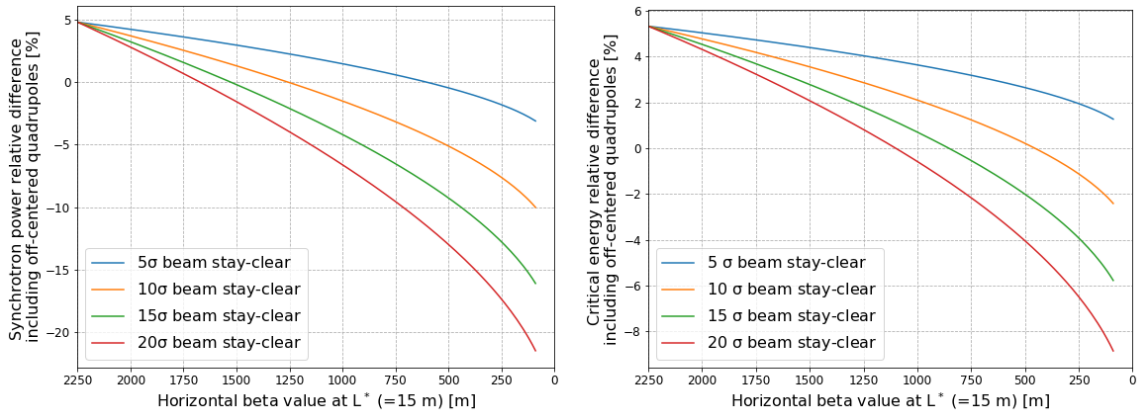


**Figure 10.38:** Relative difference with respect to the single dipole separation scheme for different values of the required beam stay-clear expressed in  $\sigma$ . Left : for the power of the emitted radiation, as function of the  $\beta$ -function of the electron beam at position  $s=15\text{m}$ . Left: for the critical energy of the emitted radiation, as function of the  $\beta$ -function of the electron beam at position  $s=15\text{m}$ . The early focusing of the electron beam allows for a much reduced separation field and thus to a reduced critical energy and power of the emitted radiation. The initial beta value is 2250 m.

7476 obtained, if an electron beam optics with  $\beta_x = 90\text{ m}$  at the entrance of Q1A is used. For this  
 7477 most promising case the matched beam optics is shown in Fig. 10.39.

7478 The lower  $\beta$ -function of the electron beam at the focusing elements has the additional positive  
 7479 feature of reducing considerably the chromaticity of the new lattice, which is a crucial parameter  
 7480 for the performance of the energy recovery process (details are described below in the chapter  
 7481 on tracking calculations). Compared to the dipole based separation and a late focusing,  $Q'$  is  
 7482 reduced to a level of 13 % horizontally and to a level of 11 % in the vertical plane. The details  
 7483 are listed in Tab. 10.25. Further studies will investigate the orbit correction scheme of the new  
 IR, and an eventual interplay of the solenoid fringe field and the quadrupoles.

	Dipole based separation	Early focusing scheme
$\xi_x$	-116	-15
$\xi_y$	-294	-32

**Table 10.25:** Chromaticity of the dipole based separation scheme and the new lattice based on early focusing, off-axis quadrupole lenses.

7484

7485 The influence of the electron doublet magnets on the proton optics is marginal – as can be  
 7486 expected due to the large difference in beam rigidity: If uncorrected, the electron doublet creates  
 7487 a distortion (a so-called *beta-beat*) of the proton optics of roughly 1 %. Still it has been calculated  
 7488 and taken into account in the context of a re-match of the proton beam optics.

7489 Combining the two improvement factors, namely the effective lengthening of  $L^*$  due to the  
 7490 use of a half quadrupole in front of the superconducting triplet, and the early focusing scheme  
 7491 in the lattice of the electrons, leads to an overall improvement of the interaction region with  
 7492 respect to synchrotron radiation power and critical energy that is shown in Fig. 10.40. The  
 7493 overall improvement factor is plotted with reference to the baseline dipole separation design  
 7494 with originally  $\beta = 2250\text{ m}$  at the separation point  $s = L^*$ . Using a normal conducting half  
 7495 quadrupole in combination with the early focusing scheme, the power of the emitted synchrotron  
 7496 radiation is reduced by 48 % for an electron beam stay-clear of  $20\sigma$ .

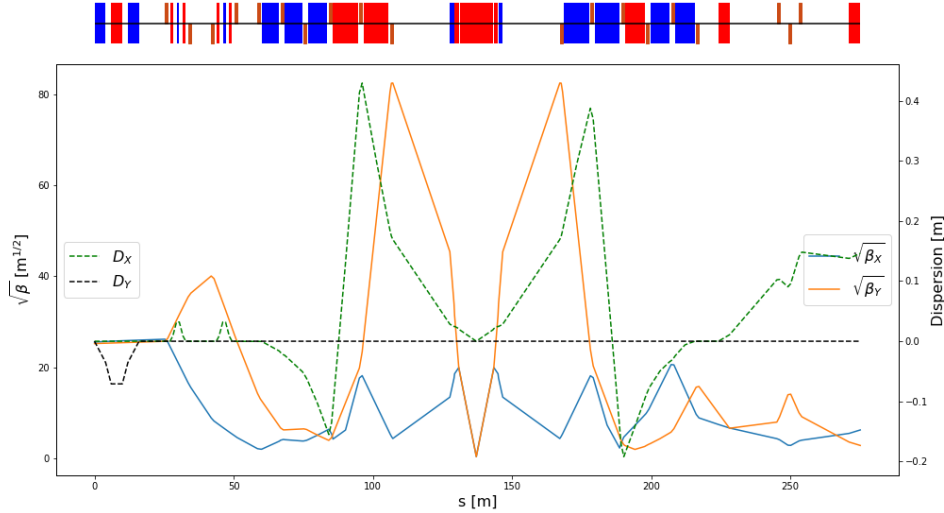


**Figure 10.39:** Electron beam optics for the new lattice including the early focusing scheme. The offset of the new doublet quadrupoles are chosen to provide the same separation field as in the dipole. The new optics is matched on the left side of the plot to the end of the acceleration linac. The right hand side is connected to Arc 6, the beginning of the decelerating ERL part. At the position of the first superconducting proton magnet the  $\beta$ -function in the (horizontal) separation plane of the electron beam is reduced to 90 m for lowest possible synchrotron radiation load.

7497 The estimated synchrotron radiation power and critical energy for the different optimisations  
 7498 are plotted in Fig. 10.40 and the results are summarised in Tab. 10.26. Referring to a beam  
 7499 energy of 49.19 GeV and the design current of 20 mA an overall power of 16.2 kW is emitted  
 7500 within one half of the interaction region.

Optimised scheme	Synchrotron radiation		Critical energy	
	Radiation power [kW]	Critical energy [keV]	Radiation power [kW]	Critical energy [keV]
Reference design	30.8	300	30.8	300
Dipole length optimum	26.8	336	30.8	300
Half quadrupole optimum	22.2	331	26.1	295
Off-centered quadrupoles opti.	19.3	290	22.1	259
Half quad. + Off-centered quad. opti.	16.2	265	17.4	255

**Table 10.26:** Synchrotron radiation power and critical energy for the different optimised separation schemes.

7501 Depending on the boundary conditions imposed by the integration of the particle detector, one  
 7502 of the two optimum layouts can be chosen – or a combination of both, i.e. an overall minimum  
 7503 defined by critical energy and radiated power.

7504 The basic main parameters of the proton mirror plate half quadrupole are summarised in  
 7505 Tab. 10.27 for the two optimum scenarios explained above: the optimum found for smallest  
 7506 synchrotron radiation power and the optimum for smallest critical energy of the emitted radi-  
 7507 ation. The values result from the optics studies of the previous sections. The presented gradients  
 7508 lead to a pole tip field of  $B_p \approx 1.3$  T.

7509 In both cases, the proton aperture radius has been chosen to include an orbit tolerance of 2 mm,  
 7510 a 10% tolerance on the beam size due to optics imperfections (beta-beating) and a beam size

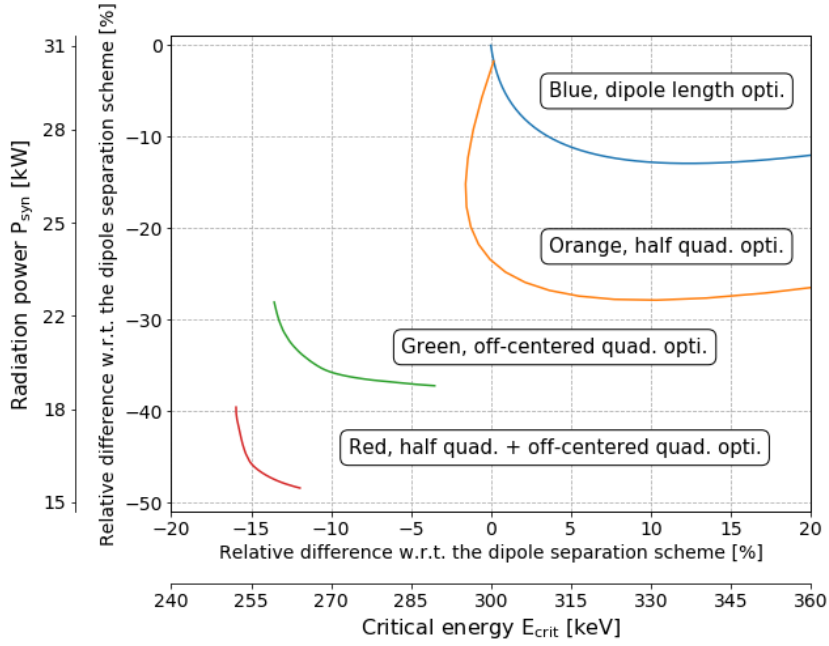


**Figure 10.40:** Relative differences with respect to the original single dipole separation scheme. The synchrotron radiated power is plotted as a function of the critical energy for different optimisation results: only optimising the dipole length (blue), only using a mirror quadrupole (orange), only using off-centered quadrupoles (green) and combining the mirror quadrupole with an earlier focusing (red).

Half quadrupole parameter	Unit	Minimum synchrotron radiation power	Minimum critical energy
$\gamma\epsilon_p$	mm-mrad	2.50	2.50
Gradient	T/m	48.2	50.7
Aperture radius	mm	27.0	25.6
Length	m	6.84	2.08

**Table 10.27:** Magnet gradient of the proposed half quadrupole for lowest synchrotron radiation power and lowest critical energy. An aperture of  $15\sigma + 20\%$  beta-beating + 2 mm orbit tolerances has been assumed.

7511 that corresponds to  $n = 15\sigma$  for a proton beam normalised emittance  $\epsilon_p = 2.50\mu m$ . A value  
7512 that is comfortably larger than the requirements of the HL-LHC standard lattice. The injection  
7513 proton optics has been taken into account and although it features a larger emittance it clearly  
7514 fit in the aperture, see the red dashed line in Fig. 10.41. The electron beam and the non-colliding  
7515 proton beam will pass through the field free region delimited by the mirror plate.

7516 The aperture requirements inside the half quadrupole are determined on one side by the colliding  
7517 proton beam optics in the main aperture of the magnet. The beam separation scheme and optics  
7518 of electron and non-colliding proton beam on the other side have to fit into the field free region  
7519 beyond the mid plane of the mirror plate. As described below, a crossing angle of 7 mrad is  
7520 assumed for the non-colliding protons. These requirements are illustrated in Fig. 10.41. For  
7521 the case of smallest synchrotron radiation power, the three beams are plotted at the entrance  
7522 and exit of the quadrupole lens. For both proton beams the beam size shown in the graph  
7523 corresponds to 15 sigma plus 2 mm orbit tolerance and 10% beam size beating. Due to the  
7524 mini-beta optics the colliding proton beam fills nearly the given aperture of the magnet. The

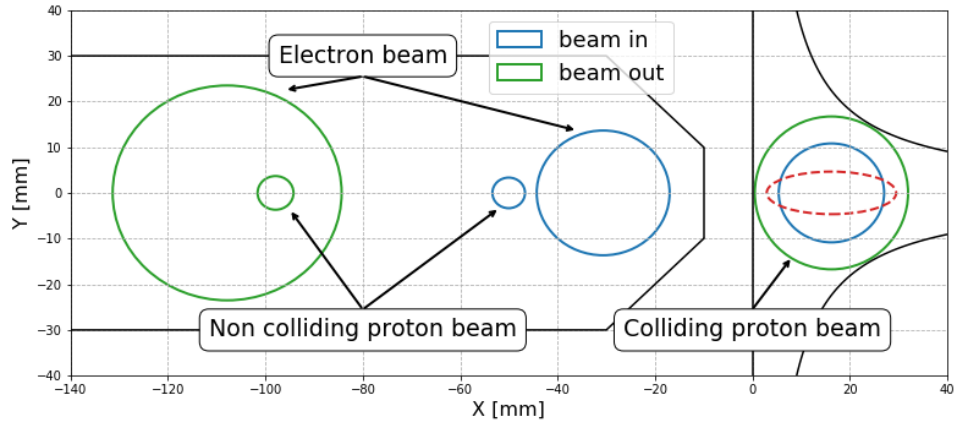


**Figure 10.41:** The position of the three beams at the entrance (blue) and exit (green) of the half quadrupole. The colliding proton beam is centered inside the main magnet aperture, while the second proton beam and the electrons are located in the field free region. The dashed red line represents the injection proton beam at the output of the half quadrupole.

7525 non-colliding proton beam follows a relaxed optics with very limited aperture need. The envelope  
 7526 of the electron beam is shown for  $20 \sigma$  beam size in both transverse planes.

7527 In contrast to the proton half quadrupole, the doublet magnets of the early focusing scheme  
 7528 will house the three beams in one single aperture. In addition to the beam envelopes, the offset  
 7529 that has been chosen to provide the beam separation effect has to be taken into account and  
 7530 included in the aperture considerations.

In Fig. 10.42 the situation is visualised. On the left side the first off-center quadrupole (powered

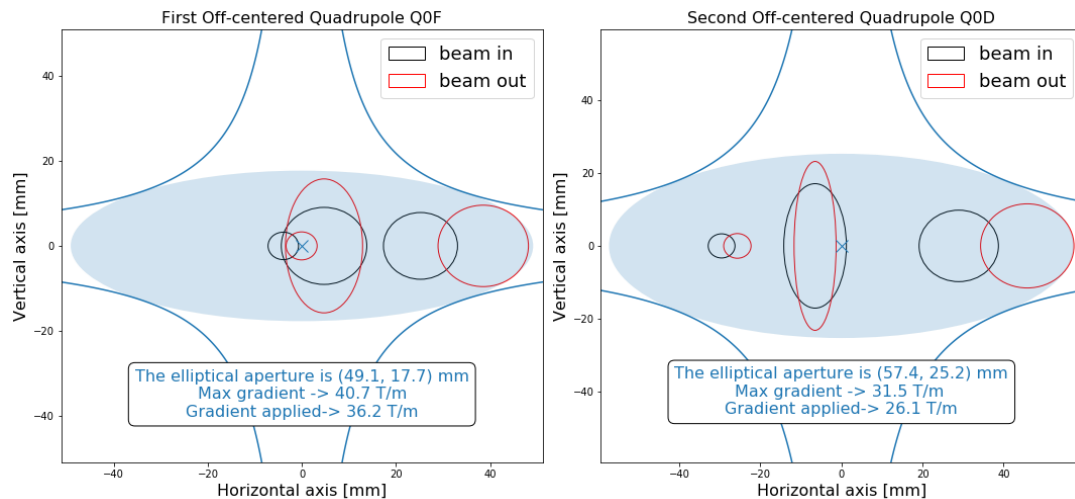


**Figure 10.42:** The position of the three beams at the entrance (black) and exit (red) of the electron doublet magnets. Following the internal convention,  $15 \sigma$  plus 20% beta beating plus 2 mm orbit tolerances beam envelopes are chosen for the proton beams. The beam size of the electrons refer to  $20 \sigma$ . From left to right the three beams are respectively the non colliding proton beam (tiny circles), electron beam (squeezed ellipses) and the colliding proton beam.

7531 as focusing lens) is presented. Following the field direction, the electron beam is offset towards  
 7532 the outer side of the ring (right side of the plot) as defined by the proton beam closed orbit.  
 7533 The right part of the figure shows the second quadrupole (powered as defocusing lens) with  
 7534

7535 the electron beam offset shifted to the other direction. In order to provide sufficient aperture  
 7536 for the three beams, an elliptical shape has been chosen for the vacuum chamber. It defines  
 7537 enough space for the beam envelopes and the off-centre design trajectories. The black ellipses  
 7538 correspond to the beams at the entrance of the magnet while the red shapes represent the beams  
 7539 at the exit. From left to right the three beams are respectively the non colliding proton beam  
 7540 (tiny circles), electron beam (squeezed ellipses) and the colliding proton beam. As defined before  
 7541 we refer to a beam size of  $20\sigma$  in case of the electrons and  $15\sigma$  plus beta-beating plus 2  
 7542 mm orbit tolerance for the colliding and non-colliding proton beam.

7543 In this context it should be pointed out that the non-colliding proton beam, travelling in the  
 7544 same direction as the electrons, is shifted in time by half the bunch spacing. While the projected  
 7545 beam envelopes in Figs. 10.42 and 10.41 seem to overlap in the transverse plane, they are well  
 7546 separated by 12.5 ns, corresponding to 3.75 m, in the longitudinal direction.

7547 The minimum required gradients and pole tip radius of the quadrupoles of the doublet are listed  
 in Tab. 10.28. Following the increasing beam size after the IP, the two quadrupoles are optimised

Parameter	Unit	Q0F	Q0D
$\gamma\epsilon_e$	mm-mrad	50	50
$\gamma\epsilon_p$	mm-mrad	2.50	2.50
Gradient	T/m	36.2	26.1
Min. pole-tip radius	mm	28.9	38.1
Length	m	1.86	1.86

**Table 10.28:** Magnet gradient and pole tip aperture of the quadrupoles of the doublet for the synchrotron power optimum.

7548 for sufficient free aperture for the colliding beams and their design orbits. Accordingly a different  
 7549 layout has been chosen for the magnets, to provide the best conditions for the radiation power  
 7550 and critical energy. An alternative approach has been studied, based on a single quadrupole  
 7551 design for both lenses of the doublet. While an optics solution still is possible, it does however  
 7552 not allow for minimum radiation power and sets more stringent requirements on the shielding  
 7553 and absorption of the synchrotron light fan.  
 7554

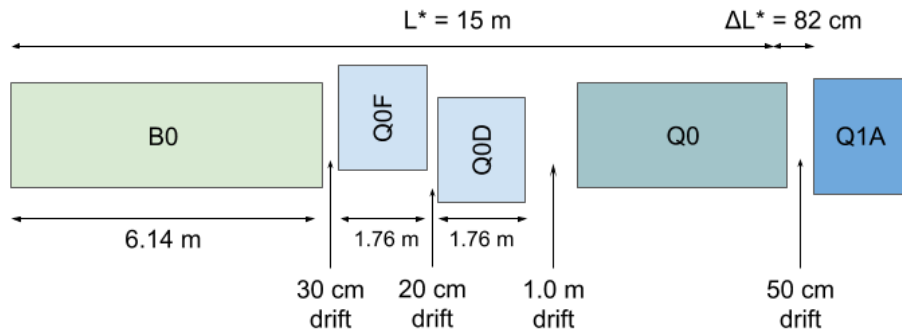


**Figure 10.43:** Possible optimised design featuring a 1.0 m drift between the off-centered quadrupoles and the half quadrupole in order to leave space for shielding material.

7555 The chromatic effect of the two lattice versions as a function of the momentum spread is shown  
 7556 in Fig. 10.44. The lattice based on a single dipole magnet and late focusing of the electron  
 7557 beam shows an increase of the  $\beta$  function of up to 40% in the vertical plane for particles with a  
 7558 momentum deviation up to the design value of  $\frac{\Delta p}{p} = 2.6 \cdot 10^{-4}$  (vertical cursor line in the graph)

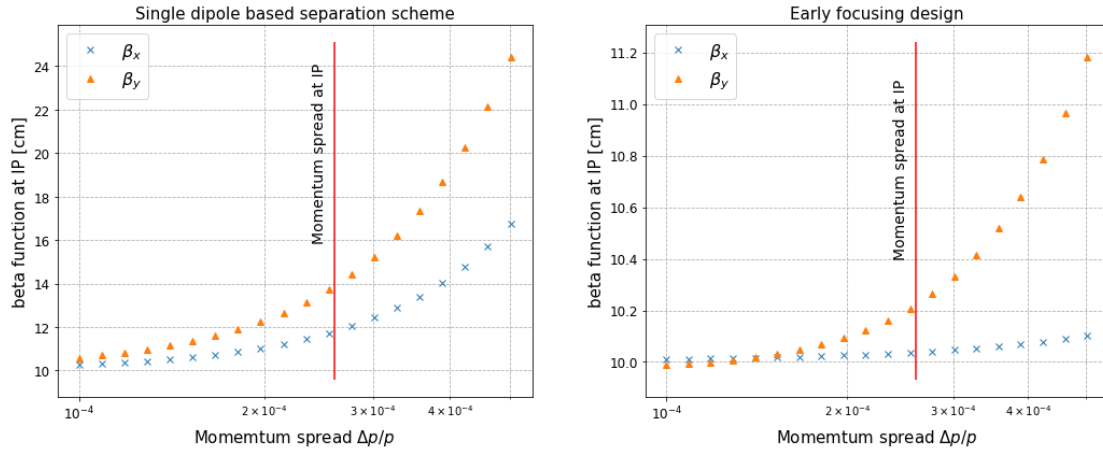


**Figure 10.44:** Beta function at the IP as a function of the momentum spread. Left : Situation for the single dipole based separation scheme. Right : With the design featuring an earlier focusing. The graphs show the increase of  $\beta^*$  due to the chromaticity of the lattice.

7559 and a corresponding luminosity loss of 20% for those particles (see Fig. 10.45). The optimised  
 7560 design, based on the early focusing scheme, shows a much reduced chromatic effect and the  
 7561 resulting off-momentum beta-beating at the IP is limited to a few percent. As direct consequence  
 7562 the luminosity loss is well below the 1.5% level. A special local chromaticity correction scheme,  
 7563 therefore, dealing with the aberrations at IP, is thus not considered as necessary. Further studies  
 7564 will include the recirculation of the beam post-collision and the energy recovery performance and  
 7565 might nevertheless highlight the need of explicit sextupoles to mitigate the growing momentum  
 7566 spread through the deceleration process and to avoid beam losses.

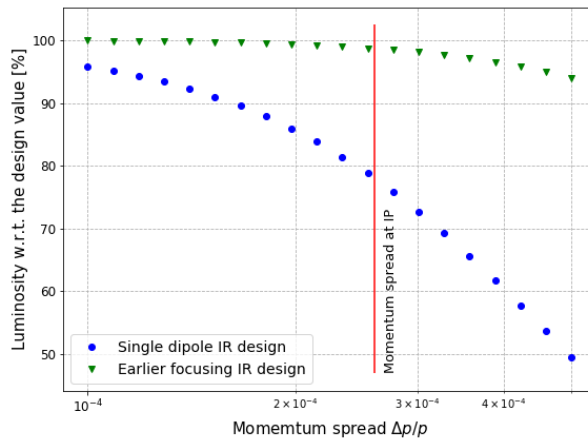


**Figure 10.45:** Luminosity as a function of the momentum spread for the single dipole based separation scheme (blue circles) and the design featuring an earlier focusing (green triangles).

## 7567 10.7.4 Interaction Region Magnet Design

### 7568 Triplet Magnet Design

7569 While the Q1 magnets remain in the range achievable with the well proven Nb-Ti superconduc-  
 7570 tors, operated at 1.8 K, the Q2 magnets require Nb<sub>3</sub>Sn technology at an operation temperature  
 7571 of 4.2 K. The working points on the load-line are given for both superconducting technologies in  
 7572 Fig. 10.46.

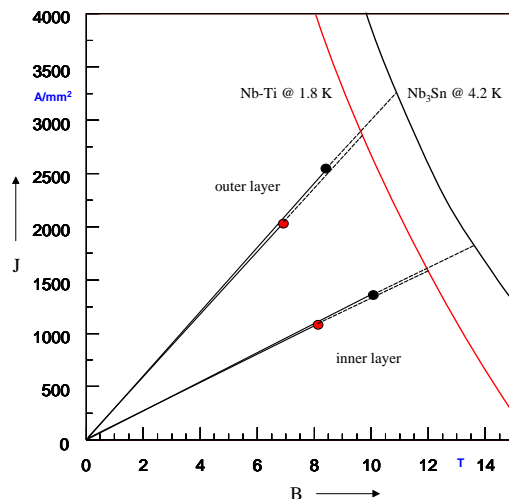


**Figure 10.46:** Working points on the load-line for both Nb-Ti and Nb<sub>3</sub>Sn variants of Q1A.

7573 The thickness of a coil layer is limited by the flexural rigidity of the cable, which will make the  
 7574 coil-end design difficult. Therefore multi-layer coils must be considered. However, a thicker,  
 7575 multi-layer coil will increase the beam separation between the proton and the electron beams.  
 7576 The results of the field computation are given in Tab. 10.29.

Magnet parameter	Unit	Magnet type			
		Q1A	Q1B	Q2 type	Q3 type
Superconductor type		Nb-Ti	Nb-Ti	Nb <sub>3</sub> Sn	Nb <sub>3</sub> Sn
Coil aperture radius $R$	mm	20	32	40	45
Nominal current $I_{\text{nom}}$	A	7080	6260	7890	9260
Nominal gradient $g$	T/m	252	164	186	175
Percentage on the load line	%	78	64	71	75
Beam separation distance $S_{\text{beam}}$	mm	106-143	148-180	233-272	414-452

**Table 10.29:** Main triplet magnet parameters

7577 Unlike with the design proposed in the CDR of 2012 [1], the increased beam separation distance  
 7578 between the colliding proton beam and the electron beam makes it possible to neglect the fringe  
 7579 fields in the electron beam pipe. For the Q2 and Q3 magnets, the electron beam is outside  
 7580 of the quadrupole cold-mass and consequently, an HL-LHC inner-triplet magnet design can be  
 7581 adapted.

7582 For the Nb<sub>3</sub>Sn material we assume composite wire produced with the internal Sn process (Nb  
 7583 rod extrusions) [843]. The non-Cu critical current density is 2900 A/mm<sup>2</sup> at 12 T and 4.2 K.  
 7584 The filament size of 46  $\mu\text{m}$  in Nb<sub>3</sub>Sn strands give rise to higher persistent current effects in  
 7585 the magnet. The choice of Nb<sub>3</sub>Sn would impose a considerable R&D and engineering design  
 7586 effort, which is however, not more challenging than other accelerator magnet projects, such as  
 7587 the HL-LHC.

7588 The conceptual design of the mechanical structure of the Q1 magnets is shown in Fig. 10.47  
 7589 (right). The necessary prestress in the coil-collar structure, which must be high enough to  
 7590 avoid unloading at full excitation, cannot be exerted with the stainless-steel collars alone. Two  
 7591 interleaved sets of yoke laminations (a large one comprising the area of the yoke keys and



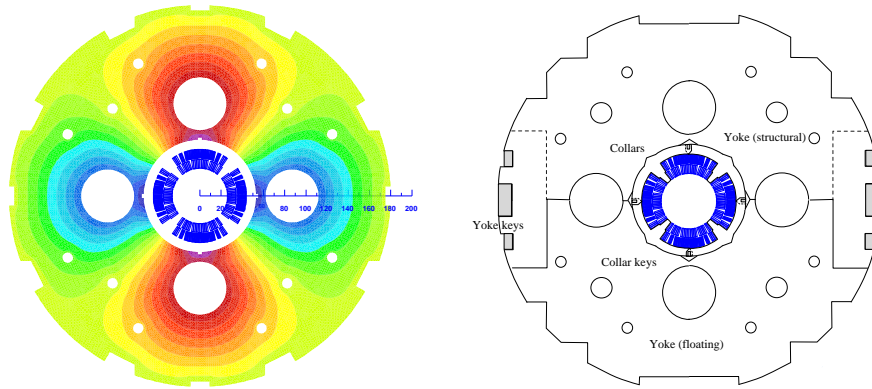


**Figure 10.47:** Conceptual design of the final focus septa Q1. Left: Magnetic vector potential (field lines). Right: Sketch of the mechanical structure.

7592 a smaller, floating lamination with no structural function) provide the necessary mechanical  
 7593 stability of the magnet during cooldown and excitation. Preassembled yoke packs are mounted  
 7594 around the collars and put under a hydraulic press, so that the keys can be inserted. The sizing  
 7595 of these keys and the amount of prestress before the cooldown will have to be calculated using  
 7596 mechanical FEM programs. This also depends on the elastic modulus of the coil, which has to  
 7597 be measured with a short-model equipped with pressure gauges. Special care must be taken to  
 7598 avoid nonallowed multipole harmonics because the four-fold symmetry of the quadrupole will  
 7599 not entirely be maintained.

7600 For the Q2 and Q3 magnets, a HL-LHC inner triplet desing using a bladder and key mechanical  
 7601 structure can be adapted.

## 7602 Normal-Conducting Magnet Design

7603 The proposed mini-beta doublet of the electron lattice, providing an early focusing of the beam,  
 7604 and the normal conducting proton-half quadrupole are new magnet concepts. These have been  
 7605 studied conceptually to determine their technical feasibility. The geometry of the QNC magnet  
 7606 is shwon in Fig. 10.48 (left). Left of the mirror plate, the field free region will provide space for  
 7607 the electron beam and the non-colliding proton beam. The thickness of the mirror plate at the  
 7608 magnet mid-plane is 20 mm, allowing for sufficient mechanical stability at the minimal beam  
 7609 separation between the electron and proton beams.

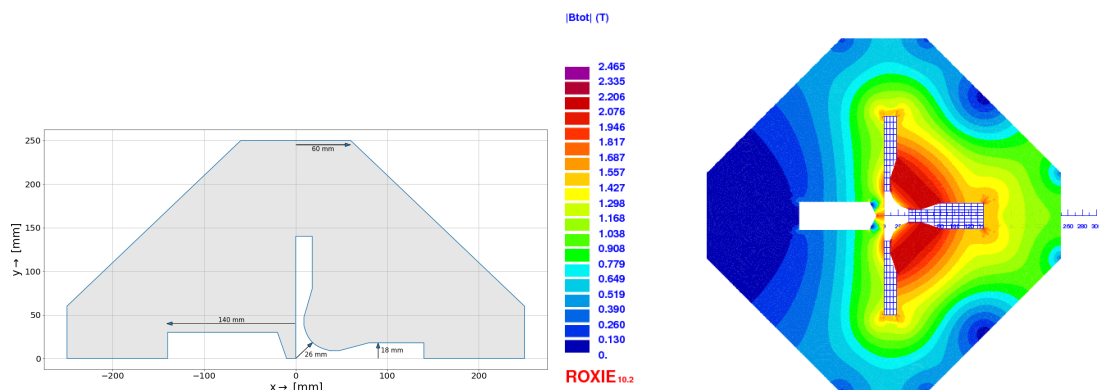


**Figure 10.48:** Left: Mechanical layout of the new half quadrupole for the proton beam. Right : Field distribution in the half quadrupole for the proton beam.

7610 Field calculations, using the magnet design code ROXIE [844] are presented in Fig. 10.48 (right).  
7611 The achieved field gradient is 50 T/m for a current of 400 A, assuming a current density of  
7612 21.14 A/mm<sup>2</sup>. This is in line with conductor geometries used for normal conducting magnets  
7613 installed in the CERN injector complex, for example, ID: PXMQNDD8WC, which is rated at  
7614 860 A corresponding to 45.45 A/mm<sup>2</sup>. A more comprehensive design study must also include a  
7615 further reduction of the multipole field components.

7616 The geometry of the Q0F and Q0D quadrupoles are given in Fig. 10.42 and the main speci-  
7617 fications are provided in Tab. 10.28. A maximum magnetic field of 1.2 T at the pole tip is well  
7618 within reach for a normal conducting quadrupole.

## 7619 10.8 Civil Engineering

7620 Since the beginning of the LHeC study which proposes a electron-hadron collider, various shapes  
7621 and sizes of the *eh* collider were studied around CERN region. Two main options were initially  
7622 considered, namely the Ring-Ring and the Linac-Ring. For civil engineering, these options  
7623 were studied taking into account geology, construction risks, land features as well as technical  
7624 constraints and operations of the LHC. The Linac-Ring configuration was selected, favouring  
7625 a higher achievable luminosity. This chapter describes the civil engineering infrastructure re-  
7626 quired for an Energy Recovery Linac (ERL) injecting into the ALICE cavern at Point 2 LHC.  
7627 Fig. 10.49 shows three options for the ERL of different sizes, represented as fractions of the LHC  
circumference, respectively 1/3, 1/4 and 1/5 of the LHC circumference.



**Figure 10.49:** Racetrack options proposed for LHeC at Point 2 of the LHC. The color coding illustrated different options with 1/3, 1/4 and 1/5 of the LHC circumference, resulting in different electron beam energies.

7628

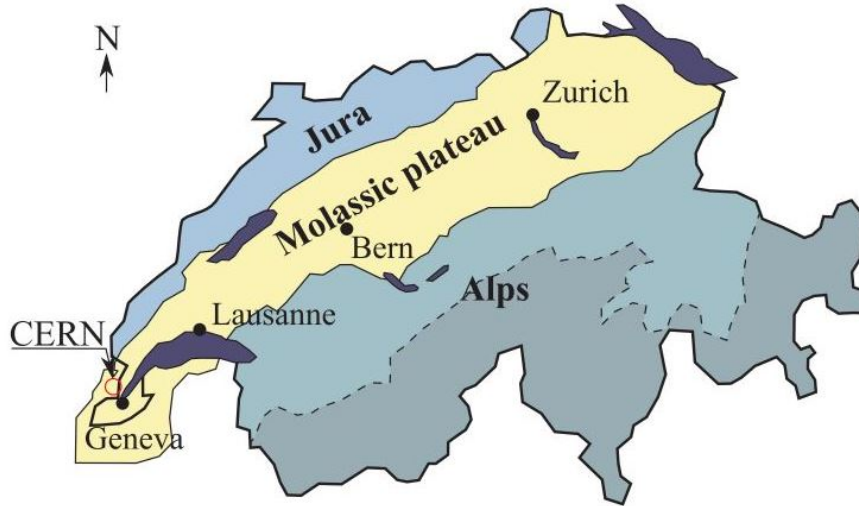


Figure 10.50: Simplified map of Swiss geology.

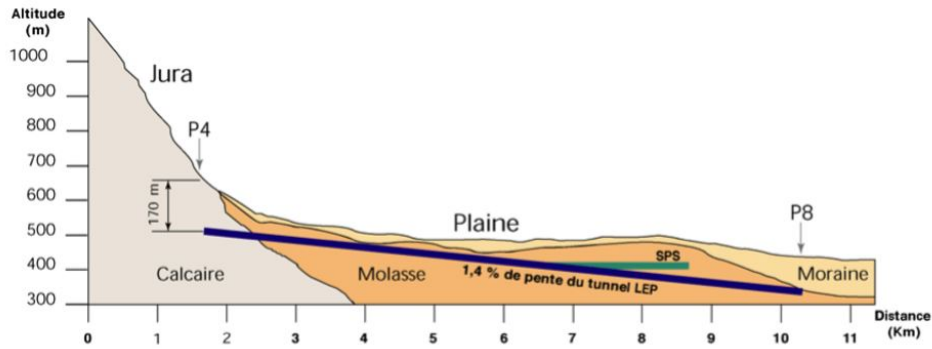
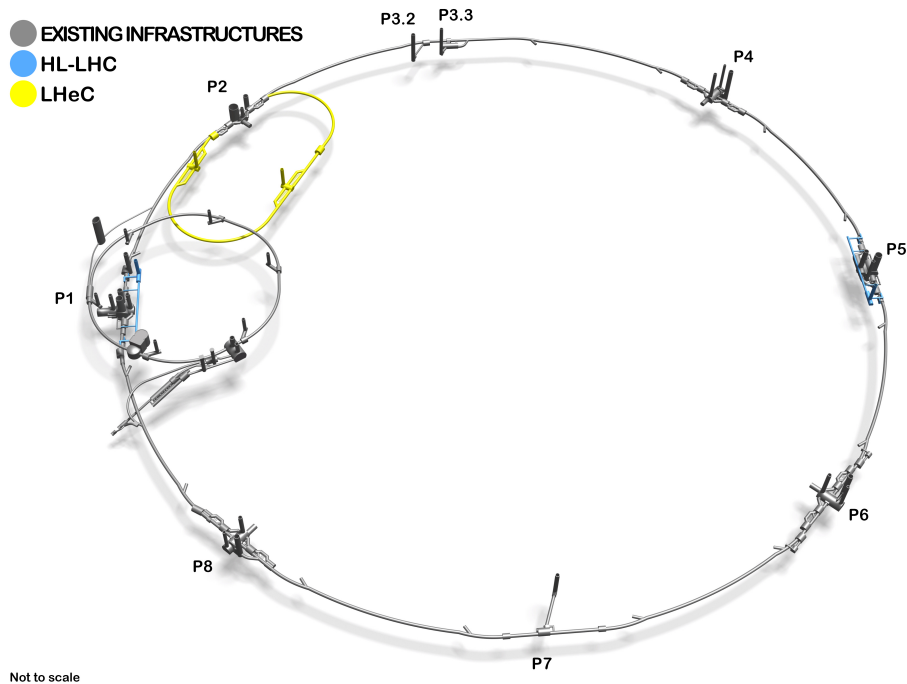


Figure 10.51: Geological profile of the LHC tunnel.

### 7629 10.8.1 Placement and Geology

7630 The proposed siting for the LHeC is in the North-Western part of the Geneva region at the  
 7631 existing CERN laboratory. The proposed Interaction Region is fully located within existing  
 7632 CERN land at LHC Point 2, close to the village of St. Genis, in France. The CERN area is  
 7633 extremely well suited to housing such a large project, with well understood ground conditions  
 7634 having several particle accelerators in the region for over 50 years. Extensive geological records  
 7635 exist from previous projects such as LEP and LHC and more recently, further ground inves-  
 7636 tigations have been undertaken for the High-Luminosity LHC project. Any new underground  
 7637 structures will be constructed in the stable molasse rock at a depth of 100–150 m in an area with  
 7638 low seismic activity.

7639 The LHeC is situated within the Geneva basin, a sub-basin of the large molassic plateau  
 7640 (Fig. 10.50). The molasse is a weak sedimentary rock which formed from the erosion of the  
 7641 Alps. It comprises of alternating layers of marls and sandstones (and formations of interme-  
 7642 diate compositions), which show a high variety of strength parameters [845]. The molasse is  
 7643 overlaid by the Quaternary glacial moraines. A simplified geological profile of the LHC is shown  
 7644 in Fig. 10.51. Although placed mainly within the molasse plateau, one sector of the LHC is  
 7645 situated in the Jura limestone.



**Figure 10.52:** 3D Schematic showing proposed underground structures of LHeC (shwon in yellow). The HL-LHC structures are highlighted in blue.

7646 The physical positioning of the LHeC has been developed based on the assumption that the  
 7647 maximum underground volume should be placed within the molasse rock and should avoid as  
 7648 much as possible any known geological faults or environmentally sensitive areas. Stable and dry,  
 7649 the molasse is considered a suitable rock type for Tunnel Boring Machines (TBM) excavation.  
 7650 In comparison, CERN has experienced significant issues with the underground construction of  
 7651 sector 3-4 in the Jura limestone. There were major issues with water ingress at and behind the  
 7652 tunnel face [846]. Another challenging factor for limestone is the presence of karsts. These are  
 7653 formed by chemical weathering of the rock and often they are filled with water and sediment,  
 7654 which can lead to water infiltration and instability of the excavation.

7655 The ERL will be positioned inside the LHC layout, in order to ensure that new surface facilities  
 7656 are located on existing CERN land. The proposed underground structures for the LHeC with  
 7657 an electron beam energy of 60 GeV are shown in Fig. 10.52. The LHeC tunnel will be tilted  
 7658 similarly to the LHC at a slope of 1.4% to follow a suitable layer of molasse rock.

### 7659 10.8.2 Underground infrastructure

7660 The underground structures proposed for LHeC option 1/3 LHC require a 9 km long tunnel  
 7661 including two LINACs. The internal diameter of the tunnel is 5.5 m. Parallel to the LINACs, at  
 7662 10m distance apart, there are the RF galleries, each 1070 m long. Waveguides of 1 m diameter  
 7663 and four connection tunnels are connecting the RF galleries and LINACs. These structures are  
 7664 listed in Tab. 10.30. Two additional caverns, 25 m wide and 50 m long are required for cryogenics  
 7665 and technical services. These are connected to the surface via two 9 m diameter shafts, provided  
 7666 with lifts to allow access for equipment and personnel. Additional caverns are needed to house  
 7667 injection facilities and a beam dump. As shown in Tab. 10.30, the underground structures  
 7668 proposed for LHeC options 1/5 LHC and 1/3 LHC are similar with the exception of the main  
 7669 tunnel and the RF galleries which have different lengths.

Structure	Quantities	Span [m]	1/3 LHC	1/5 LHC
			Length [m]	Length [m]
Machine tunnels	-	5.5	9000	5400
Service caverns	2	25	50	50
Service shafts	2	9	80	80
Injection caverns	1	25	50	50
Dump cavern	1	16.8	90	90
Junction caverns	3	16.8	20	20
RF galleries	2	5.5	1070	830
Waveguide connections	50	1	10	10
Connection tunnels	4	3	10	10

**Table 10.30:** List of underground structures for LHeC for two different options with 1/3 or 1/5 of the LHC circumference.

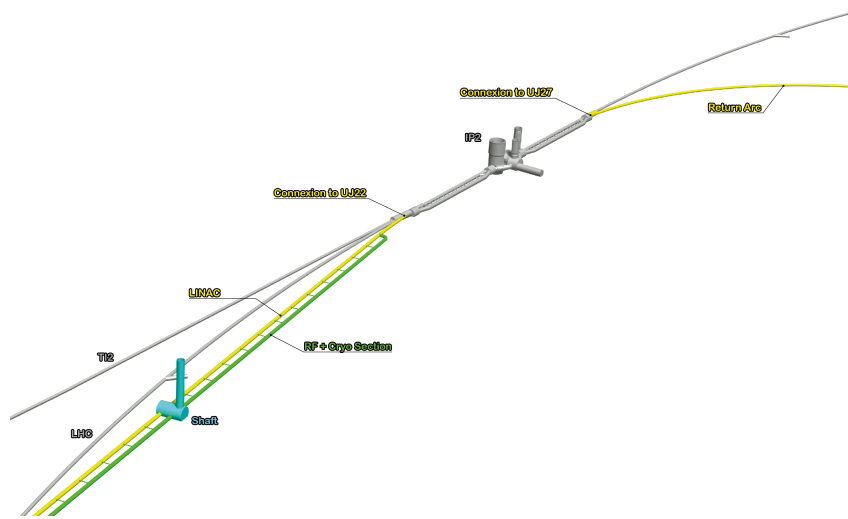


**Figure 10.53:** ERL injection area into IP2 and junction cavern

7670 Shaft locations were chosen such that the surface facilities are located on CERN land. The scope  
7671 of work for surface sites is still to be defined. New facilities are envisaged for housing technical  
7672 services such as cooling and ventilation, cryogenics and electrical distribution.

7673 In addition to the new structures, the existing LHC infrastructure requires some modifications.  
7674 To ensure connection between LHC and LHeC tunnels, the junction caverns UJ22 and UJ27  
7675 need to be enlarged. Fig. 10.53 shows the location of these caverns. Localised parts of the  
7676 cavern and tunnel lining will be broken out to facilitate the excavation of the new spaces and  
7677 the new connections, requiring temporary support.

7678 Infrastructure works for LEP were completed in 1989, for which a design lifespan of 50 years  
7679 was specified. If the LHC infrastructure is to be re-used, refurbishment and maintenance works  
7680 are needed.

### 7681 10.8.3 Construction Methods

7682 A TBM would be utilised for the excavation of the main tunnel to achieve the fastest construc-  
7683 tion. When ground conditions are good and the geology is consistent, TBMs can be two to four



**Figure 10.54:** Left: Roadheader being used for shaft excavation at HL-LHC Point 1. Right: Rockbreaker used for new service tunnels excavation at HL-LHC Point 5 (Credit: Z. Arenas).

7684 times faster than conventional methods. A double shield TBM could be employed, installing  
 7685 pre-cast segments as primary lining, and injecting grouting behind the lining.

7686 For the excavation of the shafts, caverns and connection tunnels, typical conventional techniques  
 7687 could be used. Similar construction methods used during HL-LHC construction can be adopted  
 7688 for LHeC, for example using roadheaders and rockbreakers. This machinery is illustrated in  
 7689 Fig. 10.54, showing the excavation works at Point 1. One main constraint that dictated what  
 7690 equipment to be used for the HL-LHC excavation, was the vibration limit. Considering the  
 7691 sensitivity of the beamline, diesel excavators have been modified and equipped with an electric  
 7692 motor in order to reduce vibrations that could disrupt LHC operation. Similar equipment could  
 7693 be required for LHeC, if construction works are carried out during operation of the LHC.

7694 Existing boreholes data around IP2 shows that the moraines layer is approximately 25–35 m deep  
 7695 before reaching the molasse. Temporary support of the excavation, for example using diaphragm  
 7696 walls is recommended. Once reaching a stable ground in dry conditions, common excavation  
 7697 methods can be adopted. The shaft lining will consist of a primary layer of shotcrete with  
 7698 rockbolts and an in-situ reinforced concrete secondary lining, with a waterproofing membrane  
 7699 in between the two linings.

#### 7700 10.8.4 Civil Engineering for FCC-eh

7701 A facility allowing collisions between protons and electrons was considered in the study for the  
 7702 Future Circular Collider (FCC). Fig. 10.55 shows the baseline position for FCC and the lepton  
 7703 ring located at Point L.

7704 During FCC feasibility stage, a bespoke GIS based tool (the Tunnel Optimisation Tool – TOT)  
 7705 was used to optimise the placement and layout of the FCC ring. The current baseline location  
 7706 was chosen such that the FCC tunnel is placed in preferable geology (90% of the tunnel is in  
 7707 molasse), the depth of the shafts and the overburden is minimised and tunnel under the Geneva  
 7708 Lake goes through the lake bed, passing through reasonably stable ground. More investigations  
 7709 are needed to determine the feasibility of tunnelling under the Geneva Lake. The baseline  
 7710 position also allows connections to the LHC. Fig. 10.56 shows the geological profile of the tunnel  
 7711 in baseline position. TOT was used to evaluate different layouts and positions for the FCC  
 7712 ring and assess the impact on the location of the lepton ring. The candidate locations for the  
 7713 *eh* IR were the experimental points A, B, G and L. Point L was selected because it provides  
 7714 good geological conditions, being fully housed in the molasse layer at a depth of around 180 m.  
 7715 In comparison, Point G is much deeper, Point A is challenging due to proximity of the LHC

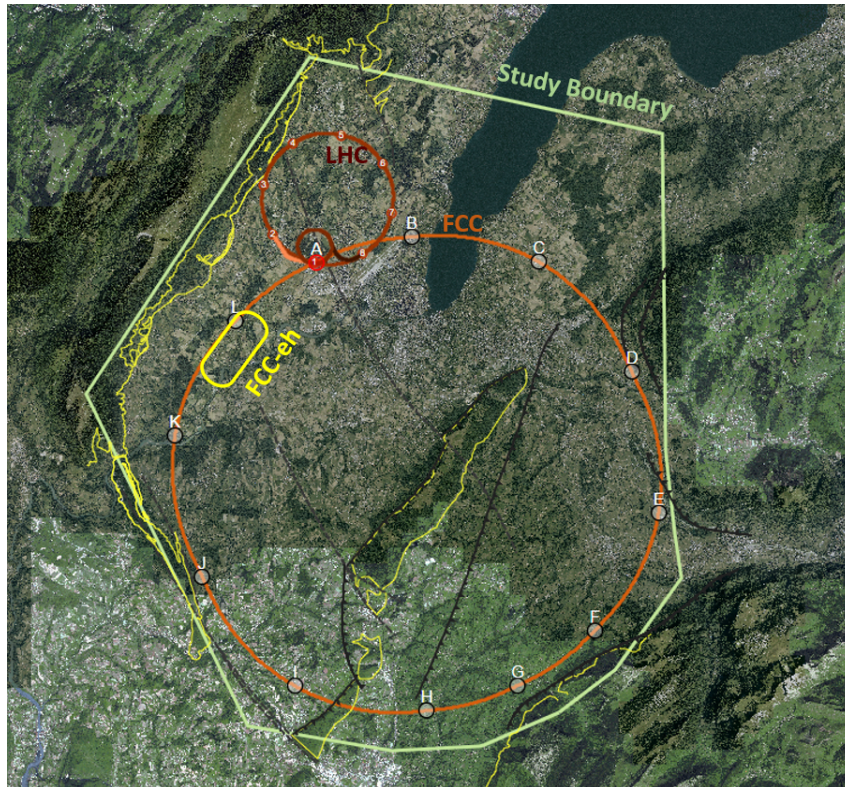


**Figure 10.55:** Baseline position and layout for FCC. The lepton ring location is shown at Point L.

7716 and Point B is located in a congested urban area. Similarly to LHeC, the lepton ring will be  
 7717 located inside the FCC ring, in this instance to avoid the Jura limestone. The entire FCC-eh  
 7718 infrastructure is located in the molasse.

7719 The geological data captured within the TOT tool was collected from various sources includ-  
 7720 ing previous underground projects at CERN, the French Bureau de Recherches Géologiques et  
 7721 Minières (BRGM), and existing geological maps and boreholes for geothermal and petroleum  
 7722 exploration. The data was processed to produce rock-head maps and to create the geological  
 7723 layers. No ground investigations have been conducted specifically for the FCC project [15]. In  
 7724 order to validate its baseline alignment and determine the geotechnical parameters required for  
 7725 the detailed design, site investigation campaigns will need to be carried out. Some boreholes  
 7726 exist in the region where the tunnel for the lepton ring will be built, reducing the uncertainty  
 7727 of the ground conditions. However, further ground investigations are needed in order to verify  
 7728 the boundary between geological layers. The geological features of interest in this region are the  
 7729 Allondon Fault and possible zones of poor rock and level of limestone, which should be avoided.

7730 The IP will be in the experimental cavern at point L, defined as an experimental point for FCC-  
 7731 hh. The layout of the ERL and the underground infrastructure for the FCC-eh is similar to  
 7732 LHeC (see Table 10.30), with the exception of the shafts which are 180 m deep. The schematic  
 7733 layout and proposed civil engineering structures are shown in Fig. 10.57.

7734 The upper excavation for each shaft will be through the moraines. Based on available geological  
 7735 data, the moraines layer should be approximately 30 m deep. Similar construction methods as  
 7736 described in Section 8.8.3 could be used. For FCC, the alternative technology that has been  
 7737 considered for deep shafts is using a Vertical Shaft Sinking Machine. The junction caverns  
 7738 connecting the ERL tunnel with the FCC tunnel must be designed such that they fit the re-

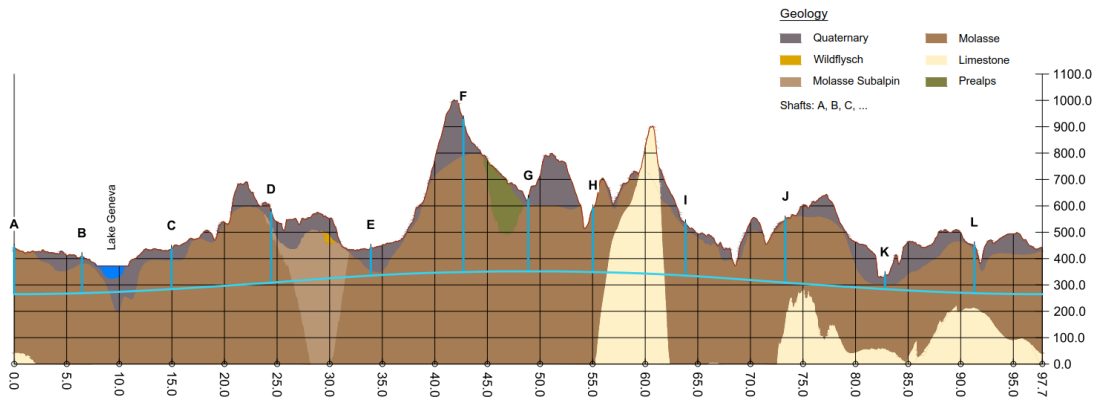


Figure 10.56: Geological profile along FCC tunnel circumference

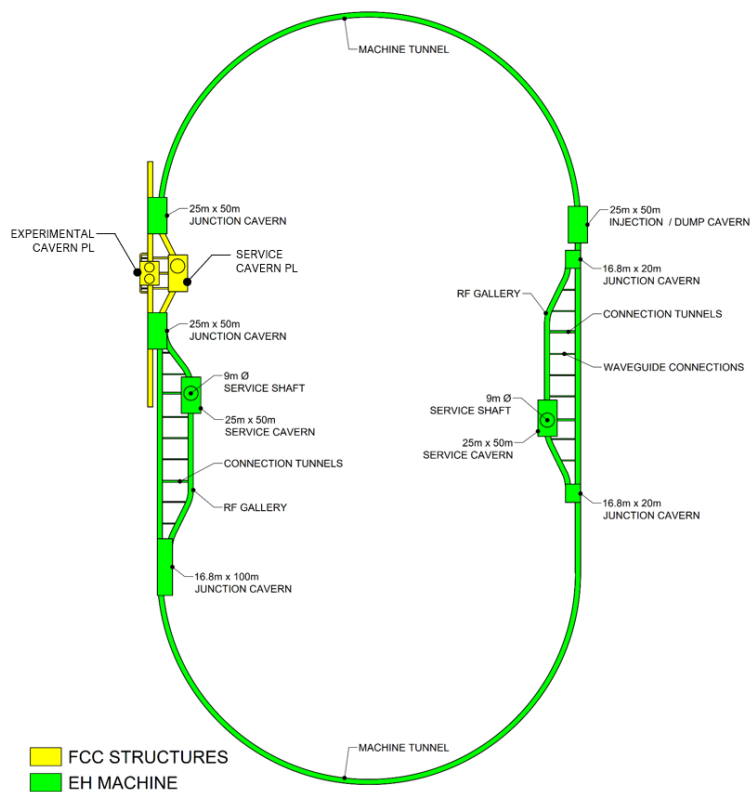


Figure 10.57: Schematic layout showing the proposed underground structures for FCC-eh



7739 quirements for the new collider and the lepton machine. The junction caverns near Point L  
7740 will connect three tunnels, the FCC main tunnel, the ERL tunnel and the RF galleries. These  
7741 caverns will have a 25 m span and 50 m length.

7742 For the FCC TBM excavations, different lining designs have been developed corresponding to  
7743 conditions of the rock [15]. Good ground conditions have been assumed based on available  
7744 geological information in the area where the ERL tunnels are positioned and a single-pass pre-  
7745 cast lining is proposed.

### 7746 **10.8.5 Cost estimates**

7747 The cost for underground civil engineering for FCC-eh facility was estimated to be approximately  
7748 430 MCHF. The construction programme for the lepton accelerator tunnels, caverns and shafts  
7749 is currently integrated into the overall FCC construction schedule.

7750 A detailed cost estimate was prepared for a 9 km ERL located at Point 2 of LHC, using the  
7751 same unit prices as for FCC. More recently for LHeC, the cost figures were adapted to fit the  
7752 smaller version, the 5.4 km racetrack at Point 2 (option 1/5 LHC). The civil engineering costs  
7753 amount to about 25 % of the total project costs. For the 9 km ERL (1/3 LHC option) the civil  
7754 engineering was estimated to 386 MCHF and for a 5.4 km configuration (1/5 LHC) the costs  
7755 would be 289 MCHF. These costs do not include surface structures. Where possible, existing  
7756 surface infrastructure will be re-used.

7757 The cost estimates include the fees for preliminary design, approvals and tender documents  
7758 (12 %), site investigations (2 %) and contractor's profit (3 %). The accuracy range of the cost  
7759 estimates at feasibility stage is  $\pm 30$  %.

### 7760 **10.8.6 Spoil management**

7761 As with all construction projects, environmental aspects play an important role. A detailed study  
7762 is being conducted at CERN to find a potential re-use for of the spoil that will be generated  
7763 from the FCC underground excavations. The total amount of spoil calculated is approximately  
7764 10 million cubic meters, of which 778,000 cubic metres of spoil would be generated from the  
7765 lepton ring tunnel construction.

## Chapter 11

# Technology of ERL and PERLE

### 11.1 Energy Recovery Linac Technology - Status and Prospects

In instances where high beam power is required, the concept of energy recovery presents an attractive solution. Energy recovering linacs (ERLs) are a class of novel accelerators which are uniquely qualified to meet the demands for a wide variety of applications by borrowing features from traditional architectures to generate linac quality beams with near storage ring efficiency [847]. After acceleration through a linac section, the electrons in an ERL are returned 180° out of phase with respect to the radio frequency (RF) accelerating field for energy recovery. The beam deposits energy into cavity fields, which can then accelerate newly injected bunches, thereby effectively canceling the beam loading effects of the accelerated beam. Therefore ERLs can accelerate very high average currents with only modest amounts of RF power. Because the beam is constantly being renewed, it never reaches an equilibrium state. Consequently this provides flexibility to manipulate the phase space and tailor the beam properties for a specific application. Further, since the energy of the decelerated beam is approximately equal to the injection energy, the dump design becomes considerably easier.

#### 11.1.1 ERL Applications

Historically, nearly all ERLs built and operated were used to drive a free-electron laser (FEL). The requirement for high peak current bunches necessitated bunch compression and handling the attendant beam dynamical challenges. In recent years, ERLs have turned from being drivers of light sources toward applications for nuclear physics experiments, Compton backscattering sources and strong electron cooling. Unlike an FEL, these latter use cases require long, high charge bunches with small energy spread. Where once a short bunch length was the key performance metric, now there is a premium on maintaining a small correlated energy spread (with a commensurately long bunch).

#### 11.1.2 Challenges

Energy recovery linacs are not without their own set of challenges. In the following sections a brief survey of some of the most relevant are given. These include collective effects, such as space charge, the multipass beam breakup (BBU) instability, coherent synchrotron radiation (CSR) and the microbunching instability ( $\mu$ BI), beam dynamic issues such as halo, the interaction of the beam with the RF system and other environmental impedances as well as issues related to common transport lines.

## 7798 **Space Charge**

7799 The role of space charge forces (both transverse and longitudinal) often dictate many operational  
7800 aspects of the machine. Maintaining beam brightness during the low energy injection stage is  
7801 vitally important. In addition to the low energy, ERL injectors must also preserve beam quality  
7802 through the merger system that directs the beam to the linac axis. Once injected into the  
7803 linac, the beam energy at the front end is often still low enough that space charge forces cannot  
7804 be neglected. Just as important is the longitudinal space charge (LSC) force which manifests  
7805 itself by an energy spread asymmetry about the linac on-crest phase [848]. The LSC wake acts  
7806 to accelerate the head of the bunch while decelerating the tail. Operating on the rising part  
7807 of the waveform leads to a decrease in the correlated energy spread, while accelerating on the  
7808 falling side leads to an increase. These observations inform where acceleration, and how the  
7809 longitudinal match, is performed.

## 7810 **Beam Breakup Instability**

7811 The beam breakup instability is initiated when a beam bunch passes through an RF cavity  
7812 off-axis, thereby exciting dipole higher-order modes (HOMs). The magnetic field of an excited  
7813 mode deflects following bunches traveling through the cavity. Depending on the details of the  
7814 machine optics, the deflection produced by the mode can translate into a transverse displacement  
7815 at the cavity after recirculation. The recirculated beam induces, in turn, an HOM voltage which  
7816 depends on the magnitude and direction of the beam displacement. Thus, the recirculated beam  
7817 completes a feedback loop which can become unstable if the average beam current exceeds the  
7818 threshold for stability [849]. Beam breakup is of particular concern in the design of high average  
7819 current ERLs utilizing superconducting RF (SRF) technology. If not sufficiently damped by the  
7820 HOM couplers, dipole modes with quality factors several orders of magnitude higher than in  
7821 normal conducting cavities can exist, providing a threat for BBU to develop. For single pass  
7822 ERLs, beam optical suppression techniques – namely, interchanging the horizontal and vertical  
7823 phase spaces to break the feedback loop between the beam and the offending HOM – are effective  
7824 at mitigating BBU [850].

## 7825 **Coherent Synchrotron Radiation**

7826 Coherent synchrotron radiation poses a significant challenge for accelerators utilizing high bright-  
7827 ness beams. When a bunch travels along a curved orbit, fields radiated from the tail of the bunch  
7828 can overtake and interact with the head. Rather than the more conventional class of head-tail  
7829 instabilities where the tail is affected by the actions of the head, CSR is a tail-head instability.  
7830 The net result is that the tail loses energy while the head gains energy leading to an undesirable  
7831 redistribution of particles in the bunch. Because the interaction takes place in a region of dis-  
7832 persion, the energy redistribution is correlated with the transverse positions in the bend plane  
7833 and can lead to projected emittance growth. While there has been much progress in recent years  
7834 to undo the effects of CSR in the bend plane with an appropriate choice of beam optics [851],  
7835 it is more difficult to undo the gross longitudinal distortion caused by the CSR wake. This is  
7836 particularly true in applications where the intrinsic energy spread is small and/or where the  
7837 effect can accumulate over multiple recirculations. One possible mitigation is shielding the CSR  
7838 wake using an appropriately sized beam pipe [852].

## 7839 **Microbunching Instability**

7840 Microbunching develops when an initial density modulation, either from shot noise or from the  
7841 drive laser, is converted to energy modulations through short-range wakefields such as space

7842 charge and CSR. The energy modulations are then transformed back to density modulations  
7843 through the momentum compaction of the lattice. Danger arises when a positive feedback is  
7844 formed and the initial modulations are enhanced. This phenomenon has been studied exten-  
7845 sively, both theoretically and experimentally, in bunch compressor chicanes [853, 854]. Only  
7846 recently has there been a concerted effort to study the microbunching instability in recirculating  
7847 arcs [855–857]. Because the beam is subject to space charge and/or CSR throughout an ERL,  
7848 density modulations can be converted to energy modulations. And because of the native mo-  
7849 mentum compaction of the lattice (in arcs, spreaders/recombiners, chicanes, etc.) those energy  
7850 modulations may be converted back to density modulations. Therefore, ERLs offer potentially  
7851 favorable conditions for seeding the microbunching instability, which requires careful attention  
7852 in the early design stages.

### 7853 **Halo**

7854 Halo is defined as the relatively diffuse and potentially irregularly distributed components of  
7855 beam phase space that can reach large amplitudes. It is of concern because ERL beams are  
7856 manifestly non-Gaussian and can have beam components of significant intensity beyond the  
7857 beam core [858]. Though sampling large amplitudes, halo responds to the external focusing of  
7858 the accelerator transport system in a predictable manner. It is therefore not always at large  
7859 spatial amplitude, but will at some locations instead be small in size but strongly divergent.  
7860 Halo can therefore present itself as *hot spots* in a beam distribution, and thus may be thought  
7861 of as a lower-intensity, co-propagating beam that is mismatched to the core beam focusing,  
7862 timing, and energy. Beam loss due to halo scraping is perhaps the major operational challenge  
7863 for higher-power ERLs. Megawatt-class systems must control losses at unshielded locations to  
7864 better than 100 parts-per-million to stay within facility radiation envelopes. Scaling to 100 MW  
7865 suggests that control must be at the part-per-million level. This has been demonstrated – but  
7866 only at specific locations within an ERL [859].

### 7867 **RF Transients**

7868 Dynamic loading due to incomplete energy recovery is an issue for all ERLs [860]. In some  
7869 machines it is due to unintentional errors imposed on the energy recovered beam; for instance,  
7870 path length errors in large-scale systems. In other machines, such as high power ERL-based FEL  
7871 drivers, it is done intentionally. In cases where there is the potential for rapid changes in the  
7872 relative phase of the energy recovered beam, dynamic loading would be difficult to completely  
7873 control using fast tuners. In such cases adequate headroom in the RF power will have to be  
7874 designed into the system. These transient beam-loading phenomena are widely unrecognized  
7875 and/or neglected. RF drive requirements for an ERL are often viewed as *minimal*, because in  
7876 steady-state operation the recovered beam notionally provides RF power for acceleration. It  
7877 has however been operationally established that RF drive requirements for ERLs are defined  
7878 not by the steady-state, but rather by beam transients and environmental/design factors such  
7879 as microphonics [861]. As a result, the RF power required for stable ERL operation can differ  
7880 dramatically from naïve expectations.

### 7881 **Wakefields and Interaction of Beam with Environment**

7882 As with other system architectures intended to handle high-brightness beams, ERLs can be  
7883 performance-limited by wakefield effects. Not only can beam quality be compromised by in-  
7884 teraction of the beam with environmental impedances, there is also significant potential for  
7885 localized power deposition in beamline components. Resistive wall and RF heating have proven

7886 problematic during ERL operation in the past [862]. Extrapolation of this experience to higher  
7887 bunch charges and beam powers leads to serious concern regarding heating effects. Careful  
7888 analysis and management of system component impedances is required.

### 7889 **Multi-turn, Common Transport**

7890 Future systems must evolve to utilize multiple turns; it is a natural cost optimization method [863]  
7891 and multi-turn systems can in principle provide performance equal to that of 1-pass up/down  
7892 ERLs at significantly lower cost. In addition to the use of multiple turns, cost control motivates  
7893 use of extended lengths of common transport, in which both accelerated and recovered passes  
7894 are handled simultaneously using the same beam lines. This presents unique challenges for high  
7895 energy ERLs, like LHeC in particular, where energy loss due to synchrotron radiation cannot  
7896 be ignored and causes an energy mismatch for common transport lines. But addressing these  
7897 challenges will open up exciting new opportunities for ERLs. In addition to PERLE and LHeC,  
7898 a multi-turn ERL design from Daresbury illustrates the manner in which the cost/complexity  
7899 optimum lies toward shorter linacs, more turns, and multiple beams in fewer beam lines [789].  
7900 This also drives the use of multiple turns in stacking rings for hadron cooling; the more turns  
7901 the cooling beam can be utilized, the lower the current required from the driver ERL, which  
7902 mitigates challenges associated with source lifetime [864].

### 7903 **11.1.3 ERL Landscape**

7904 One way to view the current state of ERLs globally is the so-called *ERL landscape* shown in  
7905 Fig. 11.1 [865]. Every data point represents a machine that demonstrated energy recovery and is  
7906 positioned in (maximum) energy and (average) current parameter space. For clarity, the plot is  
7907 restricted to continuous-wave (CW), SRF-based ERLs only and includes legacy machines, those  
7908 under construction and currently in operation as well as the LHeC and PERLE (proposed).  
7909 The size of the marker is indicative of the charge per bunch while a black line around the  
7910 marker indicates it was/is a *true ERL*. That is, where the beam power exceeds the installed  
7911 RF power (they are represented in the plot by the three FEL drivers that were designed, built,  
7912 commissioned and operated at Jefferson Laboratory).

7913 A cursory look at Fig. 11.1 illustrates several of the challenges facing the next generation of  
7914 ERLs. While getting from the current state-of-the-art to the LHeC requires only a modest  
7915 increase in average current, it requires a significant increase in bunch charge and addressing  
7916 the consequent collective effects [866]. Most significantly, however, is the leap in energy from  
7917 systems that have operated in the 100 MeV range to several tens of GeV. Note that PERLE is  
7918 strategically positioned to address incremental changes in both average current, bunch charge  
7919 and energy. As such, it provides a convenient test bed facility to address the issues described  
7920 previously [867]. Several ERLs are still in the nascent stages and as they ramp up beam power,  
7921 will also be valuable in advancing the state-of-the-art. For instance, though it uses a Fixed Field  
7922 Alternating Gradient (FFAG) arc, the Cornell/Brookhaven ERL Test Accelerator (CBETA) will  
7923 address multi-turn energy recovery for the first time in an SRF system [868]. Note that with  
7924 only minor modifications Jefferson Laboratory's Continuous Electron Beam Accelerator Facility  
7925 (CEBAF) could be operated with multi-pass energy recovery at several GeV using common  
7926 transport with the same topology as LHeC (i.e. bisected linacs of equal energy gain with arcs  
7927 vertically separated by energy using spreaders and recombiners) [869].

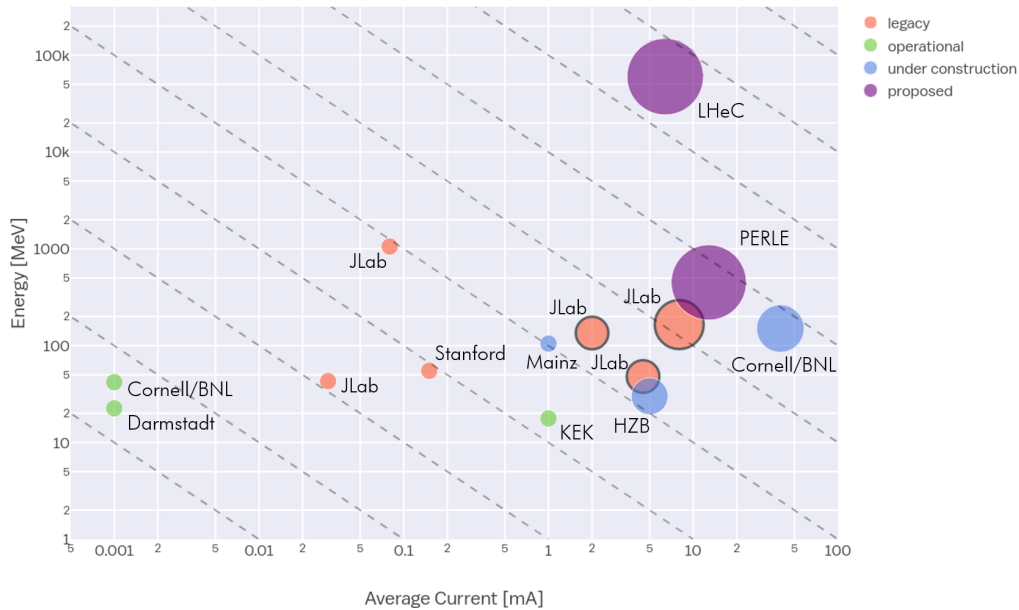


**Figure 11.1:** The *ERL landscape*, where data points are restricted to CW, SRF-based ERLs. The dashed lines represent lines of constant beam power – starting from 10 W in the lower left and going to 10 GW in the upper right. Note that both axes use a log scale.

## 11.2 The ERL Facility PERLE

7928

7929 PERLE is a compact three-pass ERL based on SRF technology, a new generation machine  
 7930 uniquely covering the 10 MW power regime of beam current and energy. Its Conceptual Design  
 7931 Report appeared recently [5]. Apart from low energy experiments it could host, thanks to its  
 7932 beam characteristics, PERLE will serve as a hub for the validation of a broad range of accelerator  
 7933 phenomena and the development of ERL technology for future energy frontiers colliders which  
 7934 was introduced above. Particularly, the basic 3-turn configuration, design challenges and beam  
 7935 parameters (see Tab. 11.1) are chosen to enable PERLE as a testbed for the injection line and  
 7936 SRF technology development, as well as multi-turn and high current ERL operation techniques  
 7937 for the Large Hadron electron Collider. While the concept and promise of ERL’s has been  
 7938 kick-started by demonstration machines based on existing accelerator technology, PERLE will  
 7939 be the first machine designed from the ground up to use fully optimised ERL-specific designs  
 7940 and hardware.

7941 The PERLE collaboration involves today CERN, Jefferson Laboratory, STFC-Daresbury, Uni-  
 7942 versity of Liverpool, BINP-Novosibirsk and the newly formed Irene Curie Lab at Orsay. Four  
 7943 of these international partners have been pioneering the development of ERL technology, the  
 7944 other are leading laboratories on SRF technology and accelerator physics. The Orsay Lab is  
 7945 leading the effort to develop and later host PERLE at Orsay campus in close collaboration with  
 7946 the LHeC coordination.

7947 The following PERLE summary focuses on the power challenge, the lattice, site and time sched-  
 7948 ule. PERLE uses a cryo-module with four 5-cell cavities like the LHeC. The prototype cavity  
 7949 production and test as well as the design status of the cryo-module are described in the LHeC  
 7950 linac chapter. There one also finds a section on the source and injector and as well arc magnets,  
 7951 dipoles of a 3-in-1 design and quadrupoles, which will similarly be used for PERLE.

### 7952 11.2.1 Configuration

7953 In its final configuration, a high average current electron beam (20 mA) is accelerated through  
7954 three passes to the maximum energy (500 MeV) in the superconducting RF CW linear acceler-  
7955 ators. The beam is then used for its intended purpose such as photon generation by Compton  
7956 back-scattering, a cooling source for ion beams or a beam for colliding against fixed targets. The  
7957 3-passes up in energy may significantly increase the energy spread or emittance of the electron  
7958 beam but the major part of the beam power remains. The beam is then sent back through the  
7959 accelerators again only this time roughly 180 degrees off the accelerating RF phase so the beam  
7960 is decelerated through the same number of passes and then sent to a beam dump at around the  
7961 injection energy. Several benefits arise from this configuration: the required RF power (and its  
7962 capital cost and required electricity) is significantly reduced to that required to establish the  
7963 cavity field; the beam power that must be dissipated in the dump is reduced by a large factor,  
7964 and often the electron beam dump energy can be reduced below the photo-neutron threshold so  
7965 that activation of the dump region can be reduced or eliminated.

### 7966 11.2.2 Importance of PERLE towards the LHeC

7967 PERLE is an important and necessary step accompanying the LHeC realisation. Together  
7968 with other ERL facilities, CBETA, bELRin-Pro and possibly others, it will bridge the gap of  
7969 power level between the currently reached maximum (CEBAF-ER at 1 MW) and the targeted  
7970 performances of LHeC (1 GW) by exploring a next higher operational power regime of around  
7971 10 MW. Moreover, sharing the same conceptual design with the LHeC, a racetrack configuration  
7972 with 3 acceleration and 3 deceleration passes, identical injection line and the same SRF system,  
7973 as well as the same beam current in the SRF cavities will allow to acquire with PERLE an  
7974 enormous insight on multiple pass operation and common transport from full energy, before and  
7975 possibly during LHeC operation too.

7976 Up to date, existing SRF systems have demonstrated stability at only a modest fraction ( $\leq 20\%$ )  
7977 of the current envisaged for the LHeC. Though threshold currents have been indirectly measured  
7978 at higher values, there is no direct evidence that multi-pass systems will be sufficiently resistant  
7979 to BBU at the higher current, nor has the sensitivity of the instability threshold to linac length,  
7980 dynamic range, and number of passes been directly or systematically measured as yet. PERLE  
7981 will provide a single datum on linac length, and can directly measure the dependence on the  
7982 number of passes and the turn-to-turn transfer matrix.

7983 The dynamic range (which is the ratio of injected/extracted energy to full energy) is a critical  
7984 design parameter, in as much as it defines the sensitivity of the overall system to magnetic  
7985 field errors. Errors at full energy drive phase/energy errors that are magnified by adiabatic  
7986 anti-damping during recovery, and can exceed the dump acceptance should the errors be too  
7987 large. Thus, the field quality needed is inversely proportional to the ratio of full energy to dump  
7988 energy: that is, a very high energy machine (or one with very low dump energy) needs very  
7989 high-quality magnets. For PERLE, the dynamic range is 70 : 1 (7 MeV injected and 490 MeV  
7990 full energy). This implies a need of  $\Delta B/B_{dipole} \simeq 0.001\%$  field flatness (extrapolated from JLAB  
7991 ERL needs) to recover cleanly enough. This implies a tight constraint on magnet performances  
7992 and impact their cost, even when it is the SRF which drives the overall cost of the facility,  
7993 for LHeC. PERLE has a very large dynamic range and a transport system with considerable  
7994 symmetry and flexibility. It is therefore a suitable tool to explore this issue and evaluate the  
7995 cost implications for larger scale systems.

7996 Existing systems have operated at maximum 1 MW full beam power. This is too low for a precise  
7997 understanding and control of beam halo. Extrapolation to 10 MW will demand suppression of

7998 localised losses to, or below, parts per million. Higher power requires a lower fractional loss.  
7999 It is not yet well understood how to do this - in particular, collimation systems require a more  
8000 optimised control of CW losses at rates observed in linacs. PERLE will provide a platform  
8001 on which the next step in understanding can be taken. Other halo effects may become visible  
8002 at only the higher CW powers under consideration in PERLE (including Touschek and intra-  
8003 beam scattering, beam-gas scattering, and ion trapping). These lead to scattering events that  
8004 adiabatically anti-damp and result in intolerable loss in the back end of the machine, limiting  
8005 dynamic range. There is no experience with these phenomena, although theoretical studies  
8006 suggest they are problematic. PERLE will be the first system capable of directly exploring  
8007 these issues.

8008 There are many collective effects that have proven challenging at lower beam powers - including  
8009 RF heating, resistive wall heating, THz emission heating... - that will have greater impact at  
8010 both higher power and higher energy. There are at present no operating ERL systems that can  
8011 study these. PERLE is the only system proposed or under construction that combines sufficient  
8012 beam power with sufficient operational flexibility to study and test mitigation algorithms and  
8013 methods. Without PERLE, higher energy/power machines will have very little insight regarding  
8014 these problems and lack the ability to test solutions.

8015 Beam quality preservation in the presence of collective effects is a significant challenge for modern  
8016 machines. In particular, Longitudinal Space Charge (LCS), Coherent Synchrotron Radiation  
8017 (CSR), and the micro-bunching instability have serious deleterious impact on performance, and  
8018 can prevent a machine from producing beam consistent with user requirements - or, worse, from  
8019 being able to operate at significant powers. PERLE probes the regions of parameter space  
8020 where these effects are observable, and offers an opportunity to benchmark models and explore  
8021 mitigation methods.

### 8022 **11.2.3 PERLE Layout and Beam Parameters**

8023 The PERLE accelerator complex is arranged in a racetrack configuration hosting two cryo-  
8024 modules (containing four, five-cell cavities operating at 801.6 MHz frequency), each located in  
8025 one of two parallel straights completed with a vertical stack of three recirculating arcs on each  
8026 side. The straights are 10 m long and the 180° arcs are 5.5 m across. Additional space is taken  
8027 by 4 m long spreaders/recombiners, including matching sections. As illustrated in Fig. 11.2, the  
8028 total footprint of PERLE is:  $24 \times 5.5 \times 0.8 \text{ m}^3$ , accounting for 40 cm vertical separation between  
8029 arcs. Each of the two cryo-modules provides up to 82 MeV energy boost per path. Therefore, in  
8030 three turns, a 492 MeV energy beam is generated. Adding the initial injection energy of 7 MeV  
8031 yields the total energy of approximately 500 MeV. The main beam parameters of PERLE facility  
8032 are summarised in Tab. 11.1

8033 As mentioned in the introduction, the essential PERLE parameters are the same as the LHeC.  
8034 The frequency choice, emittance, beam current and the time structure are chosen regarding the  
8035 requirements of the electron-proton collisions in the LHeC. Hereafter, we explain the choice of  
8036 the frequency for the LHeC and thus for PERLE.

### 8037 **11.2.4 PERLE Lattice**

8038 Multi-pass energy recovery in a racetrack topology explicitly requires that both the accelerating  
8039 and decelerating beams share the individual return arcs (Fig. 11.2). Therefore, the TWISS  
8040 functions at the linac ends have to be identical, for both the accelerating and decelerating linac  
8041 passes converging to the same energy and therefore entering the same arc.



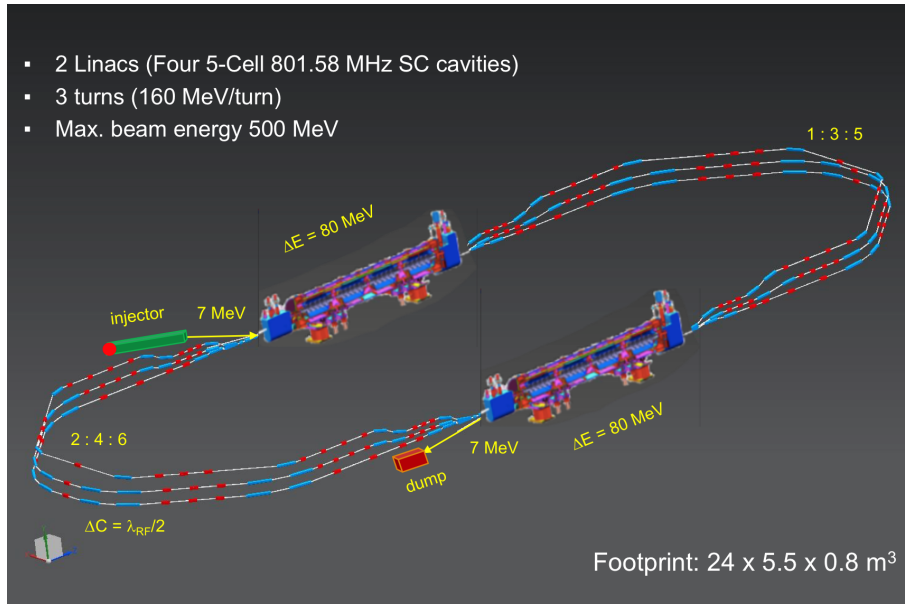


**Figure 11.2:** PERLE facility layout featuring two parallel linacs each hosting a cryomodule housing four 5-cell SC cavities, achieving 500 MeV in three passes, see text.

Target parameter	Unit	Value
Injection energy	MeV	7
Electron beam energy	MeV	500
Norm. emittance $\gamma\epsilon_{x,y}$	mm·mrad	6
Average beam current	mA	20
Bunch charge	pC	500
Bunch length	mm	3
Bunch spacing	ns	25
RF frequency	MHz	801.6
Duty factor		CW

**Table 11.1:** Summary of main PERLE beam parameters.

8042 Injection at 7 MeV into the first linac is done through a fixed field injection chicane, with its  
8043 last magnet (closing the chicane) being placed at the beginning of the linac. It closes the orbit  
8044 bump at the lowest energy, injection pass, but the magnet (physically located in the linac) will  
8045 deflect the beam on all subsequent linac passes. In order to close the resulting higher pass  
8046 bumps, the so-called re-injection chicane is instrumented, by placing two additional bends in  
8047 front of the last chicane magnet. This way, the re-injection chicane magnets are only visible by  
8048 the higher pass beams. The spreaders are placed directly after each linac to separate beams of  
8049 different energies and to route them to the corresponding arcs. The recombiners facilitate just  
8050 the opposite: merging the beams of different energies into the same trajectory before entering  
8051 the next linac. The spreader design (Fig. 11.3) consists of a vertical bending magnet, common  
8052 for all three beams, that initiates the separation. The highest energy, at the bottom, is brought  
8053 back to the horizontal plane with a chicane. The lower energies are captured with a two-step  
8054 vertical bending. The vertical dispersion introduced by the first step bends is suppressed by the  
8055 three quadrupoles located appropriately between the two steps. The lowest energy spreader is  
8056 configured with three curved bends following the common magnet, because of a large bending  
8057 angle (45°) the spreader is configured with. This minimises adverse effects of strong edge focusing

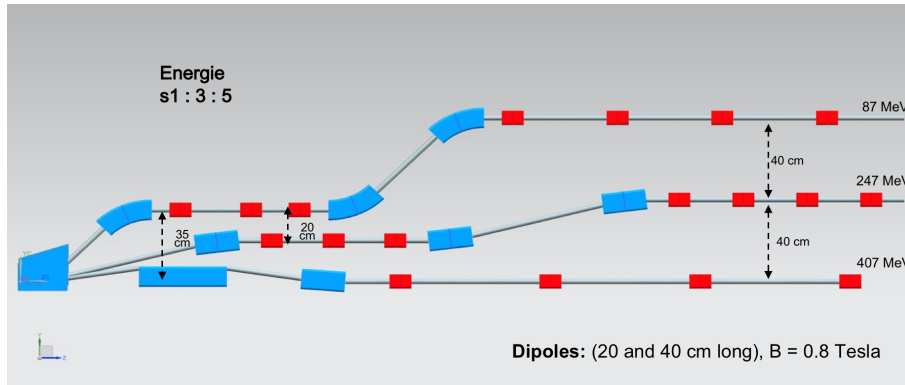


**Figure 11.3:** PERLE spreader design and matching to three circulating arcs.

8058 on dispersion suppression in the spreader. Following the spreader there are four matching quads  
 8059 to bridge the TWISS function between the spreader and the following  $180^\circ$  arc (two betas and  
 8060 two alphas). All six,  $180^\circ$  horizontal arcs are configured with Flexible Momentum Compaction  
 8061 (FMC) optics to ease individual adjustment of M56 in each arc (needed for the longitudinal  
 8062 phase-space reshaping, essential for operation with energy recovery). The lower energy arcs (1,  
 8063 2, 3) are composed of four 45.6 cm long curved  $45^\circ$  bends and of a series of quadrupoles (two  
 8064 triplets and one singlet), while the higher arcs (4, 5, 6) use double length, 91.2 cm long, curved  
 8065 bends. The usage of curved bends is dictated by a large bending angle ( $45^\circ$ ). If rectangular  
 8066 bends were used, their edge focusing would have caused significant imbalance of focusing, which  
 8067 in turn, would have had adverse effect on the overall arc optics. Another reason for using curved  
 8068 bends is to eliminate the problem of magnet sagitta, which would be especially significant for  
 8069 longer, 91.2 cm, bends. Each arc is followed by a matching section and a recombiner (both  
 8070 mirror symmetric to previously described spreader and matching segments). As required in case  
 8071 of identical linacs, the resulting arc features a mirror symmetric optics (identical betas and sign  
 8072 reversed alphas at the arc ends).

8073 The presented arc optics with modular functionality facilitates momentum compaction manage-  
 8074 ment (isochronicity), as well as orthogonal tunability for both beta functions and dispersion.  
 8075 The path-length of each arc is chosen to be an integer number of RF wavelengths except for the  
 8076 highest energy pass, arc 6, whose length is longer by half of the RF wavelength to shift the RF  
 8077 phase from accelerating to decelerating, switching to the energy recovery mode.

### 8078 11.2.5 The Site

8079 The Irene Curie Lab Orsay intends to host PERLE. The footprint of this facility occupies a  
 8080 rectangle of  $24 \times 5.5 \text{ m}^2$ . This area should be enclosed by shielding at a sufficient distance to  
 8081 allow passage and maintenance operations. We estimate the required passage and half thickness  
 8082 of the accelerator component to 2 m. A concrete shielding is assumed here to stop photons and  
 8083 neutrons produced by halo electrons. A more detailed study of the radiation generated by the  
 8084 impinging electron will be necessary at a following stage. An increase of the shielding required  
 8085 could be alleviated by the use of denser materials.

8086 The PERLE operation at the design beam parameters (Tab.11.1) required an in-depth study  
 8087 of the machine failure scenario to estimate the power left in the machine during operation after  
 8088 beam losses and how to handle and control it. The study aimed at looking if the PERLE facility  
 8089 will be classified as INB (Infrastructure Nucleaire de Base) or not, with respect to the French  
 8090 radioprotection and nuclear safety rules. This conclusion is crucial for the decision of hosting

8091 PERLE at Orsay as such INB facilities require heavy regulation procedures and a very high  
8092 investment to fulfil the requirements and ensure the safety provisions to be implemented. The  
8093 outcome of the study had concluded that PERLE shall not be considered as INB, even if the  
8094 beam parameters are quite demanding, because for several failure scenarios the energy of the  
8095 beam is brought back to the injection energy and safely dumped, thanks to the recovery mode.  
8096 For other scenarios, hard interlocks and the machine safety system are fast enough to manage  
8097 the situation. The complete report of this study has been delivered by the IRSD team at Orsay.

8098 Besides the central area required for machine implementation, space needs to be allocated for the  
8099 auxiliary systems (power converters for magnets, septa and kickers, RF power, Water cooling,  
8100 Cryogenics, Electron source, Dump). One has also to consider sufficient space for experiments  
8101 that may use the PERLE beam. These have been sketched in the PERLE CDR [5]. As a rough  
8102 estimate one would need to triple the area of the accelerator itself to accommodate all services,  
8103 with shielding included. The building that is foreseen to host this version of PERLE is a former  
8104 experimental hall (Super ACO). It is equipped with cranes and electricity. The ground of the  
8105 building is made of concrete slabs with variable ground resistance. More than half of the hall  
8106 area has a sufficient resistance to allow the installation PERLE. Being next to the tunnel of the  
8107 old Orsay Linac and close to the *Igloo*, where new accelerators are being installed currently, the  
8108 building is partially shielded and some equipment (water-cooling circuits, electrical transformer)  
8109 can be shared with the other machines. The building gives the possibility to install the RF source  
8110 and the power supplies at a different level than the accelerator. An existing control room that  
8111 overlooks the experimental hall may be used for PERLE. Since all the accelerators installed  
8112 nearby are based on warm technology, a cryogenic plant will be built. All the needed support  
8113 for infrastructure could be assured by the CPER program. Altogether, this appears to be a well  
8114 suitable place which has the great advantage to be available.

### 8115 11.2.6 Staging Strategy and Time Schedule

8116 The PERLE configuration (Cf. Fig. 11.2) entails the possibility to construct PERLE in stages,  
8117 starting by installing a single linac in the first straight and initially replacing the second one  
by beam lines. Such a consideration is determined by the existence of the SPL cryomodule

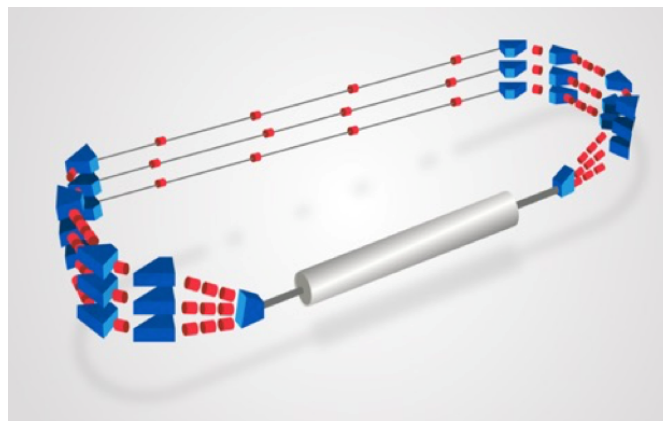


**Figure 11.4:** PERLE-Phase 1 layout featuring a single Linac in the first straight and beam line in the second straight, achieving 250 MeV in three passes.

8118  
8119 at CERN (see the discussion in Chapter 9), which will permit a rather rapid realisation of a  
8120 250 MeV machine, in what currently and tentatively is considered Phase 1 of PERLE. This will  
8121 allow in relatively short time to test with beam the various SRF components, to prove the  
8122 multi-turn ERL operation and to gain essential operation experience. Nevertheless, important

8123 achievements and steps are needed to realise these purposes. A tentative time schedule for the  
 8124 realisation of Phase 1 of PERLE is presented in Tab. 11.2.

Phase 1 milestone	Targeted date	Collaborator(s) involvement
<u>Studies &amp; prototyping</u>		
Dressed cavity design completion	Oct 2019	CERN-JLAB
SPL cryomodule design completion	May 2020	CERN
Injection line design completion	Mid 2020	STFC-Univ. Liverpool
Final design cavity fabrication and V. test	Mid 2020	JLAB-CERN
Arc and switchyard dipole prototypes	End 2020	BINP Novosibirsk
Booster cryomodule design completion	End 2021	–
Technical Design Report	End 2021	All
<u>Assembling, test &amp; installation</u>		
DC gun installation (1)	Early 2021	STFC
Booster assembly & RF test (2)	Mid 2023	STFC
Injector installation & commissioning (3)	End 2023	STFC
SPL cryomodule assembly and RF test (2)	Early 2024	CERN
Sequential installation at Orsay (4)	End 2024	–
Phase 1 operation	2025	Open to all

**Table 11.2:** Tentative time schedule to realise PERLE at Orsay in its first phase. (1) Most likely the Gun upgrade will be deferred to Phase 2 and Phase 1 will use the 5 mA ALICE DC gun which was received at Orsay on May 2019; (2) Booster test requires installation of cryogenics, RF power source, shielding, CC; (3) Injection line commissioning requires installation of cryogenics, RF power source, shielding, beam dump, diagnostics, CC, photocathode laser, vacuum, cabling, safety control systems, fluids, etc.; (4) only one spreader and one recombiner are needed for Phase 1. Final arc configuration will be installed.

8124

8125 It is foreseen from the beginning to size the infrastructure and equipment as for their final use  
 8126 (beam dump, cryogenics, cooling circuit, shielding, electrical power, etc.)

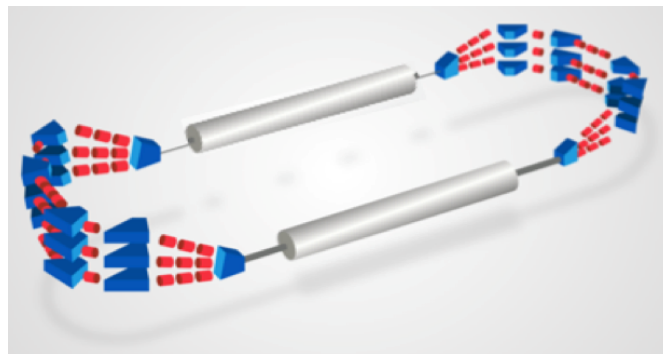


**Figure 11.5:** PERLE-Phase 2 layout featuring two Linac in each straight, achieving 500 MeV in three passes.

8127 The second phase is for the realisation of PERLE at its design parameters, as a 10 MW machine  
 8128 which requires the nominal electron current, i.e. the upgraded  $e^-$  gun and the completion of  
 8129 the production of a further cryo-module, possibly newly designed. Also, a second spreader and  
 8130 recombiner need to be installed on both sides of the second cryo-module. The timeline of this  
 8131 second phase is given in Tab. 11.3. It is expected that the PERLE Collaboration will evolve  
 8132 which will affect these plans.

Phase 2 milestone	Targeted date	Collaborator(s) involvement
DC gun upgrade	2026	STFC
Second cryomodule completion	2027	CERN
PERLE phase 2 operation	2028	Open to all

**Table 11.3:** Tentative plans for Phase 2 of PERLE.

### 8133 11.2.7 Concluding Remark

8134 Currently the focus of the planning for PERLE is on the development of ERL as a means for high  
8135 power, large energy accelerator design, technology and realisation. PERLE has a considerable  
8136 potential for low energy particle and nuclear physics too. Its intensity is orders of magnitude  
8137 higher than that of ELI. This opens a huge field of physics and industrial applications for a  
8138 user facility once the machine has been understood and operates close to its design in a reliable  
8139 manner. With recent increased interest in energy recovery technology applications at LHeC,  
8140 but also FCC and EIC, PERLE may become an important cornerstone for future high energy  
8141 and nuclear physics. The re-use of power is a *per se* green technology which is an example as to  
8142 how science may react to the low power requirements of our time.

## Chapter 12

# Experimentation at the LHeC

### 12.1 Introduction

The LHeC Conceptual Design Report [1] contained a very detailed description of a core detector concept for the LHeC. At the time of writing, the target luminosity was of order  $10^{33} \text{ cm}^{-2} \text{ s}^{-1}$  and, whilst evidence was building, the Higgs boson had yet to be discovered. A detector design based on established technologies either in use by the LHC General Purpose Detectors, ATLAS and CMS, or being developed for their upgrades was found to be adequate to realise the physics priorities of the project at the time and could comply with the  $ep$  machine constraints at an affordable cost, provided the angular acceptance was sufficient (nominally to within  $1^\circ$  of the beamline). A salient feature of experimentation at the LHeC, as compared to the LHC, is the complete absence of pile-up which can be estimated <sup>1</sup> to be around 0.1 in  $ep$  at the LHeC as compared to  $\simeq 150$  in  $pp$  at HL-LHC. Similarly, there is a reduced level of radiation in  $ep$ , by orders of magnitude lower than in  $pp$ , which enables to also consider novel technologies that are less radiation hard than conventional ones, with HV CMOS Silicon detectors as an example.

This chapter provides a short overview of a partially revised LHeC detector design, with more detail on those aspects which have developed significantly since the 2012 version (notably the central tracking). To a large extent, the considerations in the CDR are still valid and are taken forward here. However, this update also profits from the evolution of the design in the subsequent years, the updated and long term physics priorities with the higher achievable luminosities. It also introduces new technologies where they are becoming available. In more detail, the major considerations which motivate an update of the detector with respect to the 2012 baseline are:

- The increased luminosity and the confirmation of a Higgs boson discovery at a mass of around 125 GeV opens the opportunity for the LHeC to provide a set of precision measurements of the Higgs properties, in particular, percent-level measurements of several of its couplings. The possibility of obtaining world-leading measurements of couplings to beauty and charm place a heavy emphasis on the inner tracking and vertexing. The

---

<sup>1</sup>The pile-up is given as the number of events per bunch crossing, which is obtained from the instantaneous luminosity,  $L = 10^{34} \text{ cm}^{-2} \text{ s}^{-1}$ , the total cross section,  $\sigma_{tot} \simeq \sigma(\gamma p) \cdot \Phi_\gamma$ , and the bunch distance of 25 ns. The total photo-production cross section, with a minimum  $Q^2 = (M_e \cdot y)^2 / (1 - y)$ , is estimated as 220 (260)  $\mu\text{b}$  at the LHeC (FCC-he) using the parameterisation given in Ref. [870]. Here  $y$  is the inelasticity variable and  $M_e$  the electron mass. The photon flux factor in the Weizsäcker-Williams approximation is calculated as  $\Phi_\gamma = 1.03$  (1.25) for  $W = \sqrt{ys} > 1 \text{ GeV}$ . The hadronic final state at very small scattering angles,  $\theta_h \leq 0.7^\circ$  or  $|\eta| \geq 5$ , is not reaching the central detector acceptance such that at the LHeC  $W_{min}$  would be larger, about 10 GeV, which reduces the flux to about 0.6. A conservative estimate is to use  $W > 1 \text{ GeV}$ . This translates to an estimated pile-up of 0.06 at the LHeC and 0.09 at the FCC-eh which favourably compares with an estimated pile-up of 150 at HL-LHC.

8170 tracking region has therefore been extended radially with an also increased segmentation.  
8171 The requirement to maximise the acceptance for Higgs decays places an even heavier  
8172 requirement on angular coverage than was the case in 2012, with forward tracking and  
8173 vertexing being of particular importance.

- 8174 • The fast development of detector technologies and related infrastructure in some areas ne-  
8175 cessitates a fresh look at the optimum choices. Most notably, silicon detector technologies  
8176 have advanced rapidly in response to both commercial and particle physics requirements.  
8177 The low material budget, potential high granularity, and cost-effectiveness offered by mono-  
8178 lithic active pixel sensor (MAPS) solutions such as HV-CMOS are particularly attractive  
8179 and can reasonably be assumed to be in wide use in future particle physics collider detector  
8180 contexts.
- 8181 • The long term, high energy hadron collider physics program, including FCC and possi-  
8182 bilities in Asia, as well as the ultimate use of the LHC for two more decades, require the  
8183 precise, independent, and comprehensive measurements to determine PDFs, over a wider  
8184 range of  $x$  and  $Q^2$  than has previously been possible. The implication for the LHeC is a  
8185 need to further improve and extend the detector acceptance and overall performance.
- 8186 • Options in which the  $ep$  centre-of-mass energy is increased, at HE LHC or FCC-eh, require  
8187 a further reinforcement of the detector design in the forward (outgoing proton) direction,  
8188 increasing the overall size of the detector. In particular, the calorimeter depth scales  
8189 logarithmically with  $E_p$  so as to fully contain particles from very high energy forward-  
8190 going hadronic showers and to allow for precise measurements of actual and missing energy.  
8191 Using such scaling considerations, the LHeC design has been applied also to the post LHC  
8192 hadron beam configurations.

8193 The design described in the following addresses the points above. The updated detector require-  
8194 ments point in the tracking region to the need for higher spatial resolution, improved precision  
8195 in momentum measurements and enhanced primary and secondary vertexing capabilities. The  
8196 most significant change compared with 2012 is therefore a more ambitious tracking detector  
8197 design. The detector must also provide accurate measurements of hadronic jets and missing  
8198 transverse energy, as well as isolated electrons and photons. As an option compared to the CDR,  
8199 the liquid argon (LAr) choice for the main electromagnetic barrel calorimeter sampling material  
8200 is here changed to a scintillator-based solution. Both options are subsequently compared, and  
8201 as expected the long term stability and resolution performance favour a LAr calorimeter while  
8202 the modularity and installation aspects are easier solved with a warm crystal calorimeter.

8203 Both the overall event kinematics (much larger proton than electron beam energy) and the  
8204 specific acceptance requirements for the key Higgs production process imply an asymmetric  
8205 design with enhanced hadronic final state detection capabilities in the forward direction where  
8206 the deposited hadronic and electromagnetic energies are much higher than in the backward (the  
8207 electron beam) direction, see Fig. 3.2 in Sect. 3.2.

8208 A dipole magnet bends the electron beam into head-on collision with the colliding proton beam  
8209 and after the interaction point a further dipole with opposite polarity separates the orbits of  
8210 the electron and proton beam. These weak bending dipoles are placed outside of the tracker  
8211 and electromagnetic calorimeter regions. The total length is 10 m or  $2/3L^*$  as explained in the  
8212 IR section. The resulting synchrotron radiation fan has to be given free space and the beam  
8213 pipe geometry is designed specifically to accommodate it. The residual synchrotron radiation  
8214 background poses a constraint to the inner detector components.

8215 The 2012 and 2020 versions of the LHeC detector design are both realisable in terms of technology

8216 readiness. It has been a goal of this conceptual design to study the feasibility, performance and  
8217 integration of the detector, which will eventually be designed by a future  $ep/eA$  experiment  
8218 collaboration. The two designs, albeit being still similar, can be considered as two example  
8219 solutions to the LHeC requirements with differences in where the emphasis is placed in terms  
8220 of performance and cost. The current design is performed using the DD4hep [871] software  
8221 framework.

## 8222 12.2 Overview of Main Detector Elements

8223 A side projection overview of the current detector design is shown in Fig. 12.1, illustrating the  
8224 main detector components. The overall size remains compact by recent standards, with overall  
8225 dimensions of approximately 13 m in length and 9 m in diameter, small compared with ATLAS  
8226 ( $45 \times 25 \text{ m}^2$ ) and even CMS ( $21 \times 15 \text{ m}^2$ ). The inner silicon tracker contains a central barrel com-  
8227 ponent ('Tracker'), with additional disks in the forward and backward directions ('Tracker Fwd'  
8228 and 'Tracker Bwd', respectively). It is surrounded at larger radii by the Electromagnetic Barrel  
8229 ('EMC-Barrel') and in the forward and backward directions by the electromagnetic forward and  
8230 backward plug calorimeters ('FEC-Plug-Fwd' and 'BEC-Plug-Bwd', respectively). The solenoid  
8231 magnet is placed at radii immediately outside the EMC-Barrel, and is housed in a cryostat,  
8232 which it shares with the weak dipole magnet that ensures head-on collisions. It is the dipole and  
8233 cost considerations which suggest to place the solenoid there instead of surrounding the HCAL  
8234 which in terms of performance surely would have been preferable.

8235 The Hadronic-Barrel calorimeter (HCAL-Barrel) is located at radii beyond the solenoid and  
8236 dipole, whilst the forward and backward hadronic plug detectors (FHC-Plug-Fwd and BHC-  
8237 Plug-Bwd, respectively) lie beyond their electromagnetic counterparts in the longitudinal coor-  
8238 dinate. The Muon Detector forms a near-hermetic envelope around all other parts of the main  
8239 detector. It uses similar technologies to those employed by ATLAS, at much smaller surface,  
8240 see below.

8241 A magnified view of the inner part of the detector, including the magnet elements, is shown in  
8242 Fig. 12.2. The solenoid and steering dipoles enclose the electromagnetic calorimeters and the  
8243 tracker setup completely, the steering dipoles extending over the full 10 m length of the inner  
8244 detector and forward and backward plugs. If liquid argon is chosen for the sensitive material  
8245 in the EMC as in the 2012 design, the EMC will be mounted inside the cryostat, alongside the  
8246 solenoid and dipoles. The hadronic calorimeter components remain outside the cryostat and  
8247 magnet elements in all circumstances.

8248 Exploiting the current state of the art, the beam pipe is constructed of beryllium of 2.5–3 mm  
8249 thickness. As in the 2012 CDR, the beam pipe has an asymmetric shape in order to accommodate  
8250 the synchrotron radiation fan from the dipole magnets. It is thus 2.2 cm distant from the  
8251 interaction region, comparable to the HL-LHC beam pipes of the GPDs, except in the direction  
8252 of the synchrotron fan, where it is increased to 10.0 cm, giving rise to an overall circular-elliptical  
8253 profile ( illustration of the profile at IP in Fig. 12.3 ). The beam pipe shape has implications  
8254 for the design of the inner detector components, as illustrated in Fig. 12.4. The first layer of  
8255 the barrel tracker follows the circular-elliptical beam pipe shape as closely as possible, with the  
8256 profiles of subsequent layers reverting to a circular geometry.



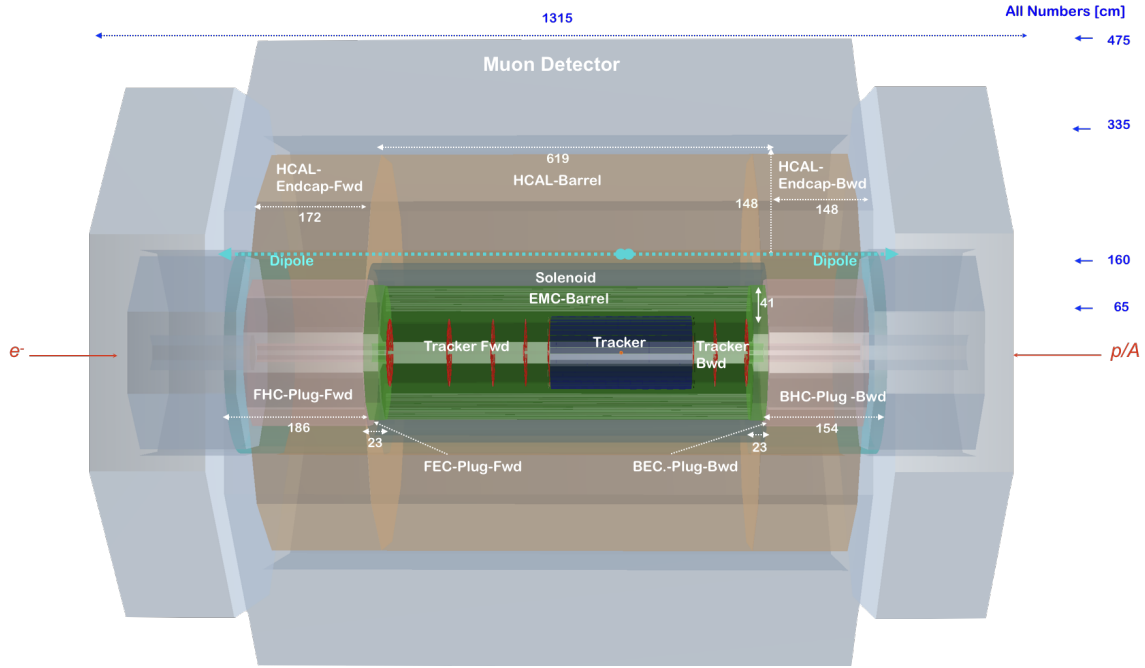


**Figure 12.1:** Side view of the updated baseline LHeC detector concept, providing an overview of the main detector components and their locations. The detector dimensions are about 13 m length and 9 m diameter. The central detector is complemented with forward ( $p$ ,  $n$ ) and backward ( $e$ ,  $\gamma$ ) spectrometers mainly for diffractive physics and for photo-production and luminosity measurements, respectively. See text for details.

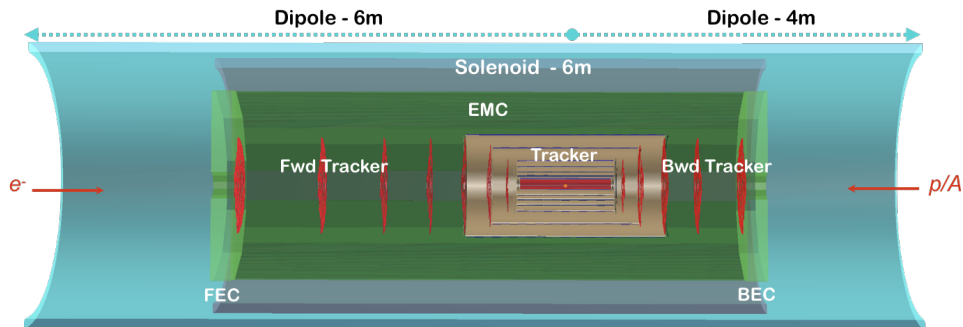


**Figure 12.2:** Side projection of the central part of the LHeC detector, illustrating also the solenoid and electron-beam-steering dipoles. See text for further details.

## 8257 12.3 Inner Tracking

### 8258 12.3.1 Overview and Performance

8259 A schematic view of the updated tracking region is shown in Fig. 12.5. The layouts in the  
 8260 central, forward and backward directions have been separately optimised using the tkLayout  
 8261 performance estimation tool for silicon trackers [873]. The result is seven concentric barrel  
 8262 layers with the innermost layer approximately 3 cm from the beam line at its closest distance  
 8263 and with approximately equal radial spacing thereafter. The tracker barrel is supplemented by  
 8264 seven forward wheels and five backward wheels of which three in each direction comprise the  
 8265 central tracker end-cap and, respectively, four and two, respectively, are mounted beyond the  
 8266 central tracker enclosure.

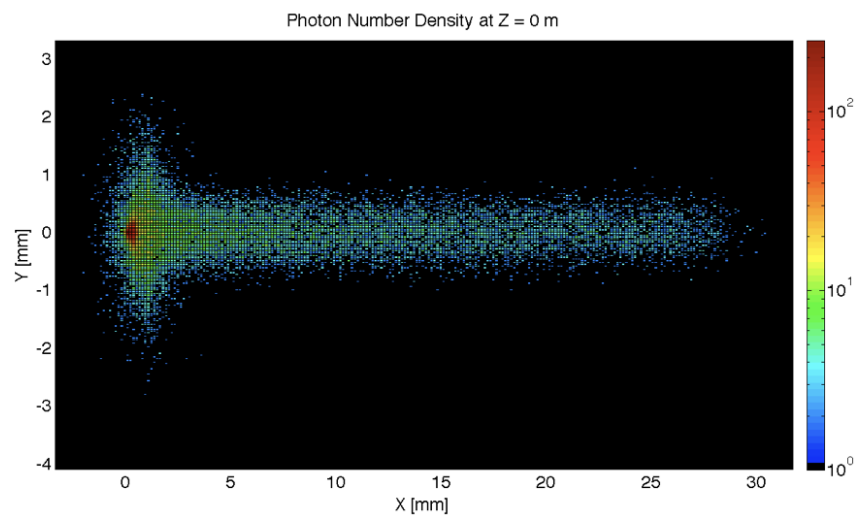


**Figure 12.3:** The simulation of synchrotron radiation profile at the IP using GEANT4 [1,872].

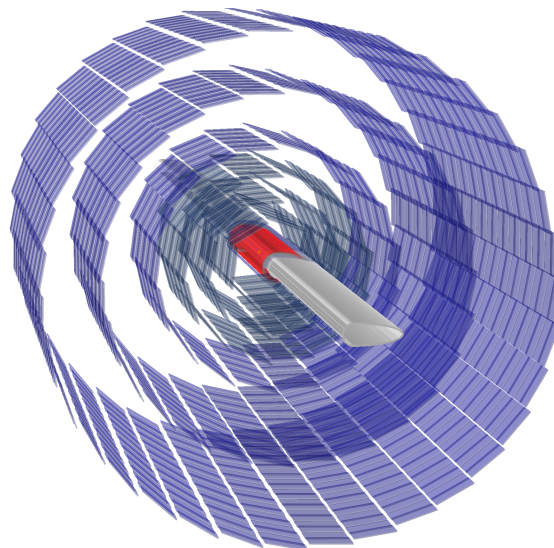


**Figure 12.4:** End-on view of the arrangement of the inner barrel tracker layers around the beam pipe.

8267 For reasons described in Sect. 12.3.2, HV-CMOS MAPS sensors can be employed, restricting  
8268 material associated with the pixel sensors to just 0.1 mm per layer. The strip detector sensors  
8269 have a larger thickness of 0.2 mm. The preferred active silicon solutions vary with radial distance  
8270 from the interaction point, so as to provide the highest spatial resolution in the layers closest  
8271 to the the interaction point. The barrel is formed from one layer of pixel-wafers, with three  
8272 layers of macro-pixels between 10 cm and 30 cm radius and a further three layers of strip-sensors  
8273 beyond 30 cm. The end-cap wheels and the forward tracker also contain combinations of the  
8274 three types of sensor, whilst the backward tracker consists of macro-pixels and strips only.

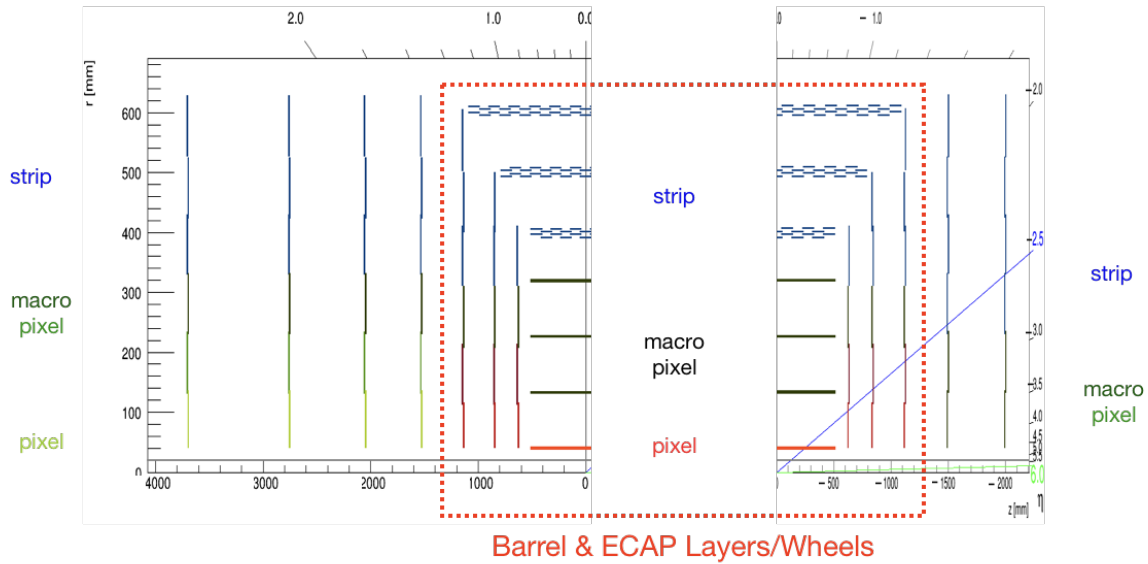


**Figure 12.5:** Schematic side-view of the tracker, subdivided into forward and backward parts and including disks as well as barrel components. The layers/wheels forming the barrel part are enclosed by the red-dotted box. The innermost pixel layers are coloured red, the macro-pixel layers are shown in black and the strip detectors in blue. For the forward and backward wheels, possibly formed with separate rings, (outside the dashed red box), the pixels, macro-pixels and strip detectors are shown in light green, dark green and blue, respectively.

8275 Tabs. 12.1 and 12.2 summarise the overall basic properties of the tracker modules, including  
8276 total numbers of channels and total area of silicon coverage, as well as spatial resolutions and  
8277 material budgets. The inner barrel has a pseudorapidity coverage  $|\eta| < 3.3$  for hits in at least  
8278 one layer, increasing to  $|\eta| < 4.1$  when the endcaps are also taken into account. The additional  
8279 disks beyond the central tracker enclosure extend the coverage to  $\eta = 5.3$  and  $\eta = -4.6$  in the  
8280 forward and backward directions, respectively. Fig. 12.6 illustrates the coverage in more detail,  
8281 displaying the numbers of layers that provide acceptance as a function of pseudorapidity in both  
8282 the forward and backward directions, also broken down into different sensor types. Charged  
8283 particles are sampled in between 5 and 8 layers throughout the entire range  $-3.5 < \eta < 4$ , with  
8284 sampling in at least two layers provided for  $-4.2 < \eta < 5$ .

8285 Spatial resolutions in the  $r - \phi$  plane, driven by the sensor pitches, reach  $7.5 \mu\text{m}$  for the pixel  
8286 layers. The resolutions are propagated using tkLayout to produce simulated charged particle  
8287 transverse momentum resolutions, as shown in Fig. 12.7. Both active and passive material  
8288 contributions are included, with a 2.5 mm Be beam pipe thickness. An excellent resolution  
8289 ( $\delta p_T/p_T$ ) at the level of 1 – 2% is achieved over a wide range of pseudorapidity and momentum.  
8290 The precision degrades slowly in the forward direction, remaining at the sub 10% level up to  
8291 very forward pseudorapidities  $\eta \sim 4.5$ . Central tracks with transverse momenta up to 1 TeV are

Tracker (LHeC)	Inner Barrel			ECAP		
	pix	pix <sub>macro</sub>	strip	pix	pix <sub>macro</sub>	strip
$\eta_{\max}, \eta_{\min}$	3.3, -3.3	2.1, -2.1	1.4, -1.4	$\pm[4.1, 1.8]$	$\pm[2.4, 1.5]$	$\pm[2.0, 0.9]$
Layers (Barrel)	1	3	3			
Wheels (ECAP)				2	1	1-3
Modules/Sensors	320	4420	3352	192	192	552
Total Si area [m <sup>2</sup> ]	0.3	4.6	17.6	0.8	5.6	3.3
Read-out-Channels [10 <sup>6</sup> ]	224.5	1738	20.6	322.4	73.3	17.0
pitch <sup><math>r-\phi</math></sup> [ $\mu\text{m}$ ]	25	100	100	25	100	100
pitch <sup><math>z</math></sup> [ $\mu\text{m}$ ]	50	400	50k <sup>2)</sup>	50	400	10k <sup>1)</sup>
Average $X_0/\Lambda_I$ [%]	7.2 / 2.2			2.2 / 0.7		

<sup>1)</sup> Reaching pitch <sup>$r-\phi$</sup>  when using two wafer layers rotated by 20 mrad is achievable.

**Table 12.1:** Summary of the main properties of the Barrel and Endcap tracker modules based on calculations performed using tkLayout [873]. For each module, the rows correspond to the pseudorapidity coverage, numbers of barrel and disk layers, numbers of sensors, total area covered by silicon sensors, numbers of readout channels, the hardware pitches affecting the ( $r - \phi$ ) and the  $z$  resolution, respectively, and the average material budget in terms of radiation lengths and interaction lengths. Where appropriate, the numbers are broken down into separate contributions from pixels, macro-pixels and strips. See Tab. 12.2 for a sum of all tracker components.

Tracker (LHeC)	Fwd Tracker			Bwd Tracker		Total
	pix	pix <sub>macro</sub>	strip	pix <sub>macro</sub>	strip	(incl. Tab. 12.1)
$\eta_{\max}, \eta_{\min}$	5.3, 2.6	3.5, 2.2	3.1, 1.6	-4.6, -2.5	-2.9, -1.6	5.3, -4.6
Wheels	2	1	3	2	4	
Modules/Sensors	180	180	860	72	416	10736
Total Si area [m <sup>2</sup> ]	0.8	0.9	4.6	0.4	1.8	40.7
Read-out-Channels [10 <sup>6</sup> ]	404.9	68.9	26.4	27.6	10.6	2934.2
pitch <sup><math>r-\phi</math></sup> [ $\mu\text{m}$ ]	25	100	100	100	100	
pitch <sup><math>z</math></sup> [ $\mu\text{m}$ ]	50	400	50k <sup>2)</sup>	400	10k <sup>1)</sup>	
Average $X_0/\Lambda_I$ [%]	6.7 / 2.1			6.1 / 1.9		
incl. beam pipe [%]						40 / 25

<sup>1)</sup> Reaching pitch <sup>$r-\phi$</sup>  when using two wafer layers rotated by 20 mrad is achievable.

**Table 12.2:** Summary of the main properties of the forward and backward tracker modules in the revised LHeC detector configuration based on calculations performed using tkLayout [873]. For each module, the rows correspond to the pseudorapidity coverage, numbers of disk layers, numbers of sensors, total area covered by silicon sensors, numbers of readout channels, the hardware pitches affecting the ( $r - \phi$ ) and the  $z$  resolution, respectively, and the average material budget in terms of radiation lengths and interaction lengths. The polar angle dependence and decomposition of  $X_0$  and  $\Lambda_I$  are shown in Fig. 12.9. Where appropriate, the numbers are broken down into separate contributions from pixels, macro-pixels and strips. The column *Total* contains the sum of corresponding values in tables 12.1 and 12.2.

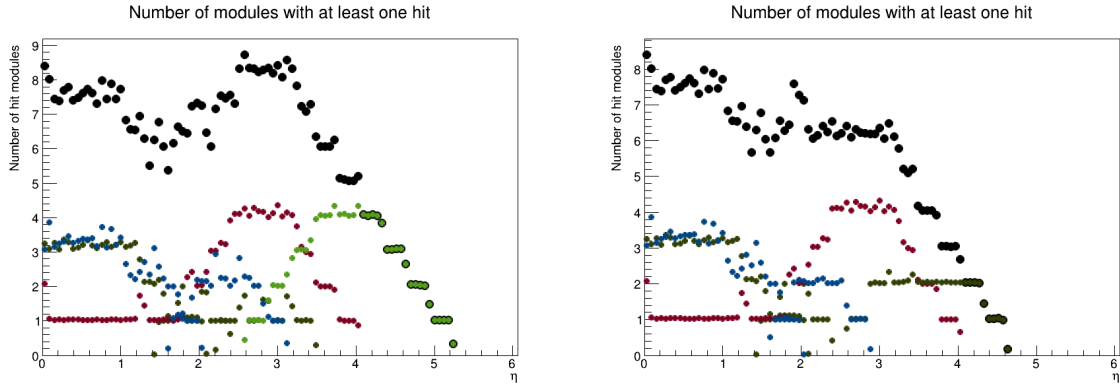


**Figure 12.6:** Numbers of silicon layers that provide acceptance for charged particles as a function of absolute value of pseudorapidity in the forward (left) and backward (right) directions, summed across the central, forward and backward trackers. The distributions are broken down according to sensor type, with colour coding of red for pixels, light or dark green for macro-pixels, blue for strips and black for the sum.

8292 measured with 10 – 20 % precision. Similar results are achieved in the (negative  $\eta$ ) backward  
 8293 direction (not shown).

8294 A major requirement of the tracking detectors will be the precise determination of vertex co-  
 8295 ordinates and track impact parameters relative to the primary vertex in order to give the best  
 8296 possible sensitivity to secondary vertices from heavy flavour decays, for example for the study of  
 8297 the Higgs in its dominant  $b\bar{b}$  decay mode. The simulated results for longitudinal and transverse  
 8298 track impact parameter resolutions using the full new tracking layout are shown in Fig. 12.8.  
 8299 The transverse spatial resolutions are at the level of 10 – 50  $\mu\text{m}$  over a wide range of transverse  
 8300 momentum and pseudorapidity, extending well into the forward direction.

8301 The material budget contributions from the sensors summed across all layers are given in  
 8302 Tabs. 12.1 and This is largest for the inner barrel, where it amounts to 7.2 % of a radiation  
 8303 length. The sensors in the central tracker endcap and the forward and backward tracking rings  
 8304 contribute 2.2 %, 6.7 % and 6.1 % of a radiation length, respectively. The material budget simula-  
 8305 tions, propagated for the full system and including passive contributions, are shown in Fig. 12.9.  
 8306 The use of thin sensors keeps the total material to the level of 0.2 – 0.4 $X_0$  throughout the entire  
 8307 tracking region up to  $\eta \sim 4.5$ . At the most forward (and backward) pseudorapidities, particles  
 8308 travel through a large effective thickness of material as they pass through the beam pipe; this  
 8309 becomes the dominant contribution for  $\eta > 3.5$ .

### 8310 12.3.2 Silicon Technology Choice

8311 Being developed for several High Luminosity-LHC (HL-LHC) upgrades and the proposed CLIC  
 8312 high-energy linear collider we envisage depleted CMOS sensor technology, also known as De-  
 8313pleted Monolithic Active Pixel Sensors (DMAPS), to be used as position sensitive detectors in  
 8314 industry standard CMOS processes or High Voltage-CMOS (HV-CMOS) processes [874]. These  
 8315 sensors are extremely attractive for experiments in particle physics as they integrate the sensing  
 8316 element and the readout ASIC in a single layer of silicon, which removes the need for inter-  
 8317 connection with complex and expensive solder bump technology. Depleted CMOS sensors also  
 8318 benefit from faster turnaround times and lower production costs when compared to hybrid sil-  
 8319 icon sensors. To achieve fast charge collection and high radiation tolerance, DMAPS can be  
 8320 implemented following two different approaches known as low fill-factor and large fill-factor.

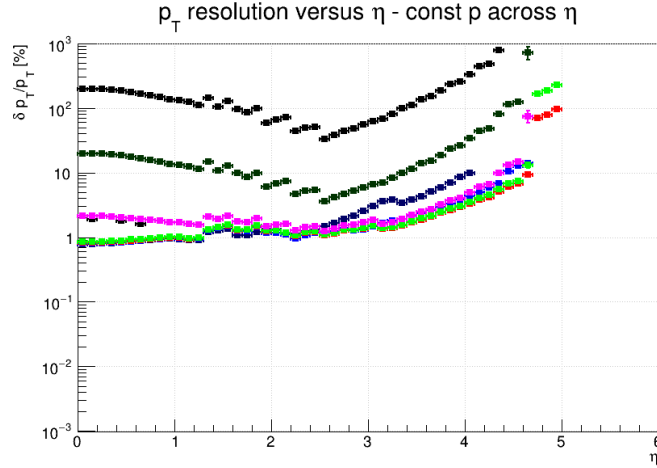


**Figure 12.7:** Simulated transverse momentum track resolution using all modules in the revised LHeC tracking system. Results are shown in terms of fractional  $p_T$  resolution as a function of pseudorapidity for several constant momenta,  $p = 100$  MeV (Black, bottom, obscured), 1 GeV (Dark Blue, obscured), 2 GeV (Light Blue, obscured), 5 GeV (Red), 10 GeV (Light Green), 100 GeV (Magenta), 1 TeV (Dark Green) and 10 TeV (Black, top).

8321 Low fill-factor DMAPS benefit from High Resistivity (HR) substrates and thick epitaxial layers  
 8322 accessible from large-scale CMOS imaging processes, while large fill-factor DMAPS exploit the  
 8323 High Voltage (HV) option developed by commercial CMOS foundries for power electronics. Re-  
 8324 cently, HR wafers have become available in the production line of foundries that manufacture  
 8325 HV-CMOS processes, thus DMAPS in HR/HV-CMOS are also possible to further improve the  
 8326 performance of the sensor. Today's most performant DMAPS detectors are  $50\mu\text{m}$  thin and have  
 8327  $50\mu\text{m} \times 50\mu\text{m}$  cell size with integrated mixed analogue and digital readout electronics,  $6\text{ns}$   
 8328 resolution and  $2 \times 10^{15} \text{1 MeV neq/cm}^2$  radiation tolerance. The typical cross-section of a large  
 8329 fill-factor DMAPS in a HV-CMOS process is shown in Fig. 12.10.

8330 DMAPS in HR/HV-CMOS have been adopted as a world first as the sensor technology of choice  
 8331 for the **Mu3e** experiment at the Paul Scherrer Institute (PSI) in Switzerland [875]. MuPix,  
 8332 the DMAPS detector for Mu3e, implements active pixels that amplify the collected charge in  
 8333 the collecting electrode and peripheral readout electronics that discriminate and process the  
 8334 amplified signals. MuPix10, the first reticle size detector for Mu3e ( $\simeq 2 \times 2 \text{cm}^2$ ) and currently  
 8335 in production, features  $250 \times 256$  pixels with an  $80 \times 80\mu\text{m}^2$  pixel size, 11-bit time-stamp, 6-bit  
 8336 Time-over-Threshold (ToT) and continuous readout. Its peripheral readout electronics include  
 8337 readout buffers, a state machine, a Phase Locked Loop (PLL) and Voltage-Controlled Oscillator  
 8338 (VCO), 8/10-bit encoders and 3 serialisers for data transmission with a rate of up to 1.6 Gbit/s.  
 8339 Previous MuPix prototypes have been thinned to  $50\mu\text{m}$  successfully and tested to achieve a  
 8340  $6\text{ns}$  time resolution after time-walk correction [876]. ATLASPix, the DMAPS development in  
 8341 HR/HV-CMOS that was originally aimed at providing an alternative sensor technology for the  
 8342 outermost pixel layer of the new ATLAS Inner Tracker (ITk) upgrade, has been tested to have  
 8343 an approximate  $150 \text{mW/cm}^2$  power consumption and be radiation tolerant up to  $2 \cdot 10^{15} \text{1 MeV}$   
 8344  $\text{neq/cm}^2$  fluences [877] DMAPS in HR-CMOS, such as the MALTA development originally aimed  
 8345 at the new ATLAS ITk upgrade as well, have achieved full efficiency after  $1 \cdot 10^{15} \text{1 MeV neq/cm}^2$   
 8346 fluences [878]. However, further research is still needed to demonstrate reticle size DMAPS in  
 8347 HR-CMOS. Research to further develop DMAPS to meet the extreme requirements of future  
 8348 experiments in particle physics is on-going.

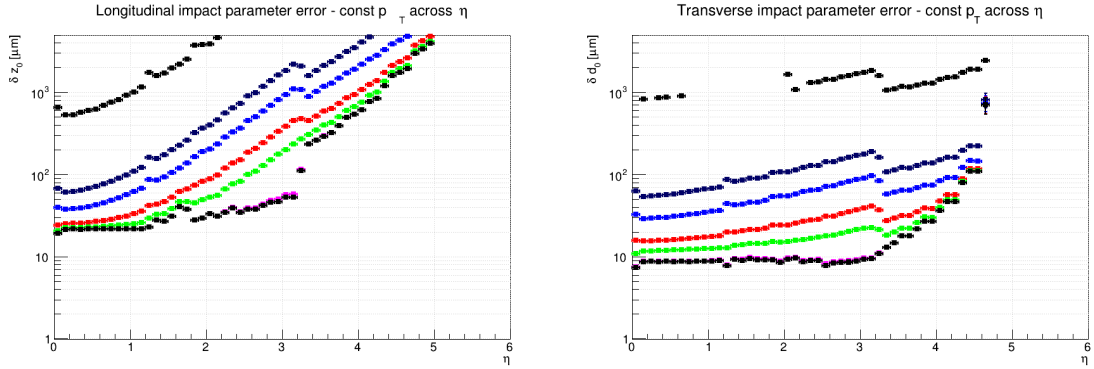


**Figure 12.8:** Simulated longitudinal (left) and transverse (right) impact parameter resolutions using all modules in the revised LHeC tracking system. Results are shown as a function of pseudorapidity for several constant momenta,  $p = 100$  MeV (Black, top), 1 GeV (Dark Blue), 2 GeV (Light Blue), 5 GeV (Red), 10 GeV (Light Green), 100 GeV (Magenta, obscured), 1 TeV (Dark Green, obscured) and 10 TeV (Black, bottom).

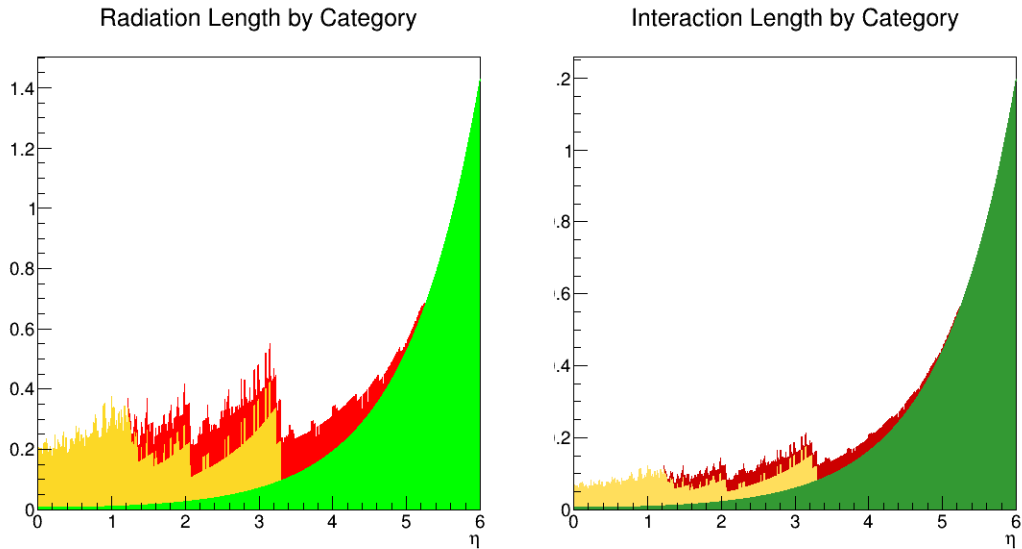


**Figure 12.9:** Material contributions from the tracking modules as a function of pseudorapidity. Results are given in terms of radiation lengths (left) and hadronic interaction lengths (right). The results are broken down into contributions from barrel modules (yellow) and endcap / additional disk modules (red) and are compared with the contribution from the 2.5 mm beam pipe (green).

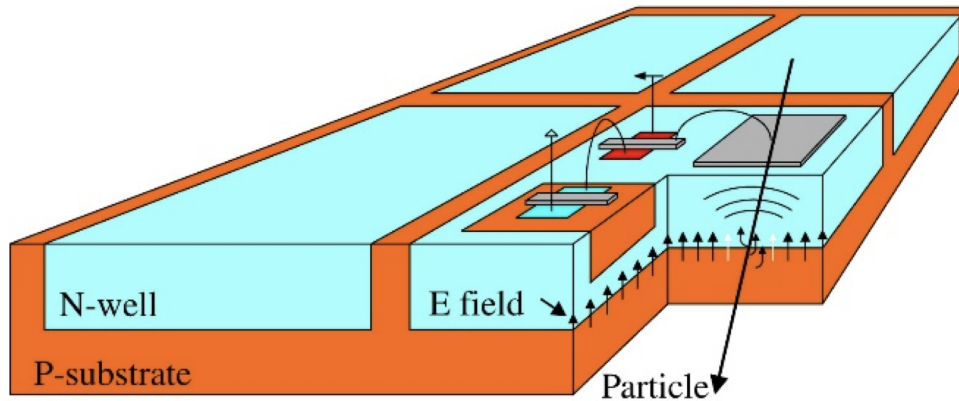


Figure 12.10: Typical sensor cross-section of a DMAPS detector in a HV-CMOS process [874].

8349 The here presented tracker design of the LHeC utilises pixel detectors for high resolution tracking  
 8350 in the inner barrel and as well the barrel endcaps and the forward tracker. The number of readout  
 8351 channels is close to  $10^9$ , with a high transverse and longitudinal segmentation provided by a pitch  
 8352 of  $25 \times 50 \mu m^2$ . One can expect that such a fine segmentation is in reach for a detector which  
 8353 would be built in a decade hence. The radiation level in electron-proton scattering is by orders  
 8354 of magnitude lower than in proton-proton interactions at the LHC and is indeed in a range  
 8355 of  $10^{15} \text{ MeV n}_{eq}/\text{cm}^2$  for which radiation hardness has been proven as indicated above. The  
 8356 monolithic CMOS detector technology leads to a significant simplification of the production of  
 8357 these detectors and a considerably reduced cost. We thus conclude that the LHeC pixel tracker  
 8358 represents a particularly suitable device for a large scale implementation of HV CMOS Silicon  
 8359 in a forthcoming collider detector.

## 8360 12.4 Calorimetry

8361 The 2012 CDR detector design leaned on technologies employed by ATLAS for calorimetry in the  
 8362 barrel region, adopting a lead / liquid argon sampling electromagnetic calorimeter with an ac-  
 8363 cordion geometry and a steel / scintillating tile sampling hadronic component. For the version of  
 8364 the LHeC detector described here, an alternative solution of a lead / scintillator electromagnetic  
 8365 calorimeter has been investigated. This has the advantage of removing the need for cryogenics,  
 8366 whilst maintaining an acceptable performance level. Comparing the lead-scintillator designs  
 8367 for the electromagnetic barrel calorimeter for the 2012 CDR with the updated setup, the **a**-term  
 8368 for shower fluctuations and transverse leakages and the **b**-term describing the back-leakages  
 8369 of the calorimeter the resolution performance of the updated design is better (**a**= 20% and  
 8370 **b**= 0.14% in the 2012 CDR and **a**= 12.4% and **b**= 1.9% in the new design). Although it is  
 8371 not discussed here, the liquid argon solution very much remains the favorable option due to its  
 8372 high level of performance and stability / radiation hardness. The fit-results in CDR 2012 the  
 8373 LAr calorimeter option show a slightly better resolution performance than the lead-scintillator  
 8374 variant. Due to the accordion shaped absorber it forces more energy deposit in the calorimeter  
 8375 volume. The CDR values for comparison: **a**= 8.47% and **b**= 0.318%. The hadronic calorime-  
 8376 ter retains the steel and scintillating tile design, similar to ATLAS. As in the 2012 CDR, plug  
 8377 sampling calorimeters are also incorporated at large  $|\eta|$ , the forward and backward components  
 8378 using tungsten and lead absorber material, respectively, with both using silicon based sensitive  
 8379 readout layers. The steel structures in the central and plug calorimetry close the outer field  
 8380 of the central solenoid. The solenoid and the dipoles are placed between the Electromagnetic-  
 8381 Barrel and the Hadronic-Calorimeter. The HCAL-Barrel sampling calorimeter using steel and



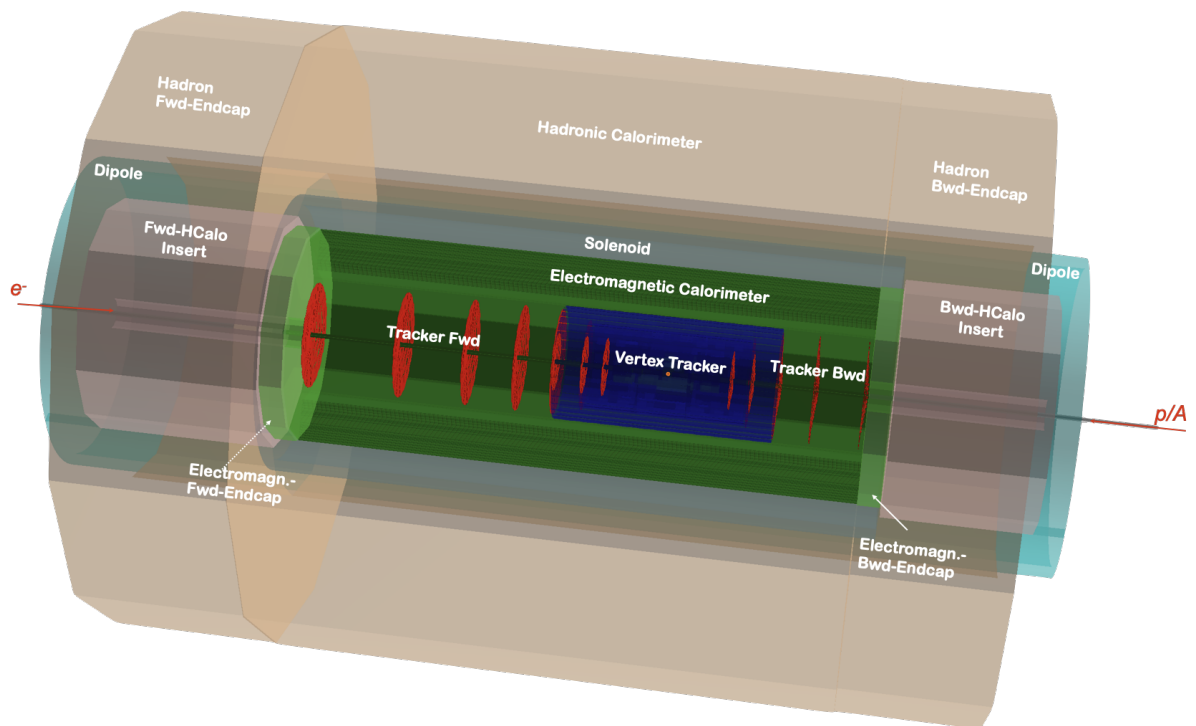


**Figure 12.11:** Three-dimensional view of the arrangement of Hadronic-Calorimeter, experimental magnets (solenoid and dipoles), the electromagnetic calorimeter and tracking detector layers.

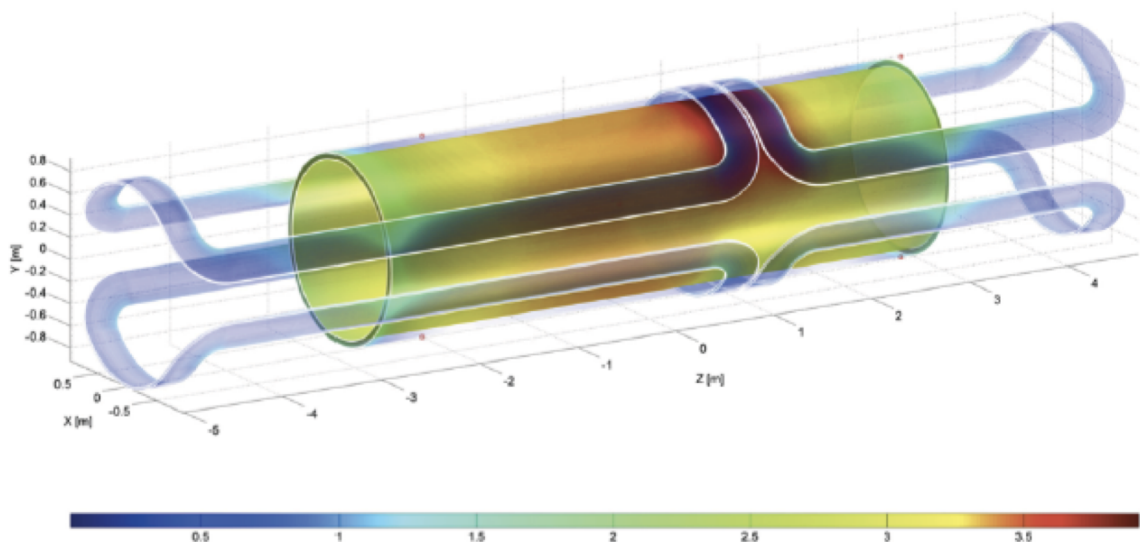


**Figure 12.12:** The coil arrangement of the solenoid and dipoles system housing in a common cryostat.

8382 scintillating tiles as absorber and active material, respectively, provides the mechanical stability  
8383 for the Magnet/Dipole cryostat and the tracking system Fig. 12.11. How the solenoid/dipoles-  
8384 system would look like has been discussed in more detail in [1] and is illustrated by Fig. 12.12.  
8385 (and the LAr cryostat in a cold EMC version) along with the iron required for the return flux of  
8386 the solenoidal field. The main features of the new calorimeter layout are summarised in Tab. 12.3  
8387 and 12.4. The pseudorapidity coverage of the electromagnetic barrel is  $-1.4 < \eta < 2.4$ , whilst  
8388 the hadronic barrel and its end cap cover  $-1.5 < \eta < 1.9$ . Also including the forward and  
8389 backward plug modules, the total coverage is very close to hermetic, spanning  $-5.0 < \eta < 5.5$ .  
8390 The total depth of the electromagnetic section is 30 radiation lengths in the barrel and backward  
8391 regions, increasing to almost  $50X_0$  in the forward direction where particle and energy densities  
8392 are highest. The hadronic calorimeter has a depth of between 7.1 and 9.6 interaction lengths,  
8393 with the largest values in the forward plug region.

Calo (LHeC)	EMC		HCAL	
	Barrel	Ecap Fwd	Barrel	Ecap Bwd
Readout, Absorber	Sci,Pb	Sci,Fe	Sci,Fe	Sci,Fe
Layers	38	58	45	50
Integral Absorber Thickness [cm]	16.7	134.0	119.0	115.5
$\eta_{\max}, \eta_{\min}$	2.4, -1.9	1.9, 1.0	1.6, -1.1	-1.5, -0.6
$\sigma_E/E = a/\sqrt{E} \oplus b$ [%]	12.4/1.9	46.5/3.8	48.23/5.6	51.7/4.3
$\Lambda_I / X_0$	$X_0 = 30.2$	$\Lambda_I = 8.2$	$\Lambda_I = 8.3$	$\Lambda_I = 7.1$
Total area Sci [m <sup>2</sup> ]	1174	1403	3853	1209

**Table 12.3:** Basic properties and simulated resolutions of barrel calorimeter modules in the new LHeC detector configuration. For each of the modules, the rows indicate the absorber and sensitive materials, the number of layers and total absorber thickness, the pseudorapidity coverage, the contributions to the simulated resolution from the sampling ( $a$ ) and material ( $b$ ) terms in the form  $a/b$ , the depth in terms of radiation or interaction lengths and the total area covered by the sensitive material. GEANT4 [872] simulation based fits using crystal ball function [879–881].

Calo (LHeC)	FHC	FEC	BEC	BHC
	Plug Fwd	Plug Fwd	Plug Bwd	Plug Bwd
Readout, Absorber	Si,W	Si,W	Si,Pb	Si,Cu
Layers	300	49	49	165
Integral Absorber Thickness [cm]	156.0	17.0	17.1	137.5
$\eta_{\max}, \eta_{\min}$	5.5, 1.9	5.1, 2.0	-1.4, -4.5	-1.4, -5.0
$\sigma_E/E = a/\sqrt{E} \oplus b$ [%]	51.8/5.4	17.8/1.4	14.4/2.8	49.5/7.9
$\Lambda_I / X_0$	$\Lambda_I = 9.6$	$X_0 = 48.8$	$X_0 = 30.9$	$\Lambda_I = 9.2$
Total area Si [m <sup>2</sup> ]	1354	187	187	745

**Table 12.4:** Basic properties and simulated resolutions of forward and backward plug calorimeter modules in the new LHeC detector configuration. For each of the modules, the rows indicate the absorber and sensitive materials, the number of layers and total absorber thickness, the pseudorapidity coverage, the contributions to the simulated resolution from the sampling ( $a$ ) and material ( $b$ ) terms in the form  $a/b$ , the depth in terms of radiation or interaction lengths and the total area covered by the sensitive material. GEANT4 [872] simulation based fits using crystal ball function [879–881].

8394 The performance of the new calorimeter layout has been simulated by evaluating the mean sim-  
8395 ulated response to electromagnetic (electron) and hadronic (pion) objects with various specific  
8396 energies using GEANT4 [872] and interpreting the results as a function of energy in terms of  
8397 sampling ( $a$ ) and material / leakage ( $b$ ) terms in the usual form  $\sigma_E/E = a/\sqrt{E} \oplus b$ . Example  
8398 results from fits are shown for the barrel electromagnetic and hadronic calorimeters in Fig. 12.13

8399 and for the forward plug electromagnetic and hadronic calorimeters in Fig. 12.14. The results  
 8400 for the  $a$  and  $b$  parameters are summarised in Tabs. 12.3 and 12.4. The response of the barrel  
 8401 electromagnetic calorimeter to electrons in terms of both sampling ( $a = 12.4\%$ ) and material  
 8402 ( $b = 1.9\%$ ) terms is only slightly worse than that achieved with liquid argon sampling in the  
 8403 2012 CDR. The resolutions of the forward and backward electromagnetic plug calorimeters are  
 8404 comparable to those achieved in the 2012 design. A similar pattern holds for the hadronic re-  
 8405 sponse, with sampling terms at the sub-50% level and material terms of typically 5% throughout  
 8406 the barrel end-caps and forward and backward plugs.

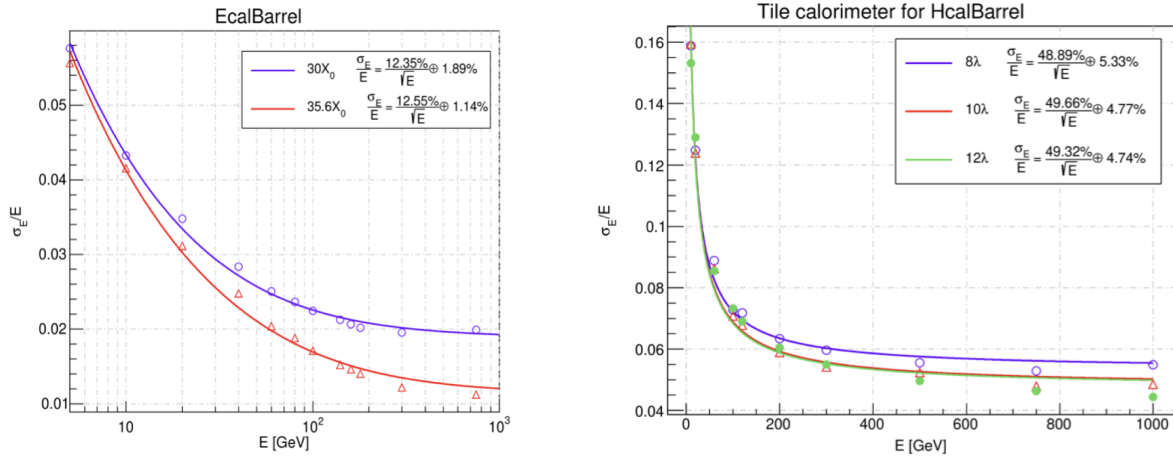


**Figure 12.13:** Crystal Ball fitted energy dependent resolution for the barrel electromagnetic (left) and barrel hadronic (right) calorimeters EMC and HCAL, respectively. The first ( $a$ ) term includes shower fluctuations and transverse leakages and the second ( $b$ ) term includes leakages from the calorimeter volume longitudinally.

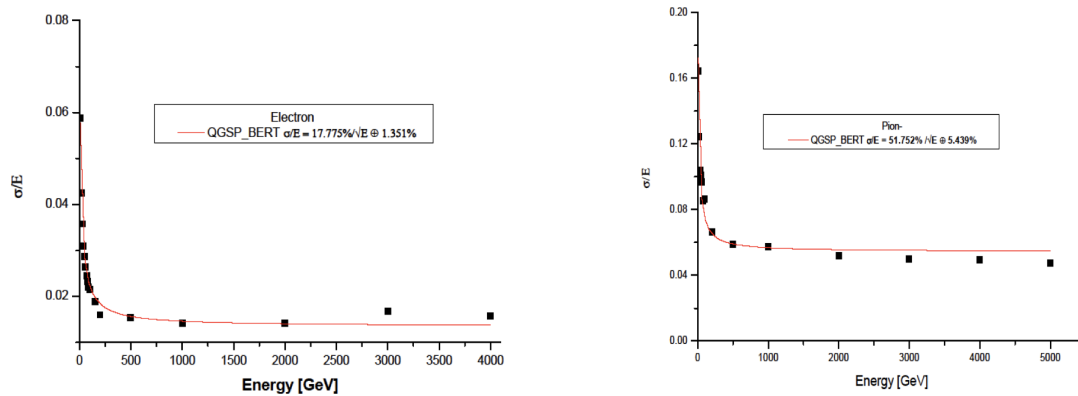


**Figure 12.14:** Crystal Ball fitted energy dependent resolution for the forward electromagnetic (left) and forward hadronic (right) plug calorimeters FEC and FHC, respectively. The first ( $a$ ) term includes shower fluctuations and transverse leakages and the second ( $b$ ) term includes leakages from the calorimeter volume longitudinally.

## 8407 12.5 Muon Detector

8408 Muon identification is an important aspect for any general purpose HEP experiment. At the  
 8409 LHeC the muon detector can widen the scope and the spectrum of many measurements, of which

8410 only a few are listed here:

- 8411 • Higgs decay,
- 8412 • Semi-leptonic decays of heavy flavoured hadrons,
- 8413 • Vector meson production,
- 8414 • Direct  $W$  and  $Z$  production,
- 8415 • Di-muon production,
- 8416 • Leptoquarks, lepton flavour violation, and other BSM phenomena.

8417 The primary target of the muon detector at the LHeC is to provide a reliable muon tag signature  
8418 which can be uniquely used in conjunction with the central detector for muon identification,  
8419 triggering and precision measurements. This specification is appropriate to the constraints of  
8420 limited space <sup>2</sup> and the lack of a dedicated magnetic field as in the baseline design. The muon  
8421 chambers surround the central detector and cover the maximum possible solid angle. They have  
8422 a compact multi-layer structure, providing a pointing trigger and a precise timing measurement  
8423 which is used to separate muons coming from the interaction point from cosmics, beam halo and  
8424 non prompt particles. This tagging feature does not include the muon momentum measurement  
8425 which is performed only in conjunction with the central detector. A trigger candidate in the  
8426 muon detector is characterised by a time coincidence over a majority of the layers in a range  
8427 of  $\eta$  and  $\phi$ , compatible with an  $ep$  interaction of interest in the main detector. The muon  
8428 candidates are combined with the trigger information coming from the central detector (mainly  
8429 the calorimetry at Level 1 trigger) to reduce the fake rate or more complex event topologies.

8430 In terms of technology choices, the options in use in ATLAS and CMS and their planned upgrades  
8431 are adequate for LHeC. Generally, muon and background rates in LHeC are expected to be  
8432 lower than in  $pp$ . The option of an LHeC muon detector composed by layers of Resistive  
8433 Plate Chambers (RPC), providing the Level 1 trigger and a two coordinate ( $\eta$ ,  $\phi$ ) measurement  
8434 possibly aided by Monitored Drift Tubes (MDT) for additional precision measurements, as  
8435 chosen for the 2012 CDR, is still valid. Recent developments as presented in the LHC Phase 2  
8436 Upgrade Technical Design Reports [882, 883] further strengthen this choice. A new thin-RPC  
8437 (1 mm gas gap) operated with lower HV, provides a sharper time response (few ns), a higher  
8438 rate capability (tens of kHz/cm<sup>2</sup>), and extends the already good aging perspective. Advances in  
8439 low-noise, high-bandwidth front-end electronics can improve the performance of older detectors.  
8440 Similar arguments also hold for smaller tube MDTs (15 mm diameter) which provide lower  
8441 occupancy and higher rate capability.

8442 Fig. 12.15 shows an adaptation for LHeC of an RPC-MDT assembly as will be implemented for  
8443 the inner muon layer of ATLAS already during the Phase-1 upgrade as a pilot for Phase-2. A  
8444 triplet of thin gap RPCs, each with 2 coordinate measurement, is combined with two superlayers  
8445 of small MDTs. It is also important to note the reduced volume of this structure, in particular  
8446 the RPC part which would provide the muon tag. For the LHeC a baseline would be to have  
8447 one or two such stations forming a near-hermetic envelope around the central detector.

8448 Finally, as already presented in the 2012 CDR, detector extensions, with a dedicated magnetic  
8449 field in the muon detector, be this a second solenoid around the whole detector or extra dipole  
8450 or toroid in the forward region are, at this stage, left open as possible developments only for  
8451 upgrade scenarios.

---

<sup>2</sup>As in the 2012 CDR, the baseline LHeC detector including the muon system and all of the services and supports is expected to fit into the octagonal shape envelope of the L3 magnet (11.6 m minimum diameter).

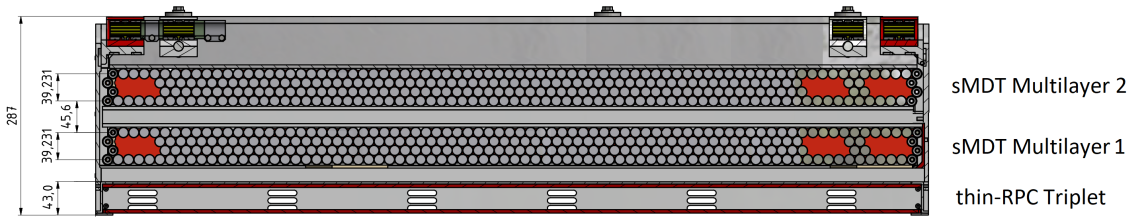


**Figure 12.15:** A transverse view of a RPC-MDT assembly as adapted from a drawing of the ATLAS Phase-1 muon upgrade [882]. In this case a station is composed of an RPC triplet for trigger and tw0-coordinate readout and two MDT superlayers for precise track measurements.

## 12.6 Forward and Backward Detectors

In the 2012 CDR, initial plans for beamline instrumentation were provided for the LHeC. In the backward direction, low angle electron and photon calorimeters were included with the primary intention of measuring luminosity via the Bethe-Heitler process  $ep \rightarrow eXp$ , also offering an electron tagger to identify photoproduction ( $\gamma p \rightarrow X$ ) processes at intermediate  $y$  values. The current design carries forward the 2012 version of this backward instrumentation.

In the forward direction, Roman pot detectors were included in the region of  $z \sim 420$  m, capable of detecting scattered protons over a range of fractional energy loss  $10^{-3} < \xi < 3 \times 10^{-2}$  and wide transverse momentum acceptance, based on extensive previous work in the LHC context by the FP420 group [884]. This also forms the basis of forward proton tagging in the revised design. However, as is the case at ATLAS and CMS / TOTEM, further Roman pot detectors in the region of 200 m and (with HL-LHC optics) perhaps around 320 m would extend the acceptance towards higher  $\xi$  values up to around 0.2 allowing the study of diffractive processes  $ep \rightarrow eXp$  where the dissociation system  $X$  has a mass extending into the TeV regime. It is worth noting that Roman pot technologies have come of age at the LHC, with the TOTEM collaboration operating 14 separate stations at its high point. Silicon sensor designs borrowed from the innermost regions of the ATLAS and CMS vertexing detectors have been used, providing high spatial resolution and radiation hardness well beyond the needs of LHeC. Very precise timing detectors based on fast silicon or Cherenkov radiation signals from traversing protons in quartz or diamond have also been deployed. It is natural that these advances and the lessons from their deployment at the LHC will be used to inform the next iteration of the LHeC design.

The forward beamline design also incorporates a zero angle calorimeter, designed primarily to detect high energy leading neutrons from semi-inclusive processes in  $ep$  scattering and to determine whether nuclei break up in  $eA$  events. This component of the detector was not considered in detail in 2012 and is therefore discussed here.

### 12.6.1 Zero-Degree (Neutron) Calorimeter

The Zero-Degree Calorimeter (ZDC) measures final state neutral particles produced at angles near the incoming hadron beam direction. They typically have large longitudinal momentum ( $x_F \gg 10^{-2}$ ), but with transverse momentum of order of  $\Lambda_{\text{QCD}}$ . Such a calorimeter has been instrumented in experiments for  $ep$  collisions (H1 and ZEUS) and for  $pp$ ,  $pA$  and  $AA$  collisions at RHIC (STAR and PHENIX) and at the LHC (ATLAS, CMS, ALICE and LHCf at the ATLAS IP). The detector's main focus is to study the soft-hard interplay in the QCD description of  $ep$  and  $eA$  collisions by studying the dependence of forward-going particles with small transverse momentum on variables such as  $Q^2$  and  $x$  that describe the hard scattering. The detector also allows the tagging of spectator neutrons to detect nuclear breakup in  $eA$  collisions and enables

8487 the precise study of the EMC effect by using neutron-tagged DIS on small systems, such as  
 8488  $e^3He \rightarrow ed + n \rightarrow eX + n$ . For heavier ions, several tens of neutrons may enter within the  
 8489 aperture of the ZDC. Inclusive  $\pi^0$  production has been measured by the LHCf experiments for  
 8490  $pp$  collisions. It is of great interest to compare with DIS measurements at the same proton  
 8491 energies. Precise understanding of the inclusive spectrum of the forward-going particles is a key  
 8492 ingredient in simulating air showers from ultra-high energy cosmic rays.

### 8493 **Physics requirement for forward neutron and $\pi^0$ production measurement**

8494 It is known from various HERA measurements that the slope parameter  $b$  is about  $8 \text{ GeV}^{-2}$  in the  
 8495 exponential parameterisation  $e^{bt}$  of the  $t$  distribution of leading neutrons. In order to precisely  
 8496 determine the slope parameter it is necessary to measure the transverse momentum of the  
 8497 neutrons up to or beyond  $1 \text{ GeV}$ . The aperture for forward neutral particles does not have to be  
 8498 very large, thanks to the large energy of the proton and heavy ion beam. For example, collisions  
 8499 with  $E_p = 7 \text{ TeV}$  need  $0.14 \text{ mrad}$  for  $p_T = 1 \text{ GeV}$  neutrons at  $E_{\text{particle}}/E_{\text{beam}} \equiv x_F = 1.0$ , or  
 8500  $0.56 \text{ mrad}$  for  $x_F = 0.25$ .

8501 The energy or  $x_F$  resolution for neutrons will not be a dominant factor thanks to the high energy  
 8502 of the produced particles. The energy resolution of a neutron with  $x_F = 0.1$  is about 2% for  
 8503 cutting-edge hadron calorimeters with  $\sigma_E/E = 50\%/\sqrt{E}$ , where  $E$  is in  $\text{GeV}$ . Such a resolution  
 8504 can be achieved if non-unity  $e/h$  can be compensated either by construction of the calorimeter  
 8505 or by software weighting, and if the size of the calorimeter is large enough so that shower leakage  
 8506 is small.

8507 On the other hand, the resolution requirement on the transverse momentum is rather stringent.  
 8508 For example,  $1 \text{ mm}$  resolution on hadronic showers from the neutron measured at  $100 \text{ m}$  down-  
 8509 stream from the interaction point corresponds to  $0.01 \text{ mrad}$  or  $70 \text{ MeV}$ , which is rather moderate  
 8510 ( $\leq 10\%$  resolution for large  $p_T$  hadrons with  $p_T > 700 \text{ MeV}$ ). For smaller  $p_T$  it is more appro-  
 8511 priate to evaluate the resolution in terms of  $t \simeq -(1 - x_F)p_T^2$  i.e.  $\Delta t \simeq 2(\Delta p_T)p_T$  at  $x_F = 1$ .  
 8512 At  $t = 0.1 \text{ GeV}^2$  or  $p_T \simeq 300 \text{ MeV}$ ,  $\Delta t$  is about 50%. A shower measurement with significantly  
 8513 better than  $1 \text{ mm}$  position resolution, therefore, would improve the  $t$ -distribution measurement  
 8514 significantly.

8515 According to the current LHC operation conditions with  $\beta^* = 5 \text{ cm}$ , the beam spread is  
 8516  $8 \times 10^{-5} \text{ rad}$  or  $0.56 \text{ GeV}$ . This is much larger than the required resolution in  $p_T$ . It is therefore  
 8517 neither possible to measure the particle flow nor to control the acceptance of the forward aper-  
 8518 ture. For precision measurement of forward particles, it is necessary to have runs with  $\beta^* \geq 1 \text{ m}$ ,  
 8519 corresponding to  $\sigma(p_T) < 70 \text{ MeV}$ .

8520 The calorimeter should be able to measure more than 30 neutrons of  $5 \text{ TeV}$  to tag spectator  
 8521 neutrons from heavy-ion collisions. The dynamic range of the calorimeter should exceed  $100 \text{ TeV}$   
 8522 with good linearity.

8523 As for  $\pi^0$  measurements, the LHCf experiment has demonstrated that a position resolution of  
 8524  $200 \mu\text{m}$  on electromagnetic showers provides good performance for the inclusive photon spectrum  
 8525 measurements [885]. This also calls for fine segmentation sampling layers.

### 8526 **ZDC location**

8527 According to the IP design, a possible location for the ZDC is after the first bending of the  
 8528 outgoing colliding proton beam at around  $Z = 110 \text{ m}$ , where no beam magnet is placed (see  
 8529 Fig. 12.16). It is anyhow planned to place a neutral particle dump around this location in order

8530 to protect accelerator components. A ZDC could serve as the first absorbing layer at zero  
 8531 degrees.

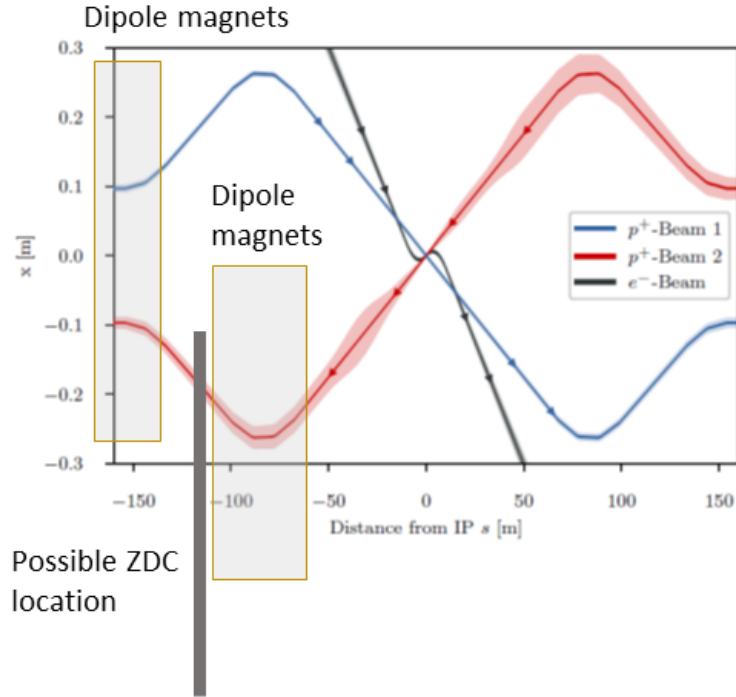


**Figure 12.16:** Possible location for a ZDC for the linac–ring design of LHeC. The solid rectangle represents the ZDC. The two boxes in front of and behind the ZDC indicate the locations of bending magnets.

8532 The aperture to the ZDC would be determined by the last quadrupole magnet at around  $z = 50$  m.  
 8533 Assuming a typical aperture for the LHC magnets of 35 mm, the aperture could be as large as  
 8534 0.7 mrad. The horizontal aperture of the dipole magnets between 75 and 100 m would be larger,  
 8535 since otherwise the magnets receive significant radiation from neutral particles produced from  
 8536 the collisions at the IP. Even if the aperture is limited by the vertical aperture of the last dipole  
 8537 at  $z = 100$  m, the aperture is 0.35 mrad, corresponding to 2.4 GeV in  $p_T$  for 7 GeV particles.  
 8538 This fulfills the physics requirement.

8539 The space for the ZDC location in the transverse direction should be at least  $\pm 2\lambda_I$  to avoid  
 8540 large leakage of hadronic showers. This can be achieved if the proton beam passes inside the  
 8541 calorimeter, about 20 cm from the centre of the calorimeter. The total size of the calorimeter  
 8542 could then be  $60 \times 60 \times 200 \text{ cm}^3$  or larger according to the current layout of the beam and  
 8543 accelerator components. This would provide about  $\pm 3\lambda_I$  in the transverse direction and about  
 8544  $10\lambda_I$  in depth.

#### 8545 Radiation requirement for the ZDC

8546 It can safely be assumed that the energy spectrum of the forward neutral particles produced in  
 8547  $ep$  and  $pp$  events are very similar. According to the LHCf simulation, their tungsten–scintillator  
 8548 sandwich calorimeter receives about  $30 \text{ Gy/nb}^{-1}$  or  $10^8 \text{ events/nb}^{-1}$  assuming  $\sigma_{pp}^{\text{tot}} = 100 \text{ mb}$ ,  
 8549 i.e.  $3 \times 10^{-7} \text{ Joule/event}$ . This means that about 1/4 of the total proton beam energy ( $7 \text{ TeV} \simeq$   
 8550  $1.12 \times 10^{-6} \text{ Joule/event}$ ) is deposited in 1 kg material in  $pp$  collisions. The  $ep$  total cross section

8551 is expected to be approximately  $68 \mu\text{b}$  or  $680 \text{ kHz}$  at  $10^{34} \text{ cm}^2\text{s}^{-1}$ . A  $7 \text{ TeV}$  beam or  $1.12 \times$   
8552  $10^{-6} \text{ Joule/event}$  corresponds to  $0.76 \text{ Joule/s}$  at this instantaneous luminosity. A quarter of the  
8553 total dose is then about  $0.2 \text{ Gy/sec}$  or  $0.02 \text{ Gy/nb}$ . The contribution from beam-gas interactions  
8554 is estimated to be much smaller ( $\mathcal{O}(100 \text{ kHz})$ ).

8555 Assuming that the ZDC is always operational during LHeC running, one year of *ep* operation  
8556 amounts to  $2.5 \text{ MGy/year}$  assuming  $10^7 \text{ sec}$  operation, or  $\mathcal{O}(10 \text{ MGy})$  throughout the lifetime of  
8557 the LHeC operation. This approximately corresponds to  $10^{14} - 10^{15}$   $1 \text{ MeV}$  neutron equivalent.

### 8558 Possible calorimeter design

8559 The high dose of  $\mathcal{O}(10 \text{ MGy})$  requires calorimeters based on modern crystals (e.g. LYSO) or  
8560 silicon as sampling layers, at least for the central part of the calorimeter where the dose is  
8561 concentrated. Since we also need very fine segmentation for photons, it is desirable to use finely  
8562 segmented silicon pads of order of  $1 \text{ mm}$ . As for the absorbers, tungsten should be used for good  
8563 position resolution of photons and the initial part of hadronic showers.

8564 In the area outside the core of the shower i.e. well outside the aperture, the dose may be much  
8565 smaller and small scintillator tiles could be used for absorbers, which allows measurements with  
8566 good  $e/h$  ratio. If we choose a uniform design using silicon across the detector, the segmentation  
8567 of the outer towers could be order of a few  $\text{cm}$ , which still makes it possible to use software  
8568 compensation technology, as developed for example for the calorimeters in the ILC design. It  
8569 may also be possible to use lead instead of tungsten for outer towers to reduce the cost.

## 8570 12.7 Detector Installation and Infrastructure

8571 The usual constraints that apply to HEP detector integration and assembly studies also apply  
8572 to the LHeC. In places, they are even tighter since the detector has to be installed in a relatively  
8573 short time, as given by the duration of an LHC machine shutdown, which is typically two years.  
8574 For the purposes of this report, it is assumed that the LHeC detector will be installed at IP2, see  
8575 Fig. 12.17. The magnet formerly used by L3 and now in use by ALICE is already present at IP2  
8576 and its support structure will be used once again by LHeC. However, the time needed to remove  
8577 the remainder of the existing detector and its services has to be included to the overall schedule.  
8578 Thus the only realistic possibility to accomplish the timely dismantling of the old detector and  
8579 the installation of the new one is to complete as much as possible of the assembly and testing  
8580 of the LHeC detector on the surface, where the construction can proceed without impacting on  
8581 the LHC physics runs. The condition for doing this is the availability of equipped free space  
8582 at the LHC-P2 surface, namely a large assembly hall with one or two cranes. To save time,  
8583 most of the detector components have been designed to match the handling means available  
8584 on site, i.e. a bridge crane in the surface hall and experiment cavern. Nevertheless, a heavy  
8585 lifting facility (about  $300 \text{ tons}$  capacity) will be rented for the time needed to lower the heaviest  
8586 detector components, such as the HCal barrel and plug modules. Large experience with this  
8587 will be acquired during LHC Long Shutdown 3, when a significant part of the ATLAS and CMS  
8588 detectors will be replaced by new elements. At CMS, for instance, a new Endcap Calorimeter  
8589 weighting about  $220 \text{ tons}$  will be lowered into the experiment cavern, a scenario very close to  
8590 what is envisaged for the LHeC detector assembly.

8591 The detector has been split into the following main parts for assembly purposes:

- 8592 • Coil cryostat, including the superconducting coil, the two integrated dipoles and eventually  
8593 the EMCal.





**Figure 12.17:** View of the surface infrastructure at Point 2, near St. Genis.

- 8594 • Five HCal tile calorimeter barrel modules, fully instrumented and cabled (5).
- 8595 • Two HCal plugs modules, forward and backward (2).
- 8596 • Two EMCal plugs, forward and backward (2).
- 8597 • Inner Tracking detector (1).
- 8598 • Beam-pipe (1).
- 8599 • Central Muon detector (1 or 2).
- 8600 • Endcaps Muon detector (2).

8601 The full detector, including the Muon chambers, fits inside the former L3 detector Magnet Yoke,  
 8602 once the four large doors are taken away. The goal is to prevent losing time in dismantling the  
 8603 L3 Magnet barrel yoke and to make use of its sturdy structure to hold the detector central part  
 8604 on a platform supported by the magnet crown, whilst the Muon chambers are inserted into  
 8605 lightweight structures (space-frames) attached to the inner surface of the octagonal L3 magnet.

8606 The assembly of the main detector elements on the surface can start at any time, without  
 8607 sensible impact on the LHC run, providing that the surface facilities are available. The Coil  
 8608 system commissioning on site is estimated to require three months and preparation for lowering  
 8609 a further three months, including some contingency. In the same time window, the L3 Magnet  
 8610 will be freed up and prepared for the new detector <sup>3</sup>. Lowering of the main detector components  
 8611 into the cavern, illustrated in Fig.12.18, is expected to take one week per piece (15 pieces in  
 8612 total). Underground integration of the central detector elements inside the L3 Magnet would

<sup>3</sup>The actual delay depends on the level of activation and the procedure adopted for dismantling the existing detector. Here again the experience acquired during the long shutdown LS2 with the upgrades of ALICE and LHCb and later with the ATLAS and CMS upgrades during LS3 will provide important insight for defining procedures and optimising the schedule.

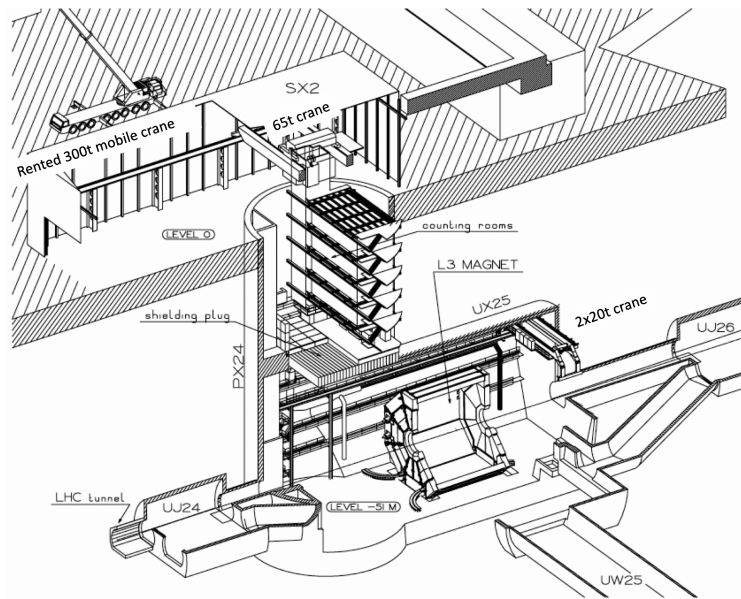


**Figure 12.18:** View of the cavern infrastructure at Point 2. The support structure of the magnet of the L3 experiment (at the centre) will house and support the LHeC detector.

8613 require about 6 months, cabling and connection to services some 8 to 10 months, in parallel  
 8614 with the installation of the Muon chambers, the Tracker and the Calorimeter Plugs. Fig.12.19  
 8615 shows the installed complete detector housed in the L3 magnet support.

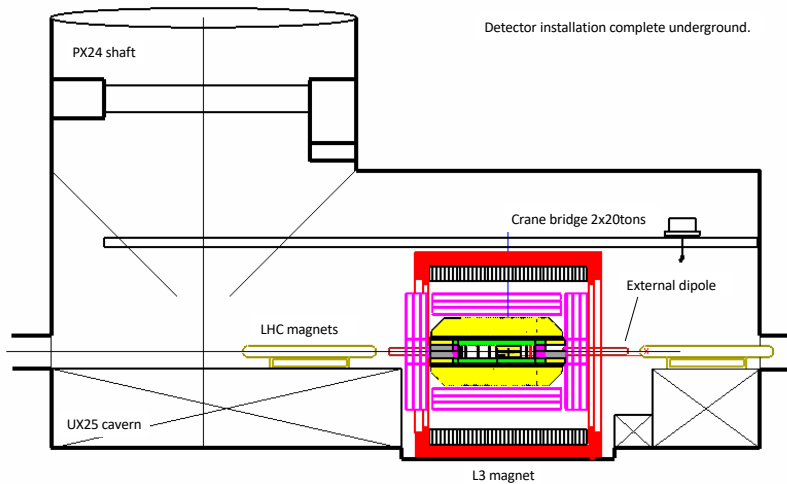


**Figure 12.19:** View of the LHeC detector, housed in the L3 magnet support structure, after installation at the interaction point.

8616 The total estimated time, from the starting of the testing of the Coil system on surface to the  
 8617 commissioning of the detector underground is thus 20 months. The beam-pipe bake out and  
 8618 vacuum pumping could take another 3 months and the final detector check-out one additional  
 8619 month. Some contingency (2–3 months in total) is foreseen at the beginning and the end of the  
 8620 installation period. A sketch of the installation schedule is provided in Fig. 12.20

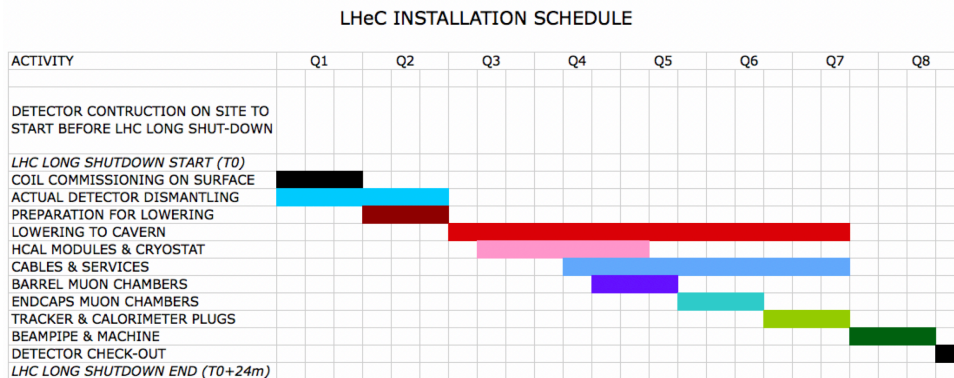


**Figure 12.20:** Time schedule of the sequential installation of the LHeC detector at point 2, as described in the text.

8621 Concerning the detector infrastructures, not much can be said at this stage. The LHeC detector  
 8622 superconducting coil will need cryogenic services and a choice has to be made between purchas-  
 8623 ing a dedicated liquid helium refrigeration plant or profiting from the existing LHC cryogenic  
 8624 infrastructure to feed the detector magnet. The electrical and water-cooling networks present at  
 8625 LHC-P2 are already well sized for the new detector and only minor interventions are expected  
 8626 there.

## 8627 12.8 Detector Design for a Low Energy FCC-eh

8628 Although not the primary focus of this report, a full detector design has also been carried  
 8629 out for an  $ep$  facility based on an FCC tunnel with proton-ring magnet strengths limited such  
 8630 that the proton energy is 20 TeV. For ease of comparison, the basic layout and the technology  
 8631 choices are currently similar to those of the LHeC detector. Similar or improved performance is  
 8632 obtained compared with the LHeC, provided that additional disks are included in the forward  
 8633 and backward trackers and the calorimeter depths are scaled logarithmically with the beam  
 8634 energies.

8635 The basic layout is shown in Fig. 12.21. The barrel and end-caps of the central tracker are  
 8636 identical to those of the LHeC design, as given in table 12.1. The design parameters for the  
 8637 FCC-eh versions of the forward and backward trackers, the barrel calorimeters and the plug  
 8638 calorimeters are given in tables 12.5, 12.6 and 12.7, respectively. Comparing the performance of  
 8639 "warm" solution (Pb-Scillator) with the "cold" variant (Pb-LAr) for the barrel electromagnetic  
 8640 calorimeter (EMC) the superior performance of the "cold" calorimeter setup again favors the  
 8641 Pb-LAr option for the lowE-FCCeh detector (see figure 12.22 and table 12.6).

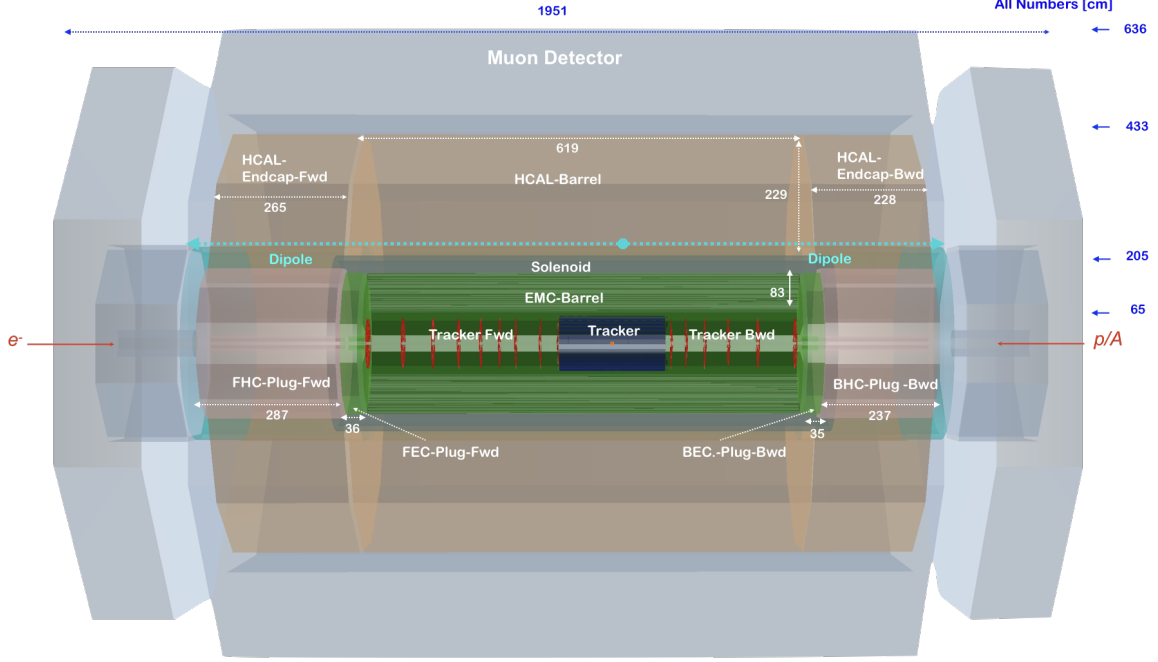


**Figure 12.21:** Side view of a low energy FCCeh ( $E_p = 20$  TeV) concept detector, designed using the DD4hep framework [871], showing the essential features. The solenoid is again placed between the ECAL-Barrel and Hadronic-Barrel calorimeters and is housed in a cryostat in common with the beam steering dipoles extending over the full length of the barrel and plug hadronic calorimeters. The sizes have been chosen such that the solenoid/dipoles and ECAL-Barrel systems as well as the whole tracker are also suitable to operate after an upgrade of the beam energy to  $E_p = 50$  TeV.

Tracker (lowE-FCCeh) <sup>1)</sup>	Fwd Tracker			Bwd Tracker		Total
	pix	pix <sub>macro</sub>	strip	pix <sub>macro</sub>	strip	(incl. Tab. 12.1)
$\eta_{\max}, \eta_{\min}$	5.6, 2.6	3.8, 2.2	3.5, 1.6	-4.6, -2.6	-2.8, -1.6	5.3, -4.6
Wheels	2	1	3	3	3	
Modules/Sensors	288	288	1376	216	1248	12444
Total Si area [m <sup>2</sup> ]	1.35	1.45	7.35	1.0	6.5	49.85
Read-out-Channels [10 <sup>6</sup> ]	647.9	110.2	42.3	82.7	38.3	3317.2
pitch <sup><math>r-\phi</math></sup> [ $\mu\text{m}$ ]	25	100	100	100	100	
pitch <sup><math>z</math></sup> [ $\mu\text{m}$ ]	50	400	50k <sup>2)</sup>	400	10k <sup>2)</sup>	
Average $X_0/\Lambda_I$ [%]	6.7 / 2.1			6.1 / 1.9		
incl. beam pipe [%]						40 / 25

<sup>1)</sup> Based on tklayout calculations [873]

<sup>2)</sup> Reaching pitch <sup>$r-\phi$</sup>  when using two wafer layers rotated by 20 mrad is achievable.

**Table 12.5:** Summary of the main properties of the forward and backward tracker modules in the low energy FCC-eh detector configuration, based on calculations performed using tkLayout. For each module, the rows correspond to the pseudorapidity coverage, the numbers of disk layers and of sensors, the total area covered by silicon sensors, the numbers of readout channels, the hardware pitches affecting the ( $r-\phi$ ) and the  $z$  resolution, and the average material budget in terms of radiation lengths and interaction lengths. The numbers are broken down into separate contributions from pixels, macro-pixels and strips. The column *Total* contains the sum of corresponding values of barrel tracker modules (identical to the LHeC barrel layout, table 12.1) and the forward and backward trackers in this table, 12.5.

Calo (lowE-FCCeh)	EMC		HCAL	
	Barrel	Ecap Fwd	Barrel	Ecap Bwd
Readout, Absorber	Sci,Pb	Sci,Fe	Sci,Fe	Sci,Fe
Layers	49	91	68	78
Integral Absorber Thickness [cm]	36.6	206.0	184.0	178.0
$\eta_{\max}, \eta_{\min}$	2.8, -2.5	2.0, 0.8	1.6, -1.4	-0.7, -1.8
$\sigma_E/E = a/\sqrt{E} \oplus b$ [%]	12.6/1.1	38.9/3.3	42.4/4.2	40.6/3.5
$\Lambda_I / X_0$	$X_0 = 66.2$	$\Lambda_I = 12.7$	$\Lambda_I = 11.3$	$\Lambda_I = 11.0$
Total area Sci [m <sup>2</sup> ]	2915	4554	12298	3903

**Table 12.6:** Basic properties and simulated resolutions of barrel calorimeter modules in a scaled configuration, suitable for a low energy FCC detector. For each of the modules, the rows indicate the absorber and sensitive materials, the numbers of layers and the total absorber thickness, the pseudorapidity coverage, the contributions to the simulated resolution from the sampling ( $a$ ) and material ( $b$ ) terms in the form  $a/b$ , the depth in terms of radiation or interaction lengths and the total area covered by the sensitive material. The resolutions are obtained from a GEANT4 [872] simulation, with fits using a crystal ball function [879–881].

Calo (lowE-FCCeh)	FHC	FEC	BEC	BHC
	Plug Fwd	Plug Fwd	Plug Bwd	Plug Bwd
Readout, Absorber	Si,W	Si,W	Si,Pb	Si,Cu
Layers	296	49	59	238
Integral Absorber Thickness [cm]	256.9	29.6	27.9	220.8
$\eta_{\max}, \eta_{\min}$	5.8, 1.8	5.4, 1.8	-1.5, -5.2	-1.5, -5.6
$\sigma_E/E = a/\sqrt{E} \oplus b$ [%]	61.9/0.5	26.5/0.4	24.7/0.4	46.7/4.4
$\Lambda_I / X_0$	$\Lambda_I = 15.5$	$X_0 = 84.7$	$X_0 = 50.2$	$\Lambda_I = 14.7$
Total area Si [m <sup>2</sup> ]	2479	364	438	1994

**Table 12.7:** Basic properties and simulated resolutions of forward and backward plug calorimeter modules in a scaled configuration, suitable for a low energy FCC detector. For each of the modules, the rows indicate the absorber and sensitive materials, the numbers of layers and the total absorber thickness, the pseudorapidity coverage, the contributions to the simulated resolution from the sampling ( $a$ ) and material ( $b$ ) terms in the form  $a/b$ , the depth in terms of radiation or interaction lengths and the total area covered by the sensitive material. The resolutions are obtained from a GEANT4 [872] simulation, with fits using a crystal ball function [879–881].

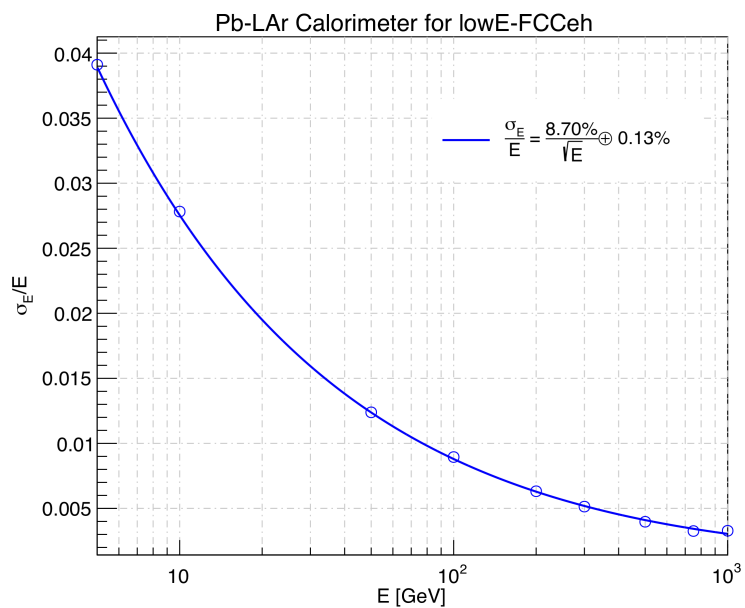


**Figure 12.22:** For comparison the achievable resolution of a cold version of an EM-calorimeter stack is shown. The sampling calorimeter setup (ATLAS type) is characterised by lead as absorber 2.2 mm thick and 3.8 mm gaps filled with liquid argon as detecting medium, a cartesian accordion geometry and stack folds having a length of 40.1 mm and an inclination angle of  $\pm 45^\circ$  to each other. The radiation length for the setup described is estimated from geantino scans using **GEANT4** [872]. The simulated calorimeter stack has a depth of 83.7 cm (approximately  $58 X_0$ ). The fits have been performed as for Fig. 12.13.

## Chapter 13

# Conclusion

The Large Hadron Collider determines the energy frontier of experimental collider physics for the next two decades. Following the current luminosity upgrade, the LHC can be further upgraded with a high energy, intense electron beam such that it becomes a twin-collider facility, in which  $ep$  collisions are registered concurrently with  $pp$ . A joint ECFA, CERN and NuPECC initiative led to a detailed conceptual design report (CDR) [1] for the Large Hadron Electron Collider published in 2012. The present paper represents an update of the original CDR in view of new physics and technology developments.

The LHeC uses a novel, energy recovery linear electron accelerator which enables TeV energy electron-proton collisions at high luminosity, of  $O(10^{34}) \text{ cm}^{-2}\text{s}^{-1}$ , exceeding that of HERA by nearly three orders of magnitude. The discovery of the Higgs boson and the surprising absence of BSM physics at LHC demand to extend the experimental base of particle physics suitable to explore the energy frontier, beyond  $pp$  collisions at the LHC. The LHC infrastructure is the largest single investment the European and global particle physics community ever assembled, and the addition of an electron accelerator a seminal opportunity way to build on it, and to sustain the HL-LHC programme by adding necessary elements which are provided by high energy deep inelastic scattering. As has been shown in this paper, the external DIS input transforms the LHC to a much more powerful facility, with a new level of resolving matter substructure, a more precise Higgs programme, challenging and complementing that of a next  $e^+e^-$  collider, and with a hugely extended potential to discover physics beyond the Standard Model.

The very high luminosity and the substantial extension of the kinematic range in deep inelastic scattering, compared to HERA, make the LHeC on its own a uniquely powerful TeV energy collider. Realising the *Electrons for LHC* programme developed with the previous and the present “white” papers, will create the cleanest, high resolution microscope accessible to the world, one may term the “CERN Hubble Telescope for the Micro-Universe”. It is directed to unravel the substructure of matter encoded in the complex dynamics of the strong interaction, and provide the necessary input for precision and discovery physics at the HL-LHC and for future hadron colliders.

This programme, as has been described in this paper, comprises the complete resolution of the partonic densities in an unexplored range of kinematics, the foundations for new, generalised views on proton structure and the long awaited clarification of the QCD dynamics at high densities, as are observed at small Bjorken  $x$ . New high precision measurements on diffraction and vector mesons will shed new light on the puzzle of confinement. As a complement to the LHC and a possible future  $e^+e^-$  machine, the LHeC would scrutinise the Standard Model (SM) deeper

8677 than ever before, and possibly discover new physics in the electroweak and chromodynamic  
8678 sectors.

8679 Through the extension of the kinematic range by about three orders of magnitude in lepton-  
8680 nucleus (eA) scattering, the LHeC is the most powerful electron-ion research facility one can  
8681 build in the next decades, for elucidating the chromodynamic origin of the Quark-Gluon-Plasma  
8682 and clarifying the partonic substructure and dynamics inside nuclei for the first time.

8683 The Higgs programme at the LHeC has been astonishing in its precision. It relies on CC and  
8684 NC precision measurements for which an inverse atobarn of luminosity is desirable to achieve.  
8685 The prospect results on the Higgs couplings from the HL-LHC when combined with those from  
8686 the LHeC will determine the couplings in the most frequent six Higgs decay channels to one  
8687 per cent level. This is as precise as one expects measurements from linear  $e^+e^-$  colliders but  
8688 obtained dominantly from  $gg$  and  $WW$  fusion respectively, as compared to  $ZH$ -strahlung in  
8689 electron-positron scattering which has the advantage of providing a Higgs width determination  
8690 too. Consequently, the LHC facility at CERN can be expected to remain the centre of Higgs  
8691 physics for two more decades.

8692 Searches for BSM physics at the LHeC offer great complementarity to similar searches at the  
8693 HL-LHC. The core advantage of the LHeC is the clean, QCD-background and pileup-free envi-  
8694 ronment of an electron-proton collider with a cms energy exceeding a TeV. This enables discov-  
8695 eries of signatures that could be lost in the hadronic noise at  $pp$  or possibly unaccessible due to  
8696 the limited center-of-mass energy at  $ee$ .

8697 Prominent examples for discovery enabled with  $ep$  are heavy neutral leptons (or sterile neutri-  
8698 nos) that mix with the electron flavour, dark photons below the di-muon threshold, which are  
8699 notoriously difficult to detect in other experiments, long-lived new particles in general or new  
8700 physics scenarios with a compressed mass spectrum, such as SUSY electrowinos and heavy  
8701 scalar resonances with masses around and below 500 GeV, which may exist but literally be  
8702 buried in di-top backgrounds at the LHC.

8703 The LHeC physics programme reaches far beyond any specialised goal which underlines the  
8704 unique opportunity for particle physics to build a novel laboratory for accelerator based energy  
8705 frontier research at CERN. The project is fundable within the CERN budget, and not preventing  
8706 much more massive investments into the further future. It offers the possibility for the current  
8707 generation of accelerator physicists to build a new collider using and developing novel technology  
8708 while preparations proceed for the next grand step in particle physics for generations ahead.

8709 The main technical innovation through the LHeC is the first ever high energy application of  
8710 energy recovery technology, based on high quality superconducting RF developments, a major  
8711 contribution to the development of *green* collider technology which is an appropriate response  
8712 to demands of our time. The ERL technique is more and more seen to have major further  
8713 applications, beyond ep at HE-LHC and FCC-eh, such as for FCC-ee, as a  $\gamma\gamma$  Higgs facility or,  
8714 beyond particle physics, as the highest energy XFEL of hugely increased brightness.

8715 The paper describes the plans and configuration of PERLE, the first 10 MW power ERL facility  
8716 which is being prepared in international collaboration for built at Irene Curie Laboratory at  
8717 Orsay. PERLE has adopted the 3-pass configuration, cavity and cryomodule technology, source  
8718 and injector layout, frequency and electron current parameters from the LHeC. This qualifies  
8719 it to be the ideal machine to accompany the development of the LHeC. However, through its  
8720 technology innovation and its challenging parameters, such as an intensity exceeding that of  
8721 ELI by orders of magnitude, PERLE has an independent, far reaching low energy nuclear and  
8722 particle physics programme with new and particularly precise measurements. It also has a



8723 possible program on industrial applications, which have not been discussed in the present paper.

8724 The LHeC provides an opportunity for building a novel collider detector which is sought for as  
8725 the design of the HL-LHC detector upgrades is approaching completion. A novel *ep* experiment  
8726 enables modern detection technology, such as HV CMOS Silicon tracking, to be further developed  
8727 and exploited in a new generation,  $4\pi$  acceptance, no pile-up, high precision collider detector in  
8728 the decade(s) hence. This paper presented an update of the 2012 detector design, in response  
8729 to demands from the development of physics, especially Higgs and BSM, and technology in  
8730 detectors and analysis. The LHeC requires to be installed at IP2 at the LHC for there is no  
8731 other interaction region available while the heavy ion programme at the LHC is presently limited  
8732 to the time until LS4. In the coming years it will have to be decided whether this or alternative  
8733 proposals for using IP2 during the final years of LHC operation are considered attractive enough  
8734 and realistic to be realised.

8735 The next steps in this development are rather clear: it needs PERLE to proceed, limited funds for  
8736 prototypes, especially of the IR magnets, be made available and a proto-detector Collaboration  
8737 to emerge such that in a few years time a decision on building the LHeC at CERN may be taken,  
8738 in the context also of what these years may bring for physics, with higher LHC luminosity, for  
8739 Asia, with decisions about ILC and CEPC, and for the further future and support of CERN as  
8740 the world's leading laboratory for particle physics, including its way of cooperation globally and  
8741 with its surrounding major laboratories.

8742 The recent history teaches a lesson about the complementarity required for energy frontier  
8743 particle physics. In the seventies and eighties, CERN hosted the  $p\bar{p}$  energy frontier, with UA1  
8744 and UA2, and the most powerful DIS experiments with muons (EMC, BCDMS, NMC) and  
8745 neutrinos (CDHSW, CHARM), while  $e^+e^-$  physics was pursued at PEP, PETRA and also  
8746 TRISTAN. Following this, the Fermi scale could be explored with the Tevatron, HERA and  
8747 LEP. The here advertised next logical step is to complement the HL-LHC by a most powerful  
8748 DIS facility, the LHeC, while preparations will take shape for a next  $e^+e^-$  collider, currently at  
8749 CERN and in Asia. Hardly a decision on LHeC may be taken independently of how the grand  
8750 future unfolds. Still, this scenario would give a realistic and yet exciting base for completing the  
8751 exploration of TeV scale physics which may not be achieved with solely the LHC.

8752 The ERL concept and technology here presented has the potential to accompany the FCC for  
8753 realising the FCC-eh machine when the time comes for the next, higher energy hadron collider,  
8754 and the search for new physics at the O(10) TeV scale.

## 8755 Acknowledgement

8756

8757 The analyses and developments here presented would not have been possible without the CERN  
8758 Directorate and other laboratories and universities supporting this study. We thank the techni-  
8759 cians contributing to this work, such as with their competence in building the first 802 MHz SC  
8760 cavity. We thank many colleagues for their interest in this work and a supportive attitude when  
8761 time constraints could have caused lesser understanding. Special thanks are also due to the  
8762 members and chair of the International Advisory Committee for their attention and guidance  
8763 to the project. From the beginning of the LHeC study, it has been supported by ECFA and its  
8764 chairs which was a great help and stimulus for undertaking this work which has been performed  
8765 outside our usual duties. During the time, a number of students, in master and PhD courses,

8766 have made very essential contributions to this project for which we are especially grateful. This  
8767 also extends to colleagues with whom we have been working closely but who meanwhile left this  
8768 development, perhaps temporarily, or work at non-particle physics institutions while wishing  
8769 LHeC success. The current situation of particle physics reminds us on the potential we have  
8770 when resources and prospects are unified, for which this study is considered to be a contribution.

8771 The authors would like to thank the Institute of Particle Physics Phenomenology (IPPP) at  
8772 Durham for the award of an IPPP Associateship to support this work, and gratefully acknowl-  
8773 edges support from the state of Baden-Württemberg through bwHPC and the German Research  
8774 Foundation (DFG) through grant no INST 39/963-1 FUGG. Financial support by Ministerio  
8775 de Ciencia e Innovación of Spain under projects FPA2017-83814-P and Unidad de Excelencia  
8776 María de Maetzu under project MDM-2016-0692, and by Xunta de Galicia (project ED431C  
8777 2017/07 and Centro singular de investigación de Galicia accreditation 2019-2022) and the Eu-  
8778 ropean Union (European Regional Development Fund – ERDF), is gratefully acknowledged. It  
8779 has been performed in the framework of COST Action CA 15213 “Theory of hot matter and  
8780 relativistic heavy-ion collisions” (THOR), MSCA RISE 823947 “Heavy ion collisions: collectiv-  
8781 ity and precision in saturation physics” (HIEIC) and has received funding from the European  
8782 Union’s Horizon 2020 research and innovation programme under grant agreement No. 824093.

## 8783 **Appendix A**

# 8784 **Statement of the International** 8785 **Advisory Committee**

8786 End of 2014, the CERN Directorate appointed an International Advisory Committee (IAC) for  
8787 advice on the direction of energy frontier electron-hadron scattering at CERN, for their mandate  
8788 see below. The committee and its chair, em. DG of CERN Herwig Schopper, was reconfirmed  
8789 when a new DG had been appointed. The IAC held regular sessions at the annual LHeC  
8790 workshops in which reports were heard by the co-coordinators of the project, Oliver Brüning  
8791 and Max Klein. Its work and opinion shaped the project development considerably and it was  
8792 pivotal for the foundation of the PERLE project. The committee was in close contact and  
8793 advised especially on the documents, on the LHeC [6,8] and PERLE [9], submitted end of 2018  
8794 to the update of the European strategy on particle physics. In line with the present updated  
8795 LHeC design report and the strategy process, the IAC formulated a brief report to the CERN  
8796 DG, in which its observations and recommendations have been summarised. This report was  
8797 also sent to the members of the European particle physics strategy group. It is reproduced here.

### 8798 **Report by the IAC on the LHeC to the DG of CERN**

8799 The development of the LHeC project was initiated by CERN and ECFA, in cooperation  
8800 with NuPECC. It culminated in the publication of the Conceptual Design Report (CDR),  
8801 arXiv:1206.2913 in 2012, which received by now about 500 citations. In 2014, the CERN Di-  
8802 rectorate invited our committee to advise the CERN Directorate, and the Coordination Group,  
8803 on the directions of future energy frontier electron-hadron scattering as are enabled with the  
8804 LHC and the future FCC (for the mandate see below). In 2016, Council endorsed the HL-LHC,  
8805 which offers a higher LHC performance and strengthened the interest in exploring the Higgs  
8806 phenomenon. In view of the imminent final discussions for the European Road Map for particle  
8807 physics, a short summary report is here presented.

### 8808 **Main Developments 2014–2019**

8809 A series of annual workshops on the LHeC and FCC-eh was held, and this report is given  
8810 following the latest workshop <https://indico.cern.ch/event/835947> , October 24/25, 2019.

8811 Based on recent developments concerning the development of the LHC accelerator and physics,  
8812 and the progress in technology, a new default configuration of the LHeC and FCC-eh has been

8813 worked out with a tenfold increased peak luminosity goal, of  $10^{34} \text{ cm}^{-2}\text{s}^{-1}$ , as compared to the  
8814 CDR. A comprehensive paper, “The LHeC at the HL-LHC”, is being finalised for publication  
8815 this year.

8816 Within this work, it has been shown that the LHeC represents the cleanest, high resolution  
8817 microscope the world can currently build, a seminal opportunity to develop and explore QCD,  
8818 to study high precision Higgs and electroweak physics and to substantially extend the range  
8819 and prospects for accessing BSM physics, on its own and in combination of pp with ep. The  
8820 LHeC, in eA scattering mode, has a unique discovery potential on nuclear structure, dynamics  
8821 and QGP physics.

8822 Intense eh collisions with LHeC and FCC-eh are enabled through a special electron-beam race-  
8823 track arrangement with energy recovery linac (ERL) technology. If LHeC were to be considered  
8824 either on its own merits, or as a bridge project to FCC-eh, it seemed important to find a config-  
8825 uration, which could be realised within the existing CERN budget. Several options were studied  
8826 and found.

8827 Before a decision on such a project can be taken, the ERL technology has to be further developed.  
8828 Considerable progress has been made in the USA, and a major effort is now necessary to develop  
8829 it further in Europe. An international collaboration (ASTeC, BINP, CERN, Jefferson Lab,  
8830 Liverpool, Orsay) has been formed to realise the first multi-turn 10 MW ERL facility, PERLE  
8831 at Orsay, with its main parameters set by the LHeC and producing the first encouraging results  
8832 on 802 MHz cavity technology, for the CDR see arXiv:1705.08783.

8833 This radically new accelerator technology, ERL, has an outstanding technical (SRF), physics  
8834 (nuclear physics) and industrial (lithography, transmutations, ..) impact, and offers possible  
8835 applications beyond ep (such as a racetrack injector or ERL layout for FCC-ee, a high energy  
8836 FEL or  $\gamma\gamma$  collider).

### 8837 **In conclusion it may be stated**

- 8838 • The installation and operation of the LHeC has been demonstrated to be commensurate  
8839 with the currently projected HL-LHC program, while the FCC-eh has been integrated into  
8840 the FCC vision;
- 8841 • The feasibility of the project as far as accelerator issues and detectors are concerned has  
8842 been shown. It can only be realised at CERN and would fully exploit the massive LHC  
8843 and HL-LHC investments;
- 8844 • The sensitivity for discoveries of new physics is comparable, and in some cases superior,  
8845 to the other projects envisaged;
- 8846 • The addition of an ep/A experiment to the LHC substantially reinforces the physics pro-  
8847 gram of the facility, especially in the areas of QCD, precision Higgs and electroweak as  
8848 well as heavy ion physics;
- 8849 • The operation of LHeC and FCC-eh is compatible with simultaneous pp operation; for  
8850 LHeC the interaction point 2 would be the appropriate choice, which is currently used by  
8851 ALICE;
- 8852 • The development of the ERL technology needs to be intensified in Europe, in national  
8853 laboratories but with the collaboration of CERN;
- 8854 • A preparatory phase is still necessary to work out some time-sensitive key elements, es-  
8855 pecially the high power ERL technology (PERLE) and the prototyping of Intersection  
8856 Region magnets.

8857 **Recommendations**

8858 i) It is recommended to further develop the ERL based ep/A scattering plans, both at LHC  
8859 and FCC, as attractive options for the mid and long term programme of CERN, resp. Before  
8860 a decision on such a project can be taken, further development work is necessary, and should  
8861 be supported, possibly within existing CERN frameworks (e.g. development of SC cavities and  
8862 high field IR magnets).

8863

8864 ii) The development of the promising high-power beam-recovery technology ERL should be in-  
8865 tensified in Europe. This could be done mainly in national laboratories, in particular with the  
8866 PERLE project at Orsay. To facilitate such a collaboration, CERN should express its interest  
8867 and continue to take part.

8868

8869 iii) It is recommended to keep the LHeC option open until further decisions have been taken.  
8870 An investigation should be started on the compatibility between the LHeC and a new heavy ion  
8871 experiment in Interaction Point 2, which is currently under discussion.

8872

8873 After the final results of the European Strategy Process will be made known, the IAC considers  
8874 its task to be completed. A new decision will then have to be taken for how to continue these  
8875 activities.

8876

8877 Herwig Schopper, Chair of the Committee,

Geneva, November 4, 2019

8878 **Mandate of the International Advisory Committee**

8879 Advice to the LHeC Coordination Group and the CERN directorate by following the develop-  
8880 ment of options of an ep/eA collider at the LHC and at FCC, especially with: Provision of  
8881 scientific and technical direction for the physics potential of the ep/eA collider, both at LHC  
8882 and at FCC, as a function of the machine parameters and of a realistic detector design, as well  
8883 as for the design and possible approval of an ERL test facility at CERN. Assistance in building  
8884 the international case for the accelerator and detector developments as well as guidance to the  
8885 resource, infrastructure and science policy aspects of the ep/eA collider. (December 2014)

8886 **Members of the Committee**

Sergio Bertolucci (Bologna)

Nichola Bianchi (INFN, now Singapore)

Frederick Bordy (CERN)

Stan Brodsky (SLAC)

Oliver Brüning (CERN, coordinator)

8887 Hesheng Chen (Beijing)

Eckhard Elsen (CERN)

Stefano Forte (Milano)

Andrew Hutton (Jefferson Lab)

Young-Kee Kim (Chicago)

Max Klein (Liverpool, coordinator)

Shin-Ichi Kurokawa (KEK)

Victor Matveev (JINR Dubna)

Aleandro Nisati (Rome I)

Leonid Rivkin (PSI Villigen)

Herwig Schopper (CERN, em.DG, Chair)

Jürgen Schukraft (CERN)

Achille Stocchi (Orsay)

John Womersley (ESS Lund)

# Bibliography

- 8889 [1] LHeC Study Group, J. L. Abelleira *et al.*, *J. Phys.* G39 (2012) 075001, [arXiv:1206.2913](#).
- 8890 [2] H. Burkhardt, *ICFA Beam Dyn. Newslett.* 58 (2012) 76.
- 8891 [3] G. Apollinari, I. Béjar Alonso, O. Brüning, P. Fessia, M. Lamont, L. Rossi and L. Tavian (eds.),  
8892 *High-Luminosity Large Hadron Collider (HL-LHC)*, vol. 4. CERN Yellow Rep. Monogr.,  
8893 CERN-2017-007-M, 2017.
- 8894 [4] L. Rossi and O. Brüning, “Progress with the High Luminosity LHC project at CERN,” in *Proceedings,*  
8895 *10th International Particle Accelerator Conference (IPAC2019): Melbourne, Australia, May 19-24, 2019,*  
8896 Jun 2019.
- 8897 [5] D. Angal-Kalinin *et al.*, *J. Phys.* G45 (2018) 065003, [arXiv:1705.08783](#).
- 8898 [6] LHeC Study Group, O. Brüning, M. Klein *et al.*, “Exploring the Energy Frontier with Deep Inelastic  
8899 Scattering at the LHC,” A Contribution to the Update of the European Strategy on Particle Physics,  
8900 CERN-ACC-NOTE-2018-0084, Dec 2018. <http://cds.cern.ch/record/2652313>.
- 8901 [7] LHeC and PERLE Collaborations, O. Brüning, M. Klein *et al.*, *J. Phys.* G46 (2019) 123001.
- 8902 [8] LHeC Study Group, O. Brüning, M. Klein *et al.*, “Addendum. Exploring the Energy Frontier with Deep  
8903 Inelastic Scattering at the LHC,” A Contribution to the Update of the European Strategy on Particle  
8904 Physics, CERN-ACC-NOTE-2018-0085, Dec 2018.
- 8905 [9] PERLE Collaboration, M. Klein, A. Stocchi *et al.*, “PERLE: A High Power Energy Recovery Facility for  
8906 Europe,” A Contribution to the Update of the European Strategy on Particle Physics,  
8907 CERN-ACC-NOTE-2018-0086, Dec 2018. <https://cds.cern.ch/record/2652336>.
- 8908 [10] S. Hossenfelder, *Lost in math*. Basic Books, New York, 2018.
- 8909 [11] G. Altarelli, *Frascati Phys. Ser.* 58 (2014) 102, [arXiv:1407.2122](#).
- 8910 [12] J. De Hondt, “Talk on the Future of Particle Physics and on ECFA Matters,” Plenary Session, ECFA,  
8911 CERN, November, 2019.
- 8912 [13] FCC Collaboration, A. Abada *et al.*, *Eur. Phys. J.* C79 (2019) 474.
- 8913 [14] FCC Collaboration, A. Abada *et al.*, *Eur. Phys. J.* ST 228 (2019) 261.
- 8914 [15] FCC Collaboration, A. Abada *et al.*, *Eur. Phys. J.* ST 228 (2019) 755.
- 8915 [16] CEPC-SPPC Study Group, M. Ahmad *et al.*, “CEPC-SPPC Preliminary Conceptual Design Report. 2.  
8916 Accelerator,” IHEP-CEPC-DR-2015-01, IHEP-AC-2015-01, 2015.
- 8917 [17] CEPC Study Group, M. Dong *et al.*, “CEPC Conceptual Design Report: Volume 2 - Physics & Detector,”  
8918 2018. [arXiv:1811.10545](#).
- 8919 [18] R. P. Feynman, *Photon-hadron interactions*. Westview Press, Reading, MA, 1972.
- 8920 [19] E. D. Bloom *et al.*, *Phys. Rev. Lett.* 23 (1969) 930.
- 8921 [20] M. Breidenbach *et al.*, *Phys. Rev. Lett.* 23 (1969) 935.
- 8922 [21] R. P. Feynman, *Phys. Rev. Lett.* 23 (1969) 1415.
- 8923 [22] J. D. Bjorken and E. A. Paschos, *Phys. Rev.* 185 (1969) 1975.
- 8924 [23] C. Y. Prescott *et al.*, *Phys. Lett.* 77B (1978) 347.
- 8925 [24] S. Weinberg, *Phys. Rev. Lett.* 19 (1967) 1264.
- 8926 [25] B. H. Wiik, *Acta Phys. Polon.* B16 (1985) 127.
- 8927 [26] M. Klein and R. Yoshida, *Prog. Part. Nucl. Phys.* 61 (2008) 343, [arXiv:0805.3334](#).

- 8928 [27] A. De Rujula, S. L. Glashow, H. D. Politzer *et al.*, *Phys. Rev. D* **10** (1974) 1649.
- 8929 [28] J. Dainton, M. Klein, P. Newman, E. Perez and F. Willeke, *JINST* **1** (2006) P10001,  
8930 [arXiv:hep-ex/0603016](#).
- 8931 [29] FCC Collaboration, A. Abada *et al.*, *Eur. Phys. J. ST* **228** (2019) 1109.
- 8932 [30] F. Marhauser *et al.*, “802 MHz ERL Cavity Design and Development,” in *Proceedings, 9th International*  
8933 *Particle Accelerator Conference (IPAC 2018): Vancouver, BC Canada, April 29-May 4, 2018*, 2018.
- 8934 [31] V. N. Litvinenko, T. Roser and M. Chamizo Llatas, [arXiv:1909.04437](#).
- 8935 [32] O. Brüning, “FCC-eh Cost Estimate,” CERN-ACC-NOTE-2018-0061, 2018.
- 8936 [33] A. Bogacz, “The LHeC ERL - Optics and Performance Optimisation,” Talk given at ERL Workshop,  
8937 Berlin, 2019.
- 8938 [34] O. Brüning, J. Jowett, M. Klein, D. Pellegrini, D. Schulte and F. Zimmermann, “Future Circular Collider  
8939 Study FCC-eh Baseline Parameters,” 2017. CERN FCC-ACC-RPT-012.
- 8940 [35] F. Bordry *et al.*, “Machine Parameters and Projected Luminosity Performance of Proposed Future  
8941 Colliders at CERN,” 2018. [arXiv:1810.13022](#).
- 8942 [36] C. Quigg, *PoS DIS2013* (2013) 034, [arXiv:1308.6637](#).
- 8943 [37] J. C. Collins, D. E. Soper and G. F. Sterman, *Factorization of Hard Processes in QCD*, vol. 5, pp. 1–91.  
8944 1989. [arXiv:hep-ph/0409313](#).
- 8945 [38] LHeC Study Group, J. L. Abelleira *et al.*, “On the Relation of the LHeC and the LHC,” 2012.  
8946 [arXiv:1211.5102](#).
- 8947 [39] G. R. Boroun, *Phys. Lett. B* **744** (2015) 142, [arXiv:1503.01590](#).
- 8948 [40] T. J. Hobbs, J. T. Londergan, D. P. Murdock and A. W. Thomas, *Phys. Lett. B* **698** (2011) 123,  
8949 [arXiv:1101.3923](#).
- 8950 [41] M. Klein, “The structure of the proton and HERA,” in *International Conference on the Structure and*  
8951 *Interactions of the Photon and 18th International Workshop on Photon-Photon Collisions and*  
8952 *International Workshop on High Energy Photon Linear Colliders*, Jan 2010.
- 8953 [42] H1 and ZEUS Collaborations, F. Aaron *et al.*, *JHEP* **1001** (2010) 109, [arXiv:0911.0884](#).
- 8954 [43] H1 and ZEUS Collaborations, H. Abramowicz *et al.*, *Eur. Phys. J. C* **75** (2015) 580, [arXiv:1506.06042](#).
- 8955 [44] HERAFitter Group, S. Alekhin *et al.*, *Eur. Phys. J. C* **75** (2015) 304, [arXiv:1410.4412](#).
- 8956 [45] H1 Collaboration, F. Aaron *et al.*, *Eur. Phys. J. C* **64** (2009) 561, [arXiv:0904.3513](#).
- 8957 [46] M. Botje, *Comput. Phys. Commun.* **182** (2011) 490, [arXiv:1005.1481](#).
- 8958 [47] M. Botje, “Erratum for the time-like evolution in QCDNUM,” 2016. [arXiv:1602.08383](#).
- 8959 [48] R. Thorne, *Phys. Rev. D* **73** (2006) 054019, [arXiv:0601245](#).
- 8960 [49] R. Thorne, *Phys. Rev. D* **86** (2012) 074017, [arXiv:1201.6180](#).
- 8961 [50] S. Alekhin, J. Blümlein and S. Moch, *Phys. Rev. D* **86** (2012) 054009, [arXiv:1202.2281](#).
- 8962 [51] S. Alekhin, J. Blümlein, S.-O. Moch and R. Placakyte, *Phys. Rev. D* **96** (2017) 014011, [arXiv:1701.05838](#).
- 8963 [52] M. Klein, “Future Deep Inelastic Scattering with the LHeC,” in *From My Vast Repertoire ...: Guido*  
8964 *Altarelli’s Legacy*, A. Levy, S. Forte and G. Ridolfi (eds.), p. 303. 2019. [arXiv:1802.04317](#).
- 8965 [53] M. Klein and V. Radescu, “Partons from the LHeC,” CERN-LHeC-Note-2013-002, Jul 2013.  
8966 <https://cds.cern.ch/record/1564929>.
- 8967 [54] S. Bentvelsen, J. Engelen and P. Kooijman, “Reconstruction of  $(x, Q^{*2})$  and extraction of structure  
8968 functions in neutral current scattering at HERA,” in *Workshop on Physics at HERA Hamburg, Germany,*  
8969 *October 29-30, 1991*, 1992.
- 8970 [55] U. Bassler and G. Bernardi, *Nucl. Instrum. Meth. A* **361** (1995) 197, [arXiv:hep-ex/9412004](#).
- 8971 [56] U. Bassler and G. Bernardi, *Nucl. Instrum. Meth.* **426** (1999) A583, [arXiv:hep-ex/9801017](#).
- 8972 [57] J. Blümlein and M. Klein, “Kinematics and resolution at future e p colliders,” in *1990 DPF Summer*  
8973 *Study on High-energy Physics: Research Directions for the Decade (Snowmass 90) Snowmass, Colorado,*  
8974 *June 25-July 13, 1990*, 1990.
- 8975 [58] R. Abdul Khalek, S. Bailey, J. Gao, L. Harland-Lang and J. Rojo, *SciPost Phys.* **7** (2019) 051,  
8976 [arXiv:1906.10127](#).
- 8977 [59] S. J. Brodsky and G. R. Farrar, *Phys. Rev. Lett.* **31** (1973) 1153.

- 8978 [60] S. J. Brodsky and G. R. Farrar, *Phys. Rev. D* 11 (1975) 1309.
- 8979 [61] V. A. Matveev, R. M. Muradian and A. N. Tavkhelidze, *Lett. Nuovo Cim.* 7 (1973) 719.
- 8980 [62] ATLAS Collaboration, G. Aad *et al.*, *Eur. Phys. J. C* 79 (2019) 970, [arXiv:1907.05120](#).
- 8981 [63] H1 and ZEUS Collaborations, H. Abramowicz *et al.*, *Eur. Phys. J. C* 78 (2018) 473, [arXiv:1804.01019](#).
- 8982 [64] J. Kuti and V. F. Weisskopf, *Phys. Rev. D* 4 (1971) 3418.
- 8983 [65] S. Dulat *et al.*, *Phys. Rev. D* 93 (2016) 033006, [arXiv:1506.07443](#).
- 8984 [66] W. G. Seligman *et al.*, *Phys. Rev. Lett.* 79 (1997) 1213, [arXiv:hep-ex/9701017](#).
- 8985 [67] NuTeV Collaboration, M. Tzanov *et al.*, *Phys. Rev. D* 74 (2006) 012008, [arXiv:hep-ex/0509010](#).
- 8986 [68] CHORUS Collaboration, G. Onengut *et al.*, *Phys. Lett.* B632 (2006) 65.
- 8987 [69] J. P. Berge *et al.*, *Z. Phys.* C49 (1991) 187.
- 8988 [70] NOMAD Collaboration, O. Samoylov *et al.*, *Nucl. Phys.* B876 (2013) 339, [arXiv:1308.4750](#).
- 8989 [71] ATLAS Collaboration, G. Aad *et al.*, *Phys. Rev. Lett.* 109 (2012) 012001, [arXiv:1203.4051](#).
- 8990 [72] CMS Collaboration, S. Chatrchyan *et al.*, *JHEP* 02 (2014) 013, [arXiv:1310.1138](#).
- 8991 [73] ATLAS Collaboration, G. Aad *et al.*, *JHEP* 05 (2014) 068, [arXiv:1402.6263](#).
- 8992 [74] ATLAS Collaboration, M. Aaboud *et al.*, *Eur. Phys. J. C* 77 (2017) 367, [arXiv:1612.03016](#).
- 8993 [75] S. Alekhin, J. Blümlein and S.-O. Moch, *Phys. Lett.* B777 (2018) 134, [arXiv:1708.01067](#).
- 8994 [76] A. M. Cooper-Sarkar and K. Wichmann, *Phys. Rev. D* 98 (2018) 014027, [arXiv:1803.00968](#).
- 8995 [77] H. Abdolmaleki *et al.*, [arXiv:1907.01014](#).
- 8996 [78] O. Behnke, A. Geiser and M. Lisovsky, *Prog. Part. Nucl. Phys.* 84 (2015) 1, [arXiv:1506.07519](#).
- 8997 [79] O. Zenaiev, *Eur. Phys. J. C* 77 (2017) 151, [arXiv:1612.02371](#).
- 8998 [80] M. A. G. Aivazis, F. I. Olness and W.-K. Tung, *Phys. Rev. Lett.* 65 (1990) 2339.
- 8999 [81] M. A. G. Aivazis, F. I. Olness and W.-K. Tung, *Phys. Rev. D* 50 (1994) 3085, [arXiv:hep-ph/9312318](#).
- 9000 [82] M. A. G. Aivazis, J. C. Collins, F. I. Olness and W.-K. Tung, *Phys. Rev. D* 50 (1994) 3102, [arXiv:hep-ph/9312319](#).
- 9001
- 9002 [83] R. S. Thorne and R. G. Roberts, *Eur. Phys. J. C* 19 (2001) 339, [arXiv:hep-ph/0010344](#).
- 9003 [84] S. Alekhin, J. Blümlein and S. Moch, *Phys. Rev. D* 89 (2014) 054028, [arXiv:1310.3059](#).
- 9004 [85] S. Alekhin, J. Blümlein, S. Klein and S. Moch, *Phys. Rev. D* 81 (2010) 014032, [arXiv:0908.2766](#).
- 9005 [86] S. Forte, E. Laenen, P. Nason and J. Rojo, *Nucl. Phys.* B834 (2010) 116, [arXiv:1001.2312](#).
- 9006 [87] A. D. Martin, W. J. Stirling, R. S. Thorne and G. Watt, *Eur. Phys. J. C* 70 (2010) 51, [arXiv:1007.2624](#).
- 9007 [88] R. D. Ball, V. Bertone, F. Cerutti, L. Del Debbio, S. Forte, A. Guffanti, J. I. Latorre, J. Rojo and M. Ubiali, *Nucl. Phys.* B849 (2011) 296, [arXiv:1101.1300](#).
- 9008
- 9009 [89] R. D. Ball, M. Bonvini and L. Rottoli, *JHEP* 11 (2015) 122, [arXiv:1510.02491](#).
- 9010 [90] S. Moch, B. Ruijl, T. Ueda, J. A. M. Vermaseren and A. Vogt, *JHEP* 10 (2017) 041, [arXiv:1707.08315](#).
- 9011 [91] F. Herzog, S.-O. Moch, B. Ruijl, T. Ueda, J. A. M. Vermaseren and A. Vogt, *Phys. Lett.* B790 (2019) 436, [arXiv:1812.11818](#).
- 9012
- 9013 [92] G. Das, S.-O. Moch and A. Vogt, [arXiv:1912.12920](#).
- 9014 [93] R. D. Ball, *AIP Conf. Proc.* 1819 (2017) 030002, [arXiv:1612.03790](#).
- 9015 [94] M. Klein and T. Riemann, *Z. Phys.* C24 (1984) 151.
- 9016 [95] A. Argento *et al.*, *Phys. Lett.* 140 (1984) B142.
- 9017 [96] S. Drell and T.-M. Yan, *Phys. Rev. Lett.* 25 (1970) 316. [Erratum: *Phys. Rev. Lett.* 25 (1970) 902].
- 9018 [97] J. Kubar, M. Le Bellac, J. Meunier and G. Plaut, *Nucl. Phys. B* 175 (1980) 251.
- 9019 [98] T.-J. Hou *et al.*, [arXiv:1912.10053](#).
- 9020 [99] A. Accardi *et al.*, *Eur. Phys. J. A* 52 (2016) 268, [arXiv:1212.1701](#).
- 9021 [100] M. Lomnitz and S. Klein, *Phys. Rev. C* 99 (2019) 015203, [arXiv:1803.06420](#).
- 9022 [101] A. V. Belitsky, X.-d. Ji and F. Yuan, *Phys. Rev. D* 69 (2004) 074014, [arXiv:hep-ph/0307383](#).
- 9023 [102] N. N. Nikolaev and B. G. Zakharov, *Z. Phys.* C49 (1991) 607.
- 9024 [103] N. Nikolaev and B. G. Zakharov, *Z. Phys.* C53 (1992) 331.



- 9025 [104] N. N. Nikolaev and B. G. Zakharov, *J. Exp. Theor. Phys.* 78 (1994) 598. [*Zh. Eksp. Teor. Fiz.* 105 (1994)  
9026 1117].
- 9027 [105] N. N. Nikolaev, B. G. Zakharov and V. R. Zoller, *Z. Phys.* A351 (1995) 435.
- 9028 [106] A. H. Müller, *Nucl. Phys.* B415 (1994) 373.
- 9029 [107] A. H. Müller and B. Patel, *Nucl. Phys.* B425 (1994) 471, [arXiv:hep-ph/9403256](#).
- 9030 [108] U. Amaldi and K. R. Schubert, *Nucl. Phys.* B166 (1980) 301.
- 9031 [109] S. Munier, A. M. Stasto and A. H. Müller, *Nucl. Phys.* B603 (2001) 427, [arXiv:hep-ph/0102291](#).
- 9032 [110] N. Armesto and A. H. Rezaeian, *Phys. Rev.* D90 (2014) 054003, [arXiv:1402.4831](#).
- 9033 [111] H. Kowalski and D. Teaney, *Phys. Rev.* D68 (2003) 114005, [arXiv:hep-ph/0304189](#).
- 9034 [112] H. Kowalski, L. Motyka and G. Watt, *Phys. Rev.* D74 (2006) 074016, [arXiv:hep-ph/0606272](#).
- 9035 [113] G. Watt and H. Kowalski, *Phys. Rev.* D78 (2008) 014016, [arXiv:0712.2670](#).
- 9036 [114] L. N. Lipatov, *Sov. Phys. JETP* 63 (1986) 904. [*Zh. Eksp. Teor. Fiz.* 90 (1986) 1536].
- 9037 [115] Y. Hatta, B.-W. Xiao and F. Yuan, *Phys. Rev. Lett.* 116 (2016) 202301, [arXiv:1601.01585](#).
- 9038 [116] T. Altinoluk, N. Armesto, G. Beuf and A. H. Rezaeian, *Phys. Lett.* B758 (2016) 373, [arXiv:1511.07452](#).
- 9039 [117] H. Mäntysaari, N. Muller and B. Schenke, *Phys. Rev.* D99 (2019) 074004, [arXiv:1902.05087](#).
- 9040 [118] F. Salazar and B. Schenke, *Phys. Rev.* D100 (2019) 034007, [arXiv:1905.03763](#).
- 9041 [119] H. Mäntysaari and B. Schenke, *Phys. Rev. Lett.* 117 (2016) 052301, [arXiv:1603.04349](#).
- 9042 [120] H. Mäntysaari and B. Schenke, *Phys. Rev.* D94 (2016) 034042, [arXiv:1607.01711](#).
- 9043 [121] H. Mäntysaari and B. Schenke, *Phys. Lett.* B772 (2017) 832, [arXiv:1703.09256](#).
- 9044 [122] H. Mäntysaari and B. Schenke, *Phys. Rev.* D98 (2018) 034013, [arXiv:1806.06783](#).
- 9045 [123] J. Cepila, J. G. Contreras and J. D. Tapia Takaki, *Phys. Lett.* B766 (2017) 186, [arXiv:1608.07559](#).
- 9046 [124] D. Bendova, J. Cepila and J. G. Contreras, *Phys. Rev.* D99 (2019) 034025, [arXiv:1811.06479](#).
- 9047 [125] M. Krelina, V. P. Goncalves and J. Cepila, *Nucl. Phys.* A989 (2019) 187, [arXiv:1905.06759](#).
- 9048 [126] A. J. Baltz, *Phys. Rept.* 458 (2008) 1, [arXiv:0706.3356](#).
- 9049 [127] S. R. Klein, *Nucl. Phys. A* 967 (2017) 249, [arXiv:1704.04715](#).
- 9050 [128] G. Zweig, “An SU(3) model for strong interaction symmetry and its breaking. Version 1,” 1964.  
9051 CERN-TH-401.
- 9052 [129] H. Fritzsch, M. Gell-Mann and H. Leutwyler, *Phys. Lett.* 47B (1973) 365.
- 9053 [130] D. J. Gross and F. Wilczek, *Phys. Rev. Lett.* 30 (1973) 1343.
- 9054 [131] H. D. Politzer, *Phys. Rev. Lett.* 30 (1973) 1346.
- 9055 [132] G. Dissertori, *Adv. Ser. Direct. High Energy Phys.* 26 (2016) 113, [arXiv:1506.05407](#).
- 9056 [133] Particle Data Group, M. Tanabashi *et al.*, *Phys. Rev.* D98 (2018) 030001.
- 9057 [134] D. d’Enterria *et al.*, *PoS ALPHAS2019* (2019) 001, [arXiv:1907.01435](#).
- 9058 [135] K. H. Streng, T. F. Walsh and P. M. Zerwas, *Z. Phys.* C2 (1979) 237.
- 9059 [136] H1 Collaboration, F. D. Aaron *et al.*, *Eur. Phys. J.* C67 (2010) 1, [arXiv:0911.5678](#).
- 9060 [137] S. D. Ellis and D. E. Soper, *Phys. Rev.* D48 (1993) 3160, [arXiv:hep-ph/9305266](#).
- 9061 [138] H1 Collaboration, C. Adloff *et al.*, *Eur. Phys. J.* C13 (2000) 397, [arXiv:hep-ex/9812024](#).
- 9062 [139] H1 Collaboration, C. Adloff *et al.*, *Eur. Phys. J.* C19 (2001) 289, [arXiv:hep-ex/0010054](#).
- 9063 [140] H1 Collaboration, C. Adloff *et al.*, *Phys. Lett.* B542 (2002) 193, [arXiv:hep-ex/0206029](#).
- 9064 [141] H1 Collaboration, A. Aktas *et al.*, *Eur. Phys. J.* C33 (2004) 477, [arXiv:hep-ex/0310019](#).
- 9065 [142] H1 Collaboration, A. Aktas *et al.*, *Eur. Phys. J.* C37 (2004) 141, [arXiv:hep-ex/0401010](#).
- 9066 [143] H1 Collaboration, A. Aktas *et al.*, *Phys. Lett.* B653 (2007) 134, [arXiv:0706.3722](#).
- 9067 [144] H1 Collaboration, F. D. Aaron *et al.*, *Eur. Phys. J.* C65 (2010) 363, [arXiv:0904.3870](#).
- 9068 [145] H1 Collaboration, V. Andreev *et al.*, *Eur. Phys. J.* C75 (2015) 65, [arXiv:1406.4709](#).
- 9069 [146] H1 Collaboration, V. Andreev *et al.*, *Eur. Phys. J.* C77 (2017) 215, [arXiv:1611.03421](#).
- 9070 [147] ZEUS Collaboration, J. Breitweg *et al.*, *Phys. Lett.* B479 (2000) 37, [arXiv:hep-ex/0002010](#).

- 9071 [148] ZEUS Collaboration, S. Chekanov *et al.*, *Eur. Phys. J. C*23 (2002) 13, [arXiv:hep-ex/0109029](#).
- 9072 [149] ZEUS Collaboration, S. Chekanov *et al.*, *Phys. Lett. B*547 (2002) 164, [arXiv:hep-ex/0208037](#).
- 9073 [150] ZEUS Collaboration, S. Chekanov *et al.*, *Eur. Phys. J. C*35 (2004) 487, [arXiv:hep-ex/0404033](#).
- 9074 [151] ZEUS Collaboration, S. Chekanov *et al.*, *Nucl. Phys. B*765 (2007) 1, [arXiv:hep-ex/0608048](#).
- 9075 [152] ZEUS Collaboration, S. Chekanov *et al.*, *Phys. Lett. B*649 (2007) 12, [arXiv:hep-ex/0701039](#).
- 9076 [153] ZEUS Collaboration, H. Abramowicz *et al.*, *Eur. Phys. J. C*70 (2010) 965, [arXiv:1010.6167](#).
- 9077 [154] ZEUS Collaboration, H. Abramowicz *et al.*, *Phys. Lett. B*691 (2010) 127, [arXiv:1003.2923](#).
- 9078 [155] CMS Collaboration, V. Khachatryan *et al.*, *JHEP* 03 (2017) 156, [arXiv:1609.05331](#).
- 9079 [156] K. Rabbertz, *Springer Tracts Mod. Phys.* 268 (2017) 1.
- 9080 [157] ATLAS Collaboration, M. Aaboud *et al.*, *JHEP* 09 (2017) 020, [arXiv:1706.03192](#).
- 9081 [158] ATLAS Collaboration, M. Aaboud *et al.*, *JHEP* 05 (2018) 195, [arXiv:1711.02692](#).
- 9082 [159] J. Currie, T. Gehrmann and J. Niehues, *Phys. Rev. Lett.* 117 (2016) 042001, [arXiv:1606.03991](#).
- 9083 [160] J. Currie, T. Gehrmann, A. Huss and J. Niehues, *JHEP* 07 (2017) 018, [arXiv:1703.05977](#).
- 9084 [161] T. Gehrmann *et al.*, *PoS RADCOR2017* (2018) 074, [arXiv:1801.06415](#).
- 9085 [162] J. R. Andersen *et al.*, “Les Houches 2017: Physics at TeV Colliders Standard Model Working Group Report,” 2018. [arXiv:1803.07977](#).
- 9087 [163] S. Amoroso *et al.*, “Les Houches 2019: Physics at TeV Colliders: Standard Model Working Group Report,” in *11th Les Houches Workshop on Physics at TeV Colliders: PhysTeV Les Houches*, Mar 2020. [arXiv:2003.01700](#).
- 9088
- 9089
- 9090 [164] D. Britzger *et al.*, *Eur. Phys. J. C*79 (2019) 845, [arXiv:1906.05303](#).
- 9091 [165] T. Carli, G. P. Salam and F. Siegert, “A Posteriori inclusion of PDFs in NLO QCD final-state calculations,” in *HERA and the LHC: A Workshop on the Implications of HERA for LHC Physics*, CERN, Geneva, Switzerland, October 11-13, 2004, 2005. [arXiv:hep-ph/0510324](#).
- 9092
- 9093
- 9094 [166] T. Carli *et al.*, *Eur. Phys. J. C* 66 (2010) 503, [arXiv:0911.2985](#).
- 9095 [167] T. Kluge, K. Rabbertz and M. Wobisch, “FastNLO: Fast pQCD calculations for PDF fits,” in *Proceedings, 14th International Workshop of deep inelastic scattering (DIS 2006)*, Tsukuba, Japan, April 20-24, 2006, 2006. [arXiv:hep-ph/0609285](#).
- 9096
- 9097
- 9098 [168] D. Britzger, K. Rabbertz, F. Stober and M. Wobisch, “New features in version 2 of the fastNLO project,” in *Proceedings, 20th International Workshop on Deep-Inelastic Scattering and Related Subjects (DIS 2012): Bonn, Germany, March 26-30, 2012*, 2012. [arXiv:1208.3641](#).
- 9099
- 9100
- 9101 [169] H1 Collaboration, V. Andreev *et al.*, *Eur. Phys. J. C*77 (2017) 791, [arXiv:1709.07251](#).
- 9102 [170] CMS Collaboration, V. Khachatryan *et al.*, *JINST* 12 (2017) P02014, [arXiv:1607.03663](#).
- 9103 [171] ATLAS Collaboration, M. Aaboud *et al.*, “Determination of jet calibration and energy resolution in proton-proton collisions at  $\sqrt{s} = 8$  TeV using the ATLAS detector,” 2019. [arXiv:1910.04482](#).
- 9104
- 9105 [172] R. Kogler, *Measurement of jet production in deep-inelastic  $e p$  scattering at HERA*. PhD thesis, Hamburg U., 2011.
- 9106
- 9107 [173] J. R. Ellis, E. Gardi, M. Karliner and M. A. Samuel, *Phys. Lett. B*366 (1996) 268, [arXiv:hep-ph/9509312](#).
- 9108 [174] S. J. Brodsky and X.-G. Wu, *Phys. Rev. D*85 (2012) 034038, [arXiv:1111.6175](#). [Erratum: *Phys. Rev. D*86 (2012) 079903].
- 9109
- 9110 [175] S. J. Brodsky and X.-G. Wu, *Phys. Rev. Lett.* 109 (2012) 042002, [arXiv:1203.5312](#).
- 9111 [176] S. J. Brodsky and L. Di Giustino, *Phys. Rev. D*86 (2012) 085026, [arXiv:1107.0338](#).
- 9112 [177] M. Mojaza, S. J. Brodsky and X.-G. Wu, *Phys. Rev. Lett.* 110 (2013) 192001, [arXiv:1212.0049](#).
- 9113 [178] S. J. Brodsky, M. Mojaza and X.-G. Wu, *Phys. Rev. D*89 (2014) 014027, [arXiv:1304.4631](#).
- 9114 [179] S.-Q. Wang, S. J. Brodsky, X.-G. Wu, J.-M. Shen and L. Di Giustino, *Phys. Rev. D*100 (2019) 094010, [arXiv:1908.00060](#).
- 9115
- 9116 [180] Particle Data Group, M. Tanabashi *et al.*, “2019 Update of the Review of Particle Physics,”. <http://pdg.lbl.gov/2019/>. To be published in *Prog. Theor. Exp. Phys.* 083C01 (2020).
- 9117
- 9118 [181] Flavour Lattice Averaging Group, S. Aoki *et al.*, [arXiv:1902.08191](#).
- 9119 [182] D. Boito, M. Golterman, K. Maltman, J. Osborne and S. Peris, *Phys. Rev. D*91 (2015) 034003, [arXiv:1410.3528](#).
- 9120

- 9121 [183] Gfitter Group, M. Baak *et al.*, *Eur. Phys. J. C* 74 (2014) 3046, [arXiv:1407.3792](#).
- 9122 [184] P. Azzi *et al.*, *CERN Yellow Rep. Monogr.* 7 (2019) 1, [arXiv:1902.04070](#).
- 9123 [185] I. Abt, A. M. Cooper-Sarkar, B. Foster, V. Myronenko, K. Wichmann and M. Wing, *Phys. Rev. D* 96  
9124 (2017) 014001, [arXiv:1704.03187](#). [*Phys. Rev. D* 96,014001(2017)].
- 9125 [186] J. Ablinger, J. Blümlein, S. Klein, C. Schneider and F. Wissbrock, *Nucl. Phys.* B844 (2011) 26,  
9126 [arXiv:1008.3347](#).
- 9127 [187] J. Ablinger, J. Blümlein, A. De Freitas, A. Hasselhuhn, A. von Manteuffel, M. Round, C. Schneider and  
9128 F. Wissbrock, *Nucl. Phys.* B882 (2014) 263, [arXiv:1402.0359](#).
- 9129 [188] J. Ablinger, A. Behring, J. Blümlein, A. De Freitas, A. von Manteuffel and C. Schneider, *Nucl. Phys.*  
9130 B890 (2014) 48, [arXiv:1409.1135](#).
- 9131 [189] A. Behring, I. Bierenbaum, J. Blümlein, A. De Freitas, S. Klein and F. Wißbrock, *Eur. Phys. J. C* 74  
9132 (2014) 3033, [arXiv:1403.6356](#).
- 9133 [190] J. Ablinger, J. Blümlein, A. De Freitas, C. Schneider and K. Schönwald, *Nucl. Phys.* B927 (2018) 339,  
9134 [arXiv:1711.06717](#).
- 9135 [191] J. Ablinger, J. Blümlein, A. De Freitas, A. Goedicke, C. Schneider and K. Schönwald, *Nucl. Phys.* B932  
9136 (2018) 129, [arXiv:1804.02226](#).
- 9137 [192] M. Dasgupta and G. P. Salam, *J. Phys.* G30 (2004) R143, [arXiv:hep-ph/0312283](#).
- 9138 [193] H1 Collaboration, A. Aktas *et al.*, *Eur. Phys. J. C* 46 (2006) 343, [arXiv:hep-ex/0512014](#).
- 9139 [194] ZEUS Collaboration, S. Chekanov *et al.*, *Nucl. Phys.* B767 (2007) 1, [arXiv:hep-ex/0604032](#).
- 9140 [195] D. Kang, C. Lee and I. W. Stewart, *Phys. Rev. D* 88 (2013) 054004, [arXiv:1303.6952](#).
- 9141 [196] Z.-B. Kang, X. Liu and S. Mantry, *Phys. Rev. D* 90 (2014) 014041, [arXiv:1312.0301](#).
- 9142 [197] D. Kang, C. Lee and I. W. Stewart, *PoS DIS2015* (2015) 142.
- 9143 [198] G. Abelof, R. Boughezal, X. Liu and F. Petriello, *Phys. Lett.* B763 (2016) 52, [arXiv:1607.04921](#).
- 9144 [199] S. Höche, S. Kuttimalai and Y. Li, *Phys. Rev. D* 98 (2018) 114013, [arXiv:1809.04192](#).
- 9145 [200] J. Currie, T. Gehrmann, E. W. N. Glover, A. Huss, J. Niehues and A. Vogt, *JHEP* 05 (2018) 209,  
9146 [arXiv:1803.09973](#).
- 9147 [201] T. Gehrmann, A. Huss, J. Mo and J. Niehues, *Eur. Phys. J. C* 79 (2019) 1022, [arXiv:1909.02760](#).
- 9148 [202] H1 Collaboration, C. Adloff *et al.*, *Eur. Phys. J. C* 29 (2003) 497, [arXiv:hep-ex/0302034](#).
- 9149 [203] H1 Collaboration, A. Aktas *et al.*, *Phys. Lett.* B639 (2006) 21, [arXiv:hep-ex/0603014](#).
- 9150 [204] ZEUS Collaboration, S. Chekanov *et al.*, *Phys. Rev. D* 76 (2007) 072011, [arXiv:0706.3809](#).
- 9151 [205] ZEUS Collaboration, H. Abramowicz *et al.*, *Nucl. Phys.* B864 (2012) 1, [arXiv:1205.6153](#).
- 9152 [206] M. Klasen, *Rev. Mod. Phys.* 74 (2002) 1221, [arXiv:hep-ph/0206169](#).
- 9153 [207] M. Glück, E. Reya and A. Vogt, *Phys. Rev. D* 46 (1992) 1973.
- 9154 [208] K. Sasaki, T. Ueda and T. Uematsu, *CERN Proc.* 1 (2018) 7.
- 9155 [209] H1 and ZEUS Collaborations, H. Abramowicz *et al.*, *JHEP* 09 (2015) 149, [arXiv:1503.06042](#).
- 9156 [210] A. J. Larkoski, I. Moulton and B. Nachman, [arXiv:1709.04464](#).
- 9157 [211] F. Ringer, *PoS ALPHAS2019* (2019) 010.
- 9158 [212] I. I. Balitsky and L. N. Lipatov, *Sov. J. Nucl. Phys.* 28 (1978) 822. [*Yad. Fiz.* 28 (1978) 1597].
- 9159 [213] E. A. Kuraev, L. N. Lipatov and V. S. Fadin, *Sov. Phys. JETP* 45 (1977) 199. [*Zh. Eksp. Teor. Fiz.* 72  
9160 (1977) 377].
- 9161 [214] V. S. Fadin and L. N. Lipatov, *Phys. Lett.* B429 (1998) 127, [arXiv:hep-ph/9802290](#).
- 9162 [215] M. Ciafaloni and G. Camici, *Phys. Lett.* B430 (1998) 349, [arXiv:hep-ph/9803389](#).
- 9163 [216] D. A. Ross, *Phys. Lett.* B431 (1998) 161, [arXiv:hep-ph/9804332](#).
- 9164 [217] Y. V. Kovchegov and A. H. Müller, *Phys. Lett.* B439 (1998) 428, [arXiv:hep-ph/9805208](#).
- 9165 [218] E. Levin, *Nucl. Phys.* B545 (1999) 481, [arXiv:hep-ph/9806228](#).
- 9166 [219] N. Armesto, J. Bartels and M. A. Braun, *Phys. Lett.* B442 (1998) 459, [arXiv:hep-ph/9808340](#).
- 9167 [220] J. Blümlein and A. Vogt, *Phys. Lett.* B370 (1996) 149, [arXiv:hep-ph/9510410](#).
- 9168 [221] J. Blümlein and A. Vogt, *Phys. Rev. D* 58 (1998) 014020, [arXiv:hep-ph/9712546](#).

- 9169 [222] M. Ciafaloni, *Nucl. Phys.* B296 (1988) 49.
- 9170 [223] B. Andersson, G. Gustafson and J. Samuelsson, *Nucl. Phys.* B467 (1996) 443.
- 9171 [224] J. Kwiecinski, A. D. Martin and P. J. Sutton, *Z. Phys.* C71 (1996) 585, [arXiv:hep-ph/9602320](#).
- 9172 [225] R. Ellis, Z. Kunszt and E. Levin, *Nucl. Phys. B* 420 (1994) 517. [Erratum: *Nucl. Phys.* B433 (1995) 498].
- 9173 [226] R. Ellis, F. Hautmann and B. Webber, *Phys. Lett.* B348 (1995) 582, [arXiv:hep-ph/9501307](#).
- 9174 [227] J. Kwiecinski, A. D. Martin and A. M. Stasto, *Phys. Rev.* D56 (1997) 3991, [arXiv:hep-ph/9703445](#).
- 9175 [228] S. Catani, M. Ciafaloni and F. Hautmann, *Phys. Lett.* B307 (1993) 147.
- 9176 [229] S. Catani and F. Hautmann, *Phys. Lett.* B315 (1993) 157.
- 9177 [230] S. Catani and F. Hautmann, *Nucl. Phys. B* 427 (1994) 475, [arXiv:hep-ph/9405388](#).
- 9178 [231] G. P. Salam, *JHEP* 07 (1998) 019, [arXiv:hep-ph/9806482](#).
- 9179 [232] M. Ciafaloni, D. Colferai and G. P. Salam, *JHEP* 10 (1999) 017, [arXiv:hep-ph/9907409](#).
- 9180 [233] M. Ciafaloni, D. Colferai and G. P. Salam, *Phys. Rev.* D60 (1999) 114036, [arXiv:hep-ph/9905566](#).
- 9181 [234] M. Ciafaloni, D. Colferai, G. P. Salam and A. M. Stasto, *Phys. Lett.* B576 (2003) 143,  
9182 [arXiv:hep-ph/0305254](#).
- 9183 [235] M. Ciafaloni, D. Colferai, G. P. Salam and A. M. Stasto, *Phys. Lett.* B587 (2004) 87,  
9184 [arXiv:hep-ph/0311325](#).
- 9185 [236] M. Ciafaloni, D. Colferai, G. P. Salam and A. M. Stasto, *Phys. Rev.* D68 (2003) 114003,  
9186 [arXiv:hep-ph/0307188](#).
- 9187 [237] M. Ciafaloni, D. Colferai, G. P. Salam and A. M. Stasto, *JHEP* 08 (2007) 046, [arXiv:0707.1453](#).
- 9188 [238] G. Altarelli, R. D. Ball and S. Forte, *Nucl. Phys.* B575 (2000) 313, [arXiv:hep-ph/9911273](#).
- 9189 [239] G. Altarelli, R. D. Ball and S. Forte, *Nucl. Phys.* B599 (2001) 383, [arXiv:hep-ph/0011270](#).
- 9190 [240] G. Altarelli, R. D. Ball and S. Forte, *Nucl. Phys.* B621 (2002) 359, [arXiv:hep-ph/0109178](#).
- 9191 [241] G. Altarelli, R. D. Ball and S. Forte, *Nucl. Phys.* B674 (2003) 459, [arXiv:hep-ph/0306156](#).
- 9192 [242] G. Altarelli, R. D. Ball and S. Forte, *Nucl. Phys.* B799 (2008) 199, [arXiv:0802.0032](#).
- 9193 [243] R. S. Thorne, *Phys. Rev.* D64 (2001) 074005, [arXiv:hep-ph/0103210](#).
- 9194 [244] A. Sabio Vera, *Nucl. Phys.* B722 (2005) 65, [arXiv:hep-ph/0505128](#).
- 9195 [245] M. Bonvini, S. Marzani and T. Peraro, *Eur. Phys. J.* C76 (2016) 597, [arXiv:1607.02153](#).
- 9196 [246] V. Bertone, S. Carrazza and J. Rojo, *Comput. Phys. Commun.* 185 (2014) 1647, [arXiv:1310.1394](#).
- 9197 [247] M. Bonvini, S. Marzani and C. Muselli, *JHEP* 12 (2017) 117, [arXiv:1708.07510](#).
- 9198 [248] A. H. Müller, *Nucl. Phys.* B335 (1990) 115.
- 9199 [249] R. D. Ball, V. Bertone, M. Bonvini, S. Marzani, J. Rojo and L. Rottoli, *Eur. Phys. J.* C78 (2018) 321,  
9200 [arXiv:1710.05935](#).
- 9201 [250] H. Abdolmaleki *et al.*, *Eur. Phys. J.* C78 (2018) 621, [arXiv:1802.00064](#).
- 9202 [251] J. Butterworth *et al.*, *J. Phys.* G43 (2016) 023001, [arXiv:1510.03865](#).
- 9203 [252] S. Carrazza, S. Forte, Z. Kassabov, J. I. Latorre and J. Rojo, *Eur. Phys. J.* C75 (2015) 369,  
9204 [arXiv:1505.06736](#).
- 9205 [253] H. Paukkunen and P. Zurita, *JHEP* 12 (2014) 100, [arXiv:1402.6623](#).
- 9206 [254] J. Rojo and F. Caola, “Parton distributions and small-x QCD at the Large Hadron Electron Collider,” in  
9207 *17th International Workshop on Deep-Inelastic Scattering and Related Subjects (DIS 2009): Madrid,*  
9208 *Spain, April 26-30, 2009*, Berlin, Germany, 2009. [arXiv:0906.2079](#).
- 9209 [255] R. Abdul Khalek, S. Bailey, J. Gao, L. Harland-Lang and J. Rojo, *Eur. Phys. J.* C78 (2018) 962,  
9210 [arXiv:1810.03639](#).
- 9211 [256] J. Bartels, K. J. Golec-Biernat and H. Kowalski, *Phys. Rev.* D66 (2002) 014001, [arXiv:hep-ph/0203258](#).
- 9212 [257] K. J. Golec-Biernat and S. Sapeta, *Phys. Rev.* D74 (2006) 054032, [arXiv:hep-ph/0607276](#).
- 9213 [258] K. J. Golec-Biernat and S. Sapeta, *JHEP* 03 (2018) 102, [arXiv:1711.11360](#).
- 9214 [259] J. Gao, L. Harland-Lang and J. Rojo, *Phys. Rept.* 742 (2018) 1, [arXiv:1709.04922](#).
- 9215 [260] V. Bertone, R. Gauld and J. Rojo, *JHEP* 01 (2019) 217, [arXiv:1808.02034](#).
- 9216 [261] L. N. Hand, D. G. Miller and R. Wilson, *Rev. Mod. Phys.* 35 (1963) 335.

- 9217 [262] G. Miller *et al.*, *Phys. Rev. D* 5 (1972) 528.
- 9218 [263] E. M. Riordan *et al.*, *Phys. Rev. Lett.* 33 (1974) 561.
- 9219 [264] H1 Collaboration, F. D. Aaron *et al.*, *Eur. Phys. J. C* 71 (2011) 1579, [arXiv:1012.4355](#).
- 9220 [265] G. Altarelli and G. Martinelli, *Phys. Lett.* 76B (1978) 89.
- 9221 [266] M. Glück, E. Hoffmann and E. Reya, *Z. Phys.* C13 (1982) 119.
- 9222 [267] C. Ewerz and O. Nachtmann, *Annals Phys.* 322 (2007) 1670, [arXiv:hep-ph/0604087](#).
- 9223 [268] F. Hautmann, *Phys. Lett.* B535 (2002) 159, [arXiv:hep-ph/0203140](#).
- 9224 [269] S. Marzani, R. D. Ball, V. Del Duca, S. Forte and A. Vicini, *Nucl. Phys. B* 800 (2008) 127,  
9225 [arXiv:0801.2544](#).
- 9226 [270] M. Bonvini and S. Marzani, *Phys. Rev. Lett.* 120 (2018) 202003, [arXiv:1802.07758](#).
- 9227 [271] H1 Collaboration, V. Andreev *et al.*, *Eur. Phys. J. C* 74 (2014) 2814, [arXiv:1312.4821](#).
- 9228 [272] ATLAS Collaboration, G. Aad *et al.*, *Phys. Rev. D* 85 (2012) 072004, [arXiv:1109.5141](#).
- 9229 [273] G. Altarelli, *Nuovo Cim.* C035N1 (2012) 1, [arXiv:1106.3189](#).
- 9230 [274] J. Blümlein and M. Klein, *Nucl. Instrum. Meth.* A329 (1993) 112.
- 9231 [275] T. Gehrmann, A. Huss, J. Niehues, A. Vogt and D. Walker, *Phys. Lett.* B792 (2019) 182,  
9232 [arXiv:1812.06104](#).
- 9233 [276] S. Catani, F. Fiorani and G. Marchesini, *Nucl. Phys.* B336 (1990) 18.
- 9234 [277] G. Marchesini and B. Webber, *Nucl. Phys. B* 386 (1992) 215–235.
- 9235 [278] F. Hautmann and H. Jung, *JHEP* 10 (2008) 113, [arXiv:0805.1049](#).
- 9236 [279] A. H. Mueller, *J. Phys. G* 17 (1991) 1443–1454.
- 9237 [280] J. R. Forshaw, A. Sabio Vera and B. Webber, *J. Phys. G* 25 (1999) 1511–1514, [arXiv:hep-ph/9812318](#).
- 9238 [281] F. Hautmann, *Acta Phys. Polon. B* 40 (2009) 2139–2163.
- 9239 [282] J. Bartels, V. Del Duca, A. De Roeck, D. Graudenz and M. Wusthoff, *Phys. Lett. B* 384 (1996) 300–306,  
9240 [arXiv:hep-ph/9604272](#).
- 9241 [283] J. Kwiecinski, A. D. Martin and A. Stasto, *Phys. Lett. B* 459 (1999) 644–648, [arXiv:hep-ph/9904402](#).
- 9242 [284] B. Andersson, G. Gustafson, H. Kharraziha and J. Samuelsson, *Z. Phys. C* 71 (1996) 613–624.
- 9243 [285] H. Jung *et al.*, *Eur. Phys. J. C* 70 (2010) 1237–1249, [arXiv:1008.0152](#).
- 9244 [286] F. Hautmann, H. Jung and S. T. Monfared, *Eur. Phys. J. C* 74 (2014) 3082, [arXiv:1407.5935](#).
- 9245 [287] A. van Hameren, *Comput. Phys. Commun.* 224 (2018) 371–380, [arXiv:1611.00680](#).
- 9246 [288] A. van Hameren, *PoS DIS2019* (2019) 139.
- 9247 [289] G. Chachamis and A. Sabio Vera, *Phys. Rev. D* 93 (2016) 074004, [arXiv:1511.03548](#).
- 9248 [290] S. Hoeche, F. Krauss and T. Teubner, *Eur. Phys. J. C* 58 (2008) 17–28, [arXiv:0705.4577](#).
- 9249 [291] J. R. Andersen, H. M. Brooks and L. Lönnblad, *JHEP* 09 (2018) 074, [arXiv:1712.00178](#).
- 9250 [292] F. Hautmann, H. Jung, A. Lelek, V. Radescu and R. Zlebcik, *Phys. Lett. B* 772 (2017) 446–451,  
9251 [arXiv:1704.01757](#).
- 9252 [293] F. Hautmann, H. Jung, A. Lelek, V. Radescu and R. Zlebcik, *JHEP* 01 (2018) 070, [arXiv:1708.03279](#).
- 9253 [294] A. Bermudez Martinez, P. Connor, H. Jung, A. Lelek, R. Zlebcik, F. Hautmann and V. Radescu,  
9254 *Phys. Rev. D* 99 (2019) 074008, [arXiv:1804.11152](#).
- 9255 [295] S. Höche, F. Krauss and S. Prestel, *JHEP* 10 (2017) 093, [arXiv:1705.00982](#).
- 9256 [296] S. Höche and S. Prestel, *Phys. Rev. D* 96 (2017) 074017, [arXiv:1705.00742](#).
- 9257 [297] R. Gandhi, C. Quigg, M. H. Reno and I. Sarcevic, *Phys. Rev. D* 58 (1998) 093009, [arXiv:hep-ph/9807264](#).
- 9258 [298] IceCube Collaboration, M. G. Aartsen *et al.*, *JINST* 12 (2017) P03012, [arXiv:1612.05093](#).
- 9259 [299] J. Kwiecinski, A. D. Martin and A. M. Stasto, *Phys. Rev. D* 59 (1999) 093002, [arXiv:astro-ph/9812262](#).
- 9260 [300] IceCube Collaboration, M. G. Aartsen *et al.*, *Nature* 551 (2017) 596, [arXiv:1711.08119](#).
- 9261 [301] T. K. Gaisser, *Cosmic rays and particle physics*. 1990.  
9262 <http://www.cambridge.org/uk/catalogue/catalogue.asp?isbn=0521326672>.
- 9263 [302] IceCube Collaboration, M. G. Aartsen *et al.*, *Phys. Rev. Lett.* 113 (2014) 101101, [arXiv:1405.5303](#).

- 9264 [303] G. Gelmini, P. Gondolo and G. Varieschi, *Phys. Rev. D* 61 (2000) 056011, [arXiv:hep-ph/9905377](#).
- 9265 [304] A. Bhattacharya, R. Enberg, Y. S. Jeong, C. S. Kim, M. H. Reno, I. Sarcevic and A. Stasto, *JHEP* 11  
9266 (2016) 167, [arXiv:1607.00193](#).
- 9267 [305] Pierre Auger Collaboration, A. Aab *et al.*, *Phys. Rev. D* 90 (2014) 122006, [arXiv:1409.5083](#).
- 9268 [306] Pierre Auger Collaboration, A. Aab *et al.*, *Phys. Rev. D* 90 (2014) 122005, [arXiv:1409.4809](#).
- 9269 [307] H. Drescher, A. Dumitru and M. Strikman, *Phys. Rev. Lett.* 94 (2005) 231801, [arXiv:hep-ph/0408073](#).
- 9270 [308] S. R. Klein and H. Mäntysaari, *Nature Rev. Phys.* 1 (2019) 662, [arXiv:1910.10858](#).
- 9271 [309] H1 Collaboration, C. Adloff *et al.*, *Z. Phys. C* 76 (1997) 613, [arXiv:hep-ex/9708016](#).
- 9272 [310] ZEUS Collaboration, J. Breitweg *et al.*, *Eur. Phys. J. C* 1 (1998) 81, [arXiv:hep-ex/9709021](#).
- 9273 [311] P. Newman and M. Wing, *Rev. Mod. Phys.* 86 (2014) 1037, [arXiv:1308.3368](#).
- 9274 [312] G. Ingelman and P. Schlein, *Phys. Lett. B* 152 (1985) 256.
- 9275 [313] W. Buchmüller, T. Gehrmann and A. Hebecker, *Nucl. Phys. B* 537 (1999) 477, [arXiv:hep-ph/9808454](#).
- 9276 [314] F. Hautmann, Z. Kunszt and D. Soper, *Phys. Rev. Lett.* 81 (1998) 3333, [arXiv:hep-ph/9806298](#).
- 9277 [315] F. Hautmann, Z. Kunszt and D. Soper, *Nucl. Phys. B* 563 (1999) 153, [arXiv:hep-ph/9906284](#).
- 9278 [316] S. J. Brodsky, R. Enberg, P. Hoyer and G. Ingelman, *Phys. Rev. D* 71 (2005) 074020,  
9279 [arXiv:hep-ph/0409119](#).
- 9280 [317] G. Ingelman, R. Pasechnik and D. Werder, *Phys. Rev. D* 93 (2016) 094016, [arXiv:1511.06317](#).
- 9281 [318] C. O. Rasmussen and T. Sjöstrand, *JHEP* 02 (2016) 142, [arXiv:1512.05525](#).
- 9282 [319] J. Bjorken, *Phys. Rev. D* 47 (1993) 101.
- 9283 [320] J. Bartels, J. R. Ellis, H. Kowalski and M. Wusthoff, *Eur. Phys. J. C* 7 (1999) 443,  
9284 [arXiv:hep-ph/9803497](#).
- 9285 [321] F. Hautmann and D. Soper, *Phys. Rev. D* 63 (2001) 011501, [arXiv:hep-ph/0008224](#).
- 9286 [322] F. Hautmann and D. E. Soper, *Phys. Rev. D* 75 (2007) 074020, [arXiv:hep-ph/0702077](#).
- 9287 [323] V. N. Gribov, *Sov. Phys. JETP* 29 (1969) 483. [*Zh. Eksp. Teor. Fiz.* 56 (1969) 892].
- 9288 [324] J. C. Collins, *Phys. Rev. D* 57 (1998) 3051, [arXiv:hep-ph/9709499](#). [Erratum: *Phys. Rev. D* 61 (2000)  
9289 019902].
- 9290 [325] A. Berera and D. E. Soper, *Phys. Rev. D* 53 (1996) 6162, [arXiv:hep-ph/9509239](#).
- 9291 [326] L. Trentadue and G. Veneziano, *Phys. Lett. B* 323 (1994) 201.
- 9292 [327] N. Armesto, P. R. Newman, W. Slominski and A. M. Stasto, *Phys. Rev. D* 100 (2019) 074022,  
9293 [arXiv:1901.09076](#).
- 9294 [328] H. Khanpour, *Phys. Rev. D* 99 (2019) 054007, [arXiv:1902.10734](#).
- 9295 [329] H1 Collaboration, A. Aktas *et al.*, *Eur. Phys. J. C* 48 (2006) 715, [arXiv:hep-ex/0606004](#).
- 9296 [330] ZEUS Collaboration, S. Chekanov *et al.*, *Nucl. Phys. B* 816 (2009) 1, [arXiv:0812.2003](#).
- 9297 [331] H1 Collaboration, F. Aaron *et al.*, *Eur. Phys. J. C* 72 (2012) 2074, [arXiv:1203.4495](#).
- 9298 [332] H1 and ZEUS Collaborations, F. D. Aaron *et al.*, *Eur. Phys. J. C* 72 (2012) 2175, [arXiv:1207.4864](#).
- 9299 [333] ZEUS Collaboration, S. Chekanov *et al.*, *Nucl. Phys. B* 713 (2005) 3, [arXiv:hep-ex/0501060](#).
- 9300 [334] H1 Collaboration, A. Aktas *et al.*, *Eur. Phys. J. C* 48 (2006) 749, [arXiv:hep-ex/0606003](#).
- 9301 [335] ZEUS Collaboration, S. Chekanov *et al.*, *Nucl. Phys. B* 831 (2010) 1, [arXiv:0911.4119](#).
- 9302 [336] H1 Collaboration, F. Aaron *et al.*, *Eur. Phys. J. C* 71 (2011) 1578, [arXiv:1010.1476](#).
- 9303 [337] V. N. Gribov and L. N. Lipatov, *Sov. J. Nucl. Phys.* 15 (1972) 675. [*Yad. Fiz.* 15 (1972) 1218].
- 9304 [338] V. N. Gribov and L. N. Lipatov, *Sov. J. Nucl. Phys.* 15 (1972) 438. [*Yad. Fiz.* 15 (1972) 781].
- 9305 [339] G. Altarelli and G. Parisi, *Nucl. Phys. B* 126 (1977) 298.
- 9306 [340] Y. L. Dokshitzer, *Sov. Phys. JETP* 46 (1977) 641. [*Zh. Eksp. Teor. Fiz.* 73 (1977) 1216].
- 9307 [341] J. C. Collins and W.-K. Tung, *Nucl. Phys. B* 278 (1986) 934.
- 9308 [342] R. S. Thorne and W. K. Tung, [arXiv:0809.0714](#).
- 9309 [343] J. F. Owens, *Phys. Rev. D* 30 (1984) 943.
- 9310 [344] M. Glück, E. Reya and A. Vogt, *Z. Phys. C* 53 (1992) 651.

- 9311 [345] R. S. Thorne and R. G. Roberts, *Phys. Rev. D* **57** (1998) 6871, [arXiv:hep-ph/9709442](#).
- 9312 [346] ATLAS Collaboration, G. Aad *et al.*, *Phys. Lett. B* **754** (2016) 214, [arXiv:1511.00502](#).
- 9313 [347] D. Britzger, J. Currie, T. Gehrmann, A. Huss, J. Niehues and R. Žlebčák, *Eur. Phys. J. C* **78** (2018) 538,  
9314 [arXiv:1804.05663](#).
- 9315 [348] Z. Nagy, *Phys. Rev. D* **68** (2003) 094002, [arXiv:hep-ph/0307268](#).
- 9316 [349] S. Moch, J. Vermaseren and A. Vogt, *Nucl. Phys. B* **688** (2004) 101, [arXiv:hep-ph/0403192](#).
- 9317 [350] A. Vogt, S. Moch and J. Vermaseren, *Nucl. Phys. B* **691** (2004) 129, [arXiv:hep-ph/0404111](#).
- 9318 [351] D. de Florian, G. F. Sborlini and G. Rodrigo, *JHEP* **10** (2016) 056, [arXiv:1606.02887](#).
- 9319 [352] J. Vermaseren, A. Vogt and S. Moch, *Nucl. Phys. B* **724** (2005) 3, [arXiv:hep-ph/0504242](#).
- 9320 [353] J. Ablinger, A. Behring, J. Blümlein, A. De Freitas, A. Hasselhuhn, A. von Manteuffel, M. Round,  
9321 C. Schneider and F. Wißbrock, *Nucl. Phys. B* **886** (2014) 733, [arXiv:1406.4654](#).
- 9322 [354] J. Ablinger, J. Blümlein, A. De Freitas, A. Hasselhuhn, C. Schneider and F. Wißbrock, *Nucl. Phys. B* **921**  
9323 (2017) 585, [arXiv:1705.07030](#).
- 9324 [355] J. Niehues and D. Walker, *Phys. Lett. B* **788** (2019) 243, [arXiv:1807.02529](#).
- 9325 [356] V. Hirschi, R. Frederix, S. Frixione, M. V. Garzelli, F. Maltoni and R. Pittau, *JHEP* **05** (2011) 044,  
9326 [arXiv:1103.0621](#).
- 9327 [357] F. Cascioli, P. Maierhofer and S. Pozzorini, *Phys. Rev. Lett.* **108** (2012) 111601, [arXiv:1111.5206](#).
- 9328 [358] G. Cullen *et al.*, *Eur. Phys. J. C* **74** (2014) 3001, [arXiv:1404.7096](#).
- 9329 [359] R. Frederix, S. Frixione, V. Hirschi, D. Pagani, H.-S. Shao and M. Zaro, *JHEP* **07** (2018) 185,  
9330 [arXiv:1804.10017](#).
- 9331 [360] F. Buccioni, J.-N. Lang, J. M. Lindert, P. Maierhöfer, S. Pozzorini, H. Zhang and M. F. Zoller, *Eur. Phys.*  
9332 *J. C* **79** (2019) 866, [arXiv:1907.13071](#).
- 9333 [361] J. Alwall, R. Frederix, S. Frixione, V. Hirschi, F. Maltoni, O. Mattelaer, H. S. Shao, T. Stelzer, P. Torrielli  
9334 and M. Zaro, *JHEP* **07** (2014) 079, [arXiv:1405.0301](#).
- 9335 [362] J. Bellm *et al.*, *Eur. Phys. J. C* **76** (2016) 196, [arXiv:1512.01178](#).
- 9336 [363] Sherpa Collaboration, E. Bothmann *et al.*, *SciPost Phys.* **7** (2019) 034, [arXiv:1905.09127](#).
- 9337 [364] M. Dasgupta and G. P. Salam, *JHEP* **08** (2002) 032, [arXiv:hep-ph/0208073](#).
- 9338 [365] S. J. Brodsky, P. Hoyer, C. Peterson and N. Sakai, *Phys. Lett.* **93B** (1980) 451.
- 9339 [366] S. J. Brodsky, A. Kusina, F. Lyonnet, I. Schienbein, H. Spiesberger and R. Vogt, *Adv. High Energy Phys.*  
9340 **2015** (2015) 231547, [arXiv:1504.06287](#).
- 9341 [367] S. J. Brodsky and S. Gardner, *Phys. Rev. Lett.* **116** (2016) 019101, [arXiv:1504.00969](#).
- 9342 [368] G. F. de Teramond and S. J. Brodsky, *Phys. Rev. Lett.* **102** (2009) 081601, [arXiv:0809.4899](#).
- 9343 [369] SELEX Collaboration, A. Ocherashvili *et al.*, *Phys. Lett. B* **628** (2005) 18, [arXiv:hep-ex/0406033](#).
- 9344 [370] ANDY Collaboration, L. C. Bland *et al.*, [arXiv:1909.03124](#).
- 9345 [371] S. J. Brodsky, G. F. de Teramond, H. G. Dosch and J. Erlich, *Phys. Rept.* **584** (2015) 1, [arXiv:1407.8131](#).
- 9346 [372] G. F. de Teramond, H. G. Dosch and S. J. Brodsky, *Phys. Rev. D* **87** (2013) 075005, [arXiv:1301.1651](#).
- 9347 [373] V. de Alfaro, S. Fubini and G. Furlan, *Nuovo Cim. A* **34** (1976) 569.
- 9348 [374] G. Veneziano, *Nuovo Cim. A* **57** (1968) 190.
- 9349 [375] A. Deur, S. J. Brodsky and G. F. de Teramond, *Prog. Part. Nucl. Phys.* **90** (2016) 1, [arXiv:1604.08082](#).
- 9350 [376] G. Grunberg, *Phys. Lett.* **95B** (1980) 70. [Erratum: *Phys. Lett.* **B110** (1982) 501].
- 9351 [377] J. D. Bjorken, *Phys. Rev.* **148** (1966) 1467.
- 9352 [378] A. Deur *et al.*, *Phys. Rev. Lett.* **93** (2004) 212001, [arXiv:hep-ex/0407007](#).
- 9353 [379] A. Deur, Y. Prok, V. Burkert, D. Crabb, F. X. Girod, K. A. Griffioen, N. Guler, S. E. Kuhn and  
9354 N. Kvaltine, *Phys. Rev. D* **90** (2014) 012009, [arXiv:1405.7854](#).
- 9355 [380] A. Deur *et al.*, *Phys. Rev. D* **78** (2008) 032001, [arXiv:0802.3198](#).
- 9356 [381] S. J. Brodsky and H. J. Lu, *Phys. Rev. D* **51** (1995) 3652, [arXiv:hep-ph/9405218](#).
- 9357 [382] S. J. Brodsky, G. F. de Teramond and A. Deur, *Phys. Rev. D* **81** (2010) 096010, [arXiv:1002.3948](#).
- 9358 [383] A. Deur, S. J. Brodsky and G. F. de Teramond, *Phys. Lett. B* **750** (2015) 528, [arXiv:1409.5488](#).

- 9359 [384] S. J. Brodsky, G. F. de Téramond, A. Deur and H. G. Dosch, *Few Body Syst.* 56 (2015) 621,  
9360 [arXiv:1410.0425](#).
- 9361 [385] A. Deur, V. Burkert, J.-P. Chen and W. Korsch, *Phys. Lett.* B650 (2007) 244, [arXiv:hep-ph/0509113](#).
- 9362 [386] A. Deur, V. Burkert, J. P. Chen and W. Korsch, *Phys. Lett.* B665 (2008) 349, [arXiv:0803.4119](#).
- 9363 [387] S. J. Brodsky, *J. Phys. Conf. Ser.* 1137 (2019) 012027.
- 9364 [388] G. P. Lepage and S. J. Brodsky, *Phys. Lett.* 87B (1979) 359.
- 9365 [389] A. V. Efremov and A. V. Radyushkin, *Phys. Lett.* 94B (1980) 245.
- 9366 [390] S. J. Brodsky, G. F. De Téramond and H. G. Dosch, *Phys. Lett.* B729 (2014) 3, [arXiv:1302.4105](#).
- 9367 [391] S. J. Brodsky, *Few Body Syst.* 57 (2016) 703, [arXiv:1601.06328](#).
- 9368 [392] R. S. Sufian, G. F. de Téramond, S. J. Brodsky, A. Deur and H. G. Dosch, *Phys. Rev.* D95 (2017) 014011,  
9369 [arXiv:1609.06688](#).
- 9370 [393] HLFHS Collaboration, G. F. de Teramond, T. Liu, R. S. Sufian, H. G. Dosch, S. J. Brodsky and A. Deur,  
9371 *Phys. Rev. Lett.* 120 (2018) 182001, [arXiv:1801.09154](#).
- 9372 [394] T. Gutsche, V. E. Lyubovitskij, I. Schmidt and A. Vega, *Phys. Rev.* D91 (2015) 114001,  
9373 [arXiv:1501.02738](#).
- 9374 [395] T. Gutsche, V. E. Lyubovitskij and I. Schmidt, *Phys. Rev.* D94 (2016) 116006, [arXiv:1607.04124](#).
- 9375 [396] H. G. Dosch, G. F. de Teramond and S. J. Brodsky, *Phys. Rev.* D91 (2015) 085016, [arXiv:1501.00959](#).
- 9376 [397] S. J. Brodsky, G. F. de Téramond, H. G. Dosch and C. Lorcé, *Int. J. Mod. Phys.* A31 (2016) 1630029,  
9377 [arXiv:1606.04638](#).
- 9378 [398] M. Nielsen, S. J. Brodsky, G. F. de Téramond, H. G. Dosch, F. S. Navarra and L. Zou, *Phys. Rev.* D98  
9379 (2018) 034002, [arXiv:1805.11567](#).
- 9380 [399] G. F. de Teramond, H. G. Dosch and S. J. Brodsky, *Phys. Rev.* D91 (2015) 045040, [arXiv:1411.5243](#).
- 9381 [400] S. L. Glashow, *Nucl. Phys.* 22 (1961) 579.
- 9382 [401] S. Weinberg, *Phys. Rev. Lett.* 27 (1971) 1688.
- 9383 [402] S. Weinberg, *Phys. Rev.* D5 (1972) 1412.
- 9384 [403] A. Salam and J. C. Ward, *Phys. Lett.* 13 (1964) 168.
- 9385 [404] P. W. Higgs, *Phys. Lett.* 12 (1964) 132.
- 9386 [405] P. W. Higgs, *Phys. Rev. Lett.* 13 (1964) 508.
- 9387 [406] F. Englert and R. Brout, *Phys. Rev. Lett.* 13 (1964) 321.
- 9388 [407] H1 Collaboration, A. Aktas *et al.*, *Phys. Lett.* B632 (2006) 35, [arXiv:hep-ex/0507080](#).
- 9389 [408] ZEUS Collaboration, H. Abramowicz *et al.*, *Phys. Rev.* D93 (2016) 092002, [arXiv:1603.09628](#).
- 9390 [409] H1 Collaboration, V. Andreev *et al.*, *Eur. Phys. J.* C78 (2018) 777, [arXiv:1806.01176](#).
- 9391 [410] M. Böhm and H. Spiesberger, *Nucl. Phys.* B294 (1987) 1081.
- 9392 [411] D. Yu. Bardin, C. Burdik, P. C. Khristova and T. Riemann, *Z. Phys.* C42 (1989) 679.
- 9393 [412] Hollik, W. and Bardin, D. Yu. and Blümlein, J. and Kniehl, B. A. and Riemann, T. and Spiesberger, H.,  
9394 “Electroweak parameters at HERA: Theoretical aspects,” in *Workshop on physics at HERA Hamburg,*  
9395 *Germany, October 29-30, 1991*, 1992.
- 9396 [413] M. Böhm and H. Spiesberger, *Nucl. Phys.* B304 (1988) 749.
- 9397 [414] D. Yu. Bardin, K. C. Burdik, P. K. Khristova and T. Riemann, *Z. Phys.* C44 (1989) 149.
- 9398 [415] A. Sirlin, *Phys. Rev.* D22 (1980) 971.
- 9399 [416] M. Böhm, H. Spiesberger and W. Hollik, *Fortsch. Phys.* 34 (1986) 687.
- 9400 [417] W. F. L. Hollik, *Fortsch. Phys.* 38 (1990) 165.
- 9401 [418] H1 Collaboration, F. D. Aaron *et al.*, *JHEP* 09 (2012) 061, [arXiv:1206.7007](#).
- 9402 [419] D. Britzger and M. Klein, *PoS DIS2017* (2018) 105.
- 9403 [420] H. Spiesberger, “EPRC: A program package for electroweak physics at HERA,” in *Future physics at*  
9404 *HERA. Proceedings, Workshop, Hamburg, Germany, September 25, 1995-May 31, 1996. Vol. 1, 2*, 1995.
- 9405 [421] G. Cowan, K. Cranmer, E. Gross and O. Vitells, *Eur. Phys. J.* C71 (2011) 1554, [arXiv:1007.1727](#).  
9406 [Erratum: *Eur. Phys. J.* C73 (2013) 2501].



- 9407 [422] CDF and D0 Collaborations, “2012 Update of the Combination of CDF and D0 Results for the Mass of  
9408 the W Boson,” 2012. [arXiv:1204.0042](#).
- 9409 [423] ALEPH, DELPHI, L3, OPAL, LEP Electroweak Collaboration, S. Schael *et al.*, *Phys. Rept.* **532** (2013)  
9410 [119](#), [arXiv:1302.3415](#).
- 9411 [424] ATLAS Collaboration, M. Aaboud *et al.*, *Eur. Phys. J. C* **78** (2018) 110, [arXiv:1701.07240](#). [Erratum:  
9412 *Eur. Phys. J. C* **78** (2018) 898].
- 9413 [425] J. de Blas, M. Ciuchini, E. Franco, S. Mishima, M. Pierini, L. Reina and L. Silvestrini, *JHEP* **12** (2016)  
9414 [135](#), [arXiv:1608.01509](#).
- 9415 [426] J. Haller, A. Höcker, R. Kogler, K. Mönig, T. Peiffer and J. Stelzer, *Eur. Phys. J. C* **78** (2018) 675,  
9416 [arXiv:1803.01853](#).
- 9417 [427] MuLan Collaboration, V. Tishchenko *et al.*, *Phys. Rev. D* **87** (2013) 052003, [arXiv:1211.0960](#).
- 9418 [428] M. Schott, “Global EW fits: experimental and theoretical issues,” Talk presented at the Ultimate  
9419 Precision at Hadron Colliders, Sarclay, France, 2019.
- 9420 [429] ALEPH, DELPHI, L3, OPAL, SLD Collaborations, LEP Electroweak Working Group, SLD Electroweak  
9421 Heavy Flavour Groups, S. Schael *et al.*, *Phys. Rept.* **427** (2006) 257, [arXiv:hep-ex/0509008](#).
- 9422 [430] D0 Collaboration, V. M. Abazov *et al.*, *Phys. Rev. D* **84** (2011) 012007, [arXiv:1104.4590](#).
- 9423 [431] CDF and D0 Collaborations, T. A. Aaltonen *et al.*, *Phys. Rev. D* **97** (2018) 112007, [arXiv:1801.06283](#).
- 9424 [432] LHCb Collaboration, R. Aaij *et al.*, *JHEP* **11** (2015) 190, [arXiv:1509.07645](#).
- 9425 [433] ATLAS Collaboration, “Measurement of the effective leptonic weak mixing angle using electron and muon  
9426 pairs from Z-boson decay in the ATLAS experiment at  $\sqrt{s} = 8$  TeV,” 2018. ATLAS-CONF-2018-037.
- 9427 [434] CMS Collaboration, A. M. Sirunyan *et al.*, *Eur. Phys. J. C* **78** (2018) 701, [arXiv:1806.00863](#).
- 9428 [435] J. Erler, “Global fits of the SM parameters,” in *7th Large Hadron Collider Physics Conference (LHCP*  
9429 *2019) Puebla, Puebla, Mexico, May 20-25, 2019*, 2019. [arXiv:1908.07327](#).
- 9430 [436] J. Erler and M. Schott, *Prog. Part. Nucl. Phys.* **106** (2019) 68, [arXiv:1902.05142](#).
- 9431 [437] E. Accomando *et al.*, *JHEP* **10** (2019) 176, [arXiv:1907.07727](#).
- 9432 [438] E. Accomando, J. Fiaschi, F. Hautmann and S. Moretti, *Eur. Phys. J. C* **78** (2018) 663,  
9433 [arXiv:1805.09239](#). [Erratum: *Eur.Phys.J. C* **79** (2019) 453].
- 9434 [439] E. Accomando, J. Fiaschi, F. Hautmann and S. Moretti, *Phys. Rev. D* **98** (2018) 013003,  
9435 [arXiv:1712.06318](#). [Erratum: *Phys. Rev. D* **99** (2019) 079902].
- 9436 [440] ZEUS Collaboration, S. Chekanov *et al.*, *Phys. Lett. B* **672** (2009) 106, [arXiv:0807.0589](#).
- 9437 [441] H1 Collaboration, F. D. Aaron *et al.*, *Eur. Phys. J. C* **64** (2009) 251, [arXiv:0901.0488](#).
- 9438 [442] H1 and ZEUS Collaborations, F. D. Aaron *et al.*, *JHEP* **03** (2010) 035, [arXiv:0911.0858](#).
- 9439 [443] U. Baur and D. Zeppenfeld, *Nucl. Phys. B* **325** (1989) 253.
- 9440 [444] U. Baur, B. A. Kniehl, J. A. M. Vermaseren and D. Zeppenfeld, “Single W and Z production at LEP /  
9441 LHC,” in *ECFA Large Hadron Collider Workshop, Aachen, Germany, 4-9 Oct 1990: Proceedings.2.*, 1990.
- 9442 [445] U. Baur, J. A. M. Vermaseren and D. Zeppenfeld, *Nucl. Phys. B* **375** (1992) 3.
- 9443 [446] NNPDF Collaboration, R. D. Ball *et al.*, *Nucl. Phys. B* **877** (2013) 290, [arXiv:1308.0598](#).
- 9444 [447] K. Hagiwara, S. Ishihara, R. Szalapski and D. Zeppenfeld, *Phys. Rev. D* **48** (1993) 2182.
- 9445 [448] K. Hagiwara, S. Ishihara, R. Szalapski and D. Zeppenfeld, *Phys. Lett. B* **283** (1992) 353.
- 9446 [449] A. De Rujula, M. B. Gavela, P. Hernandez and E. Masso, *Nucl. Phys. B* **384** (1992) 3.
- 9447 [450] S. S. Biswal, M. Patra and S. Raychaudhuri, [arXiv:1405.6056](#).
- 9448 [451] I. T. Cakir, O. Cakir, A. Senol and A. T. Tasci, *Acta Phys. Polon. B* **45** (2014) 1947, [arXiv:1406.7696](#).
- 9449 [452] R. Li, X.-M. Shen, K. Wang, T. Xu, L. Zhang and G. Zhu, *Phys. Rev. D* **97** (2018) 075043,  
9450 [arXiv:1711.05607](#).
- 9451 [453] M. Köksal, A. A. Billur, A. Gutiérrez-Rodríguez and M. A. Hernández-Ruíz, [arXiv:1910.06747](#).
- 9452 [454] A. Gutiérrez-Rodríguez, M. Köksal, A. A. Billur and M. A. Hernández-Ruíz, [arXiv:1910.02307](#).
- 9453 [455] CMS Collaboration, A. M. Sirunyan *et al.*, *Phys. Lett. B* **772** (2017) 21, [arXiv:1703.06095](#).
- 9454 [456] CMS Collaboration, A. M. Sirunyan *et al.*, [arXiv:1907.08354](#).
- 9455 [457] S. Villa, *Nucl. Phys. Proc. Suppl.* **142** (2005) 391, [arXiv:hep-ph/0410208](#).

- 9456 [458] S. Dutta, A. Goyal, M. Kumar and B. Mellado, *Eur. Phys. J. C*75 (2015) 577, [arXiv:1307.1688](#).
- 9457 [459] A. O. Bouzas and F. Larios, *Phys. Rev. D*88 (2013) 094007, [arXiv:1308.5634](#).
- 9458 [460] S. Oryn, X. Rouby and V. Lemaitre, “DELPHES, a framework for fast simulation of a generic collider  
9459 experiment,” 2009. [arXiv:0903.2225](#).
- 9460 [461] CMS Collaboration, V. Khachatryan *et al.*, *JHEP* 06 (2014) 090, [arXiv:1403.7366](#).
- 9461 [462] I. A. Sarmiento-Alvarado, A. O. Bouzas and F. Larios, *J. Phys. G*42 (2015) 085001, [arXiv:1412.6679](#).
- 9462 [463] H. Sun, *PoS DIS2018* (2018) 167.
- 9463 [464] CMS Collaboration, V. Khachatryan *et al.*, *Phys. Lett. B*736 (2014) 33, [arXiv:1404.2292](#).
- 9464 [465] J. A. Aguilar-Saavedra, *Acta Phys. Polon. B*35 (2004) 2695, [arXiv:hep-ph/0409342](#).
- 9465 [466] J. Charles *et al.*, *Phys. Rev. D*91 (2015) 073007, [arXiv:1501.05013](#).
- 9466 [467] S. Atag and B. Sahin, *Phys. Rev. D*73 (2006) 074001.
- 9467 [468] A. O. Bouzas and F. Larios, *Phys. Rev. D* 87 (2013) 074015, [arXiv:1212.6575](#).
- 9468 [469] B. Coleppa, M. Kumar, S. Kumar and B. Mellado, *Phys. Lett. B*770 (2017) 335, [arXiv:1702.03426](#).
- 9469 [470] NNPDF Collaboration, R. D. Ball *et al.*, *Eur. Phys. J. C* 77 (2017) 663, [arXiv:1706.00428](#).
- 9470 [471] F. Demartin, S. Forte, E. Mariani, J. Rojo and A. Vicini, *Phys. Rev. D* 82 (2010) 014002,  
9471 [arXiv:1004.0962](#).
- 9472 [472] I. Turk Cakir, A. Yilmaz, H. Denizli, A. Senol, H. Karadeniz and O. Cakir, *Adv. High Energy Phys.* 2017  
9473 (2017) 1572053, [arXiv:1705.05419](#).
- 9474 [473] O. Cakir, A. Yilmaz, I. Turk Cakir, A. Senol and H. Denizli, *Nucl. Phys. B*944 (2019) 114640,  
9475 [arXiv:1809.01923](#).
- 9476 [474] J. A. Aguilar-Saavedra and T. Riemann, “Probing top flavor changing neutral couplings at TESLA,” in  
9477 *5th Workshop of the 2nd ECFA, Obernai, France, October 16-19, 1999*, 2001. [arXiv:hep-ph/0102197](#).
- 9478 [475] Top Quark Working Group, K. Agashe *et al.*, “Working Group Report: Top Quark,” in *Community  
9479 Summer Study on the Future of U.S. Particle Physics: Minneapolis, MN, USA, July 29-August 6, 2013*,  
9480 2013. [arXiv:1311.2028](#).
- 9481 [476] S. Behera, R. Islam, M. Kumar, P. Poulouse and R. Rahaman, *Phys. Rev. D* 100 (2019) 015006,  
9482 [arXiv:1811.04681](#).
- 9483 [477] H. Sun and X. Wang, *Eur. Phys. J. C*78 (2018) 281, [arXiv:1602.04670](#).
- 9484 [478] European Muon Collaboration, J. J. Aubert *et al.*, *Phys. Lett.* 123B (1983) 275.
- 9485 [479] J. Gomez *et al.*, *Phys. Rev. D*49 (1994) 4348.
- 9486 [480] New Muon Collaboration, P. Amaudruz *et al.*, *Nucl. Phys. B*441 (1995) 3, [arXiv:hep-ph/9503291](#).
- 9487 [481] New Muon Collaboration, M. Arneodo *et al.*, *Nucl. Phys. B*441 (1995) 12, [arXiv:hep-ex/9504002](#).
- 9488 [482] New Muon Collaboration, M. Arneodo *et al.*, *Nucl. Phys. B*481 (1996) 3.
- 9489 [483] European Muon Collaboration, J. Ashman *et al.*, *Z. Phys. C*57 (1993) 211.
- 9490 [484] New Muon Collaboration, M. Arneodo *et al.*, *Nucl. Phys. B*481 (1996) 23.
- 9491 [485] New Muon Collaboration, P. Amaudruz *et al.*, *Nucl. Phys. B*371 (1992) 3.
- 9492 [486] M. Arneodo, *Phys. Rept.* 240 (1994) 301.
- 9493 [487] D. F. Geesaman, K. Saito and A. W. Thomas, *Ann. Rev. Nucl. Part. Sci.* 45 (1995) 337.
- 9494 [488] K. J. Eskola, P. Paakkinen, H. Paukkunen and C. A. Salgado, *Eur. Phys. J. C*77 (2017) 163,  
9495 [arXiv:1612.05741](#).
- 9496 [489] C. A. Salgado *et al.*, *J. Phys. G*39 (2012) 015010, [arXiv:1105.3919](#).
- 9497 [490] K. J. Golec-Biernat and M. Wusthoff, *Phys. Rev. D*59 (1998) 014017, [arXiv:hep-ph/9807513](#).
- 9498 [491] L. Frankfurt, V. Guzey and M. Strikman, *Phys. Rept.* 512 (2012) 255, [arXiv:1106.2091](#).
- 9499 [492] F. Gelis, E. Iancu, J. Jalilian-Marian and R. Venugopalan, *Ann. Rev. Nucl. Part. Sci.* 60 (2010) 463,  
9500 [arXiv:1002.0333](#).
- 9501 [493] Y. V. Kovchegov and E. Levin, *Camb. Monogr. Part. Phys. Nucl. Phys. Cosmol.* 33 (2012) 1.
- 9502 [494] Z. Citron *et al.*, “Future physics opportunities for high-density QCD at the LHC with heavy-ion and  
9503 proton beams,” in *HL/HE-LHC Workshop: Workshop on the Physics of HL-LHC, and Perspectives at  
9504 HE-LHC Geneva, Switzerland, June 18-20, 2018*, 2018. [arXiv:1812.06772](#).

- 9505 [495] B. L. Ioffe, V. S. Fadin and L. N. Lipatov, *Quantum chromodynamics: Perturbative and nonperturbative*  
9506 *aspects*, vol. 30. Cambridge Univ. Press, 2010.
- 9507 [496] J. Collins, *Foundations of perturbative QCD*, vol. 32. Cambridge University Press, Nov 2013.
- 9508 [497] H. Paukkunen, *Nucl. Phys. A*967 (2017) 241, [arXiv:1704.04036](#).
- 9509 [498] H. Paukkunen, *PoS HardProbes2018* (2018) 014, [arXiv:1811.01976](#).
- 9510 [499] K. J. Eskola, H. Paukkunen and C. A. Salgado, *JHEP* 04 (2009) 065, [arXiv:0902.4154](#).
- 9511 [500] D. de Florian, R. Sassot, P. Zurita and M. Stratmann, *Phys. Rev. D*85 (2012) 074028, [arXiv:1112.6324](#).
- 9512 [501] K. Kovarik *et al.*, *Phys. Rev. D*93 (2016) 085037, [arXiv:1509.00792](#).
- 9513 [502] H. Khanpour and S. Atashbar Tehrani, *Phys. Rev. D*93 (2016) 014026, [arXiv:1601.00939](#).
- 9514 [503] NNPDF Collaboration, R. Abdul Khalek, J. J. Ethier and J. Rojo, *Eur. Phys. J. C*79 (2019) 471,  
9515 [arXiv:1904.00018](#).
- 9516 [504] H. Paukkunen and C. A. Salgado, *JHEP* 07 (2010) 032, [arXiv:1004.3140](#).
- 9517 [505] K. Kovarik, I. Schienbein, F. I. Olness *et al.*, *Phys. Rev. Lett.* 106 (2011) 122301, [arXiv:1012.0286](#).
- 9518 [506] H. Paukkunen and C. A. Salgado, *Phys. Rev. Lett.* 110 (2013) 212301, [arXiv:1302.2001](#).
- 9519 [507] N. Armesto, *J. Phys. G*32 (2006) R367, [arXiv:hep-ph/0604108](#).
- 9520 [508] K. J. Eskola, P. Paakkinen and H. Paukkunen, *Eur. Phys. J. C*79 (2019) 511, [arXiv:1903.09832](#).
- 9521 [509] N. Armesto, H. Paukkunen, J. M. Penín, C. A. Salgado and P. Zurita, *Eur. Phys. J. C*76 (2016) 218,  
9522 [arXiv:1512.01528](#).
- 9523 [510] A. Kusina, F. Lyonnet, D. B. Clark, E. Godat *et al.*, *Eur. Phys. J. C*77 (2017) 488, [arXiv:1610.02925](#).
- 9524 [511] N. Armesto, A. Capella, A. B. Kaidalov, J. Lopez-Albacete and C. A. Salgado, *Eur. Phys. J. C*29 (2003)  
9525 531, [arXiv:hep-ph/0304119](#).
- 9526 [512] N. Armesto, A. B. Kaidalov, C. A. Salgado and K. Tywoniuk, *Eur. Phys. J. C*68 (2010) 447,  
9527 [arXiv:1003.2947](#).
- 9528 [513] M. Krelina and J. Nemchik, [arXiv:2003.04156](#).
- 9529 [514] S. J. Brodsky, I. Schmidt and J.-J. Yang, *Phys. Rev. D*70 (2004) 116003, [arXiv:hep-ph/0409279](#).
- 9530 [515] M. Klein, *EPJ Web Conf.* 112 (2016) 03002.
- 9531 [516] LHeC Study Group, H. Paukkunen, *PoS DIS2017* (2018) 109, [arXiv:1709.08342](#).
- 9532 [517] E. C. Aschenauer, S. Fazio, M. A. C. Lamont, H. Paukkunen and P. Zurita, *Phys. Rev. D*96 (2017)  
9533 114005, [arXiv:1708.05654](#).
- 9534 [518] LHCb Collaboration, R. Aaij *et al.*, *JHEP* 10 (2017) 090, [arXiv:1707.02750](#).
- 9535 [519] LHCb Collaboration, R. Aaij *et al.*, *Phys. Rev. D*99 (2019) 052011, [arXiv:1902.05599](#).
- 9536 [520] K. J. Eskola, I. Helenius, P. Paakkinen and H. Paukkunen, *JHEP* 05 (2020) 037, [arXiv:1906.02512](#).
- 9537 [521] I. Helenius, K. J. Eskola and H. Paukkunen, *JHEP* 09 (2014) 138, [arXiv:1406.1689](#).
- 9538 [522] J. Pumplin, D. Stump, R. Brock *et al.*, *Phys. Rev. D*65 (2001) 014013, [arXiv:hep-ph/0101032](#).
- 9539 [523] N. Armesto, “Nuclear pdfs.” 2nd FCC Physics Workshop (CERN, January 15th-19th 2018), 2018.
- 9540 [524] N. Armesto, *PoS HardProbes2018* (2019) 123.
- 9541 [525] HERAFitter Group, S. Alekhin *et al.*, *Eur. Phys. J. C*75 (2015) 304, [arXiv:1410.4412](#).
- 9542 [526] T. Lappi and H. Mäntysaari, *Phys. Rev. C*87 (2013) 032201, [arXiv:1301.4095](#).
- 9543 [527] STAR Collaboration, L. Adamczyk *et al.*, *Phys. Rev. C* 96 (2017) 054904, [arXiv:1702.07705](#).
- 9544 [528] T. Toll and T. Ullrich, *Phys. Rev. C* 87 (2013) 024913, [arXiv:1211.3048](#).
- 9545 [529] H. Mäntysaari, [arXiv:2001.10705](#).
- 9546 [530] V. N. Gribov and A. A. Migdal, *Sov. J. Nucl. Phys.* 8 (1969) 583. [*Yad. Fiz.* 8 (1968) 1002].
- 9547 [531] L. L. Frankfurt, G. A. Miller and M. Strikman, *Ann. Rev. Nucl. Part. Sci.* 44 (1994) 501,  
9548 [arXiv:hep-ph/9407274](#).
- 9549 [532] C. Marquet, M. R. Moldes and P. Zurita, *Phys. Lett. B*772 (2017) 607, [arXiv:1702.00839](#).
- 9550 [533] L. L. Frankfurt and M. I. Strikman, *Phys. Lett. B*382 (1996) 6.
- 9551 [534] H. Kowalski, T. Lappi, C. Marquet and R. Venugopalan, *Phys. Rev. C*78 (2008) 045201, [arXiv:0805.4071](#).
- 9552 [535] A. H. Müller and H. Navelet, *Nucl. Phys. B*282 (1987) 727.

- 9553 [536] M. Deak, F. Hautmann, H. Jung and K. Kutak, *Eur. Phys. J. C*72 (2012) 1982, [arXiv:1112.6354](#).
- 9554 [537] J. L. Albacete and C. Marquet, *Phys. Rev. Lett.* 105 (2010) 162301, [arXiv:1005.4065](#).
- 9555 [538] T. Lappi and H. Mäntysaari, *Nucl. Phys. A*908 (2013) 51, [arXiv:1209.2853](#).
- 9556 [539] A. Stasto, S.-Y. Wei, B.-W. Xiao and F. Yuan, *Phys. Lett. B*784 (2018) 301, [arXiv:1805.05712](#).
- 9557 [540] A. van Hameren, P. Kotko, K. Kutak, C. Marquet, E. Petreska and S. Sapeta, *JHEP* 12 (2016) 034, [arXiv:1607.03121](#). [Erratum: *JHEP* 02 (2019) 158].
- 9558
- 9559 [541] CMS Collaboration, V. Khachatryan *et al.*, *JHEP* 09 (2010) 091, [arXiv:1009.4122](#).
- 9560 [542] S. Schlichting and P. Tribedy, *Adv. High Energy Phys.* 2016 (2016) 8460349, [arXiv:1611.00329](#).
- 9561 [543] C. Loizides, *Nucl. Phys. A*956 (2016) 200, [arXiv:1602.09138](#).
- 9562 [544] B. Schenke, *Nucl. Phys. A*967 (2017) 105, [arXiv:1704.03914](#).
- 9563 [545] P. Romatschke, *Eur. Phys. J. C*77 (2017) 21, [arXiv:1609.02820](#).
- 9564 [546] ATLAS Collaboration, “Two-particle azimuthal correlations in photo-nuclear ultra-peripheral Pb+Pb collisions at 5.02 TeV with ATLAS,” ATLAS-CONF-2019-022, 2019.
- 9565
- 9566 [547] A. Badea, A. Baty, P. Chang, G. M. Innocenti, M. Maggi, C. McGinn, M. Peters, T.-A. Sheng, J. Thaler and Y.-J. Lee, *Phys. Rev. Lett.* 123 (2019) 212002, [arXiv:1906.00489](#).
- 9567
- 9568 [548] ZEUS Collaboration, “Two-particle azimuthal correlations as a probe of collective behaviour in deep inelastic *ep* scattering at HERA,” 2019. [arXiv:1912.07431](#).
- 9569
- 9570 [549] CMS Collaboration, S. Chatrchyan *et al.*, *Phys. Lett. B*724 (2013) 213, [arXiv:1305.0609](#).
- 9571 [550] CMS Collaboration, V. Khachatryan *et al.*, *Phys. Lett. B*765 (2017) 193, [arXiv:1606.06198](#).
- 9572 [551] S. D. Glazek, S. J. Brodsky, A. S. Goldhaber and R. W. Brown, *Phys. Rev. D*97 (2018) 114021, [arXiv:1805.08847](#).
- 9573
- 9574 [552] J. D. Bjorken, S. J. Brodsky and A. Scharff Goldhaber, *Phys. Lett. B*726 (2013) 344, [arXiv:1308.1435](#).
- 9575 [553] S. J. Brodsky, H.-C. Pauli and S. S. Pinsky, *Phys. Rept.* 301 (1998) 299, [arXiv:hep-ph/9705477](#).
- 9576 [554] P. A. M. Dirac, *Rev. Mod. Phys.* 21 (1949) 392.
- 9577 [555] D. Ashery, *Nucl. Phys. Proc. Suppl.* 161 (2006) 8, [arXiv:hep-ex/0511052](#).
- 9578 [556] G. Bertsch, S. J. Brodsky, A. S. Goldhaber and J. F. Gunion, *Phys. Rev. Lett.* 47 (1981) 297.
- 9579 [557] L. Frankfurt, G. A. Miller and M. Strikman, *Phys. Rev. D*65 (2002) 094015, [arXiv:hep-ph/0010297](#).
- 9580 [558] S. J. Brodsky, C.-R. Ji and G. P. Lepage, *Phys. Rev. Lett.* 51 (1983) 83.
- 9581 [559] S. J. Brodsky and A. H. Müller, *Phys. Lett. B*206 (1988) 685.
- 9582 [560] S. J. Brodsky, I. A. Schmidt and G. F. de Teramond, *Phys. Rev. Lett.* 64 (1990) 1011.
- 9583 [561] S. J. Brodsky and H. J. Lu, *Phys. Rev. Lett.* 64 (1990) 1342.
- 9584 [562] S. J. Brodsky, I. Schmidt and S. Liuti, [arXiv:1908.06317](#).
- 9585 [563] ATLAS Collaboration, G. Aad *et al.*, *Phys. Lett. B*716 (2012) 1, [arXiv:1207.7214](#).
- 9586 [564] CMS Collaboration, S. Chatrchyan *et al.*, *Phys. Lett. B*716 (2012) 30, [arXiv:1207.7235](#).
- 9587 [565] G. S. Guralnik, C. R. Hagen and T. W. B. Kibble, *Phys. Rev. Lett.* 13 (1964) 585. [,162(1964)].
- 9588 [566] A. A. Migdal and A. M. Polyakov, *Sov. Phys. JETP* 24 (1967) 91. [*Zh. Eksp. Teor. Fiz.* 51 (1966) 135].
- 9589 [567] S. Gori, C. Grojean, A. Juste and A. Paul, *JHEP* 01 (2018) 108, [arXiv:1710.03752](#).
- 9590 [568] T. Cohen, N. Craig, G. F. Giudice and M. McCullough, *JHEP* 05 (2018) 091, [arXiv:1803.03647](#).
- 9591 [569] J. Blümlein, G. J. van Oldenborgh and R. Rückl, *Nucl. Phys. B*395 (1993) 35, [arXiv:hep-ph/9209219](#).
- 9592 [570] J. Pumplin, D. R. Stump, J. Huston, H. L. Lai, P. M. Nadolsky and W. K. Tung, *JHEP* 07 (2002) 012, [arXiv:hep-ph/0201195](#).
- 9593
- 9594 [571] M. Kumar, X. Ruan, R. Islam, A. S. Cornell, M. Klein, U. Klein and B. Mellado, *Phys. Lett. B*764 (2017) 247, [arXiv:1509.04016](#).
- 9595
- 9596 [572] E. by M. Benedikt *et al.*, .
- 9597 [573] LHC Higgs Cross Section Working Group, D. de Florian *et al.*, [arXiv:1610.07922](#).
- 9598 [574] D. M. Asner *et al.*, “ILC Higgs White Paper,” in *Proceedings, 2013 Community Summer Study on the Future of U.S. Particle Physics: Snowmass on the Mississippi (CSS2013): Minneapolis, MN, USA, July 29-August 6, 2013*, 2013. [arXiv:1310.0763](#).
- 9599
- 9600 <http://www.slac.stanford.edu/econf/C1307292/docs/submittedArxivFiles/1310.0763.pdf>.
- 9601

- 9602 [575] H. Abramowicz *et al.*, *Eur. Phys. J. C* **77** (2017) 475, [arXiv:1608.07538](#).
- 9603 [576] Higgs Cross Section Working Group, <https://twiki.cern.ch/twiki/bin/view/LHCPhysics/CERNYellowReportPageBR>.
- 9604
- 9605 [577] T. Han and B. Mellado, *Phys. Rev. D* **82** (2010) 016009, [arXiv:0909.2460](#).
- 9606 [578] M. Tanaka, “Study of the higgs measurements at the lhec,” in *Bachelor of Science Thesis, Tokyo Institute of Technology, and Talk at DIS Workshop 2017*, 2014.
- 9607 <https://indico.cern.ch/event/568360/contributions/2523555/>.
- 9608
- 9609 [579] E. Kay, “Higgs Studies at a High Luminosity LHeC,” in *Master Thesis, University of Liverpool*, 2014.
- 9610 [580] U. Klein, *Poster at 37th International Conference on High Energy Physics (ICHEP), Valencia* (2014) .
- 9611 <https://indico.ific.uv.es/event/2025/contributions/937/>.
- 9612 [581] U. Klein, *Talk at LHeC Workshop, CERN and Chavannes-de-Bogis* (2015) .
- 9613 <https://indico.cern.ch/event/356714/contributions/844946/>.
- 9614 [582] D. Hampson, “Precision Higgs coupling measurements at a high luminosity LHeC,” in *Master Thesis, University of Liverpool*, 2016.
- 9615
- 9616 [583] I. Harris, “Finding higgs to charm decays in electron-proton collisions,” in *Bachelor of Science Theses, University of Liverpool*, 2017.
- 9617
- 9618 [584] ATLAS Collaboration, M. Aaboud *et al.*, *Phys. Lett. B* **786** (2018) 59, [arXiv:1808.08238](#).
- 9619 [585] CMS Collaboration, A. M. Sirunyan *et al.*, *Phys. Rev. Lett.* **121** (2018) 121801, [arXiv:1808.08242](#).
- 9620 [586] ATLAS and CMS Collaborations, *CERN Yellow Rep. Monogr.* **7** (2019) Addendum, [arXiv:1902.10229](#).
- 9621 [587] T. Sjöstrand, S. Mrenna and P. Skands, *JHEP* **05** (2006) .
- 9622 [588] U. Klein, *Talk at Workshop on the LHeC, Chavannes-de-Bogis* (2014) .
- 9623 <https://indico.cern.ch/event/278903/contributions/631181>.
- 9624 [589] J. de Favereau, C. Delaere, P. Demin, A. Giammanco, V. Lematre, A. Mertens and M. Selvaggi, *Journal of High Energy Physics* **02** (2014) .
- 9625
- 9626 [590] A. Höcker *et al.*, “TMVA - Toolkit for Multivariate Data Analysis,” CERN-OPEN-2007-007, 2007.
- 9627 [arXiv:physics/0703039](#).
- 9628 [591] S. Greder, *b quark tagging and cross-section measurement in quark pair production at D0*. PhD thesis, Louis Pasteur U., Strasbourg I, 2004.
- 9629
- 9630 [592] Y. Banda, T. Lastovicka and A. Nomerotski, “Measurement of the Higgs boson decay branching ratio to charm quarks at the ILC,” 2009. [arXiv:0909.1052](#).
- 9631
- 9632 [593] ATLAS Collaboration, G. Aad *et al.*, *Phys. Rev. D* **100** (2019) 032007, [arXiv:1905.07714](#).
- 9633 [594] ATLAS Collaboration, M. Aaboud *et al.*, *Eur. Phys. J. C* **77** (2017) 361, [arXiv:1702.05725](#).
- 9634 [595] C. Englert, R. Kogler, H. Schulz and M. Spannowsky, *Eur. Phys. J. C* **76** (2016) 393, [arXiv:1511.05170](#).
- 9635 [596] LHC Higgs Cross Section Working Group Collaboration, S. Dittmaier *et al.*, [arXiv:1101.0593](#).
- 9636 [597] T. Barklow, K. Fujii, S. Jung, R. Karl, J. List, T. Ogawa, M. E. Peskin and J. Tian, *Phys. Rev. D* **97** (2018) 053003, [arXiv:1708.08912](#).
- 9637
- 9638 [598] M. Trott, *Invited Talk at the LHeC Workshop, Chavannes* (2014) .
- 9639 <https://indico.cern.ch/event/278903/contributions/631177/>.
- 9640 [599] S. D. Rindani, P. Sharma and A. Shivaji, *Phys. Lett. B* **761** (2016) 25, [arXiv:1605.03806](#).
- 9641 [600] S. S. Biswal, R. M. Godbole, B. Mellado and S. Raychaudhuri, *Phys. Rev. Lett.* **109** (2012) 261801, [arXiv:1203.6285](#).
- 9642
- 9643 [601] A. Alloul, N. D. Christensen, C. Degrande, C. Duhr and B. Fuks, *Comput. Phys. Commun.* **185** (2014) 2250, [arXiv:1310.1921](#).
- 9644
- 9645 [602] R. D. Ball *et al.*, *Nucl. Phys. B* **867** (2013) 244, [arXiv:1207.1303](#).
- 9646 [603] Y.-L. Tang, C. Zhang and S.-h. Zhu, *Phys. Rev. D* **94** (2016) 011702, [arXiv:1508.01095](#).
- 9647 [604] C. Bernaciak, T. Plehn, P. Schichtel and J. Tattersall, *Phys. Rev. D* **91** (2015) 035024, [arXiv:1411.7699](#).
- 9648 [605] R. J. Cashmore *et al.*, *Phys. Rept.* **122** (1985) 275.
- 9649 [606] S. Buddenbrock, A. S. Cornell, Y. Fang, A. Fadol Mohammed, M. Kumar, B. Mellado and K. G. Tomiwa, *JHEP* **10** (2019) 157, [arXiv:1901.05300](#).
- 9650
- 9651 [607] W. Liu, H. Sun, X. Wang and X. Luo, *Phys. Rev. D* **92** (2015) 074015, [arXiv:1507.03264](#).

- 9652 [608] X. Wang, H. Sun and X. Luo, *Adv. High Energy Phys.* 2017 (2017) 4693213, [arXiv:1703.02691](#).
- 9653 [609] ATLAS Collaboration, M. Aaboud *et al.*, *Phys. Rev. D* 98 (2018) 032002, [arXiv:1805.03483](#).
- 9654 [610] CMS Collaboration, V. Khachatryan *et al.*, *JHEP* 02 (2017) 079, [arXiv:1610.04857](#).
- 9655 [611] J. Hernandez-Sanchez, O. Flores-Sanchez, C. G. Honorato, S. Moretti and S. Rosado, *PoS*  
9656 *CHARGED2016* (2017) 032, [arXiv:1612.06316](#).
- 9657 [612] CMS Collaboration, A. M. Sirunyan *et al.*, *JHEP* 11 (2018) 115, [arXiv:1808.06575](#).
- 9658 [613] CMS Collaboration, V. Khachatryan *et al.*, *JHEP* 12 (2015) 178, [arXiv:1510.04252](#).
- 9659 [614] S. P. Das, J. Hernandez-Sanchez, S. Moretti and A. Rosado, [arXiv:1806.08361](#).
- 9660 [615] H. Sun, X. Luo, W. Wei and T. Liu, *Phys. Rev. D* 96 (2017) 095003, [arXiv:1710.06284](#).
- 9661 [616] G. Azuelos, H. Sun and K. Wang, *Phys. Rev. D* 97 (2018) 116005, [arXiv:1712.07505](#).
- 9662 [617] CMS Collaboration, A. M. Sirunyan *et al.*, *Phys. Rev. Lett.* 119 (2017) 141802, [arXiv:1705.02942](#).
- 9663 [618] CMS Collaboration, A. M. Sirunyan *et al.*, *Phys. Rev. Lett.* 120 (2018) 081801, [arXiv:1709.05822](#).
- 9664 [619] C. Mosomane, M. Kumar, A. S. Cornell and B. Mellado, *J. Phys. Conf. Ser.* 889 (2017) 012004,  
9665 [arXiv:1707.05997](#).
- 9666 [620] L. Delle Rose, O. Fischer and A. Hammad, *Int. J. Mod. Phys. A* 34 (2019) 1950127, [arXiv:1809.04321](#).
- 9667 [621] CMS Collaboration, A. M. Sirunyan *et al.*, *JHEP* 06 (2018) 127, [arXiv:1804.01939](#). [Erratum: *JHEP* 03  
9668 (2019) 128].
- 9669 [622] CMS Collaboration, “Search for a new scalar resonance decaying to a pair of Z bosons at the  
9670 High-Luminosity LHC,” CMS-PAS-FTR-18-040, 2019.
- 9671 [623] S. P. Das, J. Hernández-Sánchez, S. Moretti, A. Rosado and R. Xoxocotzi, *Phys. Rev. D* 94 (2016) 055003,  
9672 [arXiv:1503.01464](#).
- 9673 [624] S. P. Das and M. Nowakowski, *Phys. Rev. D* 96 (2017) 055014, [arXiv:1612.07241](#).
- 9674 [625] A. Senol, *Nucl. Phys. B* 873 (2013) 293, [arXiv:1212.6869](#).
- 9675 [626] I. T. Cakir, O. Cakir, A. Senol and A. T. Tasci, *Mod. Phys. Lett. A* 28 (2013) 1350142, [arXiv:1304.3616](#).
- 9676 [627] H. Hesari, H. Khanpour and M. Mohammadi Najafabadi, *Phys. Rev. D* 97 (2018) 095041,  
9677 [arXiv:1805.04697](#).
- 9678 [628] S. Liu, Y.-L. Tang, C. Zhang and S.-h. Zhu, *Eur. Phys. J. C* 77 (2017) 457, [arXiv:1608.08458](#).
- 9679 [629] D. Curtin, K. Deshpande, O. Fischer and J. Zurita, *JHEP* 07 (2018) 024, [arXiv:1712.07135](#).
- 9680 [630] G. Azuelos, M. D’Onofrio, S. Iwamoto and K. Wang, [arXiv:1912.03823](#).
- 9681 [631] C. Han, R. Li, R.-Q. Pan and K. Wang, *Phys. Rev. D* 98 (2018) 115003, [arXiv:1802.03679](#).
- 9682 [632] S. Kудay, *J. Korean Phys. Soc.* 64 (2014) 1783, [arXiv:1304.2124](#).
- 9683 [633] R.-Y. Zhang, H. Wei, L. Han and W.-G. Ma, *Mod. Phys. Lett. A* 29 (2014) 1450029, [arXiv:1401.4266](#).
- 9684 [634] X.-P. Li, L. Guo, W.-G. Ma, R.-Y. Zhang, L. Han and M. Song, *Phys. Rev. D* 88 (2013) 014023,  
9685 [arXiv:1307.2308](#).
- 9686 [635] J. A. Evans and D. Mckeen, “The Light Gluino Gap,” 2018. [arXiv:1803.01880](#).
- 9687 [636] D. Curtin, K. Deshpande, O. Fischer and J. Zurita, *Phys. Rev. D* 99 (2019) 055011, [arXiv:1812.01568](#).
- 9688 [637] S. Antusch and O. Fischer, *JHEP* 05 (2015) 053, [arXiv:1502.05915](#).
- 9689 [638] S. Antusch, E. Cazzato and O. Fischer, *Int. J. Mod. Phys. A* 32 (2017) 1750078, [arXiv:1612.02728](#).
- 9690 [639] S. Antusch, O. Fischer and A. Hammad, [arXiv:1908.02852](#).
- 9691 [640] A. Das, S. Jana, S. Mandal and S. Nandi, *Phys. Rev. D* 99 (2019) 055030, [arXiv:1811.04291](#).
- 9692 [641] ATLAS Collaboration, G. Aad *et al.*, [arXiv:1905.09787](#).
- 9693 [642] S. Antusch, E. Cazzato and O. Fischer, *Phys. Lett. B* 774 (2017) 114, [arXiv:1706.05990](#).
- 9694 [643] DELPHI Collaboration, P. Abreu *et al.*, *Z. Phys. C* 74 (1997) 57. [Erratum: *Z. Phys. C* 75 (1997) 580].
- 9695 [644] MEG Collaboration, J. Adam *et al.*, *Phys. Rev. Lett.* 110 (2013) 201801, [arXiv:1303.0754](#).
- 9696 [645] L. Duarte, G. A. González-Sprinberg and O. A. Sampayo, *Phys. Rev. D* 91 (2015) 053007,  
9697 [arXiv:1412.1433](#).
- 9698 [646] L. Duarte, G. Zapata and O. A. Sampayo, *Eur. Phys. J. C* 78 (2018) 352, [arXiv:1802.07620](#).
- 9699 [647] S. Mondal and S. K. Rai, *Phys. Rev. D* 93 (2016) 011702, [arXiv:1510.08632](#).

- 9700 [648] M. Lindner, F. S. Queiroz, W. Rodejohann and C. E. Yaguna, *JHEP* 06 (2016) 140, [arXiv:1604.08596](#).
- 9701 [649] S. Mondal and S. K. Rai, *Phys. Rev. D* 94 (2016) 033008, [arXiv:1605.04508](#).
- 9702 [650] A. Das and S. Mandal, [arXiv:2006.04123](#).
- 9703 [651] Planck Collaboration, N. Aghanim *et al.*, [arXiv:1807.06209](#).
- 9704 [652] S. Jana, N. Okada and D. Raut, [arXiv:1911.09037](#).
- 9705 [653] A. Das, S. Mandal and T. Modak, [arXiv:2005.02267](#).
- 9706 [654] B. Holdom, *Phys. Lett.* 166B (1986) 196.
- 9707 [655] M. D’Onofrio, O. Fischer and Z. S. Wang, “Searching for Dark Photons at the LHeC and FCC-he,” 2019.  
9708 [arXiv:1909.02312](#).
- 9709 [656] LHCb Collaboration, R. Aaij *et al.*, *Phys. Rev. Lett.* 120 (2018) 061801, [arXiv:1710.02867](#).
- 9710 [657] S. Heeba and F. Kahlhoefer, “Probing the freeze-in mechanism in dark matter models with  $U(1)'$  gauge  
9711 extensions,” 2019. [arXiv:1908.09834](#).
- 9712 [658] C.-X. Yue, M.-Z. Liu and Y.-C. Guo, *Phys. Rev. D* 100 (2019) 015020, [arXiv:1904.10657](#).
- 9713 [659] K. O. Mikaelian, M. A. Samuel and D. Sahdev, *Phys. Rev. Lett.* 43 (1979) 746.
- 9714 [660] S. J. Brodsky and R. W. Brown, *Phys. Rev. Lett.* 49 (1982) 966.
- 9715 [661] R. W. Brown, K. L. Kowalski and S. J. Brodsky, *Phys. Rev. D* 28 (1983) 624. [Addendum: *Phys.*  
9716 *Rev.* D29,2100(1984)].
- 9717 [662] M. A. Samuel and J. H. Reid, *Prog. Theor. Phys.* 76 (1986) 184.
- 9718 [663] HFLAV Collaboration, Y. S. Amhis *et al.*, [arXiv:1909.12524](#).
- 9719 [664] J. C. Pati and A. Salam, *Phys. Rev. D* 10 (1974) 275. [Erratum: *Phys. Rev. D* 11 (1975) 703].
- 9720 [665] W. Buchmüller, R. Rückl and D. Wyler, *Phys. Lett.* B191 (1987) 442. [Erratum: *Phys. Lett.* B448 (1999)  
9721 320].
- 9722 [666] I. Doršner, S. Fajfer, A. Greljo, J. F. Kamenik and N. Košnik, *Phys. Rept.* 641 (2016) 1,  
9723 [arXiv:1603.04993](#).
- 9724 [667] ATLAS Collaboration, “ATLAS Exotics Searches,”. [https://atlas.web.cern.ch/Atlas/GROUPS/  
9725 PHYSICS/CombinedSummaryPlots/EXOTICS/ATLAS\\_Exotics\\_Summary/ATLAS\\_Exotics\\_Summary.pdf](https://atlas.web.cern.ch/Atlas/GROUPS/PHYSICS/CombinedSummaryPlots/EXOTICS/ATLAS_Exotics_Summary/ATLAS_Exotics_Summary.pdf).
- 9726 [668] CMS Collaboration, “Overview of CMS Exo Results,”.  
9727 <http://cms-results.web.cern.ch/cms-results/public-results/publications/EXO/index.html>.
- 9728 [669] J. Zhang, C.-X. Yue and Z.-C. Liu, *Mod. Phys. Lett.* A33 (2018) 1850039.
- 9729 [670] I. Doršner and A. Greljo, *JHEP* 05 (2018) 126, [arXiv:1801.07641](#).
- 9730 [671] M. Bahr *et al.*, *Eur. Phys. J.* C58 (2008) 639, [arXiv:0803.0883](#).
- 9731 [672] S. Mandal, M. Mitra and N. Sinha, *Phys. Rev. D* 98 (2018) 095004, [arXiv:1807.06455](#).
- 9732 [673] R. Padhan, S. Mandal, M. Mitra and N. Sinha, [arXiv:1912.07236](#).
- 9733 [674] S. Antusch, A. Hammad and A. Rashed, [arXiv:2003.11091](#).
- 9734 [675] ATLAS Collaboration, M. Aaboud *et al.*, *Phys. Rev. D* 98 (2018) 092008, [arXiv:1807.06573](#).
- 9735 [676] ATLAS Collaboration, G. Aad *et al.*, *Phys. Lett.* B796 (2019) 68, [arXiv:1903.06248](#).
- 9736 [677] BaBar Collaboration, B. Aubert *et al.*, *Phys. Rev. Lett.* 104 (2010) 021802, [arXiv:0908.2381](#).
- 9737 [678] K. Hayasaka *et al.*, *Phys. Lett.* B687 (2010) 139, [arXiv:1001.3221](#).
- 9738 [679] Y.-J. Zhang, L. Han and Y.-B. Liu, *Phys. Lett.* B768 (2017) 241.
- 9739 [680] Y.-B. Liu, *Nucl. Phys.* B923 (2017) 312, [arXiv:1704.02059](#).
- 9740 [681] L. Han, Y.-J. Zhang and Y.-B. Liu, *Phys. Lett.* B771 (2017) 106.
- 9741 [682] A. Ozansoy, V. Arı and V. Çetinkaya, *Adv. High Energy Phys.* 2016 (2016) 1739027, [arXiv:1607.04437](#).
- 9742 [683] A. Caliskan, *Adv. High Energy Phys.* 2017 (2017) 4726050, [arXiv:1706.09797](#).
- 9743 [684] A. Caliskan and S. O. Kara, *Int. J. Mod. Phys.* A33 (2018) 1850141, [arXiv:1806.02037](#).
- 9744 [685] Y. O. Günaydın, M. Sahin and S. Sultansoy, *Acta Phys. Polon.* B49 (2018) 1763, [arXiv:1707.00056](#).
- 9745 [686] M. Sahin, *Acta Phys. Polon.* B45 (2014) 1811, [arXiv:1302.5747](#).
- 9746 [687] Y. C. Acar, U. Kaya, B. B. Oner and S. Sultansoy, *J. Phys.* G44 (2017) 045005, [arXiv:1605.08028](#).
- 9747 [688] ZEUS Collaboration, H. Abramowicz *et al.*, *Phys. Lett.* B757 (2016) 468, [arXiv:1604.01280](#).

- 9748 [689] A. F. Zarnecki, “Leptoquarks and Contact Interactions at LeHC,” in *Proceedings, 16th International*  
9749 *Workshop on Deep Inelastic Scattering and Related Subjects (DIS 2008): London, UK, April 7-11, 2008,*  
9750 2008. [arXiv:0809.2917](https://arxiv.org/abs/0809.2917).
- 9751 [690] P. C. M. Yock, *Int. J. Theor. Phys.* 2 (1969) 247.
- 9752 [691] J. S. Schwinger, *Science* 165 (1969) 757.
- 9753 [692] ATLAS Collaboration, G. Aad *et al.*, *Phys. Rev. Lett.* 124 (2020) 031802, [arXiv:1905.10130](https://arxiv.org/abs/1905.10130).
- 9754 [693] R. Hofstadter, *Rev. Mod. Phys.* 28 (1956) 214.
- 9755 [694] A. F. Zarnecki, *Eur. Phys. J. C*11 (1999) 539, [arXiv:hep-ph/9904334](https://arxiv.org/abs/hep-ph/9904334).
- 9756 [695] ATLAS Collaboration, M. Aaboud *et al.*, *JHEP* 10 (2017) 182, [arXiv:1707.02424](https://arxiv.org/abs/1707.02424).
- 9757 [696] CMS Collaboration, A. M. Sirunyan *et al.*, *JHEP* 04 (2019) 114, [arXiv:1812.10443](https://arxiv.org/abs/1812.10443).
- 9758 [697] A. Michel and M. Sher, *Phys. Rev. D*100 (2019) 095011, [arXiv:1909.10627](https://arxiv.org/abs/1909.10627).
- 9759 [698] G. R. Boroun, *Chin. Phys. C*41 (2017) 013104, [arXiv:1510.02914](https://arxiv.org/abs/1510.02914).
- 9760 [699] G. R. Boroun, B. Rezaei and S. Heidari, *Int. J. Mod. Phys. A*32 (2017) 1750197, [arXiv:1606.02864](https://arxiv.org/abs/1606.02864).
- 9761 [700] H.-Y. Bi, R.-Y. Zhang, H.-Y. Han, Y. Jiang and X.-G. Wu, *Phys. Rev. D*95 (2017) 034019,  
9762 [arXiv:1612.07990](https://arxiv.org/abs/1612.07990).
- 9763 [701] K. He, H.-Y. Bi, R.-Y. Zhang, X.-Z. Li and W.-G. Ma, *J. Phys. G*45 (2018) 055005, [arXiv:1710.11508](https://arxiv.org/abs/1710.11508).
- 9764 [702] H.-Y. Bi, R.-Y. Zhang, X.-G. Wu, W.-G. Ma, X.-Z. Li and S. Owusu, *Phys. Rev. D*95 (2017) 074020,  
9765 [arXiv:1702.07181](https://arxiv.org/abs/1702.07181).
- 9766 [703] ATLAS Collaboration, “Prospect for a measurement of the Weak Mixing Angle in  $pp \rightarrow Z/\gamma^* \rightarrow e^+e^-$   
9767 events with the ATLAS detector at the High Luminosity Large Hadron Collider,”  
9768 ATL-PHYS-PUB-2018-037, CERN, Geneva, Nov 2018. <https://cds.cern.ch/record/2649330>.
- 9769 [704] CMS Collaboration, “A proposal for the measurement of the weak mixing angle at the HL-LHC,”  
9770 CMS-PAS-FTR-17-001, CERN, Geneva, 2017. <https://cds.cern.ch/record/2294888>.
- 9771 [705] W. J. Barter, “Prospects for measurement of the weak mixing angle at LHCb,” LHCb-PUB-2018-013.  
9772 CERN-LHCb-PUB-2018-013, CERN, Geneva, Nov 2018. <https://cds.cern.ch/record/2647836>.
- 9773 [706] L. A. Harland-Lang, A. D. Martin, P. Motylinski and R. S. Thorne, *Eur. Phys. J. C*75 (2015) 204,  
9774 [arXiv:1412.3989](https://arxiv.org/abs/1412.3989).
- 9775 [707] ATLAS Collaboration, G. Aad *et al.*, *JHEP* 09 (2015) 049, [arXiv:1503.03709](https://arxiv.org/abs/1503.03709).
- 9776 [708] ATLAS Collaboration, “Prospects for the measurement of the W-boson mass at the HL- and HE-LHC,”  
9777 ATL-PHYS-PUB-2018-026, CERN, Geneva, Oct 2018. <http://cds.cern.ch/record/2645431>.
- 9778 [709] F. Zimmermann, *ICFA Beam Dynamics Newsletter* 72 (2017) 138.
- 9779 [710] M. E. Peskin and T. Takeuchi, *Phys. Rev. D*46 (1992) 381.
- 9780 [711] J. De Blas *et al.*, *Eur. Phys. J. C*80 (2020) 456, [arXiv:1910.14012](https://arxiv.org/abs/1910.14012).
- 9781 [712] M. Cepeda *et al.*, *CERN Yellow Rep. Monogr.* 7 (2019) 221, [arXiv:1902.00134](https://arxiv.org/abs/1902.00134).
- 9782 [713] J. Campbell and T. Neumann, *JHEP* 12 (2019) 034, [arXiv:1909.09117](https://arxiv.org/abs/1909.09117).
- 9783 [714] B. Mistlberger, *JHEP* 05 (2018) 028, [arXiv:1802.00833](https://arxiv.org/abs/1802.00833).
- 9784 [715] F. Dulat, A. Lazopoulos and B. Mistlberger, *Comput. Phys. Commun.* 233 (2018) 243, [arXiv:1802.00827](https://arxiv.org/abs/1802.00827).
- 9785 [716] LHC Higgs Cross Section Working Group Collaboration, A. David *et al.*, “LHC HXSWG interim  
9786 recommendations to explore the coupling structure of a Higgs-like particle,” 2012. [arXiv:1209.0040](https://arxiv.org/abs/1209.0040).
- 9787 [717] ATLAS Collaboration, G. Aad *et al.*, *Phys. Rev. D*101 (2020) 012002, [arXiv:1909.02845](https://arxiv.org/abs/1909.02845).
- 9788 [718] J. de Blas *et al.*, *JHEP* 01 (2020) 139, [arXiv:1905.03764](https://arxiv.org/abs/1905.03764).
- 9789 [719] ATLAS Collaboration, “Study of correlation of PDF uncertainty in single top and top pair production at  
9790 the LHC,” ATL-PHYS-PUB-2015-010, Geneva, May 2015.
- 9791 [720] CMS Collaboration, V. Khachatryan *et al.*, *Phys. Rev. D*94 (2016) 072002, [arXiv:1605.00116](https://arxiv.org/abs/1605.00116).
- 9792 [721] Tevatron Electroweak Working Group, T. Aaltonen *et al.*, “Combination of CDF and D0 results on the  
9793 mass of the top quark using up  $9.7 \text{ fb}^{-1}$  at the Tevatron,” 2016. [arXiv:1608.01881](https://arxiv.org/abs/1608.01881).
- 9794 [722] CMS Collaboration, V. Khachatryan *et al.*, *Phys. Rev. D*93 (2016) 072004, [arXiv:1509.04044](https://arxiv.org/abs/1509.04044).
- 9795 [723] ATLAS Collaboration, M. Aaboud *et al.*, *Phys. Lett. B*761 (2016) 350, [arXiv:1606.02179](https://arxiv.org/abs/1606.02179).
- 9796 [724] CMS Collaboration, A. M. Sirunyan *et al.*, *Eur. Phys. J. C*77 (2017) 354, [arXiv:1703.02530](https://arxiv.org/abs/1703.02530).



- 9797 [725] CMS Collaboration, A. M. Sirunyan *et al.*, *Eur. Phys. J. C* **78** (2018) 891, [arXiv:1805.01428](#).
- 9798 [726] ATLAS Collaboration, “Prospects for measurement of the top quark mass using  $t\bar{t}$  events with  
9799  $J/\psi \rightarrow \mu^+\mu^-$  decays with the upgraded ATLAS detector at the High Luminosity LHC,”  
9800 ATL-PHYS-PUB-2018-042, Geneva, Dec 2018. <http://cds.cern.ch/record/2649882>.
- 9801 [727] D. Britzger, K. Rabbertz, D. Savoiu, G. Sieber and M. Wobisch, *Eur. Phys. J. C* **79** (2019) 68,  
9802 [arXiv:1712.00480](#).
- 9803 [728] ATLAS Collaboration, M. Aaboud *et al.*, *Phys. Rev. D* **98** (2018) 092004, [arXiv:1805.04691](#).
- 9804 [729] ATLAS Collaboration, M. Aaboud *et al.*, *Eur. Phys. J. C* **77** (2017) 872, [arXiv:1707.02562](#).
- 9805 [730] M. Johnson and D. Maître, *Phys. Rev. D* **97** (2018) 054013, [arXiv:1711.01408](#).
- 9806 [731] T. Klijsma, S. Bethke, G. Dissertori and G. P. Salam, *Eur. Phys. J. C* **77** (2017) 778, [arXiv:1708.07495](#).
- 9807 [732] CMS Collaboration, A. M. Sirunyan *et al.*, *Submitted to: Eur. Phys. J.* (2019) , [arXiv:1904.05237](#).
- 9808 [733] CMS Collaboration, A. M. Sirunyan *et al.*, “Determination of the strong coupling constant  $\alpha_S(m_Z)$  from  
9809 measurements of inclusive  $W^\pm$  and Z boson production cross sections in proton-proton collisions at  $\sqrt{s} =$   
9810 7 and 8 TeV,” 2019. [arXiv:1912.04387](#).
- 9811 [734] D. d’Enterria and A. Poldaru, *JHEP* **06** (2020) 016, [arXiv:1912.11733](#).
- 9812 [735] B. Bouzid, F. Iddir and L. Semlala, [arXiv:1703.03959](#).
- 9813 [736] M. Grazzini, S. Kallweit, D. Rathlev and M. Wiesemann, *Phys. Lett. B* **761** (2016) 179, [arXiv:1604.08576](#).
- 9814 [737] M. Grazzini, S. Kallweit and M. Wiesemann, *Eur. Phys. J. C* **78** (2018) 537, [arXiv:1711.06631](#).
- 9815 [738] ATLAS Collaboration, M. Aaboud *et al.*, *Eur. Phys. J. C* **79** (2019) 535, [arXiv:1902.05759](#). Auxiliary  
9816 figure.
- 9817 [739] CMS Collaboration, A. M. Sirunyan *et al.*, *JHEP* **04** (2019) 122, [arXiv:1901.03428](#).
- 9818 [740] X. Cid Vidal *et al.*, *CERN Yellow Rep. Monogr.* **7** (2019) 585, [arXiv:1812.07831](#).
- 9819 [741] ATLAS Collaboration, M. Aaboud *et al.*, *Phys. Rev. D* **97** (2018) 112001, [arXiv:1712.02332](#).
- 9820 [742] CMS Collaboration, A. M. Sirunyan *et al.*, *JHEP* **05** (2018) 025, [arXiv:1802.02110](#).
- 9821 [743] NNPDF Collaboration, R. D. Ball *et al.*, *JHEP* **04** (2015) 040, [arXiv:1410.8849](#).
- 9822 [744] C. Schmidt, J. Pumplin, C. P. Yuan and P. Yuan, *Phys. Rev. D* **98** (2018) 094005, [arXiv:1806.07950](#).
- 9823 [745] B.-T. Wang, T. J. Hobbs, S. Doyle, J. Gao, T.-J. Hou, P. M. Nadolsky and F. I. Olness, *Phys. Rev. D* **98**  
9824 (2018) 094030, [arXiv:1803.02777](#).
- 9825 [746] T. J. Hobbs, B.-T. Wang, P. M. Nadolsky and F. I. Olness, *PoS DIS2019* (2019) 247, [arXiv:1907.00988](#).
- 9826 [747] C. Brenner Mariotto and M. Machado, *Phys. Rev. D* **86** (2012) 033009, [arXiv:1208.5685](#).
- 9827 [748] R. Coelho and V. Goncalves, [arXiv:2002.10713](#).
- 9828 [749] R. Coelho and V. Goncalves, *Nucl. Phys. B* **956** (2020) 115013.
- 9829 [750] M. Bonvini, *Eur. Phys. J. C* **78** (2018) 834, [arXiv:1805.08785](#).
- 9830 [751] M. Bonvini, R. Gauld, T. Giani and S. Marzani in preparation.
- 9831 [752] M. Bonvini and F. Silveti in preparation.
- 9832 [753] J. C. Collins, D. E. Soper and G. F. Sterman, *Nucl. Phys. B* **250** (1985) 199.
- 9833 [754] R. Angeles-Martinez *et al.*, *Acta Phys. Polon. B* **46** (2015) 2501, [arXiv:1507.05267](#).
- 9834 [755] M. Diehl, *Eur. Phys. J. A* **52** (2016) 149, [arXiv:1512.01328](#).
- 9835 [756] T. C. Rogers, *Eur. Phys. J. A* **52** (2016) 153, [arXiv:1509.04766](#).
- 9836 [757] I. Balitsky and A. Tarasov, *JHEP* **06** (2016) 164, [arXiv:1603.06548](#).
- 9837 [758] S. Catani, M. Ciafaloni and F. Hautmann, *Phys. Lett. B* **242** (1990) 97.
- 9838 [759] S. Catani, M. Ciafaloni and F. Hautmann, *Nucl. Phys. B* **366** (1991) 135.
- 9839 [760] J. C. Collins and R. Ellis, *Nucl. Phys. B* **360** (1991) 3.
- 9840 [761] E. Levin, M. Ryskin, Y. Shabelski and A. Shuvaev, *Sov. J. Nucl. Phys.* **53** (1991) 657.
- 9841 [762] T. Altinoluk and R. Boussarie, *JHEP* **10** (2019) 208, [arXiv:1902.07930](#).
- 9842 [763] N. Armesto and E. Scomparin, *Eur. Phys. J. Plus* **131** (2016) 52, [arXiv:1511.02151](#).
- 9843 [764] W. Busza, K. Rajagopal and W. van der Schee, *Ann. Rev. Nucl. Part. Sci.* **68** (2018) 339,  
9844 [arXiv:1802.04801](#).

- 9845 [765] P. Romatschke and U. Romatschke, *Relativistic Fluid Dynamics In and Out of Equilibrium*. Cambridge  
9846 Monographs on Mathematical Physics. Cambridge University Press, 2019. [arXiv:1712.05815](#).
- 9847 [766] Y. Mehtar-Tani, J. G. Milhano and K. Tywoniuk, *Int. J. Mod. Phys. A*28 (2013) 1340013,  
9848 [arXiv:1302.2579](#).
- 9849 [767] A. Andronic *et al.*, *Eur. Phys. J. C*76 (2016) 107, [arXiv:1506.03981](#).
- 9850 [768] “Proceedings, 9th International Conference on Hard and Electromagnetic Probes of High-Energy Nuclear  
9851 Collisions: Hard Probes 2018 (HP2018),” SISSA, 2018. <https://pos.sissa.it/345>.
- 9852 [769] H. A. Andrews *et al.*, [arXiv:1808.03689](#).
- 9853 [770] ALICE Collaboration, B. B. Abelev *et al.*, *Phys. Lett. B*734 (2014) 314, [arXiv:1311.0214](#).
- 9854 [771] H. Song, S. A. Bass, U. Heinz, T. Hirano and C. Shen, *Phys. Rev. Lett.* 106 (2011) 192301,  
9855 [arXiv:1011.2783](#). [Erratum: *Phys. Rev. Lett.* 109 (2012) 139904].
- 9856 [772] H. Niemi, K. J. Eskola and R. Paatelainen, *Phys. Rev. C*93 (2016) 024907, [arXiv:1505.02677](#).
- 9857 [773] J. Liu, C. Shen and U. Heinz, *Phys. Rev. C*91 (2015) 064906, [arXiv:1504.02160](#). [Erratum: *Phys. Rev.*  
9858 *C*92 (2015) 049904].
- 9859 [774] B. Schenke, P. Tribedy and R. Venugopalan, *Phys. Rev. Lett.* 108 (2012) 252301, [arXiv:1202.6646](#).
- 9860 [775] J.-Y. Ollitrault, A. M. Poskanzer and S. A. Voloshin, *Phys. Rev. C*80 (2009) 014904, [arXiv:0904.2315](#).
- 9861 [776] STAR Collaboration, J. Adams *et al.*, *Phys. Rev. C*72 (2005) 014904, [arXiv:nuc1-ex/0409033](#).
- 9862 [777] STAR Collaboration, B. I. Abelev *et al.*, *Phys. Rev. C*79 (2009) 034909, [arXiv:0808.2041](#).
- 9863 [778] CMS Collaboration, A. M. Sirunyan *et al.*, [arXiv:1905.01486](#).
- 9864 [779] V. Guzey and M. Zhalov, *JHEP* 10 (2013) 207, [arXiv:1307.4526](#).
- 9865 [780] J. G. Contreras, *Phys. Rev. C*96 (2017) 015203, [arXiv:1610.03350](#).
- 9866 [781] V. Guzey and M. Klasen, *Eur. Phys. J. C*79 (2019) 396, [arXiv:1902.05126](#).
- 9867 [782] ATLAS Collaboration, M. Aaboud *et al.*, *Phys. Rev. Lett.* 121 (2018) 212301, [arXiv:1806.08708](#).
- 9868 [783] ATLAS Collaboration, M. Aaboud *et al.*, *Phys. Rev. C*100 (2019) 034903, [arXiv:1901.10440](#).
- 9869 [784] R. Aaij *et al.*, “Expression of Interest for a Phase-II LHCb Upgrade: Opportunities in flavour physics, and  
9870 beyond, in the HL-LHC era,” CERN-LHCC-2017-003, CERN, Geneva, Feb 2017.
- 9871 [785] O. Brüning, “Accelerator design.” Presented at the lhec workshop, June 2015.  
9872 <https://indico.cern.ch/event/356714/contributions/844912/>.
- 9873 [786] D. Brandt, H. Burkhardt, M. Lamont, S. Myers and J. Wenninger, *Rept. Prog. Phys.* 63 (2000) 939.
- 9874 [787] D. Pellegrini, A. Latina, D. Schulte and S. A. Bogacz, *Phys. Rev. ST Accel. Beams* 18 (2015) 121004.
- 9875 [788] S. A. Bogacz *et al.*, *ICFA Beam Dynamics Newsletter* 71 (2017) 135.
- 9876 [789] P. Williams, “A Staged, Multi-User X-Ray Free Electron Laser and Nuclear Physics Facility based on a  
9877 Multi-Pass Recirculating Superconducting CW Linac,” in *Proceedings, Future Light Sources 2018,*  
9878 *Shanghai*, 2018.
- 9879 [790] 12 GeV CEBAF Upgrade, Reference Design: [www.jlab.org/physics/GeV/accelerator](http://www.jlab.org/physics/GeV/accelerator) (2012).
- 9880 [791] G. H. Hoffstaetter and I. V. Bazarov, *Phys. Rev. ST Accel. Beams* 7 (2004) 054401,  
9881 [arXiv:physics/0405106](#).
- 9882 [792] J. S. Schwinger, *Phys. Rev.* 70 (1946) 798.
- 9883 [793] D. Pellegrini, *Ph.D. Thesis, EPFL, Switzerland* (2016) .
- 9884 [794] A. Milanese, *Talk presented at the LHeC workshop at CERN* (2014) .
- 9885 [795] J. Jowett *et al.*, “The 2018 heavy-ion run of the LHC,” in *Proceedings, 10th International Particle*  
9886 *Accelerator Conference (IPAC2019): Melbourne, Australia, May 19-24, 2019*, 2019.
- 9887 [796] T. Argyropoulos, T. Bohl, A. Lasheen, G. Papotti, D. Quartullo and E. Shaposhnikova, “Momentum  
9888 slip-stacking in CERN SPS for the ion beams,” in *Proceedings, 10th International Particle Accelerator*  
9889 *Conference (IPAC2019): Melbourne, Australia, May 19-24, 2019*, 2019.
- 9890 [797] M. Schaumann, *Phys. Rev. ST Accel. Beams* 18 (2015) 091002, [arXiv:1503.09107](#).
- 9891 [798] O. Brüning *et al.*, *ICFA Beam Dynamics Newsletter* 68 (2015) 46.
- 9892 [799] R. Calaga and E. Jensen, “A Proposal for an ERL Test Facility at CERN,” in *Proceedings, 4th*  
9893 *International Particle Accelerator Conference (IPAC 2013): Shanghai, China, May 12-17, 2013*, 2013.  
9894 <http://JACoW.org/IPAC2013/papers/wepwo049.pdf>.

- 9895 [800] F. Marhauser, “Cost Rationales for an SRF Proton Linac,” in *Proceedings, 5th International Particle*  
9896 *Accelerator Conference (IPAC 2014): Dresden, Germany, June 15-20, 2014*, 2014.
- 9897 [801] F. Marhauser, “Recent results on a multi-cell 802 mhz bulk nb cavity.” Presented at fcc week 2018,  
9898 [https://indico.cern.ch/event/656491/contributions/2932251/attachments/1629681/2597650/5\\_](https://indico.cern.ch/event/656491/contributions/2932251/attachments/1629681/2597650/5_cell_Cavity_Marhauser.pdf)  
9899 [cell\\_Cavity\\_Marhauser.pdf](https://indico.cern.ch/event/656491/contributions/2932251/attachments/1629681/2597650/5_cell_Cavity_Marhauser.pdf), 2018.
- 9900 [802] W. Schneider, I. Campisi, E. Daly *et al.*, “Design of the sns cryomodule,” in *Proceedings, the 2001 Particle*  
9901 *Accelerator Conference (PACS2001)*, 2001.
- 9902 [803] V. Parma *et al.*, “Conceptual design of the superconducting proton linac short cryo-module,” in  
9903 *Proceedings of the SRF2011, Chicago, July*, 2011.
- 9904 [804] G. Olivier, J. Thermeau and P. Bosland, “Ess cryomodules for elliptical cavities,” in *Proceedings of the*  
9905 *2013 Superconducting Radio Frequency Conference*, 2013.
- 9906 [805] H. Bluem, D. Dowell, A. Todd and L. Young, “High Brightness Thermionic Electron Gun Performance,”  
9907 in *Procings, 50th Advanced ICFA Beam Dynamics Workshop on Energy Recovery Linacs (ERL’11)*,  
9908 *Tsukuba, Japan, Oct. 2011*, 2011.
- 9909 [806] F. Sannibale *et al.*, “The VHF-Gun, the LBNL High-Brightness Electron Photo-Injector for MHz-Class  
9910 **Repetition-Rate Applications**,” in *High-Brightness Sources and Light-Driven Interactions*, Optical Society  
9911 of America, 2016.
- 9912 [807] Z. Wang, Q. Gu, G. Wang and M. Zhao, “Injector Physics Design at SHINE,” in *Proceedings, 10th*  
9913 *International Particle Accelerator Conference (IPAC’19), Melbourne, Australia, 19-24 May 2019*, JACoW  
9914 Publishing, Geneva, Switzerland, Jun. 2019.
- 9915 [808] G. Shu, Y. Chen, S. Lal, H. Qian, H. Shaker and F. Stephan, “FIRST DESIGN STUDIES OF A NC CW  
9916 **RF GUN FOR EUROPEAN XFEL**,” in *Proceedings, 10th International Particle Accelerator Conference*  
9917 *(IPAC’19), Melbourne, Australia, 19-24 May 2019*, JACoW Publishing, Geneva, Switzerland, Jun. 2019.
- 9918 [809] J. Teichert *et al.*, *Nuclear Instruments and Methods in Physics Research Section A: Accelerators,*  
9919 *Spectrometers, Detectors and Associated Equipment* 743 (2014) 114.
- 9920 [810] J. Bisognano *et al.*, “Wisconsin srf electron gun commisioning,” in *Proceedings, North American Particle*  
9921 *Accelerator Conf. (NAPAC’13), Pasadena, CA, USA, Sep.-Oct. 2013*, 09 2013.  
9922 <http://accelconf.web.cern.ch/AccelConf/PAC2013/papers/tupma19.pdf>.
- 9923 [811] E. Vogel *et al.*, “SRF Gun Development at DESY,” JACoW, Geneva, Sep 2018.
- 9924 [812] A. Neumann, and others, “Status of SRF Gun for bERLinPro,” in *Proceedings, ERL’19, Berlin,*  
9925 *Germany, Sept. 2019*, 2019.
- 9926 [813] Belomestnykh, S.A. and others, “Commissioning of the 112 MHz SRF Gun,” in *Proceedings, 17th Int.*  
9927 *Conf. RF Superconductivity, Whistler, Canada, Sep. 2015*, 2015.
- 9928 [814] Hernandez-Garcia, C. and others, “JLab FEL DC Gun,” in *Proceedings, 45th ICFA Advanced Beam*  
9929 *Dynamics Workshop on Energy Recovery LINAC Workshop (ERL’09), Ithaca, NY, USA, June 2009* ,  
9930 2009.
- 9931 [815] L. B. Jones, J. W. McKenzie, K. J. Middleman, B. L. Militsyn, Y. M. Saveliev and S. L. Smith, *Journal of*  
9932 *Physics: Conference Series* 298 (2011) 012007.
- 9933 [816] R. Kato, Y. Honda, H. Kawata, T. Miyajima, N. Nakamura, H. Sakai, M. Shimada, Y. Tanimoto, K.  
9934 Tsuchiya, “Ir-fel project at the cerl and future euv-fel lithography,” in *Presented at the 39th Int. Free*  
9935 *Electron Laser Conf. (FEL’19), Hamburg, Germany, Aug. 2019*, 2019.
- 9936 [817] Hoffstaetter, G.H. and others, “CBETA: The Cornell/BNL 4-turn ERL with FFAG Return Arcs for  
9937 **eRHIC Prototyping**,” in *Proceedings, 28th Linear Accelerator Conf. (LINAC’16)*, East Lansing, MI, USA,  
9938 2016.
- 9939 [818] B. Hounsell, W. Kaabi, M. Klein, B. Militsyn and C. Welsch, “Optimisation of the PERLE injector,” in  
9940 *Proceedings, ERL’19, Berlin, Germany, Sept. 2019*, 2019.
- 9941 [819] R. Suleiman, P. Adderley, J. Grames, J. Hansknecht, M. Poelker and M. Stutzman, *AIP Conference*  
9942 *Proceedings* 1970 (2018) 050007, <https://aip.scitation.org/doi/pdf/10.1063/1.504022>.
- 9943 [820] C. K. Sinclair *et al.*, “Performance of a very high voltage photoemission electron gun for a high brightness,  
9944 high average current ERL injector,” in *Proceedings, 22nd Particle Accelerator Conf. (PAC’07)*,  
9945 *Albuquerque, NM, USA, 2007*. <https://accelconf.web.cern.ch/AccelConf/p07/PAPERS/TUPMS021.PDF>.
- 9946 [821] N. Nishimori, R. Nagai, S. Matsuba, R. Hajima, M. Yamamoto, T. Miyajima, Y. Honda, H. Iijima,  
9947 M. Kuriki and M. Kuwahara, *Applied Physics Letters* 102 (2013) 234103.

- 9948 [822] N. Nishimori, R. Nagai, R. Hajima, M. Yamamoto, Y. Honda, T. Miyajima and T. Uchiyama, *Phys. Rev.*  
9949 *Accel. Beams* 22 (2019) 053402.
- 9950 [823] W. Liu, Y. Chen, W. Lu, A. Moy, M. Poelker, M. Stutzman and S. Zhang, *Applied Physics Letters* 109  
9951 (2016) 252104, <https://doi.org/10.1063/1.4972180>.
- 9952 [824] E. Wang, *AIP Conference Proceedings* 1970 (2018) 050008,  
9953 <https://aip.scitation.org/doi/pdf/10.1063/1.5040227>.
- 9954 [825] A. Zaltsman and R. Lambiase, *Proceedings of the 24-th Particle Accelerator Conference, PAC-2011,*  
9955 *TUP125* (2011) .
- 9956 [826] B. Parker, “Latest Developments and Progress on the IR magnet design.” presented at the LHeC and  
9957 FCC-eh Workshop, Sept 2017.
- 9958 [827] B. Parker, “Superconducting Magnet Concepts for Electron Hadron Collider IRs.” Presented at the  
9959 electrons for the lhc - lhec/fccee and perle workshop, Sept 2018.
- 9960 [828] E. Cruz-Alaniz, D. Newton, R. Tomás and M. Korostelev, *Phys. Rev. ST Accel. Beams* 18 (2015) 111001.
- 9961 [829] R. Martin and R. Tomás Garcia, “Length optimization of the detector region dipoles in LHeC and  
9962 FCC-eh,” CERN-ACC-2018-0042, CERN, Geneva, Oct 2018. <http://cds.cern.ch/record/2644892>.
- 9963 [830] S. Fartoukh, *Phys. Rev. ST Accel. Beams* 16 (2013) 111002.
- 9964 [831] “Lattice repository.” <https://gitlab.cern.ch/lhec-optics/lhec-lattice>, 2019.
- 9965 [832] A. Gaddi, “Installation Issues of eh Detectors (LHC and FCC),” Talk presented at the LHeC and FCC-eh  
9966 Workshop, CERN, Sept 2017.
- 9967 [833] A. Gaddi. Private communication, Jan 2019.
- 9968 [834] R. Bruce, C. Bracco, R. De Maria, M. Giovannozzi, S. Redaelli, R. Tomás Garcia, F. M. Velotti and  
9969 J. Wenninger, “Updated parameters for HL-LHC aperture calculations for proton beams,”  
9970 CERN-ACC-2017-0051, CERN, Geneva, Jul 2017. <https://cds.cern.ch/record/2274330>.
- 9971 [835] R. De Maria *et al.*, “HLLHCv1.3 Optics repository.”  
9972 <http://lhc-optics.web.cern.ch/lhc-optics/HLLHCv1.3/>.
- 9973 [836] E. Cruz-Alaniz, R. Martin and R. Tomás, “LHeC optics with  $\beta^* = 10$  cm and  $L^* = 15$  m,”  
9974 CERN-XXX-2019-XXX, CERN, Geneva, 2019.
- 9975 [837] Sixtrack web site: <http://sixtrack.web.cern.ch/SixTrack/>.
- 9976 [838] E. Cruz-Alaniz, J. L. Abelleira, L. van Riesen-Haupt, A. Seryi, R. Martin and R. Tomás, “Methods to  
9977 increase the dynamic aperture of the fcc-hh lattice,” in *Proceedings, International Particle Accelerator*  
9978 *Conference (IPAC’18), Vancouver, Canada, 2018*, JACoW, Geneva, Switzerland, May 2018.  
9979 <https://accelconf.web.cern.ch/AccelConf/ipac2018/papers/thpak145.pdf>.
- 9980 [839] F. Zimmermann *et al.*, “Interaction-Region Design Options for a Linac-Ring LHeC,” in *Proceedings,*  
9981 *International Particle Accelerator Conference (IPAC’10), Kyoto, Japan, May 23-28, 2010*, JACoW,  
9982 Geneva, Switzerland, May 2010.
- 9983 [840] J. L. Abelleira, H. Garcia, R. Tomás and F. Zimmermann, “Final-Focus Optics for the LHeC Electron  
9984 Beam Line,” in *Proceedings, International Particle Accelerator Conference (IPAC’12), New Orleans,*  
9985 *Louisiana, USA, May 20-25, 2012*, JACoW, Geneva, Switzerland, May 2012.
- 9986 [841] LHeC Study Group, FCC-eh Study Group, PERLE Collaboration, G. Arduini, O. Brüning and M. Klein,  
9987 *PoS DIS2018* (2018) 183.
- 9988 [842] R. Tomás, “LHeC interaction region,” Talk presented at DIS 2012 Workshop, Bonn, 2012.
- 9989 [843] J. A. Parrell, M. B. Field, Y. Zhang and S. Hong, *AIP Conf. Proc.* 711 (2004) 369–375.
- 9990 [844] S. Russenschuck, *Field computation for accelerator magnets: analytical and numerical methods for*  
9991 *electromagnetic design and optimization*. Wiley, Weinheim, 2010.
- 9992 [845] E. Fern, V. Di Murro, K. Soga, Z. Li, J. Osborne and L. Scibile, *Tunnelling and Underground Space*  
9993 *Technology* 77 (2018) 249.
- 9994 [846] C. Laughton, *Int. J. of Mining and Geological Engineering* 6 (1988) 353.
- 9995 [847] C. Tennant, “Energy Recovery Linacs,” in *Challenges and Goals for Accelerators in the XXI Century,*  
9996 O. Brüning and S. Myers (eds.), World Scientific, 2016.
- 9997 [848] C. Tennant, “Progress at the Jefferson Laboratory FEL,” in *Particle accelerator. Proceedings, 23rd*  
9998 *Conference, PAC’09, Vancouver, Canada, May 4-8, 2009*, 2010.  
9999 [http://www1.jlab.org/UL/publications/view\\_pub.cfm?pub\\_id=8641](http://www1.jlab.org/UL/publications/view_pub.cfm?pub_id=8641).

- 10000 [849] G. H. Hoffstaetter and I. V. Bazarov, *Phys. Rev. ST Accel. Beams* 7 (2004) 054401.
- 10001 [850] D. R. Douglas *et al.*, *Phys. Rev. ST Accel. Beams* 9 (2006) 064403.
- 10002 [851] S. Di Mitri, M. Cornacchia and S. Spampinati, *Phys. Rev. Lett.* 110 (2013) 014801.
- 10003 [852] M. G. Fedurin, D. Kayran, V. Yakimenko, A. V. Fedotov, V. Litvinenko and P. Muggli, *Conf. Proc.* C110328 (2011) 1677.
- 10004
- 10005 [853] S. Heifets, G. Stupakov and S. Krinsky, *Phys. Rev. ST Accel. Beams* 5 (2002) 064401.
- 10006 [854] Z. Huang and K.-J. Kim, *Phys. Rev. ST Accel. Beams* 5 (2002) 074401.
- 10007 [855] S. Di Mitri and M. Cornacchia, *EPL (Europhysics Letters)* 109 (2015) 62002.
- 10008 [856] C.-Y. Tsai, D. Douglas, R. Li and C. Tennant, *Phys. Rev. Accel. Beams* 19 (2016) 114401.
- 10009 [857] C.-Y. Tsai, S. Di Mitri, D. Douglas, R. Li and C. Tennant, *Phys. Rev. Accel. Beams* 20 (2017) 024401.
- 10010 [858] D. Douglas *et al.* Jefferson Laboratory Technical Note 12-017, 2012.
- 10011 [859] R. Alarcon *et al.*, *Phys. Rev. Lett.* 111 (2013) 164801.
- 10012 [860] T. Powers and C. Tennant, “Implications of incomplete energy recovery in srf-based energy recovery linacs,” in *Proceedings of the 2007 ICFA Workshop on Energy Recovery Linacs, Daresbury, UK*, 2007.
- 10013
- 10014 [861] T. Powers, “Control of Microphonics for Narrow Control Bandwidth Cavities,” Talk presented at the 2017 International Conference on RF Superconductivity, Lanzhou, China, 2017.
- 10015
- 10016 [862] S. Benson *et al.*, *Conf. Proc. C070625* (2007) 79.
- 10017 [863] T. Powers, “Optimization of SRF Linacs,” in *Proceedings of the 2013 International Conference on RF Superconductivity, Paris, France*, 2013.
- 10018
- 10019 [864] S. Benson *et al.*, “Development of a Bunched-Beam Electron Cooler for the Jefferson Lab Electron-Ion Collider,” in *Proceedings, 9th International Particle Accelerator Conference (IPAC 2018), Vancouver, BC Canada*, 2018.
- 10020
- 10021
- 10022 [865] C. Tennant. <https://userweb.jlab.org/~tennant/>.
- 10023 [866] C. Tennant, “Analysis of the Baseline PERLE Lattice,” Jefferson Laboratory Technical Note 18-031, 2018.
- 10024 [867] D. Douglas *et al.*, ““Why PERLE?” Historical Context and Technological Motivation,” Jefferson Laboratory Technical Note 18-014, 2018.
- 10025
- 10026 [868] G. H. Hoffstaetter *et al.*, “CBETA Design Report, Cornell-BNL ERL Test Accelerator,” 2017.
- 10027 [arXiv:1706.04245](https://arxiv.org/abs/1706.04245).
- 10028 [869] T. Satogata *et al.*, “ER@CEBAF: A test of 5-pass energy recovery at CEBAF,” Program Advisory Committee Proposal, Jun 2016.
- 10029
- 10030 [870] A. Donnachie and P. Landshoff, *Phys. Lett.* B296 (1992) 227, [arXiv:hep-ph/9209205](https://arxiv.org/abs/hep-ph/9209205).
- 10031 [871] M. Frank, F. Gaede, M. Petric and A. Sailer, “Aidasoft/dd4hep,” Oct. 2018.
- 10032 [872] GEANT4 Collaboration, S. Agostinelli *et al.*, *Nucl. Instrum. Meth.* A506 (2003) 250.
- 10033 [873] CMS Collaboration, G. Bianchi, *JINST* 9 (2014) C03054.
- 10034 [874] I. Peric, *Nucl. Instrum. Meth.* A582 (2007) 876.
- 10035 [875] A. Blondel *et al.*, “Research Proposal for an Experiment to Search for the Decay  $\mu \rightarrow eee$ ,” Jan 2013.
- 10036 [arXiv:1301.6113](https://arxiv.org/abs/1301.6113).
- 10037 [876] A. Schöning *et al.*, “MuPix and ATLASPix - Architectures and Results,” in *28th International Workshop on Vertex Detectors*, Feb 2020. [arXiv:2002.07253](https://arxiv.org/abs/2002.07253).
- 10038
- 10039 [877] M. Prathapan *et al.*, *PoS TWEPP2019* (2020) 010.
- 10040 [878] M. Dyndal *et al.*, *JINST* 15 (2020) P02005, [arXiv:1909.11987](https://arxiv.org/abs/1909.11987).
- 10041 [879] M. Oreglia, *A Study of the Reactions  $\psi' \rightarrow \gamma\gamma\psi$* . PhD thesis.
- 10042 <https://search.proquest.com/docview/303269954>.
- 10043 [880] J. E. Gaiser, *Charmonium Spectroscopy From Radiative Decays of the  $J/\psi$  and  $\psi'$* . PhD thesis.
- 10044 <https://search.proquest.com/docview/303269954>.
- 10045 [881] T. Skwarnicki, *A study of the radiative CASCADE transitions between the Upsilon-Prime and Upsilon resonances*. PhD thesis, Cracow, INP, 1986.
- 10046
- 10047 <http://www-library.desy.de/cgi-bin/showprep.pl?DESY-F31-86-02>.
- 10048 [882] ATLAS Collaborartion Collaboration, “Technical Design Report for the Phase-II Upgrade of the ATLAS Muon Spectrometer,” 2017.
- 10049
- 10050 [883] CMS Collaboration, “The Phase-2 Upgrade of the CMS Muon Detectors,” 2017.
- 10051 [884] FP420 R&D Collaboration, M. G. Albrow *et al.*, *JINST* 4 (2009) T10001, [arXiv:0806.0302](https://arxiv.org/abs/0806.0302).
- 10052 [885] LHCf Collaboration, O. Adriani *et al.*, *Phys. Lett.* B780 (2018) 233, [arXiv:1703.07678](https://arxiv.org/abs/1703.07678).